

Photo-Ionisation and Density Functional Theory Studies of Gold Doped Cerium Oxide Clusters

Robert Hardy

B.Sc. (Hons)

A thesis submitted in total fulfillment of the requirements for the degree
of Doctor of Philosophy



THE UNIVERSITY
of ADELAIDE

July, 2018

Department of Chemistry
School of Physical Sciences
The University of Adelaide

Statement of Originality

I certify this work contains no material which has been accepted for the award of any other degree or diploma in any university or other tertiary institution and, to the best of my knowledge and belief, contains no material previously published or written by another person, except where due reference has been made in the text. In addition, I certify that no part of this work will, in the future, be used in a submission for any other degree or diploma in any university or other tertiary institution without the prior approval of The University of Adelaide and, where applicable, any partner institution responsible for the joint-award of this degree.

I give consent to this copy of my thesis when deposited in the University Library, being made available for loan and photocopying, subject to the provisions of the Copyright Act 1968. The author acknowledges that copyright of published works contained within this thesis resides with the copyright holder(s) of those works.

I give permission for the digital version of my thesis to be made available on the web, via the University's digital research repository, the Library catalogue, and also through web search engines, unless permission has been granted by the University to restrict access for a period of time.

Robert Hardy

July, 2018

Abstract

This thesis presents experimental and theoretical work on small cerium oxide (Ce_mO_n , $m=2,3$; $n=0-2m$) and gold-doped cerium oxide (AuCe_mO_n , $m=2,3$; $n=0-2m$) clusters. These cluster systems are considered as simple models for larger gold-ceria systems which have shown potential for use as catalysts in low-temperature CO oxidation processes. Experimental work is also presented for the Ce_4O_n ($n=0-5$) clusters without any supporting computational data.

Ce_mO_n and AuCe_mO_n clusters are prepared in the gas phase via dual laser ablation and detected experimentally using Time-of-Flight Mass Spectrometry (TOFMS) coupled with threshold laser ionisation. Photo-Ionisation Efficiency (PIE) spectroscopy is performed on the cluster ions detected in the mass spectra following photo-ionisation (which include the Ce_2 , Ce_2O , Ce_2O_2 , Ce_3 , Ce_3O , Ce_3O_2 , Ce_3O_3 , Ce_3O_4 , Ce_4 , Ce_4O , Ce_4O_2 , Ce_4O_3 , Ce_4O_4 , Ce_4O_5 , AuCe_2 , AuCe_2O , AuCe_2O_2 , AuCe_3 , AuCe_3O , AuCe_3O_2 and AuCe_3O_3 species) over the 3.92 – 5.17 eV (240 – 315.75 nm) energy range to record the depletion of each cluster ion with decreased photon energy. Experimental PIE spectra are presented for these species. The highly oxidised Ce_2O_3 , Ce_2O_4 , Ce_3O_5 , Ce_3O_6 , AuCe_2O_3 , AuCe_2O_4 , AuCe_3O_4 , AuCe_3O_5 and AuCe_3O_6 cluster ions – which approach the stoichiometric $n=2m$ ratio of bulk ceria - are either not detected or are detected in trace quantities in all photo-ionisation mass spectra recorded during this work.

DFT calculations are used to identify the lowest energy structures for each cluster species and their corresponding cationic states. Potential ionisation transitions for each cluster are investigated using Zero Electron Kinetic Energy simulations which are subsequently combined and integrated to produce a calculated PIE spectrum. The calculated and experimental PIE spectra are then compared to (i) ascertain the adiabatic ionisation energy (IE) for each cluster species and (ii) verify that the geometric and electronic properties of the relevant cluster species can be inferred from their DFT-calculated structures. Excellent agreement is found between the experimental and calculated PIE spectra for all Ce_mO_n and AuCe_mO_n ($m=2,3$; $n=0-2m$) cluster species detected in this work. Moreover, DFT calculations predict high ionisation energies for all cluster species not detected in the photo-ionisation mass spectra.

The interactions between cerium oxide and adsorbed gold atoms – and their subsequent effects on catalytic CO oxidation – are explored via calculations which involve comparison of the undoped and gold-doped geometric structures, Hirshfeld charges, HOMO/LUMO energies and bonding energies (involving O, Au and CeO₂ fragments). The preferential site of Au deposition on the Ce_mO_n cluster is found to vary with oxidation; the Au atom adsorbs to an oxygen vacancy site on highly reduced Ce_mO_n clusters [AuCe₂O_n (*n*=0-3); AuCe₃O_n (*n*=0-4) and CeO₃ and CeO₂ vacancy sites on moderately reduced and stoichiometric clusters, respectively (i.e. AuCe₂O₄, AuCe₃O₅, AuCe₃O₆). Both Au→Ce and Ce→Au charge transfer mechanisms are calculated; the former occurs when Au adsorbs to an oxygen vacancy site while the latter occurs when Au adsorbs to a CeO₂/CeO₃ vacancy site. The adsorbed Au atom is proposed to enhance the catalytic properties of the AuCe_mO_n cluster by (i) stabilising the negatively charged Au atom on reduced AuCe_mO_n clusters to enhance nucleophilicity; (ii) increasing the electron accepting capability of the AuCe_mO_{2m} species; (iii) destabilising the electronic structure of the AuCe_mO_{2m} cluster to potentially reduce the energy cost associated with a catalytic redox cycle; and (iv) facilitating the release of additional oxygen atoms to adsorbed gas phase reactants while having minimal negative effect on subsequent oxygen vacancy healing processes.

Acknowledgements

By far the greatest acknowledgement should go to my principal supervisor, Professor Greg Metha. I can't speak highly enough of Greg's inexhaustible enthusiasm for science which, while not always appreciated at the time, certainly kept me going through some of the more difficult periods. Thanks for giving me the space to make my own mistakes, for not getting too upset when those mistakes involved expensive laser equipment, and for your valuable input and guidance.

Associate Professor Tak Kee as my second supervisor. Thanks for your support over the years which usually came in the form of either beer or last-minute signatures on my Annual Reviews.

Dr Alex Gentleman for, as the name suggests, being both a gentleman and a scholar. Thanks for your invaluable guidance for all things experimental, your moral support and your mutual appreciation of Simpsons references.

Peter Apoefis for fixing the relentless supply of broken pumps and vacuum equipment over the years, and for always doing it with a smile.

Matthew Bull for support with LabVIEW programming, for dealing with all our weird and wonderful electrical problems and mostly just preventing me from electrocuting myself.

Dr Matt Addicoat for the computational scripts and oracle-like advice whenever the calculations didn't work.

eResearchSA and the National Computational Infrastructure for the provision of computational resources. Special thanks to Rika Kobayashi for support during some of the earlier computational work.

Aidan Karayilan for experimental support. Thanks for the 213 nm mass spectra; for running the never-ending supply of “just a few more” calculations; for tolerating my sleep-deprived, expletive-laden rants and for helping me keep a sense of humour throughout the thesis writing stage.

Trevor from Property Services for always flipping our circuit breakers back on without asking questions.

Dr Jason Gascooke for support with laser alignment and the much-appreciated loan of laser dyes.

Alex Button, Simon Blackett, Georgina Sylvia and Stella Child for support during research placements. Thanks for your infectious enthusiasm for science which showed even while doing soul-destroying data analysis and programming tasks.

Past and present members of the Laser Lab for making me socialise occasionally.

My family for their love and support during my PhD. Thanks for not questioning my life choices too much, even when you probably should have.

Table of Contents

Chapter 1. Introduction	1
1.1. Clusters as Catalysts	1
1.2. Clusters Deposited on Surface Defect Sites as Catalysts	3
1.3. Carbon Monoxide Oxidation with Gold-Ceria Catalysts	5
1.4. Motivation for this Work	8
1.5. Clusters as Surface Analogues	11
1.6. Previous Work: Gas Phase Bimetal Oxide Clusters	12
1.7. Scope of this Work	15
1.8. References	18
Chapter 2. Experimental Apparatus, Theory and Methodology	28
2.1. Generation of Gas Phase Metal Clusters	29
2.1.1. A Brief History of Cluster Production Methods	29
2.1.2. Generation of Bi-Metallic Clusters in the Gas Phase	31
2.1.3. Experimental Details for Cluster Production	32
2.2. Time of Flight Mass Spectrometry	38
2.2.1. Theoretical Background	38
2.2.2. Single and Dual Stage Ion Extraction Methods; Wiley McLaren TOFMS	40
2.2.2.1. Spatial Distributions in TOFMS	41
2.2.2.2. Velocity Distributions in TOFMS	42
2.2.3. Details for Wiley McLaren TOFMS	43
2.3. Detection and Elucidation of Cluster Properties	45
2.3.1. Current Spectroscopic Methods Utilised for Metal Clusters	45
2.3.2. Spectroscopic Theory - The Born-Oppenheimer Approximation	46
2.3.3. The Franck-Condon Principle	48
2.3.4. Electronic Spectroscopy	51
2.3.5. Photo-Ionisation Spectroscopy	53
2.3.6. The Photo-Ionisation Efficiency Spectrum	56
2.3.7. Zero Electron Kinetic Energy Spectroscopy	60
2.3.8. Details for the PIE Experiment	61

2.4.	References	67
 <i>Chapter 3. Computational Theory and Methodology</i>		76
3.1.	Theoretical Background	77
3.1.1.	The Schrödinger Equation	77
3.1.2.	The Born Oppenheimer Approximation (Revisited)	78
3.1.3.	The Variational Principle	79
3.1.4.	The Hartree-Fock Method	80
3.1.5.	Density Functional Theory	81
3.1.6.	Exchange and Correlation Functionals	83
3.1.6.1.	Local Density Approximation Functionals	83
3.1.6.2.	Generalised Gradient Approximation Functionals	83
3.1.6.3.	Hybrid Functionals	84
3.1.7.	Computational Search Methods	84
3.1.8.	Basis Sets	86
3.1.8.1.	Theoretical Background	86
3.1.8.2.	Pople Basis Sets	88
3.1.8.3.	Split Valence Basis Sets	88
3.1.8.4.	Basis Set Selection and Justification	89
3.1.9.	Effective Core Potentials	89
3.1.9.1.	Theoretical Background	89
3.1.9.2.	Effective Core Potential Selection and Justification	90
3.2.	DFT Optimisation Procedure	92
3.3.	Comparison of Calculated and Experimental Properties	94
3.3.1.	Ionisation Energy Calculations	94
3.3.2.	Zero Electron Kinetic Energy and Photo-Ionisation Efficiency Simulations	95
3.4.	References	105
 <i>Chapter 4. Benchmarking Calculations</i>		109
4.1.	Effective Core Potentials for Lanthanides	110
4.2.	Requirement for a Benchmark Study of Cerium ECPs	111
4.3.	Effective Core Potentials Selected for Benchmarking Study	112

4.4.	Benchmark Calculations of Ce ₂ , CeO and AuCe Dimers	113
4.5.	ECP Benchmarking of Ce ₂ O _n (n=0-4) Clusters	116
4.5.1.	Ce ₂ O _n Ionisation Energies	116
4.5.2.	Ce ₂ O _n Cluster Geometries	118
4.6.	Computational Expense of Effective Core Treatments for Cerium	122
4.7.	Selection of Effective Core Potential Treatment	124
4.8.	References	125

Chapter 5. Photo-Ionisation Efficiency Spectroscopy, Density Functional Theory Calculations and Zero Electron Kinetic Energy Simulations of Ce₂O_n Clusters **127**

5.1.	Mass Spectrum Analysis	128
5.2.	Appearance of Cluster Ion Signal for the Ce ₂ O _n (n=0-2) Series	130
5.3.	PIE Spectrum and DFT Results for Ce ₂	133
5.3.1.	Ce ₂ Experimental PIE Spectrum	133
5.3.2.	DFT Calculations for Ce ₂	134
5.3.3.	ZEKE Spectral Simulations for Ce ₂	137
5.3.4.	Comparison of Simulated and Experimental PIE Spectra for Ce ₂	141
5.4.	PIE Spectrum and DFT Results for Ce ₂ O	143
5.4.1.	Ce ₂ O Experimental PIE Spectrum	143
5.4.2.	DFT Calculations for Ce ₂ O	144
5.4.3.	ZEKE Spectral Simulations for Ce ₂ O	147
5.4.4.	Comparison of Experimental and Simulated PIE Spectra for Ce ₂ O	152
5.5.	PIE Spectrum and DFT Results for Ce ₂ O ₂	155
5.5.1.	Ce ₂ O ₂ Experimental PIE Spectrum	155
5.5.2.	DFT Calculations for Ce ₂ O ₂	156
5.5.3.	ZEKE Spectral Simulations for Ce ₂ O ₂	158
5.5.4.	Comparison of Experimental and Simulated PIE Spectra for Ce ₂ O ₂	160
5.6.	PIE Spectrum and DFT Results for Ce ₂ O ₃	161
5.6.1.	Ce ₂ O ₃ Experimental PIE Spectrum	161
5.6.2.	DFT Calculations for Ce ₂ O ₃	161
5.6.3.	ZEKE Spectral Simulations for Ce ₂ O ₃	165
5.6.4.	Simulated PIE Spectrum for Ce ₂ O ₃	167

5.7.	PIE Spectrum and DFT Results for Ce ₂ O ₄	168
5.7.1.	Ce ₂ O ₄ Experimental PIE Spectrum	168
5.7.2.	DFT Calculated Structures for Ce ₂ O ₄	168
5.7.3.	ZEKE Spectral Simulations for Ce ₂ O ₄	171
5.7.4.	Simulated PIE Spectrum for Ce ₂ O ₄	173
5.8.	Comparison of Experimental and Calculated Ce ₂ O _n Ionisation Energies	174
5.9.	References	177
 <i>Chapter 6. Photo-Ionisation Efficiency Spectroscopy, Density Functional Theory Calculations and Zero Electron Kinetic Energy Simulations of Ce₃O_n Clusters</i>		179
6.1.	Ce _m O _n Mass Spectrum Analysis	180
6.2.	Appearance of Cluster Ion Signal for the Ce ₃ O _n (n=0-4) Series	181
6.3.	PIE Spectrum and DFT Results for Ce ₃	183
6.3.1.	Ce ₃ Experimental PIE Spectrum	183
6.3.2.	DFT Calculations for Ce ₃	184
6.3.3.	ZEKE Spectral Simulations for Ce ₃	187
6.3.4.	Comparison of Simulated and Experimental PIE Spectra for Ce ₃	190
6.4.	PIE Spectrum and DFT Results for Ce ₃ O	192
6.4.1.	Ce ₃ O Experimental PIE Spectrum	192
6.4.2.	DFT Calculations for Ce ₃ O	193
6.4.3.	ZEKE Spectral Simulations for Ce ₃ O	196
6.4.4.	Comparison of Simulated and Experimental PIE Spectra for Ce ₃ O	198
6.5.	PIE Spectrum and DFT Results for Ce ₃ O ₂	199
6.5.1.	Ce ₃ O ₂ Experimental PIE Spectrum	199
6.5.2.	DFT Calculations for Ce ₃ O ₂	200
6.5.3.	ZEKE Spectral Simulations for Ce ₃ O ₂	202
6.5.4.	Comparison of Simulated and Experimental PIE Spectra for Ce ₃ O ₂	206
6.6.	PIE Spectrum and DFT Results for Ce ₃ O ₃	207
6.6.1.	Ce ₃ O ₃ Experimental PIE Spectrum	207
6.6.2.	DFT Calculations for Ce ₃ O ₃	208
6.6.3.	ZEKE Spectral Simulations for Ce ₃ O ₃	210
6.6.4.	Comparison of Simulated and Experimental PIE Spectra for Ce ₃ O ₃	214

6.7.	PIE Spectrum and DFT Results for Ce_3O_4	216
6.7.1.	Ce_3O_4 Experimental PIE Spectrum	216
6.7.2.	DFT Calculations for Ce_3O_4	217
6.7.3.	ZEKE Spectral Simulations for Ce_3O_4	222
6.7.4.	Comparison of Simulated and Experimental PIE Spectra for Ce_3O_4	225
6.8.	PIE Spectrum and DFT Results for Ce_3O_5	228
6.8.1.	Ce_3O_5 Experimental PIE Spectrum	228
6.8.2.	DFT Calculations for Ce_3O_5	228
6.8.3.	ZEKE Spectral Simulations for Ce_3O_5	232
6.8.4.	Simulated PIE Spectrum for Ce_3O_5	234
6.9.	PIE Spectrum and DFT Results for Ce_3O_6	236
6.9.1.	Ce_3O_6 Experimental PIE Spectrum	236
6.9.2.	DFT Calculations for Ce_3O_6	236
6.9.3.	ZEKE Spectral Simulations for Ce_3O_6	238
6.9.4.	Simulated PIE Spectrum for Ce_3O_6	239
6.10.	Comparison of Experimental and Calculated Ce_3O_n Ionisation Energies	240
6.11.	References	243
<i>Chapter 7. Photo-Ionisation Efficiency Spectroscopy of Ce_4O_n Clusters</i>		244
7.1.	Ce_4O_n Mass Spectrum and Ion Signal Appearance	235
7.2.	Photo-Ionisation Efficiency Spectra for Ce_4O_n ($n=0-5$) Clusters	249
7.2.1.	Ce_4 PIE Spectrum	249
7.2.2.	Ce_4O PIE Spectrum	251
7.2.3.	Ce_4O_2 PIE Spectrum	253
7.2.4.	Ce_4O_3 PIE Spectrum	255
7.2.5.	Ce_4O_4 PIE Spectrum	257
7.2.6.	Ce_4O_5 PIE Spectrum	259
7.3.	Appearance Energy Trends for Ce_4O_n Clusters	260
7.4.	References	263

Chapter 8. Photo-ionisation Efficiency Spectroscopy, Density Functional Theory Calculations and Zero Electron Kinetic Energy Simulations of AuCe₂O_n Clusters	264
8.1. AuCe _m O _n Mass Spectrum Analysis	265
8.2. Appearance of Cluster Ion Signal for the AuCe ₂ O _n (n=0-2) Series	266
8.3. PIE Spectrum and DFT Results for AuCe ₂	268
8.3.1. AuCe ₂ Experimental PIE Spectrum	268
8.3.2. DFT Calculations for AuCe ₂	269
8.3.3. ZEKE Spectral Simulations for AuCe ₂	272
8.3.4. Comparison of Simulated and Experimental PIE Spectra for AuCe ₂	276
8.4. PIE Spectrum and DFT Results for AuCe ₂ O	277
8.4.1. AuCe ₂ O Experimental PIE Spectrum	277
8.4.2. DFT Calculations for AuCe ₂ O	278
8.4.3. ZEKE Spectral Simulations for AuCe ₂ O	280
8.4.4. Comparison of Simulated and Experimental PIE Spectra for AuCe ₂ O	283
8.5. PIE Spectrum and DFT Results for AuCe ₂ O ₂	284
8.5.1. AuCe ₂ O ₂ Experimental PIE Spectrum	284
8.5.2. DFT Calculations for AuCe ₂ O ₂	286
8.5.3. ZEKE Spectral Simulations for AuCe ₂ O ₂	290
8.5.4. Comparison of Simulated and Experimental PIE Spectra for AuCe ₂ O ₂	294
8.6. PIE Spectrum and DFT Results for AuCe ₂ O ₃	296
8.6.1. AuCe ₂ O ₃ Experimental PIE Spectrum	296
8.6.2. DFT Calculations for AuCe ₂ O ₃	296
8.6.3. ZEKE Spectral Simulations for AuCe ₂ O ₃	298
8.6.4. Simulated PIE Spectrum for AuCe ₂ O ₃	300
8.7. PIE Spectrum and DFT Results for AuCe ₂ O ₄	301
8.7.1. AuCe ₂ O ₄ Experimental PIE Spectrum	301
8.7.2. DFT Calculations for AuCe ₂ O ₄	301
8.7.3. ZEKE Spectral Simulations for AuCe ₂ O ₄	304
8.7.4. Simulated PIE Spectrum for AuCe ₂ O ₄	305
8.8. Comparison of Experimental and Calculated AuCe ₂ O _n Ionisation Energies	306
8.9. Comparison of Experimental Appearance Energies for Ce ₂ O _n and AuCe ₂ O _n Clusters	308
8.10. References	311

Chapter 9. Photo-Ionisation Efficiency Spectroscopy, Density Functional Theory Calculations and Zero Electron Kinetic Energy Simulations of AuCe₃O_n Clusters	313
9.1. AuCe ₃ O _n Mass Spectrum	314
9.2. Appearance of Cluster Ion Signal for the AuCe ₃ O _n (n=0-3) Series	317
9.3. PIE Spectrum and DFT Results for AuCe ₃	320
9.3.1. AuCe ₃ Experimental PIE Spectrum	320
9.3.2. DFT Calculations for AuCe ₃	321
9.3.3. ZEKE Spectral Simulations for AuCe ₃	323
9.3.4. Comparison of Simulated and Experimental PIE Spectra for AuCe ₃	327
9.4. PIE Spectrum and DFT Results for AuCe ₃ O	328
9.4.1. AuCe ₃ O Experimental PIE Spectrum	328
9.4.2. DFT Calculations for AuCe ₃ O	329
9.4.3. ZEKE Spectral Simulations for AuCe ₃ O	333
9.4.4. Comparison of Simulated and Experimental PIE Spectra for AuCe ₃ O	335
9.5. PIE Spectrum and DFT Results for AuCe ₃ O ₂	338
9.5.1. AuCe ₃ O ₂ Experimental PIE Spectrum	338
9.5.2. DFT Calculations for AuCe ₃ O ₂	339
9.5.3. ZEKE Spectral Simulations for AuCe ₃ O ₂	342
9.5.4. Comparison of Simulated and Experimental PIE Spectra for AuCe ₃ O ₂	346
9.6. PIE Spectrum and DFT Results for AuCe ₃ O ₃	349
9.6.1. AuCe ₃ O ₃ Experimental PIE Spectrum	349
9.6.2. DFT Calculations for AuCe ₃ O ₃	351
9.6.3. ZEKE Spectral Simulations for AuCe ₃ O ₃	356
9.6.4. Comparison of Simulated and Experimental PIE Spectra for AuCe ₃ O ₃	359
9.7. PIE Spectrum and DFT Results for AuCe ₃ O ₄	361
9.7.1. AuCe ₃ O ₄ Experimental PIE Spectrum	361
9.7.2. DFT Calculations for AuCe ₃ O ₄	361
9.7.3. ZEKE Spectral Simulations for AuCe ₃ O ₄	365
9.7.4. Simulated PIE Spectrum for AuCe ₃ O ₄	367
9.8. PIE Spectrum and DFT Results for AuCe ₃ O ₅	368
9.8.1. AuCe ₃ O ₅ Experimental PIE Spectrum	368
9.8.2. DFT Calculations for AuCe ₃ O ₅	368

9.8.3.	ZEKE Spectral Simulations for AuCe ₃ O ₅	372
9.8.4.	Simulated PIE Spectrum for AuCe ₃ O ₅	375
9.9.	PIE Spectrum and DFT Results for AuCe ₃ O ₆	376
9.9.1.	AuCe ₃ O ₆ Experimental PIE Spectrum	376
9.9.2.	DFT Calculations for AuCe ₃ O ₆	377
9.9.3.	ZEKE Spectral Simulations for AuCe ₃ O ₆	380
9.9.4.	Simulated PIE Spectrum for AuCe ₃ O ₆	382
9.10.	Comparison of Experimental and Calculated AuCe ₃ O _n Ionisation Energies	383
9.11.	Comparison of Experimental Appearance Energies for Ce ₃ O _n and AuCe ₃ O _n Clusters	385
9.12.	References	387
 <i>Chapter 10. Effects of Gold Adsorption on the Catalytic Properties of AuCe_mO_n (m=2,3; n=0-2m) Clusters</i>		388
10.1.	Au Deposition Site: Ce Vacancy or O vacancy?	389
10.2.	Hirshfeld Charge Analysis	396
10.2.1.	Au Atomic Charge	396
10.2.2.	Au-Ce _m O _n Charge Transfer Interactions	397
10.3.	Effects of Au on AuCe _m O _n Catalytic Properties	399
10.3.1.	HOMO and LUMO Energies	399
10.3.2.	Bonding Energies of Au, O and CeO ₂ Fragments	408
10.4.	Ce _m O _n and AuCe _m O _n Photon Absorption Pathways	412
10.5.	References	416
 <i>Chapter 11. Conclusions and Future Directions</i>		418
 <i>Appendix A. Mass Spectra of Ce_mO_n Clusters</i>		422
<i>Appendix B. Calculated Vibrational Frequencies for Ce_mO_n and AuCe_mO_n (m=2,3; n=0-2m) Clusters</i>		424
<i>Appendix C. Calculated Low-Intensity Ce_mO_n and AuCe_mO_n (m=2,3; n=0-2m) ZEKE Spectra</i>		453
<i>Appendix D. ZEKE Simulation Parameters and Test Calculations</i>		462

1.1. Clusters as Catalysts

Small transition metal clusters, both in the gas phase and deposited on metal oxide supports, have received significant attention over the past 40 years for their unique ability to catalyse industrially and environmentally relevant gas phase processes at lower temperatures than their bulk counterparts. Some of the more pertinent of these reactions include, but are not limited to, fuel production via water-gas shift¹⁻⁵, steam reforming^{1,6,7} and Fischer-Tropsch⁸⁻¹² processes; CO oxidation/NO_x reduction reactions for atmospheric pollution reduction¹³⁻¹⁷; and selective reactions such as partial oxidation¹⁸ and hydrogenation¹⁹ processes. Recent developments have even shown that clusters can be utilized to potentially facilitate enantioselective processes with high stereoselectivity^{20,21}.

A cluster is defined as an ensemble of [metal] atoms bound together to form a discrete unit. The size regime of clusters is not strictly defined, but typically encompasses anything between 3 and approximately 100 atoms. Clusters are unique when compared to their bulk phase counterparts in that their electronic and reactive properties do not scale with size. While these non-size scalable properties have been reported extensively²²⁻³³, one of the more pertinent examples comes from Berces et al.³⁴ who in 1998 investigated the rate coefficients for the reactions of niobium clusters with D₂, N₂ and O₂. They reported a marked fluctuation in the reactivities of the niobium clusters with the sequential addition of a single niobium atom. The most profound difference was recorded for the Nb₁₁ cluster, which showed a ten thousand-fold increase in reactivity with D₂ relative to the Nb₁₀ cluster. Moreover, the increased reactivity of Nb₁₁ compared to Nb₁₀ was primarily restricted to the D₂ molecule; reactivity with N₂ showed only a hundred-fold increase in the rate constant, while no significant change in reactivity with O₂ was observed. This highly specific dependence of the cluster composition on its reactive properties facilitates the potential development of catalysts with unprecedented reactivity, selectivity and specificity.

The catalytic activity displayed by metal clusters has been largely attributed to two key features. The first is the electronic structure, which is highly sensitive to both the number and type of atoms in the cluster motif. Some examples of this include work by Schulze et al.³⁵ and

Smalley et al.³⁶ who reported oscillatory trends in the ionisation energies and electron affinities respectively for gold clusters containing 12 or fewer atoms. The odd-numbered clusters, owing to their open valence shells, all displayed lower ionisation energies and higher electron affinities than the even-numbered clusters. Both groups accordingly claimed the open electronic shells of the odd-numbered clusters were responsible for reduced electronic stabilities and higher reactivities. Studies by Kaya et al.²⁸ on vanadium-doped cobalt clusters revealed an inertness in the Co₁₂V cluster toward H₂ adsorption which was not shared by either the Co₁₃ or Co₁₁V₂ clusters. The authors assumed all three clusters adopted the same structure which comprised a central atom surrounded by the remaining 12 atoms in either a face-centred cubic or hexagonal close-packed type arrangement. For the Co₁₂V cluster they proposed the V atom occupied the central position in the structure and withdrew electron density from the surrounding Co atoms to cause deactivation of the exterior sites on the cluster surface. This effect was negated by the substitution of a second V atom, which took an exterior position on the cluster surface to provide an electron-rich site for H₂ adsorption.

The second – and far more complex – feature of clusters which facilitates their unique reactivities is a phenomenon known as *dynamic structural fluxionality*. In this process, clusters can transition fluidly between low-lying geometric isomers. Transition state barriers for chemical reactions are lowered through these deformations in the cluster geometry which can facilitate low-temperature reactions. While the concept of dynamic structural fluxionality within metal clusters is well documented^{37–51}, detailed investigations into the isomerisation pathways between low-lying cluster geometries and how these pathways facilitate catalysis of adsorbed reactants are still in their infancy - with only a few computational studies reported^{52–61}. The effects of dynamic structural fluxionality within metal clusters are beyond the scope of this work; however, the phenomenon deserves a mention since it is a highly pertinent attribute unique to clusters that is not displayed by materials in the bulk phase.

1.2. Clusters Deposited on Surface Defect Sites as Catalysts

While metal clusters have drawn considerable interest as catalysts in their own right, recent attention has turned towards the development of catalysts utilising metal clusters deposited on metal oxide supports. Pioneering work by Sinfelt⁶² in 1973 showed ruthenium-copper and osmium-copper clusters deposited on a silica surface were able to catalyse both ethane hydrogenolysis to methane, and cyclohexane dehydrogenation to benzene. This discovery unleashed a flurry of research into surface-supported clusters, with an exhaustive number of transition metal cluster-metal oxide catalysts since reported^{10,16,63–75}. One of the more noteworthy examples comes from Heiz et al.⁵² who in 2005 reported CO oxidation at 140 K using Au₈ clusters deposited on MgO thin films. This represents an extraordinary improvement on the bulk phase catalyst systems conventionally used for CO oxidation which, utilising particles made up of precious metals such as platinum, palladium and rhodium deposited on mixed oxide surfaces of ceria, alumina and zirconia, typically perform CO oxidation at temperatures around 700 K⁷⁶.

Two salient features of surface-supported clusters have been instrumental in driving the shift towards their favourable employment as catalysts over gas phase clusters. The first is that a solid-state catalyst is much more commercially viable than a gas phase catalyst. The second, and quite unexpected feature of heterogeneous cluster-support catalysts was reported in the previously mentioned work by Heiz et al.⁵², where a unique interaction between the metal oxide surface and the adsorbed cluster was found to strongly influence subsequent catalytic processes. In this work, the authors recorded the IR absorption bands of ¹³CO molecules adsorbed to Au₈-MgO cluster-surface systems where the MgO surface was prepared as either defect-free or with surface F-centre defects (also known as oxygen vacancies) prior to Au₈ deposition. They noticed a red-shift in the stretching frequencies of the ¹³CO molecules adsorbed to Au₈ clusters on the defect-rich MgO surface compared to the defect-free surface, which were reported as 2049 cm⁻¹ and 2102 cm⁻¹, respectively. The authors further showed via Local Density of States calculations a transfer of electron density from the F-centre to the deposited Au₈ cluster. This unprecedented finding, which shows the interaction between the support and the cluster – particularly at defect sites – plays a crucial role in catalytic processes,

revolutionised the field of cluster-support catalysis where the cluster and support were traditionally considered to be non-interacting.

Further to the discovery by Heiz et al. that clusters display enhanced reactivity at defect sites, subsequent work by Freund et al.^{77,78} revealed metal atoms and clusters in fact deposit preferentially to defect sites on metal oxide surfaces. Their work, which involved exposing defect-rich MgO and CeO₂ thin films to small concentrations of gold atoms before investigating the surface composition via scanning tunnelling microscopy, found most gold atoms adsorbed to the defect-rich step sites as shown in Figure 1.1. Minimal gold adsorption was observed on the defect-poor terraces. Moreover, exposure of the metal oxide surfaces to higher gold concentrations further revealed that the gold adatoms[†] at the defect sites act as nucleation points for cluster and nanoparticle growth. Surface defect sites on metal oxide surfaces have since been recognised as highly pertinent regions that both provide anchor points for chemisorption of metal clusters and enhance the ability of adsorbed clusters to catalyse heterogeneous chemical processes.

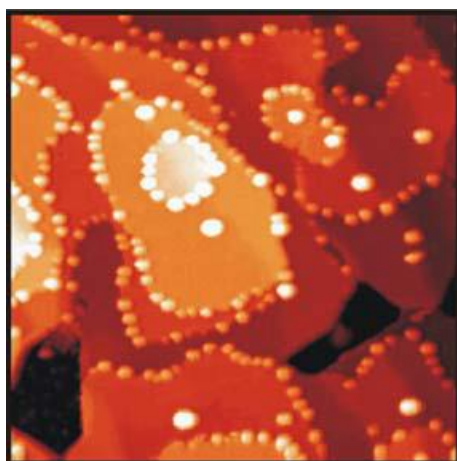
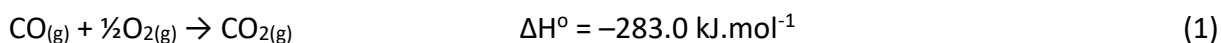


Figure 1.1: STM image of 0.1 ML Au on a ceria [111] film. Gold adsorption occurs primarily at the step sites; minimal adsorption occurs at the terraces. Reprinted by permission from Springer Nature: Lu, J. L.; Gao, H. J.; Shaikhutdinov, S.; Freund, H. J. *Catal. Letters* **2007**, 114 (1–2), 8, Copyright 2007.

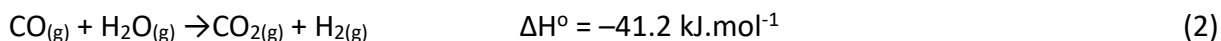
[†] The term *adatom* is a portmanteau of “adsorbed atom”.

1.3. Carbon Monoxide Oxidation with Gold-Ceria Catalysts

Over the past few years, significant effort has been directed towards using nanoscale catalysts to achieve low-temperature carbon monoxide (CO) oxidation. The reaction mechanism for CO oxidation is as follows:



Catalysed CO oxidation has attracted considerable interest for two key reasons. Firstly, carbon monoxide is a highly toxic by-product from internal combustion engines. Given that up to 95% of CO emissions in cities originate from motor vehicles⁷⁹, and that current automotive catalytic converters are only effective at temperatures above 700 K, the development of a catalyst which can perform low-temperature CO oxidation presents a one-stop solution to all but eliminating global CO emissions. CO oxidation can also be coupled with the simultaneous reduction of H₂O as steam to produce hydrogen gas in the water-gas shift (WGS) reaction as shown below:



The water-gas shift reaction is both spontaneous at room temperature and has potential applications in emerging fuel cell technology; hydrogen and oxygen gases can be combined electrochemically – i.e. in a non-combustive process – to produce electricity. Thus CO, which is a product of incomplete fossil fuel combustion, can itself be utilised in fuel generation.

The second reason for the interest in catalytic CO oxidation is that the mechanism by which CO becomes catalytically activated is quite straightforward: the catalyst initiates a π -backbonding donation to the CO π^* antibonding orbital which weakens the CO bond⁸⁰. This provides a simple benchmark by which the plethora of potential nanoscale catalytic systems

can be measured; the more a catalyst can weaken a CO bond, the better a catalyst it is likely to be.

Small gold clusters deposited on cerium oxide (ceria) surfaces are regarded as promising candidates for catalysing low-temperature CO oxidation processes. One of the unusual features of these catalysts lies in the utilisation of gold which, until recently, had been perceived as catalytically uninteresting due to its inertness in the bulk phase. However, a ground-breaking discovery by Haruta et al.⁸¹ in 1989 found gold to be highly reactive when reduced to particles in the nanometre and sub-nanometre size regimes. This high reactivity of gold, which is due to the simultaneous relativistic contraction and expansion of the 6s and 5d orbitals, respectively, is masked in the bulk phase by the tendency of gold to undergo aurophilic bonding. In this phenomenon, gold atoms bind preferentially to other gold atoms and thus become inert toward gas-phase reactants. The strong relativistic effects in gold also contribute to the high ionisation energy (9.22 eV⁸²), high electron affinity (2.31 eV⁸²) and strong electronegativity – which is comparable to that of sulfur – making it the most electronegative transition metal element⁸². Despite its high electronegativity, gold can also be oxidized quite readily to either +1 or +3 formal oxidation states⁸²; these contrasting properties allow gold to participate in either electron-accepting or electron-donating roles.

The reactivities of small gold clusters have been shown to be size-dependent. Studies of Au_n^- ($n=4-20$) cluster anions in CO oxidation processes by both Wallace and Whetten¹³, and by Hagen et al.⁸³ revealed odd-numbered Au_n^- clusters were generally unreactive due to a full valence shell. Even-numbered clusters, however, displayed varied reactivities which were driven largely by their propensity to adsorb molecular oxygen. Those clusters which facilitated CO oxidation were shown to uniquely display co-operative co-adsorption of O₂ and CO, where pre-adsorption of either O₂ or CO increased the adsorption rate of the other reactant.

The potential for cerium oxide to act as an effective support lies in both its high natural abundance – offering cheap procurement and commercial viability – and its ability to undergo

both oxidation ($\text{Ce}^{3+} \rightarrow \text{Ce}^{4+} + \text{e}^-$) and reduction ($\text{Ce}^{4+} + \text{e}^- \rightarrow \text{Ce}^{3+}$) processes readily via electron transfer to/from the cerium 4f shell. Oxygen vacancy sites on the ceria surface are thus quite stable; allowing up to 14% of surface cerium atoms to be reduced at any time⁸⁴. The effect of this low redox potential is threefold in that it (i) provides defect sites for metal cluster adsorption; (ii) facilitates the catalytic activation of adsorbed cluster species through charge transfer processes; and (iii) supports oxidation and reduction of adsorbed reactants via formation and healing of oxygen vacancies, respectively, adjacent to cluster deposition sites^{85,86}.

The efficacy of nanoscale gold-ceria catalysts in performing CO oxidation has been well documented^{1,2,7,17,87–105}. Numerous publications by Flytzani-Stephanopoulos et al.^{1,90–93,95,99,101,104,105} have shown small gold clusters (<1 nm) supported on nanostructured ceria can provide thermally stable catalysts for the water-gas shift reaction at temperatures below 250 °C (ca. 520 K). This represents a considerable decrease in reaction temperature compared to commercial WGS processes, where the High Temperature Shift typically operates in the 310–450 °C temperature range¹⁰⁶. Moreover, Huang et al.¹⁰⁰ reported CO oxidation catalysed by small gold colloids (ca. 2–5 nm diameter) deposited on cerium nanorods and nanoparticles – which largely comprise the [110] and [100] surfaces, respectively - with 50% conversion at temperatures of 270 K and 310 K, respectively. While neither of these examples are as impressive as the previously discussed work by Heiz et al. – who reported CO oxidation using Au₈-MgO catalysts at 140 K – they both show significant improvement over conventional bulk-scale catalysts with regard to facilitating low-temperature CO oxidation and WGS. Moreover, the simple benchtop methods of catalyst preparation undertaken by both Flytzani-Stephanopoulos et al. and Huang et al. – each utilising a variety of co-precipitation and precipitation-deposition procedures – would potentially be easier to implement in commercial manufacturing processes than the gas phase cluster soft-landing methods employed by the Heiz group and others.

1.4. Motivation for this Work

While nanoscale gold-ceria systems have been established as effective catalysts for CO oxidation, the numerous publications on this subject propose a variety of different reaction mechanisms and cluster-surface interactions. Topics of contention include both the deposition site of the gold particle – whether catalytic CO oxidation is achieved by gold clusters deposited on oxygen vacancies, cerium vacancies or on the defect-free surface – and the subsequent charge transfer processes between the cerium oxide surface and the adsorbed gold cluster. Nolan^{85,86}, Fabris et al.¹⁰⁷ and Tibiletti et al.¹⁰⁸, with the former two employing Density Functional Theory (DFT) calculations and the latter using EXAFS studies, all propose CO oxidation by cationic gold clusters deposited in cerium vacancies. However, the authors offer different reaction mechanisms for the CO oxidation process itself.

Calculations by Nolan have shown an exothermic CO oxidation cycle on the gold-doped [110] bulk ceria surface – where a gold atom is deposited into a Ce⁴⁺ vacancy site – with a calculated reaction energy of –2.53 eV. Nolan claims the gold atom provides a supporting role to the ceria surface – through a reduction of the oxygen vacancy formation energy, which allows surface oxygen atoms to be abstracted by CO more readily – but does not directly participate in the oxidation process itself. Fabris et al. similarly propose gold adatoms adopting a +3 oxidation state, however with significant participation of gold – via the reduction of Au³⁺ to Au⁺ – in the oxidation process. Tibiletti et al., who reported CO oxidation via the WGS pathway, propose gold adopting a +1 charge in the cerium vacancy site; the Au⁺ cation is then reduced to Au⁰ during the oxidation process.

In contrast to the work by the above groups, Flytzani-Stephanopoulos et al.^{1,101} report CO oxidation via the WGS process using gold particles deposited on the defect-free ceria surface. The authors, who investigated both surface characteristics and WGS reactivities of nanoscale Au-ceria systems using a combination of STEM/EDX, H₂-TPR and X-ray techniques (XRD, XPS), found agreement with all of Nolan, Fabris et al. and Tibiletti et al. in that the Au-ceria sites responsible for CO oxidation contained ionised gold particles; metallic gold particles were

found to be largely inert in the WGS scheme. However, they propose that strongly bonded Au-O-Ce sites on the defect free surface are the active sites; not gold-doped cerium vacancies. DFT calculations by Jenkins et al. largely supported the findings of Flytzani-Stephanopoulos et al.; particularly with regard to the repudiation of CO oxidation by gold-doped cerium vacancies¹⁰⁹. The authors calculated the formation energies of cerium vacancy sites on the ceria [111] surface to be over 10 eV greater than the formation energies of oxygen vacancies¹⁰⁹. Thus, the deposition of Au atoms to cerium vacancy sites was rejected by the authors on the grounds that Ce⁴⁺ vacancies are too energetically unfavourable to be formed in the first place. The authors also calculate the energetics of Au deposition to larger vacancy sites such as CeO₂ vacancies – where one cerium atom and two oxygen atoms are displaced – which are found to be more favourable than Au deposition to Ce⁴⁺ vacancy sites. The authors attribute this to the lower energy associated with formation of the electronically neutral CeO₂ vacancy site compared to the Ce⁴⁺ vacancy – where creation of a single Ce⁴⁺ vacancy leads to significant charge depletion of the seven surrounding oxygen atoms¹¹⁰ – however do not explore these larger vacancy sites any further.

Calculations by Jenkins et al.¹¹¹ of Au atoms adsorbed to the defect-free ceria surface were also found to agree with Flytzani-Stephanopoulos et al.; the most stable configuration was initially calculated as a gold atom centred above a surface oxygen. Jenkins et al. further proposed – via Bader charge analysis – a charge transfer from the Au adatom to a Ce⁴⁺ ion adjacent the adsorption site, without any direct Au-Ce bond (denoted i.e. Au^{δ+}→Ce⁴⁺). This charge transfer was proposed to occur via quantum tunnelling. However, in a later work¹¹⁰ the Jenkins group calculated a more energetically stable arrangement involving a gold atom bridging two oxygen atoms on the defect-free surface. The authors proposed a similar Au^{δ+}→Ce⁴⁺ charge transfer via quantum tunnelling from the Au atom to a Ce⁴⁺ ion neighbouring the Au-O bond.

To further complicate matters, Jenkins et al.^{110,111} have also calculated a stable Au-ceria interaction involving a gold atom positioned atop an oxygen vacancy site. Au binding energies to the reduced site and the defect-free surface were calculated as –2.58 eV and –1.20 eV,

respectively, implying preferable Au adsorption to oxygen vacancy sites than defect-free regions of the ceria surface. The authors calculated a charge transfer from the reduced cerium atoms neighbouring the defect site to the adsorbed gold atom (denoted $\text{Ce}^{3+} \rightarrow \text{Au}^{\delta-}$). The authors rule out any CO oxidation from a single gold atom adsorbed to an oxygen vacancy – the sites are inert toward CO – but propose the adsorbed Au atom can act as a nucleation point for larger cluster growth. Subsequent calculations by the same group¹¹² on Au_n ($n=1-11$) clusters deposited on reduced ceria surfaces showed a 3-dimensional growth mechanism where the gold cluster formed several layers above the defect site. The gold atoms in the first layer – except for the Au atom bound to the oxygen vacancy site – formed Au-O bonds on the defect-free regions surrounding the vacancy site. Moreover, the positive Bader charges calculated for the Au atoms in the first layer were consistent with the $\text{Au}^{\delta+} \rightarrow \text{O}^{2-}$ charge transfer proposed by Flytzani-Stephanopoulos et al. Jenkins et al.¹¹² proposed the positively charged bottom layer of the supported Au_n cluster could provide sites for CO adsorption – facilitated by the empty 6s orbital on $\text{Au}^{\delta+}$ – and activation along the gold-ceria interface. Gold atoms in subsequent layers were mostly stacked above the defect site with negative Bader charges due to electron abstraction from the O vacancy site. The authors proposed these higher layers were largely metallic in nature and thus less receptive to CO adsorption. Experimental work by Wang et al.¹¹³, who used synchrotron-based X-ray techniques to investigate WGS catalysis of Au-ceria systems, also found that neutral gold clusters deposited on oxygen vacancies form the active sites for CO oxidation. However, they dismiss the involvement of $\text{Au}^{\delta+}$ cations in WGS catalysis.

Numerous experimental studies^{13,14,45,83,114} have also shown that small gold clusters and nanoscale ceria particles can each function as catalysts in their own right. It is therefore possible that the entire CO oxidation cycle is performed on the either the gold cluster surface or the cerium oxide surface; with the other simply providing a supporting role.

Most experimental studies of Au-ceria catalysts so far have involved non-size selected gold particles deposited on inhomogeneous ceria surfaces. This presents difficulties in isolating the specific Au-ceria interactions – and subsequent CO oxidation mechanisms – occurring at each

catalytic site, since different interactions may be occurring at different sites. The problem lies in the catalyst preparation methods where gold particles are typically produced via reduction of HAuCl_4 while cerium oxide is precipitated from aqueous cerium salts. These methods offer the advantages of being fast, simple and potentially bulk-scalable. However, they tend to produce a distribution of gold particle sizes – from individual atoms to colloids ca. 10 nm in diameter – in addition to ceria surfaces which expose numerous surface planes – including the [100], [110] and [111] planes – and defect sites. Given the catalytic abilities of nanoscale Au-ceria systems are strongly dependent on both the size of the adsorbed gold cluster and the nature of the ceria surface^{52,90,100}, it follows that a study of size-selected gold particles deposited on a designated ceria surface would be greatly beneficial. Plane-wave pseudopotential DFT and DFT+U calculations have achieved moderate success in this regard. In these studies, plane-wave basis sets are combined with frozen core treatments of Ce atoms to describe large ceria surfaces at low computational expense. On-site Coulombic interactions of localised electrons, particularly in defect sites, are described by a (semi-empirical) Hubbard-like term (U). Plane-wave basis set methods, however, describe a rigid lattice and do not account for atomic relaxation which can lead to an inaccurate description of defect sites¹¹⁵⁻¹¹⁷. Moreover, as highlighted by Jenkins et al.¹¹⁰, the results derived from DFT+U calculations can be highly dependent on the parameters selected for the calculations – particularly the U term, which affects the degree of *f* orbital localisation – which are user-defined.

1.5. Clusters as Surface Analogues

Given the ground-breaking work by Heiz et al.⁵² who showed the reactivities of cluster-surface catalysts are heavily influenced by cluster-surface interactions, and the established ability of nanoscale gold-ceria systems to catalyse a variety of chemical processes, it follows that a thorough understanding of the interactions between gold and ceria in the nanoscale size regime would be beneficial toward the development of highly selective, low-temperature catalysts. Bimetallic clusters have been shown to perform quite well as experimentally tractable models for heterogeneous catalysts since catalytic activity often occurs at the cluster-surface interface¹¹⁸. Moreover, defect sites – particularly steps and edges - have been

shown to exhibit cluster-like bonding due to their non-uniform structures and low coordination numbers^{119,120}. It is therefore proposed that a detailed study into the properties of gold-doped ceria oxide clusters may provide some insight into the Au-ceria interactions which influence catalytic activity. Isolated regions of the ceria surface can be investigated using different cluster species, as shown in Figure 1.2. By selecting clusters with the stoichiometric configuration of a defect-free surface or a vacancy site, the subsequent interactions of these particular sites with adsorbed gold can be considered separately. The use of clusters as model surfaces in this context is advantageous to conventional bulk surfaces since they are smaller – and hence easier to study via both spectroscopic and computational methods. This is particularly relevant for the latter, where the treatment of cluster systems with atomic-centred basis sets allows for atomic relaxation to occur during calculations. This provides a better representation of the electronic and geometric properties of defect sites in comparison to conventional DFT+U calculations of defect sites on bulk surfaces.

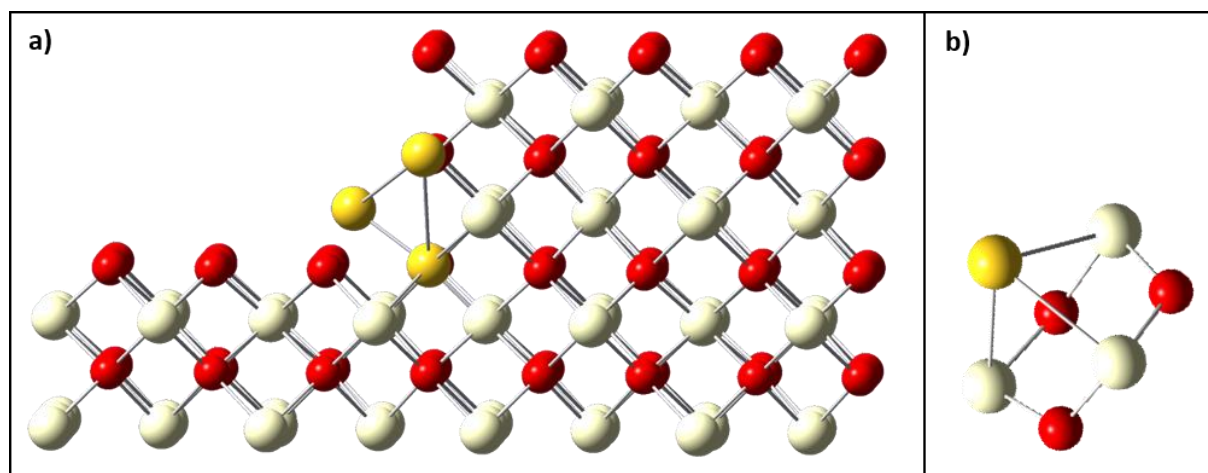


Figure 1.2: **a).** Schematic representation for an Au_3 cluster adsorbed to at a step site on the ceria [100] surface. The anchoring Au atom is occupying an oxygen vacancy. **b).** Example of a cluster model used to isolate a portion of the surface representing the gold-ceria interface.

1.6. Previous Work: Gas Phase Bimetal Oxide Clusters

Transition metal oxide clusters have been well established as analogues of bulk surface defect sites. One of the more pertinent examples draws from the Castleman group^{121–132}, who investigated the reactivities of size-selected group V transition metal oxide clusters V_mO_n ,

Nb_mO_n and Ta_mO_n . They found the reactivities of these clusters – and by extrapolation, the corresponding defect sites – were largely governed by several key factors which included: (i) cluster size, (ii) the identity of the transition metal, (iii) the availability of stable oxidation states, (iv) the coordinative saturation of the metal atoms and (v) the charge state of the cluster. Exploring these points in more detail, the authors found that smaller clusters – which are analogous of more pronounced defects – were more reactive than larger clusters. Reactivity studies of M_2O_5^+ ($\text{M} = \text{V}, \text{Nb}, \text{Ta}$) clusters with *n*-butane showed the preferential reaction pathway of the V_2O_5^+ cluster involved an oxygen transfer process with V_2O_4^+ and oxygenated *n*-butane as the products. Conversely, Ta_2O_5^+ and Nb_2O_5^+ clusters, yielded products of $\text{M}_2\text{O}_5\text{C}_2\text{H}_4^+$, which the authors proposed to be C-C activation of *n*-butane. V_mO_n clusters, which can possess stable V^{3+} and V^{4+} metal centres in addition to the natural V^{5+} state, were found to perform better in reduction processes than Ta_mO_n and Nb_mO_n clusters where the metal centres do not form stable complexes in +3 and +4 oxidation states. Coordinatively unsaturated clusters were found to be highly reactive due to the provision of sterically and electronically accessible metal centres for adsorption sites¹²³. The charge states of clusters were found to strongly affect their reactivities due to both the facilitation of electron transfer processes with reactant molecules – i.e. whether the cluster functions as an electron donor or acceptor – and the stability of the cluster valence configuration; closed shell clusters were typically more stable and thus less reactive.

Bimetal oxide clusters have not garnered as much attention as clusters comprising a single metal species. There are, however, a few notable works worth mentioning. Janssens et al.¹³³ used infrared multiple photon dissociation spectroscopy to investigate the effects of sequentially substituting vanadium atoms with titanium in the $(\text{V}_{4-n}\text{Ti}_n\text{O}_{10})^-$ [$n=0,1,\dots,4$] cluster anion. They found minimal change in the geometric structure throughout the substitution process – the cluster maintained an icosahedral geometry. However, the induced strain from the isomorphous substitution resulted in unpaired electrons accompanying each interchange of V with Ti. Nonose et al.²⁸ used a similar method to investigate the reactivity effects of adding aluminium atoms to niobium and cobalt clusters in the $n=8,9,\dots,12$ and $n=10,12,15,20$ size regimes, respectively. The authors reported sequential Al additions being accompanied

by increased reactivities with H_2 in all but the small Nb_n clusters ($n=4,5,6,7$), which showed decreased reactivities following each Al addition. Finally, Jarrold et al.^{134–151} used a combination of photoelectron spectroscopy, DFT calculations and Franck Condon simulations to investigate anionic molybdenum oxide clusters doped with vanadium, tungsten and niobium. By comparing the structures of $Mo_xM_yO_z^-$ ($M = V, W, Nb$) clusters to the corresponding $Mo_{x+y}O_z^-$ and $M_{x+y}O_z^-$ clusters species, they were able to infer the effects of atomic substitution on both intramolecular bonding and catalytic reactivity.

A handful of experimental studies have been performed on cerium oxide clusters; with the majority published in the past decade. Akin et al.¹⁵² have explored the photo-dissociation channels of small $Ce_mO_n^+$ ($m=3,4$) cluster cations to find 2 unique fragmentation pathways. Clusters with the stoichiometry $CeO(CeO_2)_n^+$ lose neutral CeO_2 units upon fragmentation, whereas cluster species with a higher oxygen content dissociate via the loss of O_2 . Recent work by Hayakawa et al.^{153,154} characterised the properties of numerous small cerium oxide cluster cations in the $Ce_3O_n^+$ ($n=4-7$) size regime using x-ray absorption spectroscopy. Through comparison of the pre-K-edge peaks for each of the clusters, the authors were able to infer that the base $Ce_3O_4^+$ geometry did not change significantly following oxidation; additional oxygen atoms instead occupied positions on the periphery of the structure. Ding et al.^{155,156} explored the reactivities of small cerium oxide cluster cations with small hydrocarbons via a combination of mass spectrometry and DFT. The authors observed increases in the intensities of the $Ce_mO_{2m-1}^+$ ion peaks when the $Ce_mO_{2m}^+$ clusters were exposed to acetylene. From their DFT calculations of potential reaction pathways, the authors proposed a mechanism whereby the $Ce_mO_{2n}^+$ cluster undergoes two-oxygen atom transfer with acetylene to produce ethanedial $(CHO)_2$. A two-oxygen atom transfer process was also reported by Nagata et al.¹⁵⁷ who were able to remove an O_2 fragment from $Ce_nO_{2n}^+$ clusters with intense heating. Hirabayashi et al.^{158,159} used a combination of mass spectrometry and DFT to study the reactivities of $Ce_mO_n^+$ ($m=2-6; n \leq 2m$) clusters with CO and NO gases. The authors found only the $n=2m$ clusters were reactive; oxygen deficient clusters were inert toward CO and NO. DFT calculations showed the CO oxidation mechanism possessing a small activation barrier whereas NO oxidation was calculated as a barrierless process. Several other publications have

also explored the properties and reactivities of small cerium oxide – and oxyhydroxide¹⁶⁰ – clusters including their structures^{115,161}, photoelectron spectra¹⁶² and reactivities^{163–166}.

Very few studies have been performed on bi-metal lanthanide oxide clusters. However, the increased number of published works in recent years shows promise. Slagtern et al.¹⁴⁸ and Olsby et al.¹⁴⁹ independently showed that rhodium doped lanthanide oxide clusters could be used for the partial oxidation of methane to synthesis gas. However, they did not investigate the interactions between the lanthanide oxide surface and the rhodium adsorbent. These interactions were later explored by Gentleman et al.¹⁶⁷ – as part of the Metha group – who used complementary Photo-Ionisation Efficiency experiments and DFT studies of RhHo_2O_n ($n=0,1,2$) clusters to identify the charge transfer interactions occurring within the RhHo_2 metal trimer upon sequential oxidation. The authors reported a charge transfer from the Ho atoms to the Rh atom in all of the RhHo_2O_n ($n=0,1,2$) clusters. However, the extent of charge transfer was found to depend strongly on the oxidation state of the cluster. The strongest Ho→Rh charge transfer was recorded in the RhHo_2O cluster species, with far weaker charge transfer interactions occurring in both the RhHo_2 and RhHo_2O_2 species. Unpublished results by Gentleman and Metha¹⁶⁸ on the properties of AuPr_2O_n ($n=0,1,2$) clusters using the same method have shown a similar charge transfer process occurring from the praseodymium atoms to the gold atom. Mafune et al.¹⁶⁹ have investigated the reactivities of a limited number of small gold-cerium oxide cluster cations – including $\text{AuCe}_2\text{O}_4^+$ and $\text{AuCe}_2\text{O}_5^+$ – with CO using a combination of temperature programmed desorption experiments and DFT calculations. Unusually, the authors claim that the $\text{AuCe}_2\text{O}_4^+$ species is reactive towards CO oxidation whereas the more highly oxidised $\text{AuCe}_2\text{O}_5^+$ cluster is inert. From their DFT calculations, the authors propose that Au functions as an adsorption site for CO while an oxygen centred radical provides the active site for oxidation.

1.7. Scope of this Work

The aim of this thesis is to conduct a detailed investigation into the Au-ceria interactions that potentially facilitate catalytic activity using small cerium oxide clusters doped with gold. Ce_mO_n and AuCe_mO_n clusters are generated in the gas phase using a similar method to that

employed by Gentleman et al.¹⁶⁷. The adiabatic ionisation energies of the generated cluster species are determined experimentally using Photo-Ionisation Efficiency (PIE) spectroscopy; the experimental setup and methodology are discussed in Chapter 2. Density Functional Theory calculations are used to predict geometric structures for Ce_mO_n and $AuCe_mO_n$ cluster species in both the neutral and cationic states. Using these calculated structures and subsequent Zero Electron Kinetic Energy simulations, calculated PIE spectra are compared to experimental PIE spectra; a good correlation between these experimental and calculated spectra then allows geometric properties of the pertinent cluster species to be inferred from the calculated structures. The calculated adiabatic ionisation energies are also compared to those attained from experimental PIE spectra to confirm the electronic structures of the calculated species. These methods will be detailed in Chapter 3. This is followed by a benchmarking study in Chapter 4 to determine an accurate method of calculating Ce_mO_n and $AuCe_mO_n$ clusters – particularly with regard to the treatment of core electrons – at a reasonable computational expense.

Experimental and computational results for the Ce_2O_n , Ce_3O_n and Ce_4O_n clusters are presented in Chapters 5, 6 and 7 respectively. Chapters 5 and 6 further present experimental PIE spectra for all Ce_2O_n and Ce_3O_n clusters detected during experiments. The experimental spectra are compared to ZEKE and PIE simulations of DFT-calculated structures to determine the adiabatic IEs for the Ce_2O_n and Ce_3O_n clusters. Chapter 7 presents only experimental PIE spectra for the Ce_4O_n cluster species. Since calculations for the Ce_4O_n cluster species were too computationally expensive to yield any decisive results, experimental appearance energies for the Ce_4O_n clusters are presented in lieu of adiabatic ionisation energies.

Experimental PIE spectra, DFT calculations and PIE simulations for the $AuCe_2O_n$ and $AuCe_3O_n$ cluster systems are presented in Chapters 8 and 9. These chapters are presented in the same format as discussed for the Ce_2O_n and Ce_3O_n systems.

Chapter 10 presents a discussion on the Au-ceria interactions occurring within AuCe_mO_n clusters with regard to existing CO oxidation mechanisms. This includes an investigation of the bonding arrangements within the calculated AuCe_mO_n clusters and an analysis of Hirshfeld charges to determine the binding sites and subsequent charge transfer interactions for Au atoms adsorbed to ceria clusters. Comparisons of calculated HOMO/LUMO energies and molecular orbitals for the Ce_mO_n and AuCe_mO_n systems are presented to explore the effects of Au on the electronic structure of Ce_mO_n . Calculated oxygen affinities for the Ce_mO_n and AuCe_mO_n cluster species provide insight to how gold adsorption may affect oxygen vacancy formation and healing on the Ce_mO_n cluster surface. Finally, the ionisation energies and oxygen binding energies for the Ce_mO_n and AuCe_mO_n clusters are compared to investigate the potential photon absorption pathways for each cluster species with regard to future photo-ionisation studies.

1.8. References

- (1) Yi, N.; Si, R.; Saltsburg, H.; Flytzani-Stephanopoulos, M. *Energy Environ. Sci.* **2010**, *3*, 831.
- (2) Li, Y.; Fu, Q.; Flytzani-Stephanopoulos, M. *Appl. Catal. B Environ.* **2000**, *27* (3), 179.
- (3) Rodriguez, J. A.; Ma, S.; Liu, P.; Hrbek, J.; Evans, J.; Pérez, M. *Science (80-.)*. **2007**, *318* (5857), 1757.
- (4) Bricker, J. C.; Nagel, C. C.; Shore, S. G. *J. Am. Chem. Soc.* **1982**, *104* (5), 1444.
- (5) Burch, R. *Phys. Chem. Chem. Phys.* **2006**, *8* (47), 5483.
- (6) Koh, A. C. W.; Leong, W. K.; Chen, L.; Ang, T. P.; Lin, J.; Johnson, B. F. G.; Khimyak, T. *Catal. Commun.* **2008**, *9* (1), 170.
- (7) Boucher, M. B.; Yi, N.; Gittleson, F.; Zugic, B.; Saltsburg, H.; Flytzani-Stephanopoulos, M. *J. Phys. Chem. C* **2011**, *115* (4), 1261.
- (8) Demitras, G. C.; Muetterties, E. L. *J. Am. Chem. Soc.* **1977**, *99* (8), 2796.
- (9) Feller, A.; Claeys, M.; Steen, E. van. *J. Catal.* **1999**, *185* (1), 120.
- (10) Fraenkel, D.; Gates, B. C. *J. Am. Chem. Soc.* **1980**, *102* (7), 2478.
- (11) Giannelis, E. P.; Rightor, E. G.; Pinnavaia, T. J. *J. Am. Chem. Soc.* **1988**, *110* (12), 3880.
- (12) Jacobs, G.; Patterson, P. M.; Zhang, Y.; Das, T.; Li, J.; Davis, B. H. *Appl. Catal. A Gen.* **2002**, *233* (1–2), 215.
- (13) Wallace, W. T.; Whetten, R. L. *J. Am. Chem. Soc.* **2002**, *124* (25), 7499.
- (14) Häkkinen, H.; Landman, U. *J. Am. Chem. Soc.* **2001**, *123* (39), 9704.
- (15) Huber, H.; McIntosh, D.; Ozin, G. A. *Inorg. Chem.* **1977**, *16* (5), 975.
- (16) Choudhary, T. V.; Goodman, D. W. *Top. Catal.* **2002**, *21* (1–3), 25.
- (17) Pillai, U. R.; Deevi, S. *Appl. Catal. A Gen.* **2006**, *299* (1–2), 266.
- (18) Hayashi, T.; Tanaka, K.; Haruta, M. *J. Catal.* **1998**, *178*, 566.
- (19) Bond, G. C.; Sermon, P. A.; Webb, G.; Buchanan, D. A.; Wells, P. B. *J. Chem. Soc. Chem. Commun.* **1973**, No. 444, 444b.

-
- (20) Farrag, M.; Tschurl, M.; Heiz, U. *Chem. Mater.* **2013**, *25* (6), 862.
- (21) Lechtken, A.; Schooss, D.; Stairs, J. R.; Blom, M. N.; Furche, F.; Morgner, N.; Kostko, O.; von Issendorff, B.; Kappes, M. M. *Angew. Chemie Int. Ed.* **2007**, *46*, 2944.
- (22) Ackermann, R. J. *J. Chem. Phys.* **1976**, *65* (3), 1027.
- (23) Deng, H. T.; Guo, B. C.; Kerns, K. P.; Castleman, A. W. *Int. J. Mass Spectrom. Ion Process.* **1994**, *138*, 275.
- (24) Knickelbein, M. B. *J. Chem. Phys.* **1995**, *102* (1), 1.
- (25) Koretsky, G. M.; Knickelbein, M. B. *Eur. Phys. J. D - At. Mol. Opt. Plasma Phys.* **1998**, *2*, 273.
- (26) Kaldor, A.; Cox, D. M. *J. Chem. Soc. Faraday Trans.* **1990**, *86* (13), 2459.
- (27) Hoshino, K.; Naganuma, T.; Watanabe, K.; Nakajima, A.; Kaya, K. *Chem. Phys. Lett.* **1993**, *211* (6), 571.
- (28) Nonose, S.; Sone, Y.; Onodera, K.; Sudo, S.; Kaya, K. *J. Phys. Chem.* **1990**, *94*, 2744.
- (29) Nonose, S.; Sone, Y.; Onodera, K.; Sudo, S.; Kaya, K. *Chem. Phys. Lett.* **1989**, *164* (4), 427.
- (30) Yang, S.; Knickelbein, M. B. *J. Chem. Phys.* **1990**, *93* (3), 1533.
- (31) Knickelbein, M. B. *Chem. Phys. Lett.* **1992**, *192* (1), 129.
- (32) Knickelbein, M. B.; Yang, S.; Riley, S. J. *J. Chem. Phys.* **1990**, *93* (1), 94.
- (33) Koretsky, G. M.; Knickelbein, M. B. *J. Chem. Phys.* **1997**, *106* (23), 9810.
- (34) Berces, A.; Hackett, P. A. *J. Chem. Phys.* **1998**, *108* (13), 5476.
- (35) Jackschath, C.; Rabin, I.; Schulze, W. *Berichte der Bunsengesellschaft für Phys. Chemie* **1992**, *96* (9), 1200.
- (36) Taylor, K. J.; Pettiette-Hall, C. L.; Cheshnovsky, O.; Smalley, R. E. *J. Chem. Phys.* **1992**, *96* (4), 3319.
- (37) Farrugia, L. J. *Organometallics* **1989**, *8* (10), 2410.
- (38) Ewing, P.; Farrugia, L. J.; Rycroft, D. S. *Organometallics* **1988**, *7* (4), 859.

- (39) Gansow, O. A.; Gill, D. S.; Bennis, F. J.; Hutchinson, J. R.; Vidal, J. L.; Schoening, R. C. *J. Am. Chem. Soc.* **1980**, *102* (7), 2449.
- (40) Ghosh, P.; Farnesi Camellone, M.; Fabris, S. *J. Phys. Chem. Lett.* **2013**, *4* (14), 2256.
- (41) Bradford, A. M.; Kristof, E.; Rashidi, M.; Yang, D.-S.; Payne, N. C.; Puddephatt, R. J. *Inorg. Chem.* **1994**, *33* (11), 2355.
- (42) Lin, L.; Höltzl, T.; Gruene, P.; Claes, P.; Meijer, G.; Fielicke, A.; Lievens, P.; Nguyen, M. T. *ChemPhysChem* **2008**, *9* (17), 2471.
- (43) Vargas, A.; Santarossa, G.; Iannuzzi, M.; Baiker, A. *Phys. Rev. B* **2009**, *80* (19), 195421.
- (44) Arenz, M.; Landman, U.; Heiz, U. *ChemPhysChem* **2006**, *7* (9), 1871.
- (45) Xing, X.; Li, X.; Yoon, B.; Landman, U.; Parks, J. H. *Int. J. Mass Spectrom.* **2014**, *377*, 393.
- (46) Gu, X.; Bulusu, S.; Li, X.; Zeng, X. C.; Li, J.; Gong, X. G.; Wang, L.-S. *J. Phys. Chem. C* **2007**, *111* (23), 8228.
- (47) Benfield, R. E.; Johnson, B. F. G. *Transit. Met. Chem.* **1981**, *6* (3), 131.
- (48) Day, V. W.; Day, R. O.; Kristoff, J. S.; Hirsekorn, F. J.; Muetterties, E. L. *J. Am. Chem. Soc.* **1975**, *97* (9), 2571.
- (49) Puddephatt, R. J.; Manojlovic-Muir, L.; Muir, K. W. *Polyhedron* **1990**, *9* (23), 2767.
- (50) Sergeeva, A. P.; Popov, I. A.; Piazza, Z. A.; Li, W.-L.; Romanescu, C.; Wang, L.-S.; Boldyrev, A. I. *Acc. Chem. Res.* **2014**, *47* (4), 1349.
- (51) Geoffroy, G. L. *Acc. Chem. Res.* **1980**, *13* (12), 469.
- (52) Yoon, B.; Häkkinen, H.; Landman, U.; Wörz, A. S.; Antonietti, J.-M.; Abbet, S.; Judai, K.; Heiz, U. *Science* **2005**, *307* (5708), 403.
- (53) Zhai, H.; Alexandrova, A. N. *J. Chem. Theory Comput.* **2016**, *12* (12), 6213.
- (54) Barrio, L.; Liu, P.; Rodríguez, J. A.; Campos-Martín, J. M.; Fierro, J. L. G. *J. Chem. Phys.* **2006**, *125* (16), 164715.
- (55) Vilhelmsen, L. B.; Hammer, B. *Phys. Rev. Lett.* **2012**, *108* (12), 126101.

- (56) Beret, E. C.; Ghiringhelli, L. M.; Scheffler, M. *Faraday Discuss.* **2011**, *152*, 153.
- (57) Gao, M.; Lyalin, A.; Takagi, M.; Maeda, S.; Taketsugu, T. *J. Phys. Chem. C* **2015**, *119* (20), 11120.
- (58) Fung, V.; Jiang, D. *J. Phys. Chem. C* **2017**, *121* (20), 10796.
- (59) Gao, M.; Lyalin, A.; Maeda, S.; Taketsugu, T. *J. Chem. Theory Comput.* **2014**, *10* (4), 1623.
- (60) Remediakis, I. N.; Lopez, N.; Nørskov, J. K. *Appl. Catal. A Gen.* **2005**, *291* (1), 13.
- (61) Koizumi, K.; Nobusada, K.; Boero, M. *J. Phys. Chem. C* **2015**, *119* (27), 15421.
- (62) Sinfelt, J. H. *J. Catal.* **1973**, *29* (2), 308.
- (63) Arrii, S.; Morfin, F.; Renouprez, A. J.; Rousset, J. L. *J. Am. Chem. Soc.* **2004**, *126* (4), 1199.
- (64) Ichikawa, M. *J. Catal.* **1979**, *59* (1), 67.
- (65) Bus, E.; Prins, R.; van Bokhoven, J. A. *Catal. Commun.* **2007**, *8* (9), 1397.
- (66) Herzing, A. A.; Kiely, C. J.; Carley, A. F.; Landon, P.; Hutchings, G. J. *Science* **2008**, *321* (5894), 1331 LP.
- (67) Deeba, M.; Gates, B. C. *J. Catal.* **1981**, *67* (2), 303.
- (68) Valden, M.; Lai, X.; Goodman, D. W. *Science* **1998**, *281* (5383), 1647.
- (69) Gates, B. C. *J. Mol. Catal. A Chem.* **2000**, *163* (1), 55.
- (70) Watanabe, M.; Uchida, M.; Motoo, S. *J. Electroanal. Chem. Interfacial Electrochem.* **1987**, *229* (1), 395.
- (71) Guzman, J.; Carrettin, S.; Corma, A. *J. Am. Chem. Soc.* **2005**, *127* (10), 3286.
- (72) Turner, M.; Golovko, V. B.; Vaughan, O. P. H.; Abdulkin, P.; Berenguer-Murcia, A.; Tikhov, M. S.; Johnson, B. F. G.; Lambert, R. M. *Nature* **2008**, *454* (7207), 981.
- (73) Lee, S.; Fan, C.; Wu, T.; Anderson, S. L. *J. Am. Chem. Soc.* **2004**, *126* (18), 5682.
- (74) Argo, A. M.; Odzak, J. F.; Lai, F. S.; Gates, B. C. *Nature* **2002**, *415* (6872), 623.
- (75) Scott, R. W. J.; Sivadinarayana, C.; Wilson, O. M.; Yan, Z.; Goodman, D. W.; Crooks, R.

- M. J. Am. Chem. Soc. **2005**, 127 (5), 1380.
- (76) Kašpar, J.; Fornasiero, P.; Hickey, N. *Catal. Today* **2003**, 77 (4), 419.
- (77) Sterrer, M.; Yulikov, M.; Fischbach, E.; Heyde, M.; Rust, H.-P.; Pacchioni, G.; Risse, T.; Freund, H.-J. *Angew. Chem. Int. Ed. Engl.* **2006**, 45 (16), 2630.
- (78) Lu, J. L.; Gao, H. J.; Shaikhutdinov, S.; Freund, H. J. *Catal. Letters* **2007**, 114 (1–2), 8.
- (79) Report on the Environment: Carbon Monoxide Emissions <https://www.epa.gov.au/roe/> (accessed Jul 11, 2017).
- (80) Atkins, P. W.; Overton, T.; Rourke, J.; Weller, M.; Armstrong, F. *Shriver & Atkins' Inorganic Chemistry*; Oxford University Press: Oxford, 2010.
- (81) Haruta, M.; Yamada, N.; Kobayashi, T.; Iijima, S. *J. Catal.* **1989**, 115 (2), 301.
- (82) NIST Atomic Spectra Database physics.nist.gov/ (accessed Jun 30, 2016).
- (83) Hagen, J.; Socaciu, L. D.; Elijazyfer, M.; Heiz, U.; Bernhardt, T. M.; Woste, L. *Phys. Chem. Chem. Phys.* **2002**, 4 (10), 1707.
- (84) Hayes, W.; Stoneham, A. M. *Defects and Defect Processes in Nonmetallic Solids*; John Wiley & Sons: New York, 2004.
- (85) Nolan, M.; Verdugo, V. S.; Metiu, H. *Surf. Sci.* **2008**, 602 (16), 2734.
- (86) Nolan, M. *J. Chem. Phys.* **2009**, 130 (14), 144702.
- (87) Si, R.; Flytzani-Stephanopoulos, M. *Angew. Chemie Int. Ed.* **2008**, 47 (15), 2884.
- (88) Fu, Q.; Kudriavtseva, S.; Saltsburg, H.; Flytzani-Stephanopoulos, M. *Chem. Eng. J.* **2003**, 93 (1), 41.
- (89) Deng, W.; Jesus, J. De; Saltsburg, H.; Flytzani-Stephanopoulos, M. *Appl. Catal. A Gen.* **2005**, 291 (1–2), 126.
- (90) Yi, N.; Rui, S.; Saltsburg, H.; Flytzani-Stephanopoulos, M. *Energy Environ. Sci.* **2010**, 3, 831.
- (91) Deng, W.; Flytzani-Stephanopoulos, M. *Angew. Chemie* **2006**, 118 (14), 2343.
- (92) Deng, W.; Frenkel, A. I.; Si, R.; Flytzani-Stephanopoulos, M. *J. Phys. Chem. C* **2008**, 112

- (33), 12834.
- (93) Flytzani-Stephanopoulos, M. *Acc. Chem. Res.* **2014**, *47* (3), 783.
- (94) Lee, Y.; He, G.; Akey, A. J.; Si, R.; Flytzani-Stephanopoulos, M.; Herman, I. P. *J. Am. Chem. Soc.* **2011**, *133* (33), 12952.
- (95) Boucher, M. B.; Goergen, S.; Yi, N.; Flytzani-Stephanopoulos, M. *Phys. Chem. Chem. Phys.* **2011**, *13* (7), 2517.
- (96) Zhou, Z.; Flytzani-Stephanopoulos, M.; Saltsburg, H. *J. Catal.* **2011**, *280* (2), 255.
- (97) Manzoli, M.; Boccuzzi, F.; Chiorino, A.; Vindingi, F.; Deng, W.; Flytzani-Stephanopoulos, M. *J. Catal.* **2007**, *245* (2), 308.
- (98) Deng, W.; Carpenter, C.; Yi, N.; Flytzani-Stephanopoulos, M. *Top. Catal.* **2007**, *44* (1–2), 199.
- (99) Zhou, Z.; Kooi, S.; Flytzani-Stephanopoulos, M.; Saltsburg, H. *Adv. Funct. Mater.* **2008**, *18* (18), 2801.
- (100) Huang, X. S.; Sun, H.; Wang, L. C.; Liu, Y. M.; Fan, K. N.; Cao, Y. *Appl. Catal. B Environ.* **2009**, *90* (1–2), 224.
- (101) Fu, Q.; Deng, W.; Saltsburg, H.; Flytzani-Stephanopoulos, M. *Appl. Catal. B Environ.* **2005**, *56* (1–2), 57.
- (102) Andreeva, D. *Gold Bull.* **2002**, *35* (3), 82.
- (103) Tabakova, T.; Boccuzzi, F.; Manzoli, M.; Andreeva, D. *Appl. Catal. A Gen.* **2003**, *252* (2), 385.
- (104) Fu, Q.; Saltsburg, H.; Flytzani-Stephanopoulos, M. *Science* **2003**, *301* (5635), 935.
- (105) Fu, Q.; Weber, A.; Flytzani-Stephanopoulos, M. *Catal. Letters* **2001**, *77* (1–3), 87.
- (106) Callaghan, C. A. Kinetics and Catalysis of the Water-Gas-Shift Reaction: A Microkinetic and Graph Theoretic Approach, PhD Thesis, Worcester Polytechnic Institute, 2006.
- (107) Camellone, M. F.; Fabris, S. *J. Am. Chem. Soc.* **2009**, *131* (30), 10473.
- (108) Tibiletti, D.; Amieiro-Fonseca, A.; Burch, R.; Chen, Y.; Fisher, J. M.; Goguet, A.; Hardacre, C.; Hu, P.; Thompsett, D. *J. Phys. Chem. B* **2005**, *109* (47), 22553.

- (109) Zhang, C.; Michaelides, A.; King, D. A.; Jenkins, S. J. *J. Phys. Chem. C* **2009**, *113* (16), 6411.
- (110) Zhang, C.; Michaelides, A.; King, D. A.; Jenkins, S. J. *J. Chem. Phys.* **2008**, *129* (19), 1.
- (111) Liu, Z. P.; Jenkins, S. J.; King, D. A. *Phys. Rev. Lett.* **2005**, *94* (19), 196102.
- (112) Zhang, C.; Michaelides, A.; King, D. A.; Jenkins, S. J. *J. Am. Chem. Soc.* **2010**, *132* (7), 2175.
- (113) Wang, X.; Rodriguez, J. A.; Hanson, J. C.; Pérez, M.; Evans, J. *J. Chem. Phys.* **2005**, *123* (22), 221101.
- (114) Sayle, T. X. T.; Parker, S. C.; Sayle, D. C. *Phys. Chem. Chem. Phys.* **2005**, *7* (15), 2936.
- (115) Li, S. F.; Lu, H.; Li, P.; Yang, Z.; Guo, Z. X. *J. Chem. Phys.* **2008**, *128* (16).
- (116) Fabris, S.; de Gironcoli, S.; Baroni, S.; Vicario, G.; Balducci, G. *Phys. Rev. B* **2005**, *71* (4), 41102.
- (117) Nolan, M.; Grigoleit, S.; Sayle, D. C.; Parker, S. C.; Watson, G. W. *Surf. Sci.* **2005**, *576* (1–3), 217.
- (118) Armentrout, P. B. *Annu. Rev. Phys. Chem.* **2001**, *52* (1), 423.
- (119) Somorjai, G. A. *Introduction to Surface Chemistry and Catalysis*; John Wiley & Sons: New York, 1994.
- (120) Somorjai, G. A. *J. Phys. Chem.* **1990**, *94* (3), 1013.
- (121) Zemski, K. A.; Justes, D. R.; Castleman, A. W. *J. Phys. Chem. B* **2002**, *106* (24), 6136.
- (122) Zemski, K. A.; Justes, D. R.; Castleman, A. W. *J. Phys. Chem. A* **2001**, *105* (45), 10237.
- (123) Anderson-Fredeen, D.; Russell, D. H. *J. Am. Chem. Soc.* **1985**, *107* (13), 3762.
- (124) Rybtchinski, B.; Milstein, D. *J. Am. Chem. Soc.* **1999**, *121* (18), 4528.
- (125) Bell, R. C.; Zemski, K. A.; Castleman, A. W. *J. Clust. Sci.* **1999**, *10* (4), 509.
- (126) Bell, R. C.; Zemski, K. A.; Castleman, A. W. *J. Phys. Chem. A* **1999**, *103* (11), 1585.
- (127) Zemski, K. A.; Justes, D. R.; Bell, R. C.; Castleman, A. W. *J. Phys. Chem. A* **2001**, *105* (18), 4410.

- (128) Schwerdtfeger, P.; Fischer, T.; Dolg, M.; Igelmann, G.; Nicklass, A.; Stoll, H.; Haaland, A. *J. Chem. Phys.* **1995**, *102* (5), 2050.
- (129) Zemski, K. A.; Bell, R. C.; Castleman, A. W. *J. Phys. Chem. A* **2000**, *104* (24), 5732.
- (130) Deng, H. T.; Kerns, K. P.; Castleman, A. W. *J. Phys. Chem.* **1996**, *100* (32), 13386.
- (131) Kung, H. H. *Transition Metal Oxides: Surface Chemistry and Catalysis*; Elsevier: New York, 1989.
- (132) Bell, R. C.; Zemski, K. A.; Kerns, K. P.; Deng, H. T.; Castleman, A. W. *J. Phys. Chem. A* **1998**, *102* (10), 1733.
- (133) Janssens, E.; Santambrogio, G.; Brümmer, M.; Wöste, L.; Lievens, P.; Sauer, J.; Meijer, G.; Asmis, K. R. *Phys. Rev. Lett.* **2006**, *96* (23), 233401.
- (134) Rothgeb, D. W.; Mann, J. E.; Jarrold, C. C. *J. Chem. Phys.* **2010**, *133* (5), 054305.
- (135) Wyrwas, R. B.; Jarrold, C. C. *J. Am. Chem. Soc.* **2006**, *128* (42), 13688.
- (136) Mann, J. E.; Waller, S. E.; Rothgeb, D. W.; Jarrold, C. C. *J. Chem. Phys.* **2011**, *135* (10), 104317.
- (137) Waller, S. E.; Mann, J. E.; Rothgeb, D. W.; Jarrold, C. C. *J. Phys. Chem. A* **2012**, *116* (39), 9639.
- (138) Wyrwas, R. B.; Robertson, E. M.; Jarrold, C. C. *J. Chem. Phys.* **2007**, *126* (21), 214309.
- (139) Mann, J. E.; Rothgeb, D. W.; Waller, S. E.; Jarrold, C. C. *J. Phys. Chem. A* **2010**, *114* (42), 11312.
- (140) Mayhall, N. J.; Rothgeb, D. W.; Hossain, E.; Raghavachari, K.; Jarrold, C. C. *J. Chem. Phys.* **2009**, *130* (12), 124313.
- (141) Mayhall, N. J.; Rothgeb, D. W.; Hossain, E.; Jarrold, C. C.; Raghavachari, K. *J. Chem. Phys.* **2009**, *131* (14), 144302.
- (142) Rothgeb, D. W.; Mann, J. E.; Waller, S. E.; Jarrold, C. C. *J. Chem. Phys.* **2011**, *135* (10), 104312.
- (143) Rothgeb, D. W.; Hossain, E.; Kuo, A. T.; Troyer, J. L.; Jarrold, C. C.; Mayhall, N. J.; Raghavachari, K. *J. Chem. Phys.* **2009**, *130* (12), 124314.

- (144) Mann, J. E.; Waller, S. E.; Jarrold, C. C. *J. Phys. Chem. A* **2013**, *117* (46), 12116.
- (145) Rothgeb, D. W.; Hossain, E.; Kuo, A. T.; Troyer, J. L.; Jarrold, C. C. *J. Chem. Phys.* **2009**, *131* (4), 044310.
- (146) Hossain, E.; Jarrold, C. C. *J. Chem. Phys.* **2009**, *130* (6), 064301.
- (147) Yoder, B. L.; Maze, J. T.; Raghavachari, K.; Jarrold, C. C. *J. Chem. Phys.* **2005**, *122* (9), 094313.
- (148) Ray, M.; Waller, S. E.; Saha, A.; Raghavachari, K.; Jarrold, C. C. *J. Chem. Phys.* **2014**, *141* (10), 104310.
- (149) Rothgeb, D. W.; Hossain, E.; Mayhall, N. J.; Raghavachari, K.; Jarrold, C. C. *J. Chem. Phys.* **2009**, *131* (14), 144306.
- (150) Richard B. Wyrwas; Bruce L. Yoder; Maze, J. T. M.; Jarrold, C. C. *J. Phys. Chem. A* **2006**, *110* (6), 2157.
- (151) Rothgeb, D. W.; Hossain, E.; Mann, J. E.; Jarrold, C. C. *J. Chem. Phys.* **2010**, *132* (6), 064302.
- (152) Akin, S. T.; Ard, S. G.; Dye, B. E.; Schaefer, H. F.; Duncan, M. A. *J. Phys. Chem. A* **2016**, *120* (15), 2313.
- (153) Hayakawa, T.; Arakawa, M.; Sarugaku, S.; Ando, K.; Tobita, K.; Kiyomura, Y.; Kawano, T.; Terasaki, A. *Top. Catal.* **2018**, *61* (1–2), 119.
- (154) Hayakawa, T.; Egashira, K.; Arakawa, M.; Ito, T.; Sarugaku, S.; Ando, K.; Terasaki, A. *J. Phys. B At. Mol. Opt. Phys.* **2016**, *49* (7), 075101.
- (155) Wu, X. N.; Zhao, Y. X.; Xue, W.; Wang, Z. C.; He, S. G.; Ding, X. L. *Phys. Chem. Chem. Phys.* **2010**, *12* (16), 3984.
- (156) Ding, X. L.; Wu, X. N.; Zhao, Y. X.; Ma, J. B.; He, S. G. *ChemPhysChem* **2011**, *12* (11), 2110.
- (157) Nagata, T.; Miyajima, K.; Hardy, R. A.; Metha, G. F.; Mafuné, F. *J. Phys. Chem. A* **2015**, *119* (22), 5545.
- (158) Hirabayashi, S.; Ichihashi, M. *J. Phys. Chem. A* **2013**, *117* (37), 9005.

- (159) Hirabayashi, S.; Ichihashi, M. *Chem. Phys. Lett.* **2013**, *564*, 16.
- (160) Aubriet, F.; Gaumet, J. J.; De Jong, W. A.; Groenewold, G. S.; Gianotto, A. K.; McIlwain, M. E.; Van Stipdonk, M. J.; Leavitt, C. M. *J. Phys. Chem. A* **2009**, *113* (22), 6239.
- (161) Wu, X.-N.; Ding, X.-L.; Bai, S.-M.; Xu, B.; He, S.-G.; Shi, Q. *J. Phys. Chem. C* **2011**, *115* (27), 13329.
- (162) Ray, M.; Felton, J. A.; Kafader, J. O.; Topolski, J. E.; Jarrold, C. C. *J. Chem. Phys.* **2015**, *142* (6), 064305.
- (163) Felton, J. A.; Ray, M.; Waller, S. E.; Kafader, J. O.; Jarrold, C. C. *J. Phys. Chem. A* **2014**, *118* (43), 9960.
- (164) Nagata, T.; Miyajima, K.; Mafuné, F. *J. Phys. Chem. A* **2015**, *119* (41), 10255.
- (165) Nagata, T.; Miyajima, K.; Mafuné, F. *J. Phys. Chem. A* **2015**, *119* (10), 1813.
- (166) Mafuné, F.; Masuzaki, D.; Nagata, T. *Top. Catal.* **2018**, *61* (1–2), 42.
- (167) Gentleman, A. S.; Addicoat, M. A.; Dryza, V.; Gascooke, J. R.; Buntine, M. A.; Metha, G. *F. J. Chem. Phys.* **2009**, *130* (16), 64311.
- (168) Gentleman, A. S. The Effect of Sequential Oxidation and Composition on the Structural and Electronic Properties of Gas Phase Transition-Lanthanide Bimetallic Clusters, PhD Thesis, The University of Adelaide, 2014.
- (169) Nagata, T.; Miyajima, K.; Mafuné, F. *J. Phys. Chem. A* **2016**, *120* (39), 7624.

Chapter Two

Experimental Apparatus, Theory and Methodology

This chapter details the methods used to (i) produce gas phase gold-cerium oxide clusters, (ii) separate photo-ionised cluster species by their mass/charge ratios, and (iii) investigate the electronic and vibrational properties of those cluster species using photo-ionisation techniques. This chapter is presented in three such parts. Each part presents a discussion on the underlying theory, details of the experimental apparatus and the experimental methodology utilised.

A general overview of cluster production techniques will initially be presented with a discussion of the methods used to produce gas phase clusters at sufficiently low rovibronic temperatures to facilitate spectroscopic probing. This will be followed by a description of time-of-flight mass spectrometry (TOFMS) techniques; beginning with an introduction to the methodology of TOFMS and then a description of the Wiley-McLaren TOF utilised in experiments. Lastly, a description of the theory underlying Photo-Ionisation Efficiency (PIE) spectroscopy will be presented followed by details of the PIE experiment and how the adiabatic ionisation energy is determined for each cluster species.

2.1. Generation of Gas Phase Metal Clusters

2.1.1. A Brief History of Cluster Production Methods

The first recorded attempts to generate gas phase metal clusters date back to 1935 with the production and subsequent recording of absorption and emission spectra for the Pb_2 dimer¹. This experiment used a thermal vapourisation method where metal powders were heated to temperatures above their boiling points, typically in excess of 1400°C. The effectiveness of this method was limited for a number of reasons. Firstly, the method was restricted to soft metals, such as lead and coinage metals, due to their relatively low boiling temperatures. Secondly, the high temperatures typically produced an ensemble of clusters in highly excited vibrational states. This greatly complicated any spectroscopic measurements due to the presence of hot band transitions. As an example, the band heads recorded in the initial Pb_2 emission spectrum discussed previously were later found to be incorrectly assigned; a correct assignment was eventually published by Bondybey and English in 1977².

In 1981 Dietz et al.³ proposed a simple, highly effective method for generating clusters of any metal species in high abundance. Their method utilised a pulsed laser which was focussed onto the surface of a metal rod or disk. The high optical density of the laser pulse produced localised boiling on the surface of the target metal – in a process known as *ablation* – causing a vapour of metal atoms to be released. A pulse of inert He gas then carried the vapourised metal atoms through a series of condensing tubes, causing two-body collisions and formation of metal clusters via association reactions. Laser ablation was found to be advantageous over the thermal vapourisation method discussed previously since it produced a metal vapour with low spatial and temporal separation; this allowed for the production of highly dense molecular beams containing the species of interest. Furthermore, the temperature of the metal rod at the focal point of the laser beam has been estimated to be as high as 10,000 K⁴; allowing clusters to be produced from most metals.

The laser ablation method developed by Smalley and co-workers additionally utilised a novel method to cool the cluster species such that spectroscopic techniques were not significantly complicated by hot band transitions. This was drawn from previous work in 1977 by Smalley,

Wharton and Levy⁵ who, borrowing from some theoretical work by Kantrowicz and Grey⁶, developed a simple method of cooling gas phase clusters utilising a supersonic expansion. The method was relatively simple and required only a high-pressure source of inert atomic gas, an aperture to pass the gas through, and an adequate pump to maintain low downstream pressure. The aperture was designed as a series of tubes with tapered diameters – known as condensing tubes – which facilitated turbulent flow of the vapourised metal particles. The condensing tubes were designed such that the internal diameter was far greater than the mean free path of the inert gas to effect a high number of collisions and subsequent cluster formation via association reactions. As the gas particles flow through the condensing tubes into an open region held under vacuum they undergo a hydrodynamic supersonic expansion process. This differs from a free expansion, in which: (i) the motion of gas particles is random and typically represented by a Maxwellian distribution; and (ii) the molecular beam both within the condensing tubes and immediately downstream of the aperture is effectively collisionless, offering no significant cooling of the entrained clusters⁵. A supersonic expansion causes the enthalpy associated with random motion to be converted to a directed mass flow in which the gas particles all display a narrow velocity distribution in a uniform direction⁶. This causes the formation of a dense cloud immediately downstream of the condensing tubes with a high collision rate between the entrained gas particles. Given the population of inert gas particles in the cloud far outweighs that of any formed cluster species, clusters will primarily undergo two body collisions with the inert gas particles to effect a cooling of both their rotational and vibrational degrees of freedom. Concomitantly, the translational degrees of freedom of the entrained clusters are cooled by the isentropic expansion of the molecular beam as it traverses the low pressure region to cause a narrowing of the velocity distribution⁵. The advantages of this are twofold. Firstly, collision rates become reduced to the point where the cluster species are effectively isolated from each other. This minimises the effects of intermolecular interactions on any subsequent spectroscopic measurements. Secondly, the narrow velocity distribution improves the resolution of any subsequent mass spectra, as will be discussed in a later section.

The inert gas utilised in supersonic expansions is usually helium, for a number of reasons. Firstly, atomic gases in general do not store energy in rotational or vibrational degrees of

freedom. Secondly, He atoms, by way of their small electron cloud – and thus weak van der Waal forces – have minimal interaction with each other; thus preventing the gas from condensing during the cooling process⁵. Finally, and most pertinently, He provides highly efficient cooling; a free jet of He gas expanded into a vacuum has been reported to reach temperatures as low as 0.03 K⁵. Unfortunately, this does not mean the cluster species entrained in the He pulse can be cooled to such cryogenic temperatures. Polyatomic cluster species, unlike a He atom, possess both rotational and vibrational modes – in addition to translational degrees of freedom – and a dense electronic structure. Cooling of both the translational and rotational degrees of freedom for clusters through collisions with He atoms have both been shown to easily achieve temperatures comparable to that of the inert gas^{5,6}. However, vibrational cooling is considerably less efficient; vibrational temperatures of supersonically expanded cluster species typically reflect the temperature of the condensing tube through which they were expanded rather than the temperature of the inert gas⁷. Therefore, unless specific effort is directed toward cooling the condensing tubes, the vibrational temperatures of the entrained clusters are generally ca. 300 K which reflects the ambient temperature. While this temperature allows some vibrational hot bands in most polyatomic species to be accessible, only the lowest energy hot bands would be accessed with any noticeable Boltzmann population in most cases. Electronic cooling is the least efficient process, and may vary significantly with the electronic state of the relevant cluster⁸.

2.1.2. *Generation of Bi-Metallic Clusters in the Gas Phase*

Following the initial work by Smalley and co-workers on metallic clusters, attention turned towards finding a suitable method to generate gas phase cluster species containing two or more metallic elements. Initial methods utilised a single laser ablation source and combined the metals of interest in either alloy rods⁹ or pressed disks¹⁰. While these methods were effective in producing mixed metal clusters with little-to-no modification of the experimental setup developed by Smalley et. al., there were considerable limitations. Not all metals were available as a powder suitable to be pressed into a disk; some combinations of metals were incompatible and not able to form alloys; and the mixing ratio of the clusters was fixed by the composition of the source material.

In 1989 Nonose et al.¹¹ proposed a unique method to generate bi-metallic clusters containing any ratio of source elements. Their method maintained the salient features of the setup initially used by Smalley et al.; however, they incorporated a second metal rod which was ablated by an independent laser. This allowed the mixing ratio to be controlled simply by adjusting the relative powers of the two ablating lasers and produced bi-metallic clusters in good abundance. A significant drawback to this method, however, is the added complexity from the employment of multiple lasers; the relative timings of each laser needs to be controlled in order to effectively produce bi-metallic clusters. More recent methods have proposed the use of a single laser coupled with a beam splitter and beam attenuators to simultaneously ablate two metal rods¹². Despite this, the dual ablation setup developed by Kaya and co-workers is a highly effective method for generating bi-metallic clusters in any mixing ratio which does not require a complex optical setup to split a single beam onto multiple targets. Moreover, the use of multiple ablating lasers allows the user to adjust both the power and the relative timings for each laser separately to optimise the mixing ratios of the metal species. The dual ablation method has been used effectively to produce clusters containing not only alkali and transition metals^{9,13-15}, but also metal-carbides¹⁰ and transition metal-lanthanide¹⁶ complexes.

2.1.3. Experimental Details for Cluster Production

The experimental method applied in this thesis is adopted from the dual ablation method developed by Kaya et al.¹¹. A schematic for the experimental setup is presented in Figure 2.1. The pertinent regions within the experimental setup include the cluster source (**A**) where gas phase bi-metallic clusters are prepared; and the time-of-flight (TOF) region (**B**) where clusters are photo-ionised, mass separated and detected. Both of these regions will be discussed in detail later in this chapter. The experimental apparatus shown in Figure 2.1 is held under a vacuum of ca. 10^{-7} Torr using two identical cryogenically cooled 6-inch diffusion pumps (Varian VHS-6) backed by identical rotary forepumps (Welch 1397) (**C**). The vacuum in both the cluster source and TOF regions are monitored using tungsten ion gauges (Duniway T100K) (**D**). Additional features built within the experimental apparatus are liquid nitrogen bellows (**E**) to facilitate vibrational cooling of the cluster species to ca. 77 K, and additional gas lines (**F**) to introduce reactant gases to the cluster species.

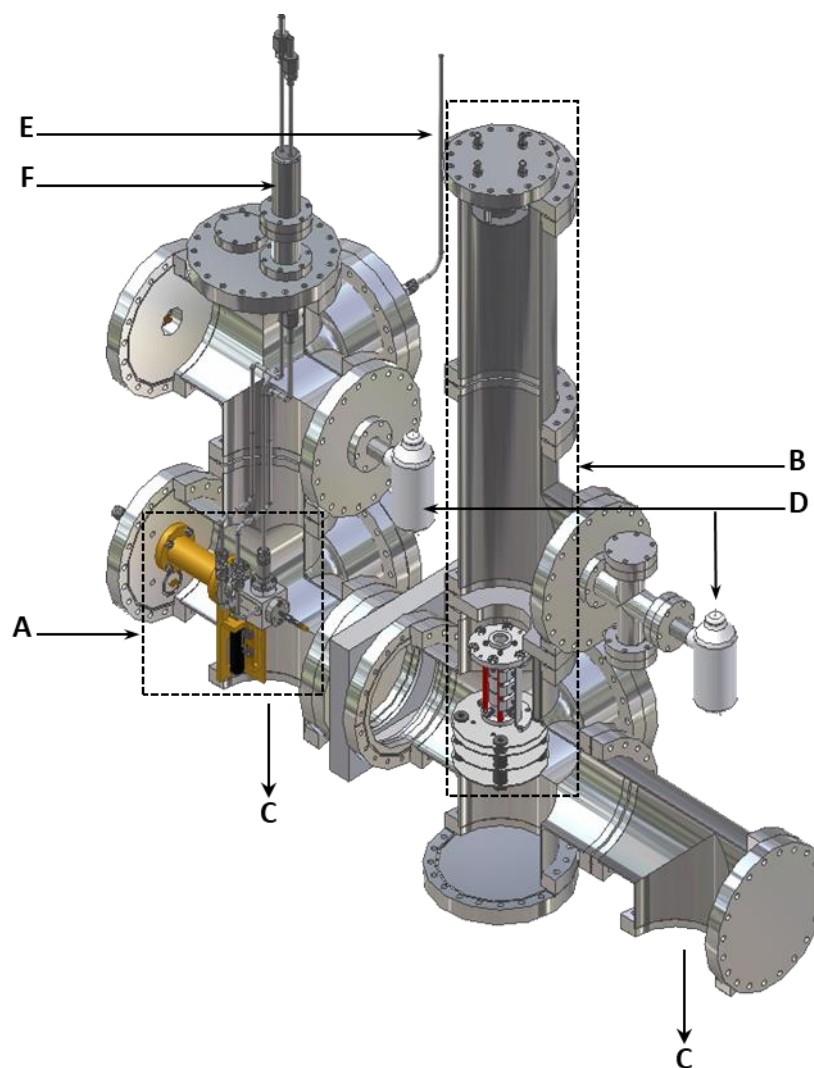


Figure 2.1: Experimental setup. Labelled components include the cluster source (A), time-of-flight region (B), diffusion pumps (C – not shown), ion gauges (D), reactant gas line (E) and cryogenic cooling bellows (F).

A detailed schematic for the cluster source region – shown as (A) in Figure 2.1 – is presented in Figure 2.2. The key components in the setup include a pulsed nozzle (General Valve, Series 9, 20 μm aperture) coupled to a gas line (1), a home-made stainless steel ablation cap with an internal ablation channel of 3 mm diameter and two bores perpendicular to the ablation channel each with 2 mm diameter (2), a 2 mm diameter gold rod (Sigma-Aldrich, 99.99%) (3), a 2 mm diameter cerium rod (DXL, 99.9%) positioned 9 mm behind the gold rod in the direction of the gas flow (4), a DC motor coupled with a translating-rotating screw mechanism

(Oriel, motor-mike 18014) (5) and a condensing tube (6). The condensing tube has a length of 25 mm with an internal diameter of 2 mm.

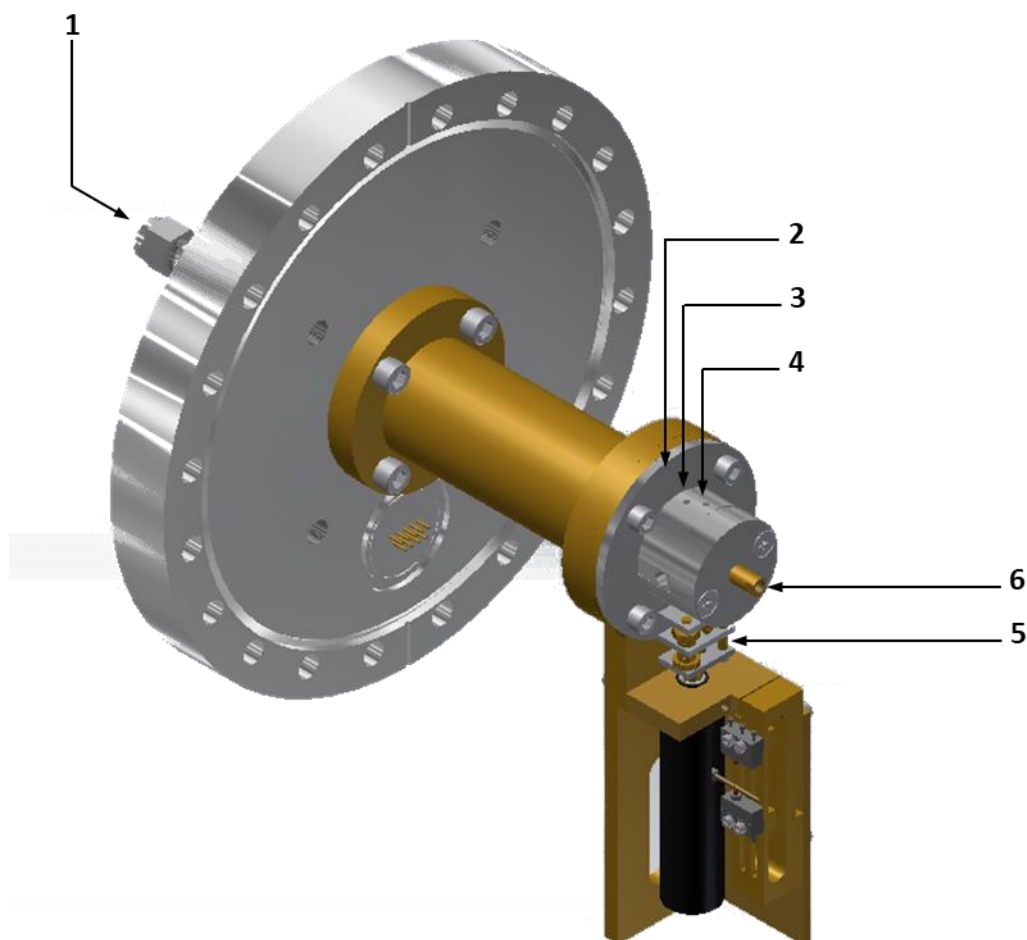


Figure 2.2: Cluster source region. Labelled components include the pulsed nozzle (1), ablation cap (2), gold rod (3), cerium rod (4), trans-rotator (5) and condensing tube (6).

Helium carrier gas (CIG gases, 99.98%) at a pressure of 80 psi is delivered via the pulsed nozzle (1) into the ablation channel (2). As this occurs, the translating-rotating gold and cerium rods (3, 4) are ablated by 532 nm pulses from the second harmonic output of two independent Q-switched Nd:YAG lasers (Big Sky Laser Ultra-CFR, 10 Hz, 532 nm and Quantel Ultra-CFR, 10 Hz, 532 nm) focused onto each rod via 250 mm focussing lenses. The constant translation and rotation of the gold and cerium rods is driven by the screw mechanism (5) and ensures that a fresh surface is provided with each laser shot. The translation ranges of the rods are set using limit switches on the screw mechanism and are typically set to cover a range of ca. 15 mm.

The laser pulses from the Nd:YAG ablation lasers are delivered to the rods via 1 mm channels in each side of the ablation cap. The gold and cerium rods – and the corresponding ablation channels – are offset by 9 mm to prevent ablation of both rods by a single laser. Laser photon densities used to ablate the gold and cerium rods are approximately 2 $\mu\text{J}/\text{pulse}$ and 12 $\mu\text{J}/\text{pulse}$, respectively, with 6 – 8 ns pulse widths for both lasers. The gold and cerium rods are ablated 540 μs and 560 μs respectively after the He gas is pulsed into the source region. The relative timings of the pulsed nozzle and the two ablation lasers – which are critical for the effective production of clusters – are controlled externally using a digital delay generator (Griffith University, TARDIS II).

Following the ablation process, the vapourised metal atoms are carried by the inert gas through a 25 mm long condensing tube with a 2 mm internal diameter (6). The turbulent flow initiated within this region induces a high collision rate where two-body collisions between metal atoms and clusters cause the formation of clusters via association reactions as follows:



Where M represents the metallic species of interest (in this case Ce and/or Au), and m and n designate the number of atoms within each cluster, which can take any integer value (for an atom, m or n equals 1). Due to both surface oxidation of the cerium rod and residual O_2 in the evacuated chamber, a number of metal oxide clusters are additionally produced in the condensation process. Oxidation occurs when metal clusters undergo 2-body collisions with atomic or molecular oxygen in similar processes to that described in Equation 2.1. Previous work by this group has shown the availability of oxygen through surface oxidation and residual O_2 is sufficient for the production of oxidised clusters in good abundance^{16,17}. Other groups, such as Castleman and co-workers, have also utilised residual oxygen to produce a number of metal oxide cluster species^{10,12,18–24}. Conversely, some groups have increased the oxygen content in the cluster source region by seeding small amounts of oxygen (ca. 1%) in the He carrier gas^{14,25,26}. Attempts were made in this work to increase the amount of available oxygen in the cluster source by both seeding various ratios of oxygen into the carrier gas (0.01% – 5%)

and feeding oxygen into the flow reactor via a second pulsed nozzle positioned between the ablation cap (2) and the condensing tube (6). Neither method produced a significant difference in the abundances of metal oxide clusters and consequentially were both discontinued.

Within the condensing tubes (6), collisions between the formed cluster species and the helium atoms induce cooling of the translational, rotational and vibrational degrees of freedom for the clusters. Whilst further translational and rotational cooling occurs during the supersonic expansion, vibrational cooling is predominantly dependent on collisions during the condensation phase. As stated previously, due to thermal equilibration of the gas with the internal walls of the condensing tube, the vibrational temperature for the clusters can only be cooled to the same temperature as the condensing tube (ca. 300 K). The experimental apparatus does have the ability to introduce cryogenic cooling using a flow reactor which can be installed between the ablation cap (2) and the condensing tube (6). The flow reactor can be cooled with liquid nitrogen to in-principle achieve temperatures of near 77 K. While attempts were made to cool the cluster species using this method, the relatively small size of the N₂ reservoir in the flow reactor caused the temperature of the internal walls to return to room temperature over a relatively short time. The non-equilibrated temperature of the condensing tubes caused variations in the pressure of the inert gas, which subsequently affected the mass flow rate of the molecular beam in the supersonic expansion. Attempts at cryogenic cooling of the cluster species were therefore not continued. Despite best efforts at collisional cooling, it is apparent in the following chapters that not all cluster species are thermally equilibrated at the time of spectroscopic probing; this is shown through residual ion signal in the PIE spectra at energies below the ionisation threshold. The causes of non-uniform cooling are twofold. Firstly, the short time spent by the clusters in the condensing tubes limits the number of cooling collisions with the inert gas. Extensive work by Duncan²⁷ has shown this issue can be somewhat alleviated through the use of expansion gases that provide more efficient cooling (the author advocates a mixture of 75% neon and 25% helium, but also advises that the most appropriate cooling gas for the relevant cluster species varies with experimental conditions such as the cluster composition and source of laser vapourisation). Secondly, and more pertinently, the internal energies of clusters tend to increase with cluster

growth^{10,18,28–30}. Larger clusters, which require more collisions and are therefore more likely to be formed near the exit of the condensing tube, can still be quite hot – in terms of both vibrational and electronic degrees of freedom – when entering the supersonic expansion.

Following cluster formation in the condensing tubes, the clusters are then supersonically expanded into a vacuum. The spectroscopic advantages of a supersonic expansion process are threefold. Firstly, the rapid expansion causes significant translational and rotational cooling to temperatures of ca. <6 K and 5 K respectively – as reported by Hopkins et. al.³¹ – to greatly simplify their thermal distribution and resultant spectroscopic profile. Secondly, the hydrodynamic-type expansion causes the clusters to be entrained in a highly dense gas pulse which greatly facilitates spectroscopic probing. Finally, the narrow velocity distribution and uniform direction of the cluster species produces a collision free environment over the time frame during which spectroscopic probing occurs (ca. 6 – 8 ns in this case, which represents the pulse width of the ionisation laser) where the clusters are essentially isolated. Clusters are therefore not affected by collision-induced non-radiative processes during spectroscopic probing³². The supersonic expansion, however, is quite inefficient with regard to cooling both the vibrational and electronic temperatures of the entrained clusters species which can lead to spectroscopic probing of a non-equilibrium of vibrational and electronic states. The former may cause an increase in thermal tailing of subsequent PIE spectra (the specifics of which are discussed later in this chapter) due to hot clusters being spectroscopically probed from vibrationally excited states. However, test calculations presented in Appendix D have shown this effect to be quite small. The latter can have an unpredictable effect on subsequent PIE spectra since the effectiveness of electronic cooling varies with the specific electronic state⁸. Thus, the existence of metastable states in the molecular beam – which may appear as secondary, weaker PIE onsets – are considered in this work.

2.2. Time of Flight Mass Spectrometry

Following the production of gas phase bi-metallic clusters and cooling by supersonic expansion, the clusters then enter the TOF region (shown as **B** in Figure 2.1) where they are photo-ionised and separated by their mass/charge ratios. A discussion of the methods used to separate the clusters by their mass/charge ratios will now be presented; details of the photo-ionisation process are presented later in this chapter.

2.2.1. Theoretical Background

Mass spectrometry presents a simple, highly accurate method of detecting cluster species by their mass/charge (m/z) ratios. A complete spectrum of cluster species is collected with each ionising laser pulse. Moreover, the mass spectrometer is connected to an oscilloscope to facilitate collection of data in real time.

The first time-of-flight (TOF) mass spectrometer was developed by Aston³³ in 1919 and consisted simply of an ion source and a detector within an evacuated chamber. While considerable improvements have been made over the years in both the methods of ion production (including electron bombardment, laser desorption and chemical ionisation processes) and ion focussing (such as delayed ion extraction and reflectrons), the basic principles remain the same. All TOF mass spectrometers require an acceleration stage, a field-free “drift region”, and a detector. A schematic of a simple TOF is presented in Figure 2.3.

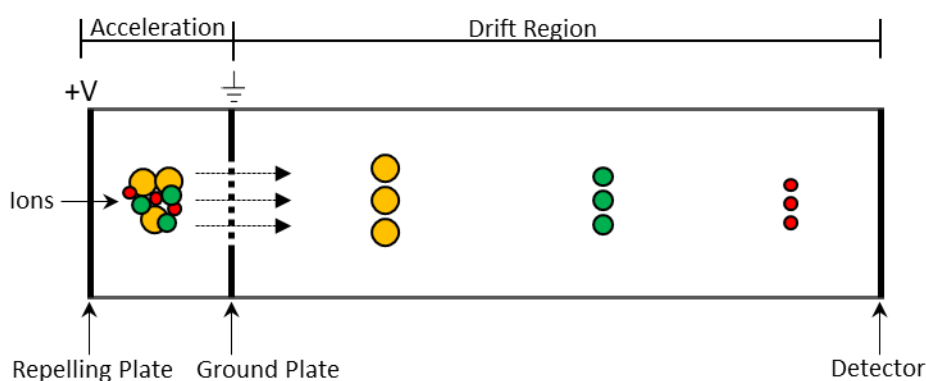


Figure 2.3: Schematic for a simple time-of-flight (TOF) Mass Spectrometer.

The acceleration region, as shown in Figure 2.3, consists of a *repelling plate* held at high voltage, and a *ground plate* which is earthed. The potential difference between the repelling and ground plates produces an equipotential electric field which can accelerate ions to high velocities. Ions subsequently enter the field-free *drift region* with velocities inversely proportional to the square root of their masses

†:

$$v = \sqrt{\frac{2Vzq}{m}} \quad (2.2)$$

For ions with mass m , velocity v and formal charge z , accelerated by a potential V . The term q represents the charge of an electron as 1.602×10^{-19} C.

Due to the field-free nature of the drift region, all ions retain a constant velocity. The time of flight through a drift region of length d is dependent on the ion m/z ratio as follows:

$$t_{drift} = \frac{d}{\sqrt{2Vzq}} \sqrt{\frac{m}{z}} = k \sqrt{\frac{m}{z}} \quad (2.3)$$

The total time of flight for an ion – from acceleration to detection – can be considered as a summation of the acceleration time, the drift time and the response time of the detector. However, the former and latter can both be treated as negligible compared to the drift time; the total time of flight can thus be approximated as the drift time:

$$TOF = t_{acceleration} + t_{drift} + t_{detection} \cong t_{drift} \quad (2.4)$$

† Derivation of this formula arises from the consideration that the ion kinetic energy is provided by the potential field, i.e. $K = \frac{1}{2}mv^2 = Vzq$

Finally, all ions discussed in the context of this work are singly charged cations (i.e. $z = +1$); the time of flight can therefore be simplified as follows:

$$TOF \cong k \sqrt{\frac{m}{z}} = k\sqrt{m} \quad (\text{for } z = +1) \quad (2.5)$$

The flight times and the intensities of each ion signal are collected in a time of flight spectrum. A mass spectrum is then constructed by fitting mass values to the peaks in the time of flight spectrum. Following from Equation 2.5, the relationship between the ion mass and the time of flight can be expressed as follows:

$$\sqrt{m} = \frac{\sqrt{z}}{k} TOF = k' TOF \quad (2.6)$$

Where k' represents a constant of proportionality. Ion masses are determined by a least-squares fit to the flight times of each ion peak in the mass spectrum. The resolution of the mass spectrometer, R , is dependent on the total flight time for particles in the drift free region as shown by the following equation:

$$R = \frac{m}{\Delta m} = \frac{t_{drift}}{2\Delta t} \quad (2.7)$$

The terms Δm and Δt in the above equation represent the smallest resolvable mass and time increments, respectively. Given that the flight time is proportional to the length of the drift free region as previously shown in Equation 2.2, the resolution of a mass spectrometer can be increased quite simply by employing a longer drift free region.

2.2.2. Single and Dual Stage Ion Extraction Methods; Wiley McLaren TOFMS

The simple TOF example described in the previous section represents the initial mass spectrometer design by Aston in 1919³³. This design utilised a single acceleration stage in a

process known as single stage ion extraction. While this method was able to successfully separate ions by their relative m/z ratios, it suffered from poor resolution due to the neglect of spatial and kinetic distributions of the neutral species in the acceleration region^{34,35}.

2.2.2.1. Spatial Distributions in TOFMS

Spatial distribution in the mass spectrometer arises from neutral species occupying different spatial coordinates in the acceleration region prior to ionisation. A neutral particle that becomes ionised closer to the repelling electrode will spend a longer time in the potential field and undergo greater acceleration than a particle that is ionised near the ground electrode. Ions with identical masses will therefore enter the drift region with a range of velocities corresponding to their respective starting points in the acceleration region. A consequence of the single stage ion extraction process is that the spatial focus plane, being the point where the particles entering the drift region with higher velocities catch up to the slower particles of identical mass, is described with the following relationship:

$$d = 2s \quad (2.8)$$

Where d and s represent the distances that particles travel in the drift region and the acceleration or extraction region, respectively. The effects of spatial distribution are minimised when the ion detector is placed in the spatial focus plane which, as a consequence of Equation 2.8, produces a very short drift free region and therefore limited resolution.

In 1955 Wiley and McLaren³⁶ devised a method to correct for spatial distributions using a dual stage ion extraction process. They utilised a low voltage extraction stage prior to the high voltage acceleration stage in order to generate a smaller velocity distribution of same-mass species. The smaller velocity difference allows for a longer flight time – and thus a longer drift region – before the faster ions catch up to the slower ions; this affords a spatial focus plane with greater resolution than the single stage ion extraction process. A schematic of the dual stage ion extraction process is shown in Figure 2.4.

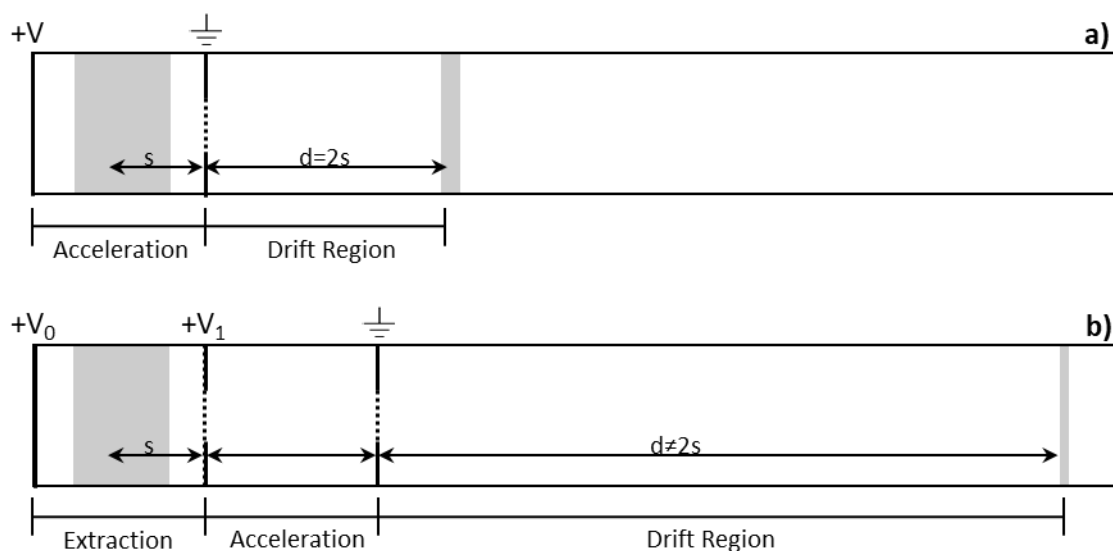


Figure 2.4: Spatial distributions for (a) a traditional TOFMS employing single stage ion extraction; and (b) a Wiley McLaren TOFMS with dual stage ion extraction. Spatial distributions of ions within the acceleration/extraction regions and at the spatial focus plane are shown in grey.

2.2.2.2. Velocity Distributions in TOFMS

Velocity distributions in the mass spectrometer result from particles situated within the same spatial plane in the acceleration region, but with different initial velocities relative to the applied potential field. Ions with an initial velocity component towards the detector will experience a greater drift velocity – and thus a shorter time of flight – than those travelling perpendicular to the applied field. Conversely, ions initially travelling toward the repelling plate will experience a turn-around time and will take longer to reach the detector³⁷. The combination of both of these events will produce a broad temporal distribution for same-mass ions reaching the detector. This effect can produce a loss in resolution due to ions with different masses reaching the detector at the same time.

Velocity distribution effects are significantly reduced in the context of this work by the supersonic expansion process which facilitates a low velocity distribution as described previously⁵. Moreover, the TOF is mounted perpendicular to the trajectory of the molecular beam. Alternative methods involve utilising a pulsed field to effect a delayed ion extraction³⁸; in this method the time delay increases the spatial distribution of the ions prior to

acceleration, which can then be corrected utilising the Wiley McLaren setup described previously.

2.2.3. Details for Wiley McLaren TOFMS

A schematic for the Time of Flight Mass Spectrometer used in the experimental setup is presented in Figure 2.5. The construction is based on the original design by Wiley and McLaren³⁶ with a mass resolution of approximately 700. The acceleration stage (**1**) comprises a three-electrode stack that is used to accelerate cations into the drift free region. This includes a repelling plate (**1a**), an extraction plate (**1b**) and a ground plate (**1c**). All three electrodes are circular aluminium plates with a 70 mm diameter and 2 mm thickness. 15 mm diameter holes are drilled in the centre of the extraction and ground plates to facilitate ion flow. Both holes are covered by a nickel mesh (90% transmission, Precision Eforming) to maintain a constant electric field between the electrodes and ensure the drift region is kept field-free. Potentials of +1809 V and +1427 V are applied to the repelling and extraction plates, respectively. Neutral clusters in the supersonically expanded molecular beam are photo-ionised between the repelling and extraction plates. The resulting cations are then accelerated into the drift region (**2**).

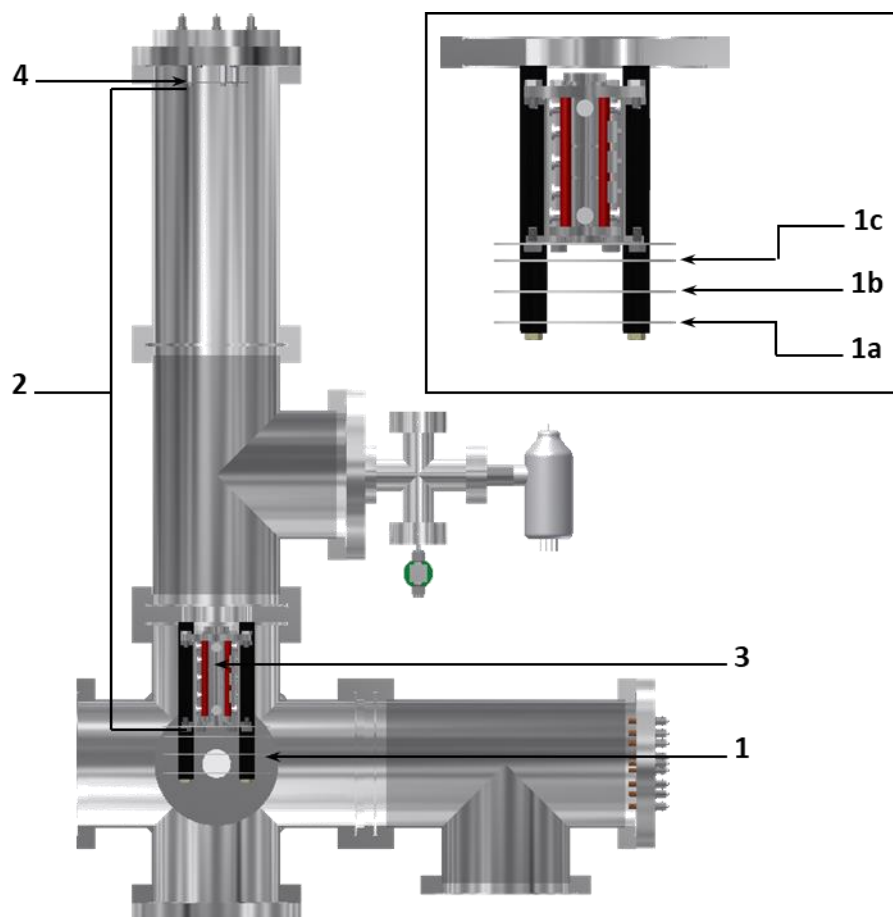


Figure 2.5: Schematic of the Wiley McLaren TOF showing the acceleration stage (1), drift region (2), einzel lens (3) and detector (4). **Inset:** Acceleration stage and einzel lens setup. The repelling plate (1a), extraction plate (1b) and ground plate (1c) are shown.

The drift region provides a field-free distance of approximately 1 m between the acceleration stage and the detector. Ions in this region are separated by their flight times corresponding to their m/z ratios. A built-in ion optics assembly containing an einzel lens (3) with an internal diameter of 10 mm and set at a voltage of -797 V is used to focus the ion beam onto the detector. The ion optics assembly additionally contains two sets of ion deflectors built perpendicular to the ion beam which correct ion trajectories in the drift region without affecting the flight time. However, these ion deflectors were not used.

Once the ions complete their flight in the drift region they collide with an ion detector (4). The detector consists of a series of three parallel plates stacked in succession which are labelled

the front plate, the back plate and the collection plate. The front and back plates are both comprised by microchannel plate detectors (EI-Mul, MCP-M585; $\phi = 25$ mm), which consist of a parallel series of continuous-dynode electron multiplier tubes³⁹. Voltages of -1100 V are applied to both the front and back plates to give a total voltage difference of -2200 V. The collection plate, which consists of a circular aluminium plate, is held at ground. The signal generated at the collection plate is amplified 25x by a pre-amplifier (Stanford Research SR250) and sent to an oscilloscope (LeCroy 9350AM, 500 MHz) where it is averaged over 1500 laser ionisation pulses.

2.3. *Detection and Elucidation of Cluster Properties*

2.3.1. *Current Spectroscopic Methods Utilised for Metal Clusters*

One of the salient features of metallic clusters is their ability to transition freely between geometric isomers with low-lying electronic minima and high degrees of vibrational freedom. Ironically, it is this property which makes the elucidation of cluster properties problematic. Direct probe techniques have so far achieved limited, albeit notable successes in resolving both the electronic and geometric properties of a number of simple clusters systems. Some of these techniques involve photo-ionisation of the species of interest, such as Photo-Ionisation Efficiency spectroscopy, resonant two-photon ionisation spectroscopy and Zero Electron Kinetic Energy spectroscopy^{16,40-80}. Other techniques such as Infrared Multiphoton Dissociation (IR-MPD) and Collision Induced Dissociation (CID) utilise IR photons and noble gas atoms respectively to dissociate clusters encapsulated in an ion trap^{24,26,28,81-127}. Direct probe techniques have been successfully utilised for a number of small transition metal clusters to determine properties such as spectroscopic constants, ionisation energies, dissociation energies and vibrational fine structure. However, these methods by themselves do not provide any information with regard to either cluster geometries or charge transfer interactions, both of which are pertinent toward the understanding of cluster-surface interactions in the cluster-surface analogue.

A pragmatic method of investigating cluster properties involves the consolidation of experimental data and computational simulations. This has been shown to be particularly

effective by Haslett, Bosnick and Moskovitis¹²⁸ who compared Raman spectra of small silver clusters embedded in an Ar matrix with calculated vibrational modes of DFT optimised Ag_n structures. Not only were the authors able to verify the correct geometries of their calculated cluster species, but they also reported several previously postulated Ag_n structures as incorrect. Moreover, the authors predicted the size at which silver clusters transition from planar to 3-dimensional structures. The consolidation of experimental and calculated data has become frequently utilised as a powerful way to elucidate the geometries and electronic structures of complex cluster species^{25,26,46,48,68,91,124,129–134}. A recent method developed by Gentleman and Dryza^{17,135} compares experimental and simulated Photo-Ionisation Efficiency spectra. This method has been shown to accurately predict the geometries of transition metal-lanthanide oxide clusters.

2.3.2. Spectroscopic Theory – The Born-Oppenheimer Approximation

A discussion of the Photo-Ionisation Efficiency spectroscopy will be presented later in this chapter. However, this discussion is best preceded by a brief description of the concepts underlying conventional electronic spectroscopy; the principles of both techniques are quite similar. A discussion of electronic spectroscopy begins with the non-relativistic Hamiltonian operator, which for any molecular system can be defined as follows¹³⁶:

$$\hat{H} = -\frac{1}{2}\sum_{i=1}^N \nabla_i^2 - \frac{1}{2}\sum_{A=1}^M \frac{1}{M_A} \nabla_A^2 - \sum_{i=1}^N \sum_{A=1}^M \frac{Z_A}{r_{iA}} + \sum_{i=1}^N \sum_{j>i}^N \frac{1}{r_{ij}} + \sum_A^M \sum_{B>A}^M \frac{Z_A Z_B}{R_{AB}} \quad (2.9)$$

In the above equation \hat{H} represents the non-relativistic Hamiltonian operator for a molecular system containing M nuclei and N electrons (the terms i, j and A, B denote individual electrons and nuclei, respectively). The term Z represents the nuclear charge while the r_{ij} , r_{iA} and R_{AB} terms represent electron-electron, electron-nuclear and nuclear-nuclear separations, respectively. The molecular Hamiltonian shown in Equation 2.9 consists of five independent operators; these include the electronic kinetic energy, nuclear kinetic energy, electron-nuclear electrostatic attraction, electronic electrostatic repulsion and nuclear electrostatic repulsion.

The Schrödinger equation, using the Hamiltonian operator shown in Equation 2.9, is unable to be solved exactly for all but the simplest of systems (the Schrödinger equation is discussed in Chapter 3). However, the Hamiltonian can be simplified greatly by taking advantage of the fact that both protons and neutrons are approximately 1800 times heavier than electrons. Given that nuclei often contain tens of protons and neutrons, a nucleus is therefore typically far heavier than the electrons orbiting it; as an example, the mass of an oxygen nucleus is nearly 30,000 times the mass of an electron. Consequentially, it is a reasonable assumption that the significantly greater masses of the nuclei will cause nuclear motion to be far slower than electronic motion. This is the premise of the Born-Oppenheimer Approximation: because nuclei move much slower than electrons, the nuclear motion within any electronic transition can be considered to be negligible. Therefore, the spatial coordinates for any nuclei can be considered as effectively fixed within the time frame of an electronic transition. The nuclear kinetic term in Equation 2.9 then becomes zero. Moreover, the nuclear-nuclear repulsion can be treated as a constant; this term can then be removed from the Hamiltonian since introducing a constant to an eigenvector will only shift the corresponding eigenvalue by a constant amount. This leaves a greatly simplified Hamiltonian operator with only three terms. The Hamiltonian can be further simplified by considering the nuclei as stationary point charges; the electron-nuclear Coulombic interaction can now be described analogous to an electron in a constant potential field. Given that all the terms in the Hamiltonian now describe electronic motion, the term “electronic Hamiltonian” is now used. The electronic Hamiltonian can be presented as follows:

$$\hat{H}_{elec} = -\frac{1}{2} \sum_{i=1}^N \nabla_i^2 - \sum_{i=1}^N \sum_{A=1}^M \frac{Z_A}{r_{iA}} + \sum_{i=1}^N \sum_{j>i}^N \frac{1}{r_{ij}} = \hat{T}_e + \hat{V}_{Ne} + \hat{V}_{ee} \quad (2.10)$$

In the above equation the terms \hat{T}_e , \hat{V}_{Ne} and \hat{V}_{ee} are used to represent the operators for the electron kinetic energy, the electron-nuclear interaction and the electron-electron repulsion, respectively. The Schrödinger equation becomes more easily soluble using the electronic Hamiltonian operator shown in Equation 2.10 compared to the complete Hamiltonian shown in Equation 2.9. The total energy of the system can be determined by solving the Schrödinger

equation for the electronic Hamiltonian, then adding the energy for nuclear-nuclear interactions as follows:

$$\hat{H}_{elec}\Psi_{elec} = E_{elec}\Psi_{elec} \quad (2.11)$$

and

$$E_{total} = E_{elec} + E_{nuc} \quad (2.12)$$

The term for nuclear motion presented in Equation 2.12 consists of both vibrational and rotational components, where the frequency of the former is typically ca. 10^3 times greater than the latter (there is also a nuclear spin component, however the energetic contribution is negligible and is ignored in this case). The Born-Oppenheimer Approximation can therefore be applied to decouple the vibrational and rotational components in the E_{nuc} term. The energy for a molecular system presented in Equation 2.12 can then be simplified further, as follows:

$$E_{total} = E_{elec} + E_{vib} + E_{rot} \quad (2.13)$$

Where E_{elec} , E_{vib} and E_{rot} represent separate energy eigenvalues corresponding to their respective electronic, vibrational and rotational wavefunctions. In the context of this work, the primary contribution to E_{total} comes from the E_{elec} and E_{vib} terms which comprise the vibronic energy for the system. The rotational energy E_{rot} is treated as negligible.

2.3.3. The Franck-Condon Principle

The Franck-Condon Principle is a logical progression from the Born-Oppenheimer Approximation when considering transitions between two different electronic states. It can be stated as follows:

Because nuclei are far more massive than electrons, an electronic transition takes place much quicker than the nuclei can respond¹³⁷.

Consider a simple molecular system in the ground electronic state with a vibrational potential energy surface defined by the Morse curve shown in Figure 2.6. Neglecting thermal effects for the moment, the molecule will be at a stationary point in the lowest vibrational quanta (i.e. the $v''=0$ state), which corresponds to an energetic minimum with an average internuclear separation of R_e'' . A transition to an upper (either excited or ionised) electronic state via absorption of a photon will cause a rearrangement in the electron distribution. Naturally, this will cause a change in the internuclear separation of the upper state, R_e' , such that $R_e' \neq R_e''$. However, the Born-Oppenheimer Approximation implies the nuclear coordinates will remain fixed at R_e'' during the electronic transition. Therefore, the electronic transition will occur from the stationary point R_e'' on the lower energy potential energy surface to a turning point on the upper state potential energy surface corresponding to the same internuclear separation¹³⁷. Following the electronic transition, the upper state will undergo a change in internuclear coordinates to R_e' – which corresponds to the minimum of the upper state potential energy surface – via vibrational relaxation.

The vibronic transition between electronic states without a change in internuclear coordinates is called a vertical transition; this transition has an intensity, I , which is proportional to the squared overlap of the wavefunctions for the lower and upper state vibrational modes, known as the Franck-Condon Factor (FCF):

$$FCF(v_i, v_k) = \left| \int \Psi_{vib}^{v_i}(R) \cdot \Psi_{vib}^{v_k}(R) dR \right|^2 \quad (2.14)$$

and

$$I \propto FCF(v_i, v_k) \quad (2.15)$$

In the above equations ν_i , ν_k and $\Psi_{vib}^{\nu_i}(r)$, $\Psi_{vib}^{\nu_k}(r)$ represent vibrational quanta and vibrational wavefunctions for the lower and upper states, respectively.

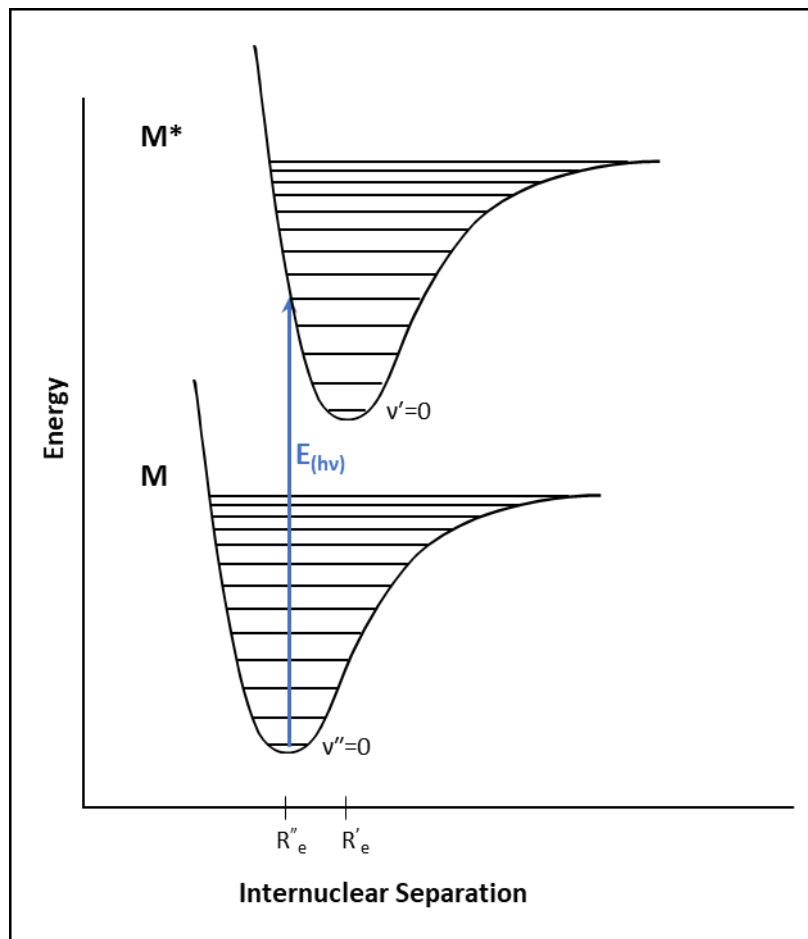


Figure 2.6: Morse curve representation of photo-excitation from a ground electronic state (M) to an excited electronic state (M^*). Photon absorption is designated by a blue arrow. Photo-excitation processes occur with no change in internuclear coordinates from the ground state; this typically corresponds to a turning point on the excited state potential energy surface.

The description of electronic transitions so far has neglected thermal effects, which can also affect the intensity of a vibronic transition. The lower electronic state may contain a number of thermally accessible vibrational overtones in addition to the ground state; these are known as hot bands. The relative population of the hot band ($v''=n$) state to the ground ($v''=0$) state is described by the Boltzmann distribution as follows:

$$\frac{N_{v''=n}}{N_{v''=0}} = \frac{g_n}{g_0} e^{\frac{-\Delta E}{kT}} \quad (2.16)$$

For a molecular system containing g_0 and g_n -degenerate $v''=0$ and $v''=n$ states with an energetic separation of ΔE , the terms $N_{v''=0}$ and $N_{v''=n}$ represent the lower and upper vibrational state populations, respectively, at temperature T . The term k is the Boltzmann constant, i.e. $1.3806 \times 10^{-23} \text{ J.K}^{-1}$. Combining the FCF and Boltzmann distributions detailed in Equations 2.15 and 2.16, an approximation for the transition intensity, I , can be presented as follows:

$$I \propto \left| \int \Psi_{vib}^{v_i}(R) \cdot \Psi_{vib}^{v_k}(R) dR \right|^2 e^{\frac{-\Delta E}{kT}} \quad (2.17)$$

2.3.4. Electronic Spectroscopy

Ignoring vibrations momentarily, absorption of a photon by molecule causes excitation of an electron from its initial electronic state, or molecular orbital, to a higher energy molecular orbital. The electronic transition is deemed "allowed" provided the selection rules for changes in parity, angular momentum and electron spin are followed. The selection rules are as follows¹³⁷:

1. *Only transitions between states with the same spin quantum number (S) are allowed [Spin Conservation Rule]^{138,139}.*
2. *The change in angular momentum between the initial and final states, ΔL (or ΔJ for spin-orbit coupled states, where $J = L + S$), must be either 0 or ± 1 . $L = 0 \leftrightarrow L = 0$ (and $J = 0 \leftrightarrow J = 0$) transitions are forbidden [Angular Momentum Conservation Rule]¹³⁷.*
3. *Any centro-symmetric molecule must undergo a change in parity following an electronic transition [Laporte Rule]¹⁴⁰.*

Provided the electronic transition is allowed, the transition intensity, I , is dependent on the transition electric dipole moment (μ_{fi}); this effectively describes the change in electron density between the initial and final states as follows:

$$I \propto |\mu_{fi}|^2 \quad (2.18)$$

Where

$$\mu_{fi} = \int \Psi_f^* \hat{\mu} \Psi_i d\tau \quad (2.19)$$

In the above equation, $\hat{\mu}$ represents the electric transition moment operator; the term τ represents the span of coordinates over which electrons are located.

Considering now a vibronic transition, in which the vibrational wavefunctions of the lower and upper states must also be taken into account, the transition intensity is additionally dependent on the Franck-Condon Factor. Furthermore, the consideration of vibrational modes also means transitions from hot bands can now occur. The transition intensity can be represented as follows:

$$I \propto |\mu_{fi}|^2 \left| \int \Psi_{vib}^{v_i}(R) \cdot \Psi_{vib}^{v_k}(R) dR \right|^2 e^{\frac{-\Delta E}{kT}} \quad (2.20)$$

For a vibronic transition to occur, the photon energy must correspond to the exact difference in energy between the lower and upper vibronic states. Any photon which does not meet this requirement is not absorbed by the molecule. An absorption spectrum for any molecule will then consist of a series of peaks which correspond to allowed vibronic transitions. The intensity of each peak will be primarily determined by the Franck-Condon overlap and the population of the initial vibronic state; assuming that all transitions within the energetic region of interest occur between the same electronic states, the electric transition moment can be regarded as a constant.

2.3.5. Photo-ionisation Spectroscopy

Photo-ionisation is the process in which an atomic or molecular species, M, absorbs a photon with sufficient energy $h\nu$ to eject an electron from either a valence or sub-valence shell in the following process:



The energy $h\nu$ required to facilitate the above process is defined as the *ionisation energy*, or IE. However, the energy does not need to be delivered by way of a photon; initial experiments to record IEs involved bombarding samples with electrons accelerated across a potential¹⁴¹. In these cases, the accelerating voltage required for an electron to ionise the sample via collision was recorded as the Ionisation Potential (IP), in units of volts (V). The energy of the accelerated electron – and therefore the IE – was equal to the same numerical value of the IP, only expressed in units of electron volts (eV)[‡]. Although modern ionisation experiments commonly utilise photo-ionisation in preference of electron bombardment, the tradition of presenting IEs in units of eV remains.

While the IE defines the energy required to remove an electron from a molecular species, it does not specify *which* electron is removed. The general rule is that unless specifically stated, the IE refers to the removal of the electron most weakly bound to the nucleus; this is typically the electron occupying the Highest Occupied Molecular Orbital (HOMO). Assuming that (i) ionisation occurs from the ground electronic state for M and (ii) no additional electronic excitation processes occurs in the M⁺ state, the IE can loosely be approximated as the negative energy of the HOMO. This draws from previous work by Koopmans¹⁴², and can be represented as follows:

$$IE \cong -E_{HOMO} \quad (2.22)$$

[‡] An electron volt is defined as the energy gained by an electron moving across a potential of 1 volt and is equal to 1.602×10^{-19} J.

Given that the energy of the HOMO is highly pertinent to chemical reactivity, measurement of the IE can be used to assist in predictions of chemical reactivity for a given species. Generally, a low IE, and therefore a weakly bound HOMO electron, corresponds to an electron donor species. A high IE conversely implies stability of the HOMO with more strongly bound electrons; these species are typically more likely to act as electron acceptors.

The process of photo-ionisation is quite similar to electronic excitation. For the most part, the cationic state can be treated the same as an electronically excited state. As with a conventional absorption spectrum, a photo-ionisation spectrum comprises a series of vibronic transitions with intensities dependent on both the Franck-Condon Factor and – in the cases of hot bands – the population of the neutral state. There are, however, some key differences between the two processes. Firstly, because the electronic charge of the cationic state is always different to that of the neutral, the transition dipole moment will always be non-zero. Secondly, photo-ionisation is not subject to Selection Rules 2 and 3 discussed previously¹⁴³. Unlike excitation, which involves promotion of an electron to a bound state (i.e. a molecular orbital), photo-ionisation simply ejects an electron into a continuum of unbound states. The change in angular momentum between the neutral and cation states can thus take any value, since the unbound electron can also take any value for l to ensure angular momentum is conserved¹⁴³. Furthermore, the Laporte Rule only applies to electronic dipole transitions, such as electronic excitation, and does not apply to photo-ionisation transitions¹⁴³. Photo-ionisation is, however, still subject to the spin selection rule; the total spin of the cation state and the unbound electron must be conserved. The final, and most pertinent difference, is that the ejected electron can retain any amount of energy following the absorption process. This means that not only are all ionisation transitions allowed (provided spin is conserved), but the neutral can now absorb photons of *any* wavelength as long as the photon energy is sufficient to eject an electron; any excess energy will simply be transferred to the electron as kinetic energy. The transfer of photon energy within the ionisation process is shown schematically in Figure 2.7.

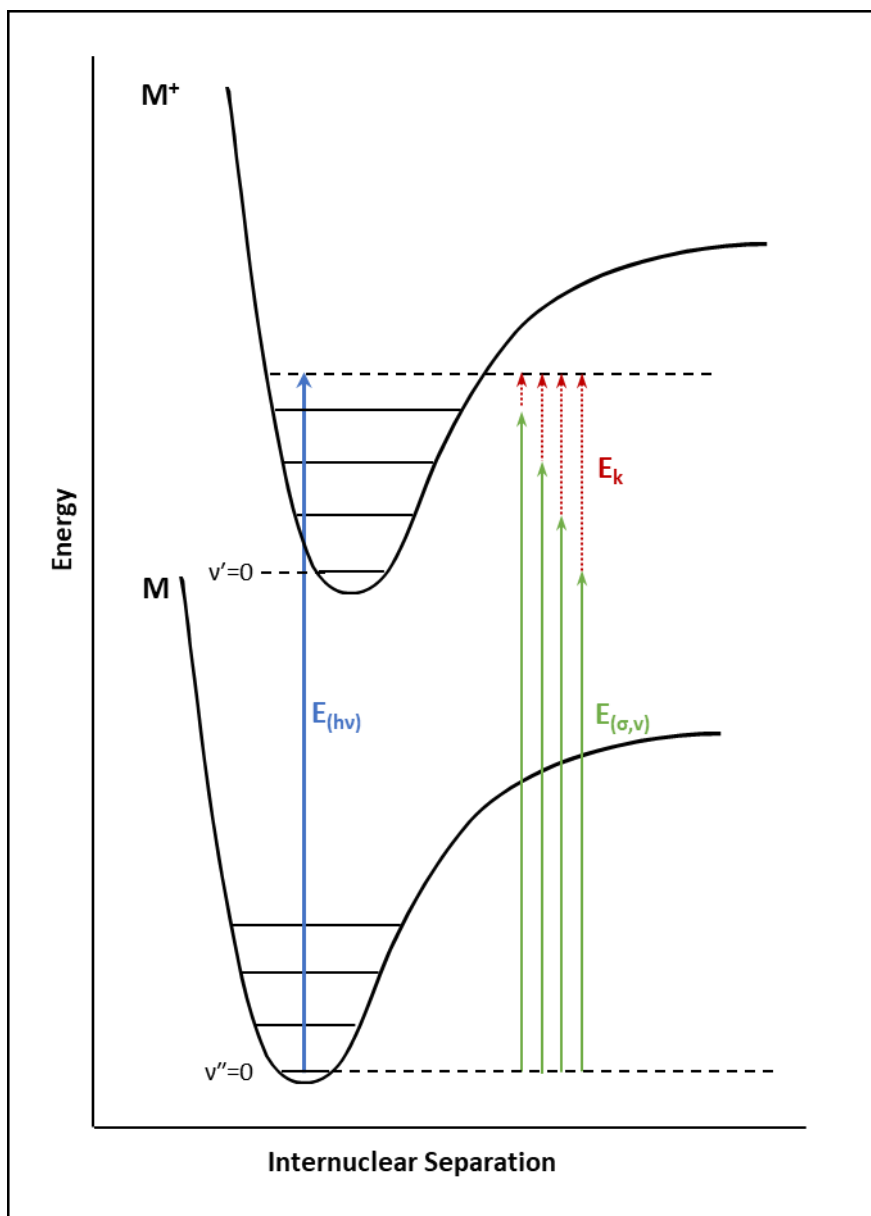


Figure 2.7: Energy transfer process during photo-ionisation. The neutral molecule (M) can absorb a photon of energy $E_{(h\nu)}$ (blue arrow) to undergo a transition to any vibrational state within the cation (M^+), with vibronic transition energy $E_{(\sigma,\nu)}$ (green arrow). The remaining energy is transferred to the ejected electron as kinetic energy E_k (red arrow).

In a macroscopic system containing a large number of M species, all vibronic transitions energetically lower than that of the incident photons are accessed simultaneously. The ion signal then becomes a summation of the intensities of all energetically accessible vibronic transitions; the intensity of any individual vibronic transition is determined by the FCF as shown in Equation 2.20. More vibronic transitions become accessible with increased photon

energy which in turn causes an increase in the ion signal. This is the premise for photo-ionisation efficiency (PIE) spectroscopy: the photon energy is scanned in the vicinity of the IE while the intensity of the ion signal is recorded. Any photon energy corresponding to a vibronic transition will see an increase in the recorded ion signal. Conversely, any photon energy which does not directly correspond to a vibronic transition will cause no change in the ion signal intensity; the additional energy will simply be transferred to the ejected electron. Because the ion signal represents a summation of all the accessible vibronic transitions at any photon energy, PIE experiments provide valuable insight into the vibrational structure of both the neutral and cationic clusters.

2.3.6. The Photo-Ionisation Efficiency Spectrum

The Photo-Ionisation Efficiency (PIE) spectrum, an example of which is presented in Figure 2.8, represents the increase in the M^+ ion signal with increased photon energy. The pertinent vibronic transitions recorded within the PIE spectrum are presented schematically in Figure 2.9.

The low energy region of the PIE spectrum typically comprises a flat region of near-zero intensity; this is known as the baseline, where the photon energy is too low to cause photo-ionisation of the species of interest. In many cases the spectral baseline intensity is not flat and can instead appear as a gradual increase in ion signal over a broad energy range; this anomaly results from photo-ionisation of metastable isomers in the molecular beam. Metastable isomers are a product of numerous cluster geometries which represent low-lying minima on the cluster potential energy surface; because metastable isomers possess the same mass as the lowest energy isomer, they are difficult to remove experimentally.

The initial onset of ion signal at low photon energy is called the *appearance energy*, or AE. The AE is defined as the point where the baseline and the ion signal onset intersect; this is found by fitting linear trend lines to both the baseline and the signal onset in the PIE spectrum. The ion signal in the immediate vicinity of the AE is called the thermal tail; vibronic transitions in

this region typically originate from hot bands and appear with a tailing effect due to the Boltzmann distribution of thermally excited states.

The ionisation energy (IE) is located slightly higher in energy than the thermal tail and can be expressed as either an *adiabatic IE* (IE_{ad}) or a *vertical IE* (IE_v). The adiabatic IE corresponds to ionisation from the lowest energy vibrational state in M to the lowest energy vibrational state in M^+ . This is otherwise known as the band origin transition which can be represented as 0_0^0 (or (0,0) for diatomics). The IE_{ad} is determined from an assignment of the vibronic transitions underlying the PIE spectrum; this is detailed in Chapter 3.

The vertical IE corresponds to the vibronic transition with the maximum FC overlap and represents the steepest slope on the PIE spectrum. The IE_v is usually the easier of the two IEs to determine accurately, usually requiring nothing more than a visual inspection of the PIE spectrum. However, the IE_{ad} is more closely aligned with Koopmans' theorem since, unlike the IE_v , the IE_{ad} does not consider vibrationally excited modes in the cation state. In the context of this work all, IE values presented are adiabatic IEs; the terms IE and IE_{ad} are used interchangeably. Any reference to vertical IEs is mentioned explicitly.

The region of the PIE spectrum which shows an increase in ion signal at higher photon energies than the IE is known as the post-band origin region. This region consists of vibronic progressions from low-lying vibrational states in M to all FC-allowed vibrational states in M^+ . Hot band transitions can also be found in this region; however, in most cases their low relative intensities generally make their contributions negligible.

The plateau of ion signal at high photon energy corresponds to the energy where all FC-allowed transitions have been accessed. From this point, any additional photon energy is imparted to the ejected electron as kinetic energy.

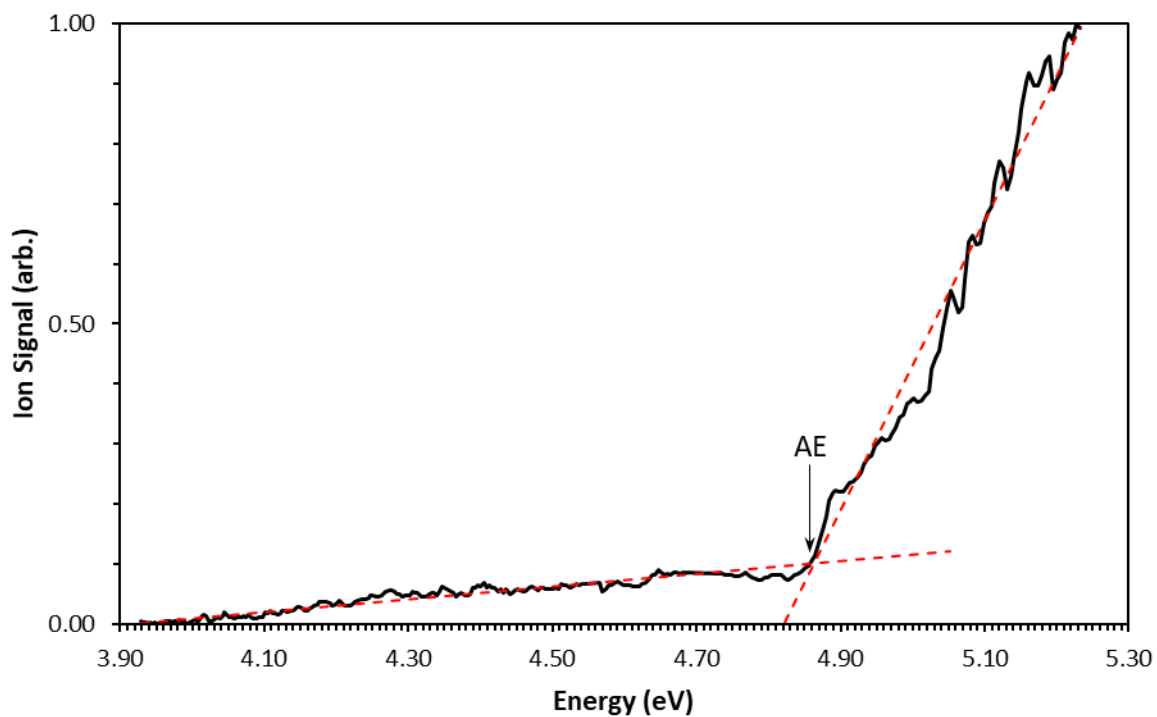


Figure 2.8: An example of a Photo-Ionisation Efficiency (PIE) spectrum showing the appearance energy (AE), adiabatic ionisation energy (IE_{ad}) and vertical ionisation energy (IE_v). Trendlines are fitted to the baseline and onset, which are shown as red dashed lines. The intersection of the trendlines corresponds to the AE.

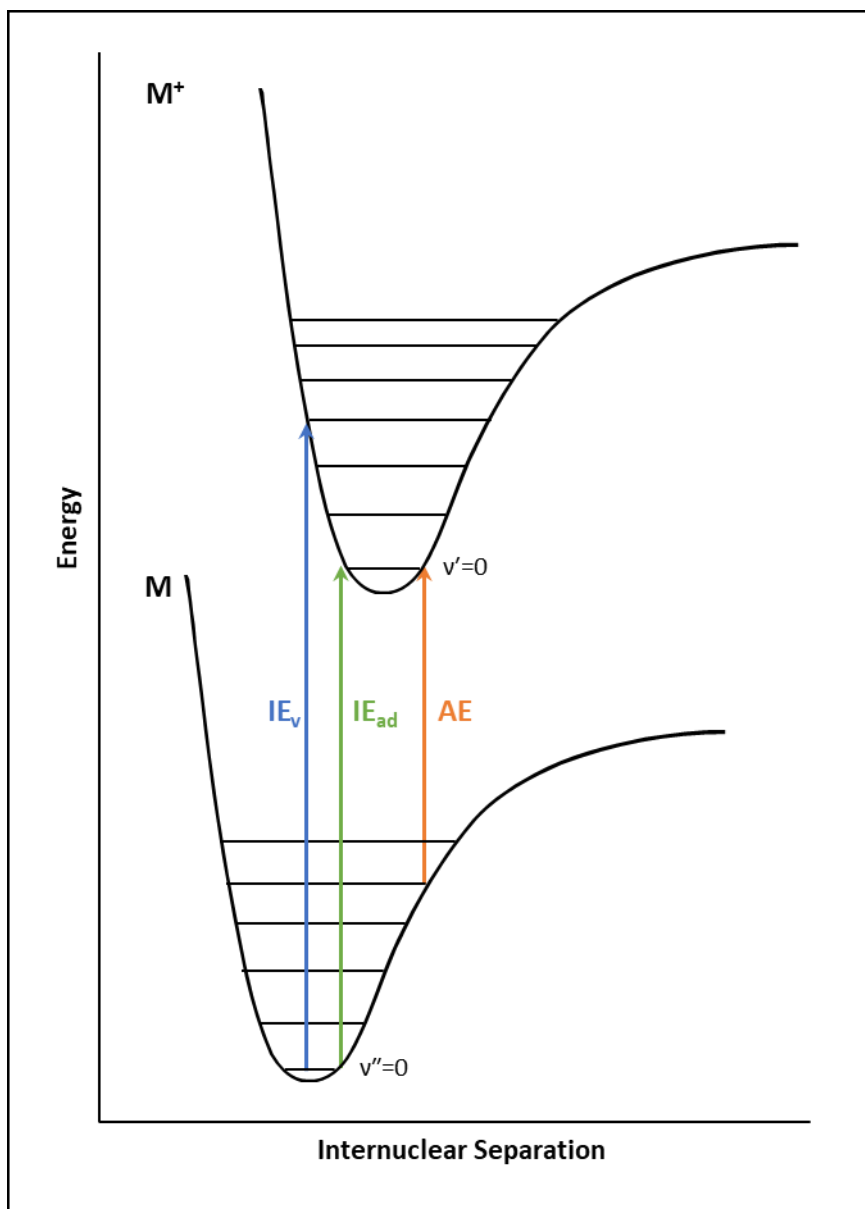


Figure 2.9: Schematic showing photo-ionisation transitions corresponding to the appearance energy (AE), adiabatic ionisation energy (IE_{ad}) and vertical ionisation energy (IE_v) – designated by orange, green and blue arrows respectively. The AE corresponds to the lowest energy FC-allowed transition. The IE_{ad} corresponds to the 0_0^0 transition. The IE_v corresponds to the maximum-FC transition.

The slope of the PIE spectrum can provide qualitative insight into the extent of structural deformation occurring following photo-ionisation. A structure which undergoes a small change when photo-ionised would expect a strong overlap of the vibrational wavefunctions for the M and M⁺ states due to the minimal change in vibrational coordinates. This would present as a steep slope in the PIE spectrum and is often correlated with short vibronic

progressions and a strong band origin transition. Conversely, any structure which undergoes substantial changes in geometry would have a poor wavefunction overlap between the M and M^+ states. In this case a PIE spectrum with a shallow slope would be expected; this is generally accompanied by long vibronic progressions and a weak band origin transition.

2.3.7. Zero Electron Kinetic Energy Spectroscopy

Experimental PIE spectra are compared to calculated PIE spectra to infer the properties of calculated structures. The calculated PIE spectra in this work are themselves produced from ZEKE spectral simulations. Therefore, while Zero Electron Kinetic Energy (ZEKE) experiments are not performed in the context of this thesis, a brief description of the technique is presented for completion. Experimental details of ZEKE spectroscopy are presented here; a discussion of ZEKE simulations is presented in Chapter 3.

The theory underlying Zero Electron Kinetic Energy (ZEKE) spectroscopy is very similar to that of PIE spectroscopy. The main difference is that PIE spectroscopy records the abundance of a cation species M^+ following photo-ionisation, whereas ZEKE spectroscopy records the abundance of ejected electrons from the photo-ionised cations¹⁴⁴. Unlike PIE spectroscopy, where all photons are absorbed regardless of energy, ZEKE spectroscopy allows for the selective detection of electrons at energies which directly correspond to vibronic transitions. This is achieved through pulsed field ionisation where a short delay occurs following photo-ionisation before a potential is applied to extract the ejected electrons. This short delay allows any electrons with residual kinetic energy, i.e. not exactly corresponding to a vibronic transition, to be removed from the acceleration region and therefore not detected^{51,62,76}. A simulated comparison of photo-ionisation and ZEKE spectra is shown in Figure 2.10. While the spectra appear quite different, they both provide information regarding IEs, vibronic structure and geometric changes. Most importantly, integration of the ZEKE spectrum with respect to photon energy yields the corresponding PIE spectrum.

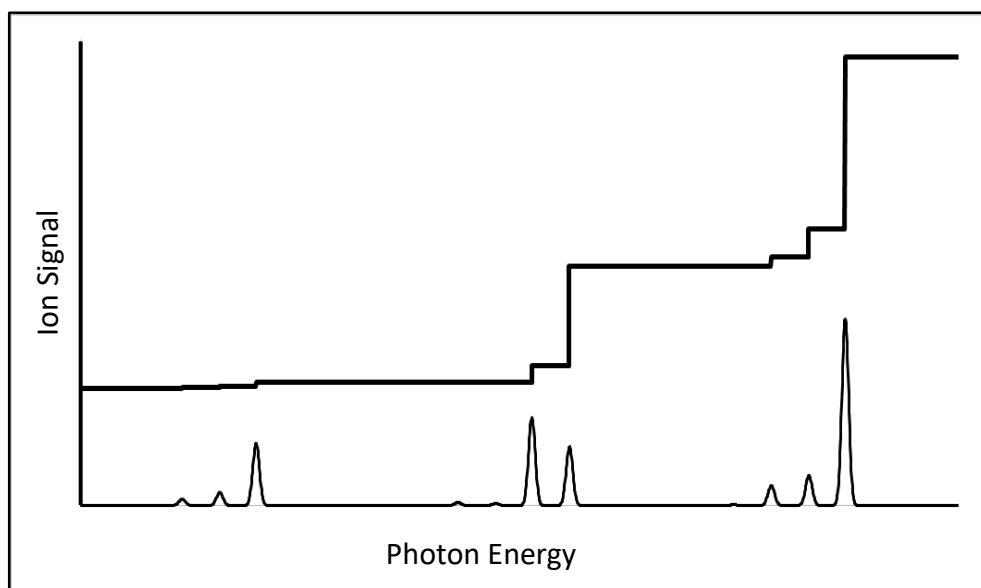


Figure 2.10: Comparison of a PIE spectrum (top) and a ZEKE spectrum (below). Integration of a ZEKE spectrum with respect to photon energy yields a PIE spectrum.

2.3.8. Details for the PIE Experiment

The experimental setup consists of three photo-ionisation sources which are used interchangeably to cover a broad range of wavelengths. The first source is a dye laser (Sirah Cobra Stretch) pumped by the 3rd harmonic output from a Nd:YAG laser (Quantel YG981C, 355 nm, 10 Hz) using a number of Coumarin, Fluorescein and Rhodamine dyes[§]. The 2nd harmonic output from this configuration is used to cover the wavelength range of 220 – 265 nm. A second dye laser (Lambdaphysik Scanmate Pro) is pumped by the 2nd harmonic output from a Nd:YAG laser (Continuum Surelite III, 532 nm, 10 Hz). The 2nd harmonic is again taken to cover the wavelength range 264 – 317.75 nm. Finally, the 5th harmonic of a Nd:YAG laser (Quantel Q-Smart, 213 nm, 10 Hz) is used to provide photo-ionisation at a fixed wavelength of 213 nm. The combination of these photo-ionisation sources gives a tuneable photo-ionisation source in the UV range of 220 – 317.75 nm (5.64 – 3.92 eV), with the ability to record ion signal at a fixed photo-ionisation wavelength of 213 nm (5.82 eV).

[§] Dyes used include Coumarins 440, 460 480, 503 and 540A; Fluorescein 548; Rhodamines 6G, B and 640. All dyes were dissolved in methanol.

The ionisation pulse is passed through a telescope consisting of two biconvex lenses with focal lengths of 75 mm and 300 mm, separated by 375 mm. This provides a 4x expansion and collimation of the ionisation pulse to reduce the photon density such that ionisation of the cluster species by multi-photon processes are minimised. An adjustable iris set at 5 mm diameter is used to select a portion of the beam with uniform photon density; this part of the photon beam is directed into the TOFMS perpendicular to the molecular train. The laser fluence of the ionisation pulse is monitored with 3 second averaging using an energy meter (Ophir Nova II) positioned behind the TOFMS. The laser fluence is maintained using a Rochon Prism controlled by a stepper motor coupled to the energy meter via a feedback loop programmed with LabVIEW. Using this setup, the photon density is typically maintained between $350 \mu\text{J}\cdot\text{cm}^{-2}$ and $400 \mu\text{J}\cdot\text{cm}^{-2}$ (measured as a pulse energy of 70-80 μJ). This is consistent with the $400 \mu\text{J}\cdot\text{cm}^{-2}$ threshold for single photon processes previously reported by Yang and Knickelbein to minimise the frequency of both two-photon processes and fragmentation events⁷⁹. On occasion the photon density of the ionising beam was reduced to fluxes as low as $250 \mu\text{J}\cdot\text{cm}^{-2}$, particularly at the ends of the laser dye tuning curves which exhibit lower lasing efficiencies. However, the linear dependence of ion signal on laser fluence reported by Yang and Knickelbein – where the laser fluence lies below the $400 \mu\text{J}\cdot\text{cm}^{-2}$ threshold – allowed for any variance in ion signal to be treated with a *post hoc* correction. Preliminary experiments in this work, which involved a visual, albeit rudimentary comparison of mass spectra for cerium oxide clusters recorded with photo-ionisation energies ranging between $250 \mu\text{J}\cdot\text{cm}^{-2}$ and $400 \mu\text{J}\cdot\text{cm}^{-2}$, showed a linear relationship between the photon fluence and ion signal consistent with single photon ionisation events. However, the absorption cross-section of any cluster is both intrinsic to the cluster itself and wavelength dependent¹⁴⁵. Therefore, despite the precautions undertaken to maintain constant photon fluence, some multi-photon events may still occur. The high energy photons used in photo-ionisation experiments also makes it difficult to rule out the occurrence of photo-fragmentation processes²⁷. A small degree of contamination of the PIE spectra in this work is therefore expected to result from multi-photon ionisation (MPI) and fragmentation events. These processes would be less likely to affect the ion signal within the photo-ionisation threshold – given the high absorption cross section within this range – but would more likely appear as residual ion signal in the pre-threshold region.

The timing of the ionisation pulse relative to the two ablation lasers and the pulsed carrier gas in the cluster source is controlled via the same digital delay generator (Griffith University, TARDIS II) as discussed previously. This is crucial to ensure that the ionising beam passes through the densest region of the supersonically expanded molecular beam to produce the maximum number of photo-ionised species. The molecular beam is photo-ionised within the extraction stage of a Wiley McLaren mass spectrometer aligned perpendicularly to both the molecular beam and ionisation pulse. Photo-ionised species are accelerated, separated by their relative m/z ratios in the drift region, and then focussed onto a dual multi-channel plate detector as described previously. The laser fluence is simultaneously averaged over the time period for which the ion signal is recorded. The ion signal, ionising wavelength and average laser fluence are all sent to a PC where they are recorded in a data file for analysis.

The ion signal for each individual species is initially recorded at low ionisation wavelength corresponding to high photon energy (240 nm or 5.17 eV). The wavelength of the ionisation beam is subsequently increased by 0.25 nm increments with a mass spectrum recorded at each wavelength. This process effectively produces a PIE spectrum in reverse, where the depletion of ion signal is measured with respect to photon energy. This ensures the ion signal is initially produced with good stability so any depletion recorded during experiments can be attributed to the decreased photon energy and not to signal fluctuation.

Each PIE scan is recorded over a maximum range of 5 nm. This ensures that the ion signal for any metal oxide cluster remains stable and is not affected by oxygen depletion from the cerium rod surface. A 30 minute “rest” interval is conducted between scans to allow re-oxidation of the cerium rod from residual oxygen in the evacuated chamber. This procedure was determined from preliminary ion stability experiments whereupon depletion of metal oxide ion peaks started to occur following periods of continual ablation longer than 90 minutes (i.e. the time taken to scan approximately 7.5 nm); peak intensities were then observed to return to their initial strength after a 30 minute “rest”. The cluster source region containing the cerium rod was exposed to the atmosphere on a daily basis to ensure sufficient availability of oxygen, since depletion of the metal oxide peaks was again observed after about 3 days of

ablation using a 90:30 ablation/rest ratio. Following the completion of each scan, a second mass spectrum was recorded at the initial ionisation wavelength; the ion signal intensities of prominent peaks in the two mass spectra were then compared to confirm the ion signal remained stable throughout the scan. Scans were recorded with 1 nm overlap to adjacent wavelength ranges in order to facilitate *post hoc* concatenation. Each wavelength region was scanned 3 times to ensure reproducibility.

The ionisation wavelength was continually increased until all ion peaks were observed to have completely disappeared; this corresponded to a wavelength of 317.75 nm (3.92 eV). Additional mass spectra were also recorded at 220 nm (5.64 eV) and 213 nm (5.82 eV). While the tuneable photo-ionisation source allowed for exploration of the 220 – 240 nm region, a comparison of mass spectra recorded following photo-ionisation at 220 nm and 240 nm revealed, with exception of the AuCe ion signal, no noticeable depletion of any ion peak. This region was therefore not explored further.

Post hoc treatment involved unweighted 13-point smoothing of the mass spectra to remove background noise. Following this treatment, individual ion peaks were identified and selected for further analysis; these include the Ce_2O_n ($n=0-2$), Ce_3O_n ($n=0-4$), Ce_4O_n ($n=0-5$), AuCe_2O_n ($n=0-2$) and AuCe_3O_n ($n=0-3$) clusters which are discussed in Chapters 5 – 9, respectively. The area of each individual ion peak was determined by trapezoidal integration; this value was divided by the averaged photon flux – to account for variances in laser fluence with wavelength – then plotted against the photon energy to produce a PIE spectrum over the given scan range. The 3 PIE spectra recorded over each wavelength range were combined and averaged to minimise any effects of ion signal fluctuation during the scans. PIE spectra over adjacent wavelength ranges were joined following the application of a scaling factor to the lower wavelength – i.e. higher energy – PIE spectrum so that the ion signals of both spectra in the overlapping range were consistent. The scaling factor was arbitrary and simply accounted for any inherent variances in ion signal strength between scans which were not wavelength dependent. The concatenated PIE spectrum was then normalised to the maximum and minimum intensity values so they were presented as 1 and 0, respectively.

Once a PIE spectrum for a particular cluster species was concatenated and normalised, the photon energies were “field-corrected” to account for the photo-ionisation processes occurring within a potential field (i.e. between the repelling and extractor plates). The applied potential field facilitates electron removal from Rydberg states (i.e. highly excited states where the electron is weakly bound to the nucleus) instead of requiring the electron to be ejected into the continuum. The result is a red shift in all recorded ionisation transition energies. The field-corrected energy is determined from the equation below, consistent with previous work by Schlag and co-workers¹⁴⁶.

$$E_{fc} = E + 6.1\sqrt{V} \quad (2.23)$$

Where E and E_{fc} are the energies before and after field correction, respectively, and V represents the applied potential between the repelling and extraction plates. Future developments of the experimental setup will likely utilise pulsed field ionisation to ensure photo-ionisation occurs in a field-free region; this will eliminate the need for *post-hoc* corrections to the photon energy.

The field-corrected PIE spectra for each cluster species are presented in Chapters 5 – 9. The adiabatic ionisation energy (IE_{ad}) is determined indirectly from the field-corrected PIE spectrum by overlaying a simulated PIE spectrum and inferring the IE value from the calculated 0_0^0 transition energy (a detailed description of this process can be found in Chapter 3). All IE_{ad} values presented in this work are assigned an error of ± 0.05 eV to maintain consistency with previous PIE studies on cerium oxide cluster IEs by Koretsky and Knickelbein⁴⁴. The authors took the vertical IE in their PIE spectra as the point of intersection between the major post-threshold portion of the ion signal and the baseline, utilising a linear extrapolation process. However, they encountered difficulties in determining whether ion signal close to the ionisation threshold reflected genuine PIE spectra or was simply due to thermal tailing effects. The authors assigned a ± 0.05 eV error to their IE values to account for uncertainties in these judgements. With the benefit of ZEKE simulations to avert such quandaries, it is likely the IEs presented in this work are, if anything, more accurate than those presented by

Koretsky and Knickelbein. The ± 0.05 eV error value can therefore be considered as a conservative estimate of errors associated with this experimental method.

2.4. References

- (1) Shawhan, E. N. *Phys. Rev.* **1935**, *48*, 343.
- (2) Bondybey, V. E.; English, J. H. *J. Chem. Phys.* **1977**, *67* (8), 3405.
- (3) Dietz, T. G.; Duncan, M. a.; Powers, D. E.; Smalley, R. E. *J. Chem. Phys.* **1981**, *74* (11), 6511.
- (4) Meiwes-Broer, K.-H. In *Advances in Metal and Semiconductor Clusters*; Duncan, M. A., Ed.; JAI Press Inc: Greenwich, Connecticut, 1993.
- (5) Smalley, R. E.; Wharton, L.; Levy, D. H. *Acc. Chem. Res.* **1977**, *10* (4), 139.
- (6) Kantrowitz, A.; Grey, J. *Rev. Sci. Instrum.* **1951**, *22* (5), 328.
- (7) Collings, B. A.; Amrein, A. H.; Rayner, D. M.; Hackett, P. A. *J. Chem. Phys.* **1993**, *99* (5), 4174.
- (8) Yardley, J. T. *Introduction to Molecular Energy Transfer*; Academic Press: New York, 1980.
- (9) Rohlfing, E. A.; Cox, D. M.; Petkovic-Linton, R.; Kaldor, A. *J. Phys. Chem.* **1984**, *88* (25), 6227.
- (10) Deng, H. T.; Guo, B. C.; Kerns, K. P.; Castleman, A. W. *Int. J. Mass Spectrom. Ion Process.* **1994**, *138*, 275.
- (11) Nonose, S.; Sone, Y.; Onodera, K.; Sudo, S.; Kaya, K. *Chem. Phys. Lett.* **1989**, *164* (4), 427.
- (12) Wagner, R. L.; Vann, W. D.; Castleman, A. W. *Rev. Sci. Instrum.* **1997**, *68*, 3010.
- (13) Bondybey, V. E.; English, J. H. *J. Chem. Phys.* **1983**, *79*, 4746.
- (14) Himeno, H.; Miyajima, K.; Yasuike, T.; Mafuné, F. *J. Phys. Chem. A* **2011**, *115* (42), 11479.
- (15) Nonose, S.; Sone, Y.; Onodera, K.; Sudo, S.; Kaya, K. *J. Phys. Chem.* **1990**, *94*, 2744.
- (16) Gentleman, A. S.; Addicoat, M. A.; Dryza, V.; Gascooke, J. R.; Buntine, M. A.; Metha, G. *F. J. Chem. Phys.* **2009**, *130* (16), 64311.
- (17) Gentleman, A. S. The Effect of Sequential Oxidation and Composition on the Structural

- and Electronic Properties of Gas Phase Transition-Lanthanide Bimetallic Clusters, PhD Thesis, The University of Adelaide, 2014.
- (18) Deng, H. T.; Kerns, K. P.; Castleman, A. W. *J. Phys. Chem.* **1996**, *100* (32), 13386.
- (19) Zemski, K. A.; Bell, R. C.; Castleman, A. W. *J. Phys. Chem. A* **2000**, *104* (24), 5732.
- (20) Bell, R. C.; Zemski, K. A.; Castleman, A. W. *J. Clust. Sci.* **1999**, *10* (4), 509.
- (21) Johnson, G. E.; Tyo, E. C.; Castleman, A. W. *Proc. Natl. Acad. Sci. U. S. A.* **2008**, *105* (47), 18108.
- (22) Zemski, K. A.; Justes, D. R.; Castleman, A. W. *J. Phys. Chem. B* **2002**, *106* (24), 6136.
- (23) Zemski, K. A.; Justes, D. R.; Bell, R. C.; Castleman, A. W. *J. Phys. Chem. A* **2001**, *105* (18), 4410.
- (24) Bell, R. C.; Zemski, K. A.; Kerns, K. P.; Deng, H. T.; Castleman, A. W. *J. Phys. Chem. A* **1998**, *102* (10), 1733.
- (25) Wu, X.; Ding, X.; Bai, S.; Xu, B.; He, S.; Shi, Q. *J. Phys. Chem. C* **2011**, *115*, 13329.
- (26) Wu, X.-N.; Ma, J.-B.; Xu, B.; Zhao, Y.-X.; Ding, X.-L.; He, S.-G. *J. Phys. Chem. A* **2011**, *115* (21), 5238.
- (27) Duncan, M. A. *Rev. Sci. Instrum.* **2012**, *83* (4), 041101.
- (28) Gregoire, G.; Duncan, M. A. *J. Chem. Phys.* **2002**, *117* (5), 2120.
- (29) Pilgrim, J. S.; Duncan, M. A. *J. Am. Chem. Soc.* **1993**, *115* (10), 4395.
- (30) Pilgrim, J. S.; Duncan, M. A. *J. Am. Chem. Soc.* **1993**, *115* (15), 6958.
- (31) Hopkins, J. B.; Langridge-Smith, P. R. R.; Morse, M. D.; Smalley, R. E. *J. Chem. Phys.* **1983**, *78* (4), 1627.
- (32) Lubman, D. M.; Rettner, C. T.; Zare, R. N. *J. Phys. Chem.* **1982**, *86* (7), 1129.
- (33) Aston, F. W. *Philos. Mag. Ser. 6* **1919**, *38* (228).
- (34) Dass, C. *Fundamentals of Contemporary Mass Spectrometry*; John Wiley & Sons: New Jersey, 2007.
- (35) Le Gac, S.; van den Berg, A. *Miniaturization and Mass Spectrometry*; Royal Society of

- Chemistry: Cambridge, 2009.
- (36) Wiley, W. C.; McLaren, I. H. *Rev. Sci. Instrum.* **1955**, *26* (12), 1150.
- (37) Guilhaus, M. J. *Mass Spectrom.* **1995**, *30*, 1519.
- (38) Brown, R. S.; Lennon, J. J. *Anal. Chem.* **1995**, *67* (13), 1998.
- (39) Wiza, J. L. *Nucl. Instruments Methods* **1979**, *162* (1), 587.
- (40) Sohnlein, B. R.; Lei, Y.; Yang, D.-S. *J. Chem. Phys.* **2007**, *127* (11), 114302.
- (41) Knickelbein, M. B. *J. Chem. Phys.* **1995**, *102* (1), 1.
- (42) Knickelbein, M. B.; Yang, S.; Riley, S. J. *J. Chem. Phys.* **1990**, *93* (1990), 94.
- (43) Koretsky, G. M.; Knickelbein, M. B. *J. Chem. Phys.* **1997**, *106* (23), 9810.
- (44) Koretsky, G. M.; Knickelbein, M. B. *Eur. Phys. J. D - At. Mol. Opt. Plasma Phys.* **1998**, *2*, 273.
- (45) Knickelbein, M. B. *Chem. Phys. Lett.* **1992**, *192* (1), 129.
- (46) Dryza, V.; Addicoat, M. A.; Gascooke, J. R.; Buntine, M. A.; Metha, G. F. *J. Phys. Chem. A* **2008**, *112* (25), 5582.
- (47) Dryza, V.; Gascooke, J. R.; Buntine, M. A.; Metha, G. F. *Phys. Chem. Chem. Phys.* **2009**, *11* (7), 1060.
- (48) Dryza, V.; Addicoat, M. A.; Gascooke, J. R.; Buntine, M. A.; Metha, G. F. *J. Phys. Chem. A* **2005**, *109* (49), 11180.
- (49) Amrein, A.; Simpson, R.; Hackett, P. *J. Chem. Phys.* **1991**, *95* (3), 1781.
- (50) von Helden, G.; van Heijnsbergen, D.; Duncan, M. A.; Meijer, G. *Chem. Phys. Lett.* **2001**, *333* (5), 350.
- (51) Yang, D.-S.; James, A. M.; Rayner, D. M.; Hackett, P. A. *Chem. Phys. Lett.* **1994**, *231*, 177.
- (52) Burton, G. R.; Xu, C.; Arnold, C. C.; Neumark, D. M. *J. Chem. Phys.* **1996**, *104* (8), 2757.
- (53) Gantefor, G. F.; Cox, D. M.; Kaldor, A. *Zeitschrift für Phys. D Atoms, Mol. Clust.* **1991**, *19* (4), 59.

- (54) Rodham, D. A.; Blake, G. A. *Chem. Phys. Lett.* **1997**, *264* (5), 522.
- (55) Miyawaki, J.; Sugawara, K. *Chem. Phys. Lett.* **2004**, *386*, 196.
- (56) Gantefor, G. F.; Cox, D. M.; Kaldor, A. *J. Chem. Phys.* **1990**, *93* (11), 8395.
- (57) Agreiter, J. K.; Knight, A. M.; Duncan, M. A. *Chem. Phys. Lett.* **1999**, *313*, 162.
- (58) Yang, D.-S.; Zgierski, M. Z.; Rayner, D. M.; Hackett, P. a.; Martinez, A.; Salahub, D. R.; Roy, P.-N. N.; Carrington, T. *J. Chem. Phys.* **1995**, *103* (13), 5335.
- (59) Baumert, T.; Thalweiser, R.; Gerber, G. *Chem. Phys. Lett.* **1993**, *209*, 29.
- (60) Taylor, S.; Lemire, G. W.; Hamrick, Y. M.; Fu, Z.; Morse, M. D. *J. Chem. Phys.* **1988**, *89* (9), 5517.
- (61) Herrmann, A.; Hofmann, M.; Leutwyler, S.; Schumacher, E.; Wöste, L. *Chem. Phys. Lett.* **1979**, *62* (2), 216.
- (62) Yang, D.-S.; Hackett, P. A. *J. Electron Spectros. Relat. Phenomena* **2000**, *106*, 153.
- (63) Labastie, P.; L'Hermite, J. -M.; Poncharal, P.; Sence, M. *J. Chem. Phys.* **1995**, *103* (15), 6362.
- (64) Handschuh, H.; Ganteför, G.; Bechthold, P. S.; Eberhardt, W. *J. Chem. Phys.* **1994**, *100* (10), 7093.
- (65) Rohlfing, E. A.; Cox, D. M.; Kaldor, A.; Johnson, K. H. *J. Chem. Phys.* **1984**, *81* (9), 3846.
- (66) James, A. M.; Kowalczyk, P.; Langlois, E.; Campbell, M. D.; Ogawa, A.; Simard, B. *J. Chem. Phys.* **1994**, *101* (6), 4485.
- (67) Ramakrishna, G.; Varnavski, O.; Kim, J.; Lee, D.; Goodson, T. *J. Am. Chem. Soc.* **2008**, *130* (15), 5032.
- (68) Häkkinen, H.; Yoon, B.; Landman, U.; Li, X.; Zhai, H.-J.; Wang, L.-S. *J. Phys. Chem. A* **2003**, *107* (32), 6168.
- (69) Powers, D. E.; Hansen, S. G.; Geusic, M. E.; Puiu, A. C.; Hopkins, J. B.; Dietz, T. G.; Duncan, M. A.; Langridge-Smith, P. R. R.; Smalley, R. E. *J. Phys. Chem.* **1982**, *86* (14), 2556.
- (70) Taylor, S.; Spain, E. M.; Morse, M. D. *J. Chem. Phys.* **1990**, *92* (5), 2698.

- (71) Bishea, G. A.; Morse, M. D. *J. Chem. Phys.* **1991**, *95* (12), 8779.
- (72) Federmann, F.; Hoffmann, K.; Quaas, N.; Toennies, J. P. *Eur. Phys. J. D - At. Mol. Opt. Plasma Phys.* **1999**, *9* (1), 11.
- (73) Sohnlein, B. R.; Yang, D.-S. *J. Chem. Phys.* **2006**, *124* (13), 134305.
- (74) Chris Wang, C. R.; Pollack, S.; Cameron, D.; Kappes, M. M. *J. Chem. Phys.* **1990**, *93* (6), 3787.
- (75) Delacrétaz, G.; Wöste, L. *Surf. Sci.* **1985**, *156*, 770.
- (76) Yang, D.-S.; Miyawaki, J. *Chem. Phys. Lett.* **1999**, *313*, 514.
- (77) Miyawaki, J.; Yang, D.-S.; Sugawara, K. *Chem. Phys. Lett.* **2003**, *372*, 627.
- (78) Knickelbein, M. B.; Yang, S. *J. Chem. Phys.* **1990**, *93* (8), 5760.
- (79) Yang, S.; Knickelbein, M. B. *J. Chem. Phys.* **1990**, *93* (3), 1533.
- (80) Knickelbein, M. B.; Menezes, W. J. C. *J. Chem. Phys.* **1991**, *94* (6), 4111.
- (81) Simard, B.; Dénoimée, S.; Rayner, D. M.; Heijnsbergen, D. van; Meijer, G.; Helden, G. von. *Chem. Phys. Lett.* **2002**, *357*, 195.
- (82) Surya, P. I.; Ranatunga, D. R. A.; Freiser, B. S. *J. Am. Chem. Soc.* **1997**, *119* (14), 3351.
- (83) Fielicke, A.; Helden, G. von; Meijer, G.; Simard, B.; Rayner, D. M. *Phys. Chem. Chem. Phys.* **2005**, *7* (23), 3906.
- (84) Chi, C.; Cui, J.; Li, Z. H.; Xing, X.; Wang, G.; Zhou, M. *Chem. Sci.* **2012**, *3* (5), 1698.
- (85) Hamilton, S. M.; Hopkins, W. S.; Harding, D. J.; Walsh, T. R.; Gruene, P.; Haertelt, M.; Fielicke, A.; Meijer, G.; Mackenzie, S. R. *J. Am. Chem. Soc.* **2010**, *132* (5), 1448.
- (86) Fielicke, A.; Meijer, G.; von Helden, G. *J. Am. Chem. Soc.* **2003**, *125* (12), 3659.
- (87) Dietrich, G.; Krückeberg, S.; Lützenkirchen, K.; Schweikhard, L.; Walther, C. *J. Chem. Phys.* **1999**, *112* (2), 752.
- (88) van Heijnsbergen, D.; Duncan, M. A.; Meijer, G.; von Helden, G. *Chem. Phys. Lett.* **2001**, *349* (3–4), 220.
- (89) Swart, I.; Fielicke, A.; Redlich, B.; Meijer, G.; Weckhuysen, B. M.; de Groot, F. M. F. *J.*

- Am. Chem. Soc.* **2007**, *129* (9), 2516.
- (90) Langsam, Y.; Ronn, A. M. *Chem. Phys.* **1981**, *54* (2), 277.
- (91) Hanley, L.; Whitten, J. L.; Anderson, S. L. *J. Phys. Chem.* **1988**, *92* (20), 5803.
- (92) Lian, L.; Su, C. -X.; Armentrout, P. B. *J. Chem. Phys.* **1992**, *97* (6), 4072.
- (93) Hales, D. A.; Su, C. -X.; Lian, L.; Armentrout, P. B. *J. Chem. Phys.* **1994**, *100* (2), 1049.
- (94) Hales, D. A.; Lian, L.; Armentrout, P. B. *Int. J. Mass Spectrom. Ion Process.* **1990**, *102*, 269.
- (95) Loh, S. K.; Hales, D. A.; Lian, L.; Armentrout, P. B. *J. Chem. Phys.* **1989**, *90* (10), 5466.
- (96) Magnera, T. F.; David, D. E.; Stulik, D.; Orth, R. G.; Jonkman, H. T.; Michl, J. *J. Am. Chem. Soc.* **1989**, *111* (14), 5036.
- (97) Grushow, A.; Ervin, K. M. *J. Chem. Phys.* **1997**, *106* (23), 9580.
- (98) Spasov, V. A.; Lee, T. H.; Maberry, J. P.; Ervin, K. M. *J. Chem. Phys.* **1999**, *110* (11), 5208.
- (99) Spasov, V. A.; Lee, T.-H.; Ervin, K. M. *J. Chem. Phys.* **2000**, *112* (4), 1713.
- (100) Rodgers, M. T.; Armentrout, P. B. *J. Phys. Chem. A* **1997**, *101* (7), 1238.
- (101) Hippler, M.; Quack, M.; Schwarz, R.; Seyfang, G.; Matt, S.; Märk, T. *Chem. Phys. Lett.* **1997**, *278* (1–3), 111.
- (102) Armentrout, P. B.; Rodgers, M. T. *J. Phys. Chem. A* **2000**, *104* (11), 2238.
- (103) Loh, S. K.; Lian, L.; Armentrout, P. B. *J. Am. Chem. Soc.* **1989**, *111* (9), 3167.
- (104) Freas, R. B.; Dunlap, B. I.; Waite, B. A.; Campana, J. E. *J. Chem. Phys.* **1987**, *86* (3), 1276.
- (105) Schultz, R. H.; Crellin, K. C.; Armentrout, P. B. *J. Am. Chem. Soc.* **1991**, *113* (23), 8590.
- (106) Kerns, K. P.; Guo, B. C.; Deng, H. T.; Castleman, A. W. *J. Chem. Phys.* **1994**, *101* (10), 8529.
- (107) Hales, D. A.; Armentrout, P. B. *J. Clust. Sci.* **1990**, *1* (1), 127.
- (108) Lian, L.; Su, C. -X.; Armentrout, P. B. *J. Chem. Phys.* **1992**, *96* (10), 7542.

- (109) de Sainte Claire, P.; Peslherbe, G. H.; Hase, W. L. *J. Phys. Chem.* **1995**, *99* (20), 8147.
- (110) Lian, L.; Su, C. -X.; Armentrout, P. B. *J. Chem. Phys.* **1992**, *97* (6), 4084.
- (111) Su, C. -X.; Armentrout, P. B. *J. Chem. Phys.* **1993**, *99* (9), 6506.
- (112) Simon, A.; Jones, W.; Ortega, J.-M.; Boissel, P.; Lemaire, J.; Maître, P. *J. Am. Chem. Soc.* **2004**, *126* (37), 11666.
- (113) Spasov, V. A.; Ervin, K. M. *J. Chem. Phys.* **1998**, *109* (13), 5344.
- (114) Su, C. -X.; Hales, D. A.; Armentrout, P. B. *J. Chem. Phys.* **1993**, *99* (9), 6613.
- (115) Rodgers, M. T.; Armentrout, P. B. *J. Phys. Chem. A* **1997**, *101* (14), 2614.
- (116) Stephan, K.; Märk, T. D. *Int. J. Mass Spectrom. Ion Phys.* **1983**, *47*, 195.
- (117) Amicangelo, J. C.; Armentrout, P. B. *J. Phys. Chem. A* **2000**, *104* (48), 11420.
- (118) Schultz, R. H.; Armentrout, P. B. *J. Phys. Chem.* **1993**, *97* (3), 596.
- (119) Butcher, C. P. G.; Johnson, B. F. G.; McIndoe, J. S.; Yang, X.; Wang, X.-B.; Wang, L.-S. *J. Chem. Phys.* **2002**, *116* (15), 6560.
- (120) Ingólfsson, O.; Busolt, U.; Sugawara, K. *J. Chem. Phys.* **2000**, *112* (10), 4613.
- (121) Gord, J. R.; Bemish, R. J.; Freiser, B. S. *Int. J. Mass Spectrom. Ion Process.* **1990**, *102*, 115.
- (122) Becker, S.; Dietrich, G.; Hasse, H.-U.; Klisch, N.; Kluge, H.-J.; Kreisler, D.; Krückeberg, S.; Lindinger, M.; Lützenkirchen, K.; Schweikhard, L.; Weidele, H.; Ziegler, J. *Zeitschrift für Phys. D Atoms, Mol. Clust.* **1994**, *30* (4), 341.
- (123) Velegrakis, M.; Mihesan, C.; Jadraque, M. *J. Phys. Chem. A* **2013**, *117* (14), 2891.
- (124) Fielicke, A.; Mitrić, R.; Meijer, G.; Bonačić-Koutecký, V.; von Helden, G. *J. Am. Chem. Soc.* **2003**, *125* (51), 15716.
- (125) de Sainte Claire, P.; Hase, W. L. *J. Phys. Chem.* **1996**, *100* (20), 8190.
- (126) van Heijnsbergen, D.; von Helden, G.; Duncan, M. A.; van Roij, A. J. A.; Meijer, G. *Phys. Rev. Lett.* **1999**, *83* (24), 4983.
- (127) van Heijnsbergen, D.; von Helden, G.; Meijer, G.; Duncan, M. A. *J. Chem. Phys.* **2002**,

- 116 (6), 2400.
- (128) Haslett, T. L.; Bosnick, K. A.; Moskovits, M. *J. Chem. Phys.* **1998**, *108* (9), 3453.
- (129) Lechtken, A.; Schooss, D.; Stairs, J. R.; Blom, M. N.; Furche, F.; Morgner, N.; Kostko, O.; von Issendorff, B.; Kappes, M. M. *Angew. Chemie Int. Ed.* **2007**, *46*, 2944.
- (130) Häkkinen, H.; Abbet, S.; Sanchez, A.; Heiz, U.; Landman, U. *Angew. Chem. Int. Ed. Engl.* **2003**, *42* (11), 1297.
- (131) Burow, M.; Wende, T.; Sierka, M.; Wlodarczyk, R.; Sauer, J.; Claes, P.; Jiang, L.; Meijer, G.; Lievens, P.; Asmis, K. R. *Phys. Chem. Chem. Phys.* **2011**, *13* (43), 19393.
- (132) Yoon, B.; Häkkinen, H.; Landman, U.; Wörz, A. S.; Antonietti, J.-M.; Abbet, S.; Judai, K.; Heiz, U. *Science* **2005**, *307* (5708), 403.
- (133) Xing, X.; Li, X.; Yoon, B.; Landman, U.; Parks, J. H. *Int. J. Mass Spectrom.* **2014**, *377*, 393.
- (134) Tibiletti, D.; Amieiro-Fonseca, A.; Burch, R.; Chen, Y.; Fisher, J. M.; Goguet, A.; Hardacre, C.; Hu, P.; Thompsett, D. *J. Phys. Chem. B* **2005**, *109* (47), 22553.
- (135) Dryza, V. Threshold Photo-ionisation and Density Functional Theory Studies of Metal-Carbide Clusters, PhD Thesis, The University of Adelaide, 2008.
- (136) Koch, W.; Holthausen, M. C. *A Chemist's Guide to Density Functional Theory*, 2nd ed.; Wiley-VCH Verlag GmbH, 2001.
- (137) Atkins, P.; de Paula, J. *Physical Chemistry*, 8th ed.; Oxford University Press: Oxford, 2006.
- (138) Neumann, J. V.; Wigner, E. *Nippon Sugaku-Buturigakkwaishi* **1929**, *3* (2), 239.
- (139) Ehrenfest, P.; Oppenheimer, J. R. *Phys. Rev.* **1931**, *37* (4), 333.
- (140) Laporte, O.; Meggers, W. F. *J. Opt. Soc. Am.* **1925**, *11* (5), 459.
- (141) Franck, J.; Hertz, G. *Verhandlungen der Dtsch. Phys. Gesellschaft* **1914**, *16*, 512.
- (142) Koopmans, T. *Physica* **1934**, *1*, 104.
- (143) Hollas, J. M. *Modern Spectroscopy*, 4th Ed.; John Wiley & Sons: Chichester, 2004.
- (144) Muller-Dethlefs, K.; Schlag, E. W. *Annu. Rev. Phys. Chem.* **1991**, 109.

- (145) Tkachenko, N. V. *Optical Spectroscopy*; Elsevier B.V.: Amsterdam, 2006.
- (146) Nemeth, G. I.; Ungar, H.; Yerezian, C.; Selzle, H. L.; Schlag, E. W. *Chem. Phys. Lett.* **1994**, 228, 1.

Chapter Three

Computational Theory and Methodology

This chapter describes the methodology employed to calculate the geometric and electronic properties of both cerium oxide and gold doped cerium oxide clusters. The chapter is presented in two parts. Firstly, a brief discussion will be presented on the theoretical background of Density Functional Theory (DFT). This will be followed by procedural details for the DFT process used in the context of this work. Secondly, the methodology behind Zero Electron Kinetic Energy spectral simulations will be detailed. This will include a discussion on the method used to construct PIE spectra for the cluster species of interest using calculated ZEKE spectra.

3.1. Theoretical Background

3.1.1. The Schrödinger Equation

All computational methods attempt to solve the time independent, non-relativistic Schrödinger Equation shown in Equation (3.1)¹.

$$E\Psi(\mathbf{q}_e, \mathbf{q}_N) = H\Psi(\mathbf{q}_e, \mathbf{q}_N) \quad (3.1)$$

Where E represents a series of eigenvalue solutions which completely describes the energy of the system. Solutions for E are dependent on the wavefunction, $\Psi(\mathbf{q}_e, \mathbf{q}_N)$, which is expressed as a function of both the electronic and nuclear coordinates \mathbf{q}_e and \mathbf{q}_N , respectively. The wavefunction is a mathematical construct comprising real and imaginary terms which, when squared (i.e. multiplied by its complex conjugate), gives the electron density. When queried by a quantum mechanical operator, the wavefunction gives the probability of a particular result. The H term is the time independent, non-relativistic Hamiltonian (energy) operator. The Hamiltonian was introduced previously in Chapter 2; it represents the summation of the kinetic and Coulombic energy contributions for each particle in the system.

In principle, the Schrödinger Equation represents the exact solution to any molecular system. However, the Schrödinger Equation is prohibitively difficult to solve for all but the simplest molecular systems; exact solutions have so far only been found for one-electron systems¹. The difficulty lies with finding an exact representation of the wavefunction, which becomes intractable once additional electrons are included due to electron-electron interactions such as Coulombic repulsion and electron exchange. The former is due to the negatively charged electrons undergoing electrostatic repulsion with all other electrons in the system. The latter results from the Pauli Exclusion Principle, which states that fermions cannot occupy the same quantum state simultaneously; electrons with the same spin state will therefore experience a short-range repulsion. The consequence of both these phenomena is that the motion of every electron in the molecular system becomes dependent on the motion of every other electron

in the molecular system. Moreover, the tendency of electrons to avoid each other through short range exchange interactions and long-range Coulombic repulsion, creating regions of low electron density; these regions are known as exchange – or Fermi – and correlation – or Coulomb – holes, respectively.

3.1.2. The Born Oppenheimer Approximation (Revisited)

Both the molecular wavefunction and the Hamiltonian operator can be simplified considerably by applying the Born Oppenheimer Approximation (discussed previously in Chapter 2). The wavefunction can then be expressed as a function of the electronic coordinates only, with regard to a set of parameterised nuclear coordinates that remain constant. This is known as the electronic wavefunction Ψ_{elec} and can be expressed as follows:

$$\Psi(\mathbf{q}_e; \mathbf{q}_N) = \Psi_{elec} \quad (3.2)$$

The nuclear coordinates \mathbf{q}_N are separated from the electronic coordinates \mathbf{q}_e by a semi-colon to denote their function as constant parameters. The Born Oppenheimer Approximation also greatly simplifies the Hamiltonian operator, as discussed previously in Chapter 2. Briefly, the nuclear kinetic term can be set to zero – since the nuclei are effectively stationary – while the nuclear-nuclear repulsion becomes constant. Because constant terms do not affect the result when an operator is applied to an eigenfunction, both these terms can be removed from the Hamiltonian. The electronic-nuclear interaction term can be expressed as the energy of each electron on a positively charged background potential which remains constant. The simplified Hamiltonian – known as the electronic Hamiltonian, H_{elec} – can be expressed in terms of the electron kinetic energy, electron-nuclear attraction and electron-electron repulsion as follows:

$$H_{elec} = -\frac{1}{2}\sum_{i=1}^N \nabla_i^2 - \sum_{i=1}^N \sum_{A=1}^M \frac{Z_A}{r_{iA}} + \sum_{i=1}^N \sum_{j>i}^N \frac{1}{r_{ij}} = \hat{T}_e + \hat{V}_{Ne} + \hat{V}_{ee} \quad (3.3)$$

The first two terms in Equation (3.3) can be solved easily. However, the final term, which represents the electron-electron interactions, is still quite difficult to solve due to electron correlation. This will be discussed further at a later point in this chapter.

3.1.3. The Variational Principle

While the wavefunction presented in Equation (3.2) is greatly simplified through the Born Oppenheimer Approximation, the exact form of the wavefunction – i.e. the wavefunction correctly describes the properties of the molecular system of interest when queried by the relevant operator – is not known. Moreover, the only requirements for a wavefunction to be solvable by the Schrödinger Equation are that it is (i) single valued at all points; (ii) continuous, with no infinite-valued regions spanning a finite length; (iii) has a continuous first derivative; and (iv) is square integrable over all space². Given the large set of available eigenfunctions which satisfy these requirements, it is not feasible to simply conduct an arbitrary search for the correct wavefunction. The Variational Principle simplifies the search for the correct wavefunction by postulating that for a set of possible trial wavefunctions – Ψ_{trial} – there will be a corresponding set of energy eigenvalues – E_{trial} – which will contain a value E_0 that represents the lower bound of the set. Therefore the closer the energy E_{trial} is to the value E_0 , the better the approximation of the wavefunction Ψ_{trial} to the actual wavefunction Ψ_0 , as shown below¹:

$$\langle \Psi_{trial}^* | \hat{H} | \Psi_{trial} \rangle = E_{trial} \geq E_0 = \langle \Psi_0^* | \hat{H} | \Psi_0 \rangle \quad (3.4)$$

A consequence of the Variational Principle is that the wavefunction which best describes the molecular system corresponds to the global minimum on the Potential Energy Surface. Many different computational methods are employed to find the correct wavefunction; the most popular ones are the Hartree-Fock method and Density Functional Theory.

3.1.4. The Hartree-Fock Method

The Hartree-Fock method simplifies the N -electron wavefunction by treating it instead as a product of N one-electron wavefunctions^{1,4}. Each one-electron wavefunction is constructed via a linear combination of Hartree products, $\chi_i(\mathbf{x}_i)$ which consist of spin-orbit functions χ_i dependent on the spin-spatial coordinates of each electron, denoted \mathbf{x}_i . Each one-electron wavefunction contains a linear combination of all spin-orbit functions to effectively give each electron a probability of occupying all orbitals. The Hartree-Fock method is advantageous in that it is (i) generalised, in that any electron can occupy any orbital; and (ii) consistent with the principle of electrons being indistinguishable. The set of one-electron wavefunctions are represented in determinantal form by a Slater Determinant. This intrinsically accounts for electron exchange since interchanging any two rows in the determinant will automatically change the sign of the wavefunction. For computational convenience, the one-electron wavefunctions are chosen to be linearly independent; in practice, this describes a non-interacting system of electrons on a positively charged background. The Slater Determinant for an N -electron system is shown in Equation (3.5).

$$\Psi_N \approx \Phi_{SD} = \frac{1}{\sqrt{N!}} \begin{vmatrix} \chi_1(\mathbf{x}_1) & \cdots & \chi_N(\mathbf{x}_1) \\ \vdots & \ddots & \vdots \\ \chi_1(\mathbf{x}_N) & \cdots & \chi_N(\mathbf{x}_N) \end{vmatrix} \quad (3.5)$$

The wavefunction is optimised iteratively using the Self-Consistent Field (SCF) process: for each electron, the one-electron Hamiltonian operator (known as the Fock operator) is applied; the orbital functions are then optimised until the energy is minimised. Once the N -electron wavefunction has been solved, the gradient of the potential energy surface is calculated and the atomic coordinates are shifted corresponding to the steepest descent on the potential energy surface. The process is then repeated until a stationary point is located. The Hartree-Fock process is popular owing to its relatively low computational expense, which typically scales with N^4 . However, the electron exchange and correlation energies are calculated poorly; the Hartree-Fock process only determines the exchange energy for a set of non-interacting electrons and ignores electron correlation entirely. Post-Hartree-Fock methods have been devised to calculate the correlation energy such as Moller-Plesset perturbation³,

Configuration Interaction⁴ and Coupled Cluster⁵⁶ methods, in addition to the Multi-Configurational Self-Consistent Field method⁷ which uses a linear combination of configuration determinants to calculate the N -electron wavefunction. While these methods have been employed successfully in computationally difficult problems such as the electronic structures of radical cations^{8,9} and proton transfer events in amino acids¹⁰⁻¹³, post-Hartree Fock methods have limited application toward metal containing clusters owing to the extensive number of electrons associated with the metal centres rendering calculations impractically expensive.

3.1.5. Density Functional Theory

Density Functional Theory (DFT) has gained increasing popularity in recent years for its ability to calculate molecular systems – including exchange and correlation energies – with a computational expense comparable to the Hartree-Fock method. Origins of DFT come from Thomas⁸ and Fermi⁹, who in 1927 independently proposed that the energy of a molecular system could be considered as a function of the electron density instead of the complex N -electron wavefunction. Unlike the wavefunction, which is a purely mathematical construct, the electron density is observable and thus can be verified experimentally. Density Functional Theory determines the energy of the system as a function of the electron density, $\rho(\mathbf{r})$, which is itself a function of the electronic coordinates. Because each electron has 3 spatial coordinates, DFT formally scales as N^3 .

Initial DFT methods developed by Thomas and Fermi described molecular systems using the uniform electron gas model whilst treating the kinetic energy, electron-nuclear interactions and electron-electron interactions in a classical manner^{14,15}. This model failed spectacularly in that for all cases the molecular system was unstable with respect to its fragments. The concept of calculating molecular systems using the electron density was then largely ignored until 1964, when Hohenberg and Kohn proposed their two existence theorems¹⁶. These theorems relate to a system of electrons moving under the influence of an external potential V_{ext} :

1. The external potential V_{ext} , and hence the total energy, is a unique functional of the electron density $\rho(\mathbf{r})$.
2. The ground state energy can be obtained using the Variational Principle. The density that minimises the total energy corresponds to the exact ground state density.

The failure of the Thomas-Fermi model was found to lie in both the crude approximation of the electron kinetic energy and the neglect of exchange and correlation terms. The former of these issues was resolved in 1965 by Kohn and Sham, who showed that any system of interacting particles had the same density as a system of non-interacting particles¹⁷. The Slater Determinant from the Hartree Fock method, which was used to approximate the wavefunction of an N -electron system, could exactly describe the wavefunction of a system of non-interacting electrons. The kinetic energy and exchange terms of the non-interacting system could therefore be computed exactly. Moreover, because electron correlation has no effect on the electron density, the correlated kinetic energy and exchange terms and the Coulombic interactions could all be ignored whilst calculating the electron density; these terms could then be calculated afterwards, using the correct electron density. This is known as the Kohn-Sham method: electrons are treated as non-interacting particles on a positively charged background to calculate the exact energy for a non-interacting system; the interaction energies from electron exchange and correlation are then approximated. The process is quite similar to the Hartree-Fock method: linearly independent one-electron wavefunctions are formed via a linear combination of Kohn-Sham orbitals; the corresponding set of one-electron energy (Fock) operators are then solved iteratively to locate a stationary point on the potential energy surface. The electron density is determined from the corresponding Kohn-Sham orbitals and used to calculate the non-interacting electronic energy. The interacting energy from both electron exchange and correlation – known as the exchange-correlation energy – is then calculated and added to the non-interacting electronic energy to give the complete electronic energy.

3.1.6. Exchange and Correlation Functionals

While the electron density and the non-interacting electronic energy can be determined exactly, an exact solution to the exchange-correlation energy – is yet to be found. This term is therefore solved by approximation. Several methods are used, which will now be discussed.

3.1.6.1. Local Density Approximation Functionals

The Local Density Approximation (LDA) – also known as the Local Spin Density Approximation (LSDA) for spin unrestricted systems – assumes the uniform electron gas model to approximate the exchange-correlation energy at each point in space as a function of the electron density at that point¹. The uniform electron gas model perfectly describes the electron distribution within an infinite homogeneous crystal and is used since it allows the exchange hole to be computed exactly in these cases. The correlation hole cannot be determined exactly and is approximated. However, unlike infinite crystal structures which have a homogeneous electron distribution, discrete molecular systems are usually characterised by non-homogeneous, rapidly varying electron densities. The LDA is thus a poor approximation for small molecular systems; particularly electron-rich species such as anions. Common LDA correlation functionals include the Vosko-Wilk-Nusair (VWN)¹⁸, Perdew-Zunger (PZ81)¹⁹ and Perdew-Wang (PW92)²⁰ functionals.

3.1.6.2. Generalised Gradient Approximation Functionals

The Generalised Gradient Approximation (GGA) accounts for the non-homogeneity of molecular systems by considering both the electron density and the electron density gradient at each point on the potential energy surface. This is performed through a first term Taylor expansion of the electron density¹. GGA exchange and correlation functionals are typically combined to yield a corresponding exchange-correlation functional. For example, the BP86 exchange-correlation functional is comprised of the Becke 1988 (B) exchange²¹ and the Perdew 1986 (P86) correlation functionals²², both of which employ a VWN Local Spin Density Approximation as well as a Generalized Gradient Approximation for improved accuracy.

3.1.6.3. Hybrid Functionals

Hybrid functionals further improve on the generalised gradient approximation for the exchange energy by including a Hartree-Fock exchange term. This term describes the exact exchange energy for the non-interacting system; the exchange energy for correlated electrons is then approximated. An example of a hybrid functional is the B3P86 exchange-correlation functional, which combines the Becke 3 parameter exchange⁵ (B3) and the P86 correlation functionals. The Becke 3 parameter exchange functional calculates the exchange energy as a combination of both the Hartree-Fock exchange energy and the correlated exchange energy; the latter is approximated using both the LSDA and the Becke GGA exchange functionals. The form of the B3P86 exchange-correlation functional is as follows:

$$E_{XC} = 0.2E_X(HF) + 0.8E_X(LSDA) + 0.72\Delta E_X(B88) + 0.81E_C(P86) + 0.19E_C(VWN) \quad (3.6)$$

Where the terms E_X and E_C represent exchange and correlation energies, respectively. Previous work by Dryza and Gentleman²³⁻²⁶ has shown the B3P86 exchange-correlation functional to reliably predict ionisation energy trends of metallic clusters with sequential addition of carbon and oxygen atoms. They also noted a tendency for the B3P86 functional to systematically calculate ionisation energies ca. 0.3 eV⁷ higher than experimental IE values. The magnitude of the error was observed to be largely dependent on the metal atoms and remained constant – to a good approximation – with sequential addition of C and O atoms. Therefore, this error – the source of which will be explained later – could be corrected quite easily. The B3P86 functional is used in all calculations presented in this thesis.

3.1.7. Computational Search Methods

The optimisation algorithms employed by the Hartree-Fock and DFT methods are both quite similar. The wavefunction is optimised for a particular atomic configuration; the first derivative is then taken to find the gradient of the potential energy surface at that point. The atomic coordinates are shifted corresponding to the steepest descent of the gradient and the

wavefunction is re-optimised. This process is repeated along the potential energy surface until the gradient converges within a set of predefined tolerances to a stationary point²⁷.

The nature of a stationary point can be determined by analysis of the vibrational modes for the converged structure. Non-linear molecular systems possess $3N-6$ vibrational modes, derived from the $3N$ degrees of freedom possessed by a molecule with N atoms (each atom can be displaced in 3 spatial coordinates). There are 6 degrees of freedom that correspond to translation and rotation – the entire molecule can translate along 3 unique spatial coordinates and rotate about 3 unique axes – which do not contribute to vibrations. Linear molecules possess $3N-5$ vibrational modes due to the absence of one rotational degree of freedom along the molecular axis.

The vibrational frequencies of the converged structure are typically determined by diagonalization of the Hessian matrix, which contains the second derivatives of the potential with respect to displacement of the atoms in Cartesian coordinates²⁸. This diagonalization process yields a series of eigenvalues which correspond to the vibrational frequencies for the molecular system. Imaginary eigenvalue solutions are known as imaginary frequencies.

Any stationary point possessing zero imaginary frequencies is identified as a minimum. The minimum corresponding to the lowest point on the potential energy surface and – thus the closest approximation to E_0 – is labelled the global minimum. All other minima are known as local minima and typically correspond to metastable structures; these constitute either structural isomers, which display a different geometric arrangement of atoms, or spin isomers, which possess the same structure in different electronic spin states.

A stationary point with one or more imaginary frequencies is known as a saddle point. Saddle points are characterised by positive and negative second derivatives in orthogonal directions. As such, a local maximum along one axial direction simultaneously corresponds to a local minimum along a different axis. n th order saddle points are characterized by the possession

of n imaginary eigenvalue solutions. A first order saddle point is often characteristic of a transition state; higher order saddle points have no chemical significance.

3.1.8. Basis Sets

3.1.8.1. Theoretical Background

A basis set comprises a set of vectors which describes the spatial boundaries for each electron. Basis sets are used in Hartree-Fock to approximate molecular orbitals and in DFT as purely mathematical constructs – labelled Kohn-Sham orbitals – to determine the electron density¹. Basis set choice is usually dependent on both the desired accuracy and the acceptable computational expense. Minimal basis sets provide low accuracy calculations at minimal computational expense which can be useful for initial geometry optimisations. Larger basis sets allow calculations with increased accuracy albeit at far greater computational expense.

Basis sets are constructed either via Slater Type Orbitals (STOs)²⁹ or Gaussian Type Orbitals (GTOs)³⁰, both of which are mathematical functions used to model atomic orbitals. The forms of STO and GTO functions are presented in Equations (3.7) and (3.8), respectively.

$$\text{STO: } \chi_{n,l,m,\zeta}(r, \theta, \varphi) = NY_{l,m}(\theta, \varphi)r^{n-1}e^{-\zeta r} \quad (3.7)$$

$$\text{GTO: } \chi_{n,l,m,\zeta}(r, \theta, \varphi) = NY_{l,m}(\theta, \varphi)r^{n-1}e^{-\zeta r^2} \quad (3.8)$$

In the above equations the terms n , l , and m represent the principal, angular and magnetic quantum numbers, respectively. Additionally, the terms r , $Y_{l,m}(\theta\varphi)$, ζ and N designate the radial distance, spherical harmonics, atomic shielding constant and normalisation factor, respectively. While STOs provide excellent models for hydrogenic atomic orbitals, they can take longer to integrate analytically. To make calculations simpler, STOs are approximated by Gaussian Type Orbitals. GTOs are a considerably poorer approximation for atomic orbitals than STOs – particularly near the nucleus – and diminish too rapidly with distance. However, contracted GTOs can be formed by a linear combination of Gaussian functions – known as

primitive Gaussian functions – to provide a better approximation of STO functions and hence hydrogenic orbitals. A contracted GTO formed from n primitive GTOs can be represented as follows:

$$STO \cong GTO(nG) = c_1 e^{-\beta_1 r^2} + c_2 e^{-\beta_2 r^2} + \dots + c_n e^{-\beta_n r^2} \quad (3.9)$$

Where c_1, c_2, \dots, c_n and $\beta_1, \beta_2, \dots, \beta_n$ are weightings determined by a least squares fit of the contracted GTO (Equation (3.9)) to a Slater Type Function (Equation (3.7))³¹. Provided that sufficient contractions are performed, contracted GTOs can give a good approximation of STOs as shown in Figure 3.1. Integration of contracted GTOs has been shown to be several orders of magnitude faster than integration of STOs; thus, contracted GTOs are used preferentially in the construction of basis sets. Depending on the specified basis set, different numbers of primitive Gaussians are used to construct the GTOs. Some commonly used basis sets are described below.

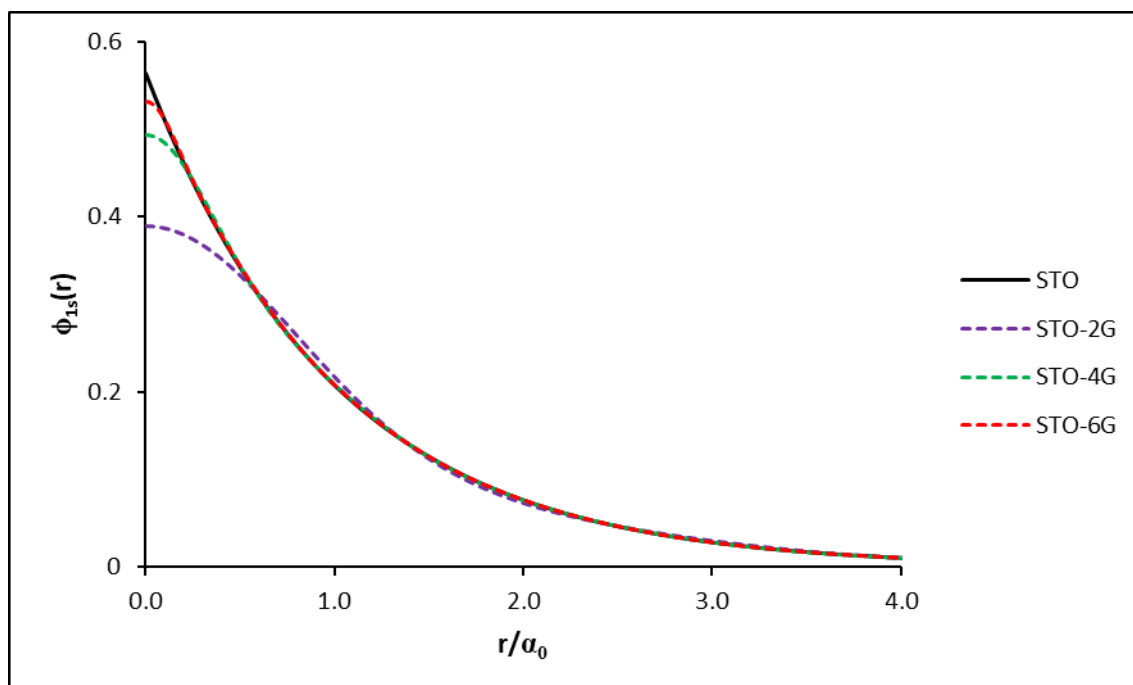


Figure 3.1: Comparison of contracted Gaussian Type Orbitals (GTOs) with Slater Type Orbitals (STOs). Contracted GTOs are labelled STO- n G, where n denotes the number of Gaussian Functions used in the contraction.

3.1.8.2. Pople Basis Sets

Initial GTO basis sets were designed by Pople in 1969 and used a linear combination of n primitive Gaussians to produce a contracted GTO³². This family of basis sets, known as STO- n G – where n denotes the number of primitive GTOs used in each contraction – gives a reasonable approximation of an STO at minimal computational expense. However, the small basis set size limits the number of trial wavefunctions available to approximate the ground state wavefunction in accordance with the Variational Principle. Moreover, because each orbital is described by only one contracted GTO, orbitals are not able to expand or contract depending on the surrounding molecular environment. Consequentially, Pople basis sets generally give a poor description of chemical bonding.

3.1.8.3. Split Valence Basis Sets

The poor flexibility in the STO- n G basis sets was resolved by Pople in 1980 with the development of split valence basis sets³³. The valence electrons, which contribute most significantly to bonding, are described by a sequential contraction of primitive Gaussians. This improves the flexibility of the basis set and allows the valence orbitals to expand or contract depending on the molecular environment. The core electrons, which do not contribute to chemical bonding, are treated in the same manner as the STO- n G basis sets. Split valence basis sets are described by the number of sequential Gaussian contractions used to construct the valence orbitals (e.g. double zeta basis sets use 2 sequential contractions). A typical example of a (double zeta) split valence basis set is the 6-31G (pronounced six-three-one-G). The core orbitals are constructed by a contraction of 6 primitive Gaussians. The valence orbitals are constructed by a contraction of 3 primitive Gaussians, followed by a subsequent contraction with 1 primitive Gaussian. Split valence basis sets which use up to six sequential contractions have been developed; however, sequential contractions come with a substantial increase in computational expense. Basis sets typically used in calculations of lanthanides and transition metals are double and triple zeta quality, respectively.

3.1.8.4. Basis Set Selection and Justification

The two basis sets available for lanthanide atoms on Gaussian09 include the Stuttgart-Dresden (SDD) and the Los Alamos National Laboratory (LANL) families of basis sets. Both basis sets are split valence, offering double zeta quality treatment of the valence electrons. However, previous benchmarking calculations by Addicoat³⁴ found the SDD basis set was more suited to calculations of small transition metal oxide clusters; particularly when utilising polarisation functions on the oxygen atoms. Gentleman^{26,35} has subsequently used the SDD basis set with the B3P86 density functional in calculations of small $Rh_xHo_mO_n$ and $Au_xPr_mO_n$ clusters; calculated IE trends and simulated PIE spectra both showed excellent agreement with experimental data. Therefore, the SDD basis set is chosen for all calculations.

The SDD basis set utilises GTO functions with contractions of (12s11p9d8f)/[9s8p6d5f] and (8s6p5d)/[7s3p4d] for Ce and Au, respectively^{36–38}. In this notation, the functions inside the parentheses denote the number of primitive Gaussian functions for each orbital type; the functions inside the square brackets denote the number and type of contracted Gaussian functions. Oxygen atoms are treated with the Dunning D95 basis set³⁹ which provides a (16s7p)/[[6s4p] contraction.

3.1.9. Effective Core Potentials

3.1.9.1. Theoretical Background

Calculations of heavy transition metals and lanthanides can be difficult owing to the large number of basis sets required to describe the many-electron system. Accordingly, all-electron calculations are not computationally feasible for all but the smallest molecular systems. Calculations of lanthanides are further complicated by the high degeneracy of the 4f subshells – in addition to open 5d and 6s shells – which can present an incredibly high number of low-lying electronic states for even the simplest lanthanide containing species. This can cause difficulties with wavefunction convergence owing to the vast number of energetically similar trial wavefunctions available. Effective Core Potentials (ECPs) and Pseudopotentials provide a computationally simpler – and less expensive – alternative to all-electron calculations. Since core electrons have only an indirect influence on chemical bonding – via interactions with the

valence shell – and do not directly participate in chemical bonding themselves, they do not require an explicit treatment. The core electrons and nuclei are therefore described by a series of analytical functions to approximate their influence on the valence shell²⁷. Valence electrons, which are strongly influenced by the molecular environment, are treated explicitly using the methods described previously. Depending on the size of the ECP, sub-valence electrons can also be afforded an explicit treatment; this is done largely to account for non-classical correlation effects – which are poorly modelled by ECPs – on the valence electrons. Effective Core Potentials furthermore allow the consideration of core relativistic effects by introducing relativistic parameters to the non-relativistic one-electron Fock operators; these are known as quasi-relativistic ECPs⁴⁰. Valence electrons, which are not included in the ECP, are afforded a classical treatment. ECPs can be limited in their ability to describe the electronic configuration of molecular systems; this is particularly the case for open shell ECPs, where unpaired electrons may be drawn into the frozen core. However, molecular properties which are not strongly dependent on the electron configuration – such as ionisation energies and vibrational frequencies – may be computed accurately at a reasonable computational expense.

3.1.9.2. *Effective Core Potential Selection and Justification*

During the course of this work, the performances of three different frozen core treatments of cerium were benchmarked with regard to predicting both the geometries of Ce₂ and CeO dimers and the IEs for the Ce₂O_n cluster series. The results of this benchmarking study can be found in Chapter 4. A total of 3 different-sized ECPs are available in Gaussian09; all of which were developed by Dolg et al.^{37,41} from Hartree-Fock all-electron calculations. The pseudopotential coefficients were optimised from a multi-electron fit to several low-lying valence states of numerous lanthanide atoms in both neutral and cation states. The ECPs are all afforded a quasi-relativistic treatment using all-electron calculations by Wood and Boring⁴². All ECPs are thus labelled MWBN (Multi-electron Wood Boring), where *N* denotes the number of electrons drawn into the frozen core. Available frozen core treatments for Ce include the MWB28, MWB47 and MWB48 ECPs, which will now be discussed.

The MWB28 ECP is a closed shell pseudopotential which draws the $n=1,2,3$ shells into the frozen core^{42,43}. The electron configuration for Ce – which has 58 electrons – is reduced to $[28]4s^24p^65s^24d^{10}5p^66s^24f^15d^1$ to maintain the valence configuration of $4f^15d^16s^2$. However, the large number of electrons requiring an explicit treatment makes this ECP quite computationally expensive.

The cerium atoms are alternatively treated with $4f^n/Q10$ and $4f^n/Q11$ open shell ECPs^{41,44}. These ECPs – which offer a generic treatment of all lanthanide atoms – afford an explicit treatment of the outer 10 and 11 electrons, respectively; all other electrons are drawn into the frozen core. In the case of cerium, which has 58 electrons, these ECPs are known as MWB48 and MWB47, respectively. Treatment of Ce with the MWB48 ECP yields the valence configuration $5s^25p^66s^2$, where both the 4f and 5d electrons are drawn into the frozen core. The MWB47 ECP yields a Ce valence configuration of $5s^25p^66s^25d^1$; the 5d electron is left in the valence shell while the 4f electron is drawn into the core. The MWB47 and MWB48 ECPs differ from the MWB28 pseudopotential in that they are not parameterized *a priori*; while the 4f and 5d electrons are initially drawn into the frozen core, the ECP does not prevent the 4f and 5d shells from later becoming occupied during wavefunction optimisation processes. The open shell nature of both ECPs means not all subshells within a particular electron shell are drawn into the frozen core. Conversely, subshells in the frozen core are not necessarily filled. While these effects prevent the electronic structure from being studied in detail, test calculations by Dolg et al.⁴⁵ have shown the $4f^n/Q10$ and $4f^n/Q11$ pseudopotentials accurately calculate bond lengths and vibrational frequencies of simple lanthanide systems such as monoxides, monohydrides and monofluorides. Moreover, both ECPs come at a greatly reduced computational expense to the MWB28 ECP.

Gold atoms are treated with the closed shell MWB60 ECP where the $n=1,2,3,4$ electron shells are drawn into the frozen core. The electronic configuration of gold is then reduced to $[60]5s^25p^65d^{10}6s^1$. The MWB60 ECP is the sole ECP available for gold in the Gaussian09 program; benchmarking studies are therefore not performed on gold ECPs. Moreover, the simple electronic configuration of the gold valence shell does not present the same issues as

cerium with regard to the explicit treatment of open subshells with high angular momenta; the 5s, 5p and 5d subshells are all fully occupied, while the remaining open 6s subshell can be treated explicitly with little difficulty due to the lack of angular nodes. Oxygen atoms are similarly afforded a 2 electron ECP treatment to yield an electronic configuration of $[2]2s^22p^4$.

3.2. DFT Optimisation Procedure

Calculations were performed using a number of computational facilities courtesies of eResearchSA and the National Computational Infrastructure. These include Tizard (a CPU cluster containing 48 SGI nodes, each containing 4 AMD 12-core 2.6 GHz CPUs)⁴⁶, Corvus (an SGI Altrix 1300 cluster with 68 Altrix XE310 nodes each containing 2 Intel Clovertown quad-core 2.66 GHz processors)⁴⁷, Vayu (a series of Sun Blade X6275 modules with 1492 nodes, each containing two quad-core 2.93 GHz Intel Nehalem CPUs)⁴⁸ and Raijin (3592 compute nodes, each containing four quad-core 2.6 GHz Intel Xeon Sandy Bridge processors)⁴⁸. Benchmark calculations were performed across all platforms to verify the consistency of calculated results.

DFT calculations in this work were performed using the B3P86 exchange correlation functional^{22,49} with the SDD basis set on the Gaussian09 suite of programs⁵⁰. Frozen core approximations for the Ce, Au and O atoms were performed using MWB28, MWB60 and MWB2 ECPs, respectively. The MWB47 and MWB48 frozen core treatments for Ce atoms were also considered during initial benchmarking calculations, which are presented in Chapter 4. The core Hamiltonian was diagonalised to form the initial wavefunction guess at each optimisation step. Calculations were performed at 298 K.

An extensive search of potential geometries was performed for each cluster species. Ce_mO_n starting structures were prepared by placing an oxygen atom near each individual atom and along each bridge and face of the $Ce_mO_{(n-1)}$ cluster. Similarly, $AuCe_mO_n$ starting structures were prepared by placing an O or Au atom near each atom and along each bridge and face of the $AuCe_mO_{(n-1)}$ and Ce_mO_n clusters, respectively. All cluster geometries were optimised in the lowest four spin states (S), otherwise expressed as the multiplicity (m) where $m=2S+1$. For

systems with an even number of electrons outside the frozen core, the $m=1,3,5,7$ multiplicities were considered. Similarly, systems with an odd number of electrons outside the frozen core were calculated in $m=2,4,6,8$ multiplicities. For systems where the $m=7$ or $m=8$ multiplicities corresponded to the lowest energy structure, higher spin states were considered. Cluster geometries were initially optimised without symmetry constraints; all structures within 1 eV of the lowest energy neutral structure with near-symmetric geometries were then constrained to the relevant point groups and re-optimised[†]. Frequency calculations were performed post-optimisation to verify convergence at a minimum on the potential energy surface. In cases where the lowest energy structure or low-lying structures were found to converge to a saddle point, the structures were distorted along the coordinates of the imaginary frequency and re-optimised. Wavefunction stability calculations were then performed on all minima within 1eV of the lowest energy structure.

Atomic charges were determined via Hirshfeld charge analysis. Hirshfeld charges were selected in favour of other methods such as Mulliken charges (which are heavily dependent on the basis set) and Bader and Weinhold (Natural Population Analysis) charges since Hirshfeld charges have been reported to offer a more chemically meaningful charge analysis⁵¹.

Cationic states were calculated for all unique neutral structures within ca. 1 eV of the lowest energy structure. The process for calculating cation geometries was the same as for the neutrals; however, the optimised neutral structures were used as starting geometries. Moreover, only $\Delta m = \pm 1$ (i.e. $\Delta S = \pm 1/2$) multiplicities relative to the neutral structure were considered in accordance with the spin conservation rule. The adiabatic ionisation energy was calculated as the difference between the combined electronic and zero-point energies of the neutral structure and the relevant cation.

[†] Symmetry constrained structures are presented where possible. While every effort was made to optimise structures constrained to their relevant point groups, this was often problematic due to convergence difficulties associated with high-symmetry structures. Unconstrained structures are presented in these cases.

3.3. Comparison of Calculated and Experimental Properties

3.3.1. Ionisation Energy Calculations

Computational chemistry packages are invaluable in exploring the geometric and electronic properties of metal clusters; particularly when combined with experimental probing techniques. Two pertinent features of clusters that can both be calculated with computational chemistry packages and determined experimentally via Photo-Ionisation Efficiency (PIE) spectroscopy include the ionisation energy (IE) – which will be discussed here – and the Franck Condon (FC) overlap between the neutral and cationic wavefunctions, which is taken from the slope of the PIE curve (this will be discussed in a later section).

Calculated and experimental IEs can be compared in order to give confidence in the calculated electronic structures – and thus inferred reactivities – of the relevant cluster species. Previous work by Dryza et al.^{24,25}, Addicoat³⁴ and Gentleman et al.^{26,35} has shown that DFT can be used to predict IE trends for metal clusters with sequential oxidation. However, while DFT methods – in particular, the B3P86 method – have been shown to match IE trends with those determined experimentally, DFT-calculated IEs tend to be systematically higher than experimental IEs by ca. 0.2 – 0.7 eV. This error arises from the implicit treatment of core electrons through the use of ECPs, which provides a poor approximation of core-valence correlation effects. This causes an over-binding of the explicitly treated valence electrons, which experience less repulsion from the core electrons and thus are more strongly bound to the cluster. Because this effect is dependent on the frozen cores, which are largely centred on the metal atoms, the IE over-prediction tends to be – to a good approximation – independent of the non-metal atoms within the cluster. Thus, the error can be treated by correcting the calculated IE of the bare metal cluster to the experimental IE; the same correction is then applied to the cluster oxides with the same metal base. An example of this process is shown in Figure 3.2. Previous work by Dryza et al.^{24,25}, Addicoat et al.³⁴ and Gentleman et al.^{26,35} have all shown that the calculated IEs, once corrected, tend to agree with experimental IE values within ca. 0.2 eV. All calculated IEs presented in this work are therefore assigned error values of ± 0.2 eV. This value accounts for errors intrinsic to the DFT process.

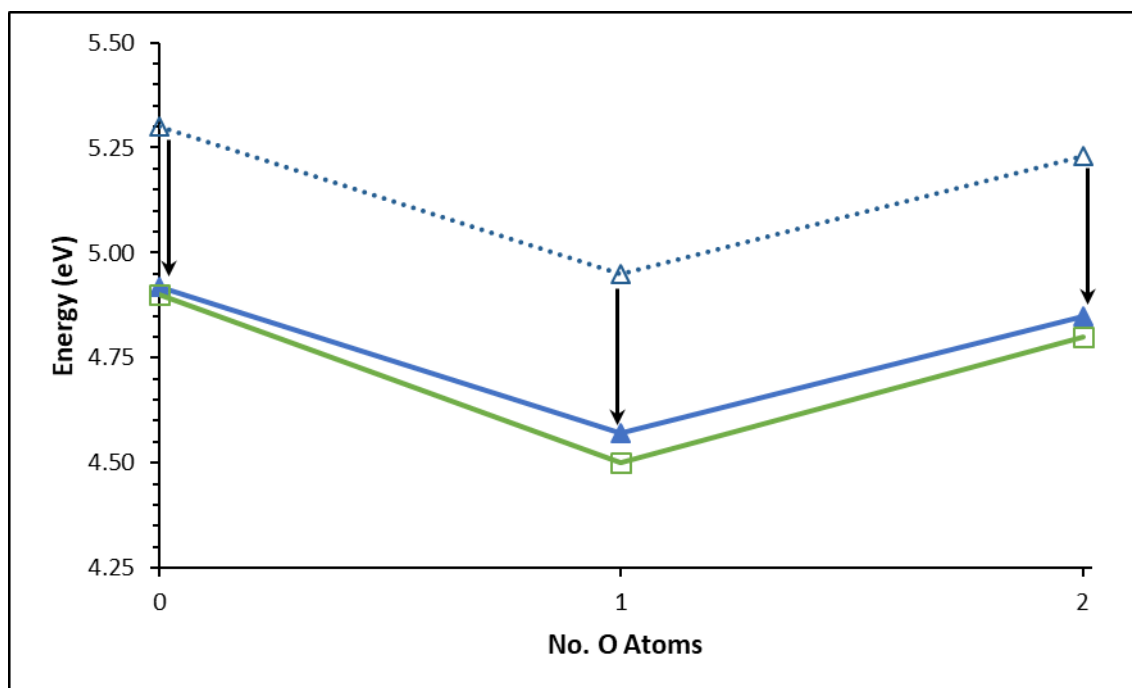


Figure 3.2: Example of calculated and experimental IEs (shown as a dotted blue line and solid green line, respectively) plotted as a function of the number of oxygen atoms within the cluster species. The calculated IE for the bare metal cluster is corrected to the experimentally determined IE. This correction is then applied to the IEs of the remaining cluster species. The corrected calculated IE is shown as a solid blue line.

3.3.2. Zero Electron Kinetic Energy and Photo-Ionisation Efficiency Simulations

The Franck-Condon overlap between the neutral and cationic cluster species, and the underlying vibronic structures of both species, are investigated by way of the PIE spectral profile. Simulated and experimentally recorded PIE spectra are compared to provide confidence in the geometries of the calculated cluster species. This novel technique developed by the Metha group³⁵ has been used to successfully correlate the experimental and calculated PIE spectra of small rhodium-holmium clusters and their oxides³⁵. The comparison of experimental and calculated PIE spectra extends from previous work by Yang et al^{52,53} who showed the ZEKE spectra of Nb₃O and Y₃C₂ clusters could be calculated to good agreement with their respective experimental spectra.

PIE spectra for potential ionisation processes are calculated implicitly using Zero Electron Kinetic Energy (ZEKE) spectral simulations. The experimental details behind ZEKE spectroscopy are discussed in Chapter 2. Briefly, a ZEKE spectrum is similar to a conventional absorption spectrum; however, photon absorption results in photo-ionisation and not photo-excitation. Each peak in the ZEKE spectrum corresponds to a vibronic transition between the neutral and cationic states. The integration of a ZEKE spectrum with regard to photon energy yields a PIE spectrum. In this work, ZEKE spectra are calculated from DFT-optimised cluster geometries, then integrated to produce a PIE spectrum. A qualitative comparison between the simulated and experimental PIE spectra is performed, where a good agreement implies the calculated neutral and cationic geometries correspond to likely structures of the relevant cluster species.

ZEKE spectra were calculated using *ezSpectrum 3.0*⁵⁴. Full-dimensional harmonic Franck Condon Factors were calculated to include Duschinsky rotations^{55,56}. The experimental appearance energy value was used as the 0_0^0 transition energy in the calculations; a post-calculation correction was then applied to the vibronic transition energies, which is discussed later in this chapter.

ZEKE spectral simulations were performed at 298 K (additional calculations performed at 1000 K and 2000 K are presented in Appendix D to show the effects of vibrationally hot clusters on subsequent ZEKE spectra). A maximum of 3 and 8 vibrational quanta were initially populated in the neutral and cationic states, respectively. In cases where the resulting ZEKE spectrum appeared truncated, additional quanta in the neutral and/or cation state were populated until a complete spectrum was calculated. The larger systems investigated in this thesis – namely Ce_3O_3 , Ce_3O_5 , Ce_3O_6 , AuCe_3O_3 , AuCe_3O_4 , AuCe_3O_5 and AuCe_3O_6 – required an extensive number of vibrational quanta to be excited which was not practical with the full Duschinsky treatment (due to memory restrictions of the program). In these cases, the Parallel Approximation was used. The Parallel Approximation assumes the vibronic coordinates in the neutral and cationic states are the same, allowing the multi-dimensional Franck Condon Factor (FCF) to be treated simply as a product of one-dimensional FCFs^{57,58}. A

consequence of this approximation is that only FCFs for $\nu'_i \leftarrow \nu''_i$ vibronic transitions are calculated; $\nu'_j \leftarrow \nu''_i$ ($i \neq j$; $i > 0$) transitions are ignored. While the Parallel Approximation is quite a crude approach to calculating FCFs, the low memory requirement from this method allows a high number of vibrational quanta – including combination modes – to be considered. Test calculations using both the Parallel Approximation and a full Duschinsky treatment showed good agreement between the calculated ZEKE spectra, where a small to moderate degree of structural change was recorded between the neutral and cationic states. These test calculations are shown in Appendix D.

Prior to calculations of the FCFs, the normal mode coordinates for the cation structure were aligned with those of the neutral structure. This was usually performed by the auto-alignment algorithm in *ezSpectrum*, which rotated the cationic structure about the Cartesian coordinate axes until the determinant of the normal modes matrix was optimised to the maximum value. In cases where the auto-align algorithm did not effectively align the neutral and cationic structures, the cationic structure was rotated manually until the determinant of the normal modes matrix was maximised. For calculations utilising the Parallel Approximation, the cationic vibrational modes were reordered to ensure the maximum Franck Condon overlap with the corresponding neutral vibrational modes.

Post-calculation treatment of the ZEKE spectra involved convoluting individual vibronic peaks with Gaussian functions to account for broadening effects from underlying rotational transitions. A home-made program convoluted all vibronic peaks to a FWHM of 0.00062 eV (ca. 5 cm^{-1}); this is consistent with previous work by Yang and co-workers⁵² who report a 5 cm^{-1} resolution of their PFI-ZEKE experiments from unresolved rotational structure. An example of the convolution process is shown in Figure 3.3. Numerous other groups have alternatively used Lorentzian functions, instead of Gaussian functions, to account for natural line broadening effects^{59–63}. Future directions by the Metha group may involve developing a peak convolution program using Voigt functions, which combine both Gaussian and Lorentzian functions⁶⁴. This will account for broadening effects due to both energetic uncertainties and unresolved rotations from thermally populated states.

All ZEKE spectra are shown in this work are normalised to the intensity of the most intense vibronic peak. This is largely for presentation purposes as it allows multiple ZEKE spectra to be shown on the same scale. The scaling factor used to normalise the most intense peak in each spectrum is shown in square brackets. The magnitude of the scaling factor is inversely proportional to the intensity of the vibronic peaks in each spectrum and by extension the FC overlap between the neutral and cationic states. The relative ZEKE intensities for each cluster system – and their potential contribution toward their respective PIE onset – can then be compared by their respective scaling factors; the more similar the scaling factors are between two – or more – ZEKE spectra, the more equally each ionisation processes will contribute to the PIE spectrum. By contrast, a set of ZEKE spectra with considerably different scaling factors will see the stronger ionisation processes overshadow the weaker ones in the PIE spectrum. This comparison becomes pertinent when considering cluster systems with a large number of potential ionisation processes as it allows the weaker transitions to be identified and excluded. ZEKE scaling factors are not compared between different cluster systems since the FC overlap is not the only factor contributing to the signal intensity of a specific cluster ion; other factors include the abundances of each neutral cluster species in the molecular beam – which will vary for each system largely due to source conditions – and their respective absorption cross sections.

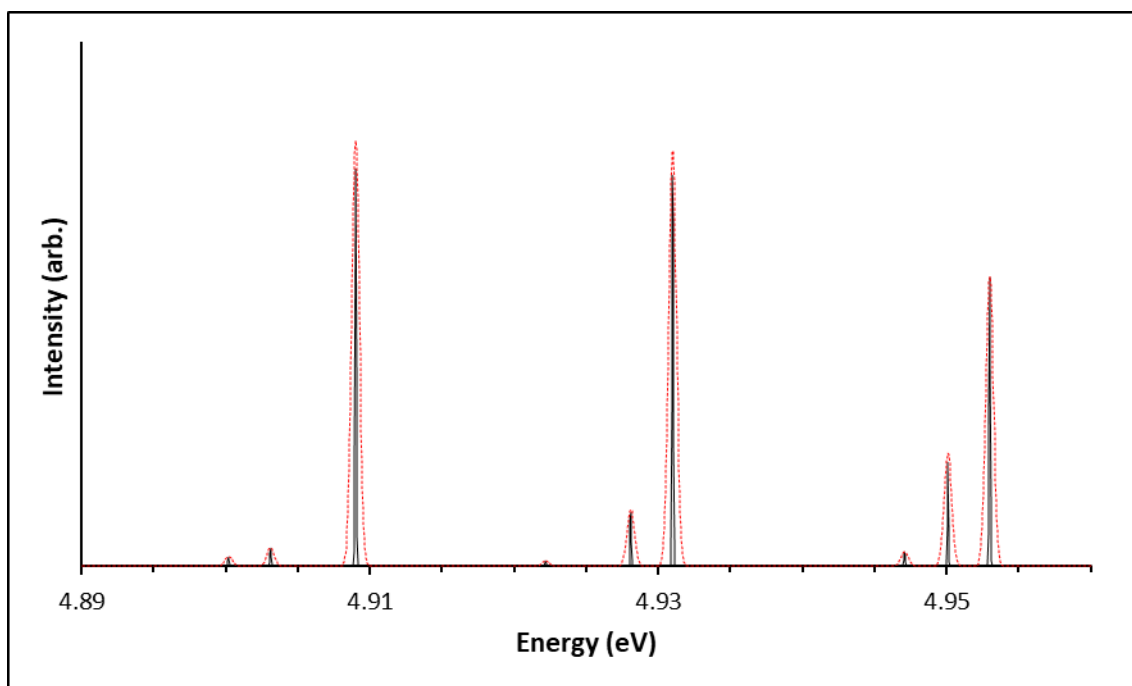


Figure 3.3: Convolution of vibronic peaks for a simulated ZEKE spectrum. Peaks are convoluted using Gaussian functions to account for thermal broadening effects. The spectrum is shown both before convolution (black) and following treatment with a Gaussian function to produce a 5 cm^{-1} ($6.2 \times 10^{-4}\text{ eV}$) FWHM (red).

Following convolution of the simulated ZEKE spectrum, the simulated PIE spectrum was produced by integrating the ZEKE spectrum with respect to energy. An example of a simulated PIE spectrum is shown in Figure 3.4. The baseline and plateau intensities were then corrected to match the corresponding experimental intensities, as shown in Figure 3.5. An arbitrary scaling factor – denoted τ in Figure 3.5 – was applied to the simulated PIE spectrum in order to match the signal intensity at the plateau to that of the experimental PIE spectrum. The simulated PIE baseline was then shifted vertically using a constant correction – denoted λ in Figure 3.5 – to match the simulated signal baseline with that of the experimental spectrum. These adjustments account for the baseline and plateau intensities in the normalised experimental PIE spectrum rarely being “0” and “1”, respectively. Anomalies in the experimental PIE spectra are discussed in detail in Chapter 2.

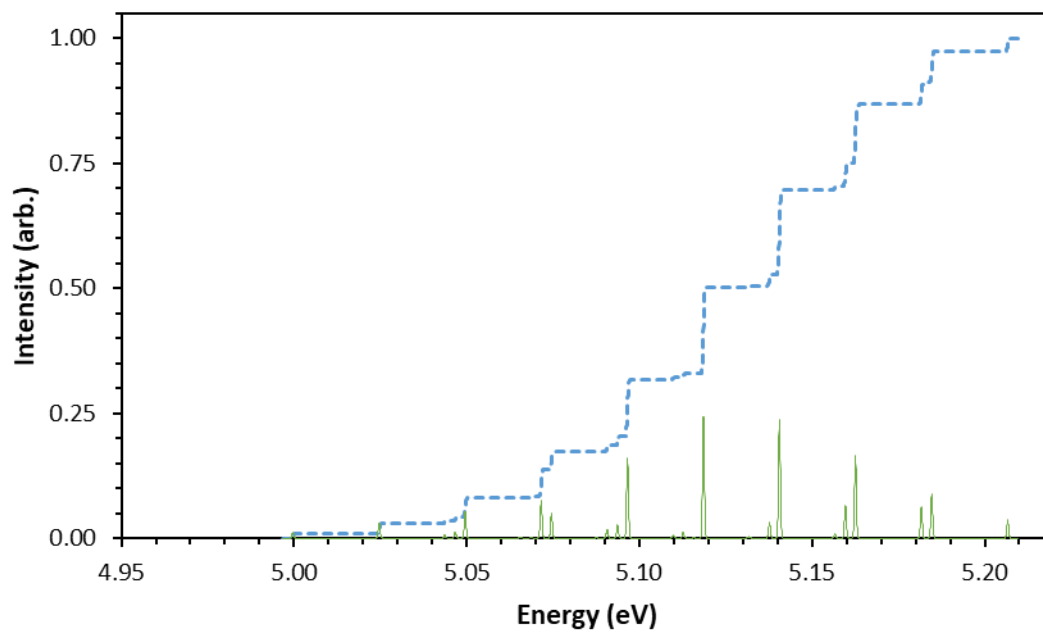


Figure 3.4: Example of a simulated ZEKE spectrum (green) and simulated PIE spectrum (blue). The PIE spectrum is constructed via integration of the ZEKE spectrum with respect to energy.

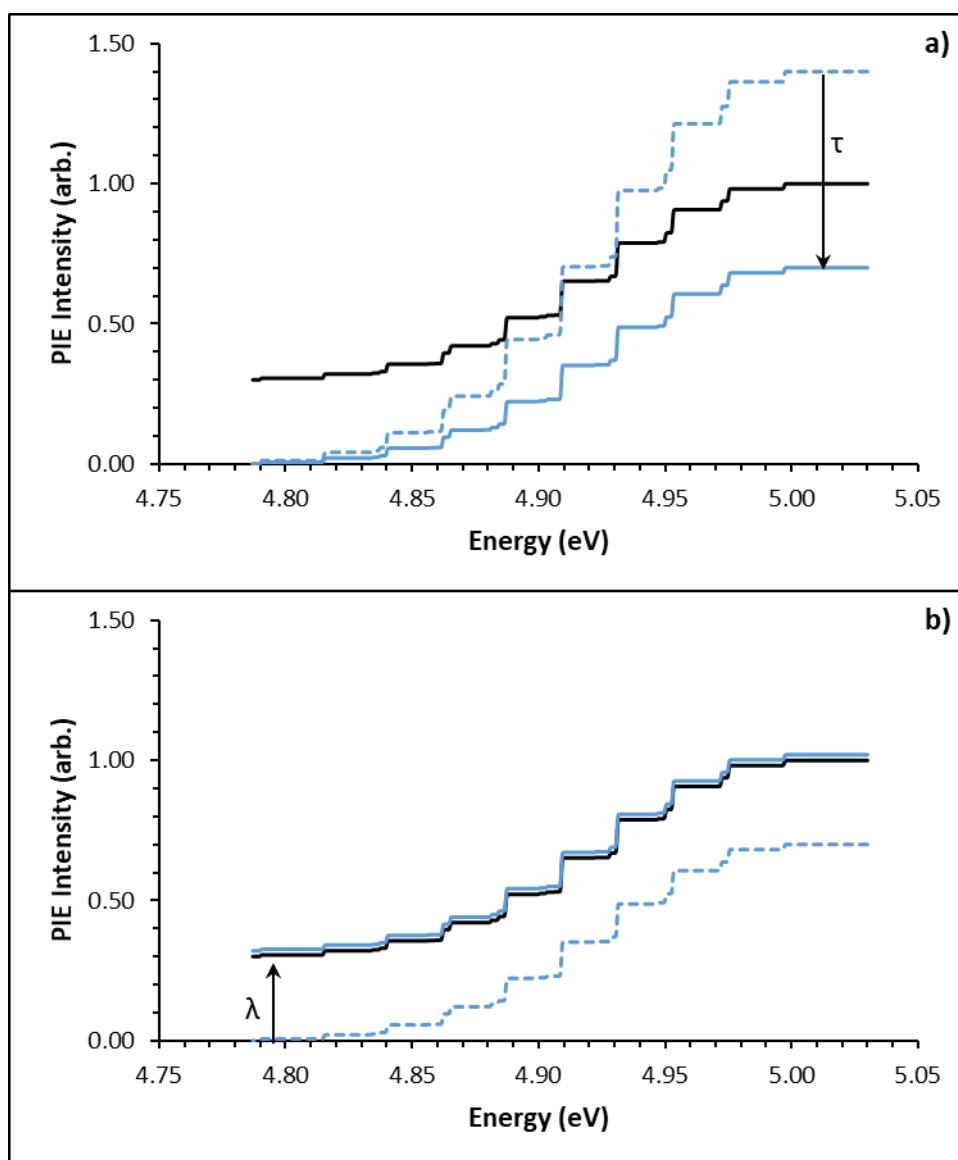


Figure 3.5: Correction of simulated PIE spectrum (blue) to experimental PIE spectrum (black). **a).** An arbitrary scaling factor τ is applied to correct the simulated ion signal plateau to the experimental plateau. **b).** A constant factor λ is then added to the intensity to correct the simulated baseline to the experimental baseline.

Following the vertical correction of the calculated PIE intensities, a horizontal correction was applied to the simulated PIE spectrum in order to match the simulated and experimental appearance energies (AEs), as shown in Figure 3.6. In this correction process the lowest energy vibronic transition – denoted LEVT in Figure 3.6 – is shifted to match the experimental AE. This will cause the simulated PIE spectrum to overlay the experimental PIE spectrum. Moreover, the calculated 0_0^0 transition energy will be corrected – to a good approximation – to

the experimental adiabatic ionisation energy. The experimental IE_{ad} value is then taken as the corrected energy of the 0_0^0 transition from the simulated PIE spectrum.

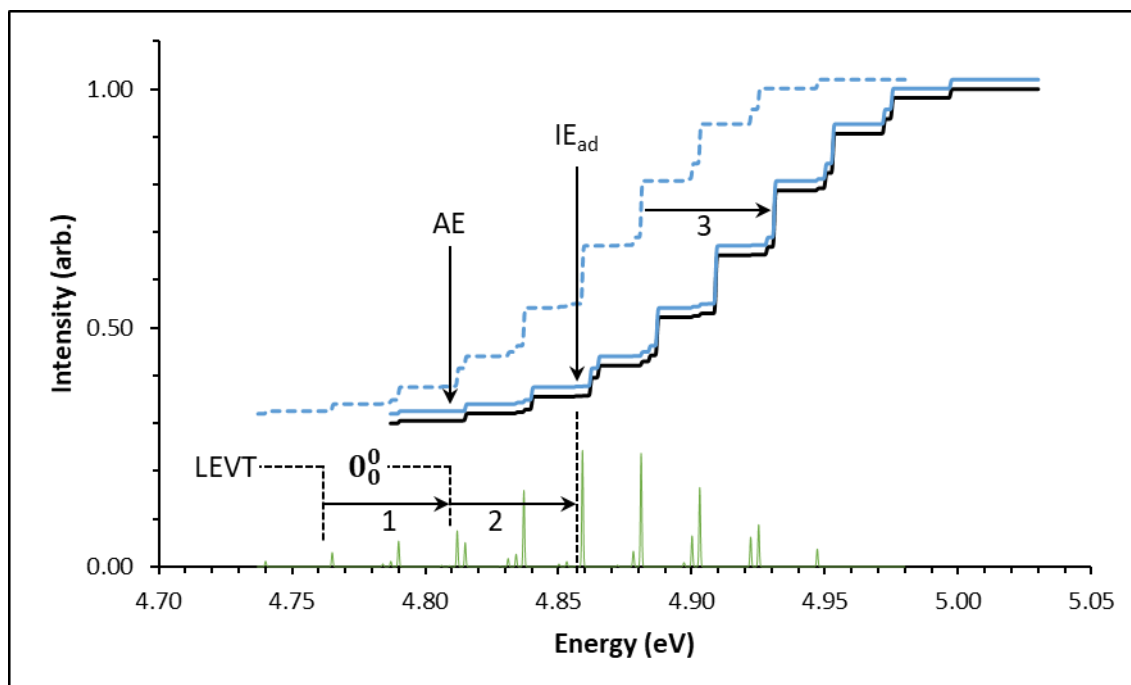


Figure 3.6: Horizontal correction of the simulated PIE spectrum (blue) to the experimental PIE spectrum (black). The 0_0^0 transition is initially assigned the value of the experimental AE for the simulations. The simulated Lowest Energy Vibronic Transition (LEVT) is then corrected to the experimental AE (1). This correction causes the calculated 0_0^0 transition to underlie the experimental IE_{ad} (2). The overall effect will be a shift of the simulated PIE spectrum so that it overlays the experimental PIE spectrum (3).

In cases where multiple ionisation transitions are attributed to the PIE spectrum, the simulated PIE spectrum is constructed from a summation of all the ZEKE spectra for the relevant transitions. The vertical correction process employed is identical to that for a PIE spectrum comprising a single ionisation transition; no scaling is made between different transitions. This ensures that ionisation transitions with stronger FCFs will be more dominant in the PIE spectrum. The horizontal correction, however, is slightly more involved. The ionisation process with the lowest calculated IE has the lowest energy vibronic transition corrected to the experimental AE in the manner described above. For all other ionisation processes, the ZEKE spectra are offset from the lowest energy ionisation transition by the

relative differences in calculated IEs, which are drawn from DFT calculations. As an example, consider a PIE spectrum in Figure 3.7 with an experimental AE of 4.81 eV. For this example, DFT calculations reveal two ionisation processes –labelled IE_1 and IE_2 – with calculated IEs of 5.05 eV and 5.25 eV, respectively. The lowest energy vibronic transition for IE_1 is calculated as 4.76 eV. The IE_1 LEVT is firstly corrected to the experimental AE at 4.81 eV. The energy of the IE_1 0_0^0 transition then becomes 4.86 eV. The energy of the IE_2 0_0^0 transition, which is calculated via DFT as 0.2 eV higher than the 0_0^0 transition of the IE_1 process, is then corrected to 5.06 eV. This process is shown schematically in Figure 3.7 and is repeated for all ionisation transitions considered; for some cluster species this included up to 6 ZEKE spectra. Following this process, the relative ionisation energies are manually adjusted by up to 0.2 eV to produce a calculated PIE spectrum which best matches the profile of the experimental PIE spectrum. This adjustment accounts for errors inherent to the DFT-calculated IEs such as the Born-Oppenheimer approximation, incomplete treatments of both correlation and relativistic effects and the use of finite basis sets⁶⁵. It should be noted that the comparison between the calculated and experimental PIE spectra is performed visually, without a least-squares fit. Moreover, the differences between calculated IEs in this work are often less than the errors associated with the DFT calculations themselves. Thus, the particular arrangement of ZEKE spectra used in this work to produce a PIE spectrum is merely one of many possible arrangements. Once a good correlation between the experimental and simulated PIE spectra is achieved, the IE_{ad} is then taken as the energy of the 0_0^0 transition from the lowest energy neutral structure to the lower energy cationic structure of the two potential $\Delta S = \pm \frac{1}{2}$ candidates. In the above example the IE_{ad} would be given as 4.86 eV.

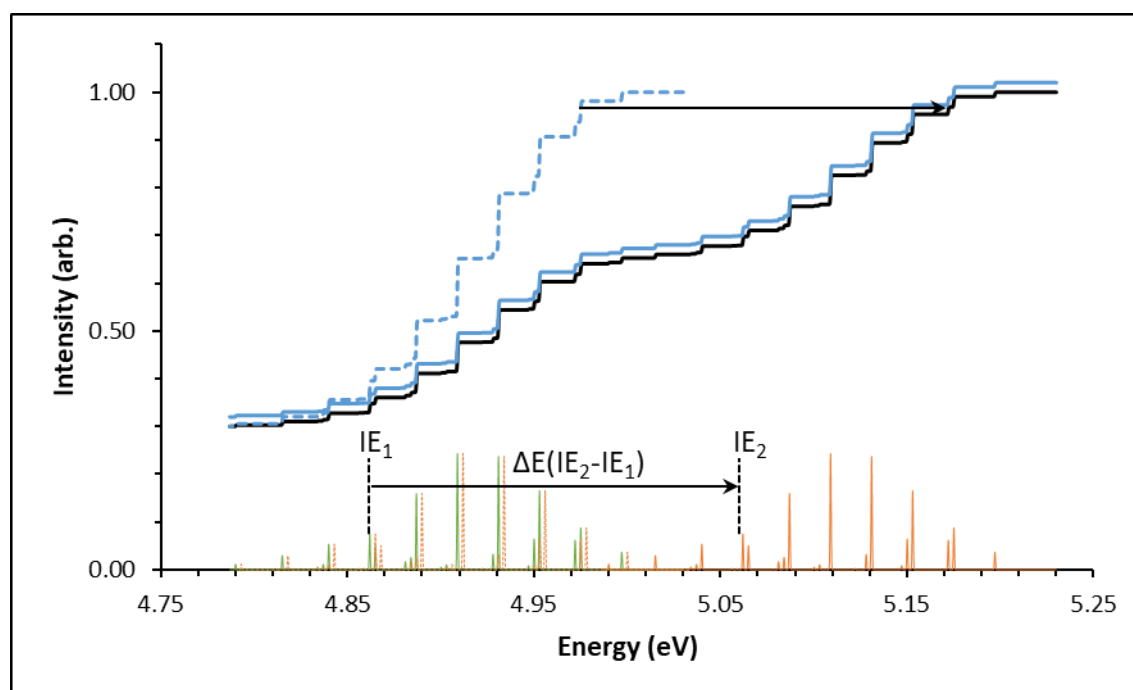


Figure 3.7: Construction of a simulated PIE spectrum with multiple photo-ionisation processes. ZEKE spectra for transitions IE_1 and IE_2 are represented by the green and dotted orange lines, respectively; the combined PIE spectrum is shown as the dotted blue line. The LEVT for IE_1 is corrected to the experimental AE. The IE_2 0_0^0 transition is then offset from the IE_1 0_0^0 transition by the calculated differences in IEs (the corrected ZEKE spectrum for IE_2 is shown as solid orange line). This process corrects the simulated PIE curve (blue) to the experimental PIE spectrum (black).

The overlaying of the simulated and experimental PIE spectra also serves the purposes of a qualitative comparison. A good correlation between the simulated and experimental PIE spectral profiles implies the FC overlap calculated between the neutral and cationic species is consistent with experimental observations. Therefore, the calculated cluster geometries and vibrational modes are representative of the actual cluster species. This complements the comparison of calculated and experimental IEs mentioned previously which signifies the correct electronic structures of the neutral and cationic species have been calculated. A good comparison of both simulated PIE spectral profiles and calculated IEs to experimental data therefore implies confidence in the calculated structures. Moreover, the geometric and electronic properties of the relevant cluster species can be inferred from the DFT calculated structures.

3.4. References

- (1) Koch, W.; Holthausen, M. C. *A Chemist's Guide to Density Functional Theory*, 2nd ed.; Wiley-VCH Verlag GmbH, 2001.
- (2) Atkins, P.; de Paula, J. *Physical Chemistry*, 8th ed.; Oxford University Press: Oxford, 2006.
- (3) Møller, C.; Plesset, M. S. *Phys. Rev.* **1934**, *46* (7), 618.
- (4) Sherrill, C. D.; Schaefer III, H. F. *Adv. Quantum Chem.* **1999**, *34*, 143.
- (5) Coester, F.; Kümmel, H. *Nucl. Phys.* **1960**, *17*, 477.
- (6) Cizek, J.; Paldus, J.; Shevitt, I. *Phys. Rev. A* **1972**, *5* (1), 50.
- (7) Hartree, D. R.; Hartree, W.; Swirles, B. *Philos. Trans. R. Soc. London. Ser. A, Math. Phys. Sciences* **1939**, *238* (790), 229.
- (8) Sodupe, M.; Bertran, J.; Rodríguez-Santiago, L.; Baerends, E. J. *J. Phys. Chem. A* **1998**, *103* (1), 166.
- (9) Barone, V.; Adamo, C. *Chem. Phys. Lett.* **1994**, *224* (5–6), 432.
- (10) Gorb, L.; Leszczynski, J. *Int. J. Quantum Chem.* **1998**, *70* (4–5), 855.
- (11) Podolyan, Y.; Gorb, L.; Leszczynski, J. *J. Phys. Chem. A* **2000**, *104* (31), 7346.
- (12) Gorb, L.; Leszczynski, J. *J. Am. Chem. Soc.* **1998**, *120* (20), 5024.
- (13) Gorb, L.; Podolyan, Y.; Dziekonski, P.; Sokalski, W. A.; Leszczynski, J. *J. Am. Chem. Soc.* **2004**, *126* (32), 10119.
- (14) Thomas, L. H. *Math. Proc. Cambridge Philos. Soc.* **1927**, *23* (05), 542.
- (15) Fermi, E. *Rend. Accad. Naz. Lincei* **1927**, *6*, 602.
- (16) Hohenberg, P.; Kohn, W. *Phys. Rev.* **1964**, *136*, 864.
- (17) Kohn, W.; Sham, L. J. *Phys. Rev. A* **1965**, *140* (4), 1133.
- (18) Vosko, S. H.; Wilk, L.; Nusair, M. *Can. J. Phys.* **1980**, *58* (8), 1200.
- (19) Perdew, J. P.; Zunger, A. *Phys. Rev. B* **1981**, *23* (10), 5048.
- (20) Perdew, J. P.; Wang, Y. *Phys. Rev. B* **1992**, *45* (23), 13246.

-
- (21) Becke, A. D. *Phys. Rev. A* **1988**, *38* (6), 3098.
- (22) Perdew, J. P. *Phys. Rev. B* **1986**, *33* (12), 8822.
- (23) Dryza, V.; Addicoat, M. A.; Gascooke, J. R.; Buntine, M. A.; Metha, G. F. *J. Phys. Chem. A* **2005**, *109* (49), 11180.
- (24) Dryza, V.; Gascooke, J. R.; Buntine, M. A.; Metha, G. F. *Phys. Chem. Chem. Phys.* **2009**, *11* (7), 1060.
- (25) Dryza, V.; Addicoat, M. A.; Gascooke, J. R.; Buntine, M. A.; Metha, G. F. *J. Phys. Chem. A* **2008**, *112* (25), 5582.
- (26) Gentleman, A. S.; Addicoat, M. A.; Dryza, V.; Gascooke, J. R.; Buntine, M. A.; Metha, G. F. *J. Chem. Phys.* **2009**, *130* (16), 64311.
- (27) Cramer, C. J. *Essentials of Computational Chemistry*, 2nd ed.; John Wiley & Sons: Chichester, 2004.
- (28) Ochterski, J. W. *Vibrational Analysis in Gaussian*; 1999.
- (29) Slater, J. C. *Phys. Rev.* **1930**, *36* (1), 57.
- (30) Boys, S. F. *Proc. R. Soc. A. Math. Phys. Eng. Sci.* **1950**, *200* (1063).
- (31) Szabo, A.; Ostlund, N. S. *Modern Quantum Chemistry: Introduction to Advanced Electronic Structure Theory*; McGraw-Hill Publishing Company: New York, 1989.
- (32) Hehre, W. J.; Stewart, R. F.; Pople, J. A. *J. Chem. Phys.* **1969**, *51* (6), 2657.
- (33) Binkley, J. S.; Pople, J. a; Hehre, W. J. *J. Am. Chem. Soc.* **1980**, *102* (3), 939.
- (34) Addicoat, M. A. Computational Investigations into the Structure and Reactivity of Small Transition Metal Clusters, PhD Thesis, The University of Adelaide, 2009.
- (35) Gentleman, A. S. The Effect of Sequential Oxidation and Composition on the Structural and Electronic Properties of Gas Phase Transition-Lanthanide Bimetallic Clusters, PhD Thesis, The University of Adelaide, 2014.
- (36) Andrae, D.; Haussermann, U.; Dolg, M.; Stoll, H.; Preuss, H. *Theor. Chim. Acta* **1991**, *78* (4), 247.
- (37) Dolg, M.; Stoll, H.; Savin, A.; Preuss, H. *Theor. Chim. Acta* **1989**, *75* (3), 173.

- (38) Schwerdtfeger, P.; Dolg, M.; Schwarz, W. H. E.; Bowmaker, G. a; Boyd, P. D. W. J. *Chem. Phys.* **1989**, *91* (3), 1762.
- (39) Dunning Jr, T. H. *J. Chem. Phys.* **1989**, *90* (2), 1007.
- (40) Dolg, M. In *Modern Methods and Algorithms of Quantum Chemistry*; John-von-Neumann-Inst. for Computing, 2000.
- (41) Dolg, M.; Stoll, H.; Preuss, H. *Theor. Chim. Acta* **1993**, *85* (6), 441.
- (42) Wood, J. H.; Boring, A. M. *Phys. Rev. B* **1978**, *18* (6), 2701.
- (43) Díaz-Megías, S.; Seijo, L. *Chem. Phys. Lett.* **1999**, *299*, 613.
- (44) Dolg, M.; Stoll, H.; Preuss, H. *J. Chem. Phys.* **1989**, *90* (3), 1730.
- (45) Dolg, M.; Stoll, H. *Theor. Chim. Acta* **1989**, *75* (5), 369.
- (46) Tizard Supercomputer <https://www.ersa.edu.au/service/hpc/tizard/> (accessed Jun 10, 2016).
- (47) eResearchSA www.ersa.edu.au (accessed Jun 10, 2016).
- (48) National Computational Infrastructure nci.org.au (accessed Jun 10, 2016).
- (49) Becke, A. D. *J. Chem. Phys.* **1993**, *98* (2), 1372.
- (50) Frisch, M. J.; Trucks, G. W.; Schlegel, H. B.; Scuseria, G. E.; Robb, M. A.; Cheeseman, J. R.; Scalmani, G.; Barone, V.; Mennucci, B.; Petersson, G. A.; Nakatsuji, H.; Caricato, M.; Li, X.; Hratchian, H. P.; Izmaylov, A. F.; Bloino, J.; Zheng, G.; Sonnenberg, J. L.; Hada, M.; Ehara, M.; Toyota, K.; Fukuda, R.; Hasegawa, J.; Ishida, M.; Nakajima, T.; Honda, Y.; Kitao, O.; Nakai, H.; Vreven, T.; Montgomery, J. A.; Peralta, J. E.; Ogliaro, F.; Bearpark, M.; Heyd, J. J.; Brothers, E.; Kudin, K. N.; Staroverov, V. N.; Kobayashi, R.; Normand, J.; Raghavachari, K.; Rendell, A.; Burant, J. C.; Iyengar, S. S.; Tomasi, J.; Cossi, M.; Rega, N.; Millam, J. M.; Klene, M.; Knox, J. E.; Cross, J. B.; Bakken, V.; Adamo, C.; Jaramillo, J.; Gomperts, R.; Stratmann, R. E.; Yazyev, O.; Austin, A. J.; Cammi, R.; Pomelli, C.; Ochterski, J. W.; Martin, R. L.; Morokuma, K.; Zakrzewski, V. G.; Voth, G. A.; Salvador, P.; Dannenberg, J. J.; Dapprich, S.; Daniels, A. D.; Farkas; Foresman, J. B.; Ortiz, J. V; Cioslowski, J.; Fox, D. J. *Gaussian 09, Revision D.01*, Gaussian, Inc., Wallingford CT. Wallingford CT 2009,.

- (51) Fonseca Guerra, C.; Handgraaf, J. W.; Baerends, E. J.; Bickelhaupt, F. M. *J. Comput. Chem.* **2004**, *25* (2), 189.
- (52) Yang, D.-S.; Zgierski, M. Z.; Rayner, D. M.; Hackett, P. a.; Martinez, A.; Salahub, D. R.; Roy, P.-N. N.; Carrington, T. *J. Chem. Phys.* **1995**, *103* (13), 5335.
- (53) Yang, D.; Zgierski, M. Z.; Hackett, P. A. *J. Chem. Phys.* **1998**, *108*, 3591.
- (54) Mozhayskiy, V. A.; Krylov, A. I. University of Southern California: Los Angeles, 2009.
- (55) Duschinsky, F. *Acta Physicochim. URSS* **1937**, *7* (551–566).
- (56) Koziol, L.; Mozhayskiy, V. A.; Braams, B. J.; Bowman, J. M.; Krylov, A. I. *J. Phys. Chem. A* **2009**, *113* (27), 7802.
- (57) Franck, J.; Dymond, E. G. *Trans. Faraday Soc.* **1926**, *21* (February), 536.
- (58) Condon, E. U. *Phys. Rev.* **1928**, *32* (6), 858.
- (59) Rothschof, G. K.; Perkins, J. S.; Li, S.; Yang, D.-S. *J. Phys. Chem. A* **2000**, *104* (35), 8178.
- (60) Yang, D.-S.; James, A. M.; Rayner, D. M.; Hackett, P. A. *Chem. Phys. Lett.* **1994**, *231*, 177.
- (61) Yang, D.-S.; Miyawaki, J. *Chem. Phys. Lett.* **1999**, *313*, 514.
- (62) Sohnlein, B. R.; Yang, D.-S. *J. Chem. Phys.* **2006**, *124* (13), 134305.
- (63) Miyawaki, J.; Yang, D.-S.; Sugawara, K. *Chem. Phys. Lett.* **2003**, *372*, 627.
- (64) Hollas, J. M. *High Resolution Modern Spectroscopy*, 2nd ed.; John Wiley & Sons: West Sussex, 1998.
- (65) Young, D. C. *Computational Chemistry: A Practical Guide for Applying Techniques to Real-World Problems*; John Wiley & Sons: New York, 2001.

Chapter Four

Benchmarking Calculations

This chapter presents benchmark calculations to determine an effective core treatment of cerium atoms appropriate to the DFT calculations in this work. Benchmark calculations are initially performed on Ce_2 , CeO and AuCe dimers which describe fundamental chemical bonds pertinent to the formation of Ce_mO_n and AuCe_mO_n clusters. Following this, an investigation into the effective core treatment of cerium atoms on both the electronic and geometric properties of the Ce_2O_n ($n=0-4$) cluster series is undertaken. Calculated adiabatic ionisation energies are compared with experimental IEs to identify an effective core treatment for Ce that provides an accurate description of the Ce_2O_n electronic structure with sequential oxidation. Finally, the computational expense associated with each ECP treatment is considered. Appropriate ECPs are then identified for calculations in the context of this work.

4.1. *Effective Core Potentials for Lanthanides*

The electronic structures of lanthanides are highly complicated by closely spaced, open 4f subshells which facilitate a dense manifold of electronic states for even the simplest of species. For example, the CeO dimer possesses 15 low-lying electronic states within 5000 cm⁻¹ of the ground state^{1,2}. Given that a study of chemical reactivity does not require an exact quantum mechanical classification of the ground state, a fully explicit treatment of the electrons in lanthanide species is both unnecessary and needlessly expensive. A suitable effective core treatment for lanthanide atoms is one which yields a good correlation with experimental data at minimal computational expense.

One of the unique properties of lanthanides – specifically Ce in the context of this work – is that the 4f electrons, while being valence-like from an energetic standpoint, are emphatically core-like from a spatial context; the 4f valence electron is spatially located at the Ce³⁰⁺ core³. The effects of this phenomenon are two-fold. Firstly, the contribution of 4f electrons to the formation of chemical bonds tends to be minimal at low oxidation states and low coordination numbers. Secondly, there are a variety of ECPs for lanthanides which can treat the 4f electrons either explicitly, to facilitate their occupation in the valence space, or implicitly, where the 4f electrons are drawn into the frozen core and replaced by an averaged potential. These are known as closed shell and open shell ECPs, respectively. The closed shell ECP has all subshells of a particular electron shell drawn into the core. An example of this type of ECP is the MWB28 core for Ce discussed in Chapter 3; the n=1,2,3 shells (where n represents the Principal Quantum Number) are drawn into the core while the n=4,5,6 shells – including the 4f electron – are treated explicitly. The size of the frozen core can be selected in a trade-off between computational efficiency and a correct description of correlation effects on the valence shell. However, the core size does not affect the valence shell configuration itself. The open shell draws part of an electron shell into the core while the remaining subshells are still treated as part of the valence space; this type of ECP is typically used exclusively with lanthanide and actinide species to allow an implicit treatment of the f electrons. This ECP simplifies calculations through exclusion of electrons for which an explicit treatment can be computationally difficult, while also providing a good description of core-valence correlation effects by allowing subshells near the valence space to be treated explicitly. Moreover, the

larger cores employed with this method often come at a reduced computational expense to the closed shell ECPs, which may require smaller cores. Examples of open shell ECPs include the MWB47 and MWB48 cores for Ce, which both treat the 4f electron implicitly.

4.2. Requirement for a Benchmark Study of Cerium ECPs

Previous calculations of lanthanide clusters performed by the Metha group^{4,5} centred on praseodymium oxide and holmium oxide clusters, in addition to those species doped with gold and rhodium respectively. Effective core treatments of Pr and Ho atoms utilised the 48 and 56 electron frozen cores, denoted MWB48 and MWB56 respectively, with the primary reason for ECP choice being the provision of an even-electron core. Both these ECPs derive from the $4f^n/Q11$ family of open shell pseudopotentials developed by Dolg and co-workers⁶⁻⁸ which afford an explicit treatment of the outer 11 electrons to give a valence configuration of $5s^25p^66s^25d^1$. The remaining electrons, including the 4f shell, are afforded an implicit pseudo-relativistic treatment. Au, Rh and O atoms were treated with MWB60, MWB28 and MWB2 closed shell ECPs respectively. This combination of ECPs was used to calculate geometries, vibrational modes and adiabatic ionisation energies for Ho_mO_n , $Rh_xHo_mO_n$, Pr_mO_n and $Au_xPr_mO_n$ clusters with excellent agreement to experimental PIE spectra.

Initial calculations of cerium oxide clusters in the context of this work treated cerium atoms with an open shell 48 electron frozen core – MWB48 – which derives from the $4f^n/Q10$ family of ECPs developed by Dolg and co-workers⁶⁻⁸. The MWB48 ECP was chosen as it afforded an even-electron core for ^{58}Ce ; similar to the treatment of ^{59}Pr and ^{67}Ho atoms by Gentleman⁵. However, the MWB48 ECP was problematic in that subsequent DFT calculations failed to correctly describe the bonding properties of the Ce_2 dimer; calculations instead predicted a van der Waals complex, as shown in Table 4.1. This surprisingly poor description of geometric properties in the simplest of cerium containing molecules prompted a search for an ECP which provides an adequate treatment of the Ce electronic structure to facilitate calculations of more complex cluster geometries.

4.3. Effective Core Potentials Selected for Benchmarking Study

The effective core potentials in the test set included the MWB48, MWB47 and MWB28 ECPs available in Gaussian09⁹. An in-depth discussion of these ECPs can be found in Chapter 3. Briefly, the MWB48 ECP ($4f^n/Q10$) draws both the cerium 4f and 5d electrons into the core to give an electron configuration of $[48]5s^25p^66s^2$ (where [N] represents the electrons drawn into the frozen core)⁶⁻⁸. The MWB47 ECP ($4f^n/Q11$) draws the 4f electron into the frozen core and leaves the 5d electron in the valence shell to give an electron configuration of $[47]5s^25p^66s^25d^1$. The MWB28 ECP draws 28 inner core electrons into the frozen core to give an electron configuration of $[28]4s^24p^65s^24d^{10}5p^66s^24f^{15}5d^1$; both the 4f and 5d electrons are included in the valence shell. The closed shell nature of the MWB28 ECP allows for a correct description of the valence shell since all valence electrons are treated explicitly. However, while the MWB28 ECP provides a more accurate description of both the valence space and core-valence effects, the MWB47 and MWB48 ECPs come with a greatly reduced computational expense. Moreover, some electronic and geometric parameters such as vibrational modes and ionisation energies are not overly dependent on the specific electron configuration; this is particularly the case for lanthanides, where the high degeneracy of the 5d and 4f orbitals tend to form electronic superconfigurations³. These properties may be predicted accurately provided an adequate treatment of correlation and relativistic effects is considered.

Effective core treatments for oxygen and gold atoms were afforded using the pseudo-relativistic MWB2 and MWB60 closed shell ECPs respectively. These ECPs draw the $n=1$ and $n=1,2,3,4$ shells respectively into the frozen core to afford electronic configurations of $[2]2s^22p^2$ for O and $[60]5s^25p^65d^{10}6s^1$ for Au. Unlike the lanthanide elements, frozen cores for the p and d-block elements in Gaussian09 are generally restricted to closed shell variants. An additional consideration for these ECPs, however, is the extent to which relativistic effects are treated. The Hartree-Fock cores (denoted SHF or MHF in Gaussian09, where “S” and “M” denote single and multi-electron fits to experimental data, respectively) ignore relativistic effects while the Wood-Boring (MWB) and Dirac-Fock (SDF and MDF) cores provide pseudo-relativistic and full relativistic treatments, respectively. However, not all ECP variants are available for all elements; for example, the MWB, MDF, SHF and MHF type cores are all

available for gold while only MWB and SDF type cores are available for oxygen. Due to the MWB type cores being the only ECPs available for the cerium atoms, these cores were also selected as appropriate frozen core treatments for oxygen and gold respectively; this ensured a consistent treatment of relativistic effects for all atoms throughout the calculations.

4.4. Benchmark Calculations of Ce₂, CeO and AuCe Dimers

Initial benchmark calculations were performed on Ce₂, CeO and AuCe dimers which are considered as relevant to describing chemical bonding within the Ce_mO_n and AuCe_mO_n cluster species. Calculations were performed in the four lowest spin multiplicities; this included singlet, triplet, quintet and septet states for even-electron species and doublet, quartet, sextet and octet states for odd-electron species. In cases where the septet or octet state yielded the lowest energy, higher spin states were considered. Calculated harmonic frequencies (ω_e) and bond lengths (r_e) for the Ce₂, CeO and AuCe dimers are presented in Table 4.1 with comparison to available known values. These known values are mostly taken from experimental data; however, in cases where such data is not available, known values are taken from high-quality simulations such as all-electron calculations.

Calculated harmonic frequencies (ω_e) for the Ce₂ dimer using the MWB28, MWB47 and MWB48 ECPs are 201.38 cm⁻¹, 194.16 cm⁻¹ and 39.58 cm⁻¹ respectively. While all ECPs predict a significantly lower ω_e than the experimental value of 245 ± 4.2 cm⁻¹, the MWB28 ECP gives the closest approximation with an 18% deviation from experiment. The MWB47 ECP performed comparably well to the MWB28 ECP with a 21% error. Unusually, the MWB48 ECP yielded an 83% deviation from the experimental value, predicting a van der Waals complex with no Ce-Ce bond. This ECP, which was developed for calculations of lanthanide atoms, monohydrides, monoxides and monofluorides,⁸ was clearly not designed to calculate the properties of lanthanide dimers. Given the failure of the MWB48 ECP to correctly describe even the simplest of cerium containing molecules, this ECP is deemed unsuitable for calculations in the context of this work.

All of the ECPs in the test set perform quite well with calculations of cerium monoxide. The MWB28 and MWB47 ECPs both predict the Ce-O bond length to within 1% of the experimental value. Additionally, the MWB28 and MWB47 ECPs predict the harmonic frequency to within 1% and 5% respectively of the experimental value. In this case the MWB28 ECP describes a slight over-binding of the CeO molecule with a greater ω_e than experiment, corresponding to a stronger force constant. Conversely, the MWB47 ECP predicts an under-binding of the CeO dimer with a ω_e value lower than experiment. The MWB48 ECP again performs the worst – albeit considerably better than for Ce₂ – with calculated r_e and ω_e values deviating from experimental values by 5% and 17%, respectively. As with the Ce₂ dimer, the MWB48 ECP again severely under-predicts the bond strength of the CeO species. The contrast between the MWB48 ECP, which systematically predicts weaker bonds in both the Ce₂ and CeO dimers compared to known values, and the MWB47 ECP, which performs quite well in both cases, highlights the pertinence of the cerium 5d electron in forming chemical bonds. By contrast, the comparable results of the MWB47 and MWB28 ECPs for both the Ce₂ and CeO dimers suggests a minimal contribution from the 4f electron to bonding within cerium containing structures which are either homonuclear or possess low oxidation ratios.

Calculations of the AuCe dimer using the MWB28 and MWB47 ECPs yielded comparable ω_e values of 142.35 cm⁻¹ and 155.91 cm⁻¹ respectively. Moreover, MWB28 and MWB47 calculated r_e values of 2.757 Å and 2.727 Å, respectively, showed only a 0.03 Å difference. While it is not possible to compare these results to known values – due to a lack of experimental data or high-quality calculations – the similar ω_e and r_e values calculated with both ECPs infers comparable performance. The MWB48 ECP again predicts a weaker bond than both the MWB28 and MWB47 cores; ω_e and r_e values were calculated respectively to be ca. 16 cm⁻¹ and 0.14 Å lower than the MWB28 calculated values. However, the differences between these ω_e and r_e values, which reflect variances of ca. 11% and 3% respectively, are quite reasonable; the MWB48 ECP would provide an acceptable frozen core treatment in this case.

Dimer	ECP	Calc ω_e (cm^{-1})	Known ω_e (cm^{-1})	Calc r_e (\AA)	Known r_e (\AA)
Ce ₂	MWB28	201.38	245.4 ± 4.2 ¹⁰	2.589	
	MWB47	194.16		2.643	
	MWB48	39.58		4.814	
CeO	MWB28/MWB2	867.58	862 ¹¹	1.801	1.820 ¹¹
	MWB47/MWB2	836.52		1.839	
	MWB48/MWB2	718.75		1.912	
AuCe	MWB60/MWB28	142.35		2.757	
	MWB60/MWB47	155.91		2.727	
	MWB60/MWB48	126.08		2.861	

Table 4.1: Effective Core Potential benchmark calculations for Ce₂, CeO and AuCe dimers. Calculations are performed using B3P86/SDD. Calculated harmonic frequencies (ω_e) and bond lengths (r_e) are compared to known values.

4.5. ECP Benchmarking of Ce_2O_n ($n=0-4$) Clusters

4.5.1. Ce_2O_n Ionisation Energies

The MWB28, MWB47 and MWB48 ECPs were additionally benchmarked against ionisation energies (IEs) for the Ce_2O_n ($n=0-4$) cluster series. This was done to compare the ability of the ECPs in the test set to correctly describe the electronic properties of cerium oxide clusters in a number of oxidation states, particularly in higher oxidation states when the contribution of the 4f electron becomes prevalent. IEs were selected as a benchmarking parameter due to (i) the ease with which IEs can be recorded for gas phase cluster species in comparison to other spectroscopic parameters, and (ii) the direct relation of the IE to the cluster electronic structure via Koopmans' Theorem¹². Due to a lack of previous experimental data for the Ce_2O_n clusters, experimental ionisation energies are presented *ad adversa*; a detailed discussion of the Ce_2O_n IEs can be found in Chapter 5.

Calculations were performed using one of the MWB28, MWB47 or MWB48 effective core treatments for Ce atoms and the MWB2 ECP for O atoms. The calculated IE for the Ce_2 dimer with each ECP was corrected to the experimental IE; this offset was subsequently applied to the IEs for all of the oxide species. This method of IE correction has been used previously by both Gentleman et al.^{5,13} and Dryza et al.¹⁴⁻¹⁷ and accounts for any systematic offsets in the calculated IEs due to the implicit treatment of the electrons in frozen cores. Because the majority of the electrons in the Ce_2O_n clusters afforded an implicit treatment are part of the Ce cores, this offset can be considered to a good approximation as being constant across the Ce_2O_n series.

A comparison of calculated and experimentally determined IEs for the Ce_2O_n cluster series is presented in Figure 4.1. The MWB28 ECP provides the best agreement with experimental data; calculated IEs for the Ce_2O and Ce_2O_2 clusters, following correction of the calculated Ce_3 IE to the experimental IE value, are predicted within 0.1 eV of their respective experimental IE values. The IE of Ce_2O_3 is additionally calculated to within 0.3 eV of the experimental value which is still a reasonable result. Moreover, it should be noted that the Ce_2O_3 IE was not accurately determined by PIE spectral analysis but estimated by bracketing of ionisation

wavelengths where the Ce_2O_3 ion peak stopped appearing in the mass spectra (the method for assigning the Ce_2O_3 IE is detailed in Chapter 5). Due to the crude method in which the Ce_2O_3 IE was assigned, it is not surprising to find a greater difference between the calculated and experimental values. The Ce_2O_4 IE is calculated as 8.561 eV which is far beyond the experimental photo-ionisation range and consistent with the non-detection of the Ce_2O_4 ion in the mass spectrum.

The MWB47 ECP performs quite well in predicting the IEs for the Ce_2O and Ce_2O_2 species; IEs are calculated within ca. 0.3 and 0.1 eV of experimental values respectively. These results are consistent with previous work by Gentleman et. al. who used the same $4f^n/\text{Q}11$ type ECPs to calculate Pr_2O_n and Ho_2O_n ($n=0,1,2$) cluster IEs with good experimental agreement^{4,5}. However, the IE for Ce_2O_3 is calculated ca. 1 eV lower than the experimental value. While experimental IE values are not available for the Ce_2O_4 cluster, the MWB47 calculated IE is ca. 2 eV lower than the MWB28 calculated value. The $4f^n/\text{Q}11$ type ECPs clearly perform quite well in systems with a low degree of oxidation, where the 4f electrons are not expected to have a significant participation in chemical bonding. However, these ECPs appear to fail once the contribution of the 4f electrons become prevalent. Thus, the MWB47 ECP is therefore not appropriate for calculations in the context of this work.

The MWB48 ECP predicts the Ce_2O IE – following correction of the calculated Ce_2 IE to the experimental IE value – to within ca. 0.35 eV of the experiment IE, which is a reasonable result. However, calculated IEs for the Ce_2O_2 and Ce_2O_3 species are both ca. 1 eV higher than their respective experimental values. The IE for Ce_2O_4 was not calculated with the MWB48 ECP; geometry optimisations predicted nonsensical structures, as discussed in the next section. The poor correlation between MWB48 calculated Ce_2O_n IEs and experimental IE values supports previous statements about the unsuitability of this ECP in calculations.

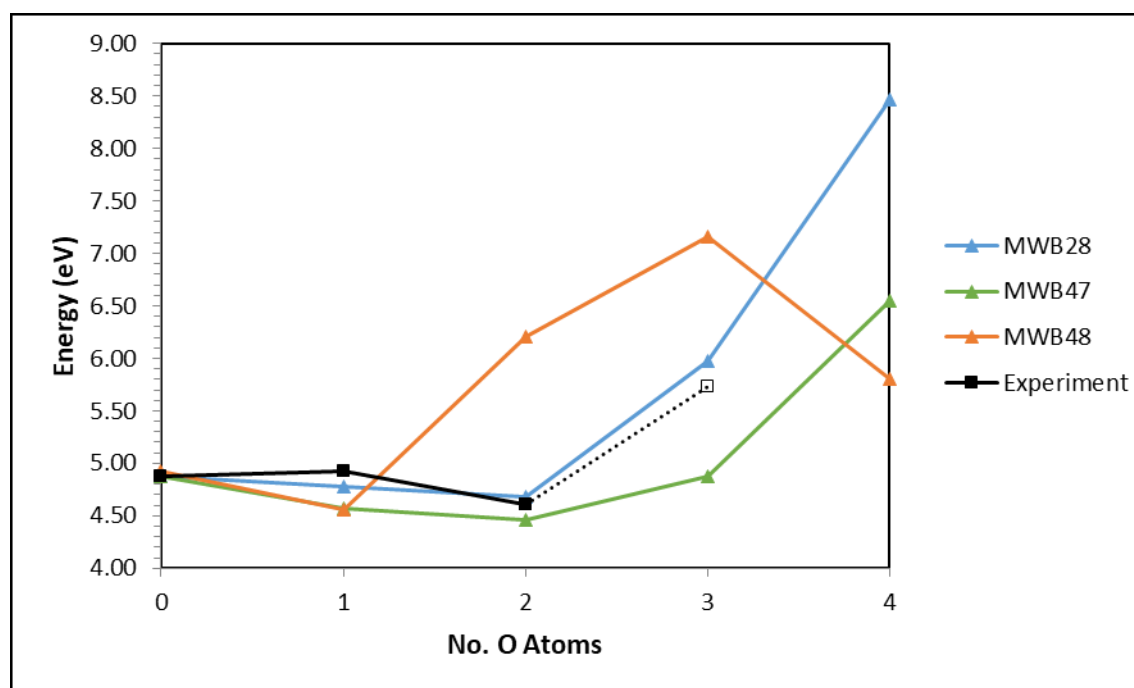


Figure 4.1: Calculated adiabatic ionisation energies for the Ce_2O_n ($n=0-4$) cluster series. Calculated IE values are corrected to the experimental IE of the bare metal cluster.

4.5.2. Ce_2O_n Cluster Geometries

Calculated geometries for neutral Ce_2O_n ($n=1-4$) systems using the MWB28, MWB47 and MWB48 effective core treatments are presented in Table 4.2. Only the lowest energy structures are shown; higher energy Ce_2O_n geometries are presented in Chapter 5. In the absence of experimental data pertaining to geometric parameters for the Ce_2O_n clusters, a rudimentary comparison between cluster geometries calculated with the different ECPs is conducted. This does not verify that the calculated structures are necessarily correct. However, a visual analysis of the calculated geometries from a standpoint of chemical intuition can allow any nonsensical structures to be identified. Furthermore, it would be interesting to compare the performances of the different ECPs with increased Ce_2O_n oxidation, where the participation of the 4f electrons becomes more prevalent.

Calculated Ce_2O structures are quite similar for all ECPs in the test set. A linear $D_{\infty h}$ structure is calculated using the MWB48 ECP, while bent C_{2v} and C_s structures are calculated with the

MWB47 and MWB28 ECPs, respectively. Calculated Ce-O bond lengths vary by up to 0.11 Å between the ECPs, which correlates to a ca. 5% difference.

Near-identical Ce₂O₂ geometries are calculated with the MWB28, MWB47 and MWB48 ECPs; the calculated structures all comprise a planar *D*_{2h} arrangement. Strong similarities are found between the MWB28 and MWB47 ECPs with regard to both the Ce-Ce and Ce-O bond lengths, which differ by ca. 0.026 Å and 0.006 Å, respectively. By contrast, the Ce-Ce and Ce-O bond lengths calculated using the MWB48 ECP are ca. 0.13 Å and 0.16 Å longer than those calculated with the MWB28 core. This again points to a tendency of the MWB48 ECP to under-predict bond strength.

Calculations of the Ce₂O₃ species show some marked geometric differences between the ECPs used in the test set. Ce₂O₃ structures calculated using the MWB28 and MWB47 ECPs both contain 3 oxygen atoms bridging a Ce-Ce bond with uniform O-Ce-Ce-O dihedral angles of 120°. The structures are, however, calculated with different point groups; the MWB28 structure is *C*₁ – albeit near-*C*_s – symmetric while the MWB47 structure has *D*_{3h} symmetry. Calculated Ce-Ce and Ce-O bond lengths differ between structures by ca. 0.6% and 1.2%, respectively. In the context of this work, these small differences between the MWB28 and MWB47 calculated structures are not significant. A more substantial difference is found between the MWB28 and MWB48 calculated structures; the MWB48 structure occupies the lower symmetry *C*₁ point group with O-Ce-Ce-O dihedral angles of ±152.7° and 54.6°, showing a considerable difference to the 120° dihedral angles calculated for the MWB28 and MWB47 species.

Calculated geometries for the Ce₂O₄ cluster reveal an even greater difference between structures with the different ECP treatments. The MWB28 calculated structure is *C*_{2h} symmetric with two O atoms singly attached to the Ce atoms of a planar Ce₂O₂-type motif. This structure is consistent with previous calculations by Chen et al.¹⁸ who used a simulated annealing search method followed by DFT calculations with the PW91 exchange-correlation functional to determine the Ce₂O₄ lowest energy structure. The MWB47 calculated structure

conversely has an O₂ unit bound to a bent Ce₂O₂ motif with C₁ symmetry. Moreover, the C_{2h} structure is energetically unfavourable when re-calculated with the MWB47 core; the re-optimised structure has a ΔE value of +2.251 eV relative to the LES. The MWB48 calculated geometry has all four O atoms bridging the Ce-Ce bond, with 3 of the O atoms in a trimeric arrangement akin to associative adsorption of an O₃ species. However, the interatomic separation of ca. 1.5 Å calculated between the O atoms in the O₃ trimer is considerably longer than the 1.278 Å bond lengths within unbound O₃¹⁹ – the bond lengths are more consistent with that of a peroxide species²⁰. This would suggest strong Ce-O bonding which may be weakening the O-O bonds within the O₃ trimer. However, the large Ce-O₃ separation of ca. 2.5 Å infers the O₃ species is weakly bound to the Ce₂O motif and would likely take the form of a van der Waals complex. Thus, the MWB48 calculated Ce₂O₄ structure is considered nonsensical and unlikely to be formed under experimental conditions.

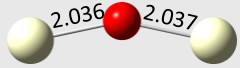
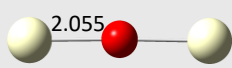

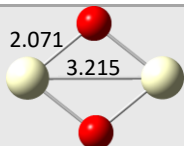
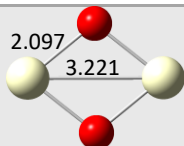
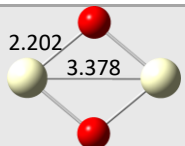
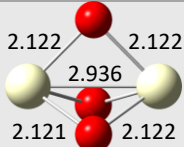
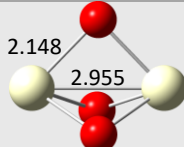
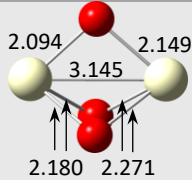
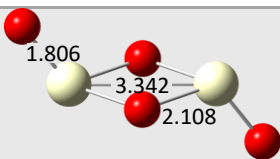
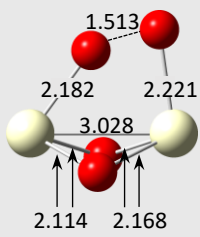
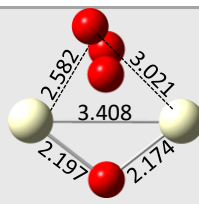
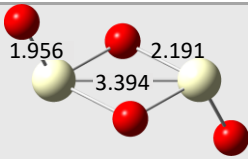
System	MWB28	MWB47	MWB48
Ce ₂ O	 $\angle\text{Ce-O-Ce} = 155.0^\circ$	 $\angle\text{Ce-O-Ce} = 178.4^\circ$	 $\angle\text{Ce-O-Ce} = 180.0^\circ$
	C_s	C_{2v}	D_{∞h}
Ce ₂ O ₂			
	D_{2h}	D_{2h}	D_{2h}
Ce ₂ O ₃			
	C₁	D_{3h}	C_s
Ce ₂ O ₄		 $\Delta E = +0.000 \text{ eV}$	
	C_{2h}	C₁	C₁
		 $\Delta E = +2.251 \text{ eV}$	
		C_{2h}	

Table 4.2: Calculated Ce₂O_n (n=1–4) structures using the MWB28, MWB47 and MWB48 ECPs. Point groups and bond lengths are shown. ΔE values are presented for higher energy structures. Chemical bonds are designated with solid lines. Interatomic distances between non-bonded atoms are designated with dashed lines.

4.6. Computational Expense of Effective Core Treatments for Cerium

The computational expense associated with each ECP for the optimisation of Ce_2O_n systems is presented in Figure 4.2. While computational accuracy is paramount, the pseudo-stochastic method employed in the context of this work – which requires optimisation of a vast number of structures in order to correctly locate the global minimum – necessitates a computationally efficient process. Therefore, a reasonable balance needs to be achieved between computational accuracy and expense. While DFT formally scales as N^3 – where N represents the number of basis functions used to represent Kohn-Sham orbitals²¹ – computational efficiency can also be highly dependent on the routines and algorithms intrinsic to the particular computational chemistry package. Moreover, the odd-electron core presented by the MWB47 ECP requires diagonalisation of the core Hamiltonian during SCF convergence cycles, which can come with an increased computational expense; the even-electron MWB28 and MWB48 ECPs do not require the core Hamiltonian to be diagonalised[†].

The computational expenses for structures optimised with the MWB28, MWB47 and MWB48 ECPs are presented in Figure 4.2. Because the number of steps required to complete geometry optimisation varied with each ECP, computational expense is recorded as average time per optimisation step. The computational expense associated with the MWB28 ECP is shown to fluctuate considerably with each Ce_2O_n system. Calculations of the Ce_2 , Ce_2O_2 and Ce_2O_4 clusters are quite comparable in expense to those of the larger MWB47 and MWB48 ECPs. In fact, the Ce_2O_2 cluster is actually less expensive to calculate with the MWB28 ECP than with the larger MWB47 core. However, Ce_2O and Ce_2O_3 calculations with the MWB28 ECP are 7 and 35 times more expensive, respectively, than their corresponding MWB47 calculations. This peculiarity is not unique to the MWB28 core; while Figure 4.2 shows the MWB47 ECP is generally more expensive than the larger MWB48 core, the Ce_2O_3 structure is optimised by the MWB47 ECP at a third of the expense of the MWB48 core. Two conclusions can be drawn

[†] Test calculations were performed on the effects of diagonalising the MWB28 and MWB48 ECPs during calculations. Calculations using the MWB48 ECP showed diagonalization of the core Hamiltonian was inconsequential; no effect on the geometries and electronic energies of optimised structures was recorded compared to the undiagonalised core. Conversely, MWB28 calculations showed diagonalisation of the core Hamiltonian in some cases lowered the electronic energies and slightly changed the geometries of optimised structures. However, the additional complexity imposed by this process on the SCF lead to convergence issues and was determined to be impractical.

from these results. Firstly, the cost associated with each ECP is not simply dependent on the core size; a more pertinent effect on computational expense appears to be the ease with which the self-consistent field – which varies with ECP selection – can be converged during each step of the optimisation process. Secondly, the cost of the MWB28 ECP is quite comparable to that of the larger MWB47 and MWB48 ECPs in most cases. However, the complexity of the electronic structure associated with the small frozen core can present difficulties with SCF convergence – due to the vast number of trial wavefunctions available, as discussed in Chapter 3 – or a significant increase in computational expense for some systems.

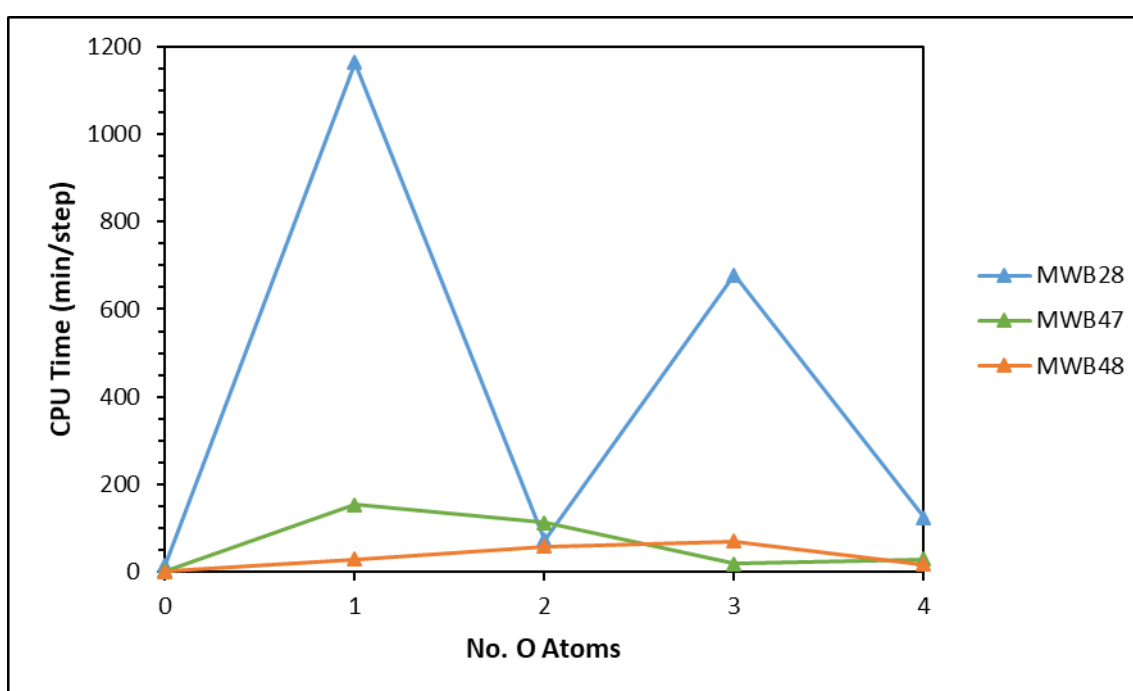


Figure 4.2: Computational expense for Ce_2O_n optimisation calculations using MWB28, MWB47 and MWB48 ECP treatments for Ce atoms.

4.7. Selection of Effective Core Potential Treatment

Given the greater accuracy of the MWB28 ECP in predicting both geometric properties and ionisation energies compared to both MWB47 and MWB48 cores, the MWB28 ECP is selected for all future calculations presented in this work. MWB60 and MWB2 effective core treatments are additionally afforded for Au and O respectively.

The complex SCF associated with the MWB28 frozen core treatment of cerium restricts the use of this ECP to cluster systems containing 2 or 3 Ce atoms. This includes the Ce_2O_n , Ce_3O_n , AuCe_2O_n and AuCe_3O_n systems presented in this work. Calculations of larger systems will require a simpler and more computationally efficient treatment of the Ce core which also allows the 4f electrons to be treated explicitly. The search for such an ECP is beyond the scope of this work.

4.8. References

- (1) Linton, C.; Dulick, M.; Field, R. W.; Carette, P.; Leyland, P. C.; Barrow, R. F. *J. Mol. Spectrosc.* **1983**, *102* (2), 441.
- (2) Linton, C. *J. Chem. Phys.* **1981**, *74* (1), 189.
- (3) Dolg, M. In *Encyclopaedia of Computational Chemistry*; Schleyer, P. v. R., Allinger, N. L., Clark, T., Gasteiger, J., Kollman, P. A., Schaefer III, P. R., Schreiner, P. R., Eds.; Wiley: Chichester, 1998; pp 1478–1486.
- (4) Gentleman, A. S.; Addicoat, M. A.; Dryza, V.; Gascooke, J. R.; Buntine, M. A.; Metha, G. *J. Chem. Phys.* **2009**, *130* (16), 64311.
- (5) Gentleman, A. S. The Effect of Sequential Oxidation and Composition on the Structural and Electronic Properties of Gas Phase Transition-Lanthanide Bimetallic Clusters, PhD Thesis, The University of Adelaide, 2014.
- (6) Dolg, M.; Stoll, H.; Preuss, H. *J. Chem. Phys.* **1989**, *90* (3), 1730.
- (7) Dolg, M.; Stoll, H. *Theor. Chim. Acta* **1989**, *75* (5), 369.
- (8) Dolg, M.; Stoll, H.; Savin, A.; Preuss, H. *Theor. Chim. Acta* **1989**, *75* (3), 173.
- (9) Frisch, M. J.; Trucks, G. W.; Schlegel, H. B.; Scuseria, G. E.; Robb, M. A.; Cheeseman, J. R.; Scalmani, G.; Barone, V.; Mennucci, B.; Petersson, G. A.; Nakatsuji, H.; Caricato, M.; Li, X.; Hratchian, H. P.; Izmaylov, A. F.; Bloino, J.; Zheng, G.; Sonnenberg, J. L.; Hada, M.; Ehara, M.; Toyota, K.; Fukuda, R.; Hasegawa, J.; Ishida, M.; Nakajima, T.; Honda, Y.; Kitao, O.; Nakai, H.; Vreven, T.; Montgomery, J. A.; Peralta, J. E.; Ogliaro, F.; Bearpark, M.; Heyd, J. J.; Brothers, E.; Kudin, K. N.; Staroverov, V. N.; Kobayashi, R.; Normand, J.; Raghavachari, K.; Rendell, A.; Burant, J. C.; Iyengar, S. S.; Tomasi, J.; Cossi, M.; Rega, N.; Millam, J. M.; Klene, M.; Knox, J. E.; Cross, J. B.; Bakken, V.; Adamo, C.; Jaramillo, J.; Gomperts, R.; Stratmann, R. E.; Yazyev, O.; Austin, A. J.; Cammi, R.; Pomelli, C.; Ochterski, J. W.; Martin, R. L.; Morokuma, K.; Zakrzewski, V. G.; Voth, G. A.; Salvador, P.; Dannenberg, J. J.; Dapprich, S.; Daniels, A. D.; Farkas, Foresman, J. B.; Ortiz, J. V.; Cioslowski, J.; Fox, D. J. *Gaussian 09, Revision D.01*, Gaussian, Inc., Wallingford CT. Wallingford CT 2009,.
- (10) Shen, X.; Fang, L.; Chen, X.; Lombardi, J. R. *J. Chem. Phys.* **2000**, *113* (6), 2233.

-
- (11) Huber, K. P.; Herzberg, G. *Molecular spectra and molecular structure of diatomic molecules*; Van Nostrand: New York, 1979.
- (12) Koopmans, T. *Physica* **1934**, *1*, 104.
- (13) Gentleman, A. S.; Addicoat, M. A.; Dryza, V.; Gascooke, J. R.; Buntine, M. A.; Metha, G. *F. J. Chem. Phys.* **2009**, *130* (16), 164311.
- (14) Dryza, V.; Addicoat, M. A.; Gascooke, J. R.; Buntine, M. A.; Metha, G. *F. J. Phys. Chem. A* **2005**, *109* (49), 11180.
- (15) Dryza, V. Threshold Photo-ionisation and Density Functional Theory Studies of Metal-Carbide Clusters, PhD Thesis, The University of Adelaide, 2008.
- (16) Dryza, V.; Gascooke, J. R.; Buntine, M. A.; Metha, G. F. *Phys. Chem. Chem. Phys.* **2009**, *11* (7), 1060.
- (17) Dryza, V.; Addicoat, M. A.; Gascooke, J. R.; Buntine, M. A.; Metha, G. F. *J. Phys. Chem. A* **2008**, *112* (25), 5582.
- (18) Chen, H.-L.; Weng, M.-H.; Ju, S.-P.; Chang, J.-G.; Chen, H.-T.; Chang, C.-S. *J. Mol. Struct.* **2010**, *963* (1), 2.
- (19) National Institute of Standards and Technology webbook.nist.gov (accessed Oct 13, 2016).
- (20) Abrahams, S. C.; Collin, R. L.; Lipscomb, W. N. *Acta Crystallogr.* **1951**, *4* (1), 15.
- (21) Cramer, C. J. *Essentials of Computational Chemistry*, 2nd ed.; John Wiley & Sons: Chichester, 2004.

Chapter Five

Photo-Ionisation Efficiency Spectroscopy, Density Functional Theory

Calculations and Zero Electron Kinetic Energy Simulations of Ce₂O_n Clusters

This chapter presents both experimentally determined and/or calculated adiabatic ionisation energies for the Ce₂O_n ($n=0-4$) cluster series. An initial analysis of the Ce_mO_n mass spectrum is discussed, followed by a comparison of experimental Photo-Ionisation Efficiency (PIE) spectra with simulated PIE spectra drawn from Zero Electron Kinetic Energy (ZEKE) simulations of DFT-optimised Ce₂O_n structures to infer cluster geometric and electronic properties.

5.1. Mass Spectrum Analysis

The mass spectrum for Ce_mO_n clusters ionised with laser radiation at 213 nm (5.82 eV) is presented in Figure 5.1. The mass spectrum shows 4 distinct groups of ion peaks with each group corresponding to the photo-ionisation of a bare metal Ce_m ($m=2,3,4,5$) cluster and its sequentially oxidised counterparts. The Ce and CeO ions, while not shown in the mass spectrum, are also detected in high abundance throughout photo-ionisation experiments. Both of these species, however, have been studied exhaustively¹⁻¹⁰ and are thus omitted from the mass spectrum.

The Ce_2O_n , Ce_3O_n and Ce_4O_n cluster ions are all detected in good abundance. Significantly weaker ion signal is recorded for the Ce_5O_n cluster ions. Previous photo-ionisation studies on Ce_m clusters by Koretsky and Knickelbein¹¹ have shown larger Ce_m clusters tend to correlate with lower IEs. The low Ce_5O_n abundances are thus unlikely to be due to high ionisation energies; they are more likely a result of both the conditions in the cluster source and the accelerating voltages in the TOF, which were optimised for the smaller Ce_2O_n , Ce_3O_n and Ce_4O_n ions. Larger Ce_mO_n cluster species, up to $Ce_{20}O_n$, have also been detected using the current experimental setup. However, the detection of these species requires a significant increase in the accelerating voltages – to produce shorter ion flight times – at the expense of reduced mass resolution. A mass spectrum showing ion peaks for larger Ce_mO_n clusters is presented in Appendix A.

The relative intensities of the cluster ion peaks presented in Figure 5.1 do follow any “magic number” trends; peak intensities are mostly dependent on the conditions within the cluster source. A higher content of surface oxygen on the cerium rod – which is achieved by exposing the cerium rod to atmosphere for ca. 8 hours every 2–3 days – yields an increased production of oxidised clusters. The absence of magic number species rules out the presence of any inherently stable cerium oxide cluster structures.

The ion peaks in the Ce_mO_n mass spectra each appear as a high intensity peak followed by a series of secondary peaks and shoulders at higher m/z . Moreover, the base of each ion peak

has a contoured appearance on the higher m/z side. These secondary peaks and contouring effects arise from Ce_mO_n clusters containing a heavier isotope of cerium – ^{142}Ce – with a natural abundance of ca. 11% compared to the 88.5% abundance of the ^{140}Ce primary isotope. A simulation of the Ce_mO_n mass spectrum showing relative isotopic abundances is presented in Figure 5.2. Cerium also exists in two other natural isotopes – ^{136}Ce and ^{138}Ce – which both have negligible relative abundances of 0.2% and 0.3%, respectively. Trace amounts of cluster hydrides – i.e. Ce_mO_nH – are also detected for some of the cluster species at +1 mass of the main ion peak. These hydride species are most likely formed from residual water in the cluster source.

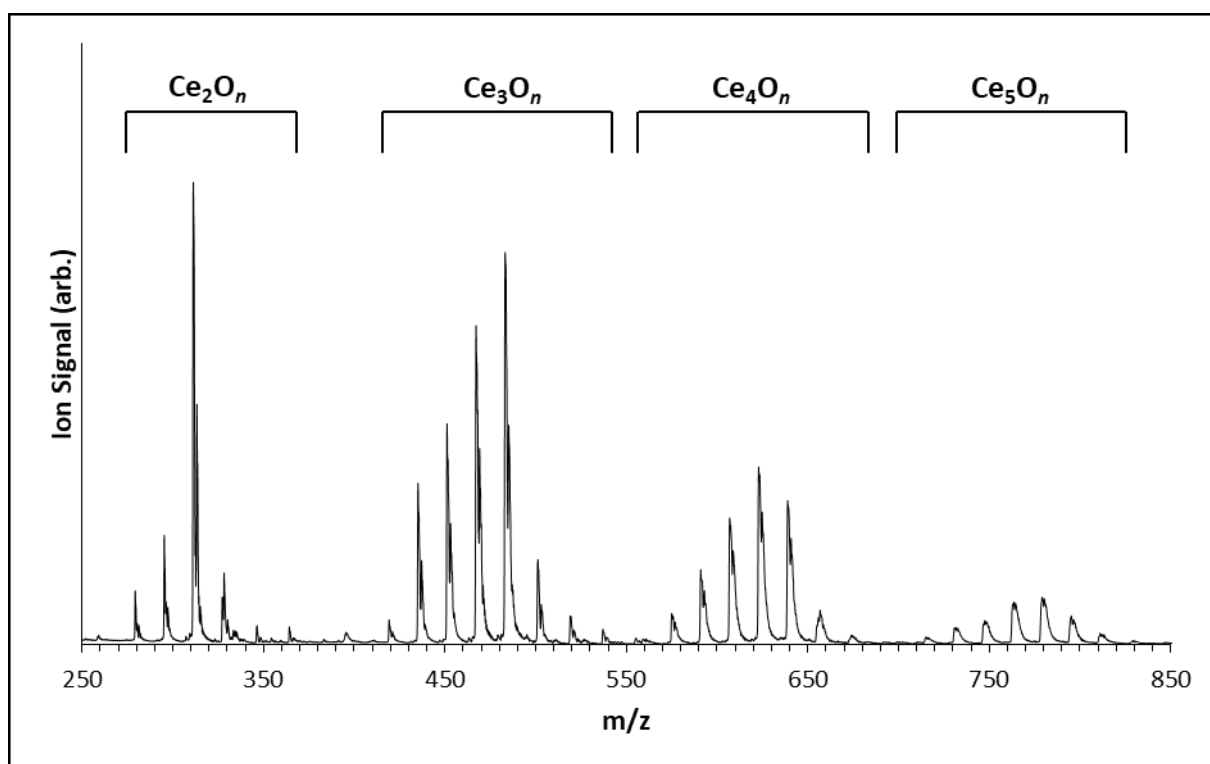


Figure 5.1: Mass spectrum for Ce_mO_n clusters following photo-ionisation at 213 nm (5.82 eV).

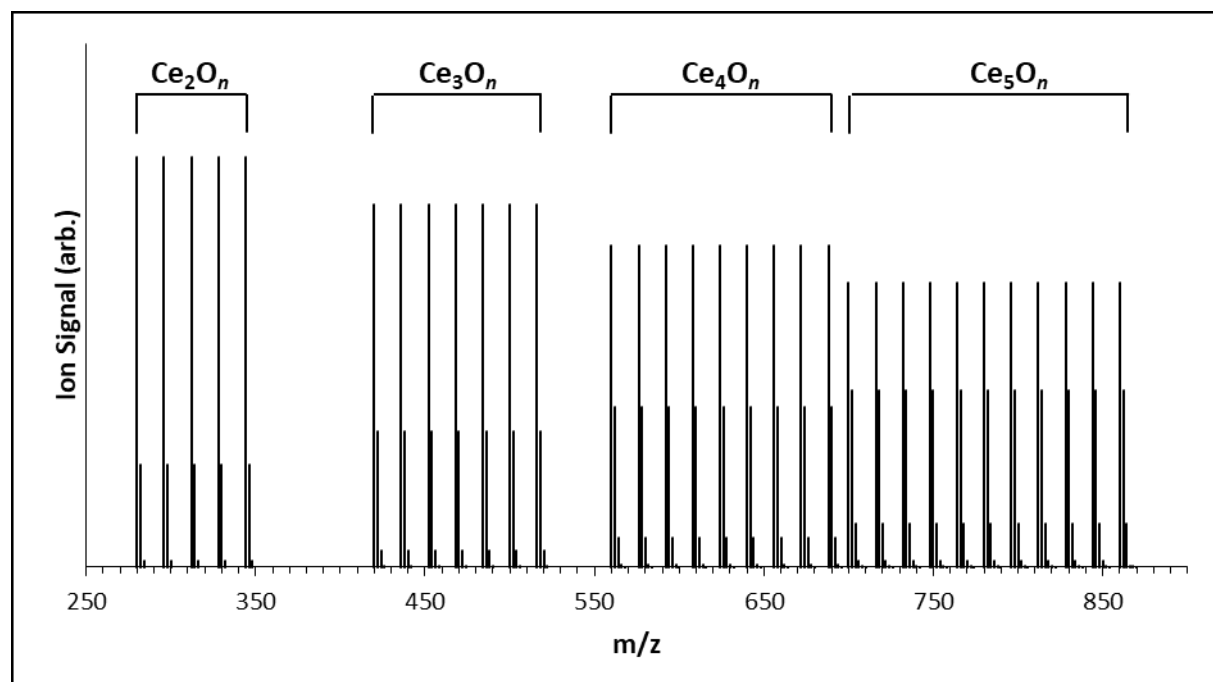


Figure 5.2: Simulated Ce_mO_n ($m=2,3,4,5$; $n=0-2m$) mass spectrum showing relative intensities of clusters comprising ^{140}Ce and ^{142}Ce isotopes. The ^{136}Ce and ^{138}Ce isotopes are not considered due to their negligible abundances.

5.2. Appearance of Cluster Ion Signal for the Ce_2O_n ($n=0-2$) Series

The appearance of the Ce_2O_n ion signal with increased photon energy was recorded over the wavelength range 240 – 317.5 nm (3.91 – 5.17 eV), as presented in Figure 5.3. While the experimental setup has the capability to explore the 220 – 317.5 nm (3.91 – 5.64 eV) wavelength range, most of the relevant peaks detected in the mass spectrum following 213 nm (5.82 eV) photo-ionisation were also detected in good abundance following 240nm (5.17 eV) photo-ionisation; therefore, the 220 – 240 nm (5.17 – 5.64 eV) range was not explored any further. The only ion peak observed to appear within the 213 – 240 nm (5.17 – 5.82 eV) range was that of the Ce_2O_3 cluster. However, mass spectra recorded following 220 nm (5.64 eV) photo-ionisation also did not show the Ce_2O_3 ion. Therefore, the Ce_2O_3 ion peak appears within the 213 – 220 nm (5.64 – 5.82 eV) range. An appropriate tuneable laser which operates within the 213 – 220 nm wavelength range is not available in the laboratory at this time. Thus, a bracketed AE of 5.64 – 5.82 eV is applied to the Ce_2O_3 cluster.

The Ce_2 , Ce_2O and Ce_2O_2 species are all observed to appear within the 240 – 279 nm (4.44 – 5.17 eV) region recorded during PIE experiments. Comparison of the mass spectra recorded following photo-ionisation at 264 nm (4.70 eV) and 245 nm (5.06 eV) – presented in Figures 5.3(b) and 5.3(c), respectively – shows the appearance of both the Ce_2 and Ce_2O ion peaks within the 4.70 – 5.06 eV energy range. The Ce_2O_2 ion peak appears at a lower energy in the 264 – 279 nm (4.44 – 4.70 eV) region, as shown by Figures 5.3(a) and 5.3(b).

The Ce_2O_4 and Ce_2O_5 ion peaks are both detected with very low intensity in the 213 nm (5.82 eV) photo-ionisation mass spectrum presented in Figure 5.1. Neither species are detected in any mass spectra recorded with lower photon energies. Due to the very weak intensities of the Ce_2O_4 and Ce_2O_5 ion peaks, it is unlikely that the ion signal for either of these species corresponds to photo-ionisation of a low-lying neutral isomer; these ion peaks could instead result from either one or a combination of photo-ionised metastable species, multi-photon ionisation processes or photo-fragmentation events. The weak ion peak recorded for the Ce_2O_4 cluster is attributed to a high IE, which will be discussed later in this chapter. The Ce_2O_5 cluster, which has a Ce:O ratio higher than the stoichiometric 1:2 ratio corresponding to the bulk surface, is not considered particularly interesting in the context of this work and is not discussed further.

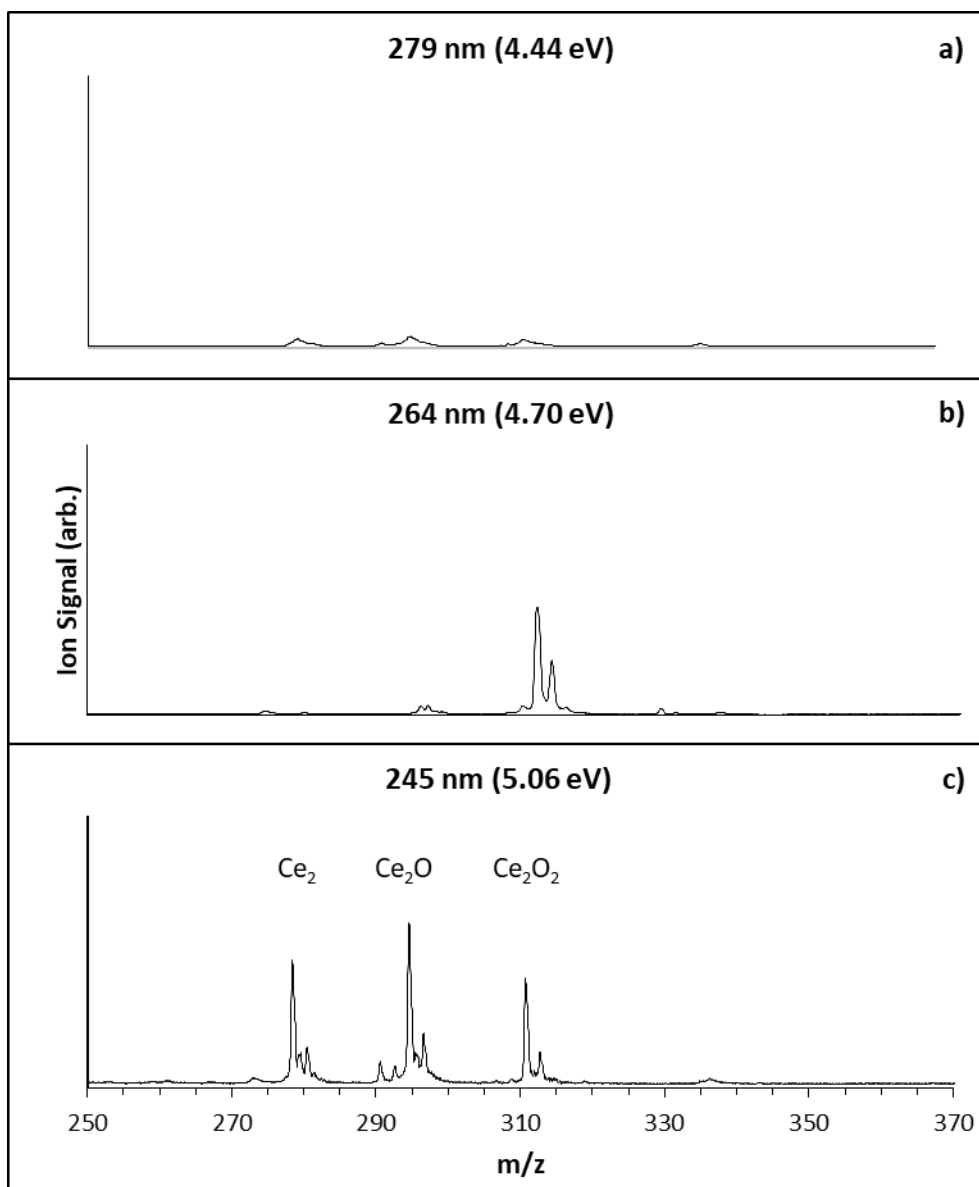


Figure 5.3: Mass spectra of Ce_2 , Ce_2O and Ce_2O_2 clusters following photo-ionisation at **a).** 279 nm (4.44 eV), **b).** 264 nm (4.70 eV) and **c).** 245 nm (5.06 eV).

5.3. PIE Spectrum and DFT Results for Ce_2

5.3.1. Ce_2 Experimental PIE Spectrum

A photo-ionisation efficiency (PIE) spectrum for the Ce_2 system recorded over the wavelength region 240 – 317.5 nm (3.92 – 5.17 eV) is presented in Figure 5.4. A relatively flat, low intensity region of ion signal is recorded between 3.92 eV and 4.87 eV; this section of the PIE spectrum is considered as the baseline. While a very minor increase in ion signal does occur over this region, this is most likely a product of photo-ionisation processes from clusters in excited electronic states (*vide infra*) or MPI. A sharp increase in ion signal begins at 4.87 eV which extends to the maximum recorded energy at 5.17 eV. The sharp onset indicates a strong Franck-Condon (FC) overlap between the neutral and cationic states correlating with a small change in the vibrational wavefunction upon ionisation. The ion signal is not observed to reach a high-energy plateau within the wavelength range over which the experiments were performed; this indicates that the highest energy FC allowed transition has not been accessed. The appearance energy (AE), which is found by the point of intersection of linear fits applied to the baseline and the onset (shown as red dashed lines in Figure 5.4), is determined to be 4.87 eV.

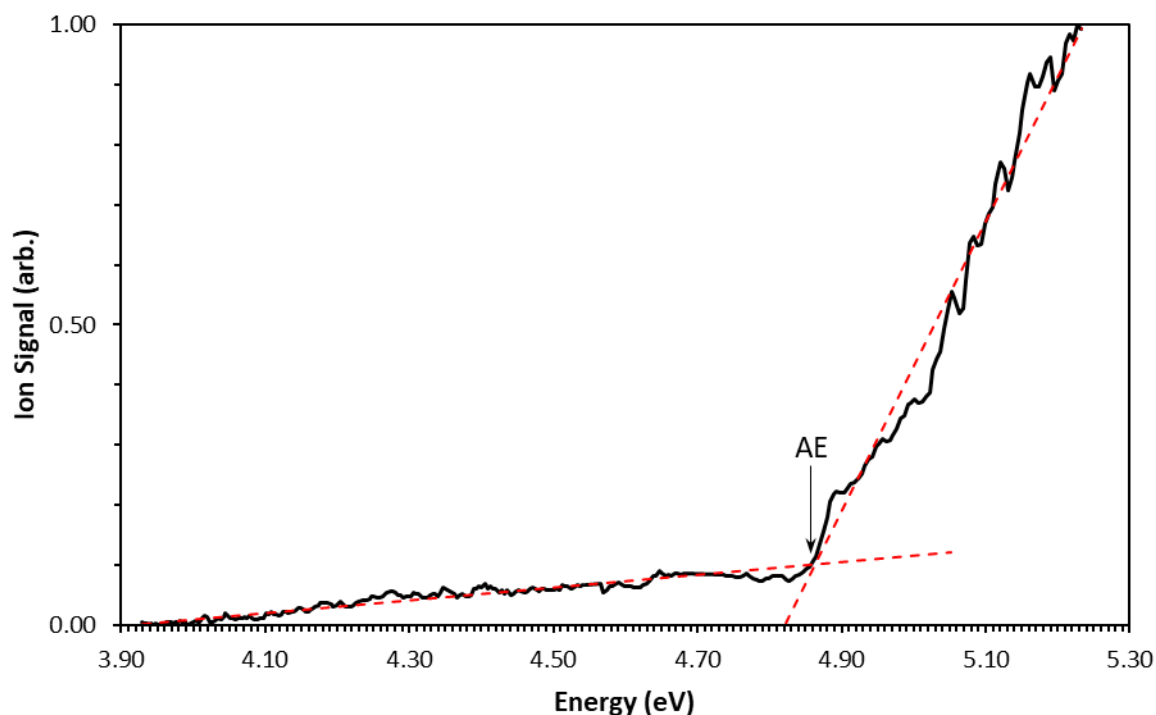


Figure 5.4: PIE spectrum for Ce_2 . Linear trendlines for the baseline and onset are presented as red dashed lines. The appearance energy is labelled with a black arrow.

5.3.2. DFT Calculations for Ce_2

DFT calculated neutral and cationic Ce_2 structures are presented with calculated vibrational frequencies and bond lengths – denoted ω_e and r_e , respectively – in Figure 5.5. Neutral Ce_2 dimers were calculated in the 1, 3, 5, 7 and 9 multiplicities. Cationic structures were subsequently found by re-optimising the neutral structures in both $\Delta S = +\frac{1}{2}$ and $\Delta S = -\frac{1}{2}$ spin states to account for ionisation processes occurring via removal of paired or unpaired electrons, respectively. The calculated electronic states for the neutral and cationic structures are presented where available. The orbital symmetries for a number of structures were unable to be identified during calculations; in these cases, electronic states are not presented.

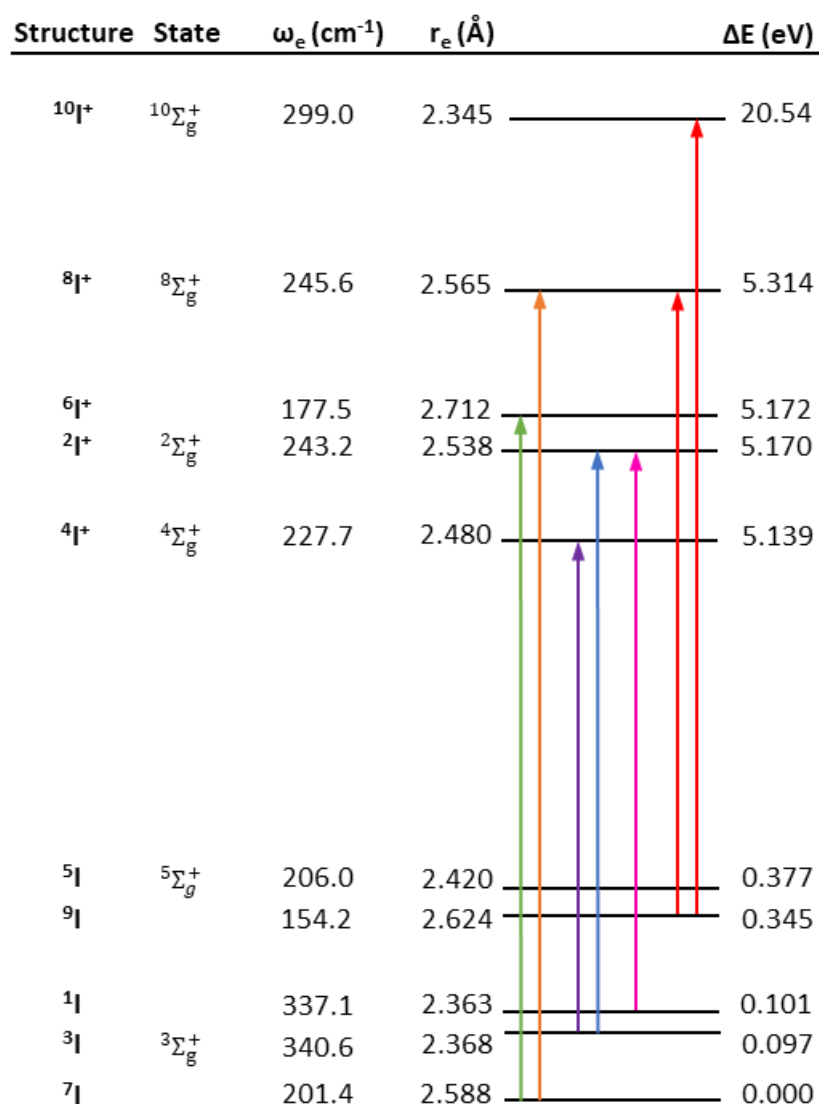


Figure 5.5: Calculated Ce_2 structures, bond lengths (r_e), harmonic frequencies (ω_e) and relative energies (ΔE). Electronic states presented where calculated. Potential ionisation transitions are shown. Ionisation transitions originating from neutral structures with prohibitively high energies are presented as red arrows.

The lowest energy neutral Ce_2 dimer is calculated as a septet (designated $7I$ in Figure 5.5) with $r_e = 2.588$ Å and $\omega_e = 201.4$ cm⁻¹. Energetically indistinguishable triplet and singlet Ce_2 states (designated $3I$ and $1I$, respectively) are also calculated with ΔE values of +0.097 eV and +0.101 eV, respectively, relative to the LES. The triplet and singlet dimers are structurally nearly identical with calculated r_e values of 2.368 Å and 2.363 Å, respectively and ω_e values of 340.6 cm⁻¹ and 337.1 cm⁻¹ respectively. This correlates well with previous *ab initio*

calculations by both Dolg et. al.¹² and Roos et. al.¹³ who predict six energetically indistinguishable singlet and triplet ($^1\Sigma_g^+$, $^1\Sigma_u^-$, $^3\Sigma_g^-$, $^3\Sigma_u^+$, $^3\sigma_u$, $^1\sigma_g$) states within 20 cm^{-1} . However, neither Dolg et al. or Roos et al. predict a septet electronic state for Ce_2 . The discrepancies between the Ce_2 calculations presented by Dolg et al. and Roos et al. compared to those presented in this work may be due to different treatments of correlation effects from the Ce 4f electron on both the 5d/6s valence shell and on 4f electrons in neighbouring Ce atoms; the most prominent effects include valence bond exchange, 4f-4f Coulombic repulsion and spin-orbit coupling. These interactions have been shown by Nikolaev¹⁴ to be highly influential on the low-lying energy spectrum of Ce_2 . Given the far more sophisticated treatments of correlation effects by both Dolg et. al. and Roos et. al. – who used CASSCF/MRCI and CASSCF/CASPT2 methods respectively – than the DFT method used in this work, the $^1\mathbf{I}$ and $^3\mathbf{I}$ species are considered as the Ce_2 LES in preference to the $^7\mathbf{I}$ species. This maintains consistency with previous works. It should be noted, however, that difficulties with correctly describing the Ce_2 ground state are more an artefact of the highly complex electronic structure of the Ce atom – which occupies the 1G_4 many-electron ground state in a rare violation of Hund's first rule¹⁵ – and subsequently, the Ce_2 dimer, rather than the inferiority of the DFT method. Moreover, an accurate description of low-lying electronic states within the Ce_2 dimer is not of particular interest within the context of this work. The pertinent electronic feature of all cluster systems in this work is the HOMO energy, which is not significantly affected by the exact superconfiguration of the ground state. DFT methods have been used previously with good success to describe the general electronic structures – particularly HOMO and LUMO energies, and spin density distribution – of small cerium oxide species^{16,17}.

Calculations also reveal neutral Ce_2 nonet and quintet species, designated $^9\mathbf{I}$ and $^5\mathbf{I}$ respectively, with energies of +0.345 eV and +0.377 eV relative to the lowest energy structure (LES). The significantly higher energies of the $^9\mathbf{I}$ and $^5\mathbf{I}$ dimers – with regard to the $^1\mathbf{I}$, $^3\mathbf{I}$ and $^7\mathbf{I}$ species – would largely preclude their existence in any noticeable abundance under the experimental conditions in this work. The $^9\mathbf{I}$ and $^5\mathbf{I}$ dimers are therefore not discussed any further.

Potential cationic structures are considered from the $\Delta S=+\frac{1}{2}$ and $\Delta S=-\frac{1}{2}$ products of the calculated 1I , 3I and 7I neutral species. This gives a total of four cationic species, designated $^4I^+$, $^2I^+$, $^6I^+$ and $^8I^+$ in order of increasing energy as shown in Figure 5.5 (the $\Delta S=+\frac{1}{2}$ and $\Delta S=-\frac{1}{2}$ products of the 1I and 3I structures converged to the same $^2I^+$ geometry). The calculated ionisation processes for the 1I , 3I and 7I neutral species show five unique transitions. These include the $^2I^+\leftarrow^1I$, $^2I^+\leftarrow^3I$, $^4I^+\leftarrow^3I$, $^6I^+\leftarrow^7I$ and $^8I^+\leftarrow^7I$ processes which are shown as green, orange, violet, blue and magenta arrows, respectively, in Figure 5.5. Calculated IEs for these processes range from 5.042 eV to 5.314 eV; given the relatively narrow range of calculated IEs, it is quite possible that all five ionisation processes contribute to the PIE onset in the experimental spectrum.

5.3.3. ZEKE Spectral Simulations for Ce_2

The $^2I^+\leftarrow^1I$, $^4I^+\leftarrow^3I$, $^2I^+\leftarrow^3I$, $^6I^+\leftarrow^7I$ and $^8I^+\leftarrow^7I$ processes were considered for ZEKE simulations owing to their similar calculated IEs. Calculated ZEKE spectra for these ionisation transitions at 300 K are presented in Figure 5.6. Energetic corrections were applied to these ZEKE spectra using the method described in Chapter 3; the corrected ZEKE spectra are shown here (this is the case for all simulated ZEKE spectra presented in this work). Comparison of the scaling factors in all five ZEKE spectra, which are applied individually to each ZEKE spectrum in order to normalise the most intense peak to a value of 1, show the scaling factors are all quite similar. Therefore, the $^2I^+\leftarrow^1I$, $^4I^+\leftarrow^3I$, $^2I^+\leftarrow^3I$, $^6I^+\leftarrow^7I$ and $^8I^+\leftarrow^7I$ transitions all have approximately equal contributions to the resulting PIE spectrum.

The simulated ZEKE spectrum for the $^2I^+\leftarrow^1I$ transition is presented in Figure 5.6(a). The spectrum presents a broad profile which consists primarily of the fundamental (n,0) progression in addition to very weak (n,1) and (n,2) hot band progressions. The fundamental and hot band progressions display an energy separation of 0.042 eV due to the calculated 1I vibrational frequency of 337.1 cm^{-1} . Vibronic peaks within each progression are separated by 0.030 eV due to the calculated $^2I^+$ vibrational frequency of 243.2 cm^{-1} . The (0,0) peak calculated at ca. 4.87 eV – labelled with a black arrow – shows very weak intensity and thus would be unlikely to have any noticeable effect on the PIE spectrum, concomitant with a weak

FC overlap between the neutral 1I and cationic $^2I^+$ structures. This is consistent with the significant elongation of the Ce-Ce bond in the $^2I^+$ structure, which is calculated as ca. 0.2 Å longer than that of the 1I dimer.

ZEKE spectral simulations for the $^4I^+ \leftarrow ^3I$ and $^2I^+ \leftarrow ^3I$ ionisation processes are presented in Figures 5.6(b) and 5.6(c) respectively. Both spectra show two vibronic progressions which include the (n,0) fundamental progression and the (n,1) hot band progression. The calculated vibrational frequency of 340.6 cm^{-1} for the neutral 3I dimer gives an energy separation of 0.042 eV between the (n,0) and (n,1) progressions in both spectra. The calculated vibrational frequencies of 227.7 cm^{-1} and 243.2 cm^{-1} for the $^4I^+$ and $^2I^+$ cations give peak separations within the progressions of 0.028 eV and 0.030 eV for the $^4I^+ \leftarrow ^3I$ or $^2I^+ \leftarrow ^3I$ spectra, respectively. The (1,1) transition is assigned as the lowest energy vibronic transition in both spectra – labelled with blue arrows in both spectra – since it is likely this transition would correspond to the beginning of the thermal tail in the PIE spectrum. While lower energy vibronic peaks are calculated in both ZEKE spectra, they are generally low intensity and sparsely located from other vibronic peaks; this would make their contribution to a PIE spectrum in an experimental setting difficult to detect. The (0,0) transitions for the $^4I^+ \leftarrow ^3I$ and $^2I^+ \leftarrow ^3I$ ionisation processes are calculated as 5.074 eV and 4.840 eV, respectively.

Comparison of the calculated $^4I^+ \leftarrow ^3I$ and $^2I^+ \leftarrow ^3I$ ZEKE spectra show markedly different spectral profiles; particularly with regard to the lengths of the (n,0) and (n,1) vibronic progressions. The $^4I^+ \leftarrow ^3I$ spectrum displays short progressions correlating with a strong FC overlap between the neutral and cationic states. Conversely, the $^2I^+ \leftarrow ^3I$ spectrum exhibits very long progressions due to the 0.17 Å difference in bond length between the 3I and $^2I^+$ dimers. Comparison of the normalisation scaling factors applied to the $^2I^+ \leftarrow ^3I$ and $^4I^+ \leftarrow ^3I$ spectra – which were 5.8 and 3.7 respectively – again points to slightly weaker FC overlap in the $^2I^+ \leftarrow ^3I$ ionisation process.

Simulated ZEKE spectra for the $^6I^+ \leftarrow ^7I$ and $^8I^+ \leftarrow ^7I$ transitions, which both originate from the septet Ce_2 structure, are shown in Figures 5.6(d) and 5.6(e) respectively. Both spectra

primarily comprise of 3 vibronic progressions which include the band origin progression (n,0) in addition to the (n,1) and (n,2) hot band progressions. Unlike the $^2I^+ \leftarrow ^1I$, $^4I^+ \leftarrow ^3I$ or $^2I^+ \leftarrow ^3I$ spectra discussed previously, the (n,2) hot band progressions are calculated with good intensity for both the $^6I^+ \leftarrow ^7I$ and $^8I^+ \leftarrow ^7I$ spectra. This is most likely due to the significantly lower vibrational frequency of the neutral 7I dimer (201.4 cm^{-1}) compared to both the 1I and 3I structures, facilitating a greater population of hot band states. Vibronic progressions in both the $^6I^+ \leftarrow ^7I$ and $^8I^+ \leftarrow ^7I$ spectra are separated by 0.025 eV corresponding to the calculated 7I vibrational frequency. Vibronic peaks within each progression in the $^6I^+ \leftarrow ^7I$ and $^8I^+ \leftarrow ^7I$ ZEKE spectra are separated 0.022 eV and 0.030 eV, respectively, correlating with the calculated $^6I^+$ and $^8I^+$ vibrational frequencies of 177.5 cm^{-1} and 245.6 cm^{-1} . The lowest energy vibronic transition in both spectra – labelled with a blue arrow – which is likely to correspond to the beginning of the thermal tail in the PIE spectrum and thus the AE, is the (0,3) transition. This transition forms part of a short (n,3) progression in the $^8I^+ \leftarrow ^7I$ ZEKE spectrum, whereas no other vibronic transition from the $v''=3$ state is calculated for the $^6I^+ \leftarrow ^7I$ ZEKE spectrum. The (0,0) transitions for the $^6I^+ \leftarrow ^7I$ and $^8I^+ \leftarrow ^7I$ spectra are calculated as 4.929 eV and 4.793 eV respectively, while the most intense peak – corresponding to the transition with maximum FC overlap – in both cases is the (2,0) peak at 4.973 eV and 5.109 eV respectively.

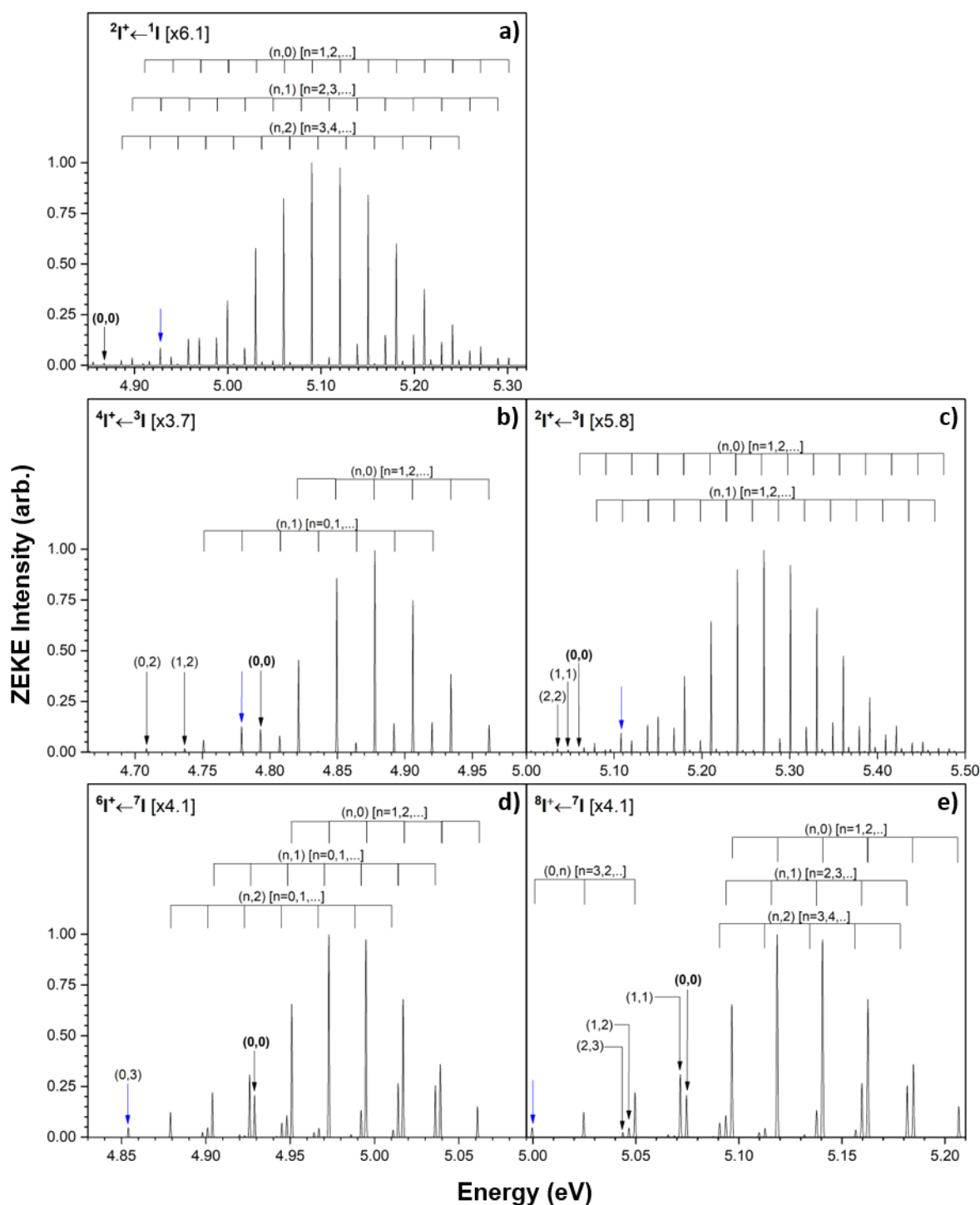


Figure 5.6: Simulated ZEKE spectra for Ce_2 ionisation transitions: **a)** $2I^+ \leftarrow -1I$, **b)** $4I^+ \leftarrow -3I$, **c)** $2I^+ \leftarrow -3I$, **d)** $6I^+ \leftarrow -7I$ and **e)** $8I^+ \leftarrow -7I$. Spectral intensities are normalised to the most intense peak in each spectrum with scaling factors shown. Prominent vibronic transitions are assigned. The vibronic transition likely to correspond to the appearance of ion signal in each spectrum is labelled with a blue arrow.

5.3.4. Comparison of Simulated and Experimental PIE Spectra for Ce_2

The simulated ZEKE spectra for the Ce_2 , $^4I^+ \leftarrow ^3I$, $^2I^+ \leftarrow ^3I$, $^2I^+ \leftarrow ^1I$, $^6I^+ \leftarrow ^7I$ and $^8I^+ \leftarrow ^7I$ transitions – listed here in order of lowest energy to highest energy – were amalgamated and then integrated to produce a simulated PIE spectrum for the Ce_2 photo-ionisation process. The similar ZEKE intensities and energies calculated for these transitions suggests all five ionisation processes would contribute to the PIE spectrum. The simulated PIE spectrum is shown overlaid against the experimental PIE spectrum in Figure 5.7. Simulated ZEKE spectra are presented underneath the PIE spectrum; these include the $^4I^+ \leftarrow ^3I$ and $^2I^+ \leftarrow ^1I$ transitions (shown as violet and magenta, respectively).

The Ce_2 adiabatic ionisation energy (IE_{ad}) is taken from the $^2I^+ \leftarrow ^1I$ band origin transition as 4.87 ± 0.05 eV (shown as a solid black arrow in Figure 5.7). This value compares well to the Ce_2 vertical IE (IE_v) previously reported by Koretsky and Knickelbein¹¹ of 4.92 ± 0.05 eV (shown as a dotted black arrow in Figure 5.7). It should be noted, however, that Koretsky and Knickelbein assigned their IE_v value through analysis of their experimental PIE spectrum only; the authors performed a linear extrapolation of the major post-threshold portion of ion signal to the baseline in order to assign the IE_v . Therefore, their assigned IE_v value does not necessarily correspond to the vibronic transition with the maximum FC overlap. Given that the Ce_2 IE assigned by Koretsky and Knickelbein occurs immediately after the thermal tail in their PIE spectrum, their assignment appears to correspond to the adiabatic transition rather than the vertical transition.

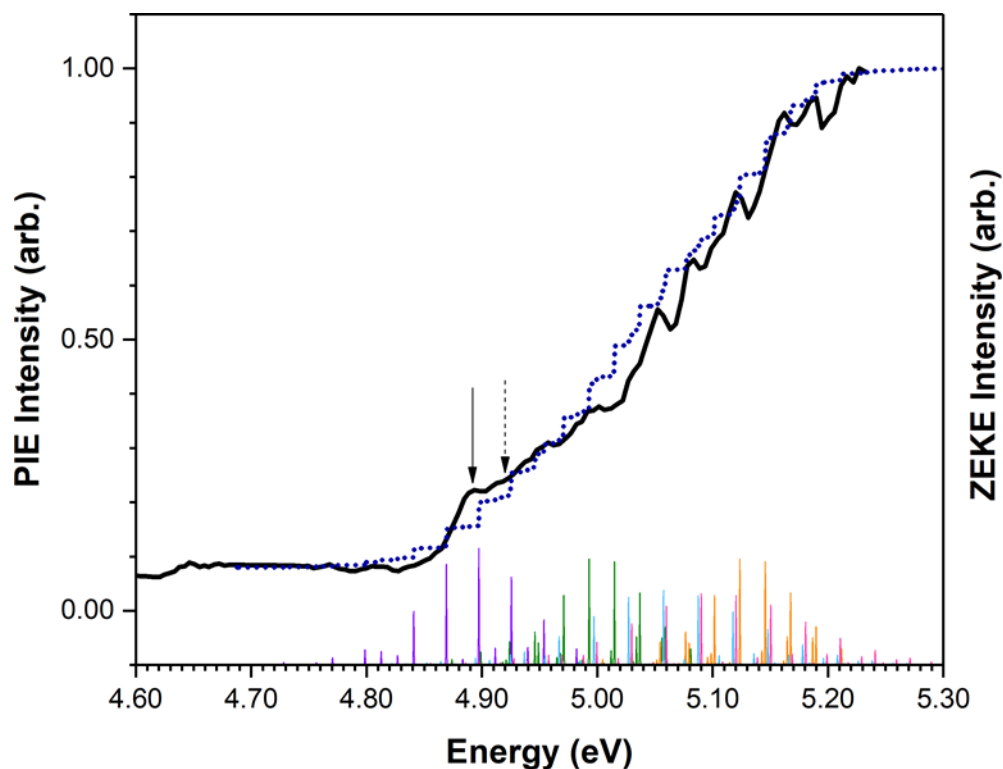


Figure 5.7: Ce_2 simulated PIE spectrum (blue dotted line) overlaid against the experimental PIE spectrum (solid black line). Calculated ZEKE spectra for the $^4f^7 \leftarrow ^3I$, $^2f^7 \leftarrow ^3I$, $^2f^7 \leftarrow ^1I$, $^6f^7 \leftarrow ^7I$ and $^8f^7 \leftarrow ^7I$ ionisation processes are shown below the PIE spectrum in violet, blue, magenta, green and orange, respectively. The adiabatic ionisation energy is labelled with a solid black arrow. The vertical ionisation energy reported by Koretsky and Knickelbein is shown with a dashed black arrow.

5.4. PIE Spectrum and DFT Results for Ce_2O

5.4.1. Ce_2O Experimental PIE Spectrum

The Ce_2O experimental PIE spectrum is presented in Figure 5.8. Two separate onsets of ion signal are observed with appearance energies of 4.85 eV and 4.45 eV, designated AE_1 and AE_2 , respectively. The higher energy onset at 4.85 eV extends to a plateau at ca. 5.03 eV with a reasonably sharp slope corresponding to a good FC overlap between the neutral and cationic states. The lower energy onset at 4.45 eV extends to a plateau at 4.55 eV with a moderate slope. The higher energy onset encompasses the majority of Ce_2O ion signal increase over the region of interest and is thus labelled the primary onset. The lower energy onset displays a modest increase in ion signal compared to the primary onset and is thus labelled the secondary onset.

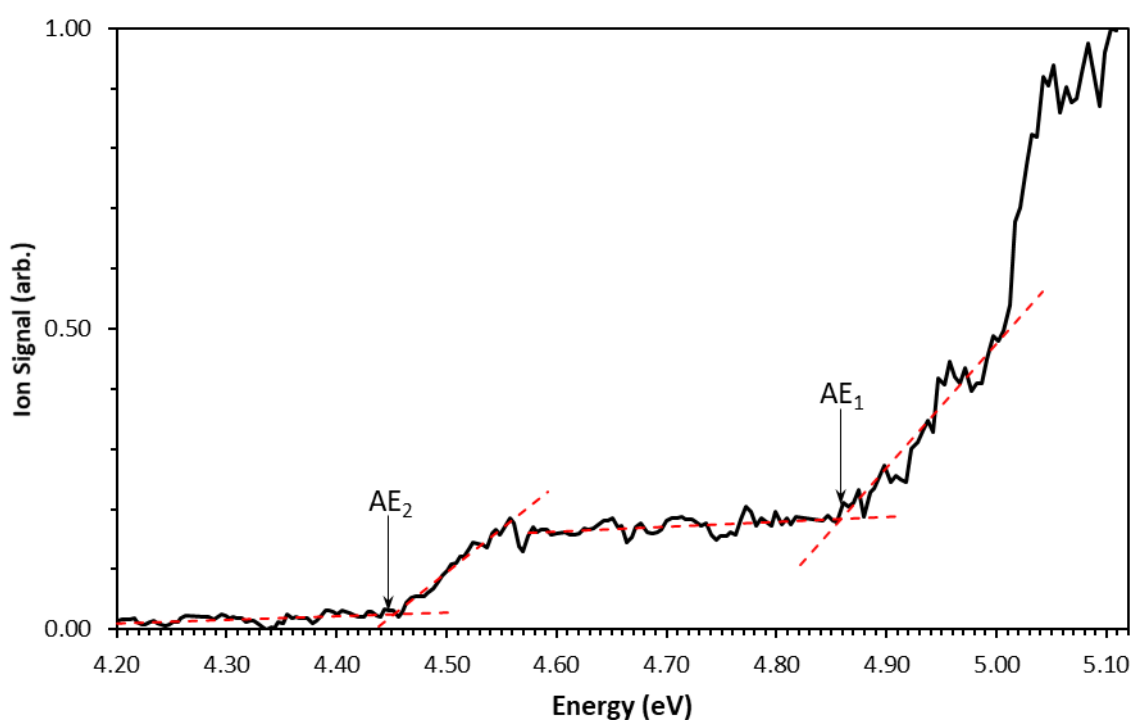


Figure 5.8: PIE spectrum for Ce_2O . Linear trendlines for the baseline and onset are presented as red dashed lines. Appearance energies for the primary and secondary onsets – designated AE_1 and AE_2 , respectively – are labelled with black arrows.

5.4.2. DFT Calculations for Ce_2O

Calculated neutral and cationic structures for Ce_2O are presented in Figures 5.9 and 5.10 (with calculated vibrational modes for all Ce_2O_n clusters shown in Appendix B). Two unique structures for the neutral Ce_2O system are calculated; these are labelled **IIA** and **IIB** in order of increasing energy. The **IIA** structure comprises an oxygen atom bound to two cerium atoms with a Ce-O-Ce bond angle of 155.0° . Only one species is calculated with this geometric arrangement, which comprises a C_s – albeit near C_{2v} – singlet in the $^1A'$ electronic state, labelled ^1IIA . While a C_{2v} symmetric ^1IIA type structure was also calculated – with an energy of +0.03 eV relative the C_s structure – the energetic and structural similarities between the C_s and C_{2v} structures makes it unlikely that the two species correspond to unique clusters. It seems more likely that the two geometries are an artefact of a single high-symmetry cluster exhibiting a Jahn-Teller distortion. Thus, the lower energy C_s structure is considered while the higher energy C_{2v} structure is ignored.

The **IIB** structure is calculated as a C_s trimer where the oxygen atom bridges a Ce-Ce bond. Attempts to constrain the **IIB** structure to a C_{2v} symmetry lead to optimised structures with imaginary frequencies corresponding to saddle points on the potential energy surface. The 2-LES and 3-LES species are calculated as spin-isomers of the same **IIB** structure in the $^5A''$ and $^3A'$ electronic states, respectively. However, these species – labelled ^5IIB and ^3IIB respectively – display a considerable energetic separation; energies for the ^5IIB and ^3IIB structures are calculated as +0.050 eV and +0.244 eV relative to the LES, respectively. This makes the ^5IIB species energetically indistinguishable from the LES, while the ^3IIB species would more likely be a metastable state in the experiment. The Ce-O bond lengths in the neutral structures are calculated in the range 2.036 – 2.079 Å; these are considerably shorter than those in the bulk ceria lattice (where Ce-O bond distances have been calculated by Nolan et al.¹⁸ to be 2.37 Å and 2.33 Å for the bulk and surface layers, respectively). However, the shorter Ce-O bond lengths calculated for the Ce_2O clusters is consistent with the contracted bond lengths reported for the surface layer due to relaxation¹⁸. Thus, the consideration of cerium oxide clusters as a highly relaxed portion of the ceria surface appears tenable. The Ce-Ce bond lengths for the ^5IIB and ^3IIB structures are calculated as 3.371 Å and 3.188 Å, respectively, while the ^1IIA Ce-Ce interatomic separation (with no Ce-Ce bond) is calculated to be

considerably longer, at 3.985 Å. The 1IIA structure is more consistent with the bulk ceria structure, where the Ce-Ce interatomic separation is 3.80 Å with no Ce-Ce bond¹⁹.

Cationic Ce_2O species are all calculated as **IIB** type geometries comprising an oxygen atom bridging a Ce-Ce bond; no cationic structures were found to display the slightly bent structure of the 1IIA neutral LES. A total of 3 cationic structures are presented as target states for the 1IIA , 5IIB and 3IIB neutral species. These species, labelled $^4IIB^+$, $^2IIB^+$ and $^6IIB^+$, are calculated as C_s symmetric structures in the $^4A''$, $^2A'$ and $^6A''$ electronic states, respectively. Symmetry constrained calculations revealed low-lying C_{2v} symmetric structures for the $^4IIB^+$, $^2IIB^+$ and $^6IIB^+$ species; each with slightly higher energies than their respective C_s structures. The C_s and C_{2v} geometries are proposed to be an artefact of Jahn Teller distortion; with both structures belonging to the same cluster. Thus, only the lower energy C_s structures are considered. This gives a total of five ionisation transitions for the Ce_2O system which include the $^2A' \leftarrow ^1A'$ ($^2IIB^+ \leftarrow ^1IIA$), $^4A'' \leftarrow ^5A''$ ($^4IIB^+ \leftarrow ^5IIB$), $^6A'' \leftarrow ^5A''$ ($^6IIB^+ \leftarrow ^5IIB$), $^4A'' \leftarrow ^3A'$ ($^4IIB^+ \leftarrow ^3IIB$) and $^2A' \leftarrow ^3A'$ ($^2IIB^+ \leftarrow ^3IIB$) processes. DFT calculated IEs for these transitions are 5.087 eV, 5.037 eV, 5.129 eV, 4.821 eV and 4.843, respectively. On comparison of these calculated IE values, the ionisation processes can be grouped into two separate onsets: the $^2A' \leftarrow ^1A'$ ($^2IIB^+ \leftarrow ^1IIA$), $^4A'' \leftarrow ^5A''$ ($^4IIB^+ \leftarrow ^5IIB$) and $^6A'' \leftarrow ^5A''$ ($^6IIB^+ \leftarrow ^5IIB$) processes correspond to the higher energy primary onset, while the $^4A'' \leftarrow ^3A'$ ($^4IIB^+ \leftarrow ^3IIB$) and $^2A' \leftarrow ^3A'$ ($^2IIB^+ \leftarrow ^3IIB$) processes correspond to the lower energy secondary onset. The $^4A'' \leftarrow ^5A''$ ($^4IIB^+ \leftarrow ^5IIB$), $^6A'' \leftarrow ^5A''$ ($^6IIB^+ \leftarrow ^5IIB$), $^4A'' \leftarrow ^3A'$ ($^4IIB^+ \leftarrow ^3IIB$) and $^2A' \leftarrow ^3A'$ ($^2IIB^+ \leftarrow ^3IIB$) processes are shown in Figure 5.9 as green, orange, violet and blue arrows, respectively. The $^2A' \leftarrow ^1A'$ ($^2IIB^+ \leftarrow ^1IIA$) transition is represented as a red dotted arrow due to low ZEKE intensities calculated for this process (vide infra).

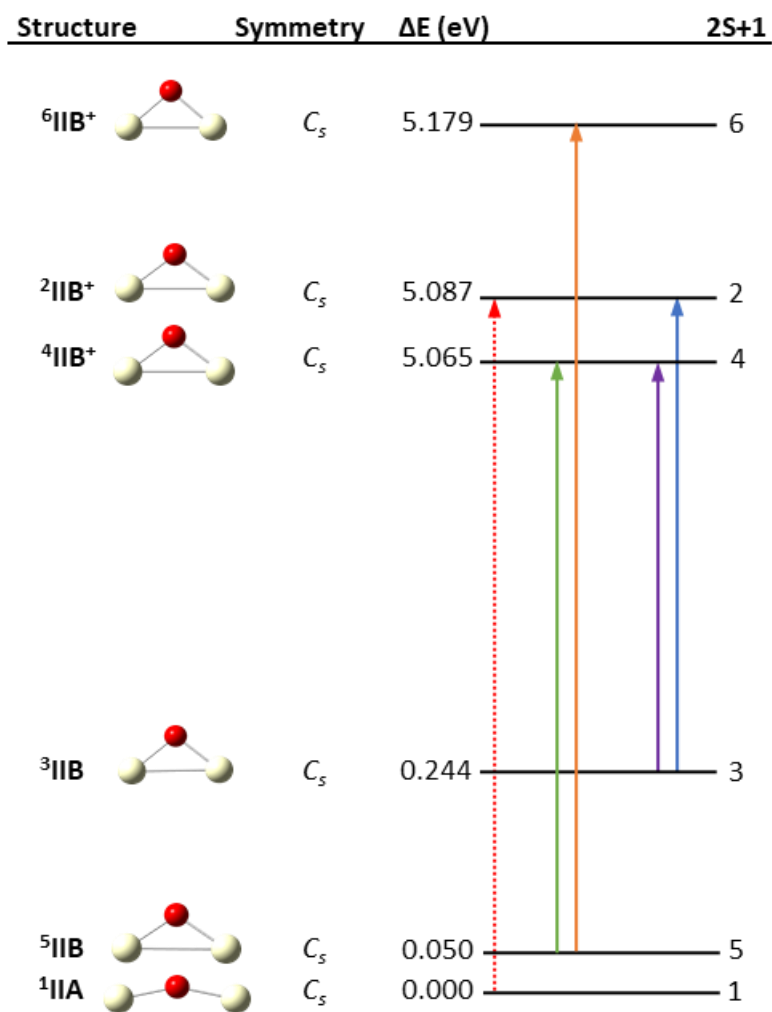


Figure 5.9: Calculated structures for Ce_2O with potential ionisation transitions. Low intensity ZEKE transitions (*vide infra*) are shown as red dotted arrows.

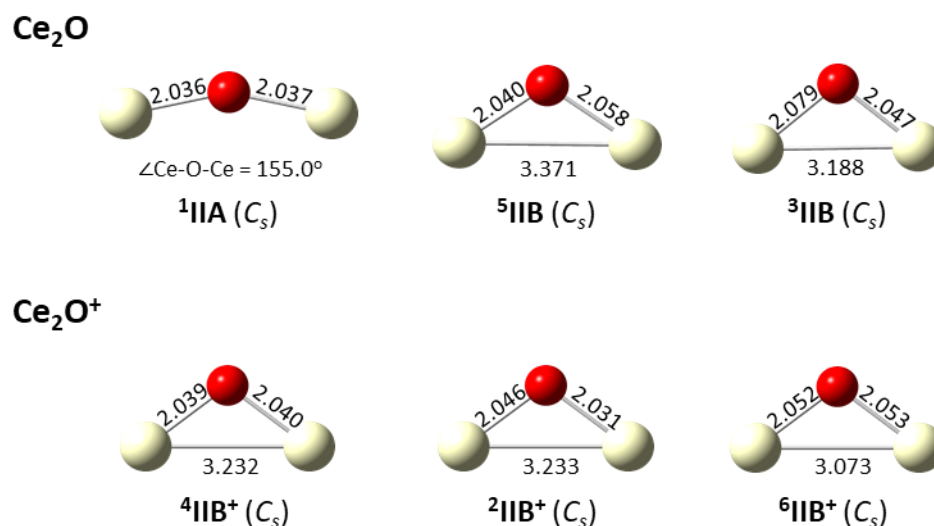


Figure 5.10: Calculated Ce_2O neutral (top) and cationic (below) structures. Bond lengths are presented in Å. Point groups are shown in brackets.

5.4.3. ZEKE Spectral Simulations for Ce_2O

Calculated ZEKE spectra for the Ce_2O ionisation transitions are presented in Figures 5.11 and 5.12; these spectra correspond to the ${}^2A' \leftarrow {}^1A'$ (${}^2IIB^+ \leftarrow {}^1IIA$), ${}^4A'' \leftarrow {}^5A''$ (${}^4IIB^+ \leftarrow {}^5IIB$) and ${}^6A'' \leftarrow {}^5A''$ (${}^6IIB^+ \leftarrow {}^5IIB$) photo-ionisation transitions underlying the primary onset and the ${}^4A'' \leftarrow {}^3A'$ (${}^4IIB^+ \leftarrow {}^3IIB$) and ${}^2A' \leftarrow {}^3A'$ (${}^2IIB^+ \leftarrow {}^3IIB$) processes underlying the secondary onset, respectively. The calculated ZEKE spectra shown here have been corrected to the experimental PIE spectrum (vide infra) using the method described in Chapter 3. Energetic corrections of +0.03 eV, +0.10 eV, -0.06 eV and -0.05 eV were applied to the ${}^6A'' \leftarrow {}^5A''$ (${}^6IIB^+ \leftarrow {}^5IIB$), ${}^4A'' \leftarrow {}^5A''$ (${}^4IIB^+ \leftarrow {}^5IIB$), ${}^4A'' \leftarrow {}^3A'$ (${}^4IIB^+ \leftarrow {}^3IIB$) and ${}^2A' \leftarrow {}^3A'$ (${}^2IIB^+ \leftarrow {}^3IIB$) ZEKE spectra, respectively, such that the calculated PIE spectrum correlated well with the experimental PIE spectrum (vide infra).

The calculated ZEKE spectrum for the ${}^2A' \leftarrow {}^1A'$ (${}^2IIB^+ \leftarrow {}^1IIA$) ionisation process – which involves ionisation from the neutral Ce_2O LES – is presented in Figure 5.11(a). Vibronic peak intensities are calculated to be ca. 10^8 times lower than for both the ${}^4A'' \leftarrow {}^5A''$ (${}^4IIB^+ \leftarrow {}^5IIB$) and ${}^6A'' \leftarrow {}^5A''$ (${}^6IIB^+ \leftarrow {}^5IIB$) spectra – presented in Figures 5.11(b) and 5.11(c), respectively – indicating an extremely weak FC overlap. The ${}^2A' \leftarrow {}^1A'$ (${}^2IIB^+ \leftarrow {}^1IIA$) process is thus considered

to have a negligible contribution toward the PIE spectrum. Consequentially, this transition is not discussed any further.

The ZEKE spectrum for the ${}^4A'' \leftarrow {}^5A''$ (${}^4IIB^+ \leftarrow {}^5IIB$) transition is presented in Figure 5.11(b). A considerable number of hot band transitions are found in the low energy end of the spectrum which begin ca. 0.036 eV before the 0_0^0 transition. These hot band transitions consist mostly of the 1_n^0 ($n=3,2,1$) progression – where ν_1 represents a bending mode – but also include the nearly degenerate $1_n^0 2_1^1$ and $1_n^0 3_1^1$ ($n=2,1$) progressions – which are separated by 8.7×10^{-4} eV (7.5 cm^{-1}) – and the 1_3^2 peak. The post-band origin region is dominated by the 1_0^n and 1_1^n progressions with the most intense peak corresponding to the 1_0^2 vibronic transition. The low degree of excitation required to achieve maximum FC overlap in this case infers minimal structural deformation following ionisation. Vibronic peaks within both the 1_0^n and 1_1^n progressions are separated by 0.0171 eV corresponding to the ν_1' vibrational frequency of 138.7 cm^{-1} .

The simulated ${}^6A'' \leftarrow {}^5A''$ (${}^6IIB^+ \leftarrow {}^5IIB$) ZEKE spectrum is presented in Figure 5.11(c). The spectral profile is considerably broader than the ${}^4A'' \leftarrow {}^5A''$ (${}^4IIB^+ \leftarrow {}^5IIB$) ZEKE spectrum, comprising several long progressions which include the 1_0^n , 1_1^n , 1_2^n and $1_0^n 2_1^1$ progressions where ν_1 and ν_2 comprise bending and asymmetric stretching modes, respectively. The peak separation of 0.0151 eV within all progressions corresponds to the ν_1' frequency of 122.2 cm^{-1} . The maximum FC transition corresponds to the 1_0^{11} vibronic peak which suggests considerable excitation of the cationic state is required to achieve vertical ionisation. Therefore, extensive structural deformation may be occurring between the 5IIB and ${}^6IIB^+$ structures.

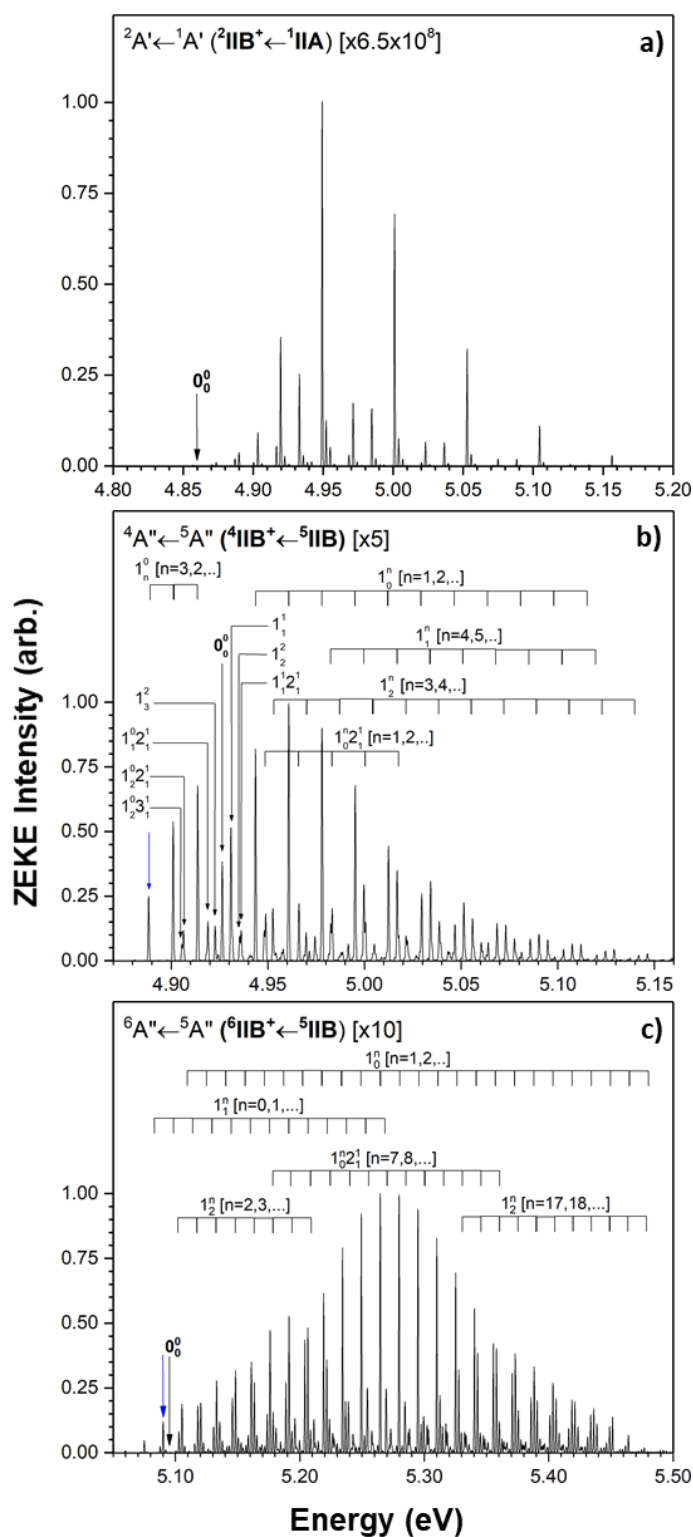


Figure 5.11: Simulated ZEKE spectra for Ce_2O primary onset ionisation transitions: **a).** ${}^2A' \leftarrow {}^1A'$ (${}^2IIB^+ \leftarrow {}^1IIA$), **b).** ${}^4A'' \leftarrow {}^5A''$ (${}^4IIB^+ \leftarrow {}^5IIB$) and **c).** ${}^6A'' \leftarrow {}^5A''$ (${}^6IIB^+ \leftarrow {}^5IIB$). Spectral intensities are normalised to the most intense peak in each spectrum with scaling factors shown. Prominent vibronic transitions are assigned. The vibronic transition likely to correspond to the appearance of ion signal in each spectrum is labelled with a blue arrow.

Simulated ZEKE spectra for the ${}^4A'' \leftarrow {}^3A'$ (${}^4IIB^+ \leftarrow {}^3IIB$) and ${}^2A' \leftarrow {}^3A'$ (${}^2IIB^+ \leftarrow {}^3IIB$) ionisation processes – corresponding to the secondary onset – are presented in Figures 5.12(a) and 5.12(b) respectively. The spectral profiles of both transitions are quite similar, spanning a small – ca. 0.15 eV – energy range which mostly consists of short vibronic progressions; this is consistent with the moderate slope of the secondary PIE onset. The 0_0^0 transition corresponds to maximum FC overlap in both cases. This suggests minimal structural change upon ionisation of the 3IIB neutral isomer to either of the ${}^2IIB^+$ or ${}^4IIB^+$ cationic states. Moreover, the similar scaling factors applied to both spectra – to normalise the peak intensities – indicates neither ionisation transition is dominant; both transitions would have similar contributions to the PIE spectrum. Both secondary onset transitions are, however, considerably more intense than the ${}^4A'' \leftarrow {}^5A''$ (${}^4IIB^+ \leftarrow {}^5IIB$) and ${}^6A'' \leftarrow {}^5A''$ (${}^6IIB^+ \leftarrow {}^5IIB$) processes corresponding to the – more dominant – primary onset. The more intense secondary onset transitions are offset by the lower population of the metastable 3IIB species, which is calculated as ca. 0.2 eV higher in energy than the 5IIB spin isomer.

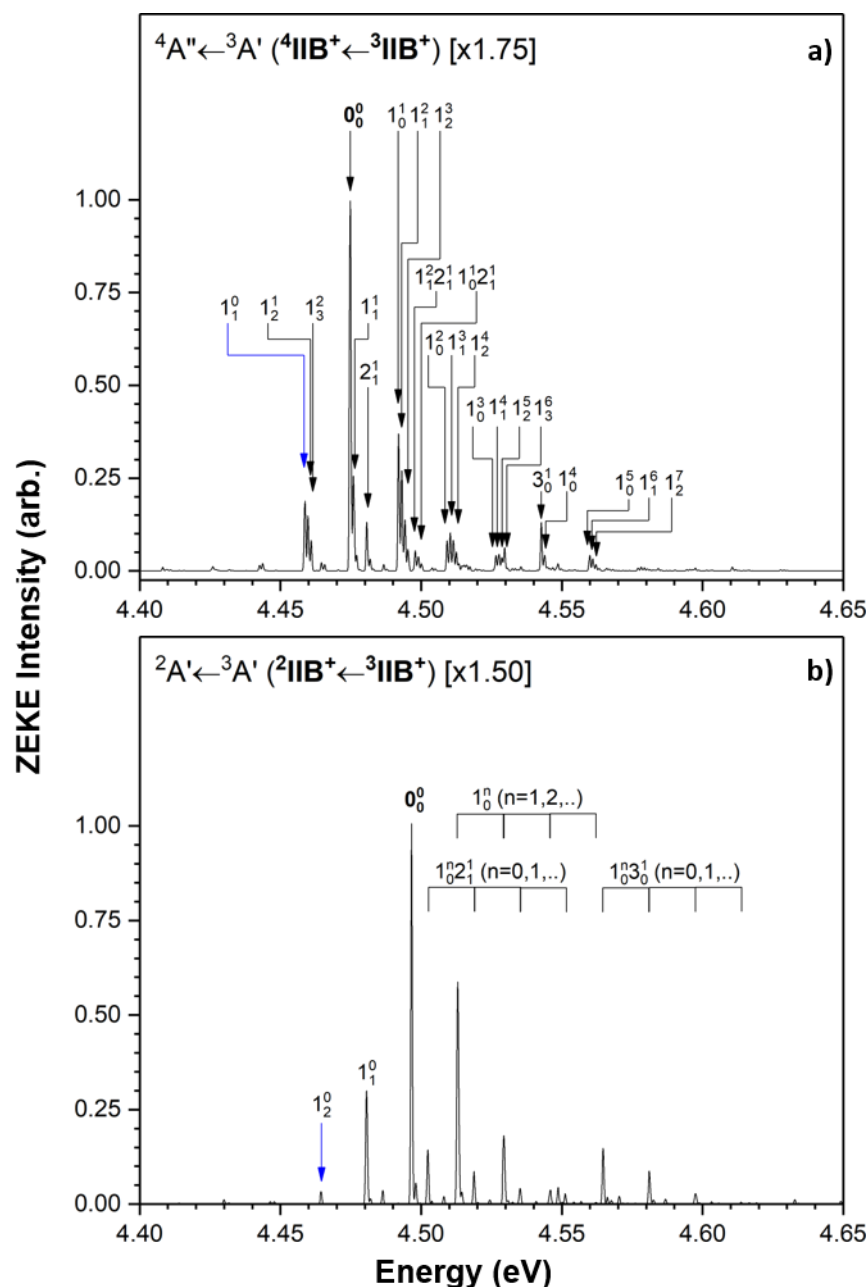


Figure 5.12: Simulated ZEKE spectra for Ce_2O secondary onset ionisation transitions: **a).** ${}^4A'' \leftarrow {}^3A'$ (${}^4IIB^+ \leftarrow {}^3IIB^+$) and **b).** ${}^2A' \leftarrow {}^3A'$ (${}^2IIB^+ \leftarrow {}^3IIB^+$). Spectral intensities are normalised to the most intense peak in each spectrum with scaling factors shown. Prominent vibronic transitions are assigned. The vibronic transition likely to correspond to the appearance of ion signal in each spectrum is labelled with a blue arrow.

5.4.4. Comparison of Experimental and Simulated PIE Spectra for Ce_2O

Simulated PIE spectra for the Ce_2O primary and secondary photo-ionisation onsets are presented in Figures 5.13 and 5.14, respectively. Both spectra are shown overlaid against the experimental PIE spectrum.

The simulated PIE spectrum for the primary onset was constructed from the integrated ${}^4A'' \leftarrow {}^5A''$ (${}^4IIB^+ \leftarrow {}^5IIB$) and ${}^6A'' \leftarrow {}^5A''$ (${}^6IIB^+ \leftarrow {}^5IIB$) ZEKE spectra. This combination of ZEKE spectra produces a calculated PIE spectrum which compares well with the experimental PIE spectrum. In this configuration, the ${}^6A'' \leftarrow {}^5A''$ (${}^6IIB^+ \leftarrow {}^5IIB$) ZEKE spectrum underlies the experimental PIE onset while the ${}^4A'' \leftarrow {}^5A''$ (${}^4IIB^+ \leftarrow {}^5IIB$) vibronic transitions extend beyond the energy range for which PIE experiments were conducted. It is possible that the ion signal plateau recorded in the experimental Ce_2O PIE spectrum represents an inflection point and does not correspond to the maximum Ce_2O ion signal. PIE experiments would need to be performed at higher photon energies to verify this. The adiabatic ionisation energy is assigned to the ${}^4A'' \leftarrow {}^5A''$ (${}^4IIB^+ \leftarrow {}^5IIB$) 0_0^0 transition – which involves ionisation to the lower energy ${}^4IIB^+$ cation – at 4.93 eV. The ${}^6A'' \leftarrow {}^5A''$ (${}^6IIB^+ \leftarrow {}^5IIB$) 1_3^0 vibronic transition is assigned to the appearance energy of the primary onset (AE_1).

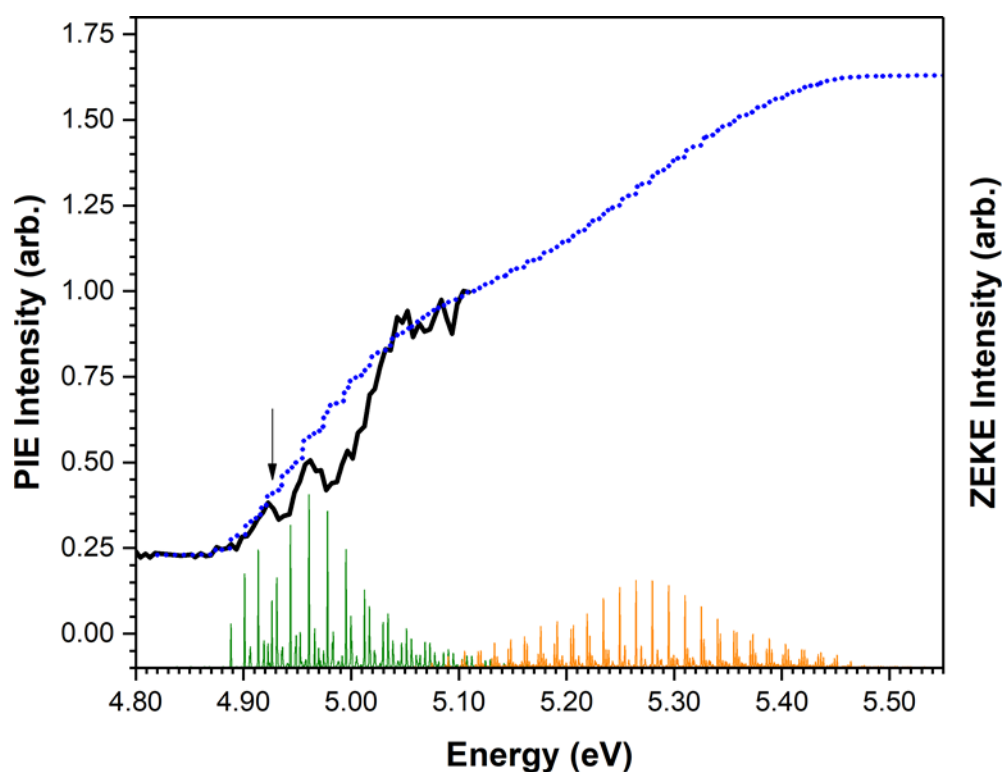


Figure 5.13: Simulated PIE spectrum for the Ce_2O primary onset (blue dotted line) overlaid against the experimental PIE spectrum (solid black line). Calculated ZEKE spectra for the ${}^4A'' \leftarrow {}^5A''$ (${}^4IIB^+ \leftarrow {}^5IIB$) and ${}^6A'' \leftarrow {}^5A''$ (${}^6IIB^+ \leftarrow {}^5IIB$) ionisation processes are shown below the PIE spectrum in green and orange, respectively. The adiabatic ionisation energy is labelled with a black arrow.

The simulated PIE spectrum corresponding to the Ce_2O secondary onset – presented in Figure 5.14 – gives an excellent fit to the experimental PIE data. The IE for the Ce_2O secondary onset can be assigned to the ${}^4A'' \leftarrow {}^3A'$ (${}^4IIB^+ \leftarrow {}^3IIB$) 0_0^0 transition at 4.48 eV. However, both onsets underlying the secondary onset involve photo-ionisation processes from metastable isomers; these ionisation processes are considered uninteresting in the context of this work. The secondary onset IE is therefore assigned for completion purposes only.

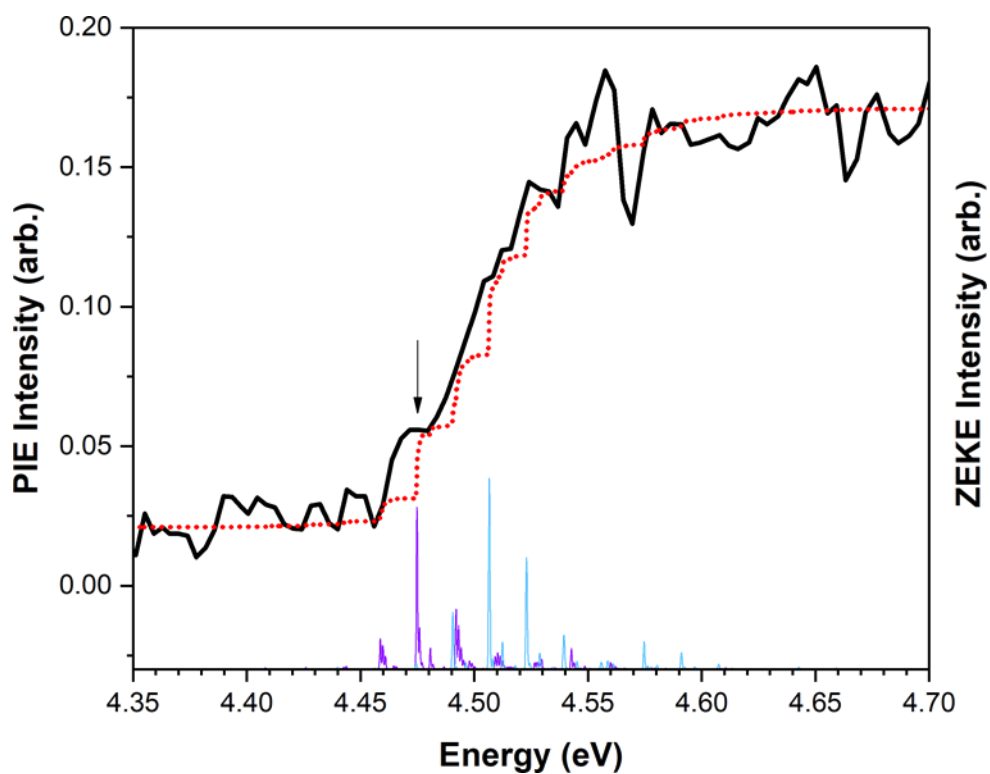


Figure 5.14: Simulated PIE spectrum for the Ce_2O secondary onset (red dotted line) overlaid against the experimental PIE spectrum (solid black line). Calculated ZEKE spectra for the $^4A'' \leftarrow ^3A'$ ($^4IIB^+ \leftarrow ^3IIB$) and $^2A' \leftarrow ^3A'$ ($^2IIB^+ \leftarrow ^3IIB$) ionisation processes are shown below the PIE spectrum in violet and blue, respectively. The adiabatic ionisation energy is labelled with a black arrow.

5.5. PIE Spectrum and DFT Results for Ce_2O_2

5.5.1. Ce_2O_2 Experimental PIE Spectrum

The experimental PIE spectrum for the Ce_2O_2 cluster species is presented in Figure 5.15. A very flat region of ion signal is recorded in the region 4.40 – 4.60 eV which is taken as the baseline. The near-zero ion signal recorded in the pre-threshold region suggests that there are no metastable species contributing to the ionisation onset. A single onset of ion signal is recorded with an appearance energy of 4.61 eV. The very sharp onset indicates a strong FC overlap between the neutral and cationic states. A shoulder at 4.65 eV suggests a second ionisation processes may be contributing to the PIE spectrum. A plateau of ion signal is recorded at 4.70 eV which indicates the highest energy FC-allowed transition has been accessed.

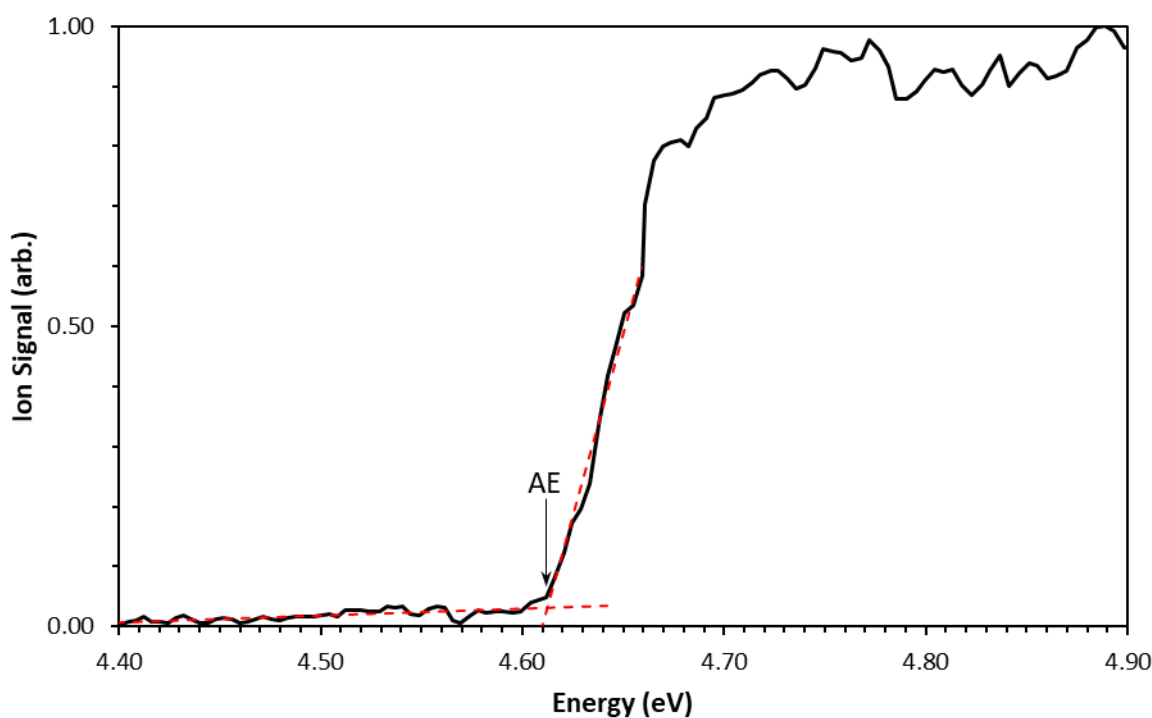


Figure 5.15: PIE spectrum for Ce_2O_2 . Linear trendlines for the baseline and onset are presented as red dashed lines. The appearance energy is labelled with a black arrow.

5.5.2. DFT Calculations for Ce_2O_2

DFT-calculated geometries of Ce_2O_2 neutral and cationic structures are presented in Figures 5.16 and 5.17. Only one unique neutral structure is shown here – labelled **III** – which comprises a D_{2h} arrangement with two oxygen atoms bridging a Ce-Ce bond. A second Ce_2O_2 structure was calculated – comprising an O_2 unit bridging the Ce-Ce bond – at an energy of ca. 5.68 eV higher than the **III** structure and is thus not shown. Two energetically indistinguishable spin isomers are calculated for the neutral **III** structure; these include a triplet in the ${}^3B_{1u}$ electronic state – labelled **³III** – and a quintet species in the ${}^5B_{2u}$ electronic state – labelled **⁵III** – with an energetic separation of 0.095 eV. Given the very similar geometric structures and vibrational frequencies calculated for the **³III** and **⁵III** species, in addition to the small energetic separation – which is well within the 0.2 eV error associated with the DFT method – it would be quite difficult to discern between these two structures experimentally. However, the **⁵III** structure is selected as the LES in preference to the **³III** species due to the lower calculated IE for this species (vide infra). The assignment of a single species to the LES is done solely for pragmatic reasons to simplify later discussions.

One unique structure is calculated for the cationic Ce_2O_2 species – with the same D_{2h} geometry as the neutral **III** structure – in two different spin states. These include the **⁴III⁺** and **²III⁺** species, which are calculated in the ${}^4B_{1u}$ and ${}^2B_{1u}$ electronic states, respectively (calculations of sextet Ce_2O_2 cations were also attempted but abandoned due to convergence difficulties). This gives 3 potential ionisation transitions which include the ${}^4B_{1u} \leftarrow {}^3B_{1u}$ (**⁴III⁺ ← ³III**), ${}^2B_{1u} \leftarrow {}^3B_{1u}$ (**²III⁺ ← ³III**) and ${}^4B_{1u} \leftarrow {}^5B_{2u}$ (**⁴III⁺ ← ⁵III**) processes; ionisation energies are calculated as 4.978 eV, 5.201 eV and 4.883 eV, respectively. The ${}^4B_{1u} \leftarrow {}^3B_{1u}$ (**⁴III⁺ ← ³III**) and ${}^4B_{1u} \leftarrow {}^5B_{2u}$ (**⁴III⁺ ← ⁵III**) processes, as the lowest energy ionisation processes with a difference in IEs of ca. 0.12 eV, are considered as potential ionisation transitions underlying the Ce_2O_2 PIE spectrum. The ${}^2B_{1u} \leftarrow {}^3B_{1u}$ (**²III⁺ ← ³III**) process – which has a calculated IE value higher than the ${}^4B_{1u} \leftarrow {}^3B_{1u}$ (**⁴III⁺ ← ³III**) and ${}^4B_{1u} \leftarrow {}^5B_{2u}$ (**⁴III⁺ ← ⁵III**) IEs by ca. 0.22 eV and 0.32 eV, respectively – is not considered to contribute to the PIE spectrum due to the comparatively higher ionisation energy. The ${}^4B_{1u} \leftarrow {}^3B_{1u}$ (**⁴III⁺ ← ³III**) and ${}^4B_{1u} \leftarrow {}^5B_{2u}$ (**⁴III⁺ ← ⁵III**) processes are shown in Figure 5.16 as green and orange arrows, respectively. The ${}^2B_{1u} \leftarrow {}^3B_{1u}$ (**²III⁺ ← ³III**) process is represented as a red dashed arrow due to the high IE for this process.

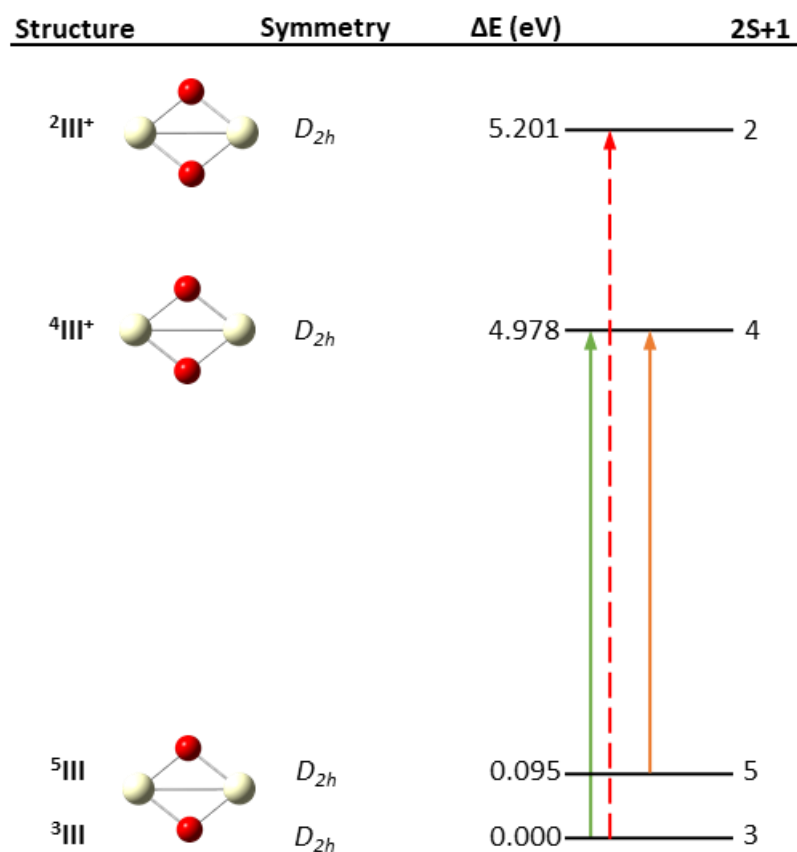


Figure 5.16: Calculated structures for Ce_2O_2 with potential ionisation transitions. Transitions with prohibitively high ionisation energies are shown as red dashed arrows.

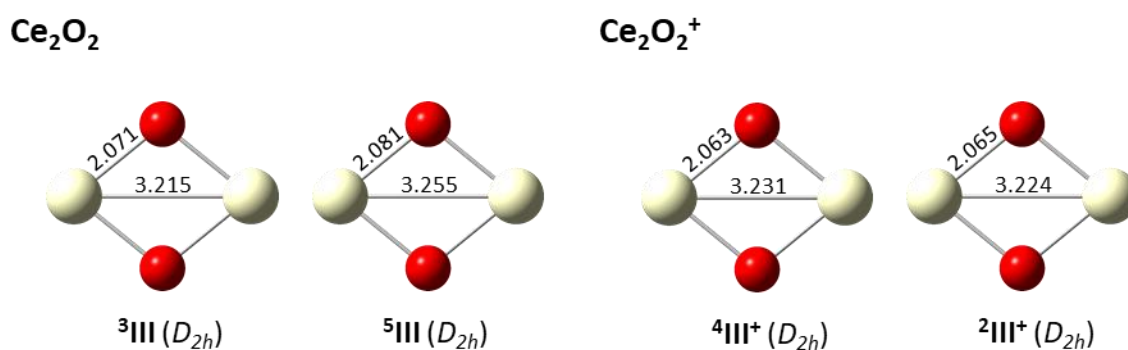


Figure 5.17: Calculated Ce_2O_2 neutral (left) and cationic (right) structures. Bond lengths are presented in Å. Point groups are shown in brackets.

5.5.3. ZEKE Spectral Simulations for Ce_2O_2

Simulated ZEKE spectra for the ${}^4B_{1u} \leftarrow {}^3B_{1u}$ (${}^4III^+ \leftarrow {}^3III$) and ${}^4B_{1u} \leftarrow {}^5B_{2u}$ (${}^4III^+ \leftarrow {}^5III$) ionisation transitions are presented in Figure 5.18. Energetic corrections of -0.005 eV and $+0.0425$ eV were applied to the ${}^4B_{1u} \leftarrow {}^3B_{1u}$ (${}^4III^+ \leftarrow {}^3III$) and ${}^4B_{1u} \leftarrow {}^5B_{2u}$ (${}^4III^+ \leftarrow {}^5III$) vibronic transitions, respectively, to improve the fit of the calculated PIE spectrum to the experimental PIE spectrum (vide infra). The corrected ZEKE spectra are shown here.

The spectral profiles of both ionisation transitions are remarkably similar owing to the near-identical neutral geometries and the common cationic structure. The 0_0^0 vibronic transitions are the most intense transitions in both spectra corresponding to the maximum FC overlap. This highlights the minimal structural change occurring within both ionisation processes and is consistent with the sharp onset observed in the experimental PIE spectrum. The ZEKE spectrum for the ${}^4B_{1u} \leftarrow {}^3B_{1u}$ (${}^4III^+ \leftarrow {}^3III$) transition presented in Figure 5.18(a) shows a hot band region which predominantly consists of the 1_n^n [$n=3,2,1$] vibronic series – where v_1 represents an out-of-plane bend – in addition to the $4_0^1 6_1^0$ peak which most likely corresponds to the AE in the PIE spectrum. The post-band origin region contains the 2_1^1 , 2_2^2 and 2_1^2 transitions – where v_2 comprises a symmetric stretch of the Ce-O bonds – in addition to some lower intensity transitions which are not assigned. The ${}^4B_{1u} \leftarrow {}^5B_{2u}$ (${}^4III^+ \leftarrow {}^5III$) ZEKE spectrum (Figure 5.18(b)) shows a similar thermal region which is again dominated by the 1_n^n [$n=3,2,1$] vibronic series whilst also containing some combination modes where the v_1 mode is coupled to the v_3 , v_4 and v_6 modes. These vibronic peaks include the $1_n^n 2_0^1$ ($n=2,1,0$) series and the 3_1^1 , 6_0^1 and $1_0^1 6_0^1$ peaks. The post-band origin region comprises mostly $v_1 v_2$ and $v_1 v_6$ combination modes.

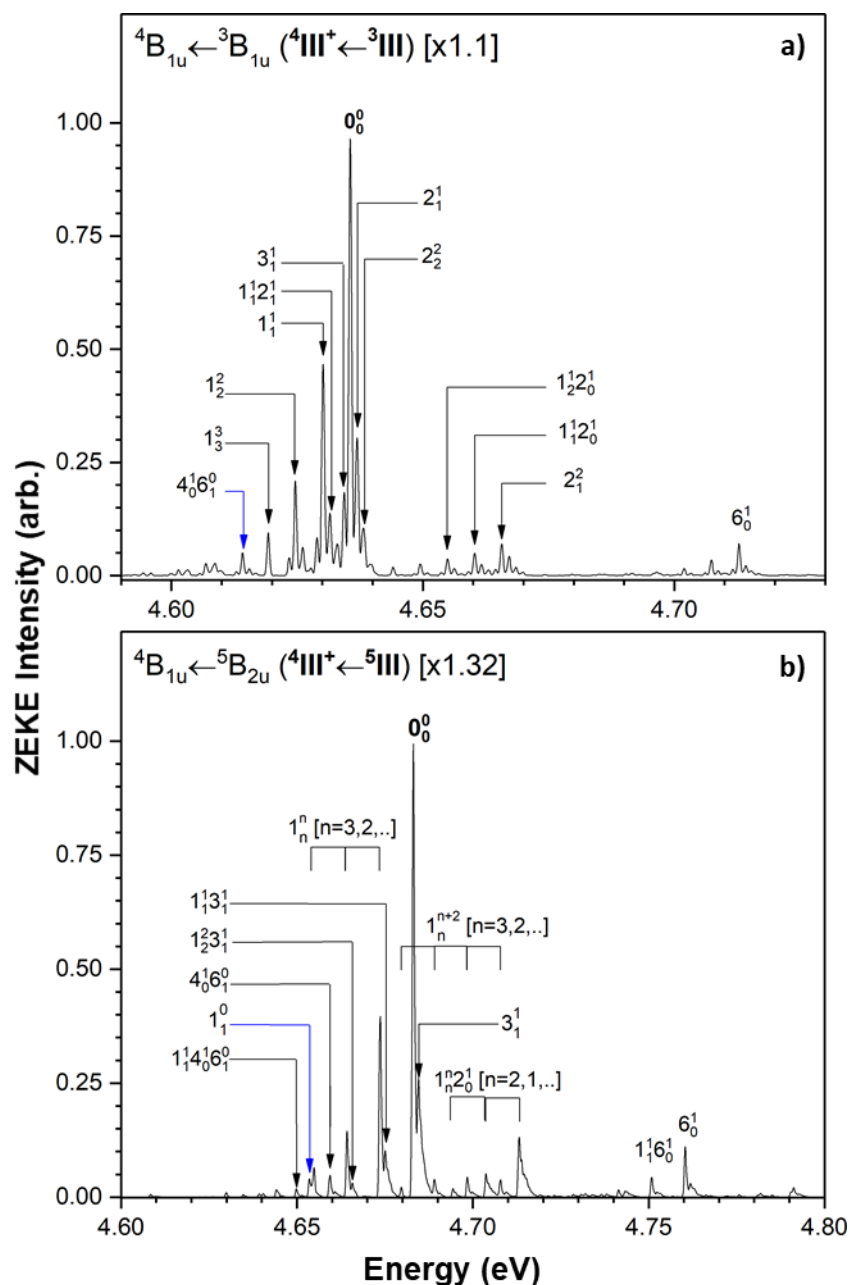


Figure 5.18: Simulated ZEKE spectra for Ce_2O_2 ionisation transitions: **a).** ${}^4B_{1u} \leftarrow {}^3B_{1u}$ (${}^4III^+ \leftarrow {}^3III$) and **b).** ${}^4B_{1u} \leftarrow {}^5B_{2u}$ (${}^4III^+ \leftarrow {}^5III$). Spectral intensities are normalised to the most intense peak in each spectrum with scaling factors shown. Prominent vibronic transitions are assigned. The vibronic transition likely to correspond to the appearance of ion signal in each spectrum is labelled with a blue arrow.

5.5.4. Comparison of Experimental and Simulated PIE Spectra for Ce_2O_2

The simulated PIE spectrum, constructed via integration of the ${}^4B_{1u} \leftarrow {}^3B_{1u}$ (${}^4III^+ \leftarrow {}^3III$) and ${}^4B_{1u} \leftarrow {}^5B_{2u}$ (${}^4III^+ \leftarrow {}^5III$) ZEKE spectra, is shown overlaid against the experimental PIE spectrum in Figure 5.19. Excellent agreement is found between the calculated and experimental PIE spectra; particularly in the thermal tail region. Moreover, the calculated shoulder at 4.62 eV from the ${}^4B_{1u} \leftarrow {}^3B_{1u}$ (${}^4III^+ \leftarrow {}^3III$) ionisation process gives a reasonable fit to the experimental shoulder at 4.65 eV. The adiabatic IE for the Ce_2O_2 species is assigned to the 0_0^0 vibronic transition of the ${}^4B_{1u} \leftarrow {}^5B_{2u}$ (${}^4III^+ \leftarrow {}^5III$) ionisation process at 4.61 eV. The experimental IE_{ad} value for the – higher energy – ${}^4B_{1u} \leftarrow {}^3B_{1u}$ (${}^4III^+ \leftarrow {}^3III$) process is assigned as 4.64 eV, which is within 0.05 eV of the ${}^4B_{1u} \leftarrow {}^5B_{2u}$ (${}^4III^+ \leftarrow {}^5III$) IE value. Given all experimental IEs in this work are assigned an error of ± 0.05 eV, the ${}^4B_{1u} \leftarrow {}^5B_{2u}$ (${}^4III^+ \leftarrow {}^5III$) and ${}^4B_{1u} \leftarrow {}^3B_{1u}$ (${}^4III^+ \leftarrow {}^3III$) ionisation processes are energetically indistinguishable.

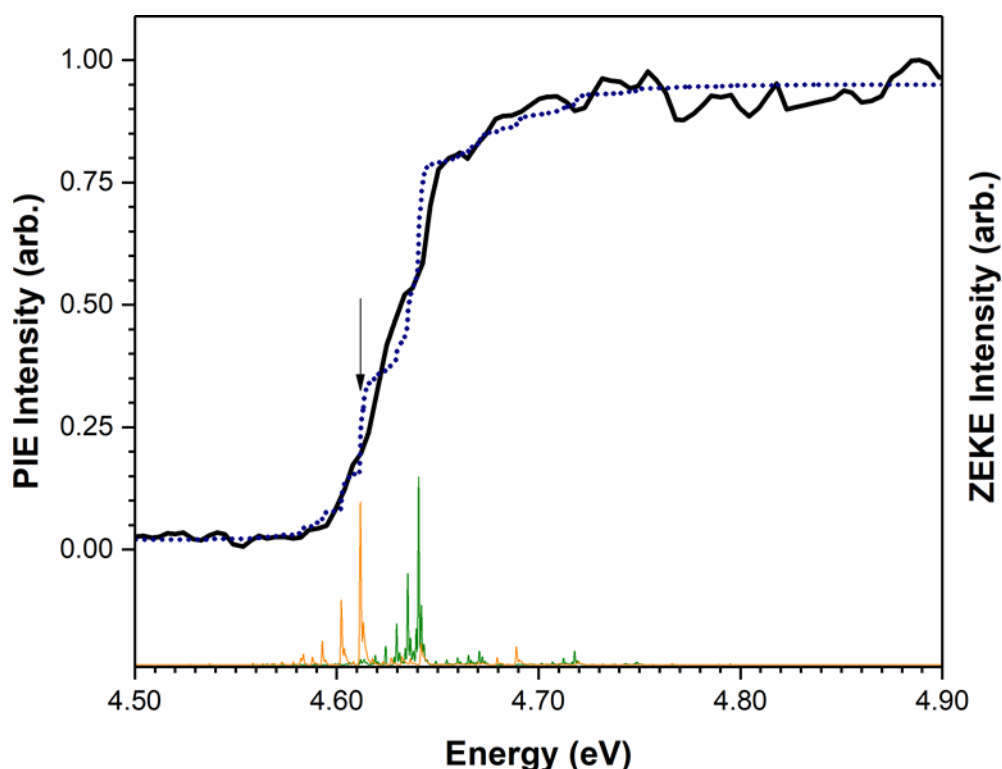


Figure 5.19: Simulated PIE spectrum for Ce_2O_2 (blue dotted line) overlaid against the experimental PIE spectrum (solid black line). Calculated ZEKE spectra for the ${}^4B_{1u} \leftarrow {}^3B_{1u}$ (${}^4III^+ \leftarrow {}^3III$) and ${}^4B_{1u} \leftarrow {}^5B_{2u}$ (${}^4III^+ \leftarrow {}^5III$) ionisation processes are shown below the PIE spectrum in green and orange, respectively. The adiabatic ionisation energy is labelled with a black arrow.

5.6. PIE Spectrum and DFT Results for Ce_2O_3

5.6.1. Ce_2O_3 Experimental PIE Spectrum

The Ce_2O_3 cluster ion was not detected within the 220 – 317.5 nm (3.92 – 5.64 eV) wavelength range available from the tuneable laser sources in this work. While The $Ce_2O_3^+$ species was detected following photo-ionisation with a 213 nm (5.82 eV) laser source – i.e. the 5th harmonic output from a Nd:YAG laser – the fixed wavelength of this laser source prevents PIE experiments from being recorded within the 213 – 220 nm (5.64 – 5.82 eV) range. Therefore, an experimental PIE spectrum has not been recorded for Ce_2O_3 . However, a bracketed IE for Ce_2O_3 is assigned as 5.64 – 5.82 eV corresponding to the appearance of the Ce_2O_3 ion peak within the 213 – 220 nm wavelength range. While the lack of an experimental PIE spectrum means structural and electronic properties of calculated Ce_2O_3 structures cannot be verified, DFT and ZEKE calculations by themselves can still provide some insight into the Ce_2O_3 cluster properties. DFT calculated Ce_2O_3 structures are presented below in addition to ZEKE and PIE spectral simulations for calculated Ce_2O_3 ionisation transitions.

5.6.2. DFT Calculations for Ce_2O_3

Calculated Ce_2O_3 neutral and cationic geometries are presented in Figures 5.20 and 5.21. Two unique Ce_2O_3 neutral isomers are calculated which are labelled **IVA** and **IVB** in order of increasing energy. The lower energy isomer – **IVA** – consists of three oxygen atoms bridging a Ce-Ce bond and is calculated in both triplet and singlet multiplicities labelled **³IVA** and **¹IVA**, respectively. The lower energy **³IVA** species – which is assigned as the LES – is calculated with C_s symmetry in the $^3A''$ electronic state. The **¹IVA** spin-isomer is calculated with C_1 – albeit near C_s – symmetry in the 1A electronic state. The geometries of both species closely approach a D_{3h} symmetry; however, symmetry-constrained calculations of the **¹IVA** and **³IVA** species in the D_{3h} point group were problematic due to convergence issues. The **³IVA** and **¹IVA** species are quite low-lying with an energetic separation of 0.120 eV. Due to similarities in the calculated energies and vibrational modes of the **³IVA** and **¹IVA** species, it would be difficult to discern between the two structures under the experimental conditions in this work.

The Ce_2O_3 **IVB** structure is calculated as a Ce_2O_2 type motif with a third oxygen atom singly attached to one of the cerium atoms. The structure is C_s symmetric with a σ plane running along the Ce-Ce bond. Two spin isomers are calculated for the **IVB** structure; these comprise singlet and triplet species in the $^1A'$ and $^3A'$ electronic states which are labelled **1IVB** and **3IVB** , respectively. Calculated energies for **1IVB** and **3IVB** species relative to the **3IVA** structure are 0.883 eV and 0.998 eV, respectively; the high energies of both these species relative to the LES would likely preclude their formation under experimental conditions.

Optimised structures for the Ce_2O_3 cation shows 3 unique species. The **$^2IVA^+$** cation is calculated as a common target state for both the **3IVA** and **1IVA** isomers. This cation maintains a similar geometry to both the **3IVA** and **1IVA** neutral isomers – albeit with a slight distortion in the Ce-O bond lengths – with C_1 symmetry in the 2A electronic state. Other calculated cations include the **$^2IVB^+$** and **$^4IVA^+$** species. The **$^2IVB^+$** cation is a target state of both the **1IVB** and **3IVB** neutral species which are energetically unfavourable isomers and thus unlikely to be formed in the cluster source. The **$^4IVA^+$** species is calculated as a high energy target state for the **3IVA** LES with an ionisation energy of 7.637 eV. This ionisation process – which corresponds to a photon wavelength of 162.4 nm – is not accessible using the photon energies available in the current experimental setup. The **$^2IVB^+$** and **$^4IVA^+$** structures are therefore not considered to be of particular interest in the context of this work. The geometries of the **$^2IVA^+$** and **$^2IVB^+$** structures compare well with the calculated $Ce_2O_3^+$ structures reported by Akin et al²⁰, who calculate very similar geometries for both species in the doublet state. Moreover, their calculated energetic separation of 0.33 eV between the two doublet states (reported as 7.7 kcal.mol⁻¹) compares well with the 0.240 eV energetic difference between the **$^2IVA^+$** and **$^2IVB^+$** structures calculated here.

Potential ionisation processes for the Ce_2O_3 system include the $^2A \leftarrow ^3A''$ (**$^2IVA^+ \leftarrow ^3IVA$**) and $^2A \leftarrow ^1A$ (**$^2IVA^+ \leftarrow ^1IVA$**) transitions with calculated IEs of 6.295 eV and 6.175 eV, respectively. Both processes contain energetically accessible neutral isomers with similar calculated IEs, therefore are both considered to contribute to the PIE spectrum. The $^2A \leftarrow ^3A''$ (**$^2IVA^+ \leftarrow ^3IVA$**)

and ${}^2A \leftarrow {}^1A$ (${}^2IV A^+ \leftarrow {}^1IV A$) transitions are shown as green and orange arrows, respectively, in Figure 5.20.

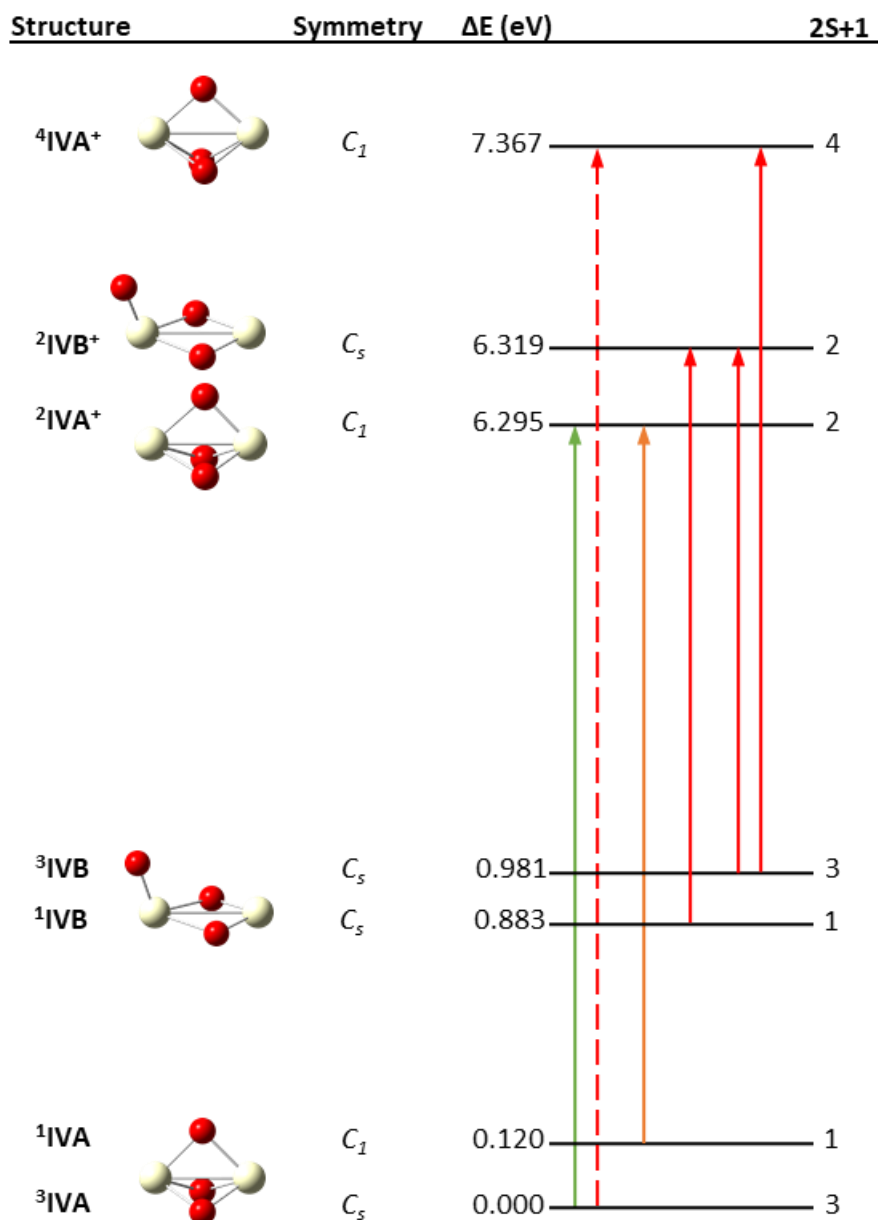


Figure 5.20: Calculated structures for Ce_2O_3 . Potential ionisation transitions are shown. Ionisation transitions from neutral structures with prohibitively high electronic energies are shown as solid red arrows. Transitions with prohibitively high ionisation energies are shown as red dashed arrows.

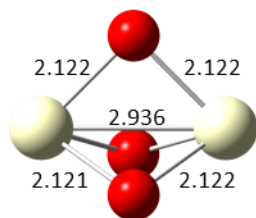
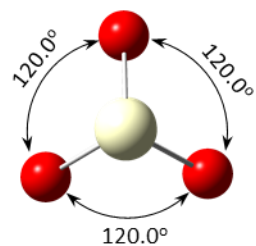
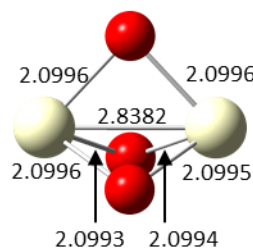
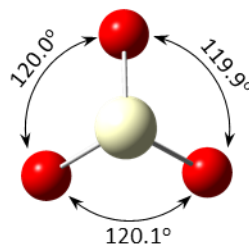
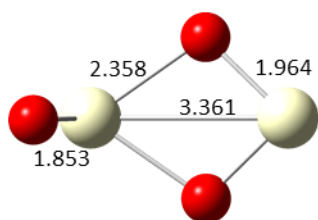
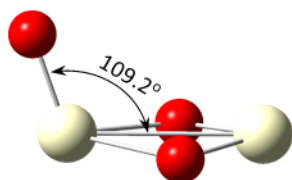
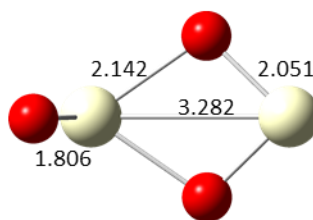
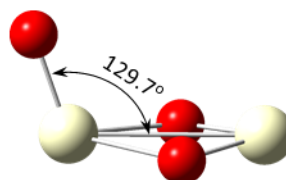
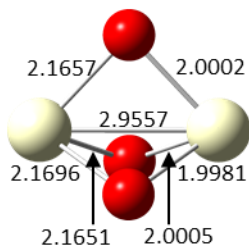
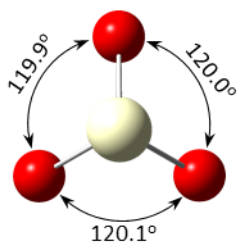
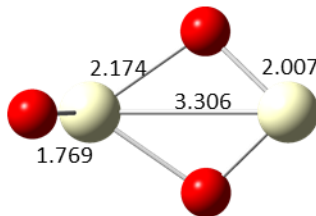
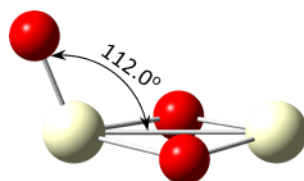
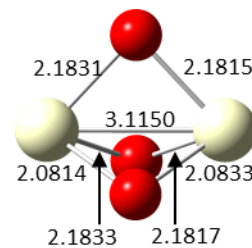
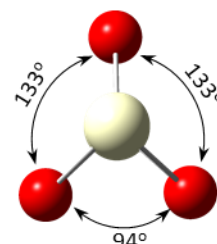
Ce_2O_3

 ${}^3IVA (C_s)$

 ${}^1IVA (C_1)$

 ${}^1IVB (C_s)$

 ${}^3IVB (C_s)$
 $Ce_2O_3^+$

 ${}^2IVA^+ (C_s)$

 ${}^2IVB^+ (C_s)$

 ${}^4IVA^+ (C_1)$

Figure 5.21: Calculated Ce_2O_3 neutral (above) and cationic (below) structures. Top and side views are presented for all structures. Bond lengths are presented in Å. Point groups are shown in brackets.

5.6.3. ZEKE Spectral Simulations for Ce_2O_3

Simulated ZEKE spectra for the Ce_2O_3 ${}^2A \leftarrow {}^3A''$ (${}^2IVA^+ \leftarrow {}^3IVA$) and ${}^2A \leftarrow {}^1A$ (${}^2IVA^+ \leftarrow {}^1IVA$) ionisation transitions are presented in Figure 5.22. Energetic corrections to the calculated ZEKE spectra were performed as follows (vide infra): vibronic transitions for the ${}^2A \leftarrow {}^1A$ (${}^2IVA^+ \leftarrow {}^1IVA$) ionisation process – which corresponds to ionisation of a higher energy spin-isomer of the LES – were corrected by -0.120 eV, corresponding to the difference between the calculated IE values for the ${}^2A \leftarrow {}^3A''$ (${}^2IVA^+ \leftarrow {}^3IVA$) and ${}^2A \leftarrow {}^1A$ (${}^2IVA^+ \leftarrow {}^1IVA$) transitions. The two spectra were overlaid and then energetically corrected such that the vibronic peak for the lowest energy vibronic transition was at 5.64 eV. This ensured that the calculated AE corresponded to the lower AE value of the bracketed Ce_2O_3 AE drawn from photo-ionisation mass spectra.

The calculated ${}^2A \leftarrow {}^3A''$ (${}^2IVA^+ \leftarrow {}^3IVA$) ZEKE spectrum presented in Figure 5.22(a) contains a very broad spectral profile with a weak 0_0^0 transition. Both of these characteristics infer a weak FC overlap between the 3IVA neutral and ${}^2IVA^+$ cationic states. The prominent vibronic peaks in the ZEKE spectrum include the $6_0^1 9_1^n$, $6_0^2 9_0^n$ and $6_0^3 9_1^n$ progressions; this suggests the cationic ${}^2IVA^+$ structure is distorted along both the ν_6 and ν_9 vibrational coordinates – which describe symmetric stretching of the Ce_1-O and Ce_2-O bonds, respectively – relative to the 3IVA neutral species.

The simulated ${}^2A \leftarrow {}^1A$ (${}^2IVA^+ \leftarrow {}^1IVA$) ZEKE spectrum is presented in Figure 5.22(b). Due to memory constraints, the ν_1 , ν_2 , ν_4 and ν_7 modes were omitted from simulations. Test calculations showed omitting these modes had minimal effect on the ZEKE spectral profile. A broad spectral profile is observed – similar to the ${}^2A \leftarrow {}^3A''$ (${}^2IVA^+ \leftarrow {}^3IVA$) ZEKE spectrum – with a very weak 0_0^0 transition, inferring a poor FC overlap between the 1IVA and ${}^2IVA^+$ structures. Moreover, comparison of the normalisation scaling factors for the ${}^2A \leftarrow {}^3A''$ (${}^2IVA^+ \leftarrow {}^3IVA$) and ${}^2A \leftarrow {}^1A$ (${}^2IVA^+ \leftarrow {}^1IVA$) processes – which are 24 and 41, respectively – shows the vibronic peak intensities in the ${}^2A \leftarrow {}^1A$ (${}^2IVA^+ \leftarrow {}^1IVA$) process are considerably weaker than for the ${}^2A \leftarrow {}^3A''$ (${}^2IVA^+ \leftarrow {}^3IVA$) transition discussed previously. The ${}^2A \leftarrow {}^3A''$ (${}^2IVA^+ \leftarrow {}^3IVA$) process is therefore expected to be the dominant process in the PIE spectrum.

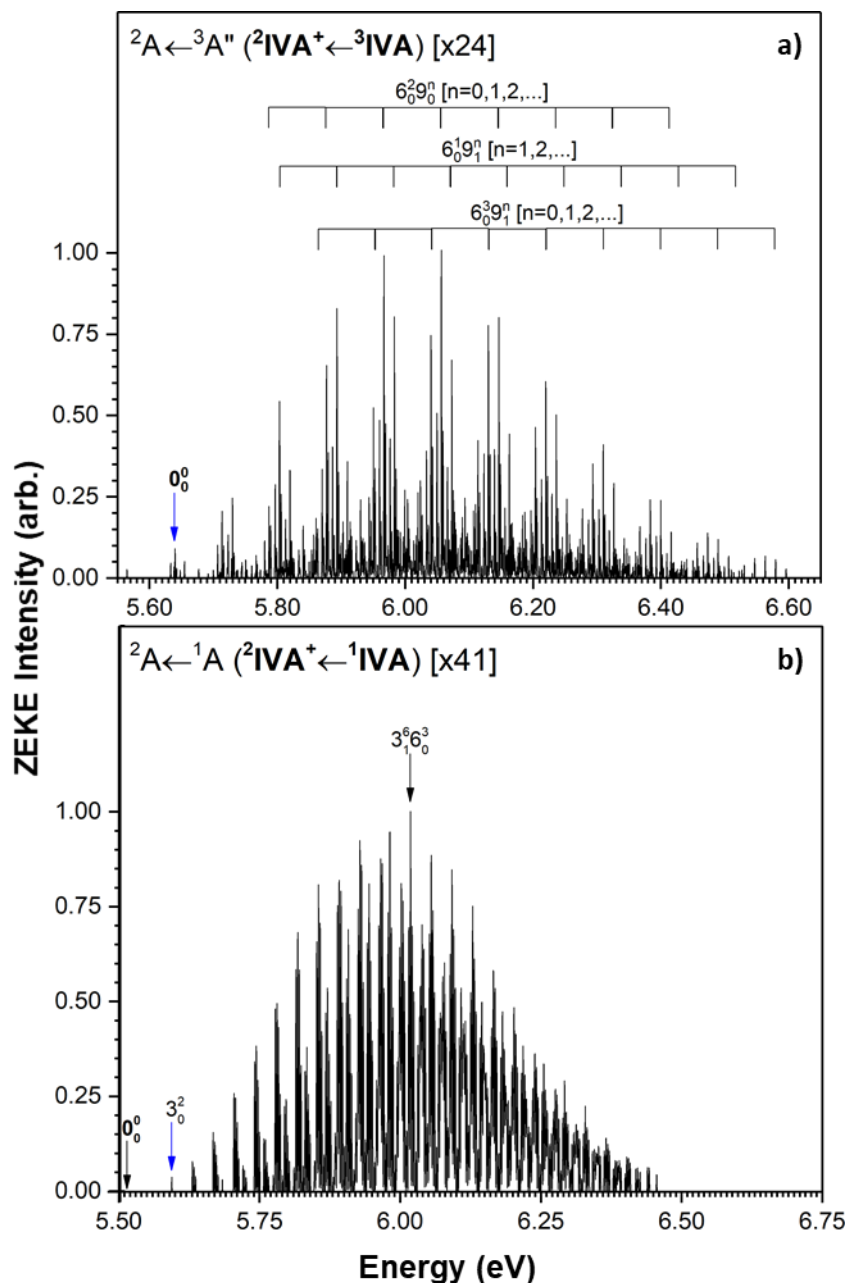


Figure 5.22: Simulated ZEKE spectra for Ce_2O_3 ionisation transitions: **a).** ${}^2A \leftarrow {}^3A''$ (${}^2IVA^+ \leftarrow {}^3IVA$) and **b).** ${}^2A \leftarrow {}^1A$ (${}^2IVA^+ \leftarrow {}^1IVA$). Spectral intensities are normalised to the most intense peak in each spectrum with scaling factors shown. Due to the significant number of peaks in both ZEKE spectra, only a small number of vibronic transitions are assigned. The vibronic transition likely to correspond to the appearance of ion signal in each spectrum is labelled with a blue arrow.

5.6.4. Simulated PIE Spectrum for Ce_2O_3

The simulated Ce_2O_3 PIE spectrum – which was constructed from a combination of the integrated ZEKE spectra for both the ${}^2A \leftarrow {}^3A''$ (${}^2IVA^+ \leftarrow {}^3IVA$) and ${}^2A \leftarrow {}^1A$ (${}^2IVA^+ \leftarrow {}^1IVA$) ionisation processes – is presented in Figure 5.23. The PIE spectrum shows a very broad onset which extends from 5.64 eV to ca. 6.35 eV. The ${}^2A \leftarrow {}^3A''$ (${}^2IVA^+ \leftarrow {}^3IVA$) 0_0^0 transition at 5.64 eV, as the lowest energy vibronic transition in the ${}^2A \leftarrow {}^3A''$ (${}^2IVA^+ \leftarrow {}^3IVA$) ZEKE spectrum, is assigned as both the adiabatic IE and the AE. The very low PIE intensity in the 5.50 – 5.75 eV region is consistent with the non-appearance of the Ce_2O_3 ion peak in the mass spectrum following photo-ionisation at 220 nm (5.64 eV). A small, albeit noticeable PIE intensity is calculated at 5.82 eV which correlates well with the weak Ce_2O_3 ion peak recorded following 213 nm (5.82 eV) photo-ionisation. The simulated spectrum reaches a plateau ca. 6.40 eV – corresponding to a photon wavelength of 193.75 nm which would be required to record the entire Ce_2O_3 PIE spectrum.

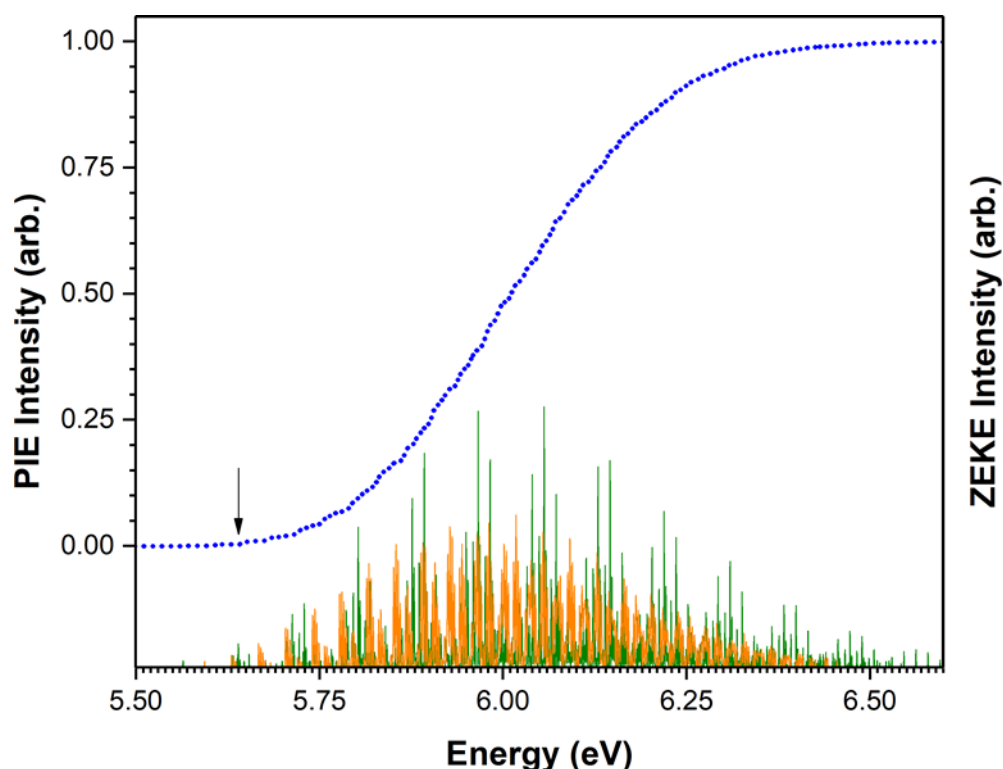


Figure 5.23: Simulated PIE spectrum for Ce_2O_3 (blue dotted line). Calculated ZEKE spectra for the ${}^2A \leftarrow {}^3A''$ (${}^2IVA^+ \leftarrow {}^3IVA$) and ${}^2A \leftarrow {}^1A$ (${}^2IVA^+ \leftarrow {}^1IVA$) ionisation processes are shown below the PIE spectrum in green and orange, respectively. The adiabatic ionisation energy is labelled with a black arrow.

5.7. PIE Spectrum and DFT Results for Ce_2O_4

5.7.1. Ce_2O_4 Experimental PIE Spectrum

The Ce_2O_4 cluster species is only detected in trace quantities following photo-ionisation at 213 nm (5.82 eV), as previously shown in Figure 5.1. The Ce_2O_4 ion is not detected in any mass spectra recorded with photon energies of 5.64 eV (220 nm) or lower. Significant effort was directed toward improving the $Ce_2O_4^+$ signal during experiments; this included changing the turbulent flow conditions in the cluster source via the pulsed valve and seeding oxygen into the carrier gas at varying concentrations (0.1% – 5%) to increase the amount of available oxygen. No increase in the Ce_2O_4 ion signal was observed, despite these attempts, whereas marked changes in the intensities of all other Ce_2O_n ion peaks were recorded. It is therefore unlikely that the low Ce_2O_4 abundance is due to the conditions in the cluster source. The weak Ce_2O_4 ion signal is instead assigned to a high ionisation energy (vide infra) which does not permit ionisation using the photon energies available with the current experimental setup.

5.7.2. DFT Calculated Structures for Ce_2O_4

Calculated neutral and cationic structures for the Ce_2O_4 cluster are presented in Figures 5.24 and 5.25. Two distinct neutral structures are calculated which are labelled **VA** and **VB** in order of increasing energy. The **VA** structure comprises a planar Ce_2O_2 motif with an additional oxygen atom attached to each of the cerium atoms in a C_{2h} symmetric arrangement. The **VA** structure is consistent with previous work by Chang et. al.²¹ who, using the PW91 exchange-correlation functional, also predicted a C_{2h} arrangement for the Ce_2O_4 cluster. Moreover, the authors calculated Ce-O bond lengths for the bridging and singly attached oxygen atoms as 2.138 Å and 1.853 Å, respectively; both of these bond length values are within 3% of the respective Ce-O bond lengths presented in this work. The **VA** structure is only presented here in the singlet 1A_g electronic state (labelled 1VA). **VA** type structures calculated in higher spin states were considerably higher in energy and are not shown.

The calculated Ce_2O_4 **VB** structure comprises three oxygen atoms bridging a Ce-Ce bond with the fourth oxygen atom bound to one cerium atom at a Ce-Ce-O bond angle of 180° . The **VB** structure is C_s symmetric and only shown here in the singlet $^1A'$ state (labelled 1VB); higher

spin states were calculated to be considerably higher in energy and thus discarded. The 1VB species is calculated with an energy of +0.376 eV relative to the LES; the significantly higher energy of the 1VB isomer suggests formation of this species is energetically unfavourable.

Cationic structures for each of the 1VA and 1VB isomers are calculated as shown in Figures 5.24 and 5.25. The cationic target for the 1VA LES, designated $^2VA^+$, is calculated as a C_1 doublet species in the 2A electronic state. The geometric structure is quite different to that of the neutral isomer; most notable is the rotation of one of the dangling oxygen atoms so that it lies within the Ce_2O_2 plane. Significant distortion of the Ce_2O_2 motif is also observed such that the cationic structure displays four unique Ce-O lengths for the bridging oxygen atoms, as opposed to the highly symmetric C_{2h} neutral 1VA structure.

The cationic target for the 1VB isomer, designated $^2VB^+$, is calculated as a C_s doublet in the 2A electronic state. Comparison to the 1VB structure shows considerable geometric differences between the two species. The bridging oxygen atoms in the $^2VB^+$ cation are all shifted parallel to the Ce-Ce bond; the oxygen atom above the Ce-Ce bond is shifted toward the left cerium atom while the two oxygen atoms below the Ce-Ce bond are shifted toward the right cerium atom. The Ce-Ce-O bond angle for the dangling oxygen atom is distorted considerably from the linear arrangement in the 1VB species to a Ce-Ce-O angle of 133.5° in the $^2VB^+$ structure.

Calculated Ce_2O_4 ionisation transitions include the Ce_2O_4 $^2A \leftarrow ^1A_g$ ($^2VA^+ \leftarrow ^1VA$) and $^2A \leftarrow ^1A'$ ($^1VB^+ \leftarrow ^2VB$) processes with calculated IEs of 9.051 eV and 8.603 eV, respectively. The high IE values calculated for both processes is consistent with the non-detection of the Ce_2O_4 cation in any mass spectra recorded during photo-ionisation experiments. The $^2A \leftarrow ^1A_g$ ($^2VA^+ \leftarrow ^1VA$) ionisation process is shown as a green arrow in Figure 5.24. The $^2A \leftarrow ^1A'$ ($^1VB^+ \leftarrow ^2VB$) process is shown as a red dotted arrow due to low ZEKE intensities calculated for this transition (vide infra).

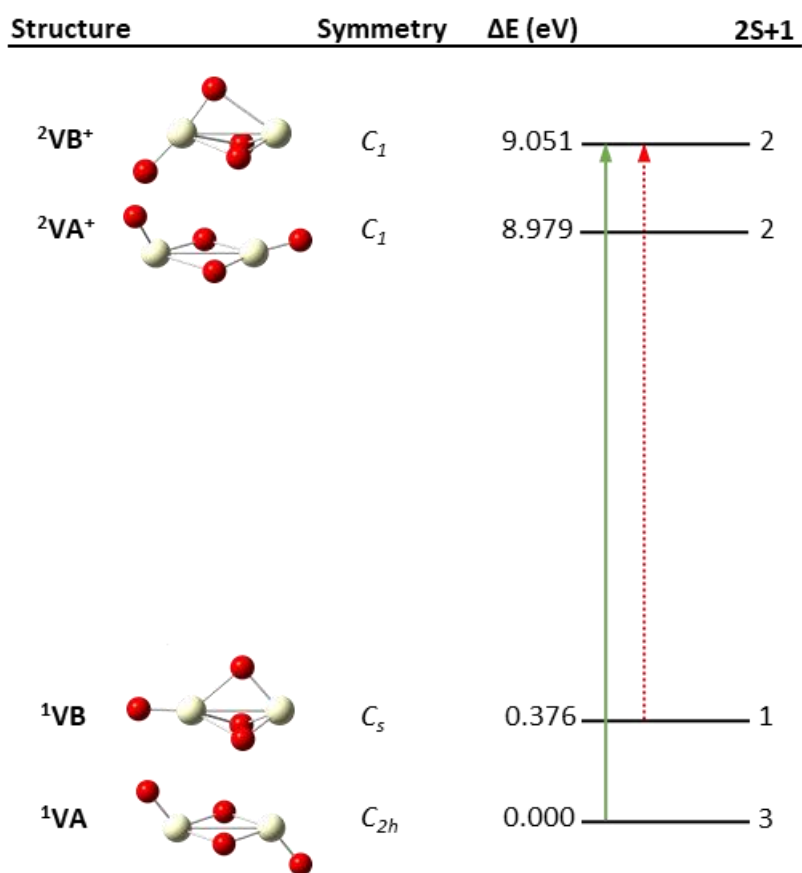


Figure 5.24: Calculated structures for Ce_2O_4 . Potential ionisation transitions are shown. Ionisation transitions with low ZEKE intensities (*vide infra*) are shown as red dotted arrows.

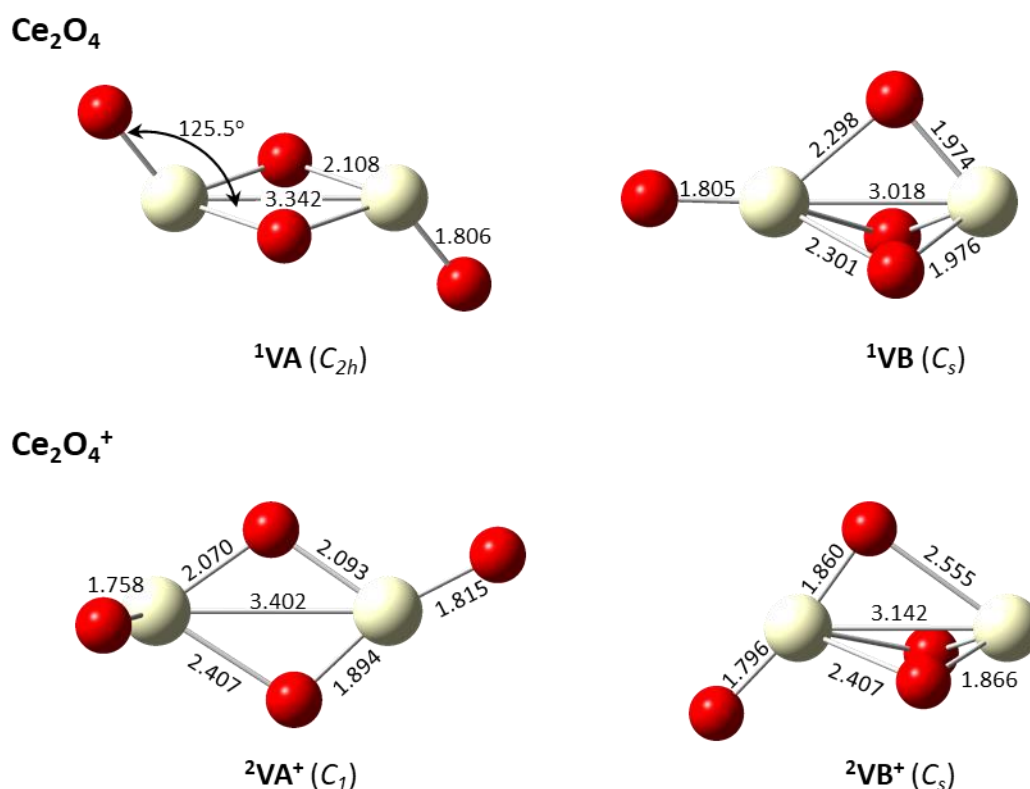


Figure 5.25: Calculated Ce_2O_4 neutral (above) and cationic (below) structures. Bond lengths are presented in Å. Point groups are shown in brackets.

5.7.3. ZEKE Spectral Simulations for Ce_2O_4

The simulated ZEKE spectrum for the ${}^2A \leftarrow {}^1A_g$ (${}^2VA^+ \leftarrow {}^1VA$) ionisation transition, which describes the ionisation process from the LES – is presented in Figure 5.26. The vibronic peaks in the spectrum display a very low intensity, with a scaling factor of 2.7×10^{23} required to normalise the most intense peak. This highlights an extremely small FC overlap between the neutral and cationic Ce_2O_4 species and may be causative towards the non-detection of the Ce_2O_4 ion in PIE experiments.

The ${}^2A \leftarrow {}^1A_g$ (${}^2VA^+ \leftarrow {}^1VA$) ZEKE spectral profile is quite broad with three separate groups of vibronic peaks separated by ca. 0.8 eV corresponding to the VA^+ v_{11} mode. The first cluster of peaks, located in the range 8.99 – 9.06 eV, mostly comprises vibronic transitions from combination modes including the $v_1 - v_4$ modes for the neutral species and the $v_1 - v_6$ modes in the cationic species. The second cluster, in the range 9.06 – 9.14 eV, again consists of

coupled $v_1 - v_4$ modes from the neutral state; however, the cationic vibrational states include the v_8 , v_{10} and v_{11} modes in addition to the $v_1 - v_4$ modes discussed previously. Minimal contribution is recorded from the v_5 and v_6 modes in this region. Finally, vibronic peaks for the third cluster in the range 9.14 – 9.20 eV involve transitions from coupled combinations of the $v_1 - v_4$ modes from the neutral and $v_1 - v_6$, v_8 , v_{10} and v_{11} modes in the cation. The 0_0^0 transition is not calculated which infers a poor FC overlap between the 1VA and $^2VA^+$ structures.

Attempts to calculate a ZEKE spectrum for the $^2A \leftarrow ^1A'$ ($VB^+ \leftarrow VB$) ionisation process were unsuccessful; no vibronic peaks were calculated above the low-intensity threshold of 1×10^{-323} set by the ezSpectrum program. The ZEKE spectrum for this ionisation transition is therefore not shown. Any contribution from the $^2A \leftarrow ^1A'$ ($VB^+ \leftarrow VB$) process to the PIE spectrum would be negligible.

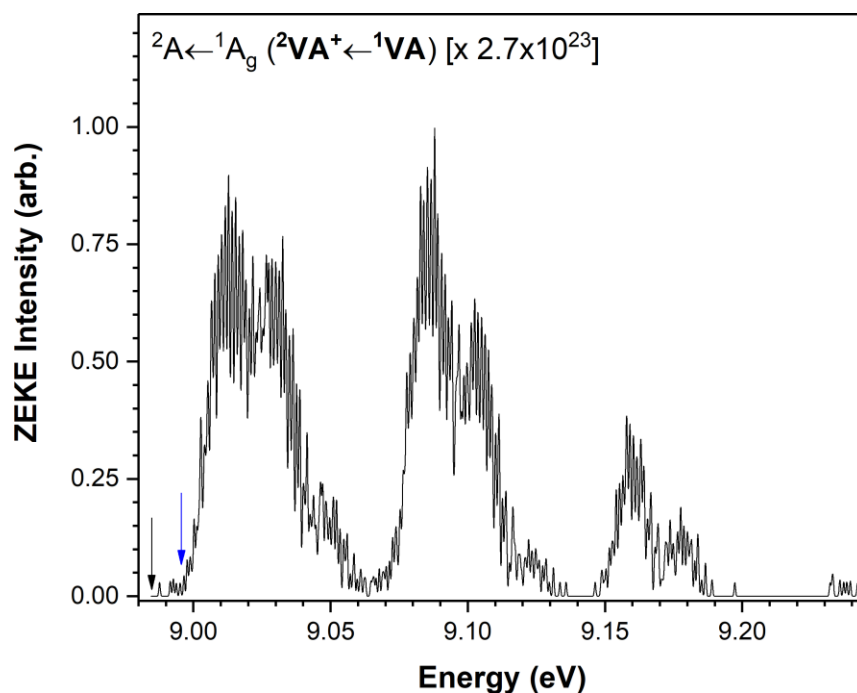


Figure 5.26: Simulated ZEKE spectrum for the Ce_2O_4 ${}^2A \leftarrow {}^1A_g$ (${}^2VA^+ \leftarrow {}^1VA$) ionisation transition. The spectral intensity is normalised to the most intense peak with scaling factor shown. The DFT-calculated IE is shown with a black arrow; the 0_0^0 transition is not recorded in calculations and thus not shown. The vibronic transition likely to correspond to the appearance of ion signal is labelled with a blue arrow.

5.7.4. Simulated PIE Spectrum for Ce_2O_4

The simulated Ce_2O_4 PIE spectrum, which was constructed via integration of the calculated ${}^2A \leftarrow {}^1A_g$ (${}^2VA^+ \leftarrow {}^1VA$) ZEKE spectrum, is presented in Figure 5.27. The spectral profile is quite broad with the appearance of three onsets corresponding to the three groups of vibronic peaks observed in the simulated ZEKE spectrum. The IE for the Ce_2O_4 species is assigned to the DFT-calculated IE of 9.051 eV. While the ionisation process cannot strictly be labelled as adiabatic – since the 0_0^0 transition was not calculated – the IE value presented here is the same as for an adiabatic ionisation process[†].

[†] This is due to the method by which the ZEKE spectra are calculated; the 0_0^0 transition energy is initially defined by the user which allows it to be used as a datum point regardless of whether the peak intensity is above the intensity threshold. All IEs in this work are therefore labelled as adiabatic IEs, regardless of whether a 0_0^0 transition is calculated, since the energies are the same. A discussion of the computational method is presented in Chapter 3.

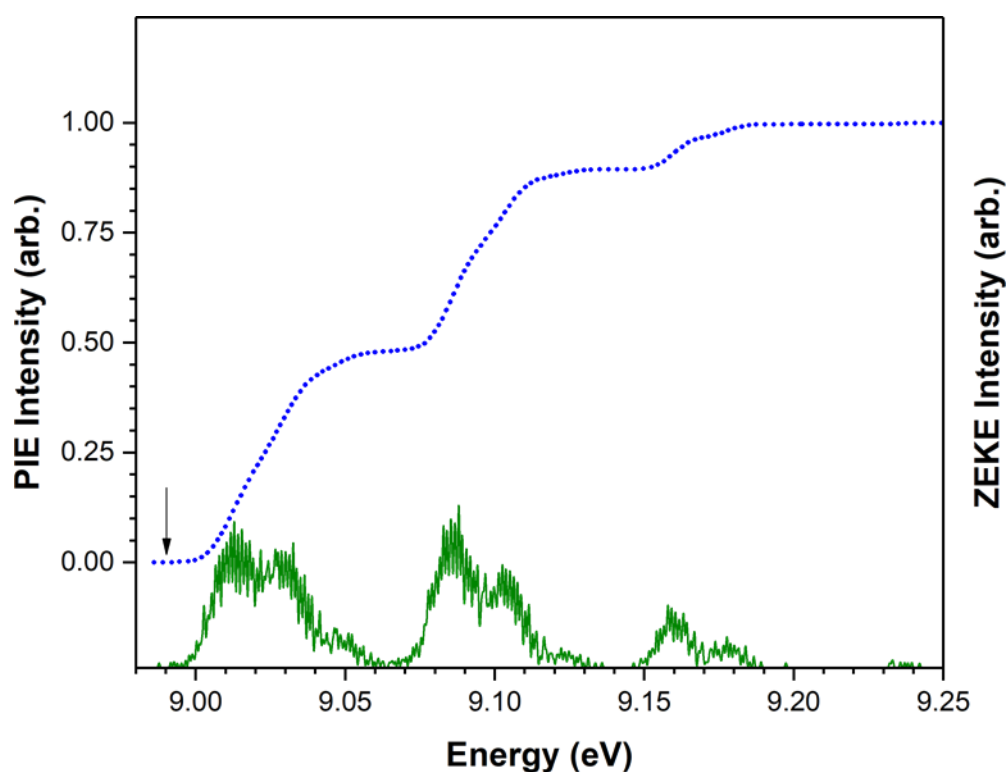


Figure 5.27: Simulated PIE spectrum for Ce_2O_4 (blue dotted line). The calculated ZEKE spectrum for the $^2A \leftarrow ^1A_g$ ($^2VA^+ \leftarrow ^1VA$) ionisation process is shown below the PIE spectrum in green. The adiabatic ionisation energy is labelled with a black arrow.

5.8. Comparison of Experimental and Calculated Ce_2O_n Ionisation Energies

Adiabatic ionisation energies for the Ce_2O_n clusters – determined both from DFT calculations and from experimental PIE spectra with the aid of ZEKE simulations – are presented in Figure 5.28. The experimental and calculated IE_{ad} values are plotted relative to the number of oxygen atoms bound to the metal cluster base. This allows for a comparison between the experimental and calculated IE trends with oxidation; the B3P86 method has been shown by the Metha group to systematically predict metal oxide IEs higher than experiment, however models IE trends with oxidation quite accurately^{22–24}. More pertinently though, an investigation into the effects of oxidation on the cluster electronic structure may provide insight to the function of cerium oxide – and gold-doped cerium oxide – in oxidative catalysis. A detailed discussion of the effects of oxidation on the catalytic properties of the Ce_2O_n clusters is presented in Chapter 10.

Experimental and calculated IEs are presented in Figure 5.28 with the respective IE trends for the primary onset shown as solid and dashed lines. Secondary onset IEs – both experimental and calculated – are also shown; however, the IE trends are not considered to be of interest. Experimental IE values are presented for the Ce_2 , Ce_2O and Ce_2O_2 clusters. An approximated IE value of 5.73 eV is presented for the Ce_2O_3 cluster; this value corresponds to the midpoint of the bracketed AE range of 5.64 – 5.82 eV. Due to this approximated IE value, the Ce_2O_2 - Ce_2O_3 IE trend is shown as a dotted line. While the experimental IE values all have assigned errors of ± 0.05 eV in accordance with previous work by Koretsky and Knickelbein¹¹, these errors are too small to be shown in Figure 5.28.

The calculated IE values are corrected to the experimental IE values using the method described in Chapter 3. Briefly, the Ce_2 calculated IE is corrected by -0.20 eV to align with the experimental Ce_2 IE value. The same correction is then applied to the calculated Ce_2O , Ce_2O_2 and Ce_2O_3 IE values. This method of offsetting the calculated IEs is consistent with previous work by both Gentleman et al.^{23,24} and Dryza et al.^{25–27} and accounts for DFT errors associated with the use of frozen cores during calculations. Error bars of ± 0.2 eV are additionally applied to all calculated IE values to account for errors inherent to the computational process. Horizontal dotted lines are shown on Figure 5.28 to represent the maximum photon energies available with the tuneable laser source (5.64 eV; 220 nm) and the fixed wavelength 5th harmonic Nd:YAG laser source (5.82 eV; 213 nm).

The Ce_2O_n experimental IE trend shows a ca. 0.05 eV increase in IE from Ce_2 to Ce_2O , followed by a ca. 0.31 eV decrease in IE for Ce_2O_2 . Thus, the Ce_2O species is recorded with the highest IE. This contrasts previous IE trends reported by Gentleman et al.^{23,24} for Ho_2O_n ($n=0-2$) and $RhHo_2O_n$ ($n=0-2$) clusters with sequential oxidation; the authors reported the monoxide cluster to have the lowest IE in both cases. However, the Ce_2O secondary IE is lower than both the Ce_2 and Ce_2O_2 IEs which agrees with the Ho_2O_n ($n=0-2$) and $RhHo_2O_n$ ($n=0-2$) IE trends.

A good correlation is found between the calculated IEs post-correction and the experimental IE values; the Ce_2O , Ce_2O_2 and Ce_2O_3 corrected IEs all match their respective experimental IE

values within a 0.2 eV margin of error. Moreover, the very high IE calculated for the Ce_2O_4 cluster – 9.05 eV, which corresponds to a corrected IE value of 8.86 eV – is consistent with the non-detection of Ce_2O_4 in experimental mass spectra. This agreement between the calculated and experimental IE values, in combination with the good correlation found between simulated and experimental PIE spectra, allows for inferences to be made about the geometric and electronic properties of Ce_2O_n clusters from the DFT calculated structures.

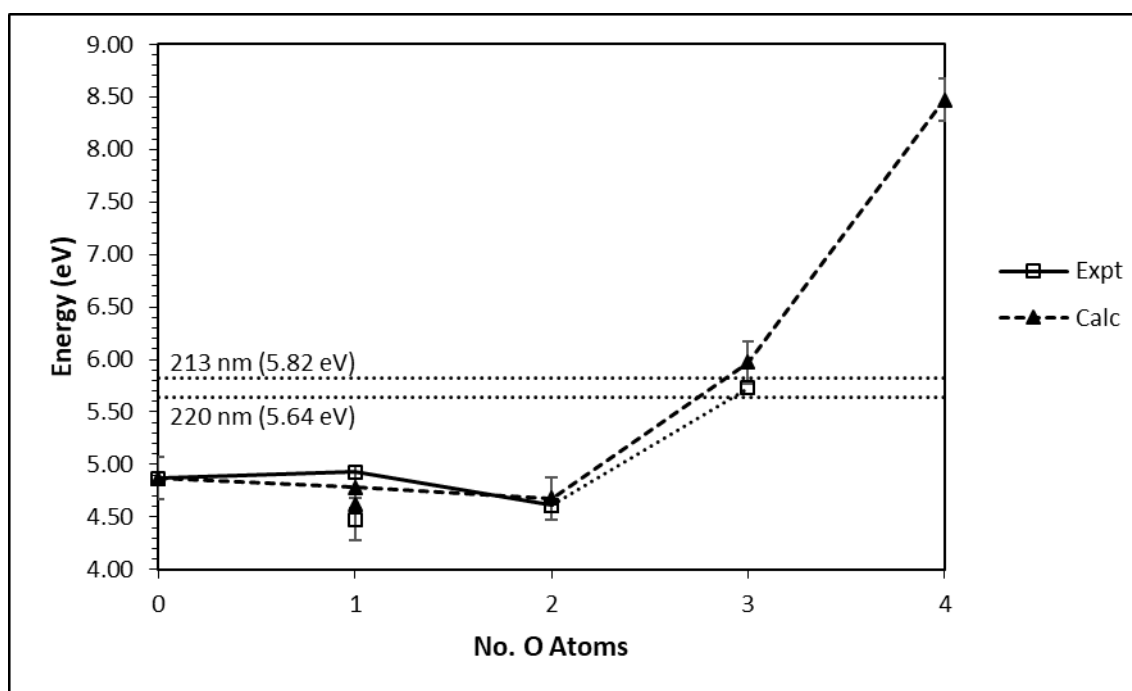


Figure 5.28: Experimental and calculated adiabatic ionisation energies for the Ce_2O_n cluster series with sequential oxidation. Primary and secondary IEs are shown for the Ce_2O species. The experimental and calculated IE trends for the primary onsets are shown as solid and dashed lines, respectively. An approximated IE is presented for Ce_2O_3 ; the Ce_2O_2 - Ce_2O_3 IE trend is therefore represented with a dotted line. Horizontal lines are drawn at 220 nm (5.64 eV) and 213 nm (5.82 eV) to represent the upper energy bound of the tuneable laser source and the highest energy for which photo-ionisation mass spectra can be recorded, respectively.

5.9. References

- (1) Barrow, R. F.; Clements, R. M.; Harris, S. M.; Jenson, P. P. *Astrophys. J.* **1979**, 229, 439.
- (2) Schall, H.; Gray, J. A.; Dulick, M.; Field, R. W. *J. Chem. Phys.* **1986**, 85 (2), 751.
- (3) Linton, C.; Dulick, M. *J. Mol. Spectrosc.* **1981**, 89 (2), 569.
- (4) Linton, C. *J. Chem. Phys.* **1981**, 74 (1), 189.
- (5) Linton, C.; Dulick, M.; Field, R. *J. Mol. Spectrosc.* **1979**, 78 (3), 428.
- (6) Ackermann, R. J. *J. Chem. Phys.* **1976**, 65 (3), 1027.
- (7) Willson, S. P.; Andrews, L. *J. Phys. Chem. A* **1999**, 103 (35), 6972.
- (8) Dulick, M.; Murad, E.; Barrow, R. F. *J. Chem. Phys.* **1986**, 85 (1), 385.
- (9) Kaledin, L. A.; Mccord, J. E.; Heaven, M. C. *J. Mol. Spectrosc.* **1993**, 158 (1), 40.
- (10) Kaledin, L. A.; Mccord, J. E.; Heaven, M. C. *J. Mol. Spectrosc.* **1995**, 170 (1), 166.
- (11) Koretsky, G. M.; Knickelbein, M. B. *Eur. Phys. J. D - At. Mol. Opt. Plasma Phys.* **1998**, 2, 273.
- (12) Cao, X.; Dolg, M. *Mol. Phys.* **2003**, 101 (13), 1967.
- (13) Roos, B. O.; Lindh, R.; Malmqvist, P.-Å.; Veryazov, V.; Widmark, P.-O.; Borin, A. C. *J. Phys. Chem. A* **2008**, 112 (45), 11431.
- (14) Nikolaev, A. V. *Phys. Rev. A - At. Mol. Opt. Phys.* **2011**, 84, 012512.
- (15) Nikolaev, A. V.; Tsvyashchenko, A. V. *Physics-Uspokhi* **2012**, 55 (7), 657.
- (16) Li, S. F.; Lu, H.; Li, P.; Yang, Z.; Guo, Z. X. *J. Chem. Phys.* **2008**, 128 (16).
- (17) Wu, X.; Ding, X.; Bai, S.; Xu, B.; He, S.; Shi, Q. *J. Phys. Chem. C* **2011**, 115, 13329.
- (18) Nolan, M.; Grigoleit, S.; Sayle, D. C.; Parker, S. C.; Watson, G. W. *Surf. Sci.* **2005**, 576 (1–3), 217.

-
- (19) *Encyclopedia of Interfacial Chemistry : Surface Science and Electrochemistry*; Wandelt, K. (Klaus), Ed.; Elsevier Inc.: Amsterdam, 2018.
- (20) Akin, S. T.; Ard, S. G.; Dye, B. E.; Schaefer, H. F.; Duncan, M. A. *J. Phys. Chem. A* **2016**, *120* (15), 2313.
- (21) Chen, H.-L.; Weng, M.-H.; Ju, S.-P.; Chang, J.-G.; Chen, H.-T.; Chang, C.-S. *J. Mol. Struct.* **2010**, *963* (1), 2.
- (22) Addicoat, M. A. Computational Investigations into the Structure and Reactivity of Small Transition Metal Clusters, PhD Thesis, The University of Adelaide, 2009.
- (23) Gentleman, A. S.; Addicoat, M. A.; Dryza, V.; Gascooke, J. R.; Buntine, M. A.; Metha, G. F. *J. Chem. Phys.* **2009**, *130* (16), 64311.
- (24) Gentleman, A. S. The Effect of Sequential Oxidation and Composition on the Structural and Electronic Properties of Gas Phase Transition-Lanthanide Bimetallic Clusters, PhD Thesis, The University of Adelaide, 2014.
- (25) Dryza, V.; Addicoat, M. A.; Gascooke, J. R.; Buntine, M. A.; Metha, G. F. *J. Phys. Chem. A* **2005**, *109* (49), 11180.
- (26) Dryza, V.; Addicoat, M. A.; Gascooke, J. R.; Buntine, M. A.; Metha, G. F. *J. Phys. Chem. A* **2008**, *112* (25), 5582.
- (27) Dryza, V.; Gascooke, J. R.; Buntine, M. A.; Metha, G. F. *Phys. Chem. Chem. Phys.* **2009**, *11* (7), 1060.

Chapter Six

Photo-Ionisation Efficiency Spectroscopy, Density Functional Theory

Calculations and Zero Electron Kinetic Energy Simulations of Ce₃O_n Clusters

This chapter presents both experimentally determined and calculated adiabatic ionisation energies for the Ce₃O_n ($n=0-4$) clusters, and calculated IEs for the Ce₃O_n ($n=5,6$) clusters. An initial analysis of the Ce_mO_n mass spectrum is discussed followed by presentations of experimental photo-ionisation efficiency (PIE) spectra for the detected cluster species. DFT calculated neutral and cationic geometries for the Ce₃O_n clusters are presented followed by calculated zero electron kinetic energy (ZEKE) and PIE spectra. The calculated PIE spectrum is compared to the experimental PIE spectrum to infer electronic and geometric properties of the relevant cluster species. For cluster systems not detected in PIE experiments, DFT calculations and ZEKE/PIE spectral simulations are presented to provide insight on geometric and electronic properties.

6.1. Mass Spectrum Analysis

A mass spectrum of the Ce_3O_n cluster series following photo-ionisation 213 nm (5.82 eV) is presented in Figure 6.1. The Ce_3 (i.e. $n=0$) bare metal cluster ion is detected with a low abundance; this is most likely due to conditions in the cluster source favouring the formation of oxidised clusters. The Ce_3 peak can be detected experimentally with a greater abundance by both reducing the pressure of the carrier gas – to decrease the collision energy between cerium atoms, thereby increasing the number of adhesive collisions – and by maintaining the cerium rod in an oxygen deficient atmosphere to minimise surface oxidation. The Ce_3O , Ce_3O_2 , Ce_3O_3 and Ce_3O_4 ions are all detected with good abundance and show a near-linear increase in peak height with increased oxidation. A significant decrease in ion signal is then recorded for the Ce_3O_5 ion, suggesting the photon wavelength may be approaching the AE for this species. The Ce_3O_6 and Ce_3O_7 ions are both detected with very weak intensity. Moreover, variation of the source conditions had no effect on the ion signal for the Ce_3O_6 and Ce_3O_7 clusters. The weak intensities of these two species are attributed to high ionisation energies, which are supported by DFT calculations (*vide infra*). While DFT calculations were not performed for the Ce_3O_7 species – since it was not considered interesting in the context of this work – the general trend observed in Ce_mO_n clusters shows increased oxidation correlating with higher ionisation energies. Therefore, the weak Ce_3O_7 ion signal is also attributed to a high IE.

Each ion peak in the mass spectrum is accompanied by a series of lower and intensity peaks and shoulders at on the higher m/z side. These correspond to clusters containing heavier isotopes of cerium, as previously discussed in Chapter 5. A simulated mass spectrum showing isotopic abundances for the Ce_3 ion is shown inset in Figure 6.1. The same isotopic pattern is observed for all Ce_3O_n ions; the ^{16}O isotope occurs in 99.76% abundance, thus secondary oxygen isotopes are negligible.

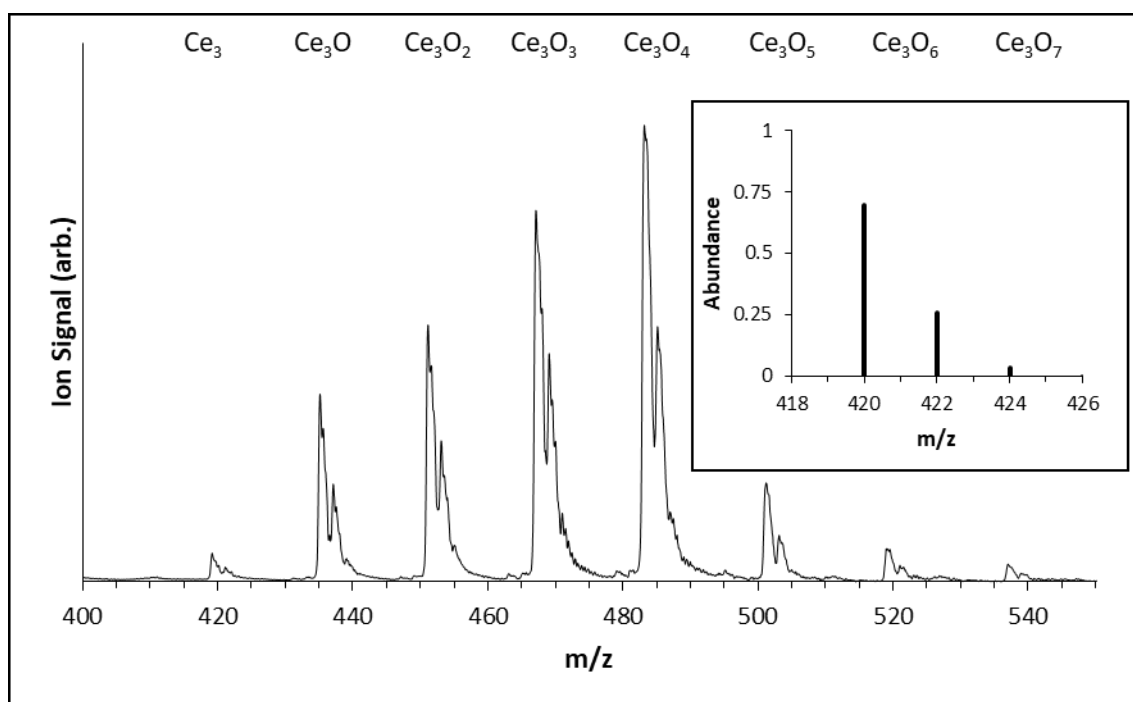


Figure 6.1: Mass spectrum for Ce_3O_n clusters following photo-ionisation at 213 nm (5.82 eV).

Inset: Simulated mass spectrum for the Ce_3 cluster showing relative isotopic abundances.

6.2. Appearance of Cluster Ion Signal for the Ce_3O_n ($n=0-4$) Series

Appearance of the Ce_3O_n ion signal with increased photon energy was recorded over the 240 – 315 nm (3.94 – 5.17 eV) wavelength range. The Ce_3 , Ce_3O , Ce_3O_2 , Ce_3O_3 and Ce_3O_4 ion peaks were all observed to appear within this region. Appearance of the Ce_3O_5 ion was observed over the 213 – 220 nm (5.64 – 5.82 eV) range by the detection of the Ce_3O_5 ion peak in the mass spectrum following photo-ionisation at 213 nm (5.82 eV) which was not evident in the mass spectrum recorded with 220 nm (5.64 eV) photo-ionisation. Because photo-ionisation experiments cannot be performed over the 213 – 220 nm wavelength range due to the lack of an appropriate tuneable laser source, PIE experiments of the Ce_3O_5 cluster were not performed. Therefore, a bracketed AE of 5.64 – 5.82 eV is assigned to the Ce_3O_5 cluster.

A series of mass spectra recorded with photo-ionisation wavelengths of 315 nm (3.94 eV), 310 nm (4.00 eV), 300 nm (4.14 eV) and 275 nm (4.51 eV) are presented in Figure 6.2 in order to bracket the appearance energies of the Ce_3O_n ($n=0-4$) cluster species. The Ce_3 and Ce_3O peaks are observed to appear in the range 4.14 – 4.51 eV; the Ce_3O_2 peak appears in the range

4.00 – 4.14 eV and the Ce_3O_4 peak appears in the range 3.94 – 4.00 eV. Trace amounts of the Ce_3O_3 peak are observed at 3.94 eV. This small ion peak may be an artefact of metastable photo-ionisation processes, multi-photon ionisation or fragmentation events.

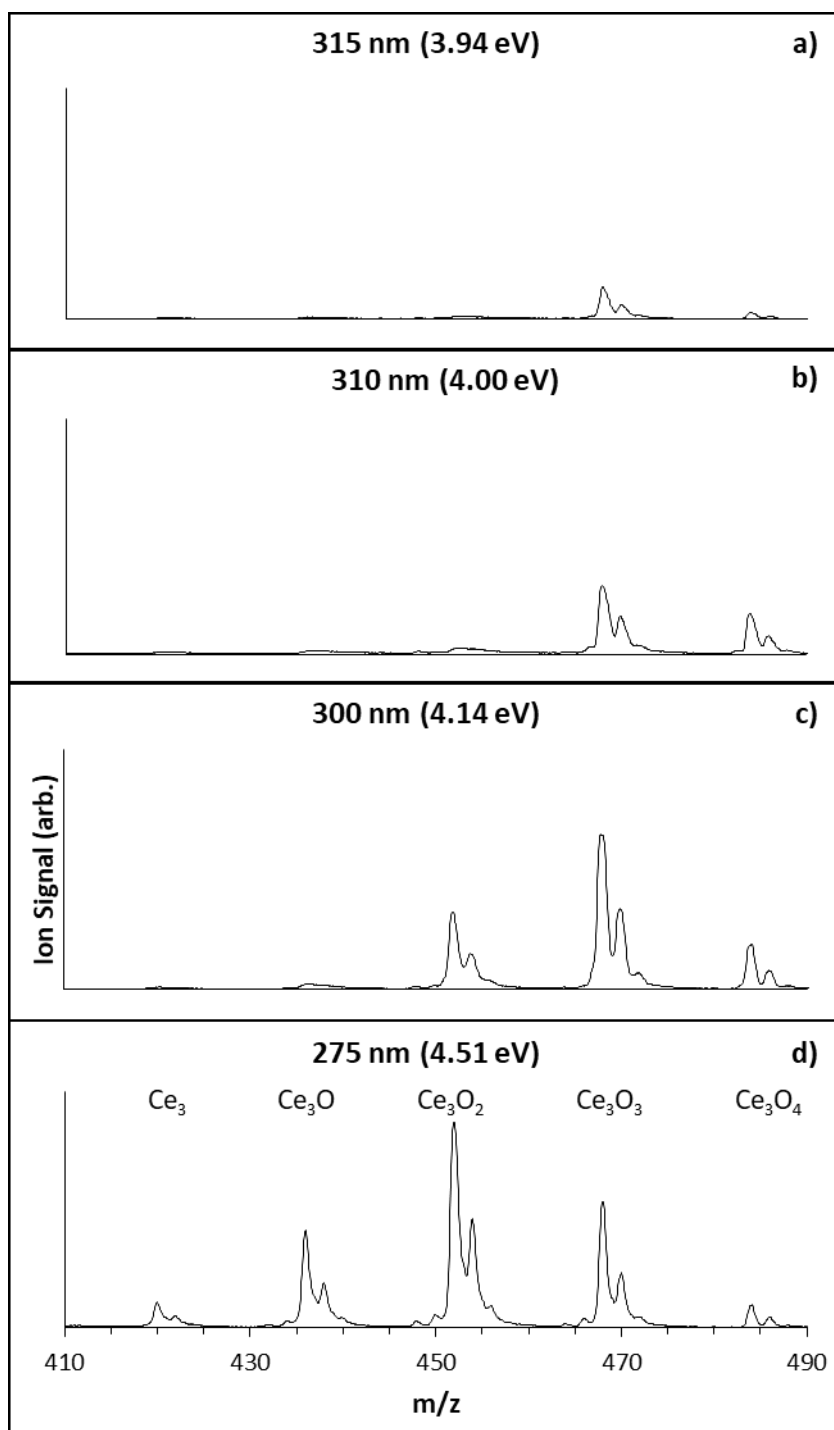


Figure 6.2: Mass spectra of the Ce_3 , Ce_3O , Ce_3O_2 , Ce_3O_3 and Ce_3O_4 clusters following photo-ionisation at **a)** 315 nm (3.94 eV), **b)** 310 nm (4.00 eV), **c)** 300 nm (4.14 eV) and **d)** 275 nm (4.51 eV).

6.3. PIE Spectrum and DFT Results for Ce_3

6.3.1. Ce_3 Experimental PIE Spectrum

The Ce_3 PIE spectrum is presented in Figure 6.3. From the lower energy end of the spectrum, a very gradual increase in ion signal is observed in the 3.92 – 4.35 eV energy region. This region is designated the baseline; the weak, albeit non-zero ion signal observed here is most likely an artefact of residual MPI, photo-ionisation of metastable isomers or fragmentation of larger clusters. A single onset of ion signal is observed with an AE of 4.35 eV; this onset extends to a plateau of maximum ion signal at 4.55 eV. The onset is characterised by two different slopes – comprising a gradual slope in the 4.35 – 4.47 eV region, and a sharper slope in the 4.47 – 4.55 eV region.

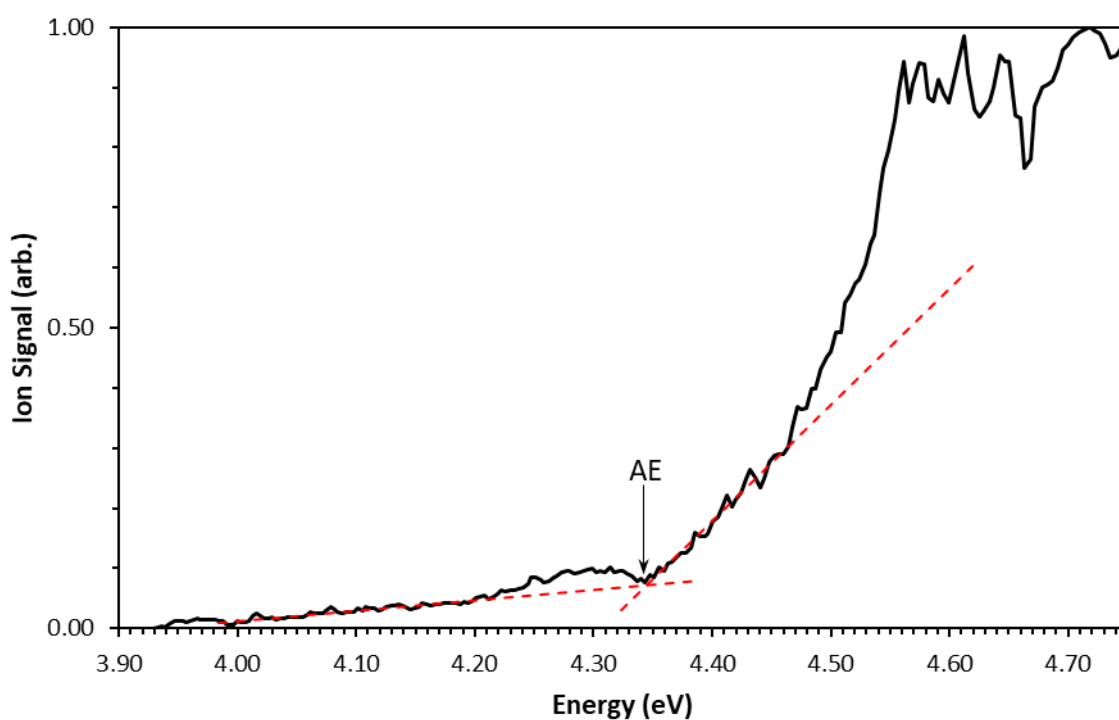


Figure 6.3: PIE spectrum for Ce_3 . Linear trendlines for the baseline and onset are presented as red dashed lines. The appearance energy is labelled with a black arrow.

6.3.2. DFT Calculations for Ce_3

DFT calculated Ce_3 structures are presented in Figures 6.4 and 6.5 (calculated vibrational modes for all Ce_3O_n species are also shown in Appendix B). Calculations were performed in the $m=1,3,5,7,9$ multiplicities. Neutral Ce_3 structures were calculated in two unique structures – labelled **VIA** and **VIB** in order of increasing energy – both comprising scalene trimers with C_s symmetry. The primary difference between the two structures lies in the length of the Ce-Ce bond forming the trimer base which are calculated as ca. 3.10 Å and 3.45 Å for the **VIA** and **VIB** structures, respectively. No optimised structure was found to form either a C_{2v} or a bent geometry.

The **VIA** structure is calculated in the $^7A''$ and $^5A''$ electronic states – labelled $^7\mathbf{VIA}$ and $^5\mathbf{VIA}$, respectively – while the **VIB** structure is calculated in the $^3A'$ and $^5A''$ electronic states, labelled $^3\mathbf{VIB}$ and $^5\mathbf{VIB}$, respectively. The comparable energies of all calculated neutral structures presented in Figure 6.5 – where all structures are within 0.2 eV of the LES – makes it likely that all four neutral species are produced with good abundance. No Ce_3 singlet states were calculated within 0.3 eV of the LES. Given the high spin states calculated for the Ce_2 dimer, presented both in Chapter 5 and elsewhere¹, the lack of low-lying singlet Ce_3 states is not unexpected. Calculations of nonet Ce_3 species also failed to yield any structures within 0.3 eV of the LES and tended to converge to flat regions of the potential energy surface with imaginary frequencies.

A total of five cationic species are presented as potential target states for the neutral Ce_3 species. These are calculated with similar geometries to the **VIA** and **VIB** structures discussed previously. The cationic structures show an energetic reordering such that the **VIB**⁺ structures are lower in energy than the **VIA**⁺ structures. The Ce_3 **VIA**⁺ structure is calculated in the $^8A''$ and $^6A''$ electronic states, labelled $^8\mathbf{VIA}^+$ and $^6\mathbf{VIA}^+$, respectively. The **VIB**⁺ structure is calculated in the $^6A''$, $^2A'$ and $^4A'$ electronic states, labelled $^6\mathbf{VIB}^+$ $^2\mathbf{VIB}^+$ and $^4\mathbf{VIB}^+$, respectively. This gives a total of 8 potential ionisation transitions: $^8A'' \leftarrow ^7A''$ ($^8\mathbf{VIA}^+ \leftarrow ^7\mathbf{VIA}$), $^6A'' \leftarrow ^7A''$ ($^6\mathbf{VIA}^+ \leftarrow ^7\mathbf{VIA}$), $^6A'' \leftarrow ^5A''$ ($^6\mathbf{VIB}^+ \leftarrow ^5\mathbf{VIA}$), $^4A' \leftarrow ^5A''$ ($^4\mathbf{VIB}^+ \leftarrow ^5\mathbf{VIA}$), $^2A' \leftarrow ^3A'$ ($^2\mathbf{VIB}^+ \leftarrow ^3\mathbf{VIB}$), $^4A' \leftarrow ^3A'$ ($^4\mathbf{VIB}^+ \leftarrow ^3\mathbf{VIB}$), $^6A'' \leftarrow ^5A''$ ($^6\mathbf{VIB}^+ \leftarrow ^5\mathbf{VIB}$) and $^4A'' \leftarrow ^5A''$ ($^4\mathbf{VIB}^+ \leftarrow ^5\mathbf{VIB}$). IEs for these processes are calculated as

4.966 eV, 5.103 eV, 4.755 eV, 4.777 eV, 4.669 eV, 4.681 eV, 4.647 eV and 4.669 eV, respectively. The ${}^2A' \leftarrow {}^3A'$ (${}^2VIB^+ \leftarrow {}^3VIB$), ${}^4A' \leftarrow {}^3A'$ (${}^4VIB^+ \leftarrow {}^3VIB$), ${}^6A'' \leftarrow {}^5A''$ (${}^6VIB^+ \leftarrow {}^5VIB$) and ${}^4A'' \leftarrow {}^5A''$ (${}^4VIB^+ \leftarrow {}^5VIB$) transitions are shown as green, orange, violet and blue arrows, respectively, in Figure 6.4. All other transitions are shown as red dotted arrows due to low ZEKE intensities (vide infra).

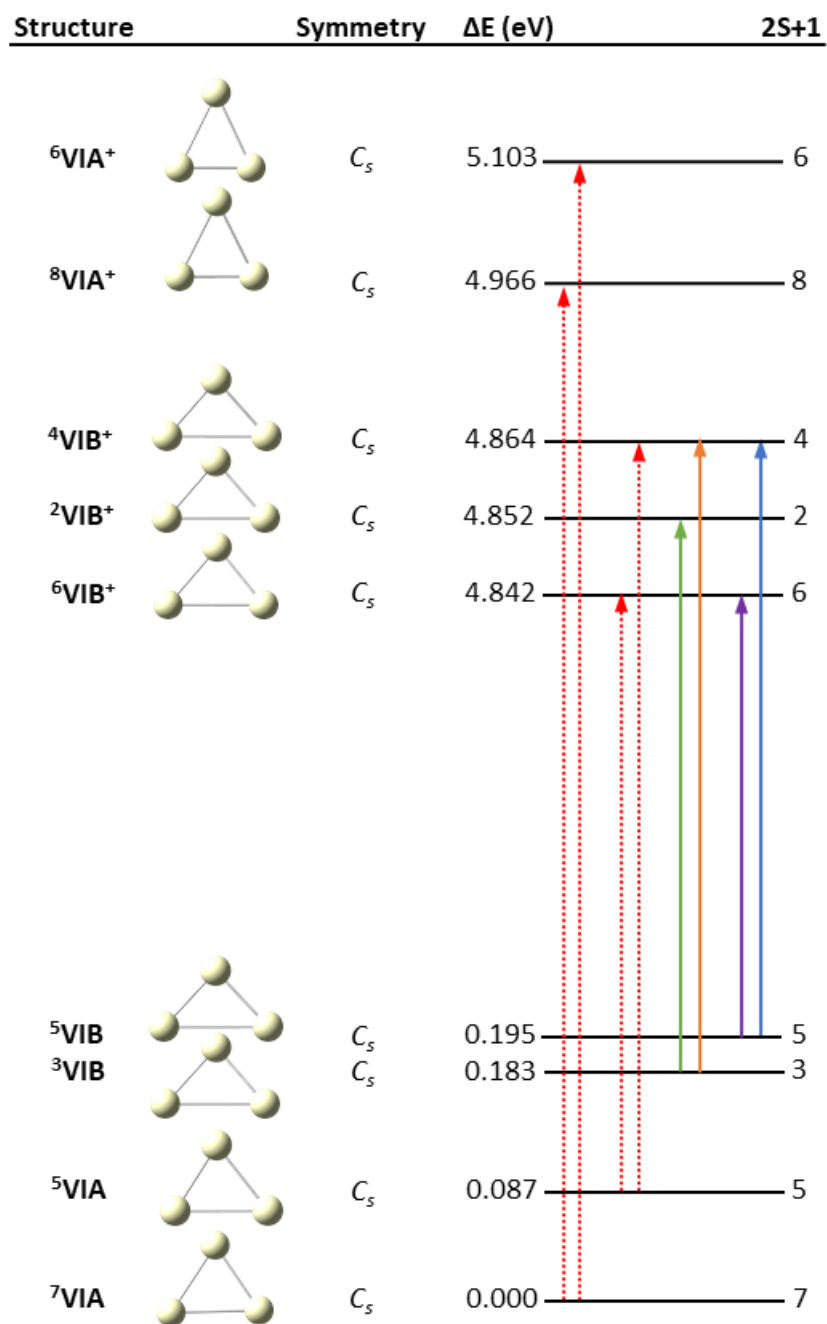


Figure 6.4: Ce_3 calculated structures with potential ionisation transitions. Transitions with low ZEKE intensities (*vide infra*) are shown as red dotted arrows.

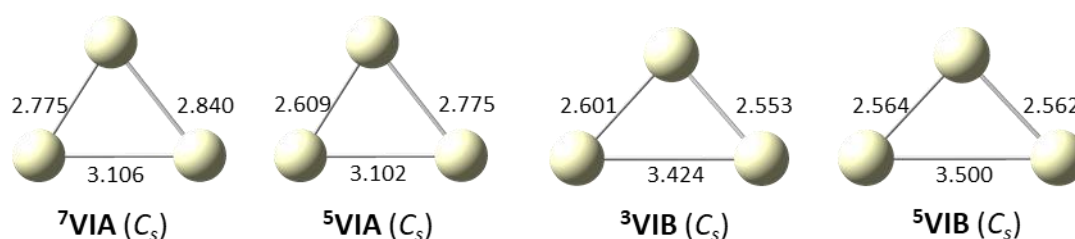
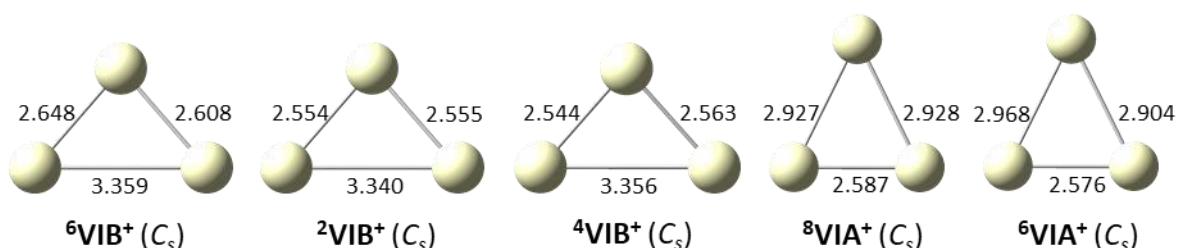
Ce_3  Ce_3^+ 

Figure 6.5: Calculated Ce_3 neutral (top) and cationic (below) structures. Bond lengths are presented in Å. Point groups are shown in brackets.

6.3.3. ZEKE Spectral Simulations for Ce_3

ZEKE spectral simulations were performed for all ionisation transitions shown in Figure 6.6. Ionisation processes from the two lowest energy neutral isomers – 7VIA and 5VIA – which include the ${}^8A'' \leftarrow {}^7A''$ (${}^8VIA^+ \leftarrow {}^7VIA$), ${}^6A'' \leftarrow {}^7A''$ (${}^6VIA^+ \leftarrow {}^7VIA$), ${}^6A'' \leftarrow {}^5A''$ (${}^6VIB^+ \leftarrow {}^5VIA$) and ${}^4A' \leftarrow {}^5A''$ (${}^4VIB^+ \leftarrow {}^5VIA$) transitions, were all calculated with very weak vibronic peak intensities corresponding to a poor FC overlap between the neutral and cationic species. Significantly higher spectral intensities were calculated for the ${}^2A' \leftarrow {}^3A'$ (${}^2VIB^+ \leftarrow {}^3VIB$), ${}^4A' \leftarrow {}^3A'$ (${}^4VIB^+ \leftarrow {}^3VIB$), ${}^6A'' \leftarrow {}^5A''$ (${}^6VIB^+ \leftarrow {}^5VIB$) and ${}^4A' \leftarrow {}^5A''$ (${}^4VIB^+ \leftarrow {}^5VIB$) processes from the – higher energy – 3VIB and 5VIB structures. Ionisation processes from the 3VIB and 5VIB structures would therefore be dominant in the PIE spectrum, making the contributions from the ${}^8A'' \leftarrow {}^7A''$ (${}^8VIA^+ \leftarrow {}^7VIA$), ${}^6A'' \leftarrow {}^7A''$ (${}^6VIA^+ \leftarrow {}^7VIA$), ${}^6A'' \leftarrow {}^5A''$ (${}^6VIB^+ \leftarrow {}^5VIA$) and ${}^4A' \leftarrow {}^5A''$ (${}^4VIB^+ \leftarrow {}^5VIA$) transitions negligible. Thus, only the Ce_3 ${}^2A' \leftarrow {}^3A'$ (${}^2VIB^+ \leftarrow {}^3VIB$), ${}^4A' \leftarrow {}^3A'$ (${}^4VIB^+ \leftarrow {}^3VIB$), ${}^6A'' \leftarrow {}^5A''$ (${}^6VIB^+ \leftarrow {}^5VIB$) and ${}^4A' \leftarrow {}^5A''$ (${}^4VIB^+ \leftarrow {}^5VIB$) ionisation processes are

considered to contribute to the PIE spectrum. Simulated ZEKE spectra for the ${}^8A'' \leftarrow {}^7A''$ (${}^8VIA^+ \leftarrow {}^7VIA$), ${}^6A'' \leftarrow {}^7A''$ (${}^6VIA^+ \leftarrow {}^7VIA$), ${}^6A'' \leftarrow {}^5A''$ (${}^6VIB^+ \leftarrow {}^5VIA$) and ${}^4A' \leftarrow {}^5A''$ (${}^4VIB^+ \leftarrow {}^5VIA$) transitions can be found in Appendix C.

The ZEKE spectra presented in Figure 6.6 were energetically corrected using the method described in Chapter 3. Subsequent energetic corrections of +0.105 eV, +0.130 eV, +0.010 eV and -0.016 eV were then applied to the calculated ${}^2A' \leftarrow {}^3A'$ (${}^2VIB^+ \leftarrow {}^3VIB$), ${}^4A' \leftarrow {}^3A'$ (${}^4VIB^+ \leftarrow {}^3VIB$), ${}^6A'' \leftarrow {}^5A''$ (${}^6VIB^+ \leftarrow {}^5VIB$) and ${}^4A'' \leftarrow {}^5A''$ (${}^4VIB^+ \leftarrow {}^5VIB$) ZEKE spectra, respectively, to improve the fit of the calculated PIE spectrum (*vide infra*) to the experimental PIE spectrum. The corrected ZEKE spectra are shown here.

Calculated ZEKE spectra for the Ce_3 ${}^2A' \leftarrow {}^3A'$ (${}^2VIB^+ \leftarrow {}^3VIB$), ${}^4A' \leftarrow {}^3A'$ (${}^4VIB^+ \leftarrow {}^3VIB$), ${}^6A'' \leftarrow {}^5A''$ (${}^6VIB^+ \leftarrow {}^5VIB$) and ${}^4A'' \leftarrow {}^5A''$ (${}^4VIB^+ \leftarrow {}^5VIB$) photo-ionisation processes are presented in Figure 6.6. Spectral profiles for the ${}^2A' \leftarrow {}^3A'$ (${}^2VIB^+ \leftarrow {}^3VIB$) and ${}^4A' \leftarrow {}^3A'$ (${}^4VIB^+ \leftarrow {}^3VIB$) ZEKE spectra shown in Figures 6.6(a) and 6.6(b) – which both describe ionisation from the 3VIB neutral structure – are quite similar. Both spectra are dominated by short progressions of the ν_1 mode – which describes an asymmetric stretch – although vibronic peaks from the ν_2 and ν_3 modes – comprising an in-plane bend and symmetric stretch, respectively – are also calculated with reasonable intensity. Some combination modes are observed but do not constitute progressions. The most intense transition in both spectra – corresponding to the maximum Franck Condon overlap – is the 0_0^0 transition, indicating minimal structural change occurring upon ionisation in both cases. A number of hot band transitions are recorded in both ZEKE spectra; this is due to simulations being performed at 300 K in order to maintain consistency with cluster rovibronic temperatures inside the supersonic expansion jet².

Calculated ZEKE spectra for the ${}^6A'' \leftarrow {}^5A''$ (${}^6VIB^+ \leftarrow {}^5VIB$) and ${}^4A'' \leftarrow {}^5A''$ (${}^4VIB^+ \leftarrow {}^5VIB$) transitions are presented in Figures 6.6(c) and 6.6(d) respectively. The ${}^6A'' \leftarrow {}^5A''$ (${}^6VIB^+ \leftarrow {}^5VIB$) spectrum largely consists of ν_1 progressions; both by itself and combined with ν_2 and ν_3 modes. The ${}^4A'' \leftarrow {}^5A''$ (${}^4VIB^+ \leftarrow {}^5VIB$) ZEKE spectrum similarly comprises mostly ν_1 progressions – both from the ground vibrational state and hot bands – albeit with minimal combination modes. The

long vibronic progressions calculated in both spectra, in combination with the weak 0_0^0 peak intensities – where the most intense vibronic transitions in the calculated ${}^6A'' \leftarrow {}^5A''$ (${}^6VIB^+ \leftarrow {}^5VIB$) and ${}^4A'' \leftarrow {}^5A''$ (${}^4VIA^+ \leftarrow {}^5VIB$) spectra are the $1_0^5 3_0^1$ and 1_0^3 peaks, respectively, and not the 0_0^0 transition as calculated for the ${}^2A' \leftarrow {}^3A'$ (${}^2VIB^+ \leftarrow {}^3VIB$) and ${}^4A' \leftarrow {}^3A'$ (${}^4VIB^+ \leftarrow {}^3VIB$) processes – both suggest a weaker FC overlap between the neutral and cationic states. These characteristics are indicative of a more substantial difference between the neutral and cationic geometries. Moreover, the spectral intensities of the ${}^6A'' \leftarrow {}^5A''$ (${}^6VIB^+ \leftarrow {}^5VIB$) and ${}^4A'' \leftarrow {}^5A''$ (${}^4VIB^+ \leftarrow {}^5VIB$) ionisation processes – with scaling factors of 6.5 and 4.0, respectively, used to normalise the most intense peak – are considerably lower than the ${}^2A' \leftarrow {}^3A'$ (${}^2VIB^+ \leftarrow {}^3VIB$) and ${}^4A' \leftarrow {}^3A'$ (${}^4VIB^+ \leftarrow {}^3VIB$) transitions, where scaling factors of 2.0 and 2.5, respectively, are applied. Thus, while all four ionisation processes would potentially contribute to the Ce_3 PIE spectrum, the stronger ${}^2A' \leftarrow {}^3A'$ (${}^2VIB^+ \leftarrow {}^3VIB$) and ${}^4A' \leftarrow {}^3A'$ (${}^4VIB^+ \leftarrow {}^3VIB$) transitions would expect to be the dominant ionisation processes.

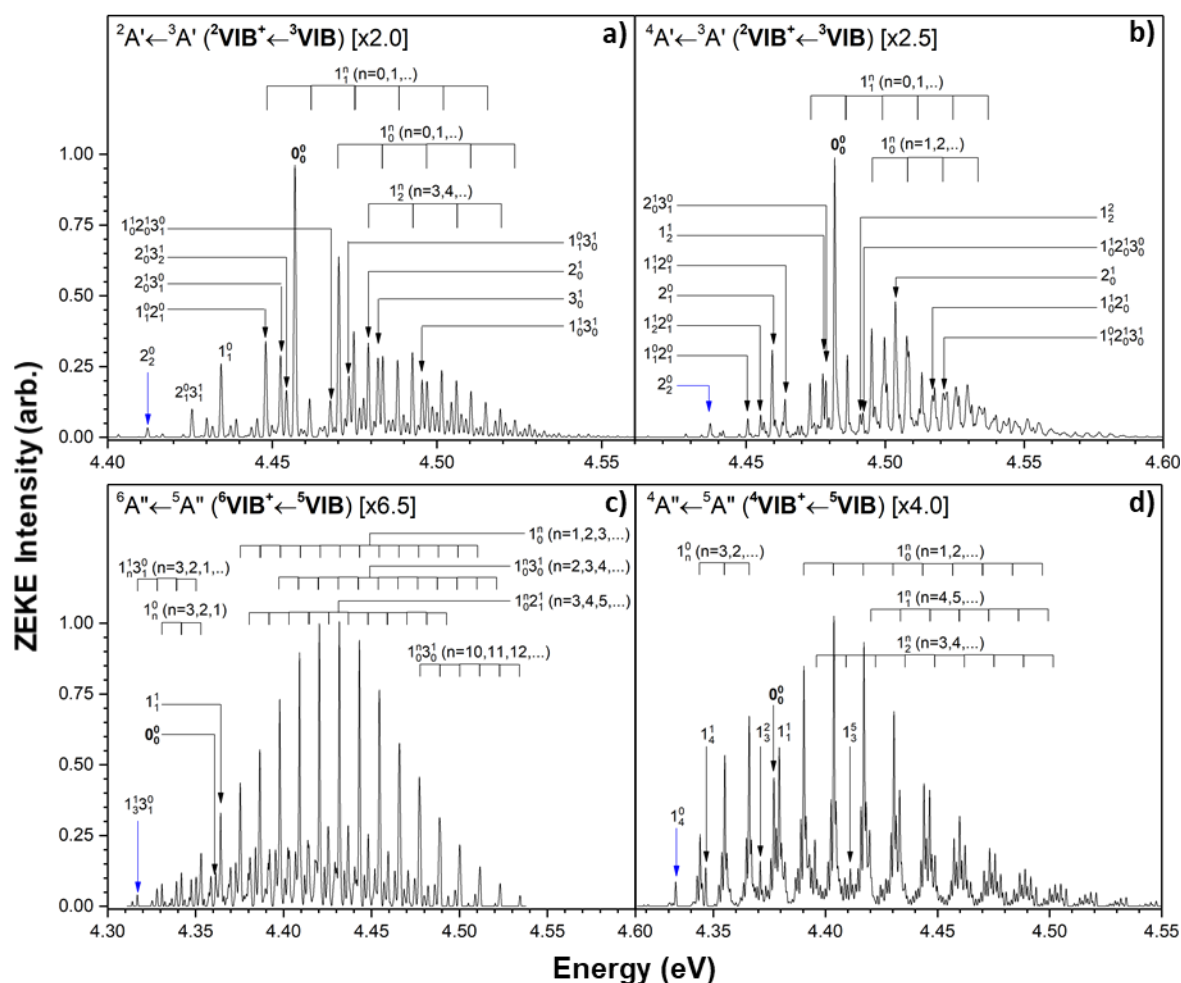


Figure 6.6: Simulated ZEKE spectra for Ce_3 ionisation transitions: **a).** ${}^2A' \leftarrow {}^3A'$ (${}^2VIB^+ \leftarrow {}^3VIB$), **b).** ${}^4A' \leftarrow {}^3A'$ (${}^4VIB^+ \leftarrow {}^3VIB$) **c).** ${}^6A'' \leftarrow {}^5A''$ (${}^6VIB^+ \leftarrow {}^5VIB$) and **d).** ${}^4A'' \leftarrow {}^5A''$ (${}^4VIB^+ \leftarrow {}^5VIB$). Spectral intensities are normalised to the most intense peak in each spectrum with scaling factors shown. Prominent vibronic peaks are assigned. The vibronic transition likely to correspond to the appearance of ion signal in each spectrum is labelled with a blue arrow.

6.3.4. Comparison of Simulated and Experimental PIE Spectra for Ce_3

The simulated PIE spectrum – constructed from a combination of the energetically corrected ${}^2A' \leftarrow {}^3A'$ (${}^2VIB^+ \leftarrow {}^3VIB$), ${}^4A' \leftarrow {}^3A'$ (${}^4VIB^+ \leftarrow {}^3VIB$), ${}^6A'' \leftarrow {}^5A''$ (${}^6VIB^+ \leftarrow {}^5VIB$) and ${}^4A'' \leftarrow {}^5A''$ (${}^4VIB^+ \leftarrow {}^5VIB$) ZEKE spectra – is presented in Figure 6.7. An excellent agreement is found between the simulated and experimental PIE spectra. The Ce_3 adiabatic IE is assigned as the energy of the 0_0^0 vibronic transition for the ${}^2A' \leftarrow {}^3A'$ (${}^2VIB^+ \leftarrow {}^3VIB$) process; this corresponds to the lowest energy photo-ionisation pathway from the lowest energy neutral species

contributing to the PIE spectrum. The Ce_3 IE_{ad} is therefore presented as 4.49 eV. An error of ± 0.05 eV is assigned to this IE value and all subsequent IE values presented in this chapter.

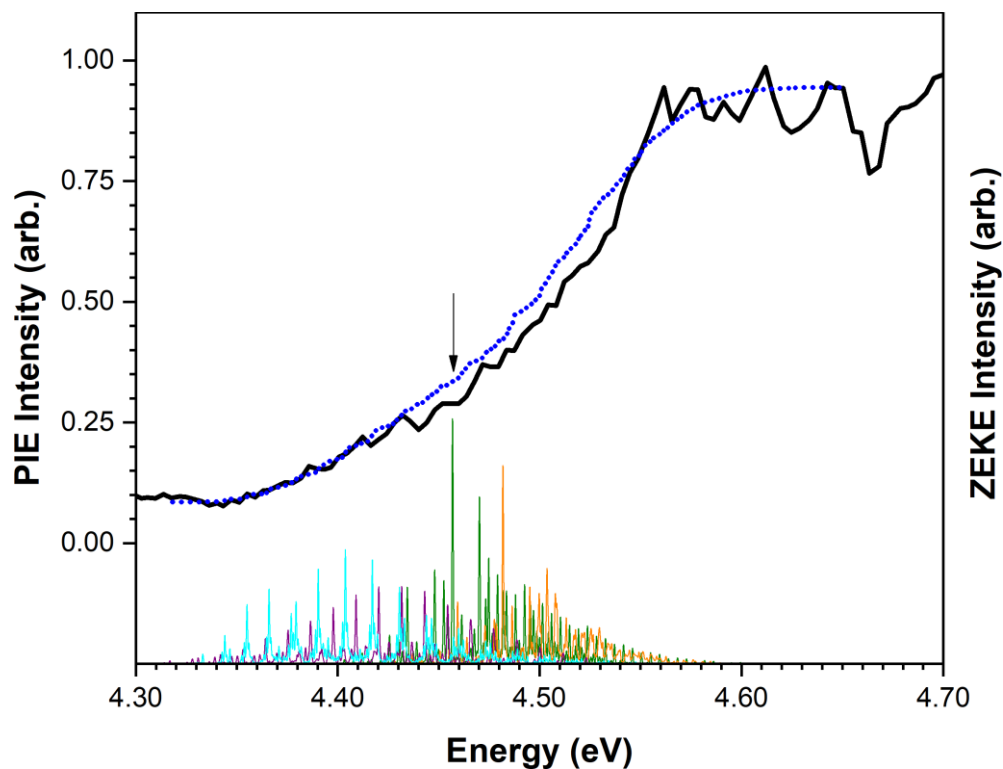


Figure 6.7: Simulated PIE spectrum for Ce_3 (blue dotted line) overlaid against the experimental PIE spectrum (solid black line). Calculated ZEKE spectra for the ${}^2A' \leftarrow {}^3A'$ (${}^2VIB^+ \leftarrow {}^3VIB$), ${}^4A' \leftarrow {}^3A'$ (${}^4VIA^+ \leftarrow {}^3VIB$), ${}^6A'' \leftarrow {}^5A''$ (${}^6VIA^+ \leftarrow {}^5VIB$) and ${}^4A'' \leftarrow {}^5A''$ (${}^4VIA^+ \leftarrow {}^5VIB$) ionisation processes are shown below the PIE spectrum in green, orange, violet and blue, respectively. The adiabatic ionisation energy is labelled with a black arrow.

6.4. PIE Spectrum and DFT Results for Ce_3O

6.4.1. Ce_3O Experimental PIE Spectrum

The Ce_3O experimental PIE spectrum is presented in Figure 6.8. A short region of zero ion signal intensity is recorded between 3.92 eV and 3.96 eV; this is followed by a slow, uniform onset of ion signal until 4.49 eV. The broad – ca. 0.6 eV – range of the onset suggest numerous ionisation processes may be involved. Furthermore, the weak ion signal intensity infers ionisation of metastable isomers and not the lowest energy structure. This onset is thus designated as a secondary ionisation onset with the appearance energy labelled AE_2 in Figure 6.8. DFT calculations for Ce_3O (vide infra) reveal 17 low-lying species within 0.5 eV of the LES which could potentially contribute to this PIE onset. This region is therefore not considered to be particularly interesting. A sharp onset of ion signal is recorded in the 4.49 – 4.56 eV region. This onset encompasses the majority of Ce_3O ion signal increase and is thus labelled the primary onset, labelled AE_1 in Figure 6.8. A plateau is recorded at 5.46 eV which corresponds to the maximum ion signal recorded over the experimental energy range of 3.92 – 5.17 eV. The appearance of the ion signal plateau indicates the highest energy FC-allowed vibronic transition has been accessed.

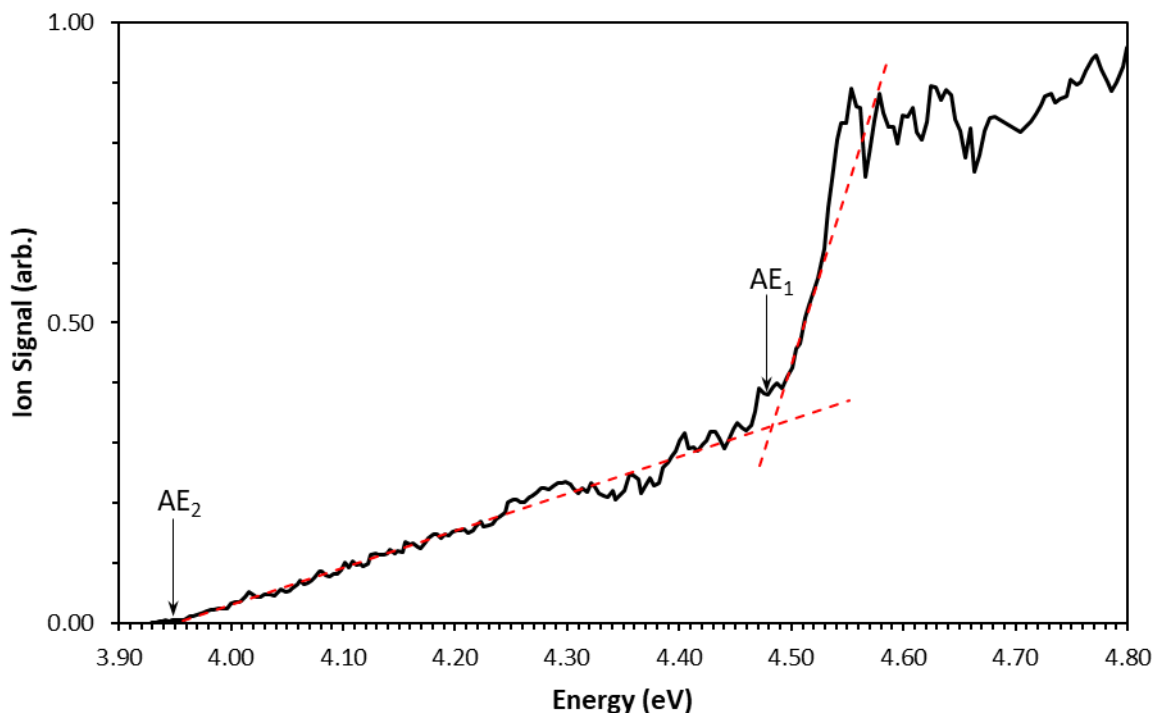


Figure 6.8: PIE spectrum for Ce_3O . Linear trendlines for the baseline and onset are presented as red dashed lines. Appearance energies for the primary and secondary onsets, labelled AE_1 and AE_2 respectively, are labelled with black arrows.

6.4.2. DFT Calculations for Ce_3O

DFT calculated Ce_3O structures are presented in Figures 6.9 and 6.10. Calculations predict a dense manifold of states, with 17 unique species calculated within 0.5 eV of the LES. It is impracticable and superfluous to present all 17 neutral structures and their corresponding cationic states; therefore, only the 3 lowest energy structures and their respective cations are presented. The neutral structures presented here are calculated with energies within ca. 0.27 eV of the LES. The remaining structures are calculated with energies of 0.27 – 0.50 eV relative to the LES. These higher energy structures would potentially contribute to the broad onset in the 3.95 – 4.49 eV range of the experimental PIE spectrum, corresponding to the secondary onset.

Two unique Ce_3O structures are calculated which are labelled **VIIA** and **VIIB** in terms of increasing energy. The **VIIA** structure consists of an oxygen atom bridging one Ce-Ce bond of

a Ce_3 trimer. The structure is C_s symmetric – calculations of the C_{2v} constrained structure converged at saddle points – and is only calculated in a quintet $^5A'$ electronic state, labelled 5VIIA . The **VIIB** structure comprises an oxygen atom facially bound to a Ce_3 trimer in a C_1 symmetric arrangement. This structure is calculated in both the 7A and 5A electronic states, which are labelled 7VIIB and 5VIIB , respectively. While not presented, all calculated neutral species within 0.5 eV of the LES display structures consistent with either the **VIIA** or **VIIB** geometries.

A total of 5 cationic species are calculated as potential target states for the neutral species presented. These species can be grouped into 2 unique geometries, labelled **VIIA**⁺ and **VIIB**⁺, which are similar to their respective neutral **VIIA** and **VIIB** geometries discussed previously. However, the cationic structures undergo an energetic reordering such that the **VIIB**⁺ structures are lower in energy than the **VIIA**⁺ structures. The calculated Ce_3O cationic species give a total of 5 potential ionisation processes; these include the $^4A \leftarrow ^5A'$ ($^4VIIA^+ \leftarrow ^5VIIA$), $^6A \leftarrow ^5A'$ ($^6VIIA^+ \leftarrow ^5VIIA$), $^6A \leftarrow ^7A$ ($^6VIIB^+ \leftarrow ^7VIIB$), $^8A \leftarrow ^7A$ ($^8VIIB^+ \leftarrow ^7VIIB$), $^6A \leftarrow ^5A$ ($^6VIIB^+ \leftarrow ^5VIIB$) and $^4A \leftarrow ^5A$ ($^4VIIB^+ \leftarrow ^5VIIB$). IEs for these processes are calculated as 4.833 eV, 5.049 eV, 4.489 eV, 4.564 eV, 4.434 eV and 4.531 eV, respectively. The $^6A \leftarrow ^5A'$ ($^6VIIB^+ \leftarrow ^5VIIA$) ionisation process is shown as a green arrow in Figure 6.9; all other ionisation processes are shown as red dotted arrows due to low ZEKE intensities (vide infra).

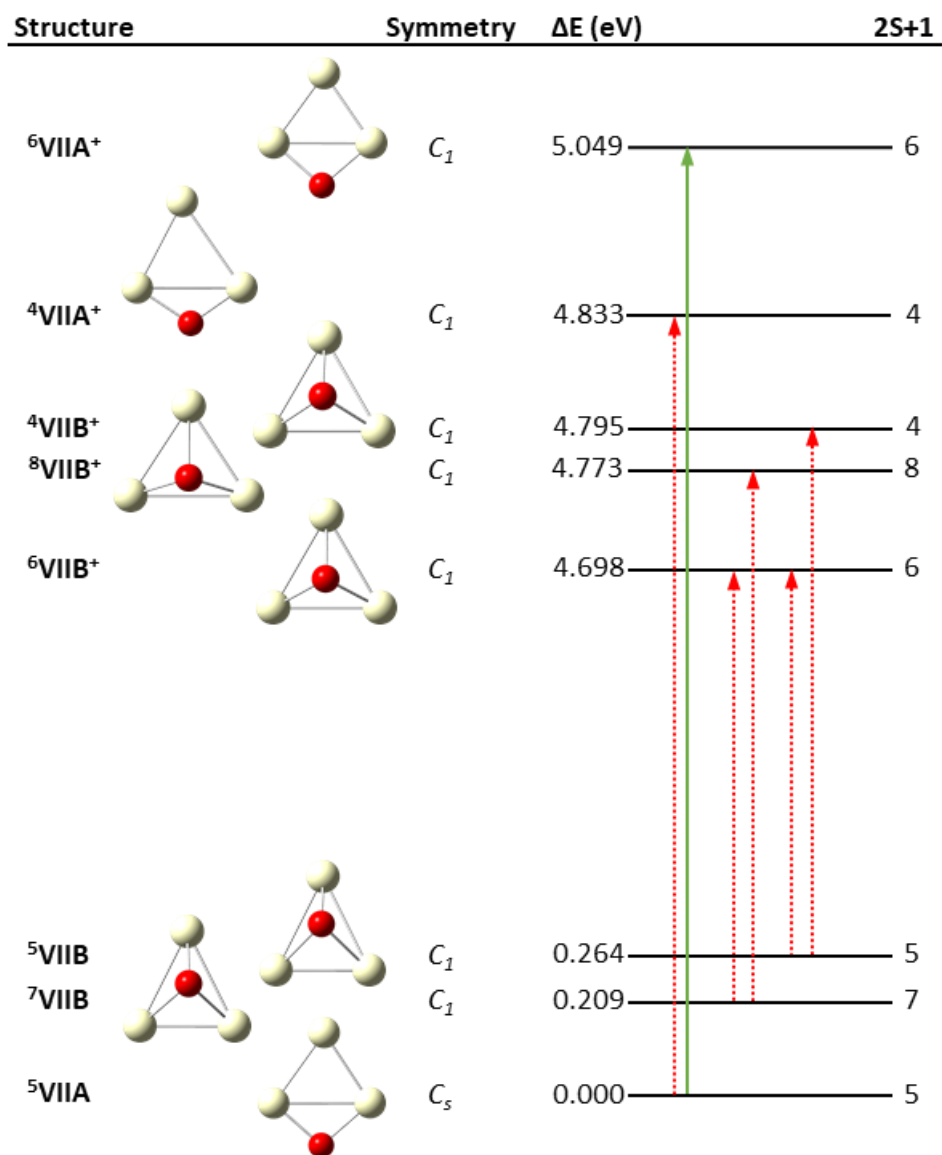


Figure 6.9: Ce_3O calculated structures. Potential ionisation transitions are shown. Transitions with low ZEKE intensities (*vide infra*) are shown as red dotted arrows.

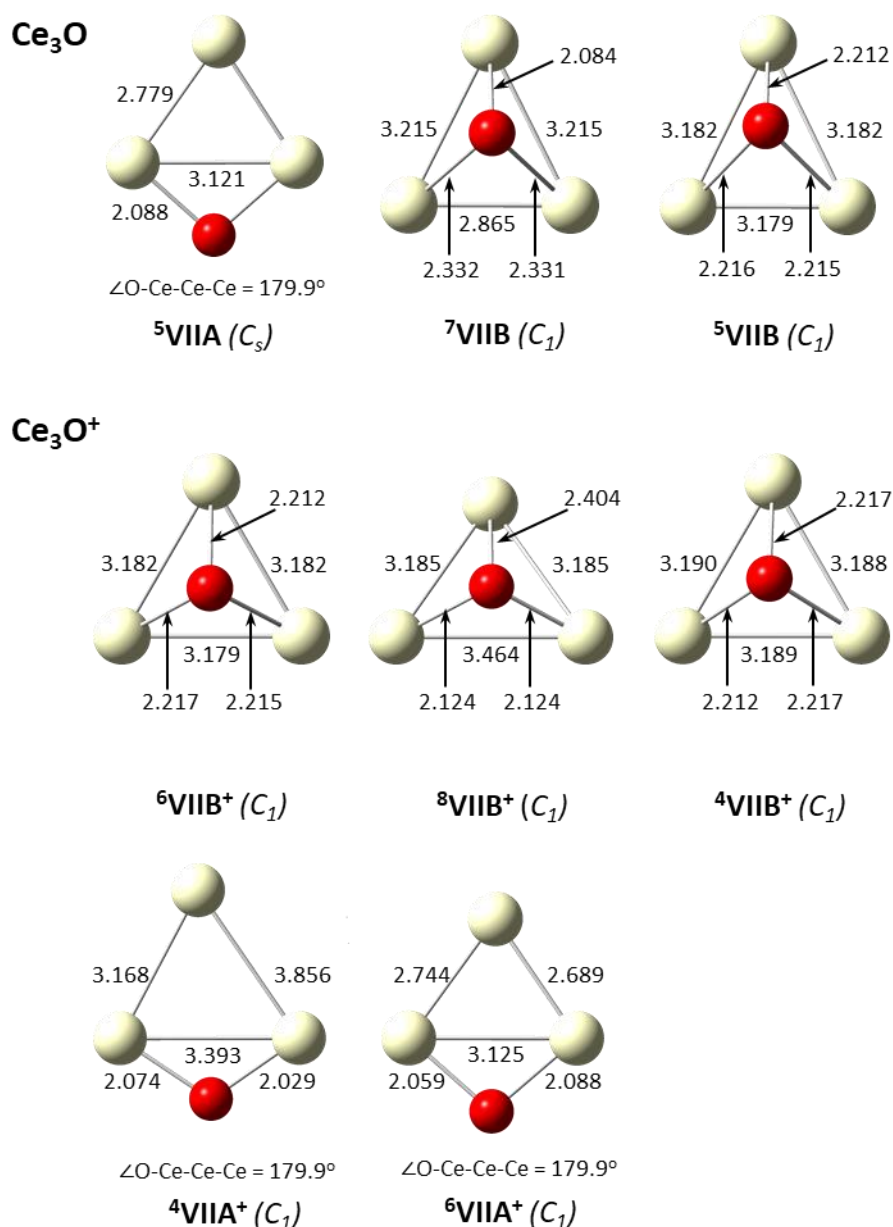


Figure 6.10: Calculated Ce_3O neutral (top) and cationic (below) structures. Bond lengths are presented in Å. Point groups are shown in brackets.

6.4.3. ZEKE Spectral Simulations for Ce_3O

The ZEKE spectrum calculated for the Ce_3O ${}^6A \leftarrow {}^5A'$ (${}^6VIIA^+ \leftarrow {}^5VIIA$) transition is presented in Figure 6.11. ZEKE spectra for all other potential ionisation transitions shown in Figure 6.9 were calculated with very low intensities and are considered to have negligible contribution to the PIE spectrum. These spectra are presented in Appendix C. A correction of -0.04 eV was applied to the simulated Ce_3O ${}^6A \leftarrow {}^5A'$ (${}^6VIIA^+ \leftarrow {}^5VIIA$) ZEKE spectrum to achieve good

agreement with the experimental PIE spectrum (vide infra). The corrected ZEKE spectrum is shown.

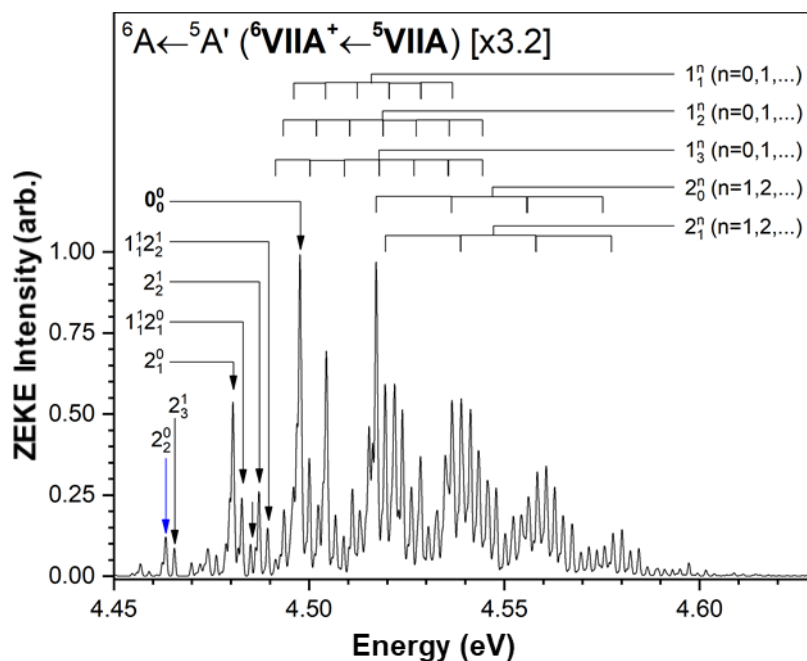


Figure 6.11: Simulated ZEKE spectrum for the Ce_3O ${}^6A \leftarrow {}^5A'$ (${}^6VIIA^+ \leftarrow {}^5VIIA$) ionisation transition. The spectral intensity is normalised to the most intense peak with scaling factor shown. Prominent vibronic peaks are assigned. The vibronic transition likely to correspond to the appearance of ion signal is labelled with a blue arrow.

Vibronic peaks in the thermal region of the ${}^6A \leftarrow {}^5A'$ (${}^6VIIA^+ \leftarrow {}^5VIIA$) ZEKE spectrum are mostly comprised of the ν_1 and ν_2 modes – which describe an asymmetric stretch of the Ce-Ce bonds and an out-of-plane bending of the Ce-O bonds, respectively – with $\nu_1\nu_2$ combination bands also observed. The post band-origin region is dominated by a number of short progressions from the ν_1 and ν_2 modes involving both the ground vibronic state and hot bands of the neutral species. Vibronic peaks in the 1_1^n , 1_2^n and 1_3^n progressions are separated by 0.0088 eV corresponding to the ν_1' frequency of 71 cm^{-1} . The 2_0^n and 2_1^n progressions similarly have vibronic peak separations of 0.013 eV corresponding to the ν_2' frequency of 108 cm^{-1} . The relatively strong intensities of the hot band progressions at a simulated temperature of 300 K is consistent with the low frequencies of the ν_1 and ν_2 modes in the neutral 5VIIA structure.

The 0_0^0 vibronic peak displays the maximum intensity – and thus maximum FC overlap – inferring minimal structural change between the neutral and cationic states.

6.4.4. Comparison of Simulated and Experimental PIE Spectra for Ce_3O

The simulated PIE spectrum for the Ce_3O ${}^6A \leftarrow {}^5A'$ (${}^6VIIA^+ \leftarrow {}^5VIIA$) transition is shown in Figure 6.12. The simulated PIE spectrum shows good agreement with the experimental PIE spectrum for the primary onset. The adiabatic IE for Ce_3O is taken as the corrected energy for the ${}^6A \leftarrow {}^5A'$ (${}^6VIIA^+ \leftarrow {}^5VIIA$) 0_0^0 vibronic transition; this gives an IE_{ad} value of 4.50 eV.

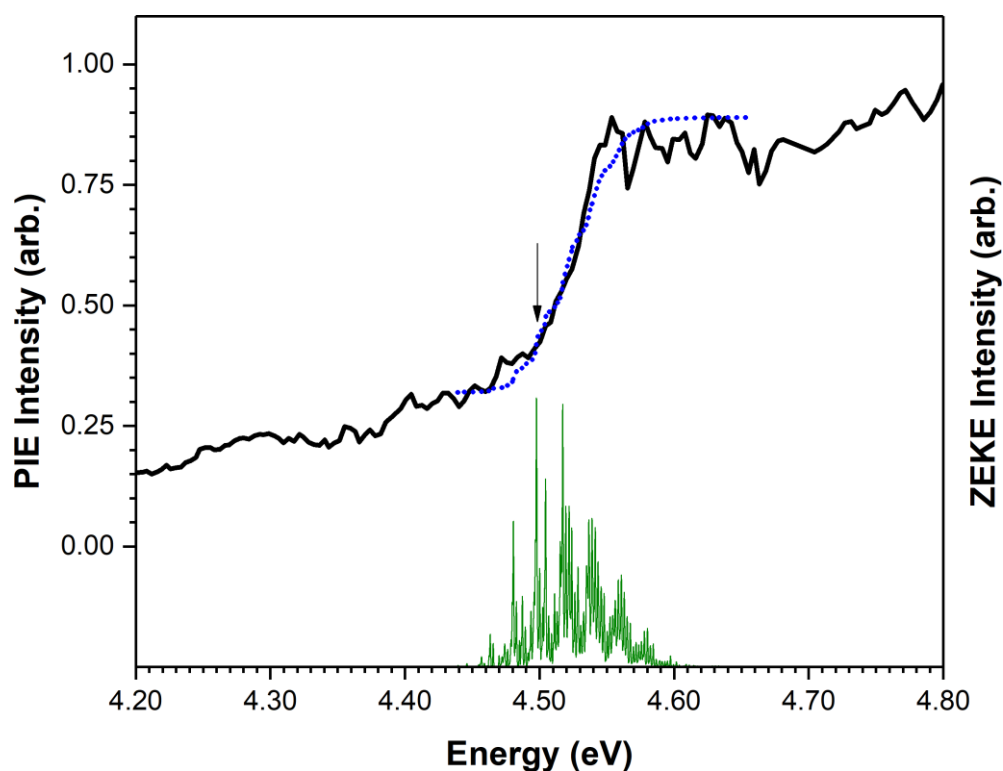


Figure 6.12: Simulated PIE spectrum for Ce_3O (blue dotted line) overlaid against the experimental PIE spectrum (solid black line). The calculated ZEKE spectrum for the ${}^6A \leftarrow {}^5A'$ (${}^6VIIA^+ \leftarrow {}^5VIIA$) ionisation process is shown below the PIE spectrum in green. The adiabatic ionisation energy is labelled with a black arrow.

6.5. PIE Spectrum and DFT Results for Ce_3O_2

6.5.1. Ce_3O_2 Experimental PIE Spectrum

The Ce_3O_2 PIE spectrum over the 3.92 – 5.17 eV (240 – 317.5 nm) energy range is presented in Figure 6.13. A flat region of near-zero ion signal intensity is initially recorded in the 3.92 – 4.02 eV range which is assigned as the baseline. A single onset of ion signal is then observed from 4.02 eV to a plateau at ca. 4.42 eV. Within this onset, considerable thermal tailing occurs from 4.02 eV until 4.06 eV as distinguished by the curved appearance of the spectrum. The AE is assigned as 4.06 eV – labelled with a black arrow in Figure 6.13 – from the intersection of trendlines fitted to the baseline and the ion signal onset. A nearly uniform slope is then observed between the AE and the ion signal plateau at 4.42 eV. The plateau corresponds to the maximum Ce_3O_2 ion signal recorded over the 3.92 – 5.17 eV (240 – 317.5 nm) energy range, indicating the highest energy FC-allowed transition has been accessed.

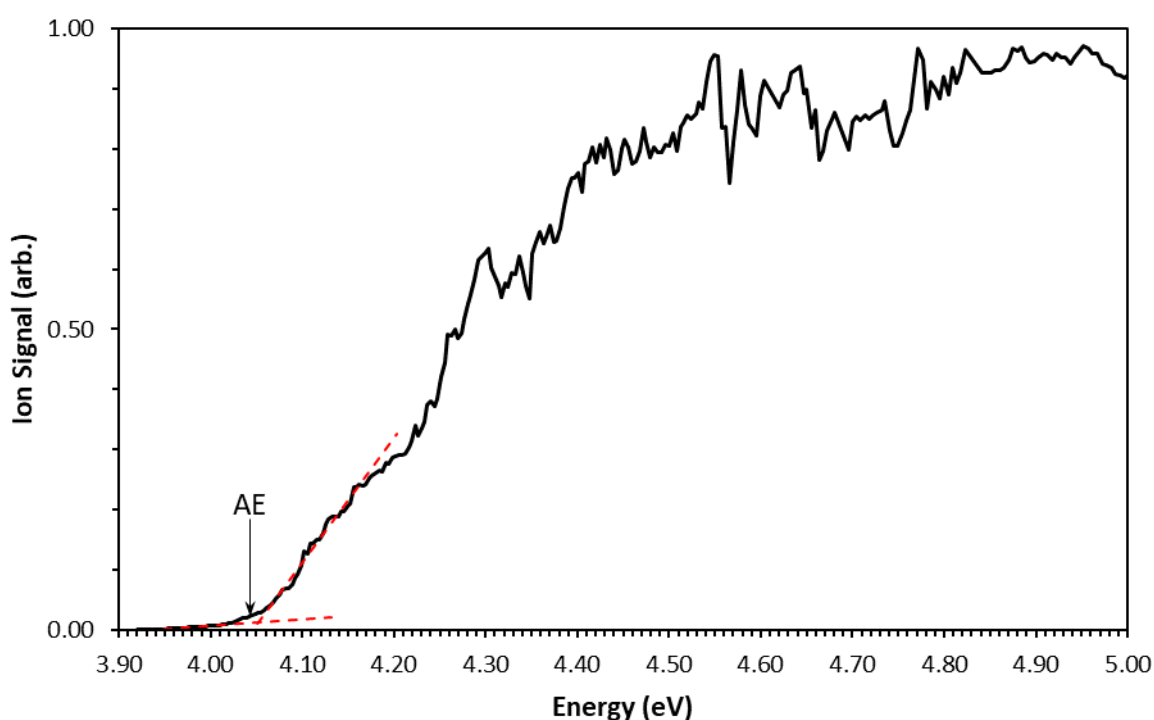


Figure 6.13: PIE spectrum for Ce_3O_2 . Linear trendlines for the baseline and onset are presented as red dashed lines. The appearance energy is labelled with a black arrow.

6.5.2. DFT Calculations for Ce_3O_2

Calculated Ce_3O_2 neutral and cationic structures are presented in Figures 6.14 and 6.15. Two unique Ce_3O_2 neutral structures are calculated which are labelled **VIIIA** and **VIIIB** in order of increasing energy. The **VIIIA** structure comprises a planar ring of oxygen and cerium atoms, with each oxygen atom inserted between 2 Ce atoms. The structure is C_{2v} symmetric and is calculated as a quintet in the 5B_2 electronic state, labelled 5VIIIA . The **VIIIB** structure contains 2 oxygen atoms bound to a Ce_3 trimer; one O atom is bound to the Ce_3 face while the other O atom bridges a Ce-Ce bond. The structure is C_1 symmetric and calculated in both triplet $-^1A-$ and quintet $-^5A-$ states, labelled 3VIIIB and 5VIIIB , respectively. The 3VIIIB and 5VIIIB structures are calculated with energies of +0.047 eV and +0.051 eV relative to the 5VIIIA LES, making all three neutral structures energetically indistinguishable in the context of this work. DFT optimisations were also performed on a trigonal bipyramidal geometry, which converged to the **VIIIB** structural arrangement.

Calculations of Ce_3O_2 cationic structures show 2 unique geometries – labelled **VIIIA**⁺ and **VIIIB**⁺ – with similar geometries to their respective neutral **VIIIA** and **VIIIB** structures. The **VIIIA**⁺ structure is calculated in the $^6A''$ and 4A electronic states – corresponding to C_s and C_1 symmetric structures, respectively – labelled $^6VIIIA^+$ and $^4VIIIA^+$, respectively. The **VIIIB**⁺ structure is calculated in the 6A , 4A and 2A electronic states – all of which have C_1 symmetric geometries – labelled $^6VIIIB^+$, $^4VIIIB^+$ and $^2VIIIB^+$, respectively. Five potential ionisation processes are considered in Figure 6.14; these include the $^6A'' \leftarrow ^5B_2$ ($^6VIIIA^+ \leftarrow ^5VIIIA$) (green), $^4A \leftarrow ^5B_2$ ($^4VIIIA^+ \leftarrow ^5VIIIA$) (orange), $^4A \leftarrow ^3A$ ($^4VIIIB^+ \leftarrow ^3VIIIB$) (blue), $^2A \leftarrow ^3A$ ($^2VIIIB^+ \leftarrow ^3VIIIB$) (violet), and $^4A \leftarrow ^5A$ ($^4VIIIB^+ \leftarrow ^5VIIIB$) (magenta) transitions with calculated IEs of 4.498 eV, 4.553 eV, 4.456 eV, 4.473 eV and 4.452 eV, respectively. The calculated IEs are all quite similar and thus consistent with the appearance of a single ionisation onset in the experimental PIE spectrum. The $^6A \leftarrow ^5A$ ($^6VIIIB^+ \leftarrow ^5VIIIB$) transition is additionally shown as a red dotted line in Figure 6.14 due to a weak ZEKE spectrum calculated for this ionisation process (vide infra).

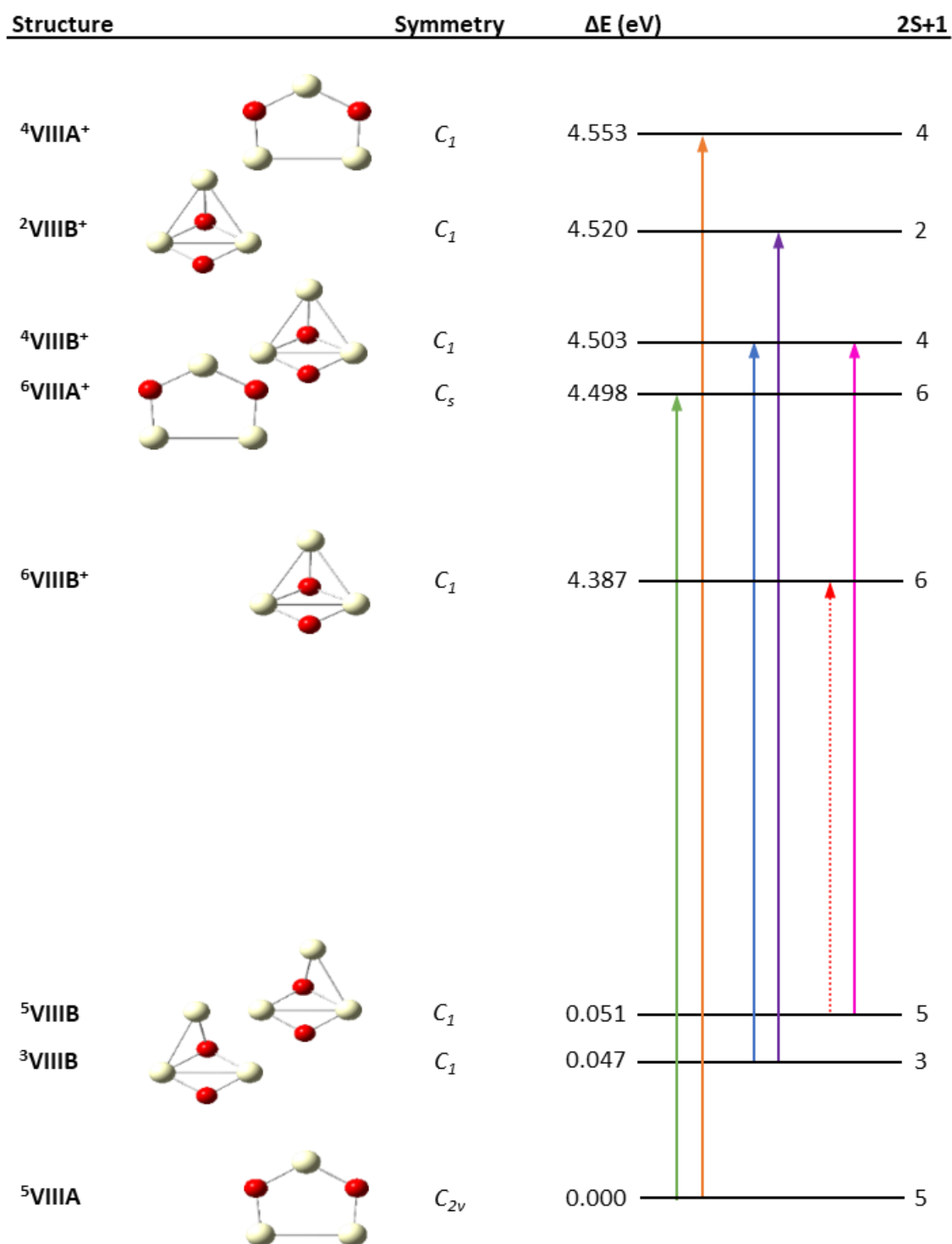


Figure 6.14: Ce_3O_2 calculated structures. Potential ionisation transitions are shown. Transitions with low ZEKE intensities (*vide infra*) are shown as red dotted arrows.

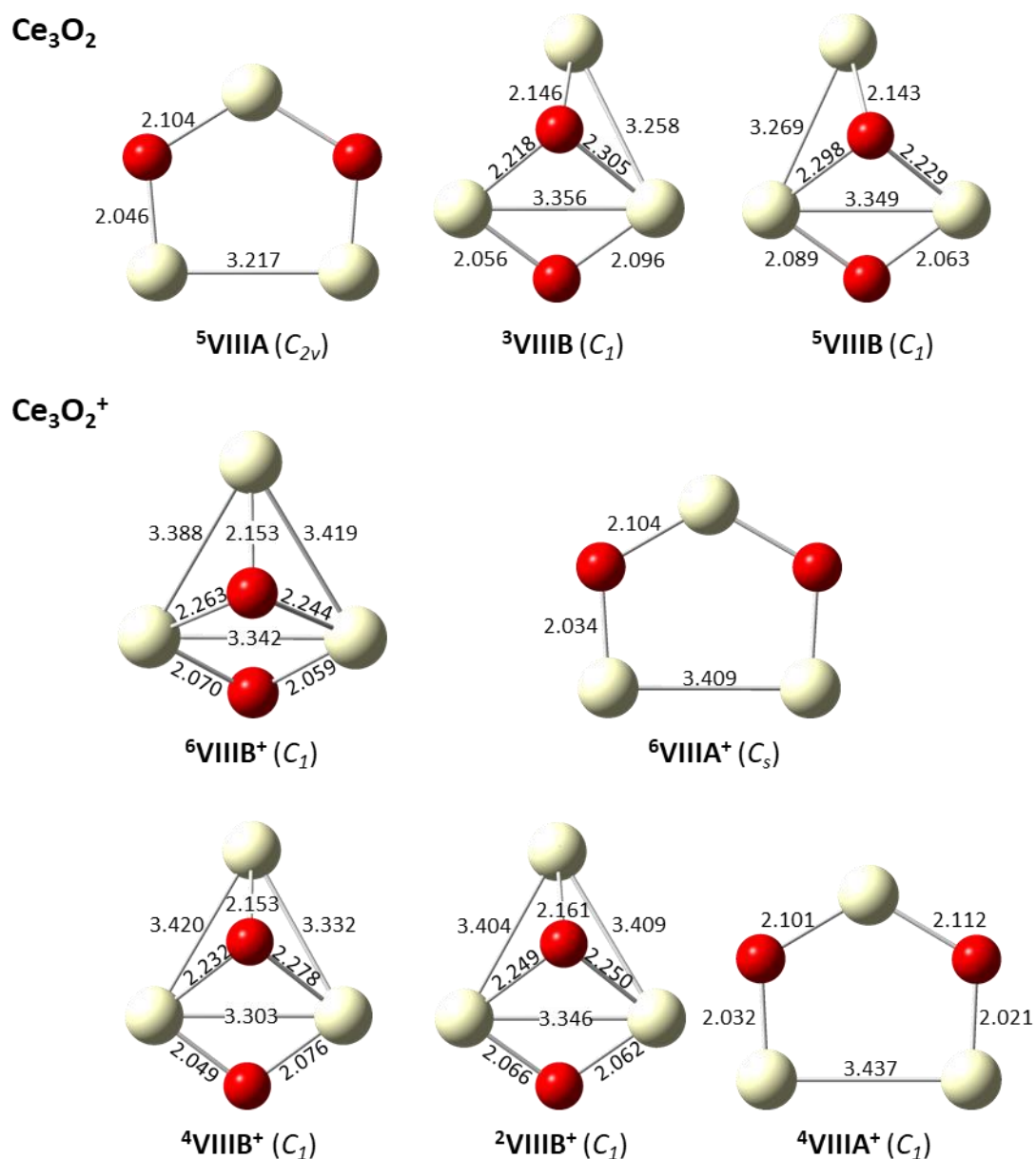


Figure 6.15: Calculated Ce_3O_2 neutral (top) and cationic (below) structures. Bond lengths are presented in Å. Point groups are shown in brackets.

6.5.3. ZEKE Spectral Simulations for Ce_3O_2

Simulated ZEKE spectra for Ce_3O_2 ionisation transitions – which include the ${}^6A'' \leftarrow {}^5B_2$ (${}^6V_{IIIA}^+ \leftarrow {}^5V_{IIIA}$), ${}^4A \leftarrow {}^5B_2$ (${}^4V_{IIIA}^+ \leftarrow {}^5V_{IIIA}$), ${}^4A \leftarrow {}^3A$ (${}^4V_{IIIB}^+ \leftarrow {}^3V_{IIIB}$), ${}^2A \leftarrow {}^3A$ (${}^2V_{IIIB}^+ \leftarrow {}^3V_{IIIB}$), ${}^6A \leftarrow {}^5A$ (${}^6V_{IIIB}^+ \leftarrow {}^5V_{IIIB}$) (red) and ${}^4A \leftarrow {}^5A$ (${}^4V_{IIIB}^+ \leftarrow {}^5V_{IIIB}$) are presented in Figure 6.16. Vibronic peak intensities for the ${}^6A \leftarrow {}^5A$ (${}^6V_{IIIB}^+ \leftarrow {}^5V_{IIIB}$) ZEKE spectrum were calculated to be

considerably weaker than the other ZEKE spectra shown in Figure 6.16; therefore, the ${}^6\text{A} \leftarrow {}^5\text{A}$ (${}^6\text{VIII B}^+ \leftarrow {}^5\text{VIII B}$) ionisation process was considered to have negligible contribution to the Ce₃O₂ PIE spectrum. The ${}^6\text{A} \leftarrow {}^5\text{A}$ (${}^6\text{VIII B}^+ \leftarrow {}^5\text{VIII B}$) ZEKE spectrum is shown in Appendix C. The ZEKE spectra were energetically corrected using the method described in Chapter 3. Subsequent corrections of +0.05 eV, +0.05 eV, +0.02 eV, +0.06 eV and +0.01 eV were applied to the ${}^6\text{A}'' \leftarrow {}^5\text{B}_2$ (${}^6\text{VIII A}^+ \leftarrow {}^5\text{VIII A}$), ${}^4\text{A} \leftarrow {}^5\text{B}_2$ (${}^4\text{VIII A}^+ \leftarrow {}^5\text{VIII A}$), ${}^4\text{A} \leftarrow {}^3\text{A}$ (${}^4\text{VIII B}^+ \leftarrow {}^3\text{VIII B}$), ${}^2\text{A} \leftarrow {}^3\text{A}$ (${}^2\text{VIII B}^+ \leftarrow {}^3\text{VIII B}$) and ${}^4\text{A} \leftarrow {}^5\text{A}$ (${}^4\text{VIII B}^+ \leftarrow {}^5\text{VIII B}$) vibronic transitions, respectively, in order to achieve a good fit between the simulated PIE spectrum (vide infra) and the experimental PIE spectrum. The corrected ZEKE spectra are shown here.

All calculated ZEKE spectra shown in Figure 6.16 generally comprise long vibronic progressions of combination modes. The 0_0^0 transition is not calculated in any of the spectra. Moreover, the lowest energy vibronic transitions in each spectrum describe vibronic transitions to highly excited vibrational modes in the cationic species; vibronic transitions corresponding to a thermal tail – i.e. transitions of the type ν_n^0 – are not calculated. These spectral characteristics infer significant structural differences between the neutral and cationic geometries.

The ${}^6\text{A}'' \leftarrow {}^5\text{B}_2$ (${}^6\text{VIII A}^+ \leftarrow {}^5\text{VIII A}$) ZEKE spectrum presented in Figure 6.16(a) comprises several combination mode progressions which include the $1_0^n 2_3^0$, $1_0^n 2_2^0 4_1^0$ and $1_0^n 2_2^0 3_0^1 4_1^0$ progressions. This implies a change in the vibrational coordinates between the neutral and cationic species, which may be attributed to the change in point group between the ${}^5\text{VIII A}$ (C_{2v}) and ${}^6\text{VIII A}^+$ (C_s) structures. A similar case can be made for the ${}^4\text{A} \leftarrow {}^5\text{B}_2$ (${}^4\text{VIII A}^+ \leftarrow {}^5\text{VIII A}$) ZEKE spectrum presented in Figure 6.16(b), which involves an ionisation transition from a C_{2v} neutral to a C_1 cation and is primarily made up of the $3_0^n 4_3^0$, $2_1^0 3_0^n 4_2^0$ and $2_1^1 3_0^n 4_2^0$ progressions. However, the strong intensities of the vibronic peaks in both spectra – as shown from the small scaling factors of 0.90 and 0.57 required to normalise the most intense peaks in the ${}^6\text{A}'' \leftarrow {}^5\text{B}_2$ (${}^6\text{VIII A}^+ \leftarrow {}^5\text{VIII A}$) and ${}^4\text{A} \leftarrow {}^5\text{B}_2$ (${}^4\text{VIII A}^+ \leftarrow {}^5\text{VIII A}$) spectra, respectively – suggests strong FC overlap between the neutral and cationic structures in both ionisation processes.

The ${}^4A \leftarrow {}^3A$ (${}^4VIII B^+ \leftarrow {}^3VIII B$) calculated ZEKE spectrum shown in Figure 6.16(c) displays very broad vibronic peaks; this is due to unresolved vibronic transitions (all vibronic peaks are convoluted with Gaussian functions to a FWHM of 5 cm^{-1}). While not all vibronic peaks were assigned, the prominent vibronic peaks describe numerous combination modes involving the ν_1 , ν_3 and ν_7 modes. The uniform separation between the vibronic peaks infers a number of vibronic progressions may be present in the ZEKE spectrum (although assigning progressions was difficult due to the number of vibronic transitions underlying each peak). The broad spectral profile – spanning a ca. 0.25 eV range – infers some structural deformation between the neutral and cationic species. However, the strong peak intensities – with a scaling factor of 0.56 required to normalise the most intense peak – suggest good FC overlap between the neutral and cationic species.

The ${}^2A \leftarrow {}^3A$ (${}^2VIII B^+ \leftarrow {}^3VIII B$) ZEKE spectrum shown in Figure 6.16(d), displays a very broad spectral profile – spanning a ca. 0.35 eV range – with is dominated by the 1_3^n , $1_3^n 7_0^1$, $1_3^n 7_0^2$ and $1_2^n 8_1^0$ progressions. The common progression of the ν_1 mode in all cases suggests structural deformation is occurring along the ν_1 vibrational coordinate. The very high peak intensities – with a scaling factor of 0.39 used to normalise the most intense peak – infers strong FC overlap between the neutral and cationic species. Moreover, the ${}^2A \leftarrow {}^3A$ (${}^2VIII B^+ \leftarrow {}^3VIII B$) transition describes the dominant ionisation process of the Ce_3O_2 cluster.

The ${}^4A \leftarrow {}^5A$ (${}^4VIII B^+ \leftarrow {}^5VIII B$) ZEKE spectrum presented in Figure 6.16(e) displays a similar spectral profile to the ${}^2A \leftarrow {}^3A$ (${}^2VIII B^+ \leftarrow {}^3VIII B$) ZEKE spectrum discussed previously. The spectrum appears quite broad – with vibronic peaks spanning a ca. 0.35 eV range – and is dominated by the 1_3^n , $1_2^n 2_1^0$, $1_2^n 2_1^0 7_0^1$ and $1_2^n 8_1^0$ progressions. The common progression of the ν_1 mode again infers deformation along the ν_1 vibrational coordinate. However, the peak intensity for the ${}^4A \leftarrow {}^5A$ (${}^4VIII B^+ \leftarrow {}^5VIII B$) ZEKE spectrum is considerably weaker than the ${}^4A \leftarrow {}^5A$ (${}^4VIII B^+ \leftarrow {}^5VIII B$) vibronic peaks – with a scaling factor of 0.7 required to normalise the most intense peak in the ${}^4A \leftarrow {}^5A$ (${}^4VIII B^+ \leftarrow {}^5VIII B$) spectrum – indicating the ${}^4A \leftarrow {}^5A$ (${}^4VIII B^+ \leftarrow {}^5VIII B$) ionisation process will have less contribution to the PIE spectrum.

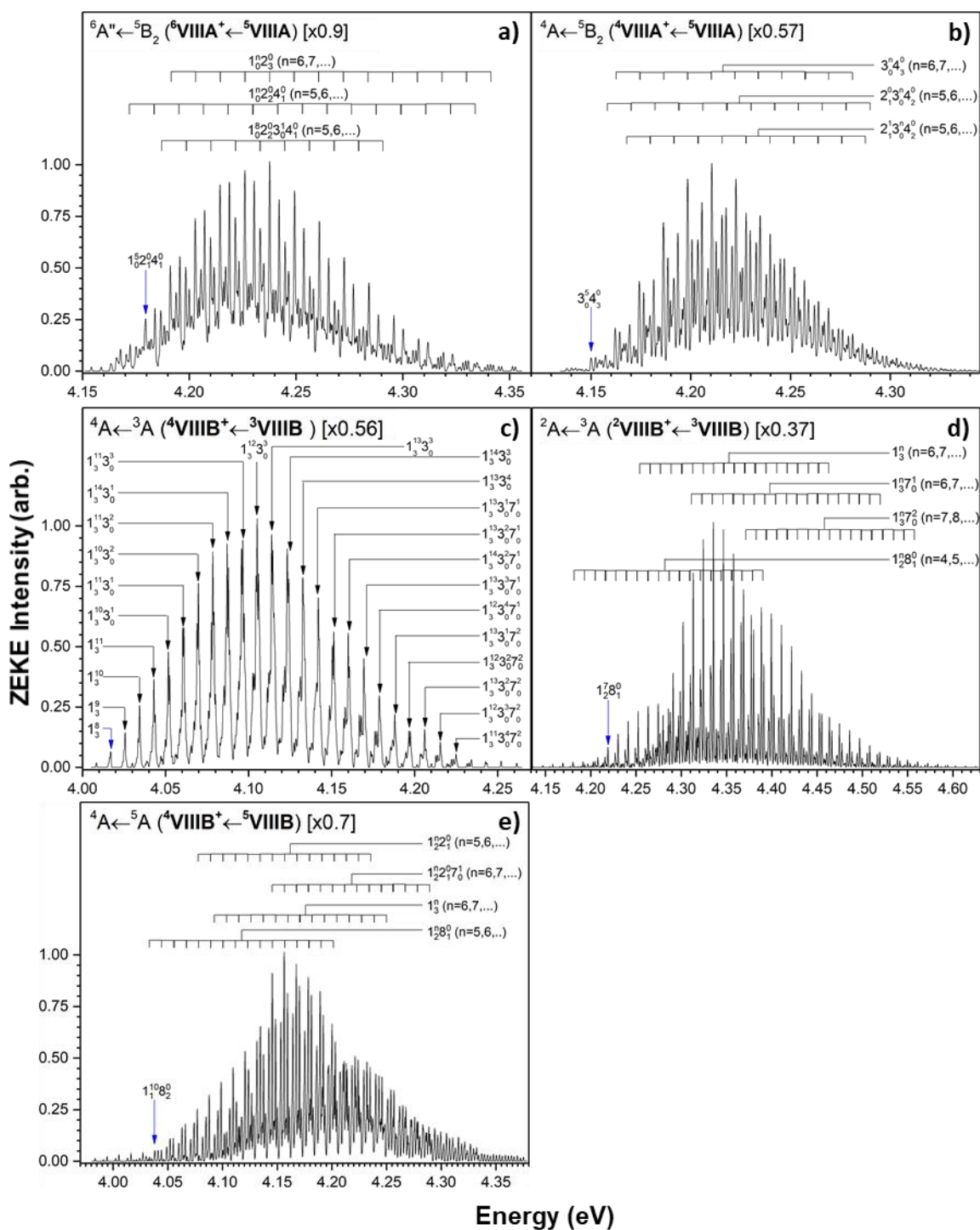


Figure 6.16: Simulated ZEKE spectra for Ce_3O_2 ionisation transitions: **a).** ${}^6A'' \leftarrow {}^5B_2$ (${}^6VIII^+ \leftarrow {}^5VIII$), **b).** ${}^4A \leftarrow {}^5B_2$ (${}^4VIII^+ \leftarrow {}^5VIII$), **c).** ${}^4A \leftarrow {}^3A$ (${}^4VIII^+ \leftarrow {}^3VIII$), **d).** ${}^2A \leftarrow {}^3A$ (${}^2VIII^+ \leftarrow {}^3VIII$) and **e).** ${}^4A \leftarrow {}^5A$ (${}^4VIII^+ \leftarrow {}^5VIII$). Spectral intensities are normalised relative to the most intense peak in each spectrum with scaling factors shown. Prominent vibronic peaks are assigned. The vibronic transition likely to correspond to the appearance of ion signal in each spectrum is labelled with a blue arrow.

6.5.4. Comparison of Simulated and Experimental PIE Spectra for Ce_3O_2

A calculated PIE spectrum for the Ce_3O_2 system – constructed via integration of the corrected ${}^6A'' \leftarrow {}^5B_2$ (${}^6VIII A^+ \leftarrow {}^5VIII A$), ${}^4A \leftarrow {}^5B_2$ (${}^4VIII A^+ \leftarrow {}^5VIII A$), ${}^4A \leftarrow {}^3A$ (${}^4VIII B^+ \leftarrow {}^3VIII B$), ${}^2A \leftarrow {}^3A$ (${}^2VIII B^+ \leftarrow {}^3VIII B$) and ${}^4A \leftarrow {}^5A$ (${}^4VIII B^+ \leftarrow {}^5VIII B$) ZEKE spectra – is presented in Figure 6.17. The simulated PIE spectrum correlates well to the experimental PIE spectrum over the entire PIE onset. The Ce_3O_2 adiabatic IE is assigned to the 0_0^0 transition for the ${}^6A'' \leftarrow {}^5B_2$ (${}^6VIII A^+ \leftarrow {}^5VIII A$) ionisation process which comprises the lowest energy ionisation process from the lowest energy neutral structure. This gives an adiabatic IE value of 4.14 eV, which is labelled with a black arrow in Figure 6.17.

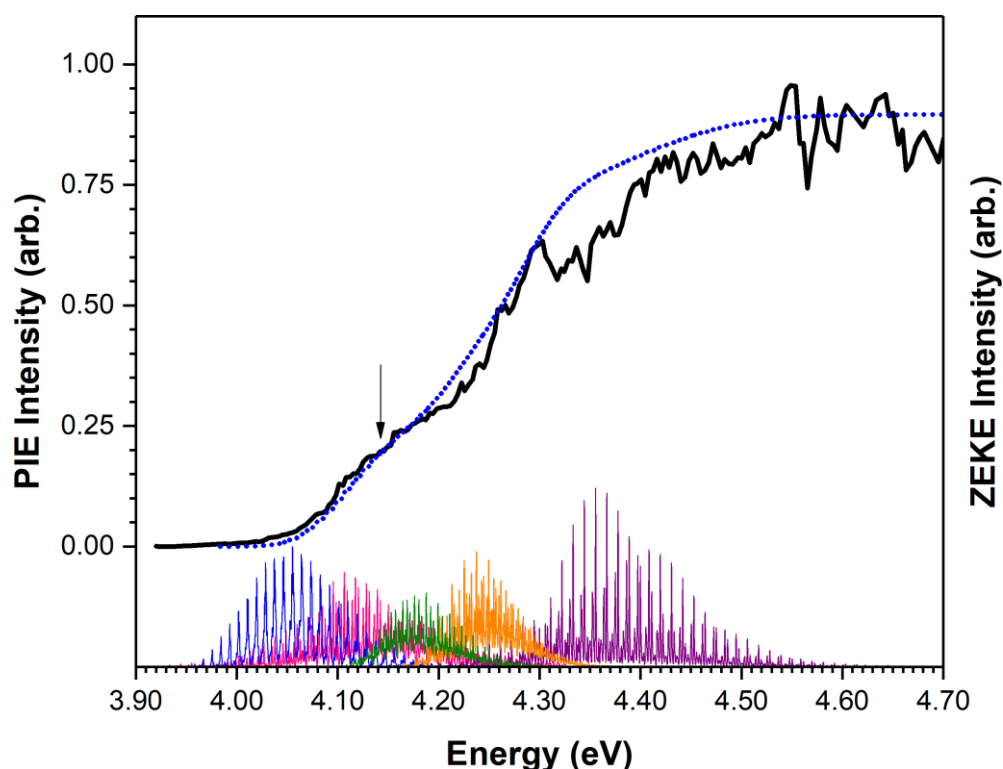


Figure 6.17: Simulated PIE spectrum for Ce_3O_2 (blue dotted line) overlaid against the experimental PIE spectrum (solid black line). Calculated ZEKE spectra for the ${}^6A'' \leftarrow {}^5B_2$ (${}^6VIII A^+ \leftarrow {}^5VIII A$), ${}^4A \leftarrow {}^5B_2$ (${}^4VIII A^+ \leftarrow {}^5VIII A$), ${}^4A \leftarrow {}^3A$ (${}^4VIII B^+ \leftarrow {}^3VIII B$), ${}^2A \leftarrow {}^3A$ (${}^2VIII B^+ \leftarrow {}^3VIII B$) and ${}^4A \leftarrow {}^5A$ (${}^4VIII B^+ \leftarrow {}^5VIII B$) transitions are shown below the PIE spectrum in green, orange, blue, violet and magenta, respectively. The adiabatic ionisation energy is labelled with a black arrow.

6.6. PIE Spectrum and DFT Results for Ce_3O_3

6.6.1. Ce_3O_3 Experimental PIE Spectrum

A PIE spectrum for the Ce_3O_3 system is presented in Figure 6.18. A flat region of zero ion signal is recorded over the range 3.92 – 3.94 eV, which is taken as the baseline. Two onset of ion signal are then observed. The lower energy onset begins at 3.94 eV and extends to a plateau at ca. 4.1 eV. The higher energy onset then appears at 4.24 eV and extends to a plateau of maximum ion signal at ca. 4.3 eV. The higher energy onset is characterised by a significantly sharper slope than the lower energy onset; however, both onsets show a comparable increase in Ce_3O_3 ion signal. The lower energy onset and higher energy onset are therefore labelled the *first onset* and *second onset*, respectively, with appearance energies shown in Figure 6.18 as AE_1 and AE_2 , respectively.

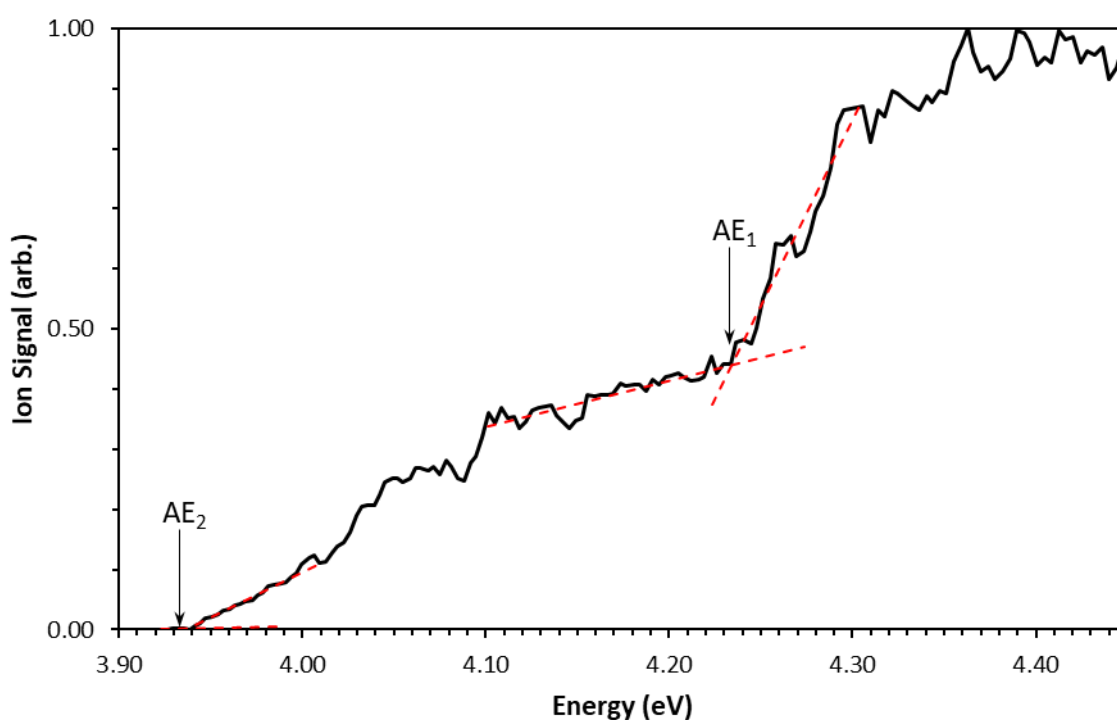


Figure 6.18: PIE spectrum for Ce_3O_3 . Linear trendlines for the baseline and onset are presented as red dashed lines. Appearance energies for the first onset and second onset – designated AE_1 and AE_2 respectively – are labelled with black arrows.

6.6.2. DFT Calculations for Ce_3O_3

Calculated Ce_3O_3 structures are presented in both Figures 6.19 and 6.20. Only one unique neutral structure is calculated – labelled **IX** – which comprises two Ce_2O_2 units bound along a common Ce-O bond. Despite numerous starting geometries, all calculations either converged to the **IX** structure or – in a small number of cases – terminated due to convergence errors. The **IX** structure is non-planar with a Ce-O-Ce – denoting the 3 atoms along the top of the Ce_3O_3 structure – angle of ca. 118° . The **IX** structure is calculated in two different spin states. These include a quintet with C_s symmetry in the $^5A'$ electronic state and a triplet with C_1 symmetry in the 3A electronic state, labelled 5IX and 3IX , respectively. The 5IX and 3IX species are energetically indistinguishable with a calculated energetic separation of 0.016 eV.

Calculations of the Ce_3O_3 cation show one unique structure – labelled **IX**⁺ which maintains a similar geometry to the neutral **IX** structure. This structure is calculated in doublet, quartet and sextet states. The doublet and quartet species – labelled $^2IX^+$ and $^4IX^+$, respectively – are nearly structurally identical; both show a decrease in the Ce-O-Ce angle – relative to the neutral **IX** structure – to ca. 105° . This is representative of an inward folding of the two Ce_2O_2 units following ionisation. These species are calculated as C_1 and C_s symmetric, respectively, in the 2A and $^4A''$ electronic states, respectively. The sextet species – labelled $^6IX^+$ – conversely shows an increase in the Ce-O-Ce angle to 132.5° , corresponding to an outward folding of the Ce_2O_2 units. This species is C_1 symmetric and is calculated in the 6A electronic state.

The calculated Ce_3O_3 neutral and cationic species give a total of 4 potential ionisation transitions; these include the $^4A'' \leftarrow ^5A'$ ($^4IX^+ \leftarrow ^5IX$), $^2A \leftarrow ^3A$ ($^2IX^+ \leftarrow ^3IX$), $^4A \leftarrow ^3A$ ($^4IX^+ \leftarrow ^3IX$) and $^6A \leftarrow ^5A'$ ($^6IX^+ \leftarrow ^5IX$) processes, which are shown in Figure 6.19 as green, orange, blue and violet arrows, respectively. IEs for these processes are calculated as 4.216 eV, 4.198 eV, 4.200 eV and 4.584 eV, respectively. The $^4A'' \leftarrow ^5A'$ ($^4IX^+ \leftarrow ^5IX$), $^2A \leftarrow ^3A$ ($^2IX^+ \leftarrow ^3IX$), $^4A \leftarrow ^3A$ ($^4IX^+ \leftarrow ^3IX$) processes, which have similar IE values, are assigned to the first onset in the Ce_3O_3 PIE spectrum. The $^6A \leftarrow ^5A'$ ($^6IX^+ \leftarrow ^5IX$) process, which has a calculated IE value ca. 0.36 eV higher than the other ionisation transitions, is assigned to the second onset. This difference in

calculated IE values is consistent with the 0.30 eV difference between the appearance energies of the first and second onsets in the experimental PIE spectrum.

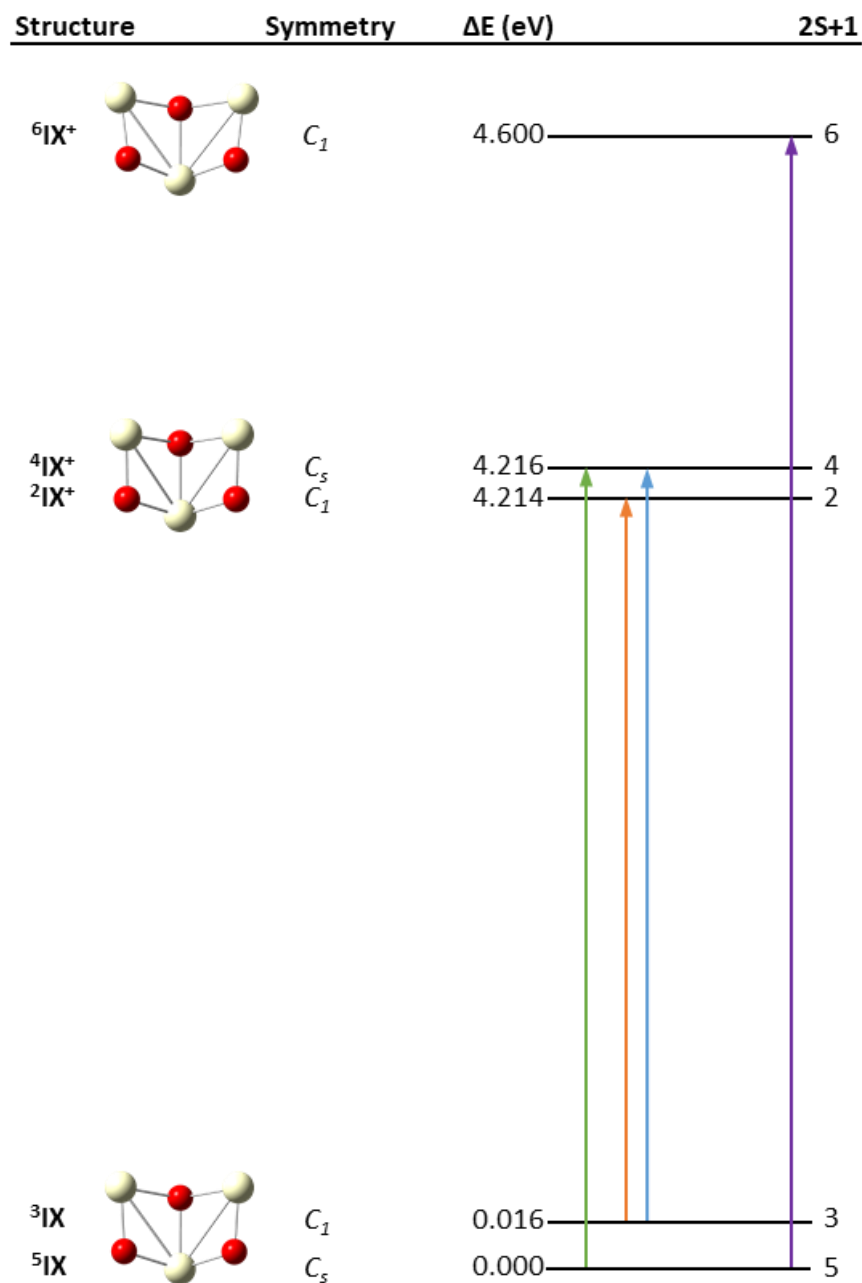


Figure 6.19: Ce_3O_3 calculated structures. Potential ionisation transitions are shown.

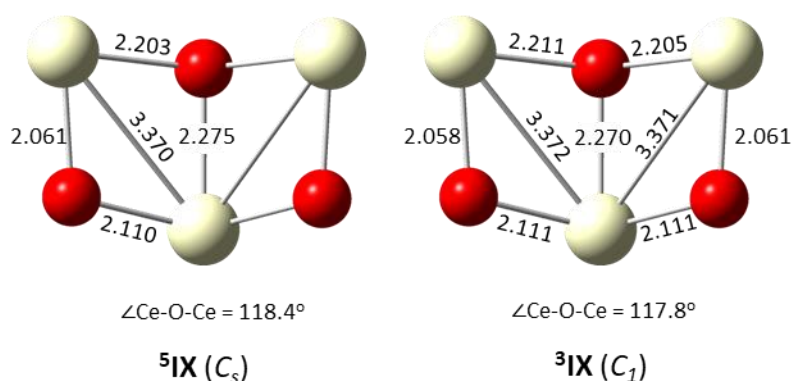
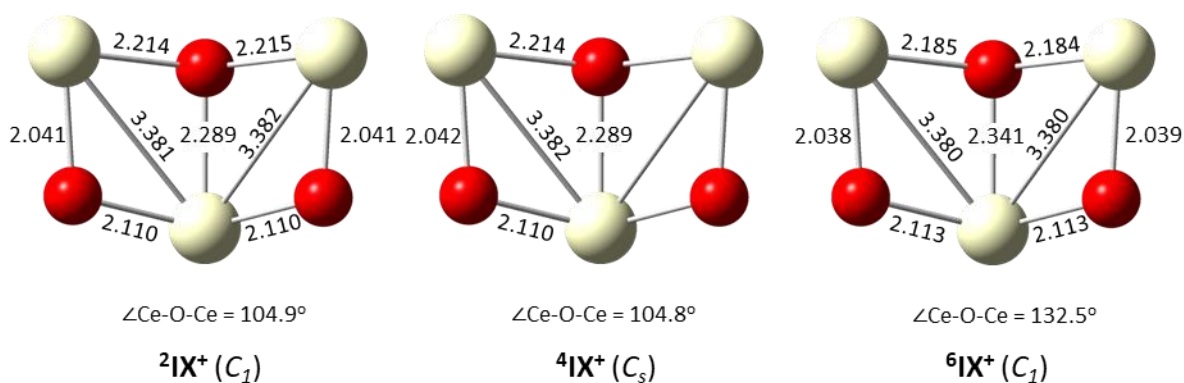
Ce_3O_3  $Ce_3O_3^+$ 

Figure 6.20: Calculated Ce_3O_3 neutral (top) and cationic (below) structures. Bond lengths are presented in Å. Point groups are shown in brackets.

6.6.3. ZEKE Spectral Simulations for Ce_3O_3

Calculated ZEKE spectra for the Ce_3O_3 $^4A'' \leftarrow ^5A'$ ($^4IX^+ \leftarrow ^5IX$), $^2A \leftarrow ^3A$ ($^2IX^+ \leftarrow ^3IX$), $^4A \leftarrow ^3A$ ($^4IX^+ \leftarrow ^3IX$) ionisation processes – corresponding to the first onset – are shown in Figure 6.21. The calculated ZEKE spectrum for the $^6A \leftarrow ^5A'$ ($^6IX^+ \leftarrow ^5IX$) transition – corresponding to the second onset – is presented in Figure 6.22. Due to the extensive number of vibrationally excited states required to be calculated for these ionisation processes, a full Duschinsky treatment was not viable. The Parallel Approximation was instead used to calculate the Ce_3O_3 ionisation processes. The relevant ZEKE spectra were corrected to the first and second onsets using the method shown in Chapter 3. This involved correcting the lowest energy vibronic transition of the lowest energy ionisation process to the AE; higher energy transitions were

then offset by their relative differences in calculated IE values. The corrected ZEKE spectra are presented here.

Spectral profiles for the ${}^4A'' \leftarrow {}^5A'$ (${}^4IX^+ \leftarrow {}^5IX$), ${}^2A \leftarrow {}^3A$ (${}^2IX^+ \leftarrow {}^3IX$) and ${}^4A \leftarrow {}^3A$ (${}^4IX^+ \leftarrow {}^3IX$) transitions shown in Figure 6.21 – which correspond to the first onset – are all quite similar. All three spectra span the ca. 3.85 – 4.25 eV energy range and are dominated by long progressions of the cationic ν_1 vibrational mode; both by itself and combined with the ν_2 and ν_3 modes of both the neutral and cationic species. The ν_1 mode corresponds to a rotation of the two Ce₂O₂ units along the common Ce-O bond in a folding motion. Vibration of the ${}^2IX^+$ and ${}^4IX^+$ species along the ν_1 coordinate yields the respective 5IX and 3IX neutral geometry. Thus, progressions of the ν_1 mode are expected. Peak separations of the 1_0^n , $1_0^n 3_0^1$ and $1_0^n 2_1^1$ progressions in the ${}^4A'' \leftarrow {}^5A'$ (${}^4IX^+ \leftarrow {}^5IX$) ZEKE spectrum and the 1_0^n , $1_1^n 3_0^1$, $1_0^n 3_0^2$ and $1_0^n 2_1^1 3_0^1$ progressions in the ${}^4A \leftarrow {}^3A$ (${}^4IX^+ \leftarrow {}^3IX$) ZEKE spectrum are calculated as 0.0130 eV corresponding to the ${}^4IX^+$ ν_1 frequency of 104.99 cm⁻¹. Similar for the ${}^2A \leftarrow {}^3A$ (${}^2IX^+ \leftarrow {}^3IX$) ZEKE spectrum, vibronic peaks in the 1_0^n , 1_2^n , $1_0^n 3_0^1$, $1_0^n 3_0^2$, $1_0^n 3_1^1$ and $1_3^n 3_0^1$ progressions all are separated by 0.129 eV corresponding to the ${}^2IX^+$ ν_1 frequency of 104.08 cm⁻¹. Comparison of the spectral intensities of the ${}^4A'' \leftarrow {}^5A'$ (${}^4IX^+ \leftarrow {}^5IX$), ${}^2A \leftarrow {}^3A$ (${}^2IX^+ \leftarrow {}^3IX$) and ${}^4A \leftarrow {}^3A$ (${}^4IX^+ \leftarrow {}^3IX$) ZEKE spectra – where scaling factors of 39.1, 34 and 26, respectively, are applied to normalise the most intense vibronic peak in each spectrum – show similar peak intensities. Therefore, all three ionisation transitions are expected to have a similar contribution to the PIE onset. While these spectral intensities are reasonable, inferring a good FC overlap, the more prominent vibronic peaks tend to correlate with significant distortion of the cationic species; the $1_0^2 3_0^1$ vibronic transition corresponds to maximum FC overlap in all three spectra. Moreover, the 0_0^0 transition is not calculated in any of the spectra.

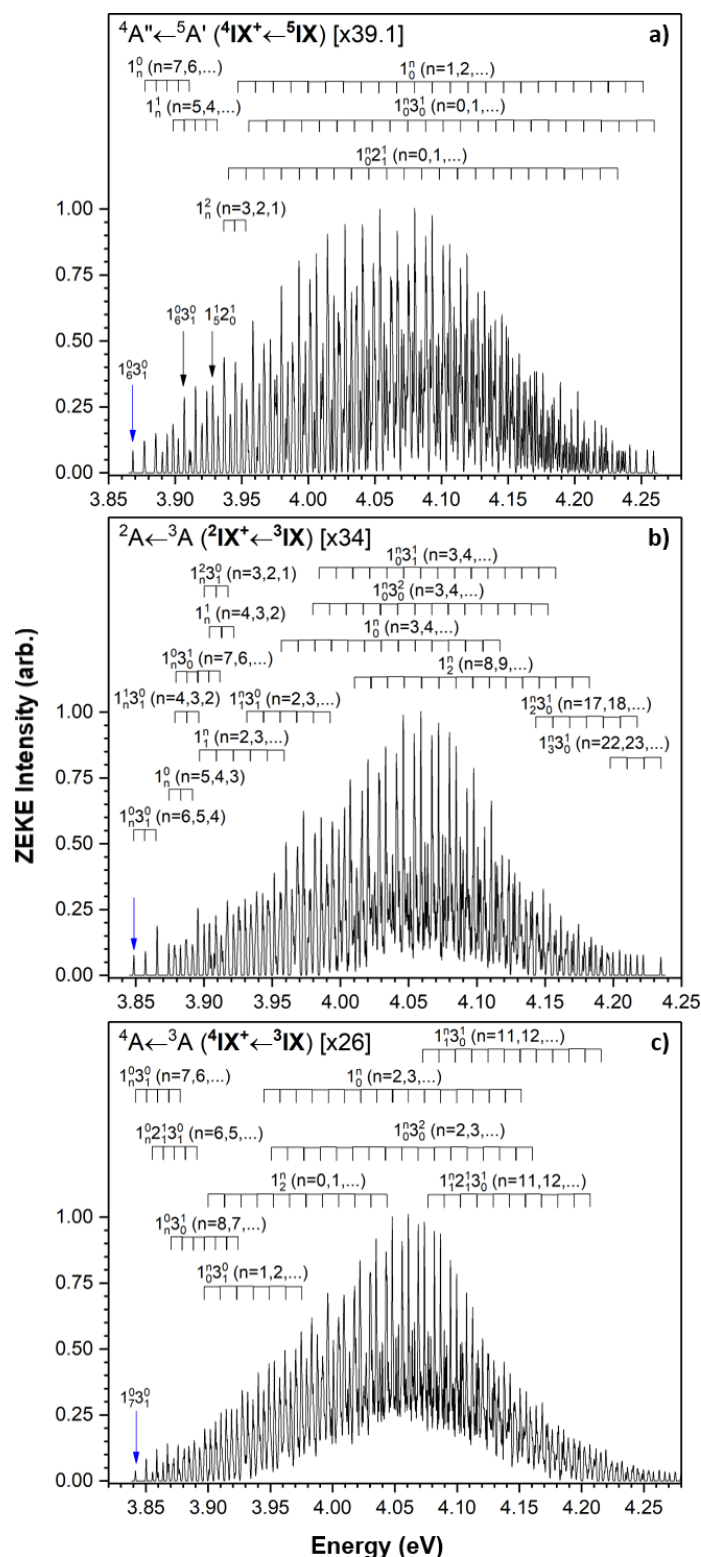


Figure 6.21: Simulated ZEKE spectra for Ce_3O_3 ionisation transitions corresponding to the first onset: **a).** ${}^4A'' \leftarrow {}^5A'$ (${}^4IX^+ \leftarrow {}^5IX$), **b).** ${}^2A \leftarrow {}^3A$ (${}^2IX^+ \leftarrow {}^3IX$) and **c).** ${}^4A \leftarrow {}^3A$ (${}^4IX^+ \leftarrow {}^3IX$). Spectral intensities are normalised relative to the most prominent peak in each spectrum with scaling factors shown. The vibronic transition likely to correspond to the appearance of ion signal in each spectrum is labelled with a blue arrow.

The simulated ZEKE spectrum for the ${}^6A \leftarrow {}^5A'$ (${}^6IX^+ \leftarrow {}^5IX$) ionisation transition – corresponding to the second onset – is presented in Figure 6.22. The vibronic peaks in this spectrum appear quite broad; with each peak containing numerous vibronic transitions which are not resolved. This broadening effect is due to closely spaced vibronic peaks which become merged following convolution with Gaussian functions to a 5 cm^{-1} FWHM during the post-calculation treatment. The spectral profile is considerably narrower than for the ${}^4A'' \leftarrow {}^5A'$ (${}^4IX^+ \leftarrow {}^5IX$), ${}^2A \leftarrow {}^3A$ (${}^2IX^+ \leftarrow {}^3IX$) and ${}^4A \leftarrow {}^3A$ (${}^4IX^+ \leftarrow {}^3IX$) spectra discussed previously – spanning a range of ca 0.2 eV – which is consistent with the shaper onset observed in the PIE spectrum. Moreover, the vibronic peak intensities in the ${}^6A \leftarrow {}^5A'$ (${}^6IXA^+ \leftarrow {}^5IXA$) ZEKE spectrum are approximately three times more intense than those calculated in the first onset ${}^4A'' \leftarrow {}^5A'$ (${}^4IX^+ \leftarrow {}^5IX$), ${}^2A \leftarrow {}^3A$ (${}^2IX^+ \leftarrow {}^3IX$) and ${}^4A \leftarrow {}^3A$ (${}^4IX^+ \leftarrow {}^3IX$) ionisation transitions. Considering that the first onset comprises three ionisation processes, while the second onset has only one underlying ionisation process, similar increases in Ce_3O_3 ion signal would be expected across both onsets; which is observed. The ${}^6A \leftarrow {}^5A'$ (${}^6IXA^+ \leftarrow {}^5IXA$) ZEKE spectrum is again dominated by progressions of the ν_1 mode, which is mostly coupled with the ν_5 mode. The maximum FC transition corresponds to the $1_0^3 5_0^1$ vibronic peak which has considerably less vibrational excitation than the $1_0^9 3_0^1$ maximum FC transition for the primary onset transitions; inferring a stronger FC overlap. However, the 0_0^0 transition is not calculated.

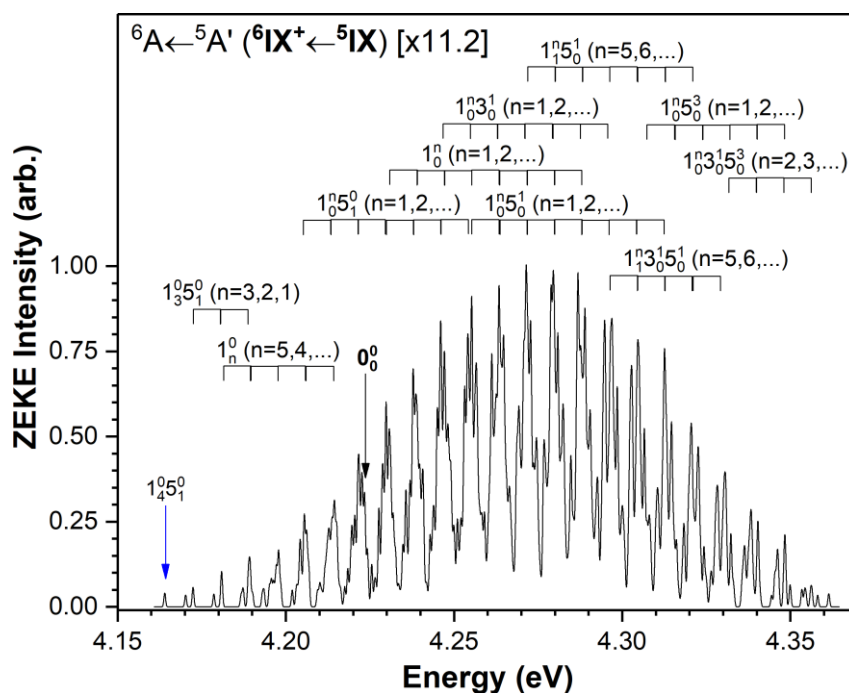


Figure 6.22: Simulated ZEKE spectrum for the Ce_3O_3 ${}^6A \leftarrow {}^5A'$ (${}^6IX^+ \leftarrow {}^5IX$) ionisation transition corresponding to the second onset. The spectral intensity is normalised relative to the most prominent peak in the spectrum with scaling factor is shown. Prominent vibronic peaks are assigned. The vibronic transition likely to correspond to the appearance of ion signal is labelled with a blue arrow.

6.6.4. Comparison of Simulated and Experimental PIE Spectra for Ce_3O_3

Simulated PIE spectra for both the first and second onsets are presented in Figure 6.23. The primary onset PIE spectrum was constructed from a combination of the integrated ${}^4A'' \leftarrow {}^5A'$ (${}^4IX^+ \leftarrow {}^5IX$), ${}^2A \leftarrow {}^3A$ (${}^2IX^+ \leftarrow {}^3IX$) and ${}^4A \leftarrow {}^3A$ (${}^4IX^+ \leftarrow {}^3IX$) ZEKE spectra. The second onset PIE spectrum was constructed via integration of the calculated ${}^6A \leftarrow {}^5A'$ (${}^6IX^+ \leftarrow {}^5IX$) ZEKE spectrum. Both calculated PIE spectra show excellent agreement with their respective experimental PIE onsets. IEs for the first and second onsets are assigned to the ${}^4A'' \leftarrow {}^5A'$ (${}^4IX^+ \leftarrow {}^5IX$) and ${}^6A \leftarrow {}^5A'$ (${}^6IX^+ \leftarrow {}^5IX$) spectra as 3.94 eV and 4.22 eV, respectively. While both IE values describe ionisation processes from the lowest energy neutral structure, the lower energy IE value is more interesting in the context of this work since it is more closely aligned with the HOMO energy of the neutral cluster. Thus, the Ce_3O_3 IE is presented as 3.94 eV.

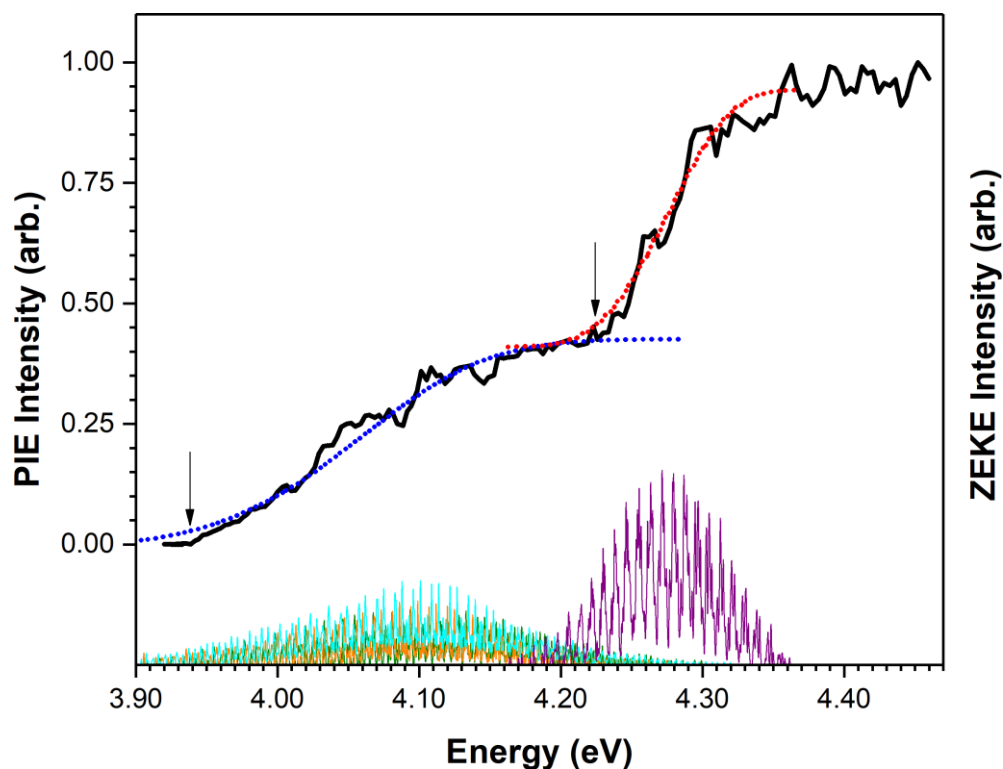


Figure 6.23: Ce_3O_3 PIE spectra for the first and second onsets (blue and red dotted lines, respectively) overlaid against the experimental PIE spectrum (solid black line). Calculated ZEKE spectra for the ${}^4A'' \leftarrow {}^5A'$ (${}^4IX^+ \leftarrow {}^5IX$), ${}^2A \leftarrow {}^3A$ (${}^2IX^+ \leftarrow {}^3IX$), ${}^4A \leftarrow {}^3A$ (${}^4IX^+ \leftarrow {}^3IX$) and ${}^6A \leftarrow {}^5A'$ (${}^6IX^+ \leftarrow {}^5IX$) processes are shown below the PIE spectrum in green, orange, blue and violet, respectively. The adiabatic ionisation energy for each onset is labelled with a black arrow.

6.7. PIE Spectrum and DFT Results for Ce_3O_4

6.7.1. Ce_3O_4 Experimental PIE Spectrum

The Ce_3O_4 PIE spectrum is presented in Figure 6.24. A very short region of zero ion signal is recorded over the 3.92 – 3.95 eV energy range; this region is assigned as the baseline. Two onsets of Ce_3O_4 ion signal are then recorded. A low energy onset begins at 3.95 eV and extends to a plateau at ca. 4.1 eV. A higher energy onset then begins at 4.21 eV and extends to a plateau of maximum ion signal at 4.64 eV; this plateau indicates the highest energy FC allowed transition has been accessed. The higher energy onset describes the majority of the Ce_3O_4 ion signal increase and is thus labelled the primary onset. The lower energy onset shows a very weak ion signal increase and is labelled the secondary onset. The appearance energies for the primary and secondary onsets – labelled AE_1 and AE_2 , respectively – are taken from the intersection of trendlines fitted to the baseline and slope of each onset to give values of 3.95 eV and 4.21 eV, respectively.

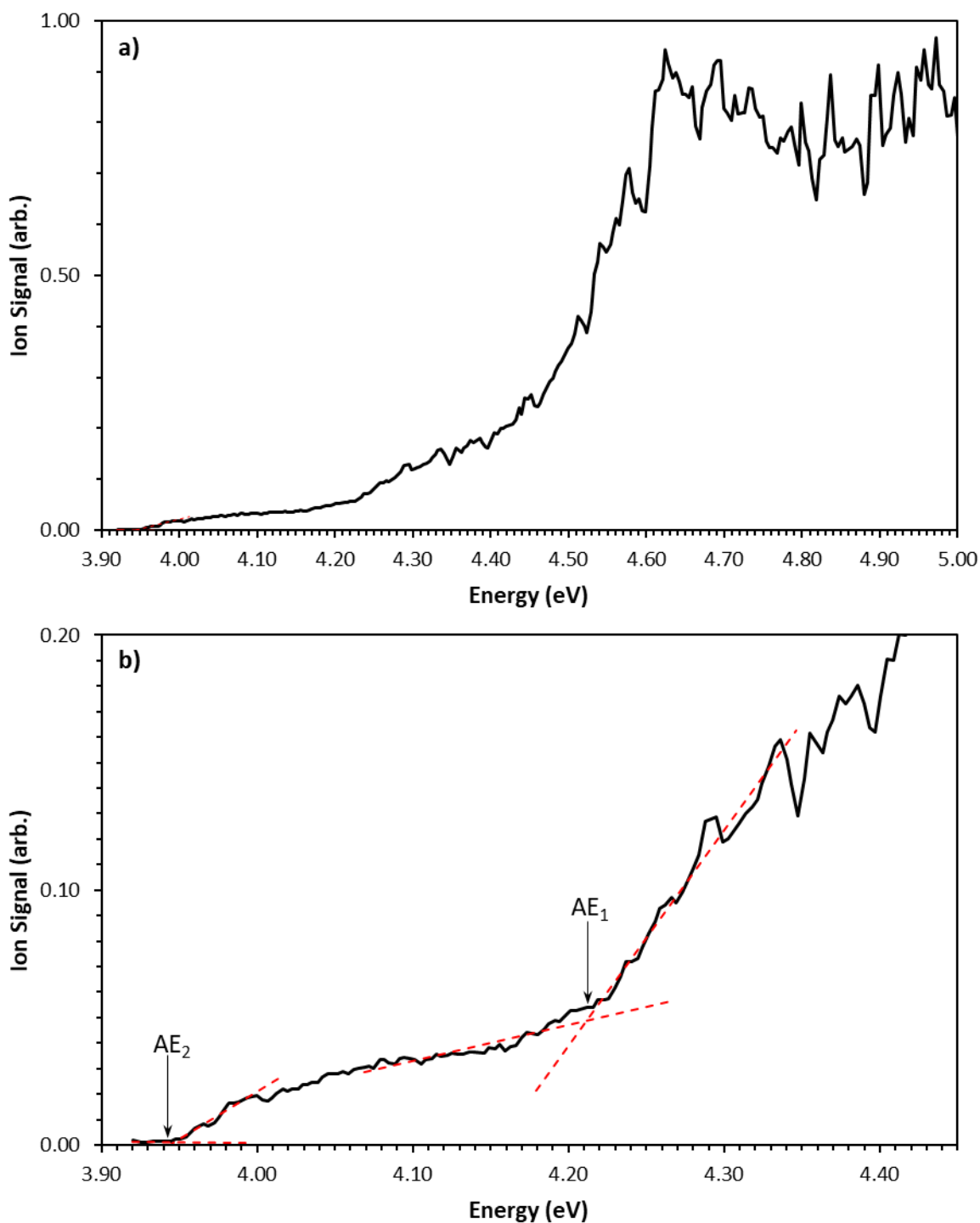


Figure 6.24: PIE spectrum for Ce_3O_4 showing (a). entire spectrum and (b). region of PIE onsets. Appearance energies for the primary and secondary onsets - designated AE_1 and AE_2 respectively - are labelled with black arrows.

6.7.2. DFT Calculations for Ce_3O_4

Calculated Ce_3O_4 structures are presented in Figures 6.25 and 6.26. Two unique structures are calculated which are labelled **XA** and **XB** in order of increasing energy. The **XA** structure comprises a Ce_3 trimer with three oxygen atoms – positioned above the Ce_3 plane – bridging each Ce-Ce bond and a fourth oxygen atom – below the Ce_3 plane – facially bound to the Ce_3 trimer. This structure is calculated as C_1 symmetric, although very closely approaches C_{3v} symmetry (calculations of the C_{3v} constrained structure were attempted but not completed due to convergence issues). The **XA** structure is calculated in a number of spin states; these include the quintet, triplet and singlet species – labelled $^5\mathbf{XA}$, $^3\mathbf{XA}$ and $^1\mathbf{XA}$, respectively – in the 5A , 3A and 1A electronic states, respectively. The small energetic differences between these spin-isomers – where the energies of the $^3\mathbf{XA}$ and $^1\mathbf{XA}$ species relative to the $^5\mathbf{XA}$ LES are calculated as +0.021 eV and +0.043 eV, respectively – makes all three **XA** species energetically indistinguishable in the context of this work.

The Ce_3O_4 **XB** structure consists of a CeO_2 unit facially bound to a Ce_2O_2 moiety. The structure is C_1 symmetric, although approaches a C_{2v} symmetry (symmetry constrained calculations were again attempted but not completed due to convergence issues). Two unique neutral spin-isomers are calculated; these include a quintet in the 5A electronic state and a triplet in the 3A state, labelled $^5\mathbf{XB}$ and $^3\mathbf{XB}$ respectively. Both species are considerably higher in energy than the **XA** structures, with calculated energies of +0.237 eV and +0.272 eV respectively relative to the $^5\mathbf{XA}$ LES.

Calculated Ce_3O_4 cations show two unique geometries which are similar to the neutral **XA** and **XB** species; these cationic structures are thus labelled \mathbf{XA}^+ and \mathbf{XB}^+ , respectively. The \mathbf{XA}^+ structure is calculated in the 2A , 4A and 6A electronic states which are labelled $^2\mathbf{XA}^+$, $^4\mathbf{XA}^+$ and $^6\mathbf{XA}^+$, respectively. The $^4\mathbf{XA}^+$ and $^2\mathbf{XA}^+$ species are energetically indistinguishable – with calculated energies of +3.899 eV and +3.900 eV relative to the $^5\mathbf{XA}$ LES, respectively – and are structurally similar to all neutral **XA** species; albeit with a ca. 0.5% elongation of the Ce-Ce bond lengths compared to the neutral **XA** structure. Conversely, the $^6\mathbf{XA}^+$ species shows considerable elongation the two Ce-O bonds of one of the bridging O atoms (the top O atom

in Figure 6.26). This ${}^6\mathbf{XA}^+$ structure is calculated as near C_s symmetric; however, the high energy of the ${}^6\mathbf{XA}^+$ structure – calculated as +8.192 eV relative to the ${}^5\mathbf{XA}$ LES – precludes the formation of this species under the ionisation conditions used in this work. Therefore, symmetry constrained calculations of the ${}^6\mathbf{XA}^+$ structure were not attempted. The \mathbf{XB}^+ structure is calculated with energetically indistinguishable quartet and doublet species in the ${}^4\mathbf{A}$ and ${}^2\mathbf{A}$ electronic states, respectively – with energies of +4.511 eV and +4.512 eV relative to the ${}^5\mathbf{XA}$ LES, respectively – in addition to a high energy sextet species in the ${}^6\mathbf{A}$ electronic state with a calculated energy of +7.956 eV relative to the LES. The high energy calculated for the sextet species would prevent formation of this cation under the ionisation conditions in this work. The quartet, doublet and sextet \mathbf{XB}^+ species are labelled ${}^4\mathbf{XB}^+$, ${}^2\mathbf{XB}^+$ and ${}^6\mathbf{XB}^+$, respectively.

Potential Ce_3O_4 ionisation transitions are presented in Figure 6.25. Ionisation transitions from the \mathbf{XA} structure include the ${}^4\mathbf{A} \leftarrow {}^5\mathbf{A}$ (${}^4\mathbf{XA}^+ \leftarrow {}^5\mathbf{XA}$), ${}^2\mathbf{A} \leftarrow {}^3\mathbf{A}$ (${}^4\mathbf{XA}^+ \leftarrow {}^3\mathbf{XA}$), ${}^4\mathbf{A} \leftarrow {}^3\mathbf{A}$ (${}^4\mathbf{XA}^+ \leftarrow {}^3\mathbf{XA}$) and ${}^2\mathbf{A} \leftarrow {}^1\mathbf{A}$ (${}^2\mathbf{XA}^+ \leftarrow {}^1\mathbf{XA}$) transitions shown – on the left side of Figure 6.25 – as green, orange, blue and violet arrows, respectively. IEs for these processes are calculated as 3.899 eV, 3.878 eV, 3.879 eV and 3.856 eV, respectively. Ionisation processes from the \mathbf{XB} structure include the ${}^4\mathbf{A} \leftarrow {}^5\mathbf{A}$ (${}^4\mathbf{XB}^+ \leftarrow {}^5\mathbf{XB}$), ${}^4\mathbf{A} \leftarrow {}^3\mathbf{A}$ (${}^4\mathbf{XB}^+ \leftarrow {}^3\mathbf{XB}$) and ${}^2\mathbf{A} \leftarrow {}^3\mathbf{A}$ (${}^4\mathbf{XB}^+ \leftarrow {}^3\mathbf{XB}$) transitions which are shown – on the right side of Figure 6.25 – as green, orange and blue arrows, respectively; IEs for these processes are calculated as 4.274 eV, 4.239 eV and 4.240 eV, respectively. The ${}^4\mathbf{A} \leftarrow {}^5\mathbf{A}$ (${}^4\mathbf{XB}^+ \leftarrow {}^5\mathbf{XB}$), ${}^4\mathbf{A} \leftarrow {}^3\mathbf{A}$ (${}^4\mathbf{XB}^+ \leftarrow {}^3\mathbf{XB}$) and ${}^2\mathbf{A} \leftarrow {}^3\mathbf{A}$ (${}^4\mathbf{XB}^+ \leftarrow {}^3\mathbf{XB}$) transitions are assigned to the primary onset – due to their higher calculated IEs – while the ${}^4\mathbf{A} \leftarrow {}^5\mathbf{A}$ (${}^4\mathbf{XA}^+ \leftarrow {}^5\mathbf{XA}$), ${}^2\mathbf{A} \leftarrow {}^3\mathbf{A}$ (${}^4\mathbf{XA}^+ \leftarrow {}^3\mathbf{XA}$), ${}^4\mathbf{A} \leftarrow {}^3\mathbf{A}$ (${}^4\mathbf{XA}^+ \leftarrow {}^3\mathbf{XA}$) and ${}^2\mathbf{A} \leftarrow {}^1\mathbf{A}$ (${}^2\mathbf{XA}^+ \leftarrow {}^1\mathbf{XA}$) processes are assigned to the secondary onset. It is quite unusual for ionisation processes from the LES to be assigned to the weaker PIE onset, while the ionisation processes from the metastable isomers are assigned to the dominant onset. It may be the case that conditions in the cluster source favour the formation of the Ce_3O_4 kinetic product (\mathbf{XB}) over the thermodynamic product (\mathbf{XA}). This would need to be verified with detailed studies of cluster formation mechanisms, which are beyond the scope of this work.

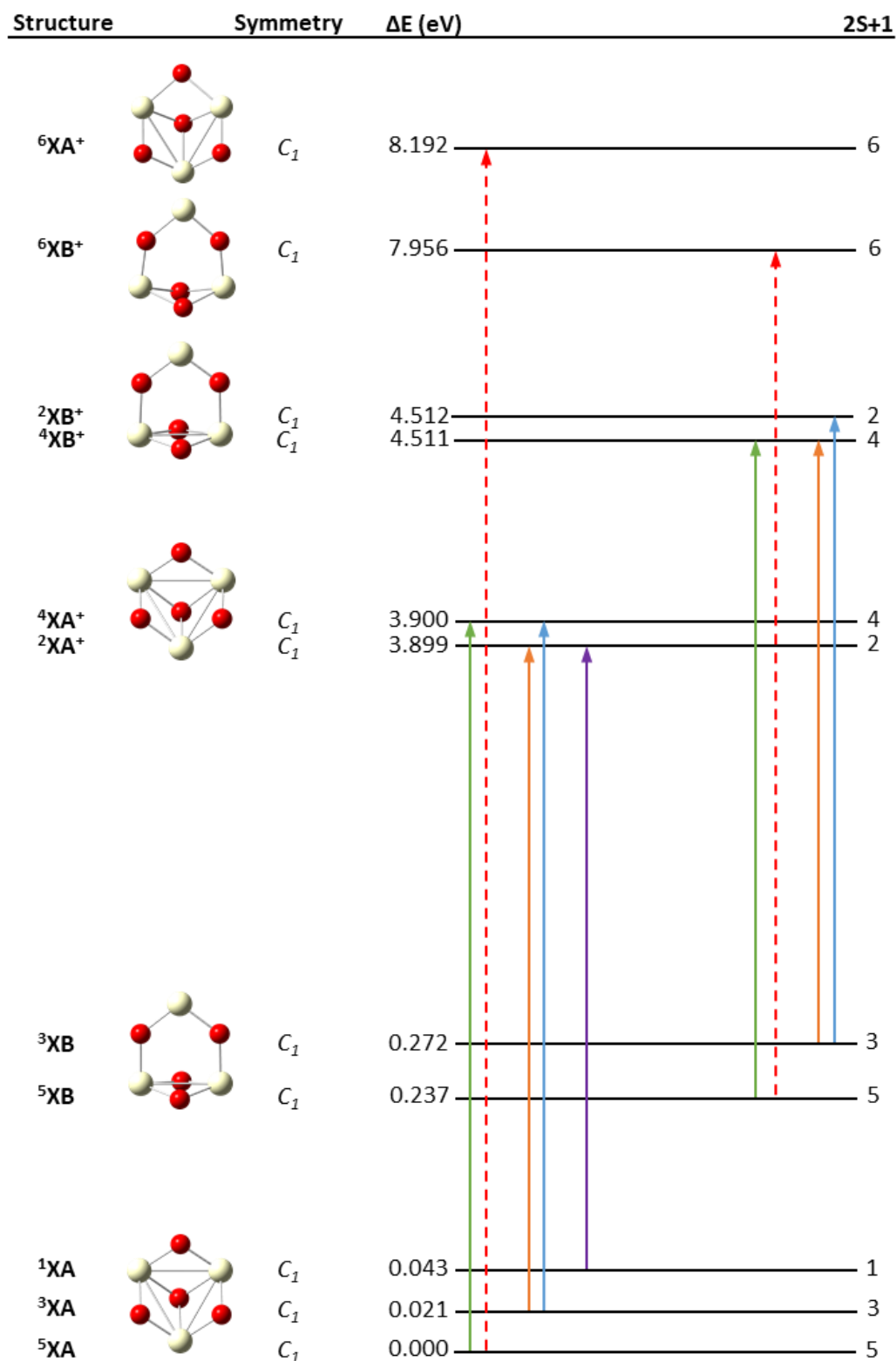


Figure 6.25: Ce_3O_4 calculated structures. Potential ionisation transitions are shown. Ionisation transitions corresponding to the secondary onset are displayed on the left; transitions corresponding to the primary onset are shown on the right. Transitions with prohibitively high ionisation energies are shown as red dashed arrows.

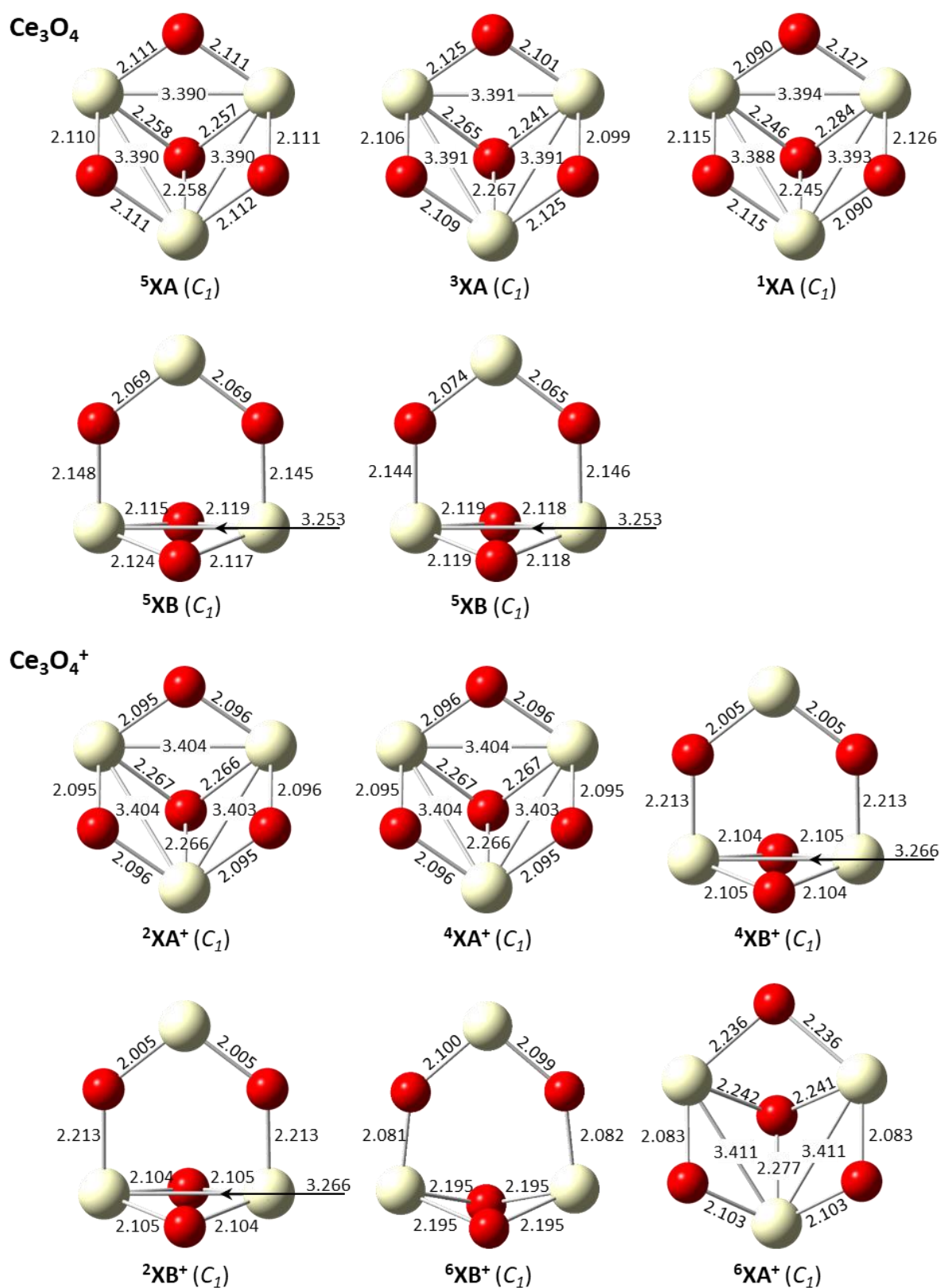


Figure 6.26: Calculated Ce_3O_4 neutral (top) and cationic (below) structures. Bond lengths are presented in Å. Point groups are shown in brackets.

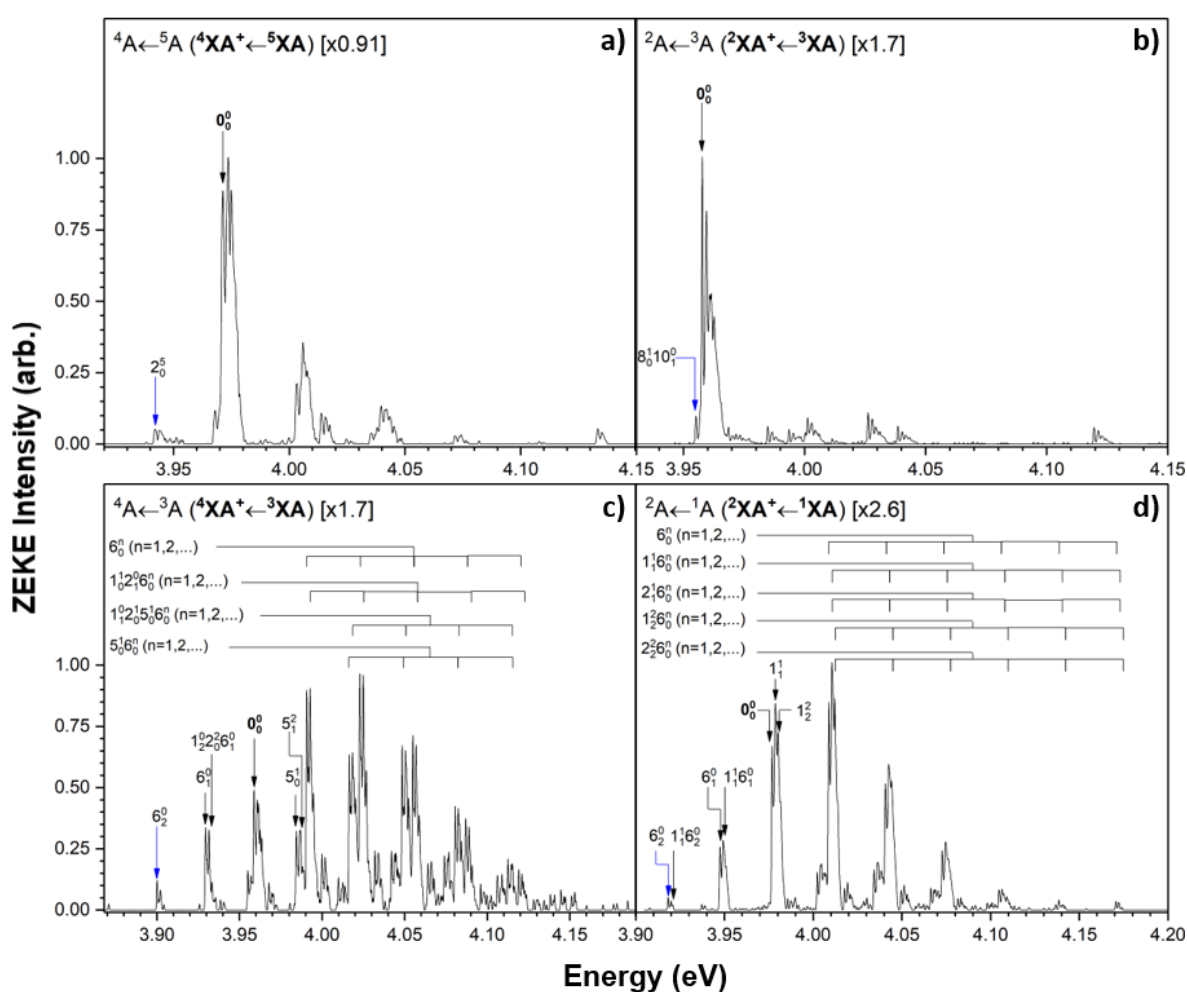
6.7.3. ZEKE Spectral Simulations for Ce_3O_4

Simulated ZEKE spectra for Ce_3O_4 $^4A \leftarrow ^5A$ ($^4XA^+ \leftarrow ^5XA$), $^2A \leftarrow ^3A$ ($^4XA^+ \leftarrow ^3XA$) $^4A \leftarrow ^3A$ ($^4XA^+ \leftarrow ^3XA$) and $^2A \leftarrow ^1A$ ($^2XA^+ \leftarrow ^1XA$) photo-ionisation transitions – corresponding to the secondary onset – are presented in Figure 6.27. These processes all describe photo-ionisation from the lower energy XA neutral structure. The ZEKE spectra were energetically corrected using the method described in Chapter 3. Subsequent corrections of -0.02 eV, -0.04 eV and -0.04 eV were then applied to the $^4A \leftarrow ^5A$ ($^4XA^+ \leftarrow ^5XA$), $^2A \leftarrow ^3A$ ($^4XA^+ \leftarrow ^3XA$) and $^4A \leftarrow ^3A$ ($^4XA^+ \leftarrow ^3XA$) ZEKE spectra respectively such that the calculated PIE spectrum (vide infra) showed good agreement with the experimental PIE spectrum. The corrected ZEKE spectra are shown here.

The spectral profiles of the calculated $^4A \leftarrow ^5A$ ($^4XA^+ \leftarrow ^5XA$) and $^2A \leftarrow ^3A$ ($^4XA^+ \leftarrow ^3XA$) processes, shown in Figures 6.27(a) and 6.27(b) respectively, are quite similar. Both spectra show the majority of the vibronic transitions grouped within one vibronic band at ca. 3.97 eV. This infers closely spaced vibronic peaks which are unresolved in the ZEKE spectra due to thermal broadening (broadening effects were calculated by convoluting all vibronic peaks to a 5 cm^{-1} FWHM using Gaussian functions). The 0_0^0 vibronic peak corresponds to the maximum FC transition which is consistent with the minimal structural change calculated between the neutral and cationic XA species. Vibronic transitions for the $^4A \leftarrow ^5A$ ($^4XA^+ \leftarrow ^5XA$) ionisation process are twice as intense as those calculated for the $^2A \leftarrow ^3A$ ($^4XA^+ \leftarrow ^3XA$) process, with scaling factors of 0.91 and 1.7 respectively used to normalise the most intense peak in each spectrum. However, the small scaling factors applied to both spectra indicate strong FC overlap between the neutral and cationic species in both ionisation processes.

The calculated $^4A \leftarrow ^3A$ ($^4XA^+ \leftarrow ^3XA$) and $^2A \leftarrow ^1A$ ($^2XA^+ \leftarrow ^1XA$) ZEKE spectra presented in Figures 6.27(c) and 6.27(d) are both significantly broader than the $^4A \leftarrow ^5A$ ($^4XA^+ \leftarrow ^5XA$) and $^2A \leftarrow ^3A$ ($^4XA^+ \leftarrow ^3XA$) spectra discussed previously, with vibronic peaks spanning a ca. 0.2 eV energy range in both spectra. These vibronic peaks comprise a number of short progressions of the ν_6 mode – which involves opposing breathing movements of the Ce_3 trimer and the bridging oxygen atoms – both by itself and combined with other modes including the ν_1 , ν_2 and ν_5 modes. Both spectra moreover show intense 0_0^0 peaks, although the maximum FC transitions

in the ${}^4A \leftarrow {}^3A$ (${}^4XA^+ \leftarrow {}^3XA$) and ${}^2A \leftarrow {}^1A$ (${}^2XA^+ \leftarrow {}^1XA$) spectra correspond to the 6_0^2 and 6_0^1 transitions, respectively. This is consistent with some small but noticeable structural change occurring with photo-ionisation. Vibronic peak intensities for the both spectra are quite strong, albeit considerably weaker than the ${}^4A \leftarrow {}^5A$ (${}^4XA^+ \leftarrow {}^5XA$) spectrum shown in Figure 6.27(a), with scaling factors of 1.7 and 2.6 used to normalise the maximum intensity peaks in the ${}^4A \leftarrow {}^3A$ (${}^4XA^+ \leftarrow {}^3XA$) and ${}^2A \leftarrow {}^1A$ (${}^2XA^+ \leftarrow {}^1XA$) spectra, respectively. The ${}^4A \leftarrow {}^3A$ (${}^4XA^+ \leftarrow {}^3XA$) and ${}^2A \leftarrow {}^1A$ (${}^2XA^+ \leftarrow {}^1XA$) transitions are both expected to have a strong contribution to the Ce_3O_4 PIE spectrum, however will be overshadowed by the ${}^4A \leftarrow {}^5A$ (${}^4XA^+ \leftarrow {}^5XA$) process.



6.27: Simulated ZEKE spectra for Ce_3O_4 ionisation transition corresponding to the secondary onset: **a).** ${}^4A \leftarrow {}^5A$ (${}^4XA^+ \leftarrow {}^5XA$), **b).** ${}^2A \leftarrow {}^3A$ (${}^2XA^+ \leftarrow {}^3XA$) **c).** ${}^4A \leftarrow {}^3A$ (${}^4XA^+ \leftarrow {}^3XA$) and **d).** ${}^2A \leftarrow {}^1A$ (${}^2XA^+ \leftarrow {}^1XA$). Spectral intensities are normalised relative to the most prominent peak in each spectrum with scaling factors shown. Prominent vibronic transitions are assigned. The vibronic transition likely to correspond to the appearance of ion signal in each spectrum is labelled with a blue arrow.

Simulated ZEKE spectra for the ${}^4A \leftarrow {}^5A$ (${}^4XB^+ \leftarrow {}^5XB$), ${}^4A \leftarrow {}^3A$ (${}^4XB^+ \leftarrow {}^3XB$) and ${}^2A \leftarrow {}^3A$ (${}^4XB^+ \leftarrow {}^3XB$) ionisation processes – corresponding to the primary PIE onset – are presented in Figure 6.28. The ZEKE spectra were energetically corrected using the method described in Chapter 3. A further energetic correction of -0.18 eV was applied to the ${}^4A \leftarrow {}^5A$ (${}^4XB^+ \leftarrow {}^5XB$) ZEKE spectrum; no additional energetic corrections were applied to either the ${}^4A \leftarrow {}^3A$ (${}^4XB^+ \leftarrow {}^3XB$) or ${}^2A \leftarrow {}^3A$ (${}^4XB^+ \leftarrow {}^3XB$) spectra. The spectral profiles for all three ionisation processes are nearly identical, comprising a number of short progressions involving the ν_7 and ν_{15} modes. The ν_7 mode involves an out of plane bending of the Ce_2O_2 unit – where the oxygen atoms are displaced while the cerium atoms remain stationary – while the ν_{15} mode involves an in-plane stretch of the Ce-O bonds within the CeO_2 unit where the oxygen atoms are displaced toward the Ce_2O_2 group. The 0_0^0 transition is calculated with strong intensity in all spectra, however does not constitute the maximum FC transition; the $7_0^1 15_0^1$ mode corresponds to the most intense transition in the ${}^4A \leftarrow {}^5A$ (${}^4XB^+ \leftarrow {}^5XB$) and ${}^4A \leftarrow {}^3A$ (${}^4XB^+ \leftarrow {}^3XB$) spectra, while the 15_0^1 mode is most intense for the ${}^2A \leftarrow {}^3A$ (${}^4XB^+ \leftarrow {}^3XB$) spectrum. This small excitation corresponds to a good FC overlap between the neutral and cationic structures for all three ionisation transitions. Comparison of the vibronic peak intensities – which are normalised to the most intense peak with scaling factors of 7, 7 and 8.5 applied to the ${}^4A \leftarrow {}^5A$ (${}^4XB^+ \leftarrow {}^5XB$), ${}^4A \leftarrow {}^3A$ (${}^4XB^+ \leftarrow {}^3XB$) and ${}^2A \leftarrow {}^3A$ (${}^4XB^+ \leftarrow {}^3XB$) ZEKE spectra, respectively – infers similar contributions of all three ionisation processes to the PIE spectrum.

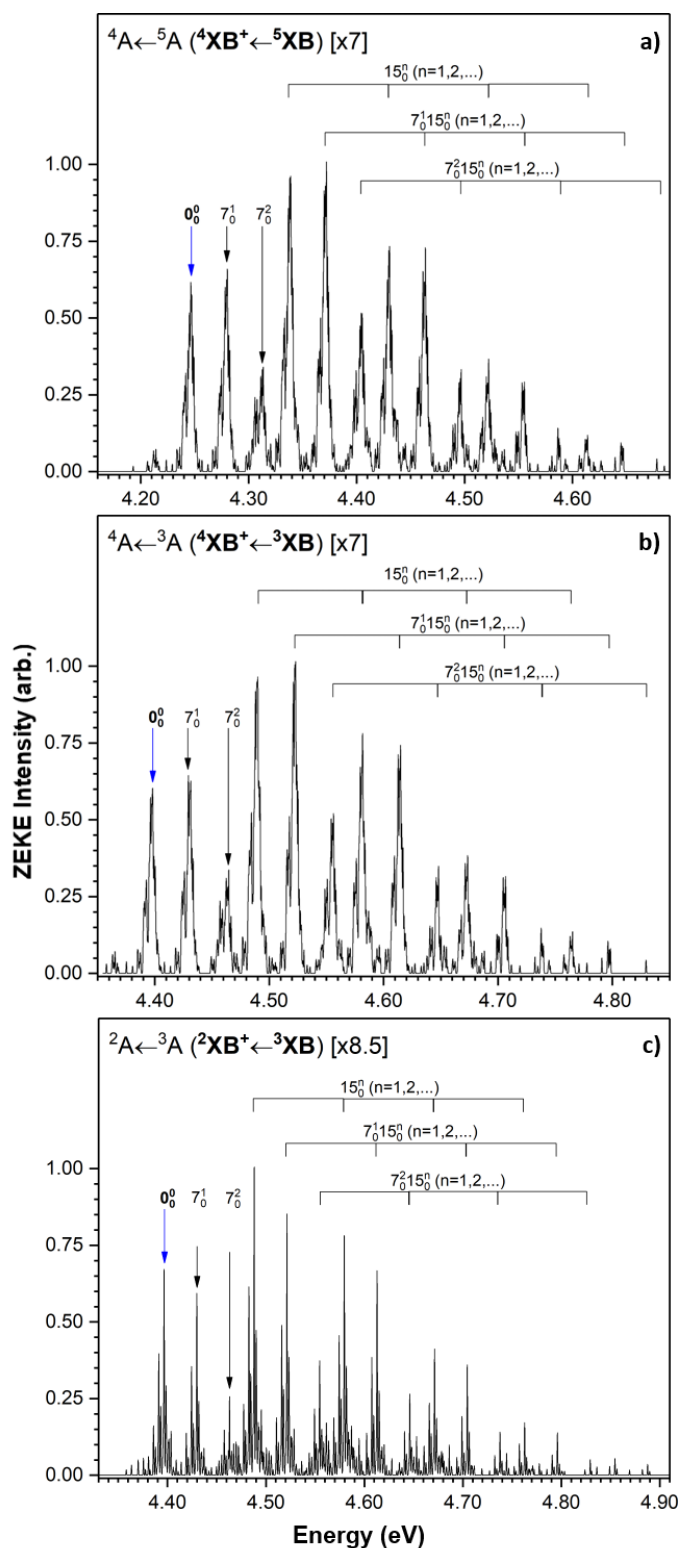


Figure 6.28: Simulated ZEKE spectra for Ce_3O_4 ionisation transitions corresponding to the primary onset: **a).** ${}^4A \leftarrow {}^5A$ (${}^4XB^+ \leftarrow {}^5XB$), **b).** ${}^4A \leftarrow {}^3A$ (${}^4XB^+ \leftarrow {}^3XB$) and **c).** ${}^2A \leftarrow {}^3A$ (${}^2XB^+ \leftarrow {}^3XB$). Spectral intensities are normalised with scaling factors shown. Prominent vibronic transitions are assigned. The vibronic transition likely to correspond to the appearance of ion signal in each spectrum is labelled with a blue arrow.

6.7.4. Comparison of Simulated and Experimental PIE Spectra for Ce_3O_4

The simulated PIE spectrum for the Ce_3O_4 secondary onset is presented in Figure 6.29. The PIE spectrum is constructed from a combination of the integrated $^4A \leftarrow ^5A$ ($^4XA^+ \leftarrow ^5XA$), $^2A \leftarrow ^3A$ ($^4XA^+ \leftarrow ^3XA$), $^4A \leftarrow ^3A$ ($^4XA^+ \leftarrow ^3XA$) and $^2A \leftarrow ^1A$ ($^2XA^+ \leftarrow ^1XA$) ZEKE spectra. Good agreement is found between the calculated and experimental spectra, particularly in the 3.95 – 4.00 eV region where the 0_0^0 transitions for all four ionisation processes are located. The Ce_3O_4 IE is thus taken from the secondary onset – despite the significantly lower intensity of ion signal compared to the primary onset – since this onset can be assigned to ionisation processes from the LES. The adiabatic IE for this onset is assigned to the $^4A \leftarrow ^5A$ ($^4XA^+ \leftarrow ^5XA$) transition which corresponds to the lowest energy ionisation process from the LES. This gives an IE value of 3.97 eV.

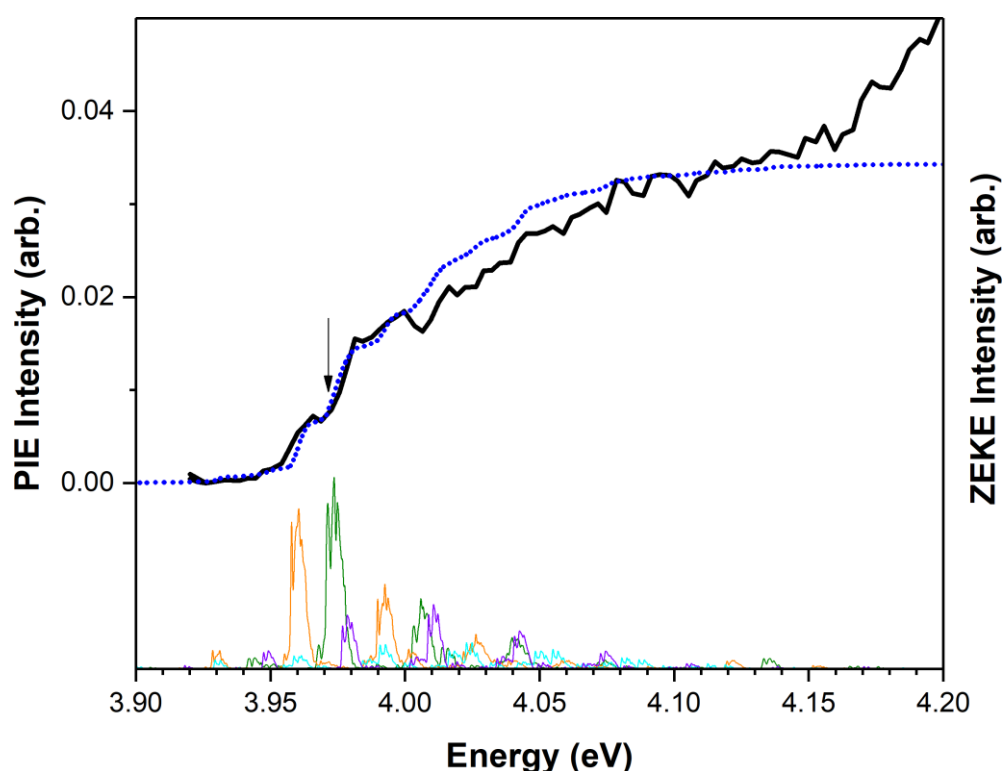


Figure 6.29: Simulated PIE spectrum for the Ce_3O_4 secondary onset (blue dotted line) overlaid against the experimental PIE spectrum (solid black line). Calculated ZEKE spectra for the $^4A \leftarrow ^5A$ ($^4XA^+ \leftarrow ^5XA$), $^2A \leftarrow ^3A$ ($^4XA^+ \leftarrow ^3XA$), $^4A \leftarrow ^3A$ ($^4XA^+ \leftarrow ^3XA$) and $^2A \leftarrow ^1A$ ($^2XA^+ \leftarrow ^1XA$) ionisation processes are shown below the PIE spectrum in green, orange, blue and violet, respectively. The adiabatic ionisation energy is labelled with a black arrow.

The simulated PIE spectrum for the primary onset is presented in Figure 6.30. The PIE spectrum was constructed from a combination of the integrated $^4A \leftarrow ^5A$ ($^4XB^+ \leftarrow ^5XB$), $^4A \leftarrow ^3A$ ($^4XB^+ \leftarrow ^3XB$) and $^2A \leftarrow ^3A$ ($^4XB^+ \leftarrow ^3XB$) ZEKE spectra to provide a reasonable agreement with the experimental PIE spectrum. The IE for the primary onset is taken as the energy of the 0_0^0 transition for the $^4A \leftarrow ^5A$ ($^4XB^+ \leftarrow ^5XB$) ionisation process – comprising the lowest energy ionisation transition from the lowest energy structure involved in this onset – as 4.25 eV.

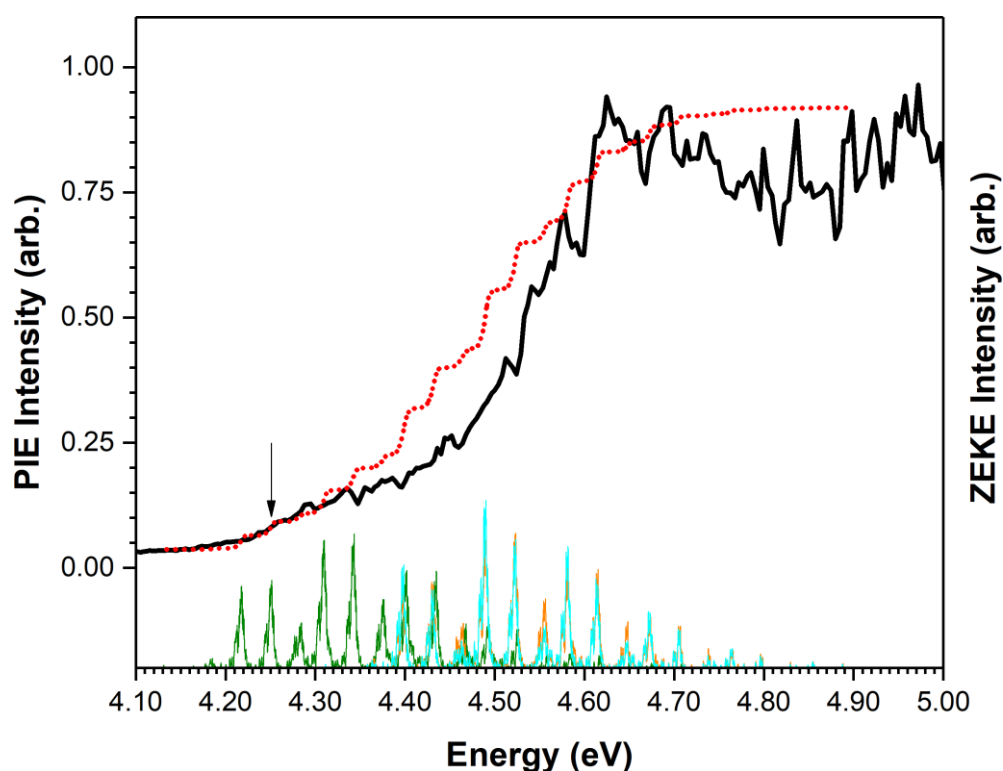


Figure 6.30: Simulated PIE spectrum for the Ce_3O_4 primary onset (red dotted line) overlaid against the experimental PIE spectrum (solid black line). Calculated ZEKE spectra for the $^4A \leftarrow ^5A$ ($^4XB^+ \leftarrow ^5XB$), $^4A \leftarrow ^3A$ ($^4XB^+ \leftarrow ^3XB$) and $^2A \leftarrow ^3A$ ($^4XB^+ \leftarrow ^3XB$) ionisation processes are shown below the PIE spectrum in green, orange and blue, respectively. The adiabatic ionisation energy is labelled with a black arrow.

6.8. PIE Spectrum and DFT Results for Ce_3O_5

6.8.1. Ce_3O_5 Experimental PIE Spectrum

A PIE spectrum was not recorded for the Ce_3O_5 cluster due to the Ce_3O_5 ion not being detected following photo-ionisation within the 220 – 317.5 nm (3.92 – 5.64 eV) wavelength range available with the tuneable laser source. However, a low intensity Ce_3O_5 peak was detected in the mass spectrum following photo-ionisation at 213 nm (5.82 eV). Therefore, a bracketed AE of 5.64 – 5.82 eV is assigned to the Ce_3O_5 cluster. While an experimental PIE spectrum is not shown, DFT calculated structures and calculated ZEKE and PIE spectra will be presented to investigate the geometric and electronic properties of the calculated Ce_3O_5 species.

6.8.2. DFT Calculations for Ce_3O_5

Calculated Ce_3O_5 structures are presented in Figures 6.31 and 6.32. Two unique neutral structures are calculated which are labelled **XIA** and **XIB** in order of increasing energy. The **XIA** structure comprises one oxygen atom attached to a Ce_3O_4 type motif via a single Ce-O bond. The structure is C_1 symmetric, although approaches a C_s symmetry (symmetry constrained calculations of all Ce_3O_5 structures were problematic due to convergence issues). The **XIA** structure is calculated in both triplet – 3A – and singlet – 1A – spin states labelled $^3\mathbf{XIA}$ and $^1\mathbf{XIA}$, respectively. The $^3\mathbf{XIA}$ structure comprises the LES while the $^1\mathbf{XIA}$ species is calculated with a relative energy of +0.149 eV.

The calculated **XIB** structure consists of a Ce_3O_4 type motif with an additional oxygen atom bound to the exposed Ce_3 face. The structure is C_1 – albeit near C_s – symmetric and is calculated in singlet – 1A – and triplet – 3A – spin states labelled $^1\mathbf{XIB}$ and $^3\mathbf{XIB}$, respectively. These spin-isomers are nearly identical, both geometrically and energetically, with calculated energies of +0.120 and +0.121 eV relative to the $^3\mathbf{XIA}$ LES, respectively.

Calculated cationic structures show two unique geometries labelled \mathbf{XIA}^+ and \mathbf{XIB}^+ corresponding to their respective **XIA** and **XIB** neutral structures. The \mathbf{XIA}^+ structure is calculated in doublet – 2A – and quartet – 4A – spin states – labelled $^2\mathbf{XIA}^+$ and $^4\mathbf{XIA}^+$,

respectively. The $^2XIA^+$ and $^4XIA^+$ structures both show considerable differences in the Ce-O bond lengths of the bridging oxygen atoms compared to their respective neutral 1XIA and 3XIA species. Moreover, the $^4XIA^+$ species shows a significant displacement of the singly attached oxygen atom – attached to the top cerium atom in Figure 6.32(b). The XIB^+ structure is calculated in doublet – 2A – and quartet – 4A – spin states labelled $^1XIB^+$ and $^3XIB^+$, respectively. The Ce-Ce bond lengths, and the Ce-O bond lengths for the facial oxygen atoms, remain similar for both the neutral and cationic species. However, significant changes in the Ce-O bond lengths for the bridging oxygen atoms are observed in both cationic species relative to the neutral structures. Comparison of the cationic geometries calculated here – in particular the $^2XIB^+$ and $^2XIA^+$ – species with those calculated by Akin et al³ – who perform calculations of doublet state cations – shows excellent agreement with regard to both the geometries and energetic ordering of the two cationic species. Moreover, the energetic separation between the $^2XIB^+$ and $^2XIA^+$ cations compares well in both works; Akin et al report an energetic separation of 0.24 eV (reported as 5.6 kcal.mol⁻¹) while it is calculated here as 0.234 eV.

A total of 6 ionisation processes are calculated for the Ce_3O_5 system; these include the $^2A \leftarrow ^3A$ ($^2XIA^+ \leftarrow ^3XIA$), $^4A \leftarrow ^3A$ ($^4XIA^+ \leftarrow ^3XIA$), $^2A \leftarrow ^1A$ ($^2XIB^+ \leftarrow ^1XIB$), $^2A \leftarrow ^3A$ ($^2XIB^+ \leftarrow ^3XIB$), $^4A \leftarrow ^3A$ ($^4XIB^+ \leftarrow ^3XIB$) and $^2A \leftarrow ^1A$ ($^2XIA^+ \leftarrow ^1XIA$) transitions with calculated IEs of 6.376 eV, 7.633 eV, 6.022 eV, 6.021 eV, 7.879 eV and 6.227 eV, respectively. The $^2A \leftarrow ^3A$ ($^2XIA^+ \leftarrow ^3XIA$) and $^2A \leftarrow ^1A$ ($^2XIA^+ \leftarrow ^1XIA$) ionisation transitions are represented as green and orange arrows, respectively, in Figure 6.31. The $^2A \leftarrow ^1A$ ($^2XIB^+ \leftarrow ^1XIB$) and $^2A \leftarrow ^3A$ ($^2XIB^+ \leftarrow ^3XIB$) ionisation processes are shown as red dotted arrows due to low ZEKE intensities calculated for these processes (vide infra). The $^4A \leftarrow ^3A$ ($^4XIA^+ \leftarrow ^3XIA$) and $^4A \leftarrow ^3A$ ($^4XIB^+ \leftarrow ^3XIB$) processes both have IEs considerably higher than those calculated for the other 4 ionisation processes and would most likely contribute to a higher energy PIE onset. These processes are shown as red dashed arrows and are not discussed any further.

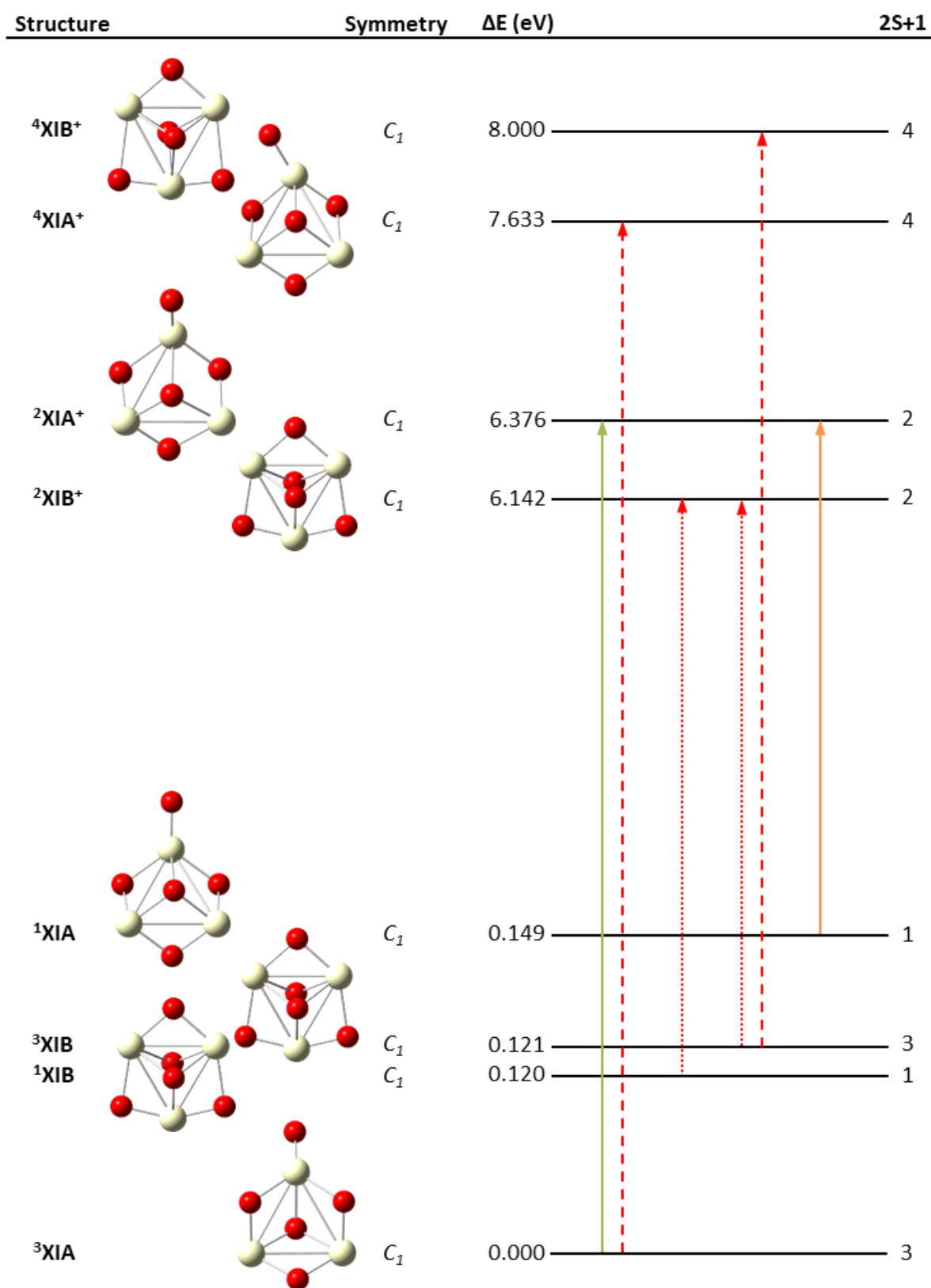


Figure 6.31: Ce_3O_5 calculated structures. Potential ionisation transitions are shown. Transitions with prohibitively high ionisation energies are shown as red dashed arrows. Transitions with low ZEKE intensities (*vide infra*) are shown as red dotted arrows.

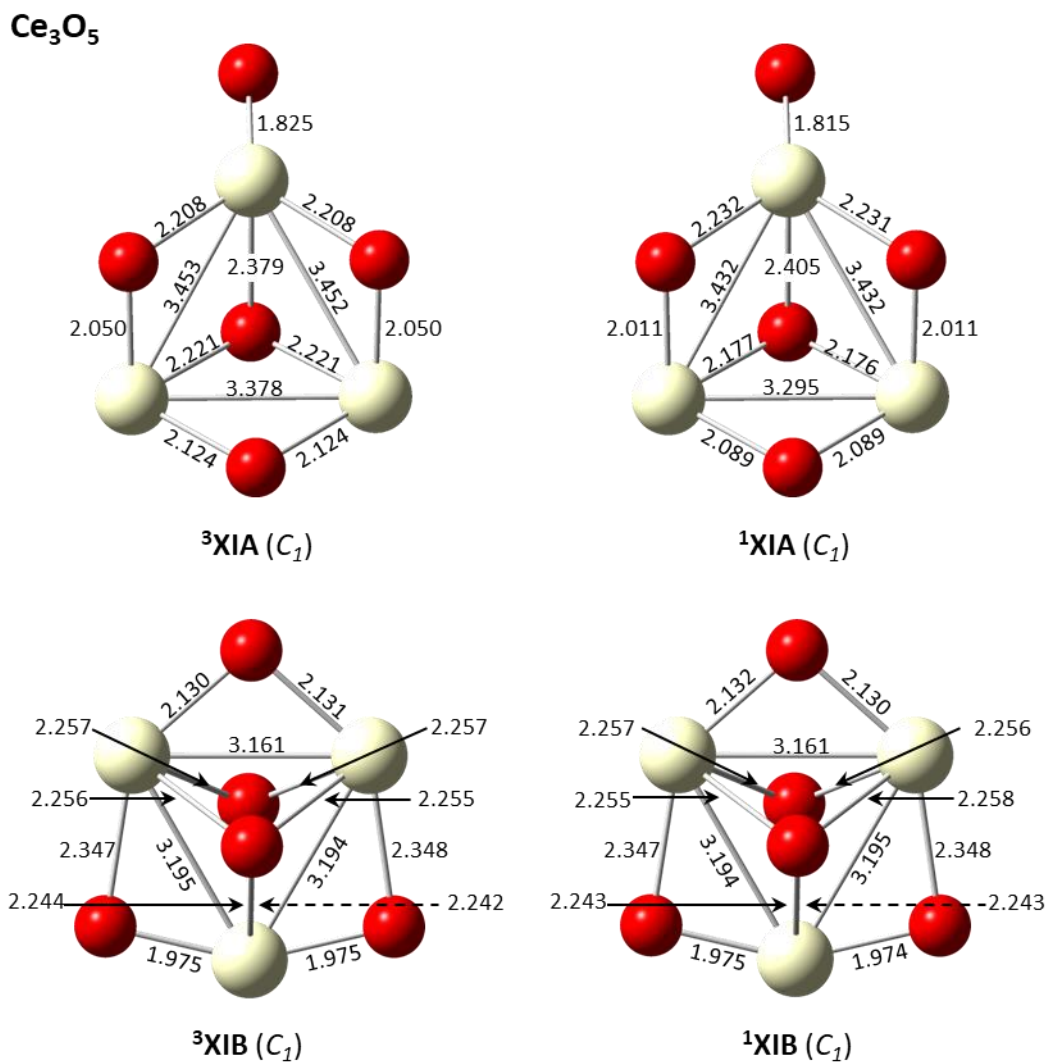


Figure 6.32(a): Calculated Ce_3O_5 neutral structures. Bond lengths are presented in Å. Point groups are shown in brackets.

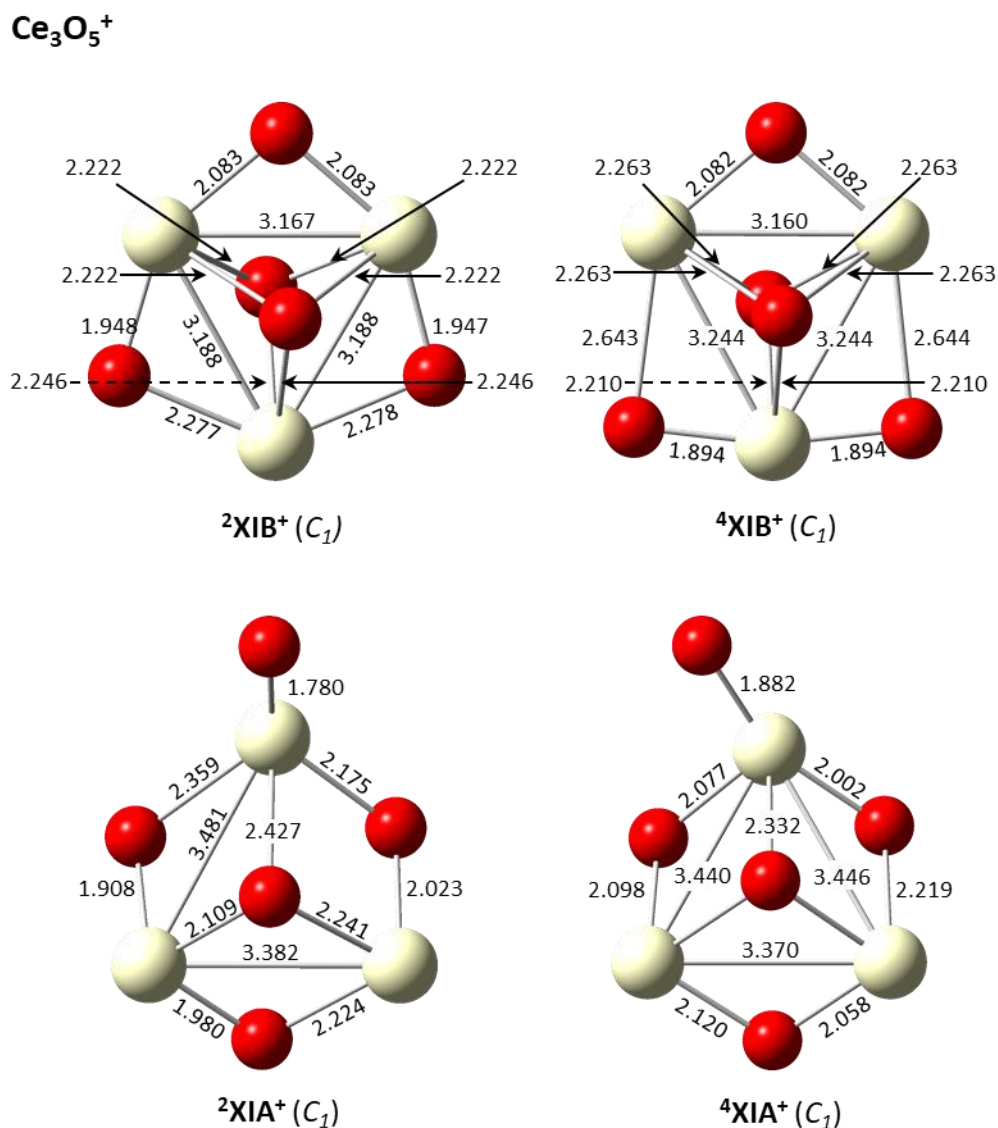


Figure 6.32(b): Calculated Ce_3O_5 cationic structures. Bond lengths are presented in Å. Point groups are shown in brackets.

6.8.3. ZEKE Spectral Simulations for Ce_3O_5

ZEKE spectral simulations were performed on potential Ce_3O_5 ionisation transitions which include the ${}^2A \leftarrow {}^3A$ (${}^2XIA^+ \leftarrow {}^3XIA$), ${}^2A \leftarrow {}^1A$ (${}^2XIB^+ \leftarrow {}^1XIB$), ${}^2A \leftarrow {}^3A$ (${}^2XIB^+ \leftarrow {}^3XIB$) and ${}^2A \leftarrow {}^1A$ (${}^2XIA^+ \leftarrow {}^1XIA$) processes. Simulations were performed using the Parallel Approximation to facilitate additional vibrational excitation of the cationic states. Due to the extensive number of vibrational modes for the Ce_3O_5 cluster species, a full Duschinsky treatment was not viable.

Calculated ZEKE spectra for the ${}^2A \leftarrow {}^1A$ (${}^2XIB^+ \leftarrow {}^1XIB$) and ${}^2A \leftarrow {}^3A$ (${}^2XIB^+ \leftarrow {}^3XIB$) ionisation processes both showed weak vibronic intensities such that neither transition was considered to contribute to the Ce_3O_5 PIE spectrum. The calculated ${}^2A \leftarrow {}^3A$ (${}^2XIB^+ \leftarrow {}^3XIB$) ZEKE spectrum is shown in Appendix C. Calculations of the ${}^2A \leftarrow {}^1A$ (${}^2XIB^+ \leftarrow {}^1XIB$) ZEKE spectrum showed no vibronic peaks with intensity above a 10^{-10} intensity threshold. This spectrum is therefore not shown.

Simulated ZEKE spectra for the Ce_3O_5 ${}^2A \leftarrow {}^3A$ (${}^2XIA^+ \leftarrow {}^3XIA$) and ${}^2A \leftarrow {}^1A$ (${}^2XIA^+ \leftarrow {}^1XIA$) ionisation transitions are presented in Figure 6.33. The ${}^2A \leftarrow {}^3A$ (${}^2XIA^+ \leftarrow {}^3XIA$) ZEKE spectrum – shown in Figure 6.33(a) – displays a very broad profile which extends over a ca. 1 eV range. The spectrum is dominated by long progressions of the ν_{17} mode – including the $1_0^1 17_0^n$ and $1_0^2 17_0^n$ progressions which are indicative of structural change along the ν_{17} vibrational coordinate (which involves asymmetric stretches Ce-O bonds for the bridging oxygen atoms). The vibronic peak intensities are weak – with a scaling factor of 1050 required to normalise the most intense peak – inferring a weak FC overlap between the 3XIA neutral and ${}^2XIA^+$ cationic species. The 0_0^0 vibronic transition is not calculated in the ZEKE spectrum. The ${}^2A \leftarrow {}^1A$ (${}^2XIA^+ \leftarrow {}^1XIA$) ZEKE spectrum presented in Figure 6.33(b) displays a broad profile, albeit significantly narrower than the ${}^2A \leftarrow {}^3A$ (${}^2XIA^+ \leftarrow {}^3XIA$) ZEKE spectrum. A slight broadening of the vibronic peaks is observed due to unresolved vibronic transitions. It was therefore impracticable to assign transition for all but the pertinent vibronic peaks. The lowest energy and maximum FC transitions correspond to the $2_0^2 8_0^2 17_0^2$ and $2_0^2 8_0^1 17_0^5$ peaks, suggesting the vibronic peaks may again include a progression of the ν_{17} mode. The 0_0^0 transition is not recorded while the most intense peak corresponds to the highly excited $2_0^2 8_0^1 17_0^5$ transition inferring a weak FC overlap between the 1XIA and ${}^2XIA^+$ structures. The spectral intensity is comparable to the ${}^2A \leftarrow {}^1A$ (${}^2XIA^+ \leftarrow {}^1XIA$) ZEKE spectrum, suggesting both spectra will have similar contributions to the PIE spectrum.

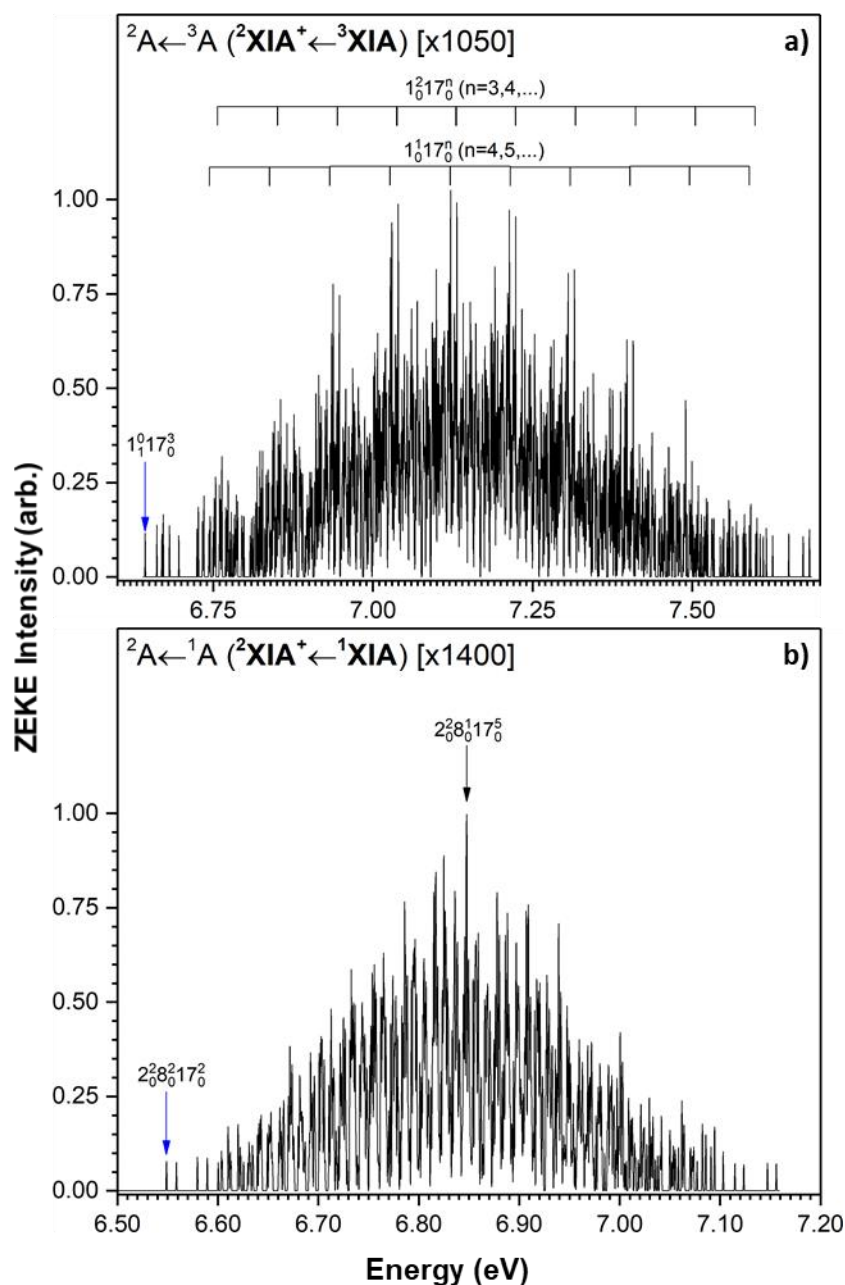


Figure 6.33: Simulated ZEKE spectra for Ce_3O_5 ionisation transitions: **a)** ${}^2A \leftarrow {}^3A$ (${}^2XIA^+ \leftarrow {}^3XIA$) and **b)** ${}^2A \leftarrow {}^1A$ (${}^2XIA^+ \leftarrow {}^1XIA$). Spectral intensities are normalised with scaling factors shown. Prominent vibronic peaks are assigned. The vibronic transition likely to correspond to the appearance of ion signal in each spectrum is labelled with a blue arrow.

6.8.4. Simulated PIE Spectrum for Ce_3O_5

The Ce_3O_5 simulated PIE spectrum is constructed from the integrated ${}^2A \leftarrow {}^3A$ (${}^2XIA^+ \leftarrow {}^3XIA$) and ${}^2A \leftarrow {}^1A$ (${}^2XIA^+ \leftarrow {}^1XIA$) ZEKE spectra; these ionisation processes were both considered to

contribute to the Ce_3O_5 PIE spectrum due to their similar calculated IEs and ZEKE intensities. The simulated PIE spectrum is shown in Figure 6.34. The PIE onset begins at 6.62 eV – corresponding to the AE – followed by a broad onset to a plateau at ca. 7.17 eV. The majority of the onset appears to be within the region of the ${}^2A \leftarrow {}^1A$ (${}^2XIA^+ \leftarrow {}^1XIA$) transition due to the high density of vibronic transitions within this process (as observed by the peak broadening in the ZEKE spectrum). The Ce_3O_5 IE is assigned from the DFT-calculated IE for ${}^2A \leftarrow {}^3A$ (${}^2XIA^+ \leftarrow {}^3XIA$) process – comprising the lowest energy ionisation transition from the lowest energy neutral structure; this gives an IE value of 6.38 eV (shown with a black arrow in Figure 6.34). Given the tendency of DFT to overpredict IE values of transition metal clusters – the calculated Ce_3O_n IEs are corrected by -0.18 eV to match their experimental IE values (vide infra) – the IE value reported here may be considerably higher than the actual IE.

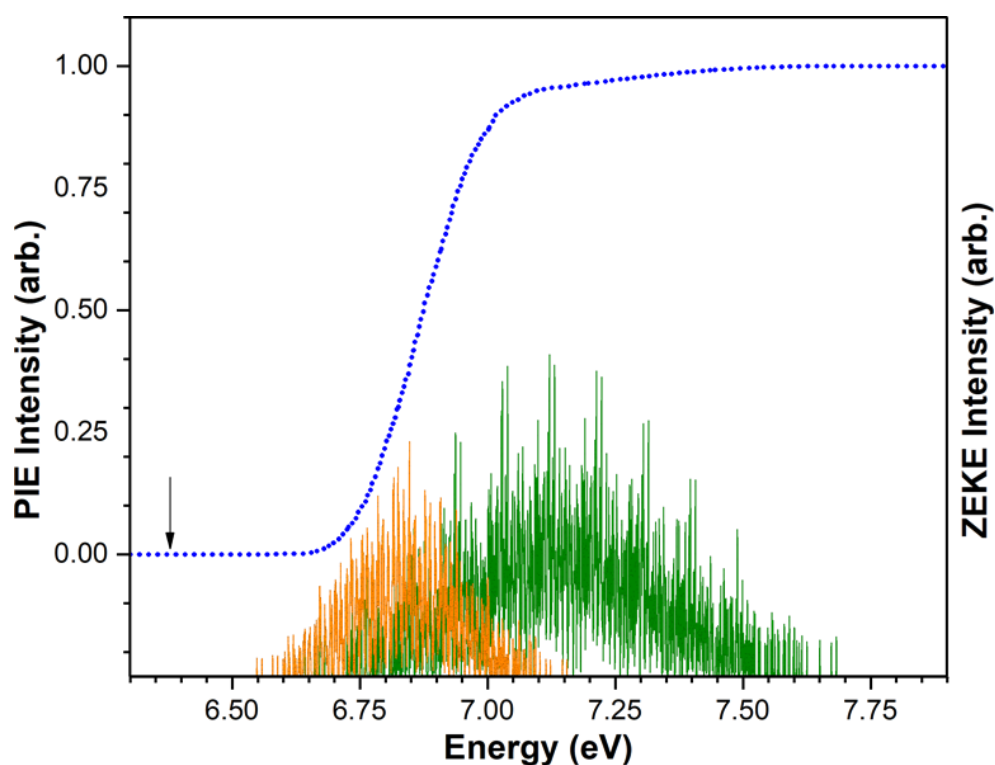


Figure 6.34: Simulated PIE spectrum for Ce_3O_5 (blue dotted line). Calculated ZEKE spectra for the ${}^2A \leftarrow {}^1A$ (${}^2XIA^+ \leftarrow {}^1XIA$) and ${}^2A \leftarrow {}^3A$ (${}^2XIA^+ \leftarrow {}^3XIA$) ionisation processes are shown below the PIE spectrum in green and orange, respectively. The adiabatic ionisation energy is labelled with a black arrow.

6.9. PIE Spectrum and DFT Results for Ce_3O_6

6.9.1. Ce_3O_6 Experimental PIE Spectrum

A PIE spectrum is not shown for the Ce_3O_6 cluster. The Ce_3O_6 ion peak was only detected in trace quantities following photo-ionisation at 213 nm (5.82 eV), as shown in Figure 6.1. Moreover, the Ce_3O_6 ion peak was not detected in the 220 – 317.5 nm (3.92 – 5.64 eV) wavelength range available using the tuneable laser source in this work. DFT calculated Ce_3O_6 neutral and cationic structures are presented below to provide some insight into the electronic and geometric properties of the Ce_3O_6 cluster. Calculated ZEKE and PIE spectra are also presented.

6.9.2. DFT Calculations for Ce_3O_6

DFT calculations for Ce_3O_6 neutral and cationic structures are presented in Figures 6.35 and 6.36. Calculations reveal only one low energy neutral structure which comprises a C_5 singlet in the $^1A'$ electronic state. This structure, labelled 1XII , describes a Ce_3O_4 motif with two additional oxygen atoms singly attached to two different cerium atoms. The singly bound and facially bound oxygen atoms are all positioned below the Ce_3 plane; the bridging oxygen atoms are all located above the Ce_3 plane. Alternative Ce_3O_6 geometries were calculated – with one of the singly attached oxygen atoms instead (i) facially bound to the Ce_3 trimer and (ii) bridging a Ce-Ce bond – which were both over 1 eV higher in energy than the 1XII structure and thus not shown. The cationic structure for the 1XII neutral species, labelled $^2XII^+$, comprises a C_1 symmetric structure in the 2A electronic state. Considerable structural changes are found between the 1XII and $^2XII^+$ species, involving displacement of the singly attached oxygen atoms – as shown in Figure 6.36 – and an asymmetric change in the two Ce-O bond lengths of the top bridging O atom; the left Ce-O bond contracts by ca. 0.13 Å relative to the neutral structure while the right Ce-O bond expands by ca. 0.28 Å.

The calculated neutral and cationic species present a single ionisation process for the Ce_3O_6 system – labelled $^2A \leftarrow ^1A'$ ($^2XIIA^+ \leftarrow ^1XIIA$) – with a calculated IE of 8.482 eV. This calculated IE value is well beyond the capabilities of the tuneable laser sources used in this work and is consistent with the non-detection of the Ce_3O_6 cation in photo-ionisation experiments.

Further calculations of Ce_3O_6 clusters presented in Chapter 10 also suggest the Ce_3O_6 cluster may undergo photo-dissociation processes in preference of photo-ionisation.

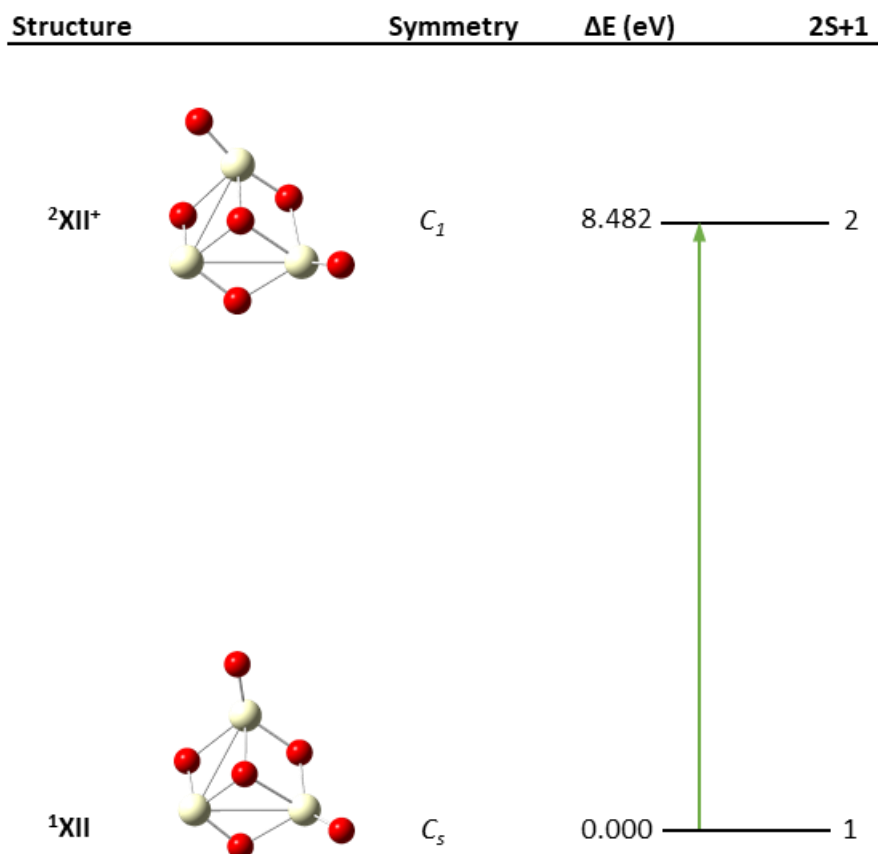


Figure 6.35: Ce_3O_6 calculated structures. Potential ionisation transitions are shown.

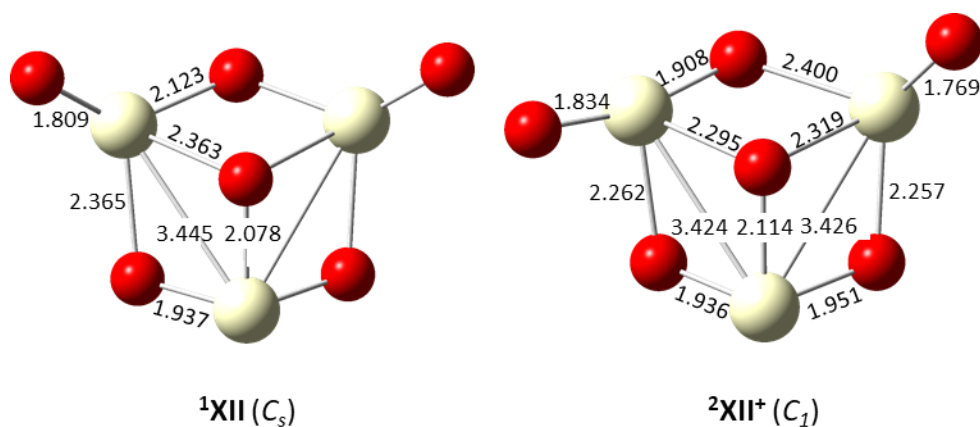


Figure 6.36: Calculated Ce_3O_6 neutral (left) and cationic (right) structures. Bond lengths are presented in Å. Point groups are shown in brackets.

6.9.3. ZEKE Spectral Simulations for Ce_3O_6

ZEKE spectral simulations were performed for the Ce_3O_6 ${}^2A \leftarrow {}^1A'$ (${}^2XII^+ \leftarrow {}^1XII$) ionisation process. Due to the extensive number of vibrational modes for this species, the Parallel Approximation was utilised. Furthermore, only transitions from the $\nu_1, \nu_2, \nu_3, \nu_4, \nu_6, \nu_8, \nu_{19}$ and ν_{20} modes were considered in order to increase the number of available vibrational quanta for the target state; this allowed for a maximum of 4 and 28 vibrational quanta to be accessed in the neutral and cationic states, respectively. Test calculations were performed to confirm that none of the omitted modes contributed significantly to the ZEKE spectrum.

The calculated ZEKE spectrum for the Ce_3O_6 ${}^2A \leftarrow {}^1A'$ (${}^2XII^+ \leftarrow {}^1XII$) transition is presented in Figure 6.37. The spectral profile is quite narrow – spanning a ca. 0.25 eV range – with a low intensity group of peaks in the range 9.34 – 9.39 eV followed by a more prominent group of peaks in the 9.39 – 9.49 eV range. These peaks appear quite broad due to unresolved vibronic transitions (post-calculation treatment of the ZEKE spectrum involved a convolution of all peaks to a 5 cm^{-1} FWHM in order to account for thermal broadening effects). This made the assignment of vibronic peaks difficult; thus, only the lowest energy and maximum FC vibronic transitions are assigned. Both transitions involve significant coupling of vibrational modes; with the lowest energy and maximum FC peaks assigned to the $3_0^6 4_3^0 6_0^3 8_0^7 19_0^6 20_0^2$ and $3_0^5 4_0^1 6_2^3 8_0^7 19_0^7 20_0^2$ transitions, respectively. A very low intensity is calculated for all vibronic

peaks, with a scaling factor of 2.7×10^6 required to normalise the intensity of the most prominent transition. Moreover, the 0_0^0 transition at 8.482 eV – in addition to all vibronic transitions below 9.34 eV – is below the low intensity threshold of the simulations and is not recorded. These observations are all consistent with a poor FC overlap between the neutral and cationic species, inferring extensive structural deformation following photo-ionisation.

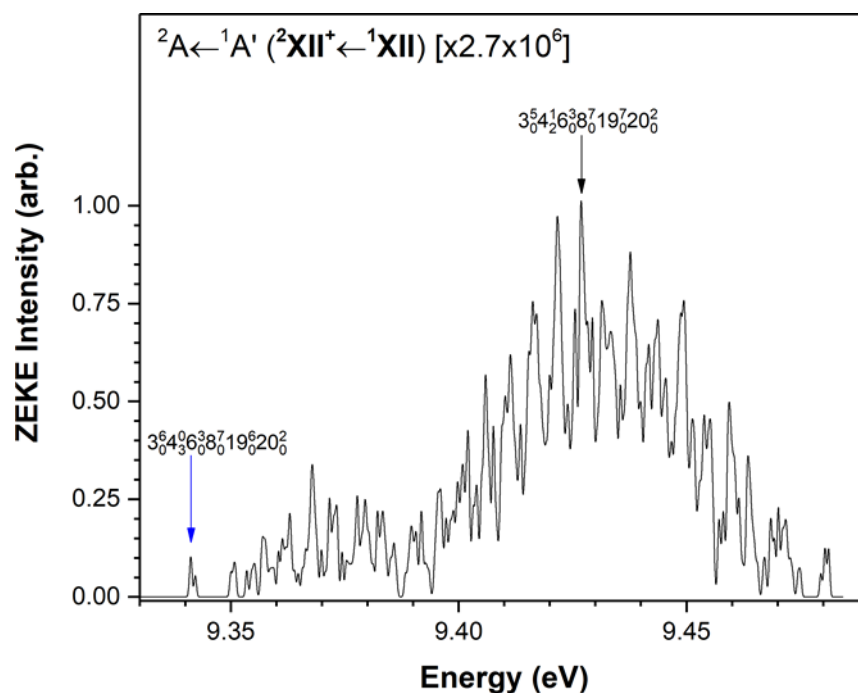


Figure 6.37: Simulated ZEKE spectrum for the Ce_3O_6 ${}^2A \leftarrow {}^1A'$ (${}^2XII^+ \leftarrow {}^1XII$) ionisation transition. The spectral intensity is normalised relative to the most prominent peak with scaling factor shown. Vibronic assignments are provided for the transition likely to correspond to the appearance of ion signal (blue arrow) and the most intense transition (black arrow). The 0_0^0 transition was not calculated and is therefore not shown.

6.9.4. Simulated PIE Spectrum for Ce_3O_6

The simulated Ce_3O_6 PIE spectrum was calculated via integration of the ${}^2A \leftarrow {}^1A'$ (${}^2XII^+ \leftarrow {}^1XII$) ZEKE spectrum and is presented in Figure 6.38. A single ionisation onset is calculated with an appearance energy of 9.36 eV. The onset initially displays a shallow slope in the range 9.36 – 9.40 eV before becoming considerably sharper in the 9.40 – 9.48 eV region. A plateau corresponding to the maximum Ce_3O_6 ion signal is calculated at 9.48 eV. The calculated

adiabatic IE of 8.48 eV – from DFT calculations – is ca. 0.9 eV lower in energy than the AE and is not shown.

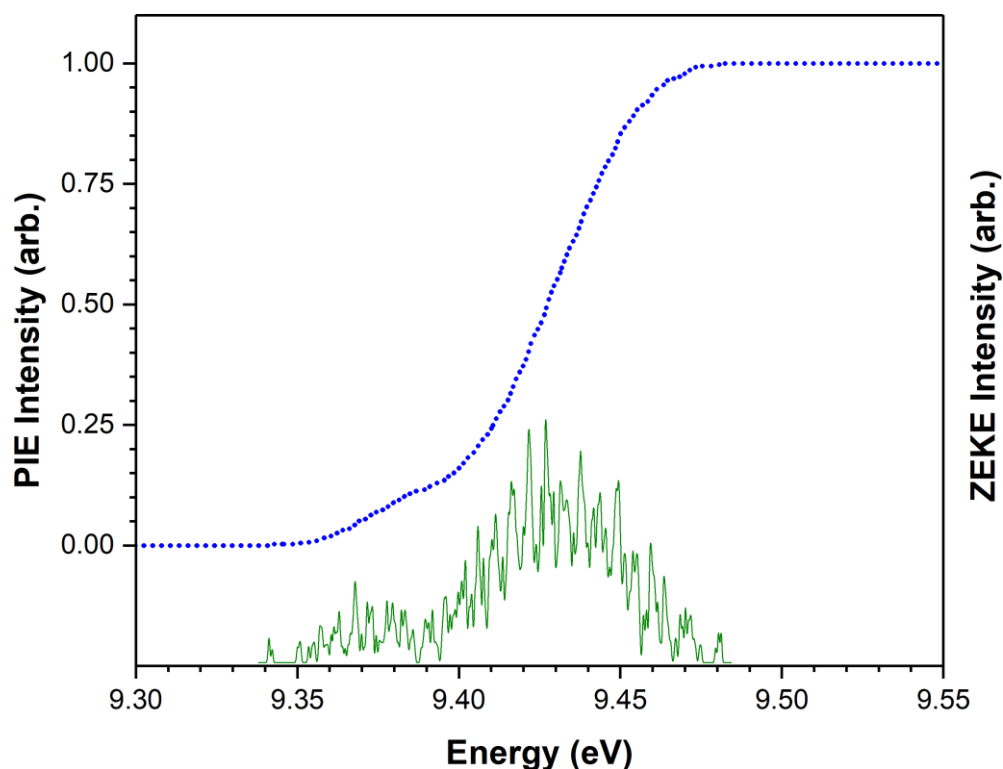


Figure 6.38: Simulated PIE spectrum for Ce_3O_6 (blue dotted line). The calculated ZEKE spectrum for the ${}^2A \leftarrow {}^1A'$ (${}^2XII^* \leftarrow {}^1XII$) ionisation transition is shown below the PIE spectrum in green. The calculated adiabatic ionisation energy at 8.482 eV is not shown.

6.10. Comparison of Experimental and Calculated Ce_3O_n Ionisation Energies

Experimental and calculated adiabatic IEs for the Ce_3O_n cluster series with sequential addition of oxygen atoms are shown in Figure 6.39. Experimental IEs are presented for the Ce_3 , Ce_3O , Ce_3O_2 , Ce_3O_3 and Ce_3O_4 clusters. An approximated IE of 5.73 eV is assigned to the Ce_3O_5 cluster – in the absence of an experimental IE value – which corresponds to the midpoint of the bracketed 5.64 – 5.82 eV AE value assigned earlier (this value is assigned for ease of presentation only). IE trends for the experimental and calculated primary onset IEs are shown as solid and dashed lines, respectively. The experimental IE trend for Ce_3O_4 – Ce_3O_5 is represented as a dotted line since the Ce_3O_5 IE is approximated. Secondary onset IEs are also presented for the Ce_3O_3 and Ce_3O_4 species; however, the IEs trends for the secondary onsets

are not of interest to this work and are not shown. Horizontal lines representing the photon energies of 220 nm (5.64 eV) and 213 nm (5.84 eV), corresponding to the maximum photon energies available with the tuneable laser source and 5th harmonic Nd:YAG laser source, respectively, are also shown. No experimental data is presented for the Ce_3O_6 cluster.

The calculated cluster IEs are corrected to the experimental IEs using the method described in Chapter 3. Briefly, the calculated IE for the Ce_3 cluster is corrected to the experimental IE (requiring a correction of -0.18 eV); the same correction is subsequently applied to the calculated IEs for rest of the Ce_3O_n series. This method of offsetting the calculated IEs is consistent with previous work by Gentleman et al.^{4,5} and Dryza et al.⁶⁻⁸. The corrected calculated IEs are shown in Figure 6.39. Additionally, error bars of ± 0.2 eV are applied to each of the calculated IE values to account for energetic uncertainties intrinsic to the DFT calculated energies. Errors of ± 0.05 eV are also applied to the experimental IE values, consistent with previous error assignments of cerium oxide cluster IPs by Koretsky and Knickelbein⁹. However, these error values are too small to be presented graphically.

A very good correlation is found between the experimental and corrected calculated IEs for the Ce_3O_n ($n=1-4$) clusters. In these cases, the corrected calculated IEs match the experimental IEs within, or very close to, the assigned errors of ± 0.2 eV. The – post-correction – calculated IEs for the Ce_3O , Ce_3O_2 and Ce_3O_3 species are all slightly higher than their respective experimental IEs, whereas the Ce_3O_4 calculated IE is slightly lower than the experimental IE value. The calculated IE for the Ce_3O_5 species is significantly higher – by 0.46 eV – than the approximated AE of 5.73 eV. However, the calculated and experimental IE trends – which both show a sharp increase in ionisation energy from the Ce_3O_4 cluster to the Ce_3O_5 cluster – match quite well. Moreover, the observed Ce_3O_5 ion signal is possibly due to metastable isomers being ionised at lower photon energies. PIE experiments would be required to provide more insight into the Ce_3O_5 system, although this would require a tuneable laser source capable of producing higher photon energies than are available with the current experimental setup. No experimental IE value is presented for the Ce_3O_6 cluster, although the high calculated IE value is consistent with the non-detection of the Ce_3O_6 ion – above trace quantities – in any mass spectra recorded during this work. This excellent agreement between the calculated and experimental IE values for the Ce_3O_n cluster series

suggests the calculated electronic structures of the Ce_3O_n clusters provide a good representation of the actual electronic structures; particularly with regard to the HOMO energy. Moreover, the good agreement between the calculated and experimental PIE spectra for the Ce_3 , Ce_3O , Ce_3O_2 , Ce_3O_3 and Ce_3O_4 clusters suggests the geometric structures of these systems have been calculated correctly. Thus, the geometric and electronic properties of the Ce_3O_n ($n=0-4$) clusters can be inferred from DFT calculations. While experimental data for the Ce_3O_5 and Ce_3O_6 clusters is not available for comparison, the good agreement between the experimental and calculated properties of the Ce_3O_n ($n=0-4$) clusters provides confidence in the DFT method. Thus, the calculated Ce_3O_5 and Ce_3O_6 geometric and electronic properties can be considered reliable.

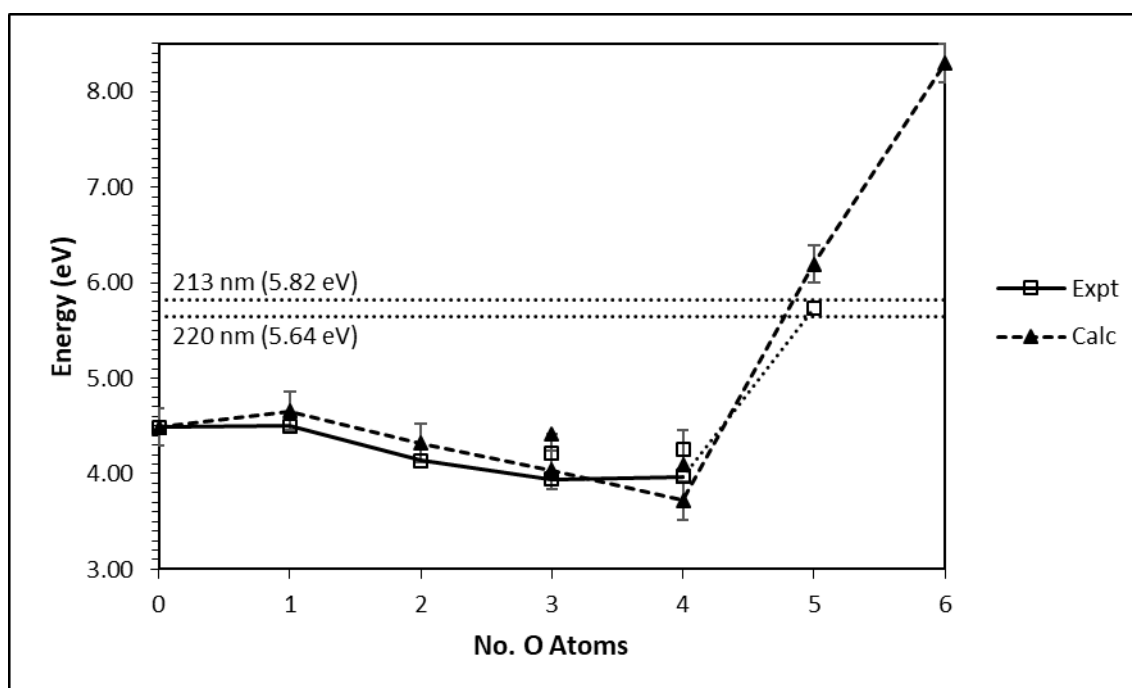


Figure 6.39: Experimental and calculated adiabatic ionisation energies for the Ce_3O_n cluster series with sequential oxidation. Primary and secondary IEs are shown for the Ce_3O_3 and Ce_3O_4 species. The experimental and calculated IE trends for the primary onsets are shown as solid and dashed lines, respectively. An approximated IE is presented for Ce_3O_5 ; the Ce_3O_4 - Ce_3O_5 IE trend is therefore represented with a dotted line. Horizontal lines are drawn at 220 nm (5.64 eV) and 213 nm (5.82 eV) to represent the upper energy bound of the tuneable laser source and the highest energy for which photo-ionisation mass spectra can be recorded, respectively.

6.11. References

- (1) Cao, X.; Dolg, M. *Mol. Phys.* **2003**, *101* (13), 1967.
- (2) Collings, B. A.; Amrein, A. H.; Rayner, D. M.; Hackett, P. A. *J. Chem. Phys.* **1993**, *99* (5), 4174.
- (3) Akin, S. T.; Ard, S. G.; Dye, B. E.; Schaefer, H. F.; Duncan, M. A. *J. Phys. Chem. A* **2016**, *120* (15), 2313.
- (4) Gentleman, A. S.; Addicoat, M. A.; Dryza, V.; Gascooke, J. R.; Buntine, M. A.; Metha, G. F. *J. Chem. Phys.* **2009**, *130* (16), 64311.
- (5) Gentleman, A. S. The Effect of Sequential Oxidation and Composition on the Structural and Electronic Properties of Gas Phase Transition-Lanthanide Bimetallic Clusters, PhD Thesis, The University of Adelaide, 2014.
- (6) Dryza, V.; Addicoat, M. A.; Gascooke, J. R.; Buntine, M. A.; Metha, G. F. *J. Phys. Chem. A* **2005**, *109* (49), 11180.
- (7) Dryza, V.; Addicoat, M. A.; Gascooke, J. R.; Buntine, M. A.; Metha, G. F. *J. Phys. Chem. A* **2008**, *112* (25), 5582.
- (8) Dryza, V.; Gascooke, J. R.; Buntine, M. A.; Metha, G. F. *Phys. Chem. Chem. Phys.* **2009**, *11* (7), 1060.
- (9) Koretsky, G. M.; Knickelbein, M. B. *Eur. Phys. J. D - At. Mol. Opt. Plasma Phys.* **1998**, *2*, 273.

Chapter Seven

Photo-Ionisation Efficiency Spectroscopy of Ce₄O_n Clusters

This chapter presents experimental PIE spectra for the Ce₄O_n ($n=0-5$) clusters. A qualitative analysis of the PIE spectral profiles is presented in addition to experimental appearance energies (AEs) for these species. AE trends for the Ce₄O_n clusters with sequential oxidation are compared to AE trends for the Ce₂O_n and Ce₃O_n clusters.

7.1. Ce_4O_n Mass Spectrum and Ion Signal Appearance

A mass spectrum for Ce_4O_n cluster ion species following photo-ionisation at 213 nm (5.82 eV) is presented in Figure 7.1. A total of 8 peaks ion peaks are detected; these correspond to the $n=0-7$ clusters. The ion peaks have a broad appearance with a number of secondary peaks and shoulders in addition to a contouring of the ion peak base on the higher mass side. These features are due to the use of a non-isotopically pure cerium rod in the production of cerium oxide clusters. Cerium has two prominent isotopes, ^{140}Ce and ^{142}Ce , with natural abundances of 88.5% and 11% respectively[†]. The calculated isotopic abundances of the Ce_4 cluster – which are the same for all Ce_4O_n clusters since the primary isotope of oxygen is over 99% abundant – are presented in Figure 7.2.

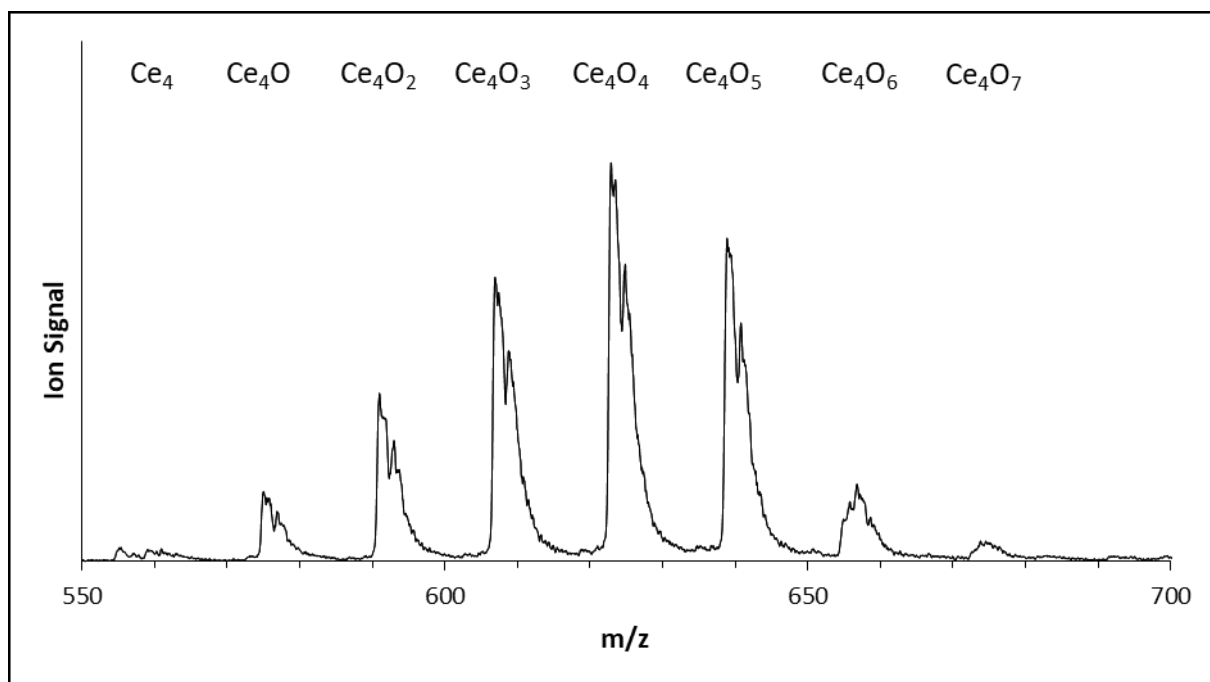


Figure 7.1: Mass spectrum for Ce_4O_n clusters following photo-ionisation at 213 nm (5.82 eV).

[†] The remaining 0.5% comprises the other two naturally occurring isotopes, ^{136}Ce and ^{138}Ce , with natural abundances of 0.2% and 0.3% respectively. Due to the low abundances of these two isotopes, the intensities of any isotopic peaks are negligible.

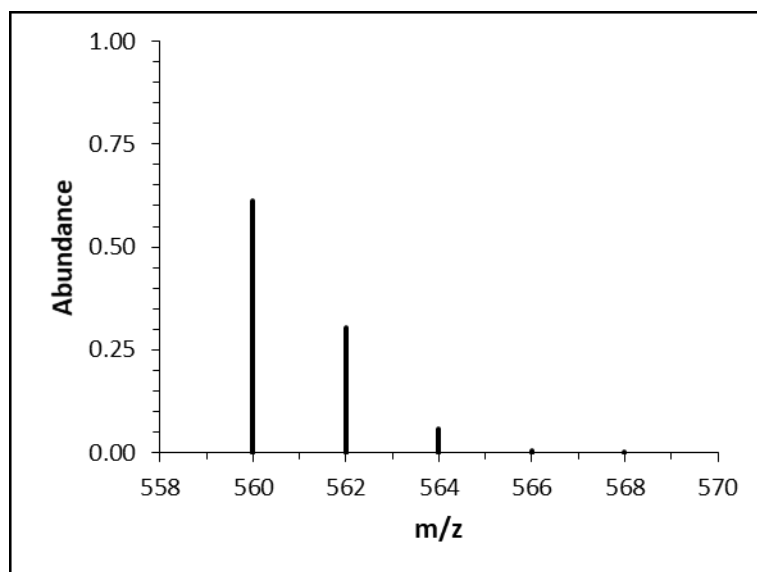


Figure 7.2: Calculated isotopic abundances for the Ce_4 cluster.

The mass spectrum shown in Figure 7.1 displays a very weak Ce_4 ion peak; this is despite the photon energy being significantly higher than the previously reported Ce_4 IE of 4.47 eV¹. The weak Ce_4 ion signal is most likely due to the conditions in the cluster source region, which were optimised for the production of oxidised cluster species and not the bare metal cluster (an in-depth discussion on the effects of the source conditions on the cluster ion signal is presented in Chapter 8). The Ce_4O , Ce_4O_2 , Ce_4O_3 and Ce_4O_4 cations are detected in increasing abundance with the Ce_4O_4 ion peak showing the strongest intensity. A slightly decreased ion signal is then observed for the Ce_4O_5 ion peak which is detected with a similar intensity to that of the Ce_4O_3 species. These peaks are all produced in good abundance and are most likely ionisation products from low-lying neutral clusters. The Ce_4O_6 and Ce_4O_7 cations show markedly lower abundances than all of the Ce_4O_n ($n=0-5$) clusters. The Ce_4O_8 cluster – which corresponds to the stoichiometric 1:2 Ce:O ratio found in bulk ceria – is not detected in any mass spectra.

Figure 7.3 shows the recorded Ce_4O_n mass spectrum following photo-ionisation at 4 different wavelengths. The Ce_4 peak intensity tends to fluctuate depending on the source conditions. However, the Ce_4 ion appears within the 290 – 305 nm (4.07 – 4.28 eV) range. The Ce_4O peak appears with weak intensity within the 290 – 305 nm (4.07 – 4.28 eV) before a moderately

stronger ion peak is observed in the mass spectrum following photo-ionisation at 280 nm (4.43 eV). The Ce_4O_2 and Ce_4O_3 clusters display similar trends where the respective ion peaks are weakly observed following photo-ionisation at 305 nm (4.07 eV) followed by strong ion peaks in the mass spectrum recorded with 290 nm (4.28 eV) photo-ionisation. The Ce_4O_4 ion peak appears with weak intensity following photo-ionisation at both 305 nm (4.07 eV) and 290 nm (4.28 eV); the ion signal within this region may be a residual ion peak from either metastable isomers, multi-photon ionisation processes or fragmentation events. The Ce_4O_4 ion peak is then recorded with good intensity following 280 nm (4.43 eV) photo-ionisation. Finally, the Ce_4O_5 ion displays a higher appearance energy than the other Ce_4O_n species considered here; with the Ce_4O_5 ion peak appearing in the 280 – 290 nm (4.28 – 4.43 eV) range.

Ion signal appearances for the Ce_4O_6 and Ce_4O_7 clusters are not shown and are assumed to be higher than 4.43 eV (280 nm). While calculated IEs for the Ce_4O_n clusters are not presented, experimental and computational IEs for the Ce_2O_n and Ce_3O_n clusters – presented in Chapters 5 and 6, respectively – both identify a general trend where Ce_mO_n clusters display a sharp increase in IE as the number of oxygen atoms in the cluster approaches a Ce:O ratio of 1:2 corresponding to the stoichiometric ratio of bulk ceria.

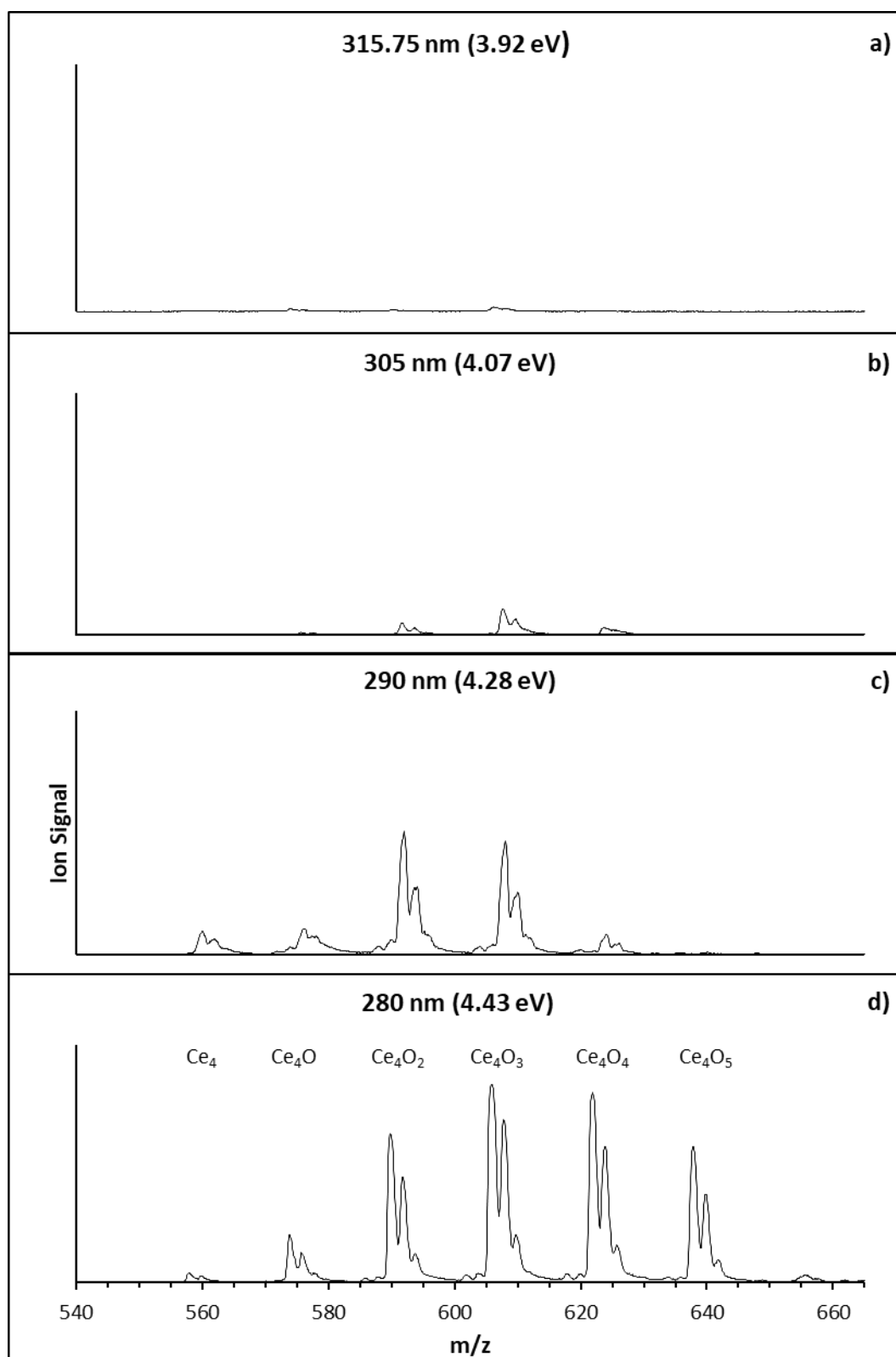


Figure 7.3: Mass spectra of Ce_4O_n ($n=0-5$) clusters following photo-ionisation at **a).** 315.75 nm (3.92 eV), **b).** 305 nm (4.07 eV), **c).** 290 nm (4.28 eV) and **d).** 280 nm (4.43 eV).

7.2. Photo-ionisation Efficiency Spectra for Ce_4O_n ($n=0-5$) Clusters

Experimental PIE spectra for the Ce_4O_n ($n=0-5$) clusters are presented in the following section. Appearance energies (AEs) for Ce_4O_n clusters are presented in lieu of adiabatic ionisation energies (IEs) due to a lack of DFT calculated structures from which to assign ionisation transitions. DFT calculations of Ce_4O_n clusters were attempted but abandoned due to convergence issues and high computational expense (with the majority of calculations unable to complete a single optimisation step within the allocated computation time). Linear trendlines are applied to both the baseline and the ion signal onset in the PIE spectrum; the appearance energy is then taken as the intersection of these trendlines.

7.2.1. Ce_4 PIE Spectrum

The Ce_4 PIE spectrum is presented in Figure 7.4. A single onset is observed with an AE at 4.17 eV; this onset extends over a range of ca. 0.41 eV to a plateau at 4.58 eV. Due to the quite extensive range of the onset (ca. 3200 cm^{-1}), the onset is unlikely to originate from a single ionisation transition. It is possible that the onset encompasses multiple overlapping ionisation processes.

The Ce_4 PIE spectrum has been previously reported by Koretsky and Knickelbein¹ as shown in Figure 7.5. Excellent agreement is found between the two spectra. The PIE spectrum reported by Koretsky and Knickelbein displays a single onset of ion signal from 4.17 eV to a point of maximum intensity at 4.56 eV. The authors do not show any PIE data for photon energies above 4.56 eV (272 nm); thus, they do not record a plateau of ion signal in their PIE spectrum. However, their reported Ce_4 ionisation potential (IP) of 4.17 eV agrees with the AE value presented here. Given the authors report their IP value from the base of their PIE onset, their IP value can also be taken as their AE value.

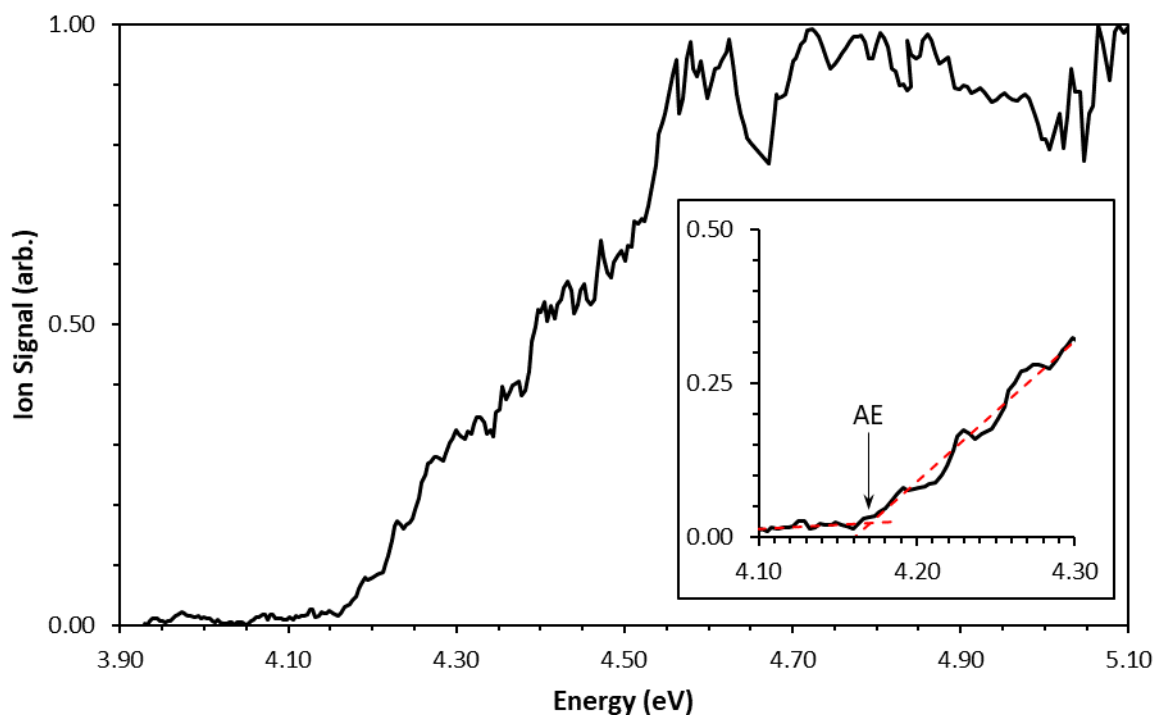


Figure 7.4: Experimental PIE spectrum for Ce_4 . **Inset:** Assignment of the appearance energy by the intersection of trendlines fitted to the baseline and onset. The appearance energy is labelled with a black arrow.

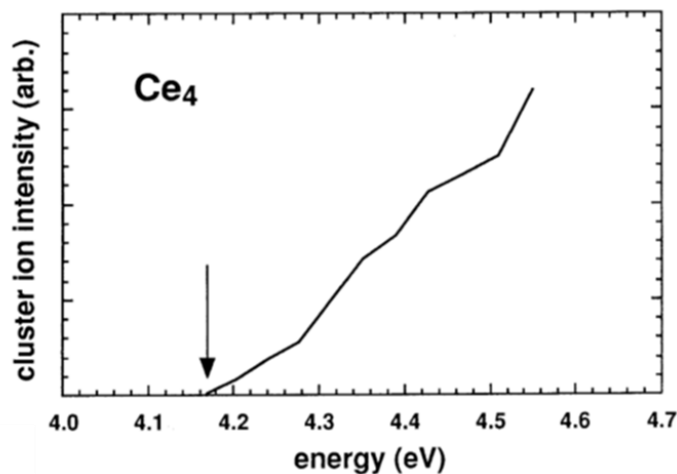


Figure 7.5: Ce_4 PIE spectrum reported by Koretsky and Knickelbein. The Ionisation Potential (IP) is labelled with a black arrow. Reprinted figure from Koretsky, G. M.; Knickelbein, M. B. *Eur. Phys. J. D - At. Mol. Opt. Plasma Phys.* **1998**, 2, 273 with kind permission of the European Physical Journal (EPJ).

7.2.2. Ce_4O PIE Spectrum

The Ce_4O PIE spectrum is presented in Figure 7.6. Two distinct onsets of ion signal are observed. The lower energy onset occurs over the 4.17 – 4.36 eV range. This onset is characterised by a shallow slope with a long thermal tail and a moderate increase in ion signal. The higher energy onset spans the 4.36 – 4.50 eV energy region and comprises a sharp slope which extends to a plateau of ion signal at ca. 4.50 eV – indicating the highest energy FC-allowed transition has been accessed. Comparison of the ion signal intensities for the two onsets shows the higher energy onset is slightly more intense than the lower energy onset. The higher energy onset is therefore labelled the primary onset; the lower energy onset is designated the secondary onset. However, the comparable intensities for both onsets suggests there may be two different low-lying Ce_4O isomers contributing to the PIE spectrum. Considerable overlap is observed between the two onsets such that the lower energy region of the primary onset masked by the secondary onset. Thus, the primary onset AE – labelled AE_1 in Figure 7.6 – is determined by a change in the slope of the PIE curve and from not an increase in ion signal from a baseline. The assigned AE_1 value may therefore not be accurate. The secondary onset AE is shown as AE_2 in Figure 7.6.

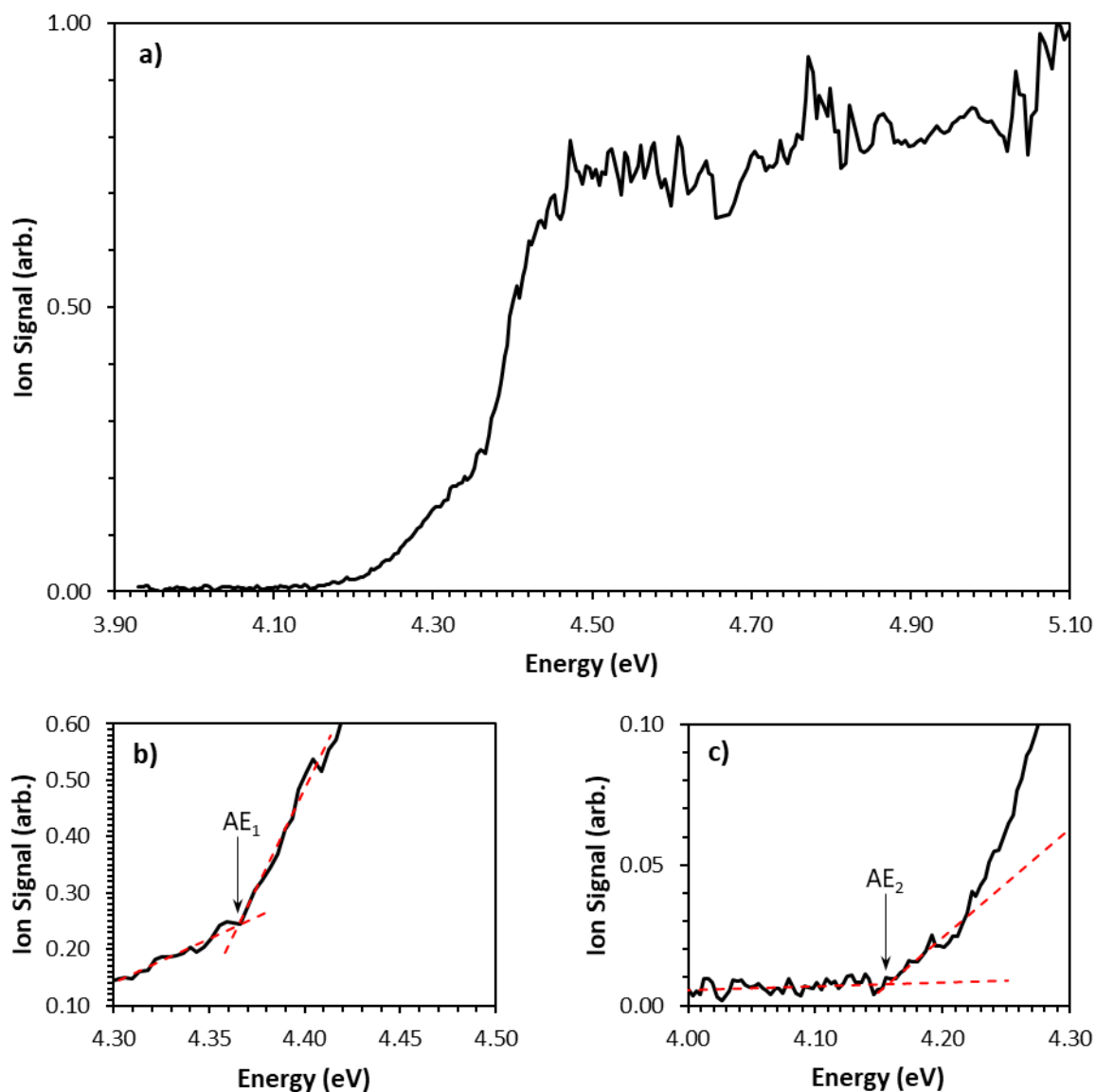


Figure 7.6: PIE spectrum for Ce_4O showing **a).** complete spectrum; **b).** primary onset and **c).** secondary onset. Linear trendlines for the baseline and onset are presented as red dashed lines. Appearance energies for the primary and secondary onsets – designated AE_1 and AE_2 , respectively – are labelled with black arrows.

7.2.3. Ce_4O_2 PIE Spectrum

The experimental PIE spectrum for Ce_4O_2 is presented in Figure 7.7. Three overlapping onsets of ion signal are observed which are characterised by the different slopes in the PIE spectrum. The lowest energy onset spans the 3.97 – 4.19 eV range with a very weak intensity. The second onset appears as an increase in the ion signal slope at 4.19 eV; this onset extends to 4.37 eV and is considerably more intense than the first onset. The highest energy onset occurs from 4.37 eV to a plateau at 4.74 eV which corresponds to the maximum ion signal intensity, indicating the highest energy FC-allowed transition has been accessed. This onset comprises the majority of the ion signal increase, and as such may be describing the photo-ionisation transition from the lowest energy neutral species. This onset is thus designated the primary onset; the 4.19 – 4.37 eV and 3.97 – 4.19 eV onsets are labelled the secondary and tertiary onsets, respectively, by their relative intensities. Due to the considerable overlap between the three onsets, the thermal tails of the primary and secondary onsets are masked by the previous onsets. Consequentially, the AE values assigned to the primary and secondary onsets may not be accurate. The primary, secondary and tertiary onset appearance energies are shown as AE_1 , AE_2 and AE_3 , respectively, in Figure 7.7.

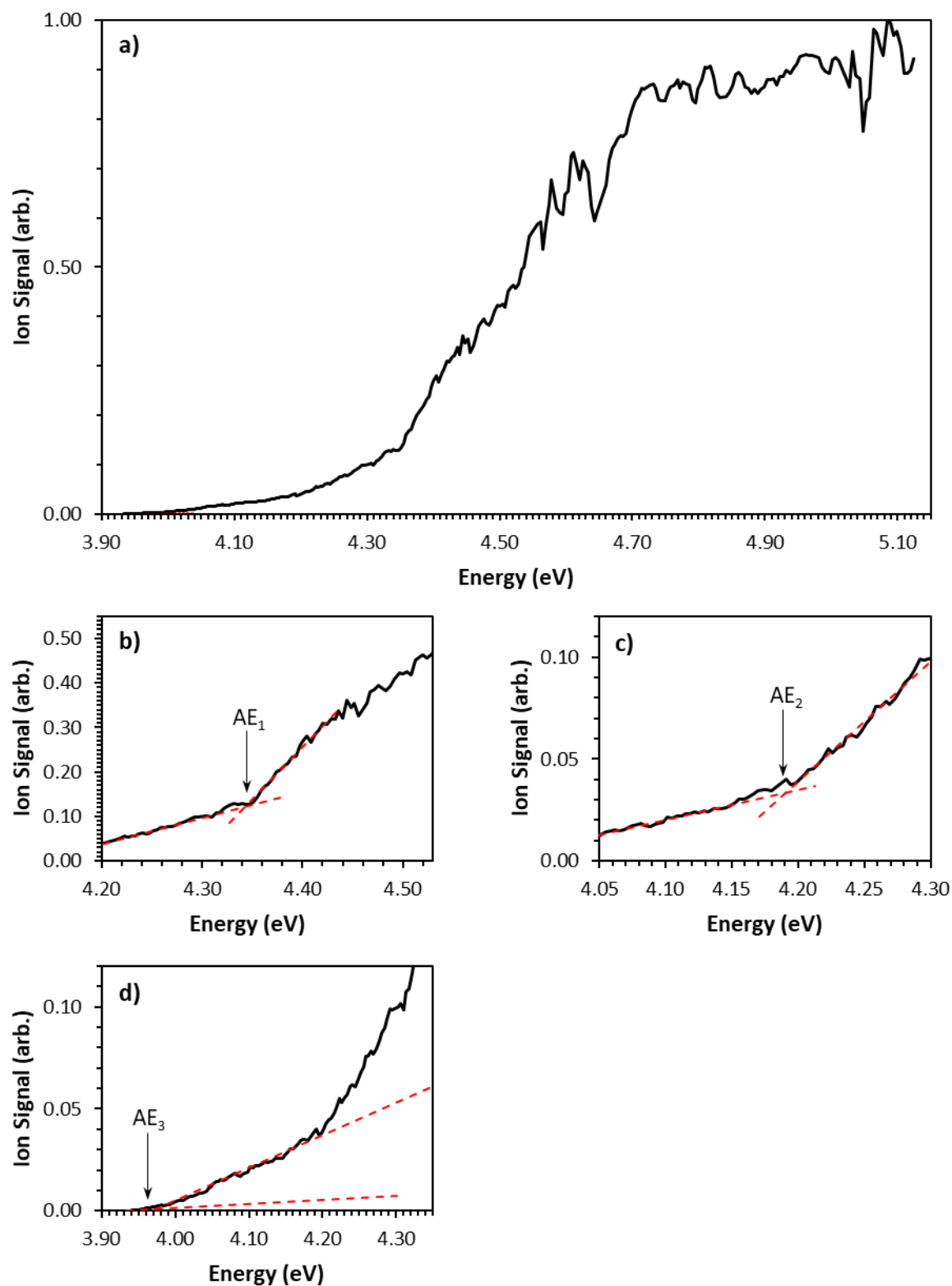


Figure 7.7: PIE spectrum for Ce_4O_2 showing **a).** complete spectrum; **b).** primary onset; **c).** secondary onset and **d).** tertiary onset. Linear trendlines for the baseline and onset are presented as red dashed lines. Appearance energies for the primary, secondary and tertiary onsets - designated AE_1 , AE_2 and AE_3 respectively - are labelled with black arrows.

7.2.4. Ce_4O_3 PIE Spectrum

The Ce_4O_3 experimental PIE spectrum is presented in Figure 7.8. The first appearance of ion signal is recorded at 3.94 eV which extends to a plateau at 4.36 eV corresponding to the maximum ion signal; this indicates that the highest energy FC-allowed transition has been accessed. Two different slopes of signal onset are observed within this energy region. The lower energy onset occurs over the 3.94 – 4.21 eV range with a broad slope. The higher energy onset spans the 4.21 – 4.36 eV range and comprises a noticeably sharper slope than the lower energy onset. The higher energy onset shows a slightly greater increase in ion signal than the lower energy onset; thus, the higher energy onset is designated the primary onset while the lower energy onset is labelled the secondary onset. The similar intensities of both onsets suggest photo-ionisation processes from two low-lying isomers may be underlying the Ce_4O_3 PIE spectrum. The primary and secondary onsets are shown as AE_1 and AE_2 , respectively, in Figure 7.8.

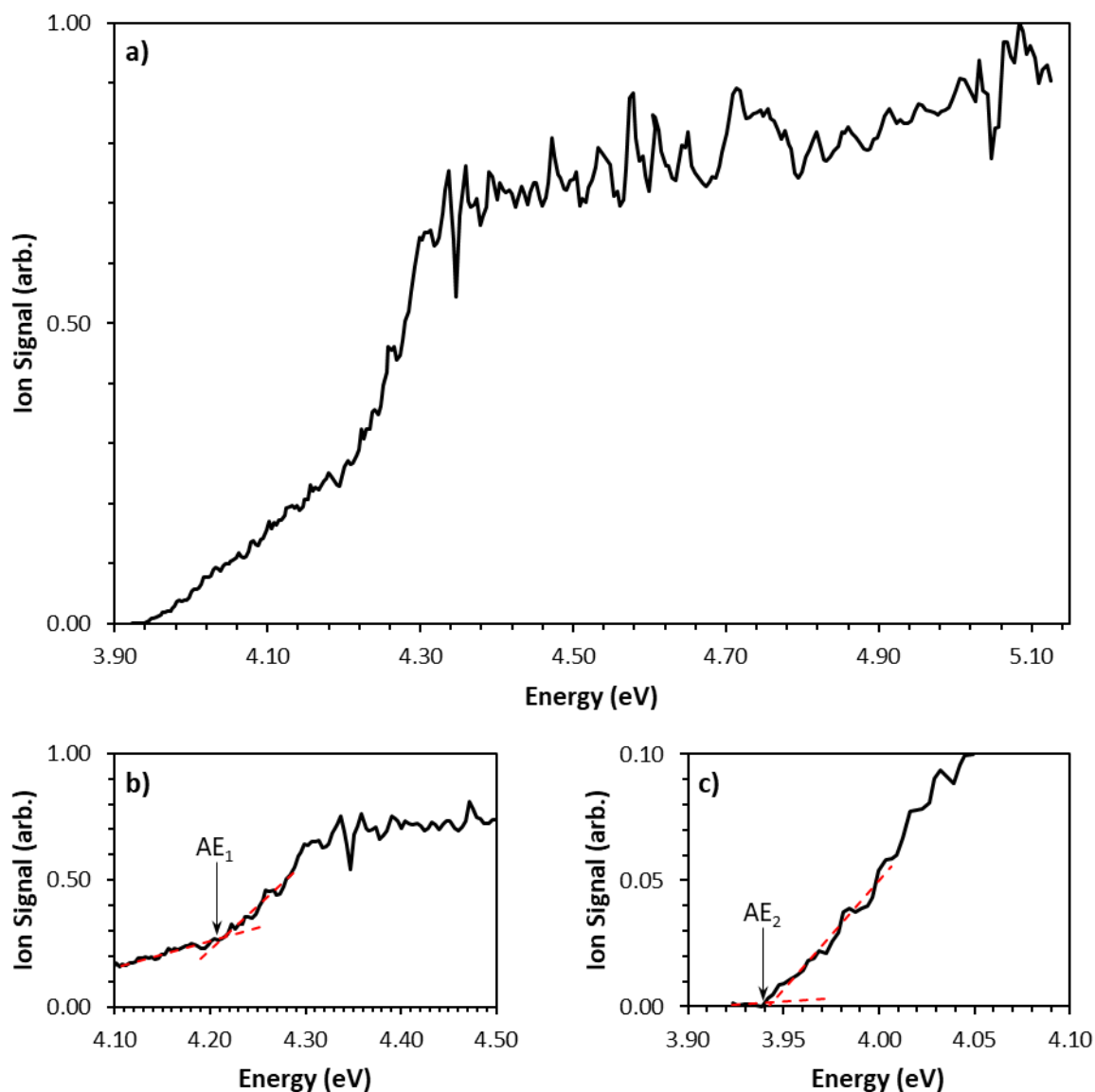


Figure 7.8: PIE spectrum for Ce_4O_3 showing **a)** complete spectrum; **b)** primary onset and **c)** secondary onset. Linear trendlines for the baseline and onset are presented as red dashed lines. Appearance energies for the primary and secondary onsets – designated AE_1 and AE_2 , respectively – are labelled with black arrows.

7.2.5. Ce_4O_4 PIE Spectrum

The Ce_4O_4 experimental PIE spectrum is presented in Figure 7.9. The initial appearance of ion signal occurs at 4.02 eV with a very weak onset to a short plateau at 4.16 eV. This is followed by a second onset at 4.20 eV which comprises the majority of the ion signal increase. Thus, this onset is labelled the primary onset while the lower energy onset is labelled the secondary onset. The primary onset extends to a plateau of maximum ion signal at 4.32 eV – indicating the highest energy FC-allowed transition has been accessed – and is characterised by a moderate slope, inferring some degree of structural deformation following ionisation. The significantly higher intensity of the primary onset compared to the secondary onset suggests that one photo-ionisation process is clearly dominant. Thus, the primary onset most likely describes photo-ionisation transitions from low-lying neutral Ce_4O_4 isomers. The weak intensity of the secondary onset suggests photo-ionisation processes may be occurring from metastable states. The primary and secondary onsets are shown as AE_1 and AE_2 , respectively, in Figure 7.9.

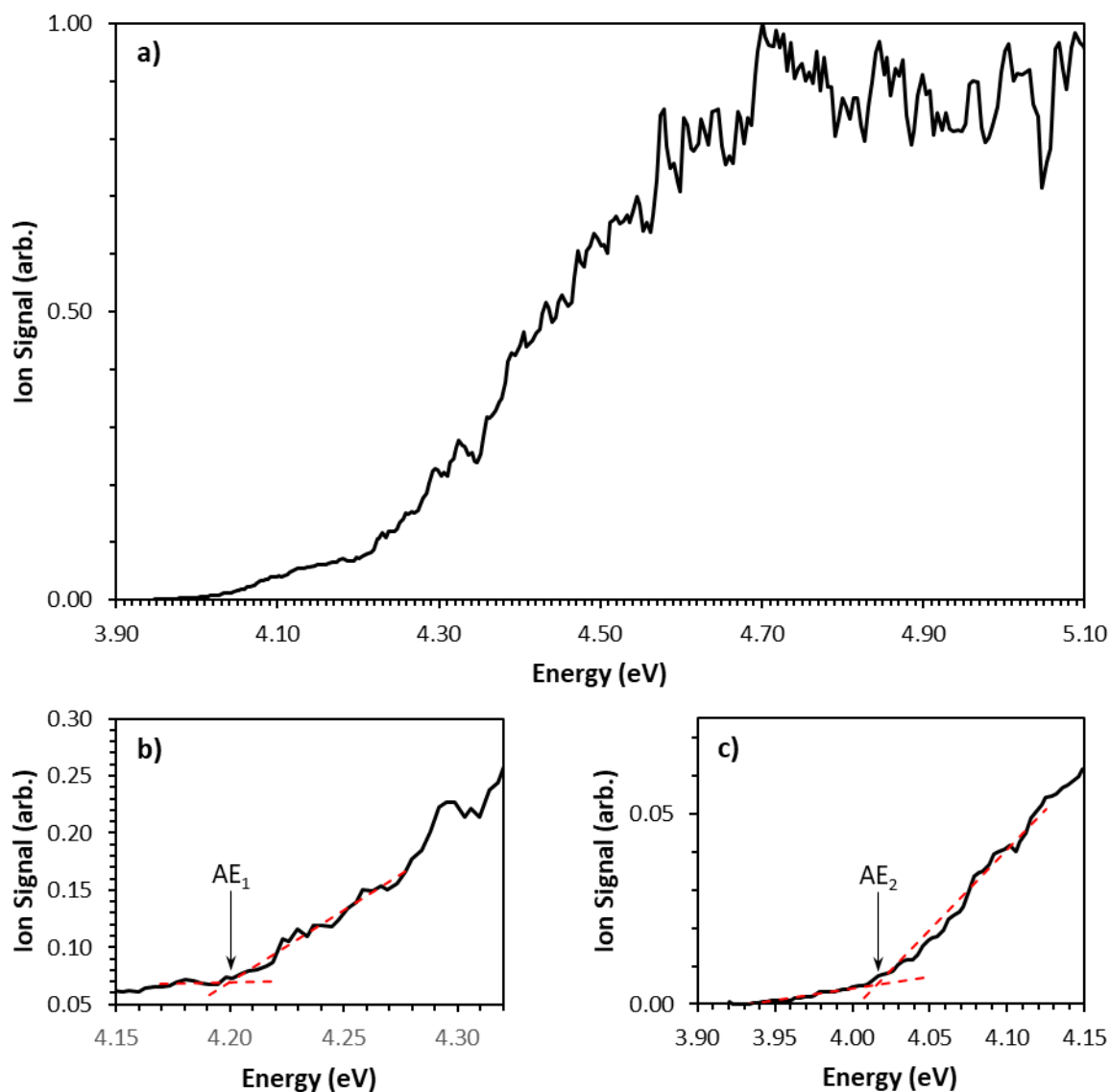


Figure 7.9: PIE spectrum for Ce_4O_4 showing **a)** complete spectrum; **b)** primary onset and **c)** secondary onset. Linear trendlines for the baseline and onset are presented as red dashed lines. Appearance energies for the primary and secondary onsets – designated AE_1 and AE_2 , respectively – are labelled with black arrows.

7.2.6. Ce_4O_5 PIE Spectrum

The Ce_4O_5 experimental PIE spectrum recorded over the 3.92 – 4.68 eV region is presented in Figure 7.10. A very weak onset of ion signal is observed between 4.20 eV and 4.35 eV. This region is assigned to photo-ionisation processes from metastable isomers and is not considered to be particularly interesting. A strong onset of ion signal is observed with an AE of 4.35 eV. The onset maintains a consistent slope – inferring photo-ionisation from one unique Ce_4O_5 neutral isomer – to a maximum ion signal at 4.68 eV which corresponds to the highest photon energy where the Ce_4O_5 ion peak was recorded in PIE experiments. The PIE spectrum does not show a plateau of ion signal, indicating the highest energy FC-allowed transition has not been accessed.

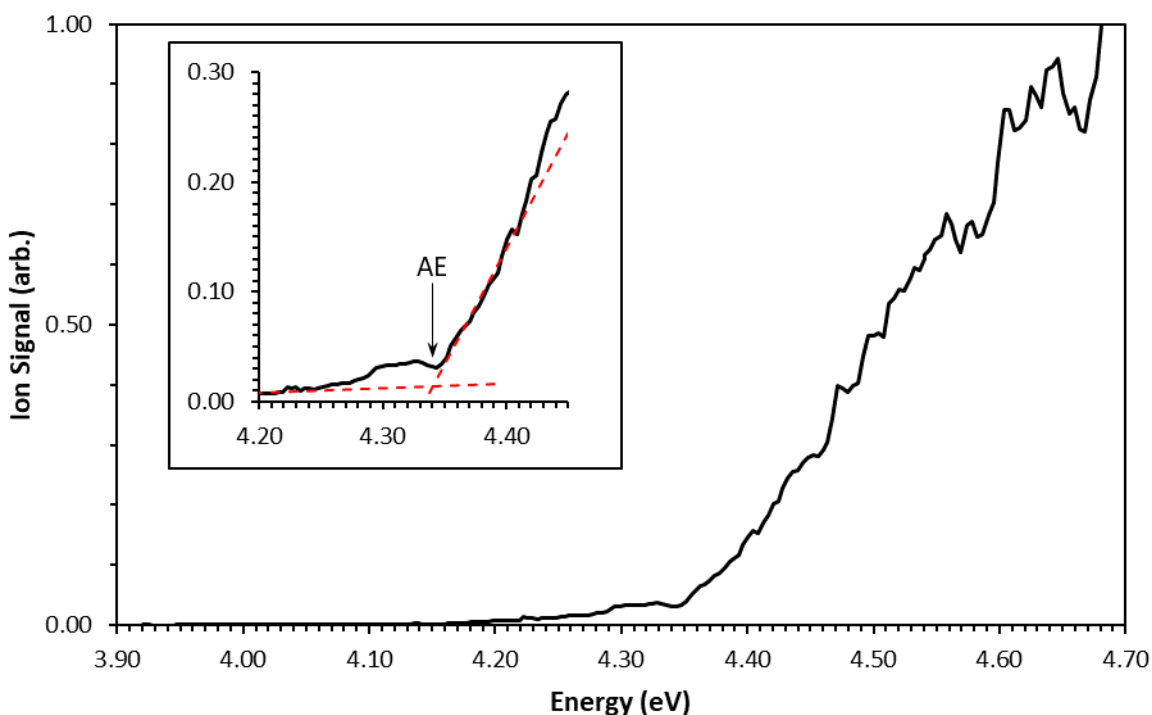


Figure 7.10: PIE spectrum for Ce_4O_5 . **Inset:** Assignment of the appearance energy by intersection of trendlines fitted to the baseline and onset. The appearance energy is labelled with a black arrow.

7.3. Appearance Energy Trends for Ce_4O_n Clusters

Appearance energy trends for the Ce_4O_n ($n=0-5$) cluster ions with sequential oxidation are presented in Figure 7.11. Due to some the Ce_4O_n PIE spectra displaying multiple AEs, two different photo-ionisation trends are plotted; these include (i) the first onset AE which corresponds to the lowest energy at which ion signal is observed, and (ii) the primary onset AE which typically correlates with ionisation process from the lowest energy neutral structure.

The Ce_4O_n first onset AE trend – presented as a dashed line in Figure 7.11 – shows similar AE values for Ce_4 and Ce_4O ; this is followed by a decrease in energy for the Ce_4O_2 , Ce_4O_3 and Ce_4O_4 species, all of which have similar AE values. A moderate increase in AE is then recorded for the Ce_4O_5 cluster. The Ce_4O_n AE trend for the primary onsets shows an increase in the AE of Ce_4O compared to Ce_4 . This is followed by a slight decrease in AE for Ce_4O_2 then a more pronounced decrease in energy for both the Ce_4O_3 and Ce_4O_4 AEs. An increase in AE is then recorded for the Ce_4O_5 cluster, which has a comparable AE to Ce_4O_2 . The Ce_4O_n primary onset AEs are all quite similar – spanning a ca. 0.25 eV energy range – suggesting oxidation/reduction of the Ce_4O_n ($n=0-5$) clusters does not have a significant effect on their HOMO energies. DFT calculations would be beneficial in exploring the electronic properties of the Ce_4O_n clusters in more detail.

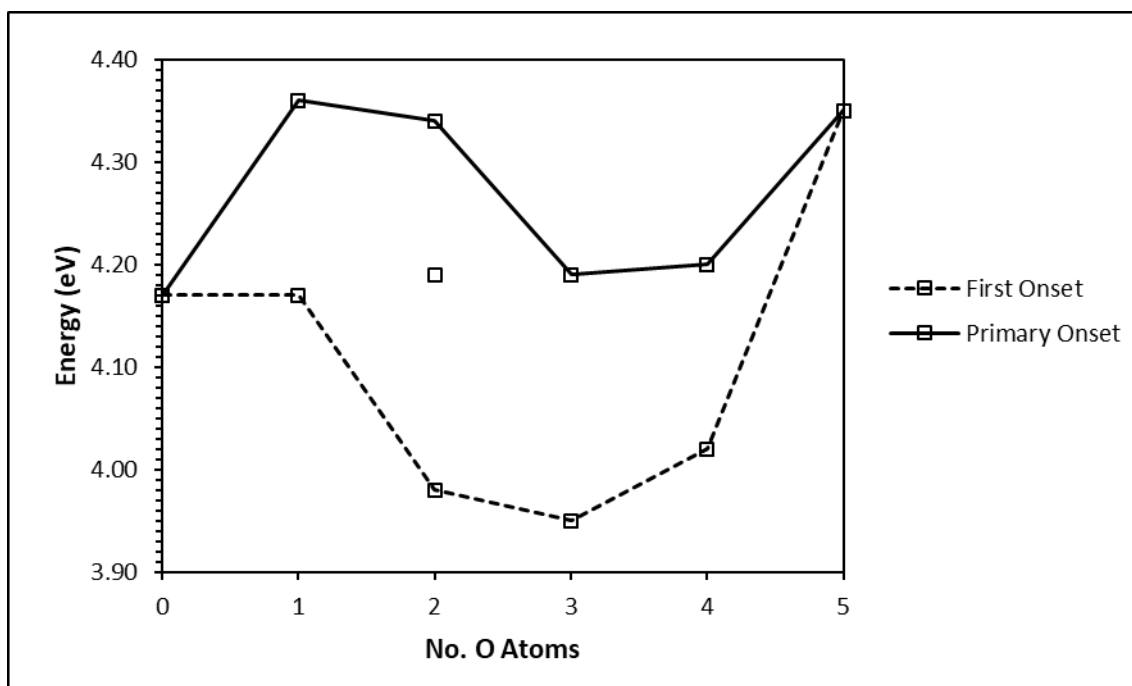


Figure 7.11: Appearance energies for the Ce_4O_n cluster series with sequential oxidation. AE trends are shown for both the first onset of ion signal (dashed line) and the primary onset (solid line).

Ce_4O_n AE trends are compared to AE trends of the Ce_2O_n and Ce_3O_n cluster series in Figure 7.12. The primary onset AE trends for the Ce_3O_n and Ce_4O_n clusters – presented as violet and green solid lines, respectively – shows comparable AEs for the $n=0,1,3$ species; with AE values for these respective Ce_3O_n and Ce_4O_n clusters within ca. 0.15 eV of each other. The Ce_4O_2 and Ce_4O_4 clusters both show primary onset AEs considerably higher – by up to ca. 0.40 eV – than their respective Ce_3O_2 and Ce_3O_4 AE values. However, both the Ce_3O_2 and Ce_3O_4 species have only one onset – therefore the first onset and primary onset AEs are the same – while the respective Ce_4O_2 and Ce_4O_4 clusters show multiple onsets; with the highest energy onset corresponding to the primary onset in both cases. A Ce_4O_n AE trend with the Ce_4O_2 and Ce_4O_4 primary onset AE values replaced by the first onset AEs is shown in Figure 7.12 as a green dotted line; this trend shows excellent agreement with the Ce_3O_n primary onset AEs.

The Ce_3O_n and Ce_4O_n first onset AE trends – presented as violet and green dashed lines, respectively – compare quite well; the Ce_4O_n AE is in most cases similar to, or slightly lower than, the respective Ce_3O_n AE. An exception is found for the Ce_4O species, where the first

onset AE is ca. 0.2 eV higher than the Ce_3O AE. Comparison of the AE values for both the Ce_3O_n and Ce_4O_n species to those of the Ce_2O_n clusters – presented as blue dashed and solid lines for first onset and primary onset AEs, respectively – shows the Ce_3O_n and Ce_4O_n AEs are ca. 0.2 – 0.6 eV lower than their corresponding Ce_2O_n AEs. Moreover, comparison of the AEs for the – bare metal – Ce_2 , Ce_3 and Ce_4 species shows a decrease in AE with increased cluster size; this is consistent with IE trends for Ce_m clusters reported by Koretsky and Knickelbein¹.

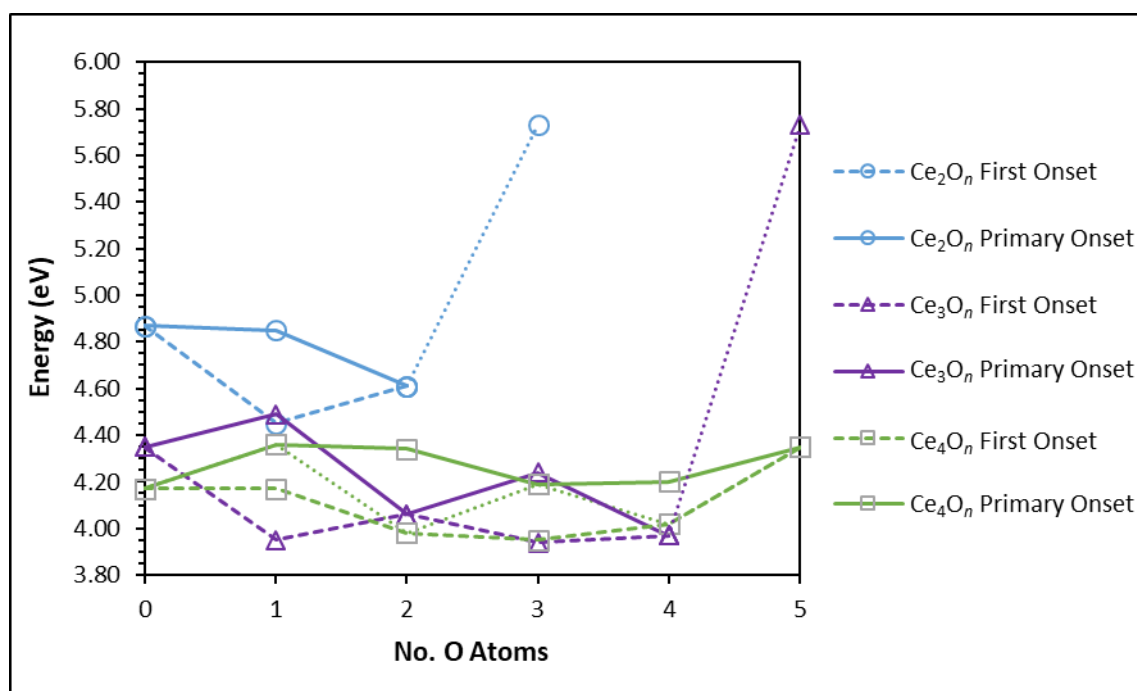


Figure 7.12: Appearance energies for the Ce_2O_n (blue), Ce_3O_n (violet) and Ce_4O_n (green) cluster series with sequential oxidation. AE trends are shown for both the first onset of ion signal (dashed line) and the primary onset (solid line). The Ce_2O_3 and Ce_3O_5 AEs are approximated; therefore, AE trends for these species are represented with dotted lines. The Ce_4O_n AE trend with the Ce_4O_2 and Ce_4O_4 first onset AEs used in place of the highest intensity AEs is shown as a green dotted line.

7.4. References

- (1) Koretsky, G. M.; Knickelbein, M. B. *Eur. Phys. J. D - At. Mol. Opt. Plasma Phys.* **1998**, *2*, 273.

Chapter Eight

Photo-Ionisation Efficiency Spectroscopy, Density Functional Theory

Calculations and Zero Electron Kinetic Energy Simulations of AuCe₂O_n Clusters

This chapter presents both experimentally determined and DFT-calculated adiabatic ionisation energies for the AuCe₂O_n ($n=0-4$) clusters. An initial analysis of the AuCe_mO_n mass spectrum is presented, followed by presentations of experimental Photo-Ionisation Efficiency (PIE) spectra for the detected cluster species. DFT calculated cluster neutral and cationic geometries are used Zero Electron Kinetic Energy (ZEKE) spectral simulations, which are integrated to produce a calculated PIE spectrum. This is compared to the experimental PIE spectrum to infer electronic and geometric properties of the relevant cluster species. For cluster systems not detected in PIE experiments, DFT calculations and ZEKE/PIE spectral simulations are still presented to provide insight on the properties of the calculated cluster species.

8.1. AuCe_mO_n Mass Spectrum

A mass spectrum for Au_xCe_mO_n clusters following photo-ionisation at 213 nm (5.82 eV) is presented in Figure 8.1. Au_xCe_mO_n ion peaks detected in the mass spectrum include the AuCe, AuCe₂O_n ($n=0-2$), AuCe₃O_n ($n=0-3$) and AuCe₄O_n ($n=0-5$) cluster species. Au_xCe_mO_n cluster ions containing 2 or more gold atoms are not detected; this is most likely due to the high ionisation energy of gold (9.23 eV¹) which increases the IE of Au_xCe_mO_n clusters relative to the extent of gold doping. Previous work by Gentleman² on the ionisation energies of RhHo₂O_n and Rh₂Ho₂O_n clusters revealed Rh₂Ho₂O_n IEs which were typically 0.3 eV higher than their RhHo₂O_n counterparts. Gentleman attributed this increased IE to the extra Rh atom which, by way of its high ionisation energy (7.46 eV³), has a stabilising effect on the electronic structure of the entire cluster.

The AuCe_mO_n ion peaks do not appear to follow any “magic number” trends in intensity. Moreover, they are typically detected with far lower intensity than their Ce_mO_n counterparts. This may be an effect of either (i) lower production of AuCe_mO_n clusters in the source compared to Ce_mO_n clusters; or (ii) photo-dissociation of AuCe_mO_n clusters in the ionisation region. With regard to the former, the optimal conditions for AuCe_mO_n cluster production were found to require the He carrier gas pressure to be only slightly higher than for Ce_mO_n cluster formation, and with weak ablation of the gold rod. While higher pressure of the inert gas induces a greater collision rate, the higher kinetic energies of the particles in the turbulent flow region may cause the particles to recoil on collision and thus reduce the frequency of Au-Ce_mO_n chemisorption processes. Likewise, strong ablation of the gold rod will introduce excess gold concentrations in the cluster source which, while increasing the Au-Ce_mO_n collision rate, will also induce greater rates of both Au-Au and Au-AuCe_mO_n collisions. Both types of collisions – which are likely to display higher chemisorption energies due to the preference of gold to undergo aurophilic bonding⁴⁻⁶ – will hinder the formation of AuCe_mO_n clusters in the source region. With regard to the latter, a detailed discussion on the atomic bonding energies within AuCe_mO_n clusters – and their implications in cluster photo-fragmentation processes – is presented in Chapter 10.

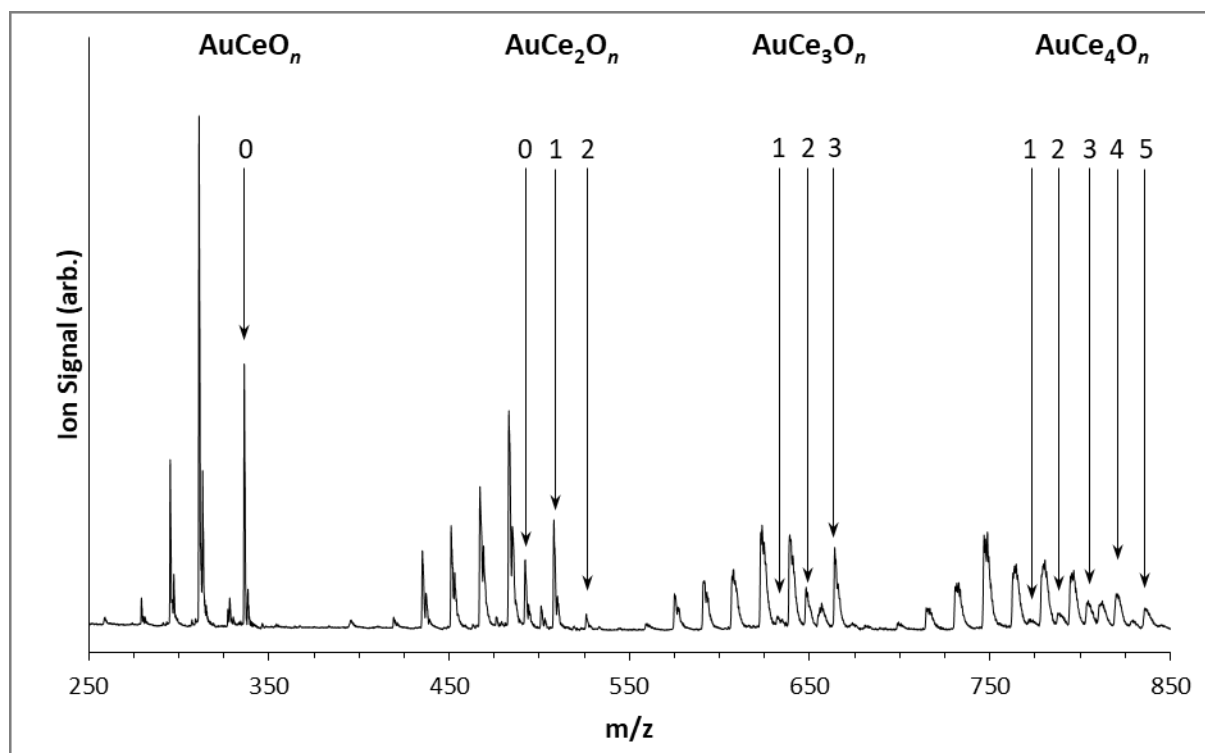


Figure 8.1: Mass spectrum of Ce_mO_n and AuCe_mO_n clusters following photo-ionisation at 213 nm (5.82 eV). Ion peaks corresponding to AuCe_mO_n clusters are labelled.

8.2. Appearance of Cluster Ion Signal for the AuCe_2O_n ($n=0-2$) Series

A series of mass spectra recorded following photo-ionisation at 240 nm (5.17 eV), 264 nm (4.70 eV) and 279 nm (4.44 eV) are presented in Figure 8.2. The AuCe_2 , AuCe_2O and AuCe_2O_2 ion peaks all appear within these wavelength ranges. Both the AuCe_2 and AuCe_2O peaks appear in the 240 – 264 nm (4.70 – 5.17 eV) range while the AuCe_2O_2 peak appears in the 264 – 279 nm (4.44 – 4.70 eV) region. The AuCe_2O_3 and AuCe_2O_4 ion peaks are not detected at any wavelength within the experimental range; this is most likely due to both species having high appearance energies – and correspondingly high ionisation energies – which prohibit photo-ionisation using the experimental setup in this work.

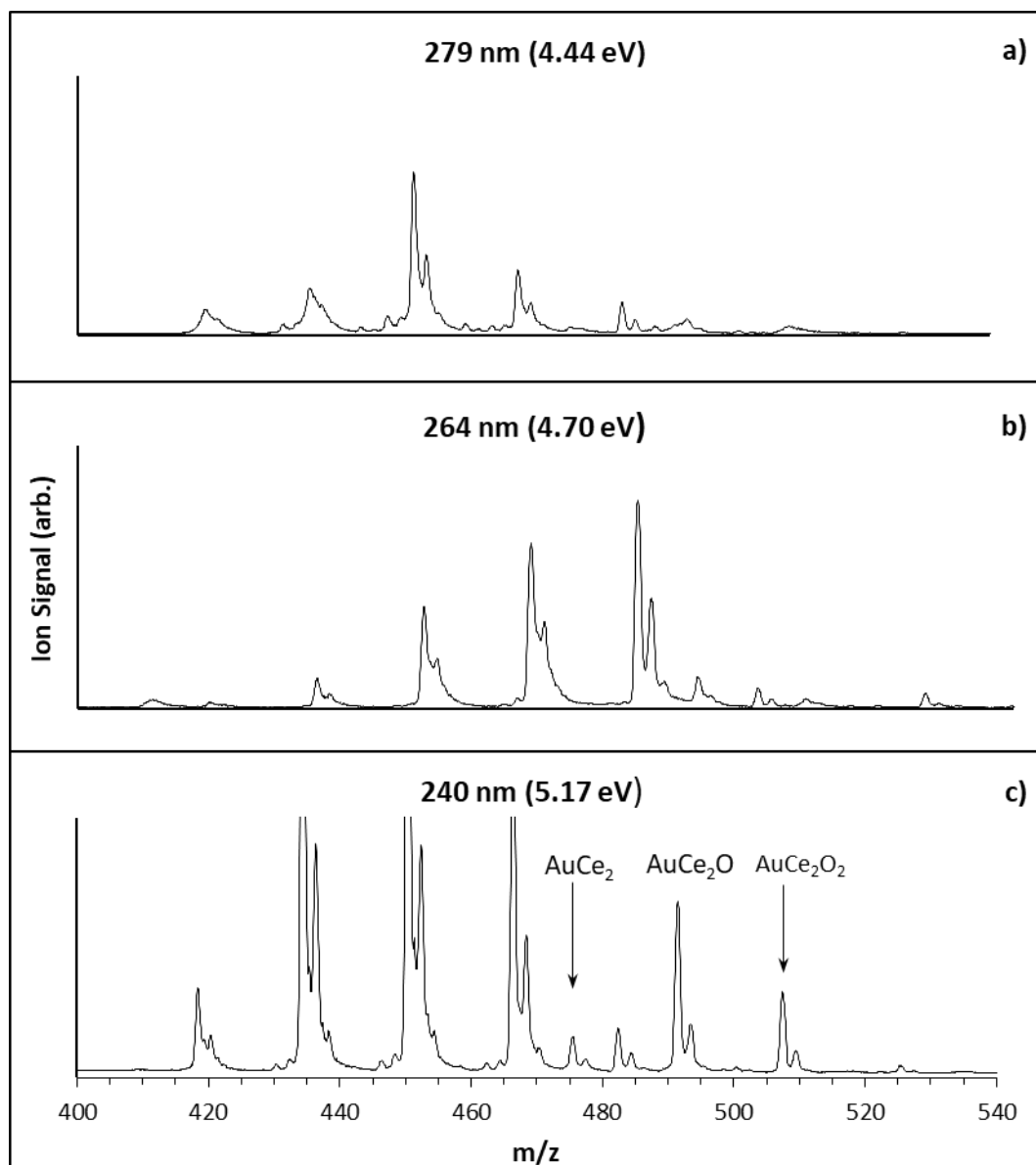


Figure 8.2: Mass spectra of AuCe_2 , AuCe_2O and AuCe_2O_2 clusters following photo-ionisation at **a).** 279 nm (4.44 eV), **b).** 264 nm (4.70 eV) and **c).** 240 nm (5.64 eV).

8.3. PIE Spectrum and DFT Results for AuCe₂

8.3.1. AuCe₂ Experimental PIE Spectrum

The Photo-Ionisation Efficiency (PIE) spectrum for AuCe₂ recorded over the energy range 4.70 – 5.12 eV is presented in Figure 8.3. A flat region of ion signal with zero intensity is initially recorded in the 4.70 – 4.78 eV region; this is assigned as the ion signal baseline. A single onset is then observed with an appearance energy of 4.78 eV. The onset has a broad profile – spanning a ca. 0.2 eV range – with a shallow slope. The onset reaches a plateau at ca. 5.0 eV, indicating the highest energy FC-allowed vibronic transition has been accessed.

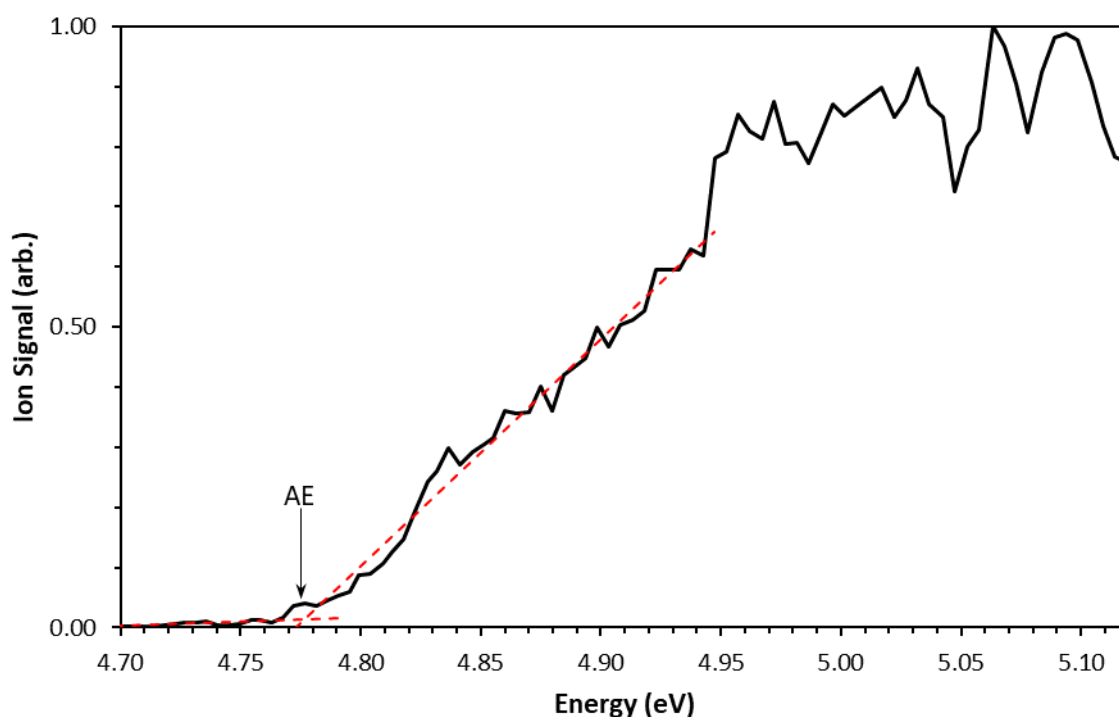


Figure 8.3: PIE spectrum for AuCe₂. Linear trendlines for the baseline and onset are presented as red dashed lines. The appearance energy is labelled with a black arrow.

8.3.2. DFT Calculations for AuCe₂

DFT calculations of neutral AuCe₂ structures were performed using an extensive number of starting geometries in the m=2,4,6,8 multiplicities. The lowest energy calculated AuCe₂ structures are shown in Figures 8.4 and 8.5. Calculated vibrational modes for all AuCe₂O_n clusters are also presented in Appendix B. The neutral AuCe₂ clusters are calculated with a very dense manifold of states; 14 unique geometric isomers and spin isomers located within 0.35 eV of the LES. The extensive number of low-lying isomers makes subsequent ZEKE and PIE simulations problematic, since constructing a PIE spectrum from 28 ionisation transitions would be both computationally expensive and inherently difficult. Therefore, a small subset of low-lying neutral structures located within 0.03 eV of the LES – comprising four neutral AuCe₂ structures – are instead considered. This still provides a good fit between simulated and experimental PIE spectra, as discussed in section 8.3.4.

The four low-lying AuCe₂ neutral structures are all calculated as trimers in either the C_s or C_{2v} point groups; the C_s and C_{2v} structures are labelled **XIIIA** and **XIIIB**, respectively. The structures are all calculated in either sextet or octet spin states. Thus, the four lowest energy species are labelled **⁶XIIIA**, **⁶XIIIB**, **⁸XIIIA** and **⁸XIIIB** in order of increasing energy. While the calculated neutral structures are energetically indistinguishable, the **⁶XIIIA** structure is considered as the LES to simplify later discussions. Electronic states for the AuCe₂ structures were unable to be calculated due to orbitals being calculated with unidentified symmetries.

A total of 3 cationic structures are calculated as target states for the **⁶XIIIA**, **⁶XIIIB**, **⁸XIIIA** and **⁸XIIIB** neutral species. These include two septet species with C_s and C_{2v} point groups – labelled **⁷XIIIA⁺** and **⁷XIIIB⁺**, respectively – and a quintet C_s structure labelled **⁵XIIIA⁺**. All calculated AuCe₂ cationic structures show an elongation of the Ce-Ce bond and contraction of the Au-Ce bonds relative to their neutral counterparts. No C_{2v}-symmetric quintet cation was calculated, however the **⁵XIIIA⁺** structure was found to very closely approach C_{2v} symmetry (C_{2v} constrained calculations of the quintet cation converged to a saddle point). Therefore, the **⁵XIIIA⁺** cation is considered as the quintet target state of both the **⁶XIIIA** and **⁶XIIIB** neutral species. AuCe₂ nonet cations – as $\Delta S = +\frac{1}{2}$ targets for the **⁸XIIIA** and **⁸XIIIB** neutral species –

were particularly difficult to calculate and tended to converge to saddle points with low imaginary frequencies (ca. 30 cm⁻¹). Moreover, distortion of these structures along the imaginary vibrational coordinate and re-optimisation simply lead to the structure converging on the original saddle point. This peculiarity typically results from a flat potential energy surface. While it is generally acceptable to ignore low imaginary frequencies as anomalies of the DFT process⁷, the *ezSpectrum* program used in this work for ZEKE simulations does not permit the use of imaginary frequencies⁸. Consequentially, nonet cationic species are not presented.

The calculated AuCe₂ neutral and cationic species gives a total of 6 potential ionisation transitions for the AuCe₂ PIE spectrum; these include the ${}^7\text{XIIIA}^+ \leftarrow {}^6\text{XIIIA}$, ${}^5\text{XIIIA}^+ \leftarrow {}^6\text{XIIIA}$, ${}^7\text{XIIIB}^+ \leftarrow {}^8\text{XIIIB}$, ${}^7\text{XIIIA}^+ \leftarrow {}^8\text{XIIIA}$, ${}^7\text{XIIIB}^+ \leftarrow {}^6\text{XIIIB}$ and ${}^5\text{XIIIA}^+ \leftarrow {}^6\text{XIIIB}$ processes. IEs for these transitions are calculated as 5.044 eV, 5.214 eV, 5.042 eV, 5.030 eV, 5.024 eV and 5.184 eV respectively; the ca. 0.17 eV variance in calculated IEs matches well with the ca. 0.2 eV onset of ion signal in the experimental PIE spectrum. The ${}^7\text{XIIIA}^+ \leftarrow {}^6\text{XIIIA}$, ${}^5\text{XIIIA}^+ \leftarrow {}^6\text{XIIIA}$, ${}^7\text{XIIIB}^+ \leftarrow {}^8\text{XIIIB}$, ${}^7\text{XIIIB}^+ \leftarrow {}^6\text{XIIIB}$ and ${}^5\text{XIIIA}^+ \leftarrow {}^6\text{XIIIB}$ processes are shown in Figure 8.4 as green, orange, blue, violet and yellow arrows, respectively. The ${}^7\text{XIIIA}^+ \leftarrow {}^8\text{XIIIA}$ transition is shown as a red dotted arrow due to low a ZEKE intensity calculated for this process (vide infra).

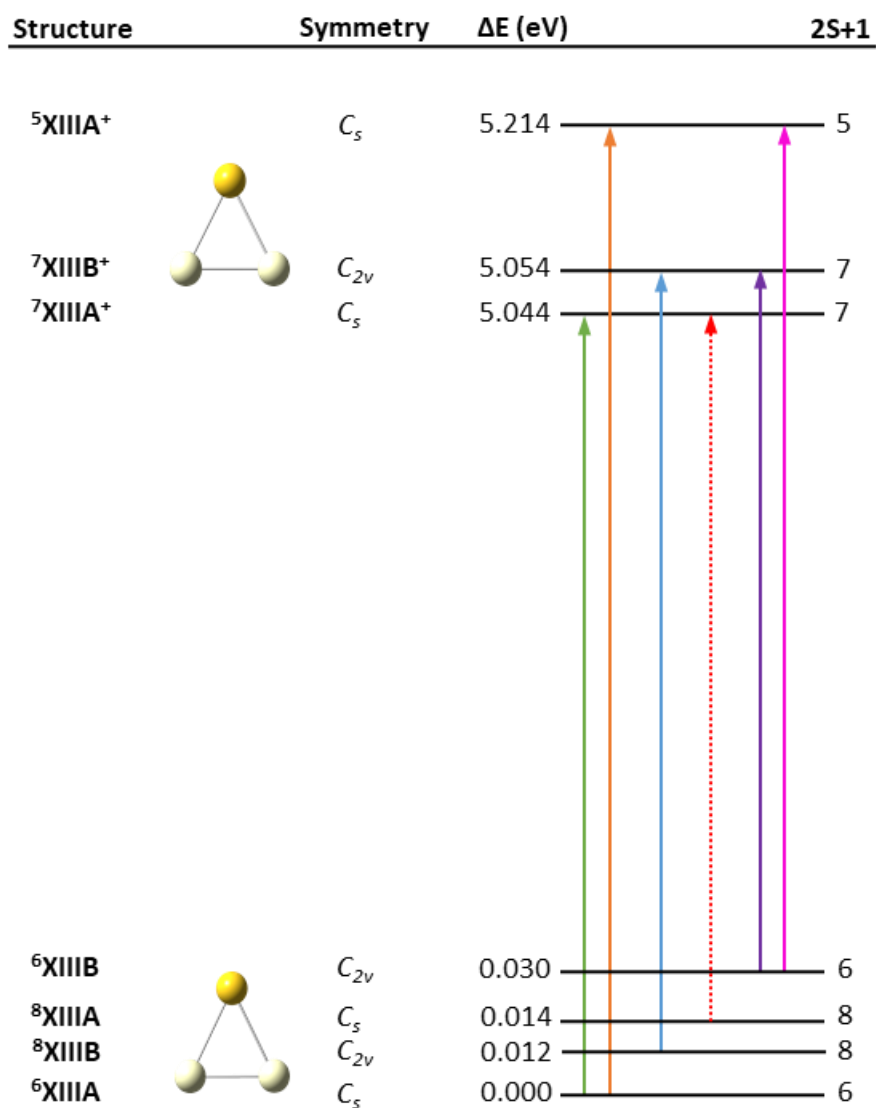


Figure 8.4: Calculated structures for the AuCe₂. Potential ionisation transitions are shown. Low intensity ZEKE transitions (*vide infra*) are shown as red dotted arrows.

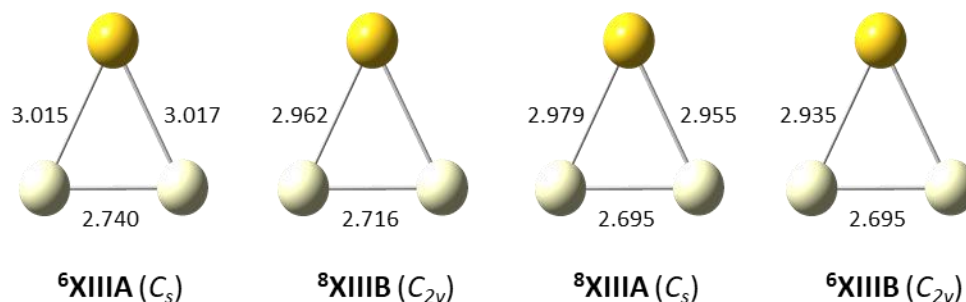
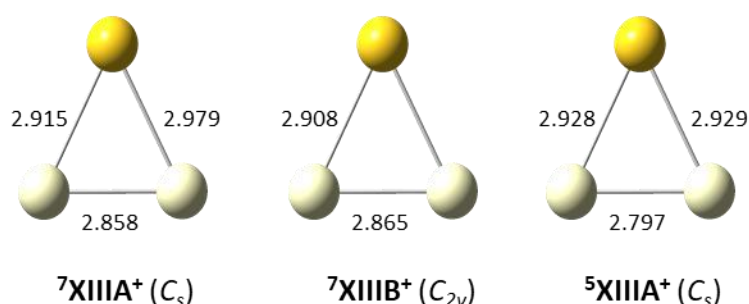
AuCe₂**AuCe₂⁺**

Figure 8.5: Calculated AuCe₂ neutral (top) and cationic (below) structures. Bond lengths are presented in Å. Point groups are shown in brackets.

8.3.3. ZEKE Spectral Simulations for AuCe₂

ZEKE spectral simulations for the AuCe₂ **⁷XIIIA⁺←⁶XIIIA**, **⁵XIIIA⁺←⁶XIIIA**, **⁷XIIIB⁺←⁸XIIIB**, **⁷XIIIB⁺←⁶XIIIB** and **⁵XIIIA⁺←⁶XIIIB** ionisation processes are presented in Figure 8.6. The calculated ZEKE spectra were energetically offset from each other using the method described in Chapter 3; further corrections of −0.13 eV, −0.02 eV, −0.04 eV and −0.02 eV were then applied to the **⁵XIIIA⁺←⁶XIIIA**, **⁷XIIIB⁺←⁸XIIIB**, **⁷XIIIB⁺←⁶XIIIB** and **⁵XIIIA⁺←⁶XIIIB** ZEKE spectra, respectively, such that a good fit was found between the calculated and experimental PIE spectra (vide infra). The corrected ZEKE spectra are shown here.

Similar intensities are calculated for all spectra – identified by the comparable scaling factors used to normalise the most intense peaks in each spectrum – although the **⁵XIIIA⁺←⁶XIIIA** and **⁵XIIIA⁺←⁶XIIIB** processes appear to be particularly dominant. Very low vibronic peak intensities were calculated for the **⁷XIIIA⁺←⁸XIIIA** process; this process is thus not considered

to contribute substantially to the PIE spectrum. The ${}^7\text{XIII A}^+ \leftarrow {}^8\text{XIII A}$ ZEKE spectrum is shown in Appendix C.

The ${}^7\text{XIII A}^+ \leftarrow {}^6\text{XIII A}$ and ${}^5\text{XIII A}^+ \leftarrow {}^6\text{XIII A}$ ZEKE spectra presented in Figures 8.6(a) and 8.6(b) – which both describe ionisation processes from the ${}^6\text{XIII A}$ LES – show markedly different spectral profiles. The ${}^7\text{XIII A}^+ \leftarrow {}^6\text{XIII A}$ spectrum comprises a number of short progressions of the ν_2 mode; both by itself and combined with the ν_1 and ν_3 modes. The ν_2 mode describes a symmetric Au-Ce stretch; the ν_2 progression thus infers structural deformation of the cationic ${}^7\text{XIII A}^+$ species along the ν_2 vibrational coordinate. The ${}^5\text{XIII A}^+ \leftarrow {}^6\text{XIII A}$ ZEKE spectrum is dominated by long progressions in the post-band origin region which mostly comprise the 2_0^n , $1_1^1 2_0^n$, $1_2^2 2_0^n$ and $1_3^3 2_0^n$ progressions; this again suggests deformation of the cationic structure occurring along the ν_2 coordinate which describes an Au-Ce symmetric stretch. The 2_0^2 vibronic peak corresponds to maximum FC overlap in both the ${}^7\text{XIII A}^+ \leftarrow {}^6\text{XIII A}$ and ${}^5\text{XIII A}^+ \leftarrow {}^6\text{XIII A}$ spectra, inferring a small degree of structural deformation between the neutral and cationic structures for both ionisation processes. However, comparison of the vibronic peak intensities of the ${}^7\text{XIII A}^+ \leftarrow {}^6\text{XIII A}$ and ${}^5\text{XIII A}^+ \leftarrow {}^6\text{XIII A}$ spectra – which are scaled by 10 and 3.72, respectively, in order to normalise the most intense peak – show stronger vibronic peak intensities, and thus greater FC overlap – in the ${}^5\text{XIII A}^+ \leftarrow {}^6\text{XIII A}$ spectrum.

The ${}^7\text{XIII B}^+ \leftarrow {}^8\text{XIII B}$ and ${}^7\text{XIII B}^+ \leftarrow {}^6\text{XIII B}$ ZEKE spectra – presented in Figures 8.6(c) and 8.6(d) respectively – involve ionisation from the C_{2v} -symmetric ${}^8\text{XIII B}$ and ${}^6\text{XIII B}$ spin-isomers to a common ${}^7\text{XIII B}^+$ cationic species. The spectral profiles are comparable owing to the similar geometries of both neutral structures. Both ZEKE spectra contain a number of long progressions of the ν_2 mode – both by itself and combined with the ν_1 and ν_3 modes – in the post-band origin region. The ν_2 mode describes a symmetric stretch of the Au-Ce bonds. The comparable peak intensities of both spectra – where the most intense vibronic peak is scaled by 13 and 14 for the ${}^7\text{XIII B}^+ \leftarrow {}^8\text{XIII B}$ and ${}^7\text{XIII B}^+ \leftarrow {}^6\text{XIII B}$ ZEKE spectra, respectively – infers similar FC overlap in both ionisation processes.

The $^5\text{XIIIA}^+ \leftarrow ^6\text{XIIIB}$ ZEKE spectrum presented in Figure 8.6(e). This spectrum shows a markedly different profile to the $^7\text{XIIIB}^+ \leftarrow ^6\text{XIIIB}$ spectrum in Figure 8.6(d) – which both describe ionisation of the $^6\text{XIIIB}$ neutral species – with significantly higher peak intensities and shorter vibronic progressions. These both point to a strong FC overlap – and thus a minimal change in geometric structure – between the neutral $^6\text{XIIIB}$ and cationic $^5\text{XIIIA}^+$ species.

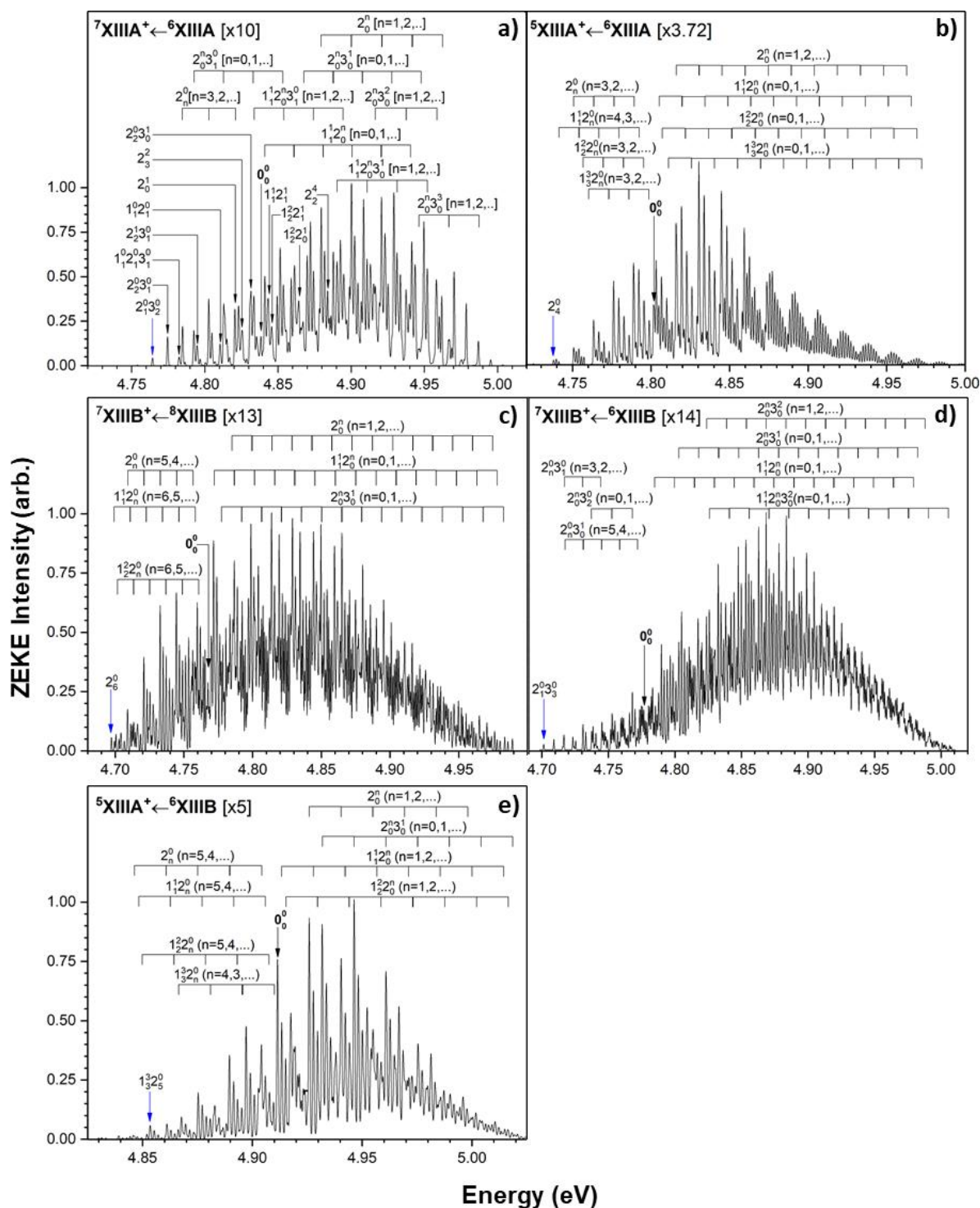


Figure 8.6: ZEKE spectra for AuCe₂ ionisation transitions: **a).** ${}^7\text{XIIIA}^+ \leftarrow {}^6\text{XIIIA}$, **b).** ${}^5\text{XIIIA}^+ \leftarrow {}^6\text{XIIIA}$ **c).** ${}^7\text{XIIIB}^+ \leftarrow {}^8\text{XIIIB}$, **d).** ${}^7\text{XIIIB}^+ \leftarrow {}^6\text{XIIIB}$ and **e).** ${}^5\text{XIIIA}^+ \leftarrow {}^6\text{XIIIB}$. Spectral intensities are normalised to the most intense peak in each spectrum with scaling factors shown. Prominent vibronic transitions are assigned. The vibronic transition likely to correspond to the appearance of ion signal in each spectrum is labelled with a blue arrow.

8.3.4. Comparison of Simulated and Experimental PIE Spectra for AuCe₂

The simulated AuCe₂ PIE spectrum is presented in Figure 8.7. This PIE spectrum was calculated via integration of the ${}^7\text{XIII A}^+ \leftarrow {}^6\text{XIII A}$, ${}^5\text{XIII A}^+ \leftarrow {}^6\text{XIII A}$, ${}^7\text{XIII B}^+ \leftarrow {}^8\text{XIII B}$, ${}^7\text{XIII B}^+ \leftarrow {}^6\text{XIII B}$ and ${}^5\text{XIII A}^+ \leftarrow {}^6\text{XIII B}$ vibronic peaks in the respective ZEKE spectra. An excellent agreement is found between the calculated and experimental PIE spectra. The adiabatic IE is assigned to the ${}^7\text{XIII A}^+ \leftarrow {}^6\text{XIII A}$ 0_0^0 transition – corresponding to the lowest energy ionisation process from the lowest energy neutral structure. This gives an IE value of 4.82 eV for the AuCe₂ cluster.

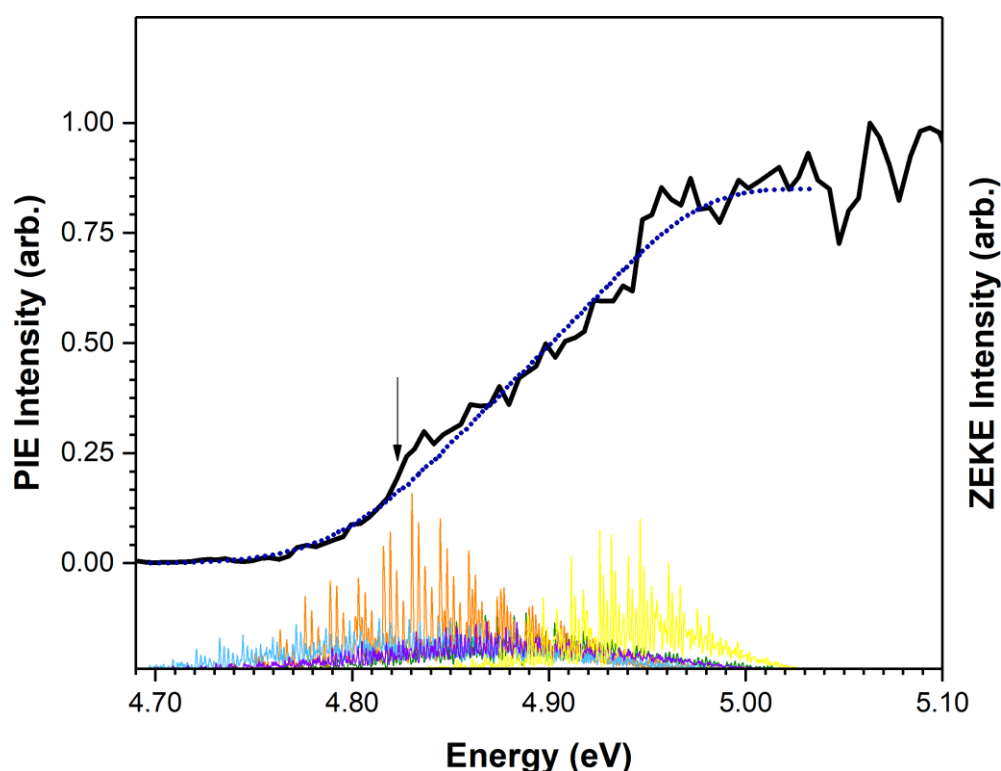


Figure 8.7: Calculated AuCe₂ PIE spectrum (blue dashed line) overlaid against the experimental PIE spectrum (solid black line). Calculated ZEKE spectra for the ${}^7\text{XIII A}^+ \leftarrow {}^6\text{XIII A}$, ${}^5\text{XIII A}^+ \leftarrow {}^6\text{XIII A}$, ${}^7\text{XIII B}^+ \leftarrow {}^8\text{XIII B}$, ${}^7\text{XIII B}^+ \leftarrow {}^6\text{XIII B}$ and ${}^5\text{XIII A}^+ \leftarrow {}^6\text{XIII B}$ ionisation processes are shown below the PIE spectrum in green, orange, blue, violet and yellow, respectively. The adiabatic ionisation energy is labelled with a black arrow.

8.4. PIE Spectrum and DFT Results for AuCe₂O

8.4.1. AuCe₂O Experimental PIE Spectrum

The PIE spectrum for the AuCe₂O cluster species is presented in Figure 8.8. A flat region of zero ion signal is initially recorded in the 4.20 – 4.40 eV region; this is followed by a very weak onset in the 4.40 – 4.54 eV energy range. The low intensity signal in this region is likely to be from metastable photo-ionisation processes; therefore, it is not regarded as particularly interesting. The 4.40 – 4.54 eV region is taken as the baseline for the PIE onset. A sharp onset is observed with an appearance energy of 4.54 eV and a shoulder at 4.62 eV. The onset extends to a plateau of maximum ion signal at ca. 4.74 eV, indicating the highest FC-allowed vibronic transition has been accessed.

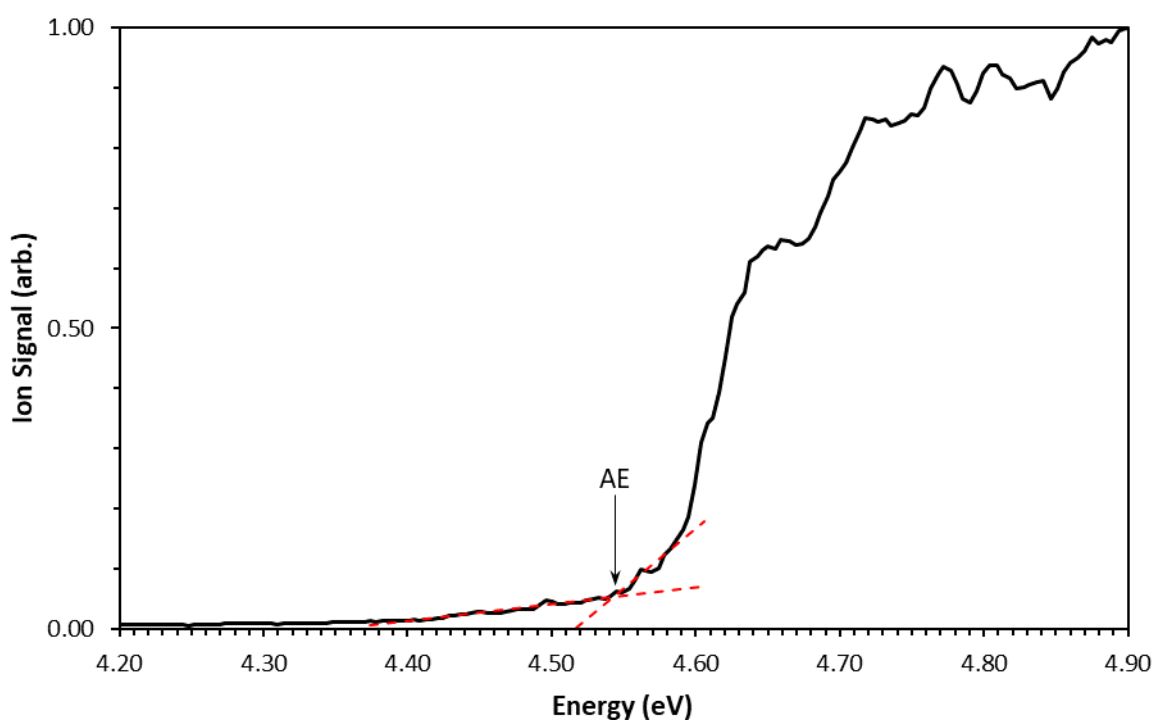


Figure 8.8: PIE spectrum for AuCe₂O. Linear trendlines for the baseline and onset are presented as red dashed lines. The appearance energy is labelled with a black arrow.

8.4.2. DFT Calculations for AuCe₂O

Calculated AuCe₂O neutral and cationic structures are presented in Figures 8.9 and 8.10. Only one unique geometric structure is calculated for the neutral AuCe₂O system. This C₁ symmetric structure, labelled **XIV**, comprises an AuCe₂ trimer with an oxygen atom bridging the Ce-Ce bond; the oxygen is positioned out of the AuCe₂ plane with a dihedral angle of 130.6°. Calculated neutral species with the **XIV** structure quartet and doublet spin-isomers – with $\Delta E = 0.003$ eV – in the ⁴A and ²A electronic states, labelled ⁴**XIV** and ²**XIV** respectively. These spin isomers are energetically indistinguishable with an energetic separation of $\Delta E = 0.003$ eV. The bonding arrangement in both structures – where the Au atom bridges two Ce atoms – is consistent with previous calculations of Au deposited to O vacancy sites on the bulk ceria surface^{9,10}. The Au-Ce bond lengths shown here – which range from 2.947 Å to 2.956 Å – are slightly shorter than those calculated by Fabris et al., who report bond lengths of 3.14 Å and 3.20 Å.

Two unique structures are calculated for the AuCe₂O cations. Both structures comprise the same atomic arrangement as the neutral **XIV** structure, with the oxygen atom positioned either within or above the AuCe₂ plane (labelled **XIVA** and **XIVB** respectively). The **XIVA** structure is calculated in quintet and triplet states – labelled ⁵**XIVA**⁺ and ³**XIVA**⁺ respectively – while the **XIVB** structure is calculated in triplet and singlet states, labelled ³**XIVB**⁺ and ¹**XIVB**⁺, respectively. A total of 4 ionisation transitions are calculated for the AuCe₂O system which include the ⁵A←⁴A (⁵**XIVA**⁺←⁴**XIV**), ³A←⁴A (³**XIVB**⁺←⁴**XIV**), ¹A←²A (¹**XIVB**⁺←²**XIV**) and ³A←²A (³**XIVA**⁺←²**XIV**) ionisation transitions. IEs are calculated as 5.021 eV, 5.029 eV, 5.046 eV and 5.104 eV, respectively; the 0.083 eV variation in calculated IE values compares well with the ca. 0.1 eV range over which the majority of the ion signal increase occurs in the experimental PIE spectrum. The ³A←⁴A (³**XIVB**⁺←⁴**XIV**) and ¹A←²A (¹**XIVB**⁺←²**XIV**) ionisation processes are presented as green and orange arrows, respectively, in Figure 8.9. The ⁵A←⁴A (⁵**XIVA**⁺←⁴**XIV**) and ³A←²A (³**XIVA**⁺←²**XIV**) transitions are shown as red dotted arrows due to low vibronic peak intensities calculated for their respective ZEKE spectra (vide infra).

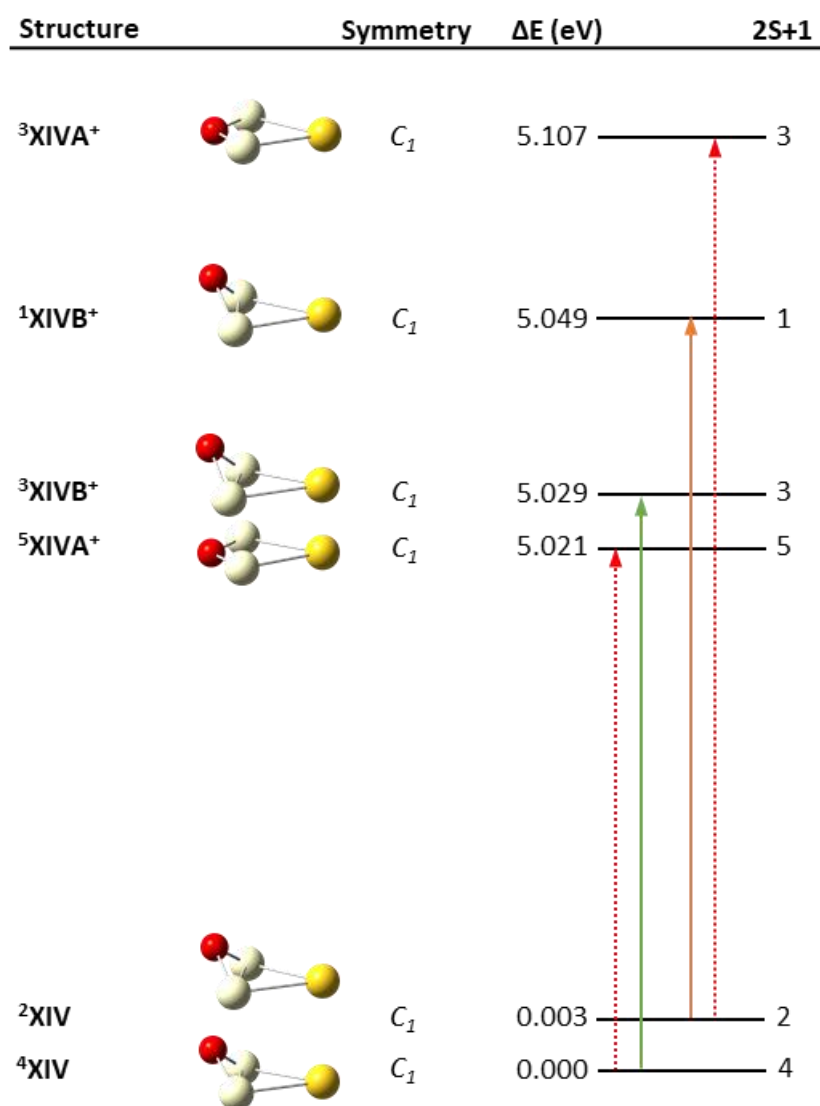


Figure 8.9: Calculated structures for AuCe₂O. Potential ionisation transitions are shown. Low intensity ZEKE transitions (*vide infra*) are presented as red dotted arrows.

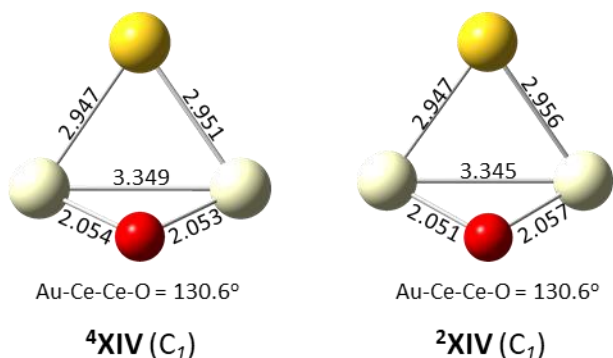
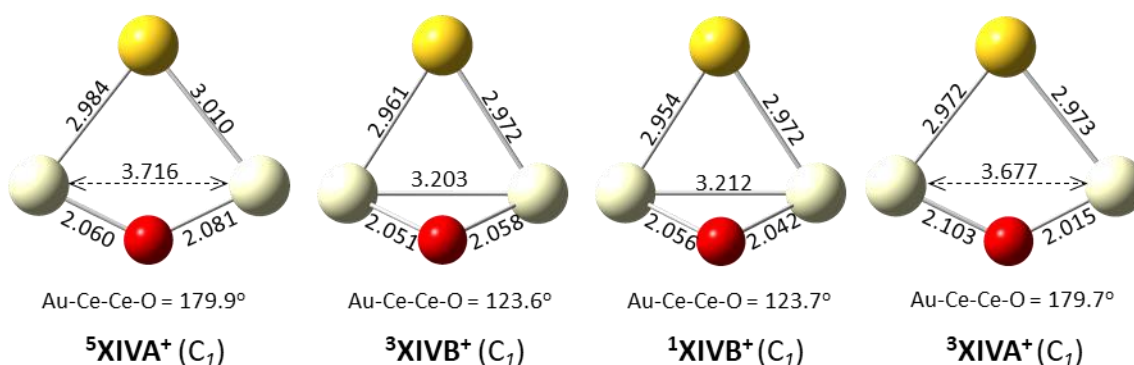
AuCe_2O  **AuCe_2O^+** 

Figure 8.10: Calculated AuCe_2O neutral (top) and cationic (below) structures. Dihedral angles are shown. Bond lengths are presented in Å. Point groups are shown in brackets.

8.4.3. ZEKE Spectral Simulations for AuCe_2O

Calculated ZEKE spectra for the AuCe_2O ${}^3\text{A} \leftarrow {}^4\text{A}$ (${}^3\text{XIVB}^+ \leftarrow {}^4\text{XIV}$) and ${}^1\text{A} \leftarrow {}^2\text{A}$ (${}^1\text{XIVB}^+ \leftarrow {}^2\text{XIV}$) ionisation processes are presented in Figure 8.11. The ZEKE spectra were corrected to the AE of the experimental PIE spectrum using the method described in Chapter 3. The corrected ZEKE spectra are shown here. The ${}^3\text{A} \leftarrow {}^4\text{A}$ (${}^3\text{XIVB}^+ \leftarrow {}^4\text{XIV}$) and ${}^1\text{A} \leftarrow {}^2\text{A}$ (${}^1\text{XIVB}^+ \leftarrow {}^2\text{XIV}$) transitions are both considered to contribute to the AuCe_2O PIE spectrum owing to the comparable intensities of both ZEKE spectra. Vibronic peak intensities for both the ${}^5\text{A} \leftarrow {}^4\text{A}$ (${}^5\text{XIVA}^+ \leftarrow {}^4\text{XIV}$) and ${}^3\text{A} \leftarrow {}^2\text{A}$ (${}^3\text{XIVA}^+ \leftarrow {}^2\text{XIV}$) processes were calculated as significantly lower than for the ${}^3\text{A} \leftarrow {}^4\text{A}$ (${}^3\text{XIVB}^+ \leftarrow {}^4\text{XIV}$) and ${}^1\text{A} \leftarrow {}^2\text{A}$ (${}^1\text{XIVB}^+ \leftarrow {}^2\text{XIV}$) transitions. This is possibly due to the geometric differences between the bent neutral and planar cationic structures, such that they were not considered to contribute substantially to the PIE spectrum. ZEKE spectra

for the ${}^3A \leftarrow {}^4A$ (${}^3XIVB^+ \leftarrow {}^4XIV$) and ${}^1A \leftarrow {}^2A$ (${}^1XIVB^+ \leftarrow {}^2XIV$) spectra are shown here; the ${}^3A \leftarrow {}^4A$ (${}^3XIVB^+ \leftarrow {}^4XIV$) and ${}^1A \leftarrow {}^2A$ (${}^1XIVB^+ \leftarrow {}^2XIV$) ZEKE spectra are shown in Appendix C.

The calculated ZEKE spectrum for the ${}^3A \leftarrow {}^4A$ (${}^3XIVB^+ \leftarrow {}^4XIV$) ionisation process is presented in Figure 8.11(a). The spectral profile is dominated by the 2_n^0 hot band progression in the thermal region and the 2_0^n progression in the post-band origin region; the ν_2 mode describes a symmetric stretch of the Au-Ce bonds. Vibronic peak separations within 2_n^0 and 2_0^n progressions are calculated as 0.0114 eV and 0.0135 eV respectively; these peak separations correspond to the 4XIV and ${}^3XIVB^+$ ν_2 frequencies of 92.3 cm⁻¹ and 108.9 cm⁻¹, respectively. The thermal onset additionally contains a number of weak hot band transitions – including the $2_1^0 3_1^1$, $2_3^0 4_0^1$, $1_2^2 2_1^0$ and $1_1^1 2_2^0 4_0^1$ transitions – while numerous $\nu_2 \nu_3 \nu_4$ coupled modes are recorded in the post-band origin region. The 2_0^2 vibronic transition corresponds to the maximum FC overlap which, in addition to the narrow spectral profile – with all vibronic peaks calculated over a ca. 0.15 eV range – is consistent with minimal structural change upon ionisation.

The calculated ZEKE spectrum for the ${}^1A \leftarrow {}^2A$ (${}^1XIVB^+ \leftarrow {}^2XIV$) transition is presented in Figure 8.11(b). The thermal region in this spectrum is dominated by the 2_n^0 progression – which again corresponds to a symmetric stretch of the Au-Ce bonds with weak $2_n^0 3_1^1$, $2_1^n 3_2^2$ and $1_1^1 2_1^n 3_1^1$ progressions also calculated. The post-band origin region mostly consists of the 2_0^n progression, with a weaker $2_0^n 6_1^1$ progression causing a tailing effect at the higher energy end of the ZEKE spectrum. Both the 2_0^n and $2_0^n 6_1^1$ progressions show peak separations of 0.0130 eV corresponding to the ${}^1XIVB^+$ ν_2 frequency of 101.5 cm⁻¹. The 2_0^1 peak corresponds to maximum FC overlap, inferring minimal structural change upon ionisation. Moreover, the 0_0^0 transition is calculated with a strong peak intensity, suggesting strong FC overlap for the adiabatic transition.

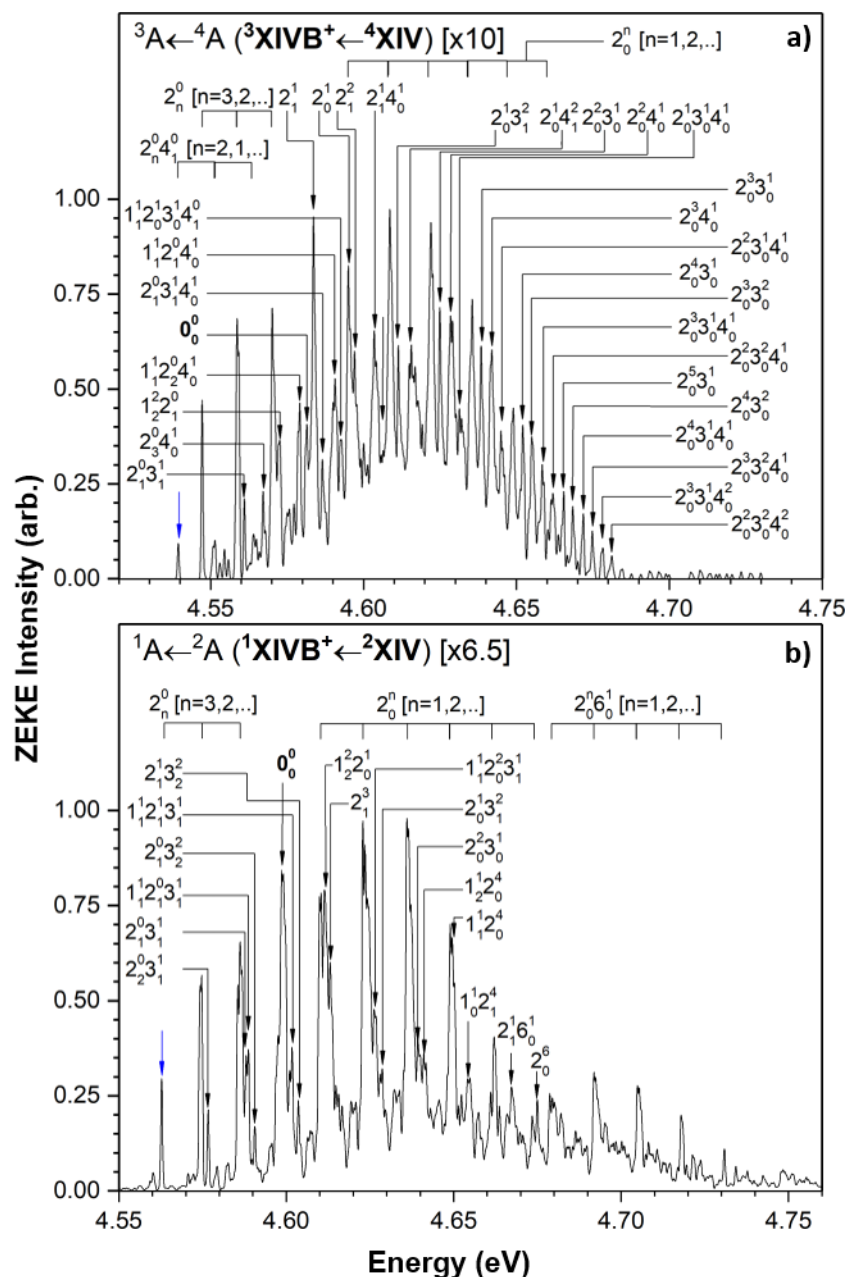


Figure 8.11: Calculated ZEKE spectra for AuCe₂O: **a).** ${}^3A \leftarrow {}^4A$ (${}^3XIVB^+ \leftarrow {}^4XIV$); **b).** ${}^1A \leftarrow {}^2A$ (${}^1XIVB^+ \leftarrow {}^2XIV$). Spectral intensities are normalised to the most intense peak in each spectrum with scaling factors shown. Prominent vibronic transitions are assigned. The vibronic transition likely to correspond to the appearance of ion signal in each spectrum is labelled with a blue arrow.

8.4.4. Comparison of Simulated and Experimental PIE Spectra for AuCe₂O

The simulated PIE spectrum is calculated via integration of the vibronic peaks for both the $^3A \leftarrow ^4A$ ($^3XIVB^+ \leftarrow ^4XIV$) and $^1A \leftarrow ^2A$ ($^1XIVB^+ \leftarrow ^2XIV$) ionisation transitions. This PIE spectrum is shown overlaid against the experimental PIE spectrum in Figure 8.12. A very good fit is found between the simulated and experimental PIE spectra; particularly in the thermal tail and band origin regions. However, unlike the experimental PIE spectrum, the simulated PIE spectrum does not include a shoulder at ca. 4.62 eV. DFT simulations do not predict any metastable ionisation transitions at ca. 4.62 eV. Therefore, the shoulder is thus considered as an experimental anomaly and may be due to ion signal fluctuation which was particularly prevalent for the AuCe_mO_n clusters. The adiabatic ionisation energy is assigned to the $^3A \leftarrow ^4A$ ($^3XIVB^+ \leftarrow ^4XIV$) 0_0^0 transition as the lowest energy ionisation process from the LES. This gives an IE value of 4.58 eV.

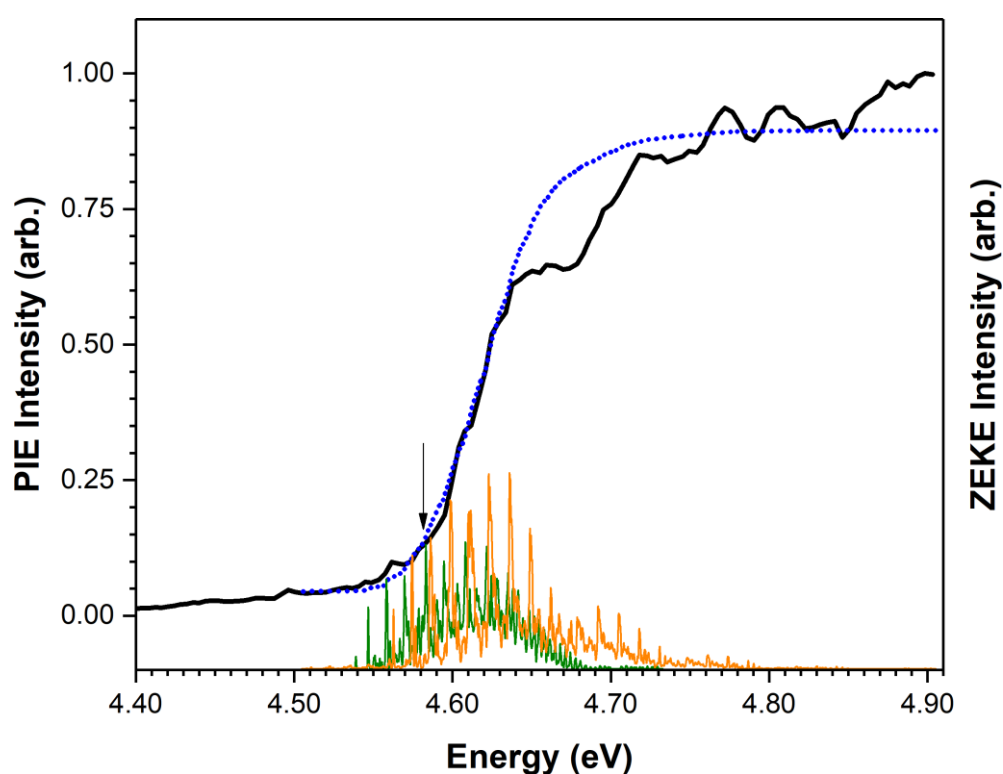


Figure 8.12: AuCe₂O simulated PIE spectrum (blue dotted arrow) overlaid against the experimentally recorded PIE spectrum (solid black arrow). Calculated ZEKE spectra for the AuCe₂O $^3A \leftarrow ^4A$ ($^3XIVB^+ \leftarrow ^4XIV$) and $^1A \leftarrow ^2A$ ($^1XIVB^+ \leftarrow ^2XIV$) ionisation processes are shown below the PIE spectrum in green and orange, respectively. The adiabatic ionisation energy is labelled with a black arrow.

8.5. PIE Spectrum and DFT Results for AuCe_2O_2

8.5.1. AuCe_2O_2 Experimental PIE Spectrum

The AuCe_2O_2 PIE spectrum recorded in the energy range 4.10 – 5.15 eV is presented in Figure 8.13. Two ionisation onsets are observed with appearance energies of 4.86 eV and 4.31 eV – presented in Figures 8.13 (b) and (c) respectively – which are labelled the primary and secondary onsets respectively due to their relative intensities. The primary onset, where the majority of the AuCe_2O_2 ion signal appears, shows a reasonably slow ion signal increase with a uniform slope that extends to a plateau at ca. 5.05 eV. While a shoulder is observed in the primary onset at 4.97 eV, this is probably an artefact of ion signal fluctuation which is exacerbated by the weak AuCe_2O_2 ion peak recorded in all mass spectra. The secondary onset shows a very gradual onset of ion signal from 4.31 eV to a plateau at ca. 4.70 eV. The very weak increase in ion signal recorded over this onset suggest that the underlying photo-ionisation processes may be occurring from metastable isomers, and not the LES.

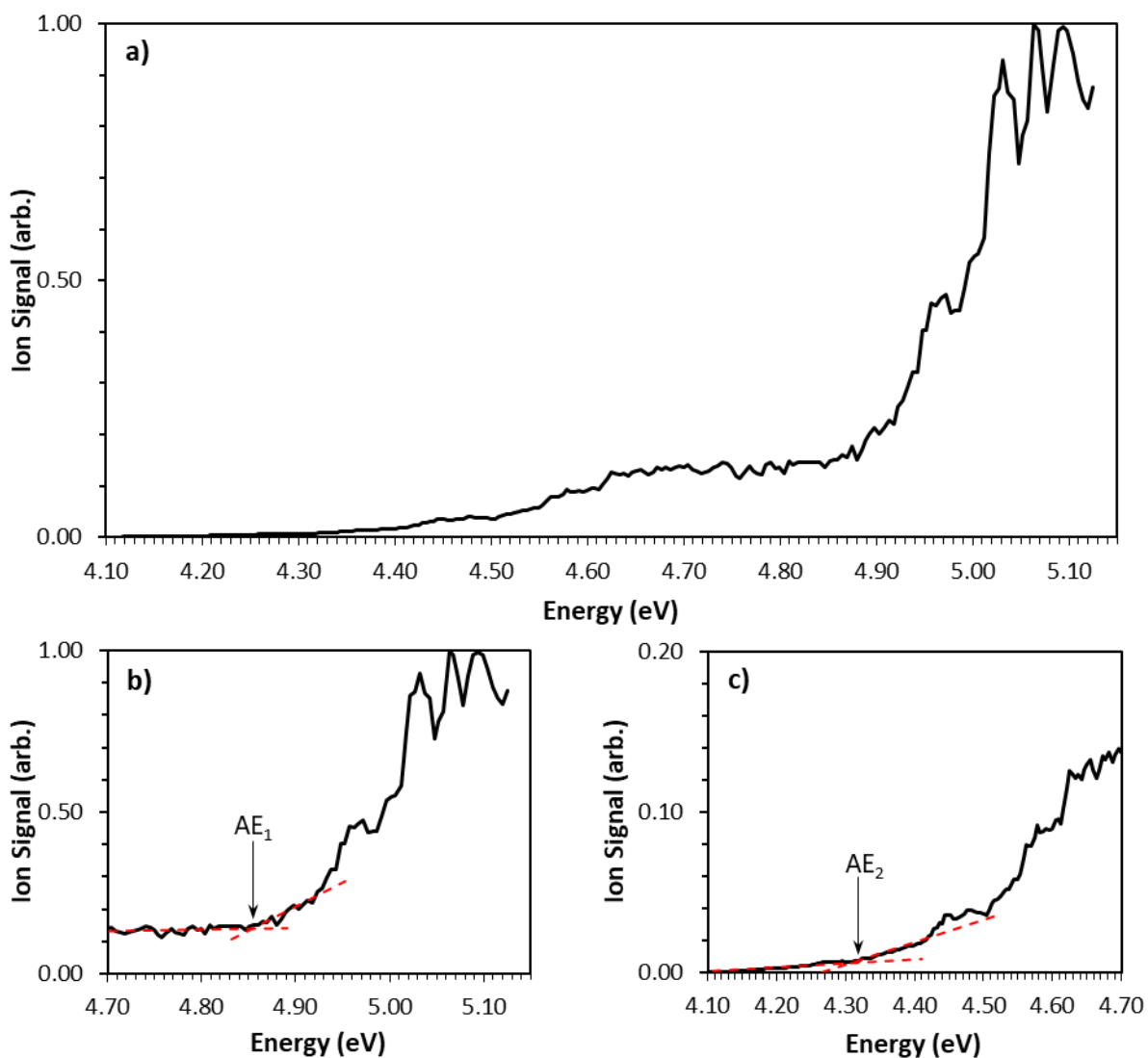


Figure 8.13: PIE spectrum for AuCe₂O₂: **a).** complete PIE spectrum; **b).** primary onset; **c).** secondary onset. Linear trendlines for the baseline and onset are presented as red dashed lines. Appearance energies for the primary and secondary onsets - designated AE₁ and AE₂, respectively – are labelled with black arrows.

8.5.2. DFT Calculations for AuCe_2O_2

DFT-calculated AuCe_2O_2 neutral and cationic structures are presented in Figures 8.14 and 8.15. One unique AuCe_2O_2 neutral geometry is calculated which comprises a gold atom bound to a Ce_2O_2 motif via a single Au-Ce bond. Calculated AuCe_2O_2 species include indistinguishable quartet ($^4\text{A}'$) and doublet (^2A) spin-isomers – labelled ^4XVA and ^2XVA , respectively – and a higher energy doublet (^2A) structure (although labelled ^2XVB for purposes of differentiation from the ^2XVA structure). While the ^4XVA and ^2XVA isomers are calculated with different point groups – as C_s and C_1 symmetric, respectively – the similarities in geometric structure would make these species difficult to differentiate experimentally. It is uncertain whether the ^2XVB structure corresponds to a higher energy isomer of the XVA structure due to a slightly greater bending of the oxygen atoms out of the Ce_2O_2 plane – with O-Ce-Ce-O dihedral angles for the XVA and XVB structures calculated as 178.4° and 177.1° , respectively – or whether the ^2XVB structure is simply an excited electronic state of the ^2XVA species.

The XVB type structure is calculated as a C_1 symmetric doublet in the ^2A electronic state, labelled ^2XVB . The geometry is very similar to the XVA structure, albeit with a slightly greater bending of the oxygen atoms out of the Ce_2O_2 plane; O-Ce-Ce-O dihedral angles for the XVA and XVB structures are calculated as 178.4° and 177.1° respectively. While this presents only a small difference in geometric structure, calculations of the Ce_2O_2 species in Chapter 5 show the planar D_{2h} arrangement is quite stable; thus, any deformation away from the planar Ce_2O_2 arrangement – or near-planar in the case of the AuCe_2O_2 XVA structure – may be energetically unfavourable. Consequentially, the ^2XVB isomer is calculated as significantly higher in energy than both the ^4XVA and ^2XVA species, with an energetic separation of ca. 0.82 eV relative to the LES.

Calculations of the AuCe_2O_2 cationic species show 2 unique structures, which are labelled XVA^+ and XVB^+ in order of increasing energy. The XVA^+ structure – calculated in both singlet and triplet electronic states – comprises a gold atom bridging the Ce-Ce bond of a Ce_2O_2 unit[†].

[†] The bridging XVA^+ structure was re-optimised in the neutral $m=2,4,6,8$ spin states but converged to the ^2XVA and ^4XVA geometries.

This presents a marked difference to both the **XVA** and **XVB** neutral structures described previously in terms of both geometric arrangement and vibrational modes; very poor FC overlap is therefore expected between both neutral **XVA** and **XVB** species and the **XVA**⁺ cation. The **XVB**⁺ cationic structure, which is calculated in the quintet state only, displays a similar geometry to the neutral **XVA** species. Thus, the **⁵XVB**⁺ cation presents a potential target state for the **⁴XVA** neutral cluster.

A total of 6 potential ionisation processes are calculated for the AuCe₂O₂ system; these include the ³A←⁴A' (**³XVA**⁺←**⁴XVA**), ⁵A←⁴A' (**⁵XVB**⁺←**⁴XVA**), ¹A←²A (**¹XVA**⁺←**²XVA**), ³A←²A (**³XVA**⁺←**²XVA**), ¹A←²A (**¹XVA**⁺←**²XVB**) and ³A←²A (**³XVA**⁺←**²XVB**) transitions. IEs for these processes are calculated as 4.879 eV, 7.838 eV, 4.870 eV, 4.875 eV, 4.050 eV and 4.805 eV respectively. The ⁵A←⁴A' (**⁵XVB**⁺←**⁴XVA**) process is not considered to contribute to the PIE spectrum due to the high calculated IE value (this process is therefore represented by a red dashed arrow in Figure 8.14). The remaining calculated IE values all lie within the photon energies used in this work. IEs for the ¹A←²A (**¹XVA**⁺←**²XVB**) and ³A←²A (**³XVA**⁺←**²XVB**) processes are both calculated as being ca. 0.8 eV lower than the ³A←⁴A' (**³XVA**⁺←**⁴XVA**), ¹A←²A (**¹XVA**⁺←**²XVA**), ³A←²A (**³XVA**⁺←**²XVA**) transitions; this compares reasonably well with the ca. 0.5 eV difference between the primary and secondary onsets in the experimental PIE spectrum. The ³A←⁴A' (**³XVA**⁺←**⁴XVA**), ¹A←²A (**¹XVA**⁺←**²XVA**) and ³A←²A (**³XVA**⁺←**²XVA**) processes, which describe ionisation transitions from the low-lying **⁴XVA** and **²XVA** isomers, are assigned to the primary onset. The ¹A←²A (**¹XVA**⁺←**²XVB**) and ³A←²A (**³XVA**⁺←**²XVB**) processes, which describe ionisation from metastable isomers, are considered for the secondary onset. The ³A←⁴A' (**³XVA**⁺←**⁴XVA**), ¹A←²A (**¹XVA**⁺←**²XVB**) and ³A←²A (**³XVA**⁺←**²XVB**) ionisation processes are shown as green, orange and violet arrows in Figure 8.14. The ¹A←²A (**¹XVA**⁺←**²XVA**), ³A←²A (**³XVA**⁺←**²XVA**) transitions are shown as red dotted arrows due to low ZEKE intensities calculated for these processes (vide infra).

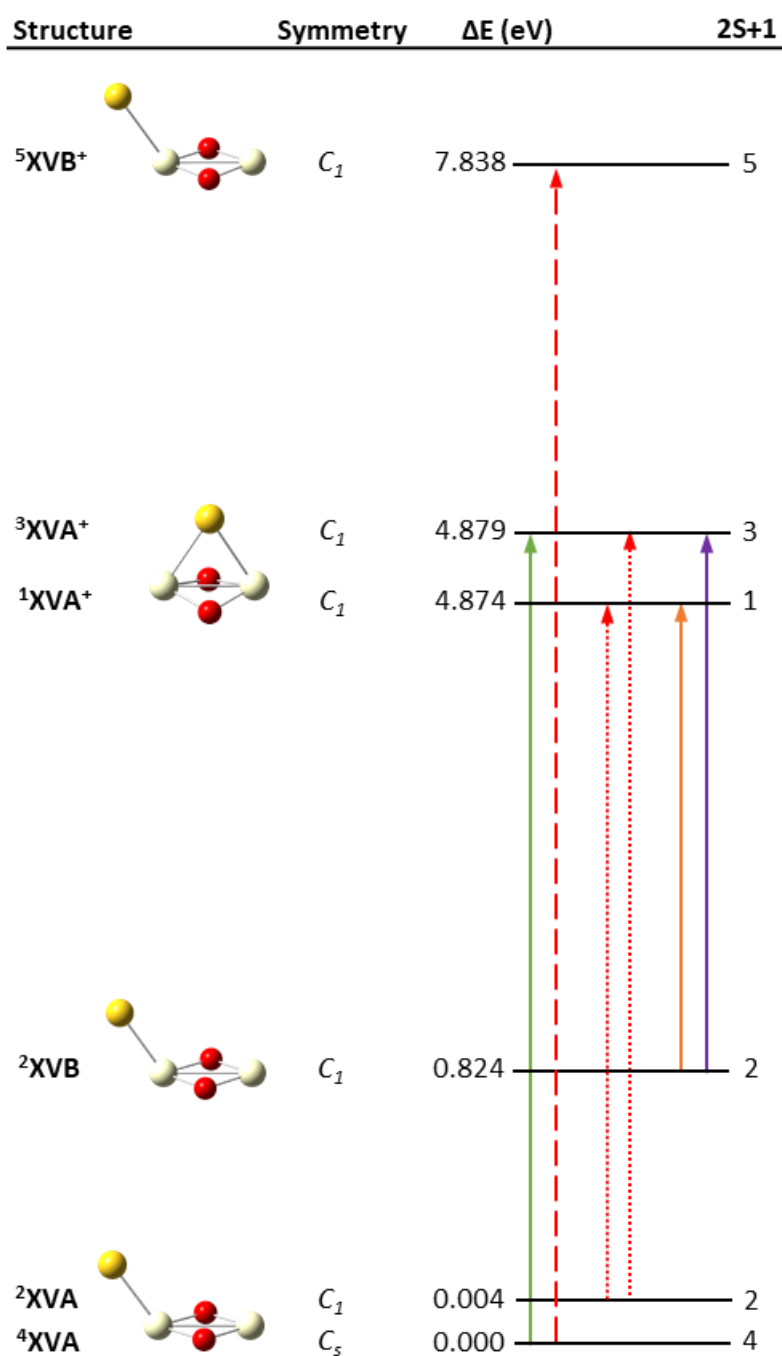


Figure 8.14: Calculated structures for AuCe₂O₂. Potential ionisation transitions are shown. Transitions with low ZEKE intensities (*vide infra*) are shown as red dotted arrows. Transitions with prohibitively high ionisation energies are shown as red dashed arrows.

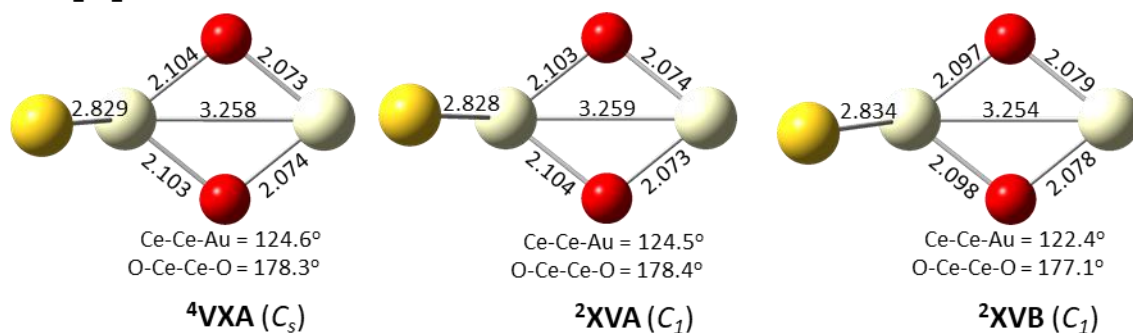
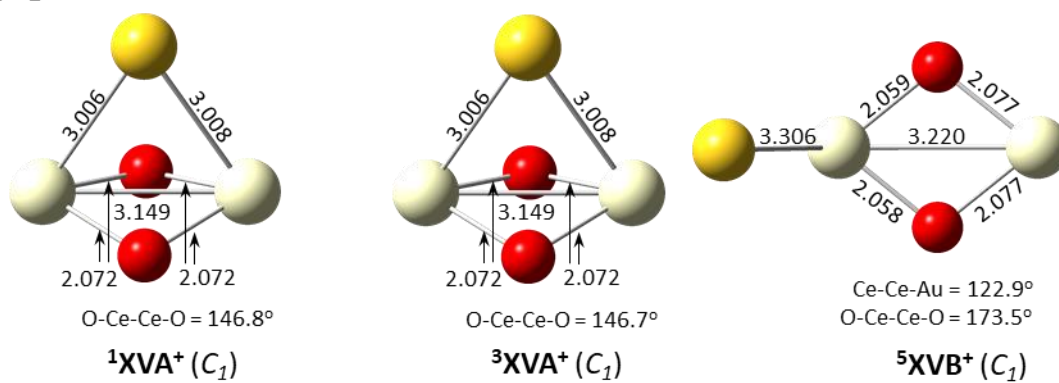
AuCe₂O₂**AuCe₂O₂⁺**

Figure 8.15: Calculated AuCe₂O₂ neutral (top) and cationic (below) structures. Pertinent bond angles and dihedral angles are shown. Bond lengths are presented in Å. Point groups are shown in brackets.

8.5.3. ZEKE Spectral Simulations for AuCe₂O₂

ZEKE spectral simulations for potential AuCe₂O₂ ionisation processes are presented in Figures 8.16 and 8.17 corresponding to the primary and secondary PIE onsets, respectively. The ${}^3A \leftarrow {}^4A'$ (${}^3XVA^+ \leftarrow {}^4XVA$) lowest energy vibronic transition is corrected to the primary onset AE, while the ${}^1A \leftarrow {}^2A$ (${}^1XVA^+ \leftarrow {}^2XVA$) and ${}^3A \leftarrow {}^2A$ (${}^3XVA^+ \leftarrow {}^2XVA$) ZEKE spectra are corrected to the secondary onset using the method described in Chapter 3. The corrected ZEKE spectra are shown here. All of the AuCe₂O₂ ionisation transitions are calculated to be extremely weak; with vibronic peak intensities on the order of 10^{-124} – 10^{-149} . While intensities such as these should preclude the relevant transitions from being observed, it is noted that (i) these are the only ionisation processes calculated for the AuCe₂O₂ cluster; and (ii) the AuCe₂O₂ ion peak is clearly observed in the experimental mass spectra. Therefore, the AuCe₂O₂ PIE spectrum is assigned to the transitions shown here in lieu of any other viable ionisation processes.

ZEKE spectral intensities for the ${}^3A \leftarrow {}^4A'$ (${}^3XVA^+ \leftarrow {}^4XVA$), ${}^1A \leftarrow {}^2A$ (${}^1XVA^+ \leftarrow {}^2XVA$) and ${}^3A \leftarrow {}^2A$ (${}^3XVA^+ \leftarrow {}^2XVA$) ionisation transitions – corresponding to the primary onset – are calculated to be on the order of 10^{-139} , 10^{-149} and 10^{-149} respectively. While all three ionisation processes are calculated as extremely weak, the ${}^3A \leftarrow {}^4A'$ (${}^3XVA^+ \leftarrow {}^4XVA$) process is, by comparison, 10^{10} times more intense than both the ${}^1A \leftarrow {}^2A$ (${}^1XVA^+ \leftarrow {}^2XVA$) and ${}^3A \leftarrow {}^2A$ (${}^3XVA^+ \leftarrow {}^2XVA$) transitions. Thus, the ${}^1A \leftarrow {}^2A$ (${}^1XVA^+ \leftarrow {}^2XVA$) and ${}^3A \leftarrow {}^2A$ (${}^3XVA^+ \leftarrow {}^2XVA$) ionisation transitions are not considered to contribute substantially to the PIE spectrum; only the ${}^3A \leftarrow {}^4A'$ (${}^3XVA^+ \leftarrow {}^4XVA$) process is considered. ZEKE spectra for the ${}^1A \leftarrow {}^2A$ (${}^1XVA^+ \leftarrow {}^2XVA$) and ${}^3A \leftarrow {}^2A$ (${}^3XVA^+ \leftarrow {}^2XVA$) processes are presented in Appendix C.

The calculated ZEKE spectrum for the ${}^3A \leftarrow {}^4A'$ (${}^3XVA^+ \leftarrow {}^4XVA$) ionisation transition is presented in Figure 8.16. Vibronic peaks predominantly consist of combination modes involving ν_1 hot bands – which describes an in-plane Ce-Ce-Au bend – coupled with the ν_2 , ν_4 , ν_6 and ν_9 modes. The 0_0^0 transition is not calculated in the ZEKE spectrum which, in addition to the very weak spectral intensity, is consistent with a poor FC overlap between the neutral and cationic species. However, the lack of alternative ionisation transitions means the ${}^3A \leftarrow {}^4A'$ (${}^3XVA^+ \leftarrow {}^4XVA$) process may still contribute to the primary onset. The poor FC overlap

(³XVA⁺←⁴XVA) ZEKE spectrum considered for the AuCe₂O₂ primary onset. This significantly higher ZEKE intensity may offset the low population of the ²XVB state – due to the +0.824 eV energetic difference calculated between the ⁴XVA and ²XVB neutral species – making both the ¹A←²A (¹XVA⁺←²XVB) and ³A←²A (³XVA⁺←²XVB) transitions viable ionisation processes for the secondary onset.

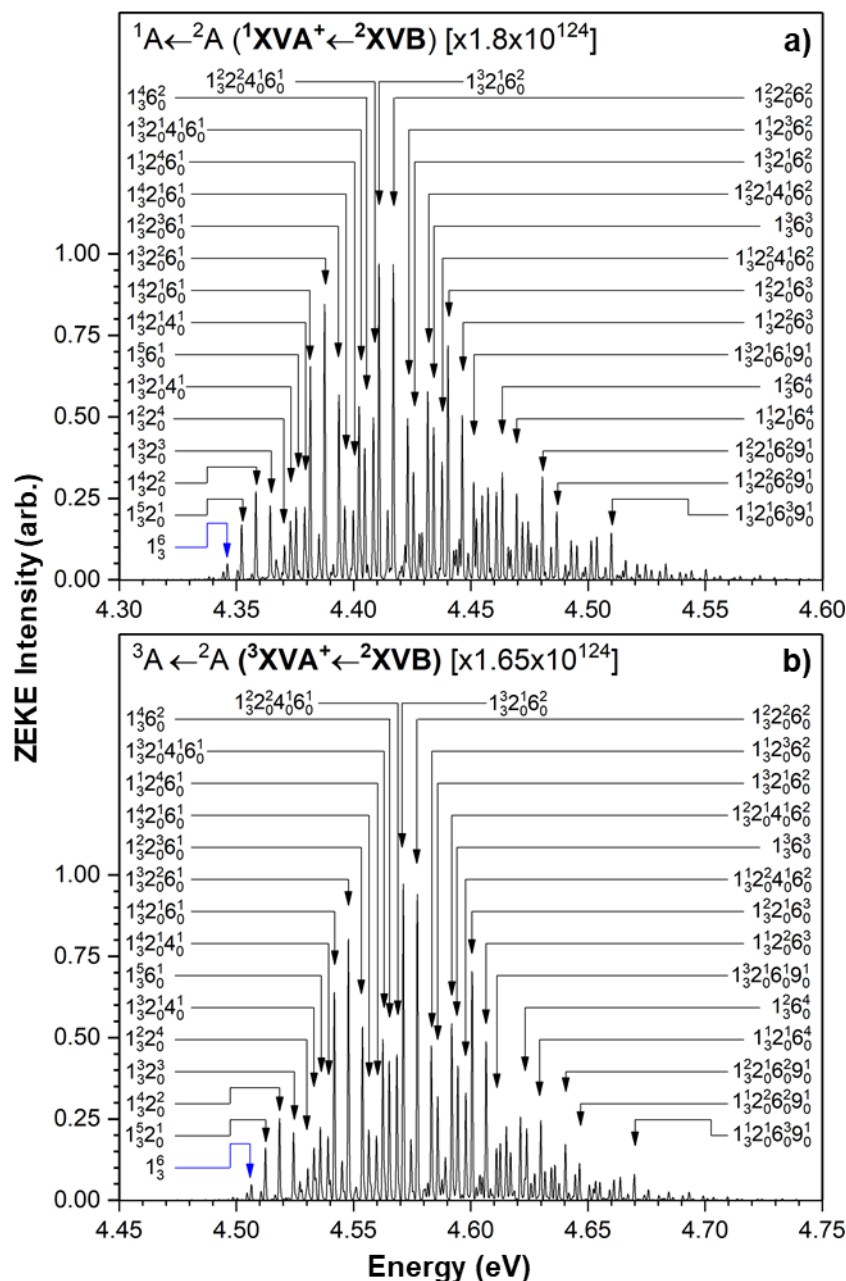


Figure 8.17: Simulated ZEKE spectra for the AuCe₂O₂ ionisation transitions corresponding to the secondary onset: **a).** ${}^1A \leftarrow {}^2A ({}^1XVA^+ \leftarrow {}^2XVB)$ and **b).** ${}^3A \leftarrow {}^2A ({}^3XVA^+ \leftarrow {}^2XVB)$. Spectral intensities are normalised to the most intense peak in each spectrum with scaling factors shown. Prominent vibronic peaks are assigned. The vibronic transition likely to correspond to the appearance of ion signal in each spectrum is labelled with a blue arrow. The 0_0^0 transition was not calculated in simulations and is not shown.

8.5.4. Comparison of Simulated and Experimental PIE Spectra for AuCe₂O₂

A PIE spectrum for the AuCe₂O₂ primary onset was calculated by integration of the ${}^3A \leftarrow {}^4A'$ (${}^3XVA^+ \leftarrow {}^4XVA$) ZEKE spectrum. This calculated PIE spectrum is presented in Figure 8.18. A reasonably good fit is found between the simulated and experimental PIE spectra. The adiabatic IE is determined to be 4.86 eV. Since the ionisation process here corresponds to the lowest energy ionisation process from the lowest energy neutral structure, this IE value is taken as the experimental AuCe₂O₂ IE.

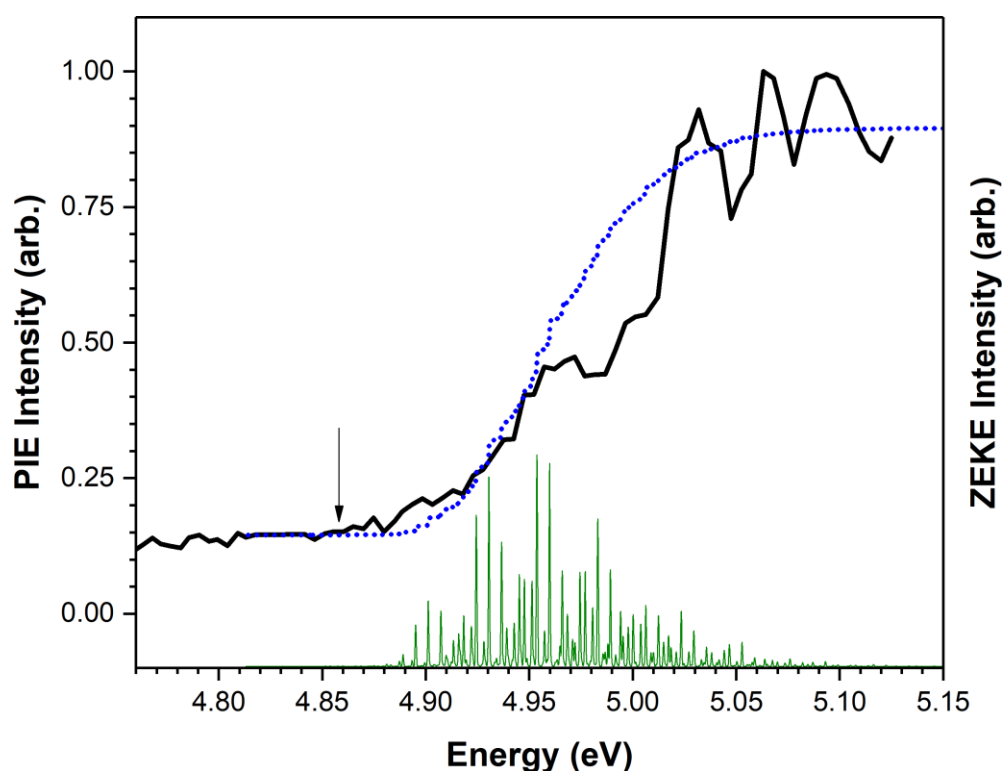


Figure 8.18: Simulated PIE spectrum for the AuCe₂O₂ primary onset (blue dotted line) overlaid against the experimental PIE spectrum (solid black line). The ZEKE spectrum for the ${}^3A \leftarrow {}^4A'$ (${}^3XVA^+ \leftarrow {}^4XVA$) ionisation process is shown below the PIE spectrum in green. The adiabatic ionisation energy is labelled with a black arrow.

The calculated PIE spectrum for the AuCe₂O₂ secondary onset – calculated via integration of the ${}^1A \leftarrow {}^2A$ (${}^1XVA^+ \leftarrow {}^2XVB$) and ${}^3A \leftarrow {}^2A$ (${}^3XVA^+ \leftarrow {}^2XVB$) ZEKE spectra - is presented in Figure 8.19. A good correlation is found between the simulated and experimental PIE spectra. The IE for this onset is assigned to the ${}^1A \leftarrow {}^2A$ (${}^1XVA^+ \leftarrow {}^2XVB$) transition – as the lower energy

ionisation process – with an IE of 4.31 eV. Thus, the secondary onset is assigned to an ionisation process from a metastable isomer.

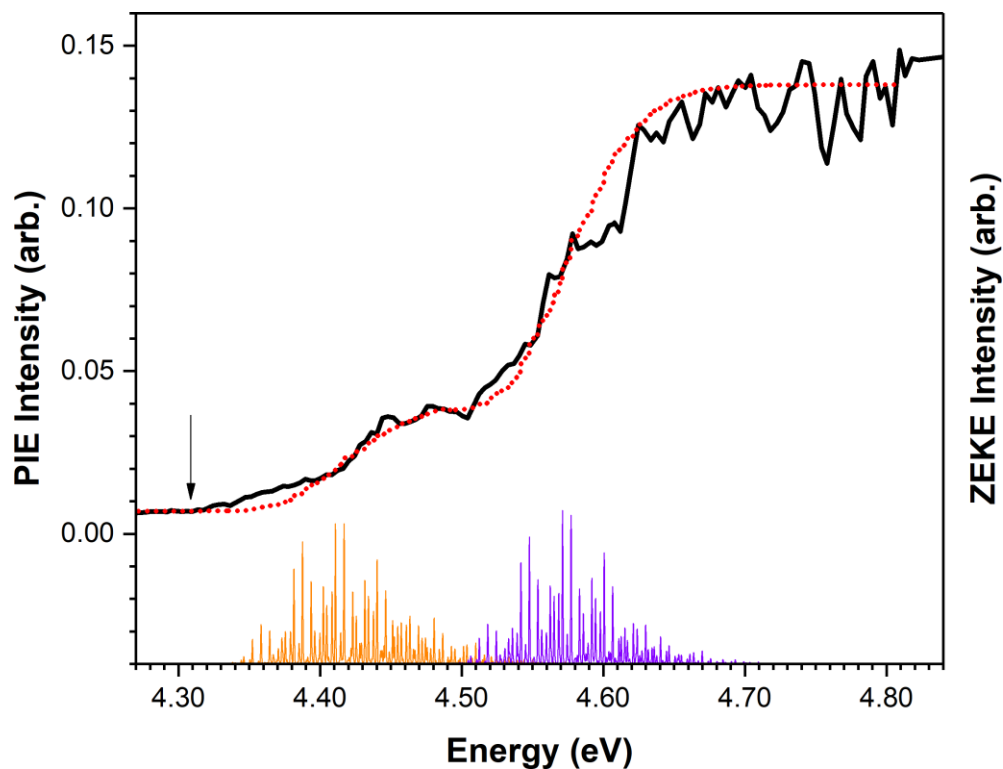


Figure 8.19: Simulated PIE spectrum for the AuCe₂O₂ secondary onset (red dotted line) overlaid against the experimental PIE spectrum (solid black line). Calculated ZEKE spectra for the $^1A \leftarrow ^2A$ ($^1XVA^+ \leftarrow ^2XVB$) and $^3A \leftarrow ^2A$ ($^3XVA^+ \leftarrow ^2XVB$) ionisation processes are shown below the PIE spectrum in orange and violet, respectively. The adiabatic ionisation energy is labelled with a black arrow.

8.6. PIE Spectrum and DFT Results for AuCe_2O_3

8.6.1. AuCe_2O_3 Experimental PIE Spectrum

The AuCe_2O_3 ion was not detected either during photo-ionisation experiments or in the mass spectrum following photo-ionisation at 213 nm (5.84 eV). Given the high ionisation energy of the Ce_2O_3 system discussed previously in Chapter 5, in addition to previous findings by Gentleman et. al^{2,11}. that doping lanthanide oxide clusters with transition metals causes a blueshift in the cluster IE, the non-detection of the AuCe_2O_3 ion is most likely due to a high ionisation energy. While no experimental PIE data has been recorded for the AuCe_2O_3 system, DFT calculated structures are presented below with simulated ZEKE and PIE spectra; some comments on these structures and spectra will be made.

8.6.2. DFT Calculations for AuCe_2O_3

Calculated structures for the AuCe_2O_3 cluster are shown in Figures 8.20 and 8.21. One unique neutral geometry is calculated comprising a Ce_2O_3 motif with a gold atom bound to one of the cerium atoms. This structure is, however, calculated in two different doublet electronic states (labelled **²XVIA** and **²XVIB** for purposes of differentiation). The **²XVIA** species displays C_1 symmetry in the ²A electronic state while the **²XVIB** isomer is C_s symmetric – with a σ_h plane running along the Ce-Ce bond – in the ²A' electronic state. The two structures differ slightly in the Au-Ce-Ce bond angle; which is calculated as 179.4° and 169.4° for the **²XVIA** and **²XVIB** structures, respectively. Given the small energy separation of 0.159 eV, both the **²XVIA** and **²XVIB** species are expected to be produced with good abundance in the cluster source.

A single cationic species is calculated as a target state for both the **²XVIA** and **²XVIB** structures. This cation, designated **¹XVI⁺**, is calculated as a singlet with C_1 symmetry in the ¹A electronic state. The **¹XVI⁺** structure displays a markedly smaller Au-Ce-Ce angle of 134.0° compared to both the **²XVIA** and **²XVIB** species. Moreover, the oxygen atoms in the **¹XVI⁺** structure are all displaced parallel to the Ce-Ce bond, akin to an O-Ce asymmetric stretch. The oxygen atom above the Ce-Ce bond – in Figure 8.21 – is shifted toward the Au atom while the two O atoms below the Ce-Ce bond are shifted away from the Au atom. Triplet state cations are not

considered as target states for the ${}^2\text{XVIA}$ and ${}^2\text{XVIB}$ species; the triplet species converged to dissociative states where the gold atom detaches from the Ce₂O₃ unit.

The calculated neutral and cationic AuCe₂O₃ structures give a total of 2 potential ionisation processes. These include the ${}^1\text{A} \leftarrow {}^2\text{A}$ (${}^1\text{XVI}^+ \leftarrow {}^2\text{XVIA}$) and ${}^1\text{A} \leftarrow {}^2\text{A}'$ (${}^1\text{XVI}^+ \leftarrow {}^2\text{XVIB}$) transitions with calculated IEs of 7.602 eV and 7.443 eV, respectively. Both calculated IEs are considerably higher than the photo-ionisation limit of 5.82 eV (213 nm) in experiments and are consistent with the non-detection of the AuCe₂O₃ ion peak in experimental mass spectra. The ${}^1\text{A} \leftarrow {}^2\text{A}'$ (${}^1\text{XVI}^+ \leftarrow {}^2\text{XVIB}$) transition is shown in Figure 8.20 as a green arrow. The ${}^1\text{A} \leftarrow {}^2\text{A}$ (${}^1\text{XVI}^+ \leftarrow {}^2\text{XVIA}$) transition is shown as a red dotted arrow due to low intensity vibronic peaks calculated in the ZEKE spectrum (*vide infra*).

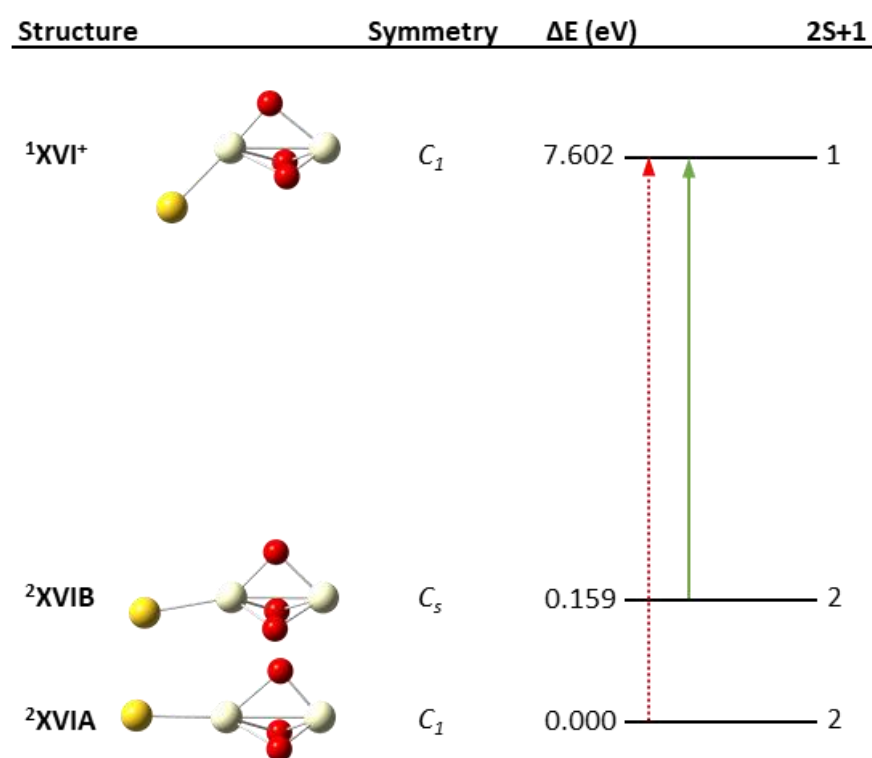


Figure 8.20: Calculated structures for AuCe₂O₃. Potential ionisation transitions are shown. Low ZEKE intensity transitions (*vide infra*) are shown with red dotted arrows.

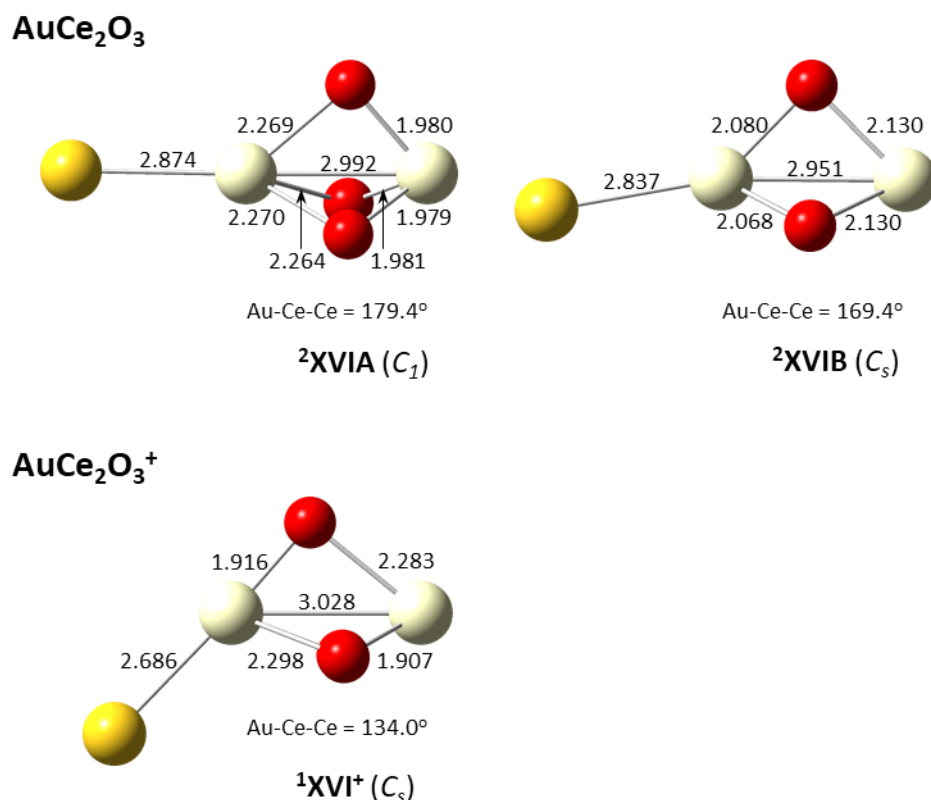


Figure 8.21: Calculated AuCe₂O₃ neutral (top) and cationic (below) structures. Au-Ce-Ce bond angles are shown. Bond lengths are presented in Å. Point groups are shown in brackets.

8.6.3. ZEKE Spectral Simulations for AuCe₂O₃

Simulated ZEKE spectra for the AuCe₂O₃ ¹A←²A (¹XVI⁺←²XVIA) and ¹A←²A' (¹XVI⁺←²XVIB) ionisation transitions are presented in Figures 8.22(a) and 8.22(b), respectively. ZEKE intensities for both the ¹A←²A (¹XVI⁺←²XVIA) and ¹A←²A' (¹XVI⁺←²XVIB) spectra are quite low, with scaling factors of 3.1x10²⁰ and 6.2x10⁸ respectively required to normalise the most intense peaks in each spectrum. The low spectral intensities – and thus weak FC overlap – are consistent with the extensive structural differences between both the ²XVIA and ²XVIB neutral isomers and the ¹XVI⁺ cation. Comparison of the spectral intensities shows the ¹A←²A' (¹XVI⁺←²XVIB) transition is ca. 10¹² times more intense than the ¹A←²A (¹XVI⁺←²XVIA) transition. The contribution of the ¹A←²A (¹XVI⁺←²XVIA) transition to the PIE spectrum is therefore considered to be negligible. Therefore, only the ¹A←²A' (¹XVI⁺←²XVIB) transition, which is presented in Figure 8.22(b), is considered to contribute to the AuCe₂O₃ PIE spectrum. This ZEKE spectrum shows a very broad onset of vibronic transitions in the 7.37 – 7.87 eV

energy range. Prominent vibronic peaks are mostly comprised of ν_1 , ν_3 , ν_4 , ν_9 and ν_{12} combination modes with no discernible progressions. The 0_0^0 transition is not recorded while the maximum FC transition corresponds to the highly excited $1_3^5 12_1^0$ peak, inferring weak FC overlap.

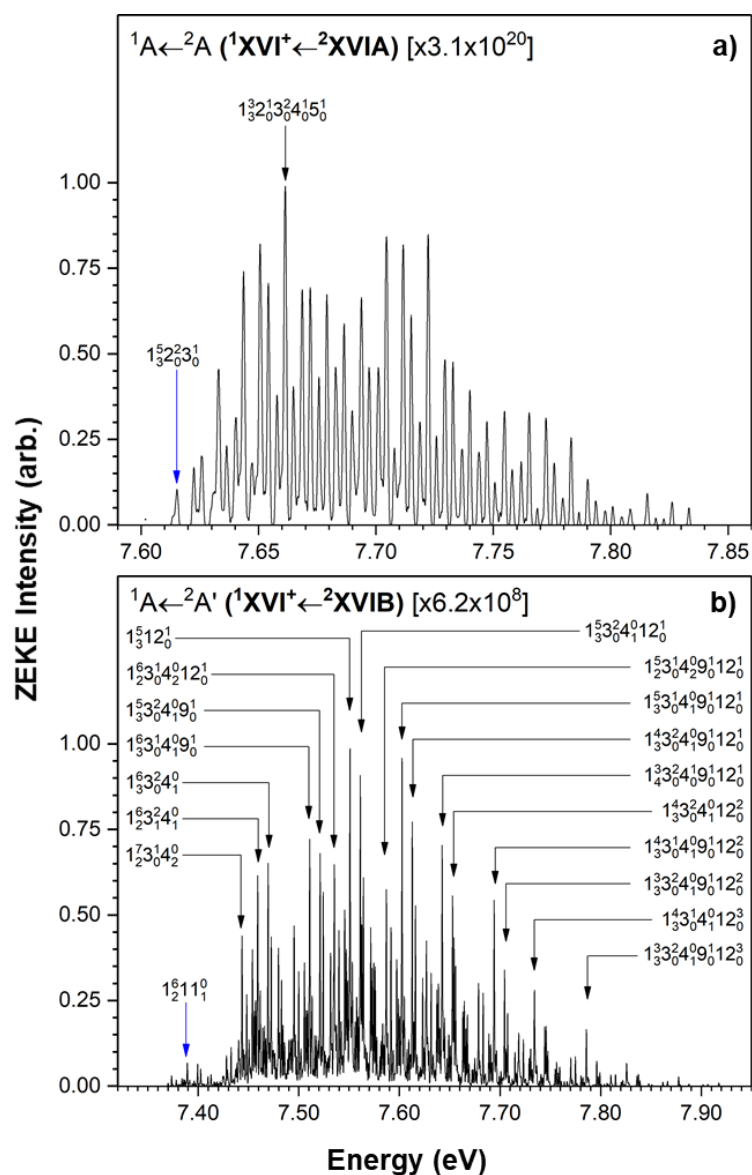


Figure 8.22: Simulated ZEKE spectra for the AuCe₂O₃: **a).** ${}^1A \leftarrow {}^2A$ (${}^1XVI^+ \leftarrow {}^2XVIA$) and **b).** ${}^1A \leftarrow {}^2A'$ (${}^3XVI^+ \leftarrow {}^2XVIB$). Spectral intensities are normalised to the most intense peak in each spectrum with scaling factors shown. Prominent vibronic peaks are assigned for the ${}^1A \leftarrow {}^2A'$ (${}^3XVI^+ \leftarrow {}^2XVIB$) ZEKE spectrum. The vibronic transition likely to correspond to the appearance of ion signal in each spectrum is labelled with a blue arrow. The 0_0^0 transition was not calculated for either spectrum and is not shown.

8.6.4. Simulated PIE Spectrum for AuCe_2O_3

A PIE spectrum for the AuCe_2O_3 cluster species is calculated via integration of the $^1\text{A} \leftarrow ^2\text{A}'$ ($^1\text{XVI}^+ \leftarrow ^2\text{XVIB}$) ZEKE spectrum and is presented in Figure 8.23. Due to the considerable structural differences calculated between the neutral $^2\text{XVIB}$ and cationic $^1\text{XVI}^+$ species, the simulated PIE spectrum shows a very slow onset from ca. 7.43 eV to a plateau at ca. 7.8 eV. Moreover, minimal thermal tailing effects are observed with no calculated band origin transition. The IE is assigned as 7.44 eV from DFT calculations. However, the DFT method used in this work tends to overpredict IEs – as described in Chapter 3 – therefore this value may be higher than the actual IE.

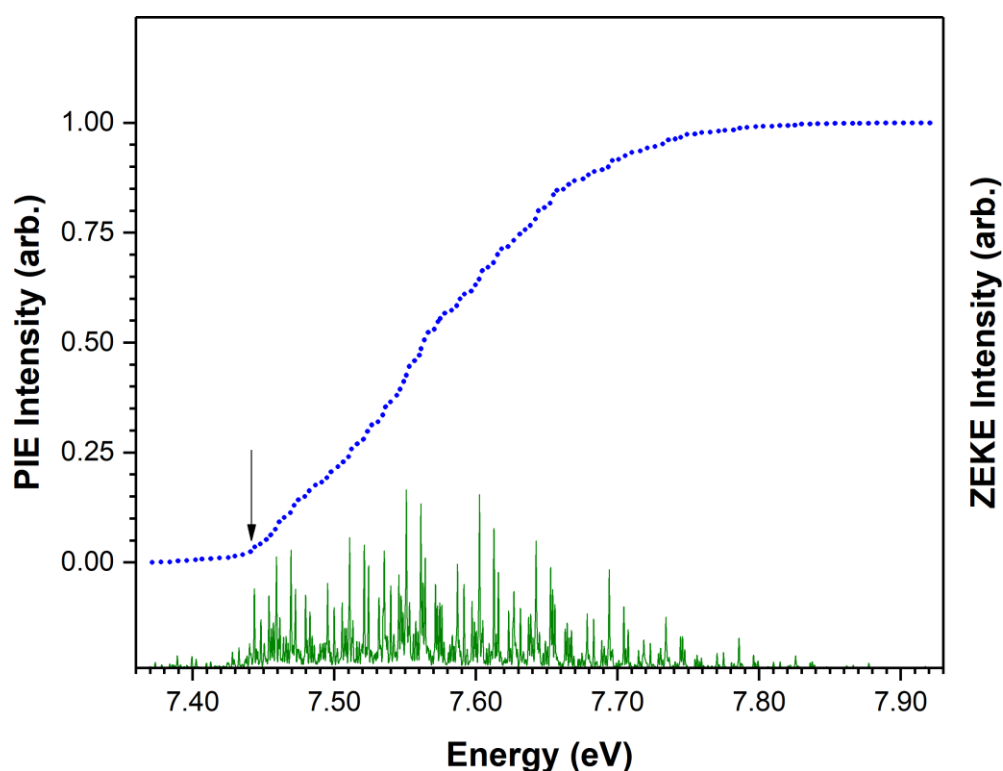


Figure 8.23: Simulated AuCe_2O_3 PIE spectrum (blue dotted line). The calculated ZEKE spectrum for the $^1\text{A} \leftarrow ^2\text{A}'$ ($^1\text{XVI}^+ \leftarrow ^2\text{XVIB}$) ionisation process is shown below the PIE spectrum in green. The adiabatic ionisation energy is labelled with a black arrow.

8.7. PIE Spectrum and DFT Results for AuCe₂O₄

8.7.1. AuCe₂O₄ Experimental PIE Spectrum

The AuCe₂O₄ ion was not detected during photo-ionisation experiments or in the mass spectrum following photo-ionisation at 213 nm (5.84 eV). As with the AuCe₂O₃ cluster discussed previously, the non-detection of the AuCe₂O₄ species is attributed to a high ionisation energy. Consequentially, a PIE spectrum for AuCe₂O₄ has not been recorded. However, DFT calculated structures and simulated ZEKE and PIE spectra are presented to provide some insight into the geometric and electronic properties of the AuCe₂O₄ cluster.

8.7.2. DFT Calculations for AuCe₂O₄

DFT-calculated structures for AuCe₂O₄ are shown in Figures 8.24 and 8.25. Calculations reveal only one unique neutral species – labelled ²XVII – which comprises an AuCe₂O₂ XVA⁺-type structure with two additional oxygen atoms bridging both Au-Ce bonds. The structure is C_s symmetric – with the AuCe₂ trimer lying in a σ plane – and is calculated as a doublet species in the ²A' electronic state. While other AuCe₂O₄ structures were calculated – including an AuO dimer attached to a Ce₂O₃ species via a Ce-O bridge – they were more than 1 eV higher in energy than the ²XVII species and thus are not shown here. The AuCe₂O₄ structure is the only AuCe₂O_n species calculated with a gold atom directly bound to an oxygen atom; this suggests the gold atom may be positively charged. A detailed analysis of atomic charges is presented in Chapter 10. The O-Au-O bridging configuration calculated for the ²XVII structure is consistent with previous calculations of Au deposition at Ce vacancy sites on bulk surfaces^{9,11-13}, where the Au atom is shown to coordinate up to 4 O atoms. The Au-O bond lengths calculated in the ²XVII structure are comparable to those calculated by Fabris et al.⁹, who report Au-O bond lengths of 2.14 Å.

DFT calculations of AuCe₂O₄ cationic species reveal unique singlet and triplet isomers, labelled ¹XVII⁺ and ³XVII⁺ respectively in order of increasing energy. Both cationic species retain similar geometric structures to the neutral ²XVII species, albeit with some noticeable differences. The ¹XVII⁺ isomer, is calculated as C_s symmetric in the ¹A' electronic state with a similar geometry to the ²XVII neutral. The ³XVII⁺ species maintains the same C_s symmetry as the ²XVII structure,

however experiences an elongation of all Ce-Ce and Ce-O bonds in the cluster. Moreover, Au-Ce bonds are not calculated for the $^3\text{XVII}^+$ cation.

The calculated AuCe_2O_4 neutral and cationic structures give a total of 2 potential ionisation processes; these include the $^1\text{A}' \leftarrow ^2\text{A}'$ ($^1\text{XVII}^+ \leftarrow ^2\text{XVII}$) and $^3\text{A}' \leftarrow ^2\text{A}'$ ($^3\text{XVII}^+ \leftarrow ^2\text{XVII}$) transitions with calculated IEs of 6.879 eV and 7.942 eV, respectively. Both calculated IEs are significantly higher than the photon energies available in the current experimental setup, which is consistent with the non-detection of the AuCe_2O_4 ion in photo-ionisation experiments. Due to the significant difference in IEs for the two ionisation processes, it is quite likely that the $^1\text{A}' \leftarrow ^2\text{A}'$ ($^1\text{XVII}^+ \leftarrow ^2\text{XVII}$) and $^3\text{A}' \leftarrow ^2\text{A}'$ ($^3\text{XVII}^+ \leftarrow ^2\text{XVII}$) transitions would produce two separate onsets in a PIE spectrum. In the context of this work, the higher energy $^3\text{XVII}^+$ cation is not particularly interesting; only the lower energy $^1\text{A}' \leftarrow ^2\text{A}'$ ($^1\text{XVII}^+ \leftarrow ^2\text{XVII}$) transition is considered. The $^1\text{A}' \leftarrow ^2\text{A}'$ ($^1\text{XVII}^+ \leftarrow ^2\text{XVII}$) transition is therefore presented as a green arrow in Figure 8.24, while the $^3\text{A}' \leftarrow ^2\text{A}'$ ($^3\text{XVII}^+ \leftarrow ^2\text{XVII}$) transition is shown as a red dashed arrow.

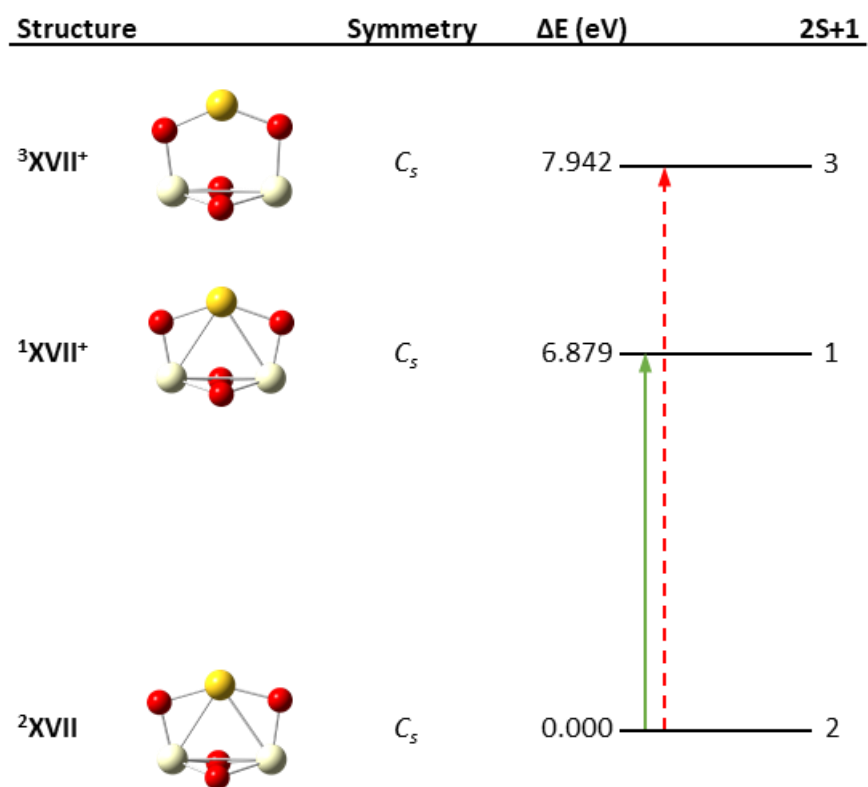


Figure 8.24: Calculated structures for AuCe₂O₄. Potential ionisation transitions are shown. Ionisation transitions with prohibitively high IEs are shown as red dashed arrows.

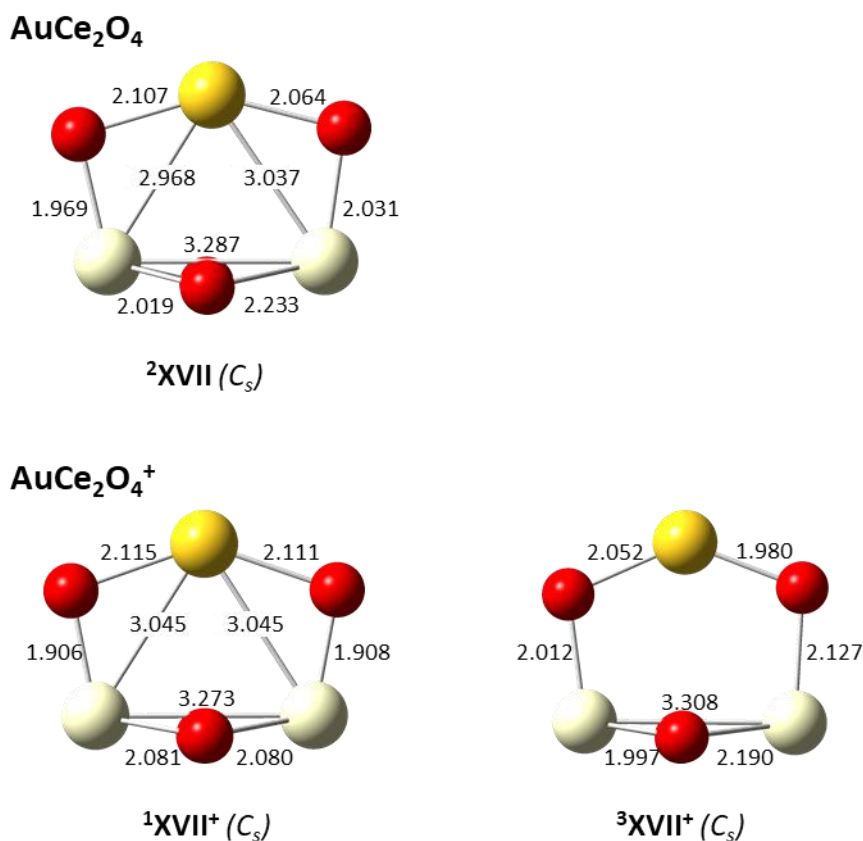


Figure 8.25: Calculated AuCe₂O₄ neutral (top) and cationic (below) structures. Bond lengths are presented in Å. Point groups are shown in brackets.

8.7.3. ZEKE Spectral Simulations for AuCe₂O₄

A simulated ZEKE spectrum for the ${}^1A' \leftarrow {}^2A'$ (${}^1\text{XVII}^+ \leftarrow {}^2\text{XVII}$) ionisation transition is presented in Figure 8.26. A very broad spectral profile is calculated – with vibronic peaks spanning a ca. 0.5 eV range – with few vibronic transitions in the thermal region and a very weak 0_0^0 transition. Prominent vibronic peaks in the ZEKE spectrum are mostly calculated as combination modes – involving the ν_1 , ν_2 , ν_7 , ν_{12} and ν_{15} modes – with no distinct vibronic progressions. The maximum FC transition is assigned to the $2_0^1 1_0^2 1_0^2$ peak. The spectral intensity is calculated as being quite weak, with a scaling factor of 95 required to normalise the most intense vibronic peak. This suggests a relatively weak FC overlap between the ${}^2\text{XVII}$ and ${}^1\text{XVII}^+$ species which is attributed to the considerable structural differences between the ${}^2\text{XVII}$ and ${}^1\text{XVII}^+$ species.

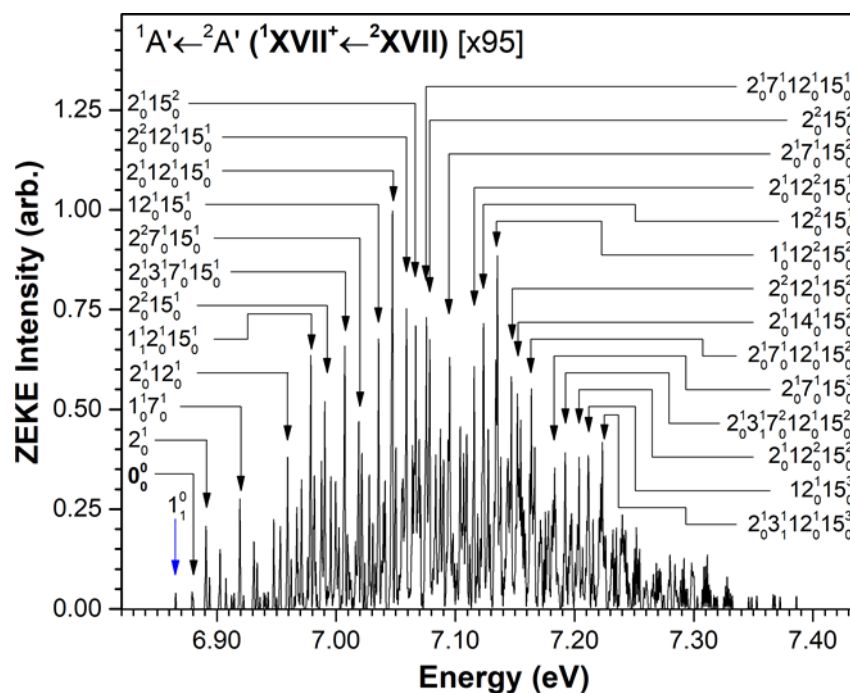


Figure 8.26: Simulated ZEKE spectrum for the AuCe₂O₄ ${}^1A' \leftarrow {}^2A'$ (${}^1XVII^+ \leftarrow {}^2XVII$) ionisation process. Spectral intensities are normalised to the most intense vibronic transition with scaling factor shown. Prominent vibronic peaks are assigned. The vibronic transition likely to correspond to the appearance of ion signal in each spectrum is labelled with a blue arrow.

8.7.4. Simulated PIE Spectrum for AuCe₂O₄

A PIE spectrum AuCe₂O₄ was calculated by integration of the ${}^1A' \leftarrow {}^2A'$ (${}^1XVII^+ \leftarrow {}^2XVII$) vibronic peaks; this spectrum is presented in Figure 8.27. The PIE spectrum appears as a single onset of ion signal with a broad slope in the 6.87 – 7.33 eV energy range. Minimal thermal tailing is calculated; it is quite likely the 0_0^0 transition energy in this case would be lower than the appearance energy. The IE is assigned as 6.88 eV from DFT calculations; however, the experimental IE may be lower than this value due to the tendency of the DFT method to over-predict ionisation energies.

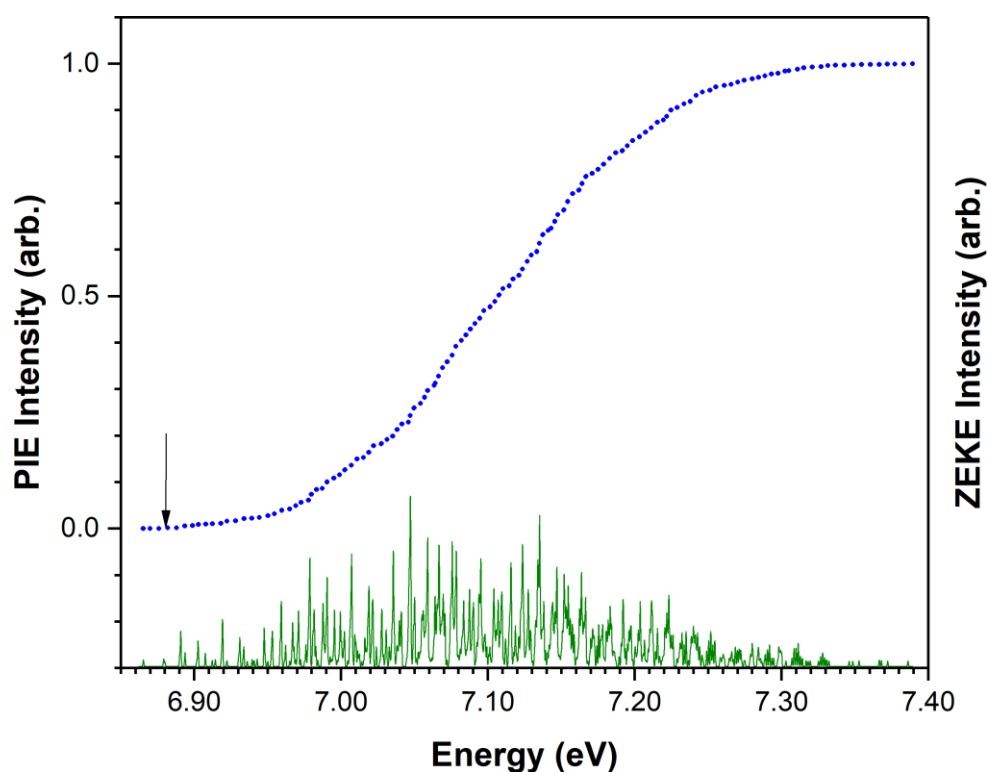


Figure 8.27: Simulated AuCe₂O₄ PIE spectrum (blue dotted line). The calculated ZEKE spectrum for the $^1A' \leftarrow ^2A'$ ($^1XVII' \leftarrow ^2XVII$) ionisation process is shown below the PIE spectrum in green. The adiabatic ionisation energy is labelled with a black arrow.

8.8. Comparison of Experimental and Calculated AuCe₂O_n Ionisation Energies

Experimental and calculated ionisation energies for the AuCe₂O_n ($n=0-4$) cluster series are presented in Figure 8.28. Experimental adiabatic IEs are shown for AuCe₂, AuCe₂O and AuCe₂O₂ while calculated IEs are presented for AuCe₂, AuCe₂O, AuCe₂O₂, AuCe₂O₃ and AuCe₂O₄. Secondary onset IEs are also shown for the AuCe₂O₂ species; however, these IEs are not of any particular interest in the context of this work. Experimental and calculated IE trends for the primary onset are shown as solid and dashed lines, respectively. The experimental IE values are assigned errors of ± 0.05 eV which are consistent with IP errors previously assigned to cerium oxide clusters by Koretsky and Knickelbein¹⁵. However, these errors are too small to be shown in Figure 8.28.

The calculated ionisation energies are corrected to experimental IE values using the methods reported by both Gentleman et al.^{2,16} and Dryza et al.¹⁷⁻¹⁹. Briefly, the AuCe₂ calculated IE

value is corrected to the experimental IE (involving a correction of -0.22 eV); the same correction is then applied to the rest of the clusters in the AuCe₂O_n series. This correction accounts for systematic errors in the calculated IEs which arise from the use of effective core potentials. Error bars of ± 0.2 eV are fitted to the calculated IE values to account for inherent energetic uncertainties in the DFT calculated energies. Horizontal lines are presented at 5.64 eV (220 nm) and 5.82 eV (213 nm) to represent the maximum photon energies available using the tuneable laser source and fixed wavelength 5th harmonic Nd:YAG laser source.

The experimental IE trend shows a decreased IE for AuCe₂O compared to AuCe₂, followed by an increase in the IE for AuCe₂O₂. This trend is consistent with previous work by Gentleman et al.¹¹, who studied ionisation trends of RhHo₂O_n clusters with sequential oxidation. The authors reported a lower IE for the monoxide species compared to both the bare metal and dioxide species.

Comparison of the calculated and experimental IEs for the AuCe₂O and AuCe₂O₂ species shows the AuCe₂O – post-correction – calculated IE is slightly higher than the experimental IE value; whereas the AuCe₂O₂ calculated IE is lower than the experimental IE. This is consistent with the calculated IE trend for the Ce₃O_n cluster series where the Ce₃O_n ($n=1-3$) IEs were all higher than their respective experimental IEs while the Ce₃O₄ IE was calculated lower than the experimental IE value. However, all calculated AuCe₂O_n IEs are within 0.2 eV of their respective experimental IE values; showing good agreement between the calculated and experimental IEs. This, in combination with the good correlations found between simulated and experimental PIE spectra, implies that the calculated AuCe₂, AuCe₂O and AuCe₂O₂ clusters are reasonable approximations of the actual cluster species in terms of both geometric and electronic structure. Thus, inferences about the reactive properties of these cluster species can be made from the calculated structures. While such inferences cannot be made for the AuCe₂O₃ and AuCe₂O₄ clusters, given the lack of experimental data for comparison, it should be noted that the AuCe₂O₃ and AuCe₂O₄ calculated IEs of 7.44 eV and 6.88 eV respectively are both consistent with the absence of these ion peaks in the mass spectra presented in this work. Moreover, the reliability of the DFT method used to calculate AuCe₂O_n ($n=0-2$)

geometric and electronic structures has been clearly shown. Thus, the reactive properties of the AuCe_2O_3 and AuCe_2O_4 clusters will be surmised from the calculated structures.

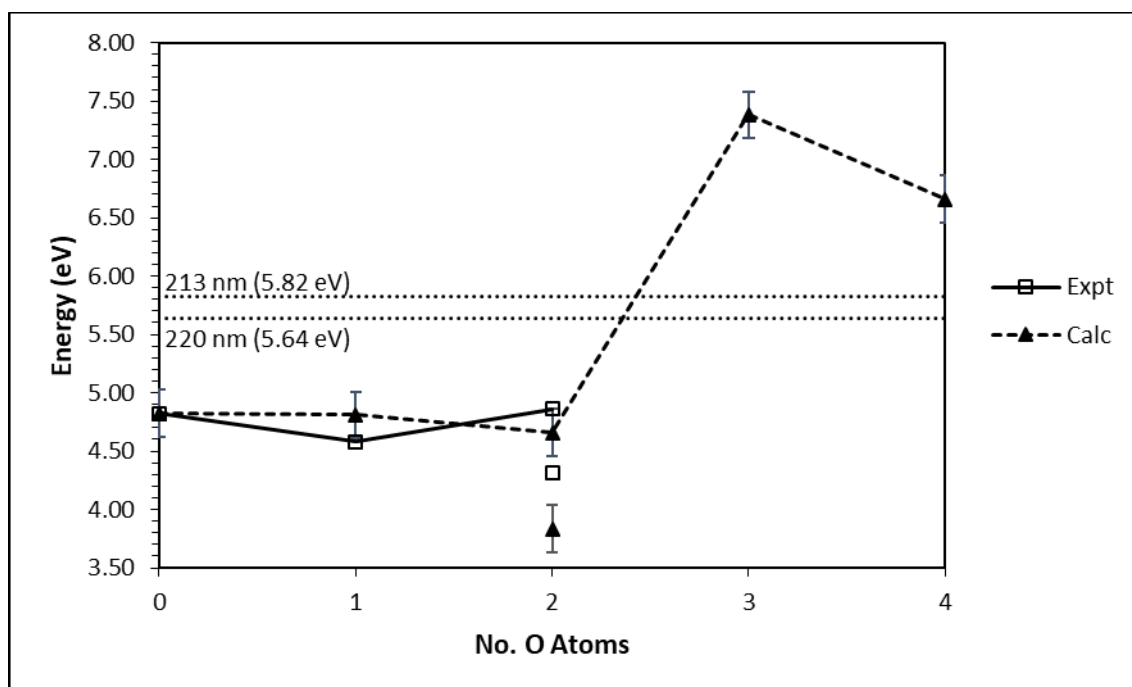


Figure 8.28: Experimental and calculated adiabatic ionisation energies for the AuCe_2O_n series with sequential oxidation. Primary and secondary IEs are shown for the AuCe_2O_2 species. The experimental and calculated IE trends for the primary onsets are shown as solid and dashed lines, respectively. Horizontal lines are drawn at 220 nm (5.64 eV) and 213 nm (5.82 eV) to represent the upper bound of the tuneable laser source and the highest photon energy for which mass spectra are recorded, respectively.

8.9. Comparison of Experimental Appearance Energies for Ce_2O_n and AuCe_2O_n Clusters

A comparison of experimental appearance energy values for the Ce_2O_n and AuCe_2O_n cluster species is presented in Figure 8.29. This comparison permits a simple analysis of the effects of gold adsorption on the ceria cluster ions using experimental data. The Ce_2O_n and AuCe_2O_n AE trends with sequential oxidation are presented as blue and gold lines in Figure 8.29, respectively. Appearance energies for both the first onset of ion signal and the highest intensity ion signal onset – corresponding to the primary onset – are both presented (as dashed and solid lines, respectively). The Ce_2O_3 AE is approximated as 5.73 eV (as the

midpoint for the bracketed AE range of 5.64–5.82 eV presented earlier). The AuCe₂O₃ AE values are not presented since this species was not detected in any mass spectra.

A direct comparison between the first onset AE values for the Ce₂O_n and AuCe₂O_n species shows no apparent correlation. The Ce₂O_n first onset AEs show an initial decrease in appearance energy for the monoxide – compared to the bare metal species – followed by an increase in AE for the dioxide species. The AuCe₂O_n first onset AEs by contrast show a decrease in AE for both the monoxide and dioxide species. Similar for the highest intensity onset AEs, no obvious correlation is noted. The Ce₂O_n highest intensity onset AE trend shows a decrease in the appearance energy of the monoxide species – compared to the bare metal cluster – followed by a further decrease in AE for the dioxide species. The AuCe₂O_n AEs by contrast show a decrease in AE for the monoxide species – compared to the bare metal cluster – followed by an increase in AE for the dioxide species. Unusually, better correlations are found by comparing the AuCe₂O_n first onset AEs with the Ce₂O_n highest intensity onset AEs, and the AuCe₂O_n highest intensity onset AEs with the Ce₂O_n first onset AEs. However, the trends drawn from these comparisons are contradictory: the former shows a decrease in AE by 0.09 – 0.31 eV due to gold adsorption, whereas the latter shows slightly higher AEs for the AuCe₂O and AuCe₂O₂ species resulting from gold doping. Comparison of the Ce₂O_n and AuCe₂O_n AE values is therefore inconclusive as to the effects of gold doping on ceria clusters. However, the similar AE values recorded for all Ce₂O_n/AuCe₂O_n clusters – which differed by up to 0.31 eV – shows any effects of Au adsorption is quite small for these particular cluster species. A more detailed analysis of the effects of gold doping on ceria cluster properties – using DFT calculations – is presented in Chapter 10.

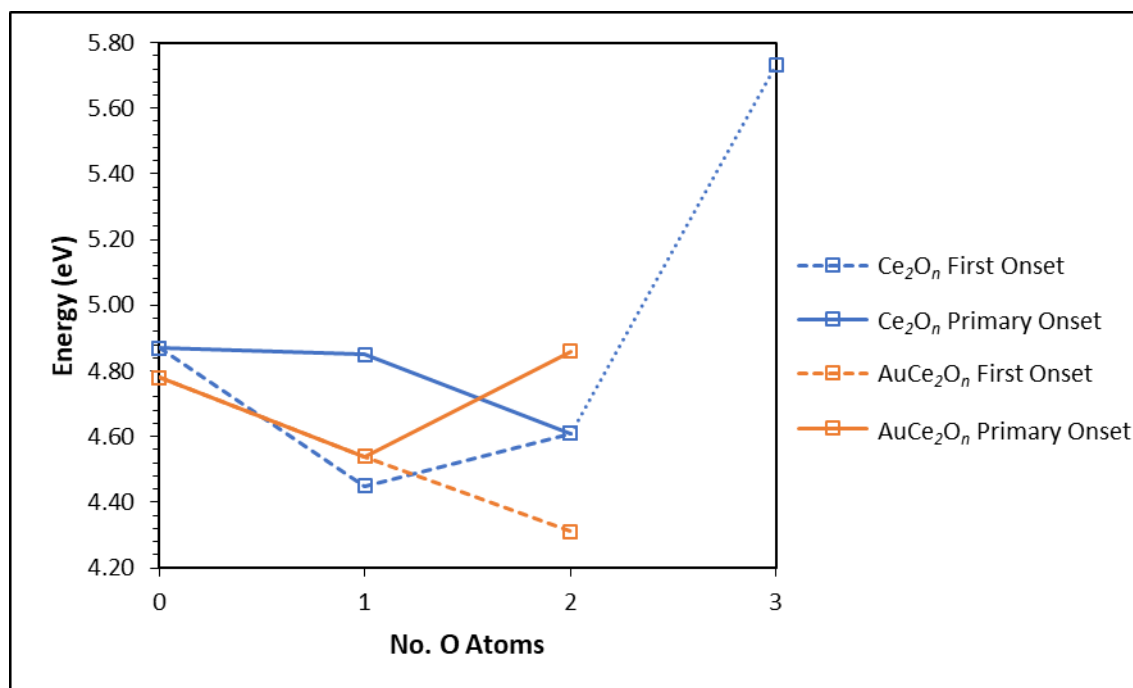


Figure 8.29: Experimental appearance energies for the Ce_2O_n (blue) and AuCe_2O_n (gold) cluster series with sequential oxidation. Appearance energy trends are shown for both the first onset of ion signal (dashed lines) and the primary onset (solid lines). The Ce_2O_3 AE is approximated, therefore the Ce_2O_2 – Ce_2O_3 AE trend is shown as a dotted line.

8.10. References

- (1) Emsley, J. *The Elements, Oxford Chemistry Guides*; Oxford University Press: New York, 1995.
- (2) Gentleman, A. S. The Effect of Sequential Oxidation and Composition on the Structural and Electronic Properties of Gas Phase Transition-Lanthanide Bimetallic Clusters, PhD Thesis, The University of Adelaide, 2014.
- (3) NIST Atomic Spectra Database physics.nist.gov/ (accessed Jun 30, 2016).
- (4) Schmidbaur, H.; Schier, A. *Chem. Soc. Rev.* **2008**, *37* (9), 1931.
- (5) Scherbaum, F.; Grohmann, A.; Huber, B.; Krüger, C.; Schmidbaur, H. *Angew. Chemie Int. Ed. English* **1988**, *27* (11), 1544.
- (6) Schmidbaur, H. *Gold Bull.* **2000**, *33* (1), 3.
- (7) Ockerski, J. W. *Vibrational Analysis in Gaussian*; 1999.
- (8) Mozhayskiy, V. A.; Krylov, A. I. *ezSpectrum 3.0: Franck-Condon Factors in the Harmonic Approximation*; 2009.
- (9) Camellone, M. F.; Fabris, S. *J. Am. Chem. Soc.* **2009**, *131* (30), 10473.
- (10) Zhang, C.; Michaelides, A.; King, D. A.; Jenkins, S. J. *J. Chem. Phys.* **2008**, *129* (19), 1.
- (11) Gentleman, A. S.; Addicoat, M. A.; Dryza, V.; Gascooke, J. R.; Buntine, M. A.; Metha, G. *F. J. Chem. Phys.* **2009**, *130* (16), 164311.
- (12) Nolan, M. *J. Chem. Phys.* **2009**, *130* (14), 144702.
- (13) Nolan, M.; Verdugo, V. S.; Metiu, H. *Surf. Sci.* **2008**, *602* (16), 2734.
- (14) Zhang, C.; Michaelides, A.; King, D. A.; Jenkins, S. J. *J. Phys. Chem. C* **2009**, *113* (16), 6411.
- (15) Koretsky, G. M.; Knickelbein, M. B. *Eur. Phys. J. D - At. Mol. Opt. Plasma Phys.* **1998**, *2*, 273.
- (16) Gentleman, A. S.; Addicoat, M. A.; Dryza, V.; Gascooke, J. R.; Buntine, M. A.; Metha, G. *F. J. Chem. Phys.* **2009**, *130* (16), 64311.
- (17) Dryza, V.; Addicoat, M. A.; Gascooke, J. R.; Buntine, M. A.; Metha, G. *F. J. Phys. Chem.*

A **2005**, 109 (49), 11180.

(18) Dryza, V.; Addicoat, M. A.; Gascooke, J. R.; Buntine, M. A.; Metha, G. F. *J. Phys. Chem.*

A **2008**, 112 (25), 5582.

(19) Dryza, V.; Gascooke, J. R.; Buntine, M. A.; Metha, G. F. *Phys. Chem. Chem. Phys.* **2009**,

11 (7), 1060.

Chapter Nine

Photo-Ionisation Efficiency Spectroscopy, Density Functional Theory

Calculations and Zero Electron Kinetic Energy Simulations of AuCe₃O_n Clusters

This chapter presents both calculated and experimentally determined adiabatic ionisation energies for the AuCe₃O_n ($n=0-3$) clusters, and calculated ionisation energies for the AuCe₃O_n ($n=4-6$) clusters. An initial analysis of the AuCe₃O_n mass spectrum is presented; this is followed by a comparison of experimental and simulated Photo-Ionisation Efficiency (PIE) spectra – with the latter derived from Zero Electron Kinetic Energy (ZEKE) simulations of DFT-calculated structures. Calculated and experimental ionisation energies are then compared to verify the reliability of the DFT calculated structures, such that the geometric and electronic properties of AuCe₃O_n clusters can be inferred from calculations.

9.1. AuCe_3O_n Mass Spectrum

A mass spectrum showing AuCe_3O_n cluster ion peaks following photo-ionisation at 213 nm (5.82 eV) is presented in Figure 9.1. A number of other peaks are also recorded in the mass spectrum; these ion peaks correspond to the Ce_4O_n clusters which are slightly lighter than the AuCe_3O_n clusters. A detailed analysis of the Ce_4O_n cluster series can be found in Chapter 7. The AuCe_3O_n ion peaks are all observed with a number of secondary peaks on the higher m/z side of each peak in addition to contouring at the peak base; this is attributed to secondary Ce isotopes. Given that Au only has one naturally occurring isotope, the isotopic peak distribution of AuCe_3O_n clusters is the same as for the Ce_3O_n clusters discussed in Chapter 6.

Ion peaks corresponding to the AuCe_3O , AuCe_3O_2 and AuCe_3O_3 clusters are all detected in good abundance following 213 nm (5.82 eV) photo-ionisation. The AuCe_3 ion is not detected in the mass spectrum; however, this is attributed to the source conditions in this case favouring the formation of oxidised clusters. As stated in previous chapters, the formation of Ce_mO_n and AuCe_mO_n clusters does not follow any “magic number” trends. Cluster abundances are instead highly dependent on the conditions in the cluster source, most notably the pressure of the carrier gas. An example of this is presented in Figure 9.2, which shows two different mass spectra of Ce_4O_n and AuCe_3O_n clusters. The mass spectrum shown in Figure 9.2(a) was recorded under similar source conditions to the mass spectrum shown in Figure 9.1. Conversely, the mass spectrum shown in Figure 9.2(b) was recorded with a lower carrier gas pressure which facilitates the formation of clusters with fewer oxygen atoms. Significantly greater abundance of both Ce_4 and AuCe_3 ion peaks can be observed in this mass spectrum. The reduced pressure of the He carrier gas in the latter case could restrict the formation of metal cluster oxides through reduction of either the collision rate or the collision energy with oxygen atoms in the turbulent flow.

Ion peaks for the AuCe_3O_4 , AuCe_3O_5 and AuCe_3O_6 clusters, unlike the AuCe_3 ion, are not detected under any source conditions following photo-ionisation at 213 nm (5.82 eV). The non-detection of the AuCe_3O_4 , AuCe_3O_5 and AuCe_3O_6 clusters is therefore attributed to

prohibitively high ionisation energies. This is supported by DFT calculations later in this chapter.

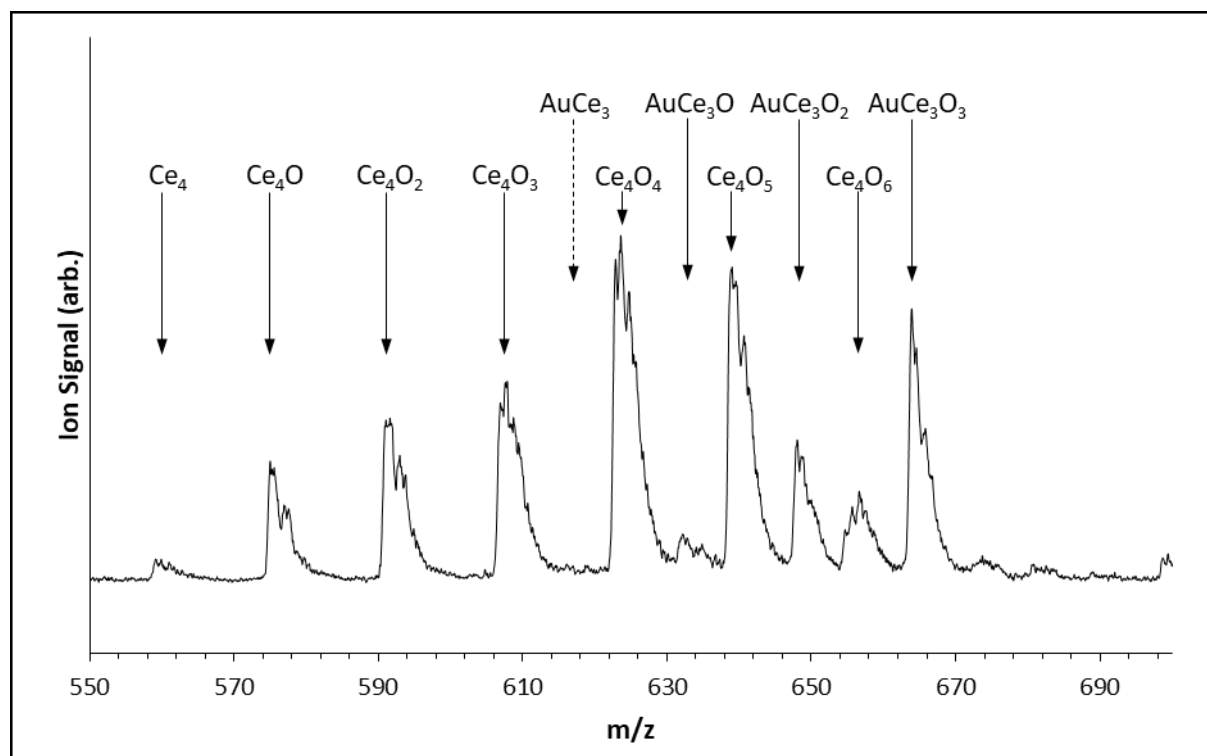


Figure 9.1: Mass spectrum of Ce_4O_n and AuCe_3O_n clusters following photo-ionisation at 213 nm (5.82 eV). Ion peaks corresponding to Ce_4O_n and AuCe_3O_n clusters are labelled. The AuCe_3 cluster is not detected in this mass spectrum due to source conditions favouring oxidised clusters; the mass corresponding to AuCe_3 is labelled with a dashed arrow.

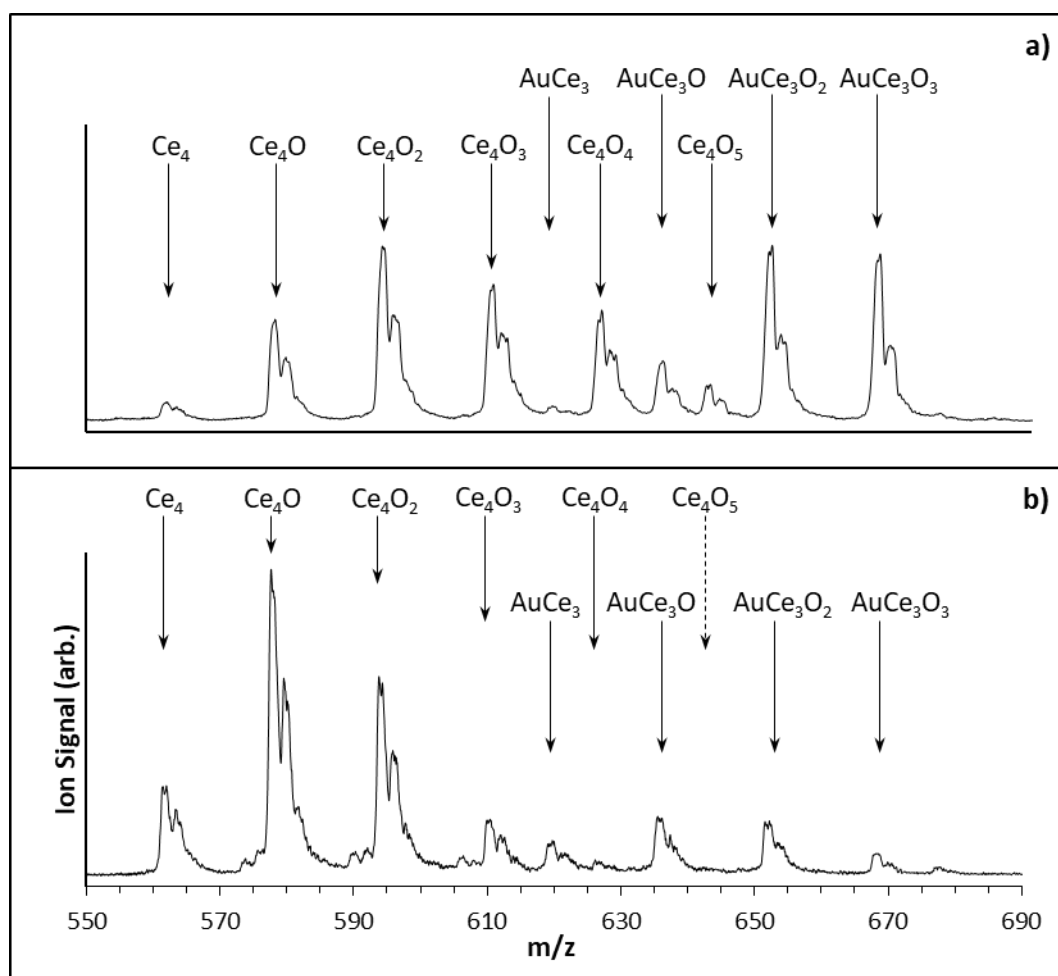


Figure 9.2: Mass spectra of Ce_4O_n and AuCe_3O_n clusters recorded under conditions favouring **a).** formation of oxidised clusters and **b).** formation of bare metal clusters. Ion peaks corresponding to the Ce_4O_n and AuCe_3O_n clusters are labelled. Mass spectra are recorded following photo-ionisation at 245.5 nm (5.05 eV). The Ce_4O_5 ion peak is not detected in Figure 9.2(b); the corresponding ion mass is labelled with the dashed arrow.

9.2. Appearance of Cluster Ion Signal for the AuCe₃O_n (n=0–3) Series

A series of AuCe₃O_n mass spectra recorded at decreasing photon wavelengths – corresponding with increasing photon energies – is presented in Figure 9.3. Source conditions for the mass spectra shown in Figures 9.3(a)-(d) are optimised for the production of metal oxide clusters; Figure 9.3(e) shows a mass spectrum optimised for the production of bare metal clusters. No AuCe₃O_n ion peaks are observed following 315.75 nm (3.92 eV) photo-ionisation, while the AuCe₃, AuCe₃O, AuCe₃O₂ and AuCe₃O₃ ion peaks are all detected following 245 nm (5.06 eV) photo-ionisation. The AuCe₃ ion peak is first detected in the mass spectrum recorded following 245 nm (5.06 eV) photo-ionisation (Figure 9.3(e)). A bracketed AE of 4.44 – 5.06 eV is assigned to the AuCe₃ cluster. The AuCe₃O ion peak is not detected following photo-ionisation at 285 nm (4.35 eV), is detected with weak intensity following 279 nm (4.44 eV) photo-ionisation and shows good intensity following 245 nm (5.06 eV) photo-ionisation. A bracketed AE of 4.35 – 5.06 eV is assigned to the AuCe₃O cluster. The AuCe₃O₂ and AuCe₃O₃ ion peaks both appear within in the 3.92 – 4.35 eV (315.75 – 285 nm) energy range with strong ion growth then observed at photon energies higher than 4.35 eV. Bracketed AEs of 3.92 – 4.35 eV are assigned to both the AuCe₃O₂ and AuCe₃O₃ cluster systems.

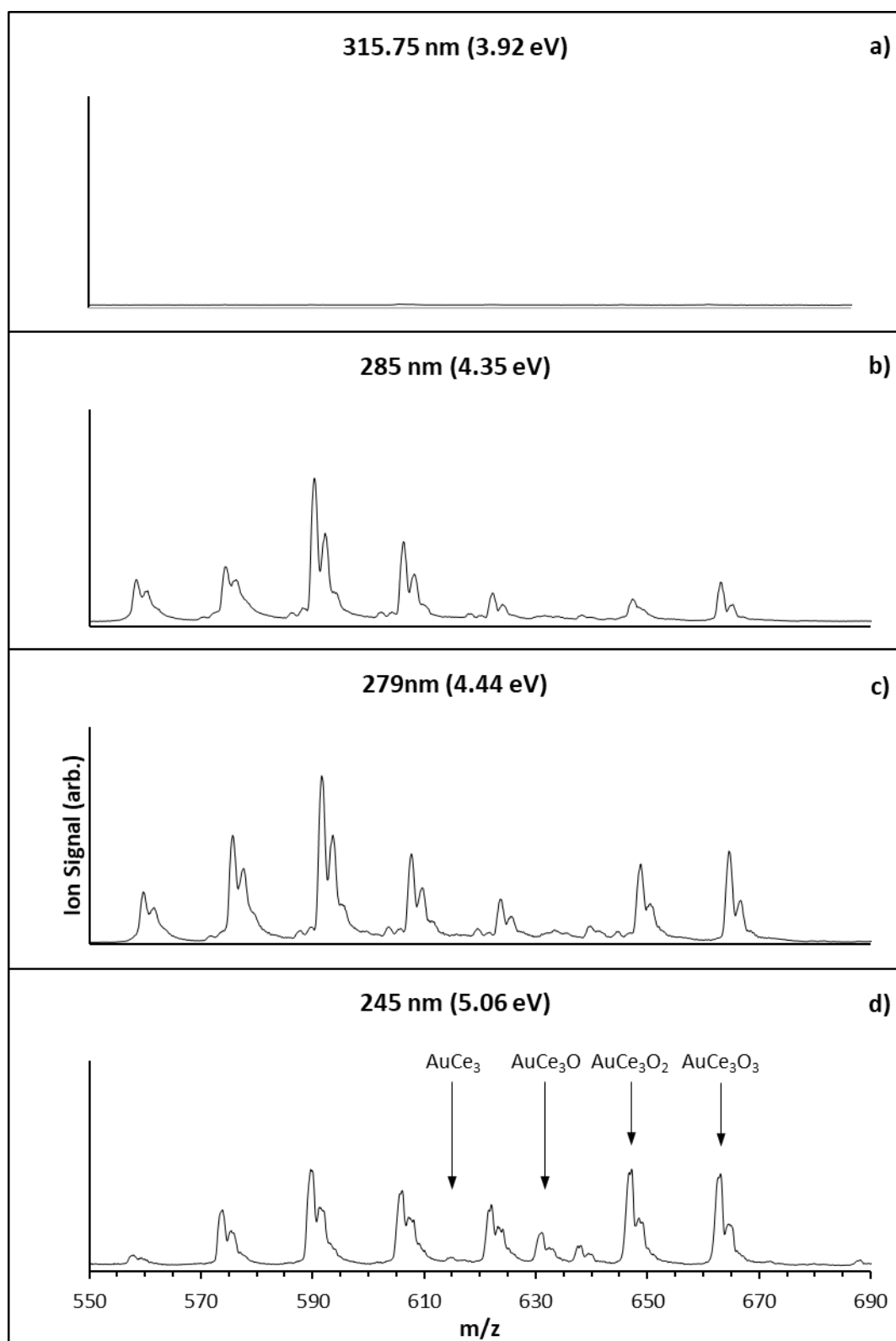


Figure 9.3: Mass spectra of AuCe_3O_n clusters recorded following photo-ionisation at **a).** 315.75 nm (3.92 eV), **b).** 285 nm (4.35 eV), **c).** 279 nm (4.44 eV) and **d).** 245 nm (5.06 eV).

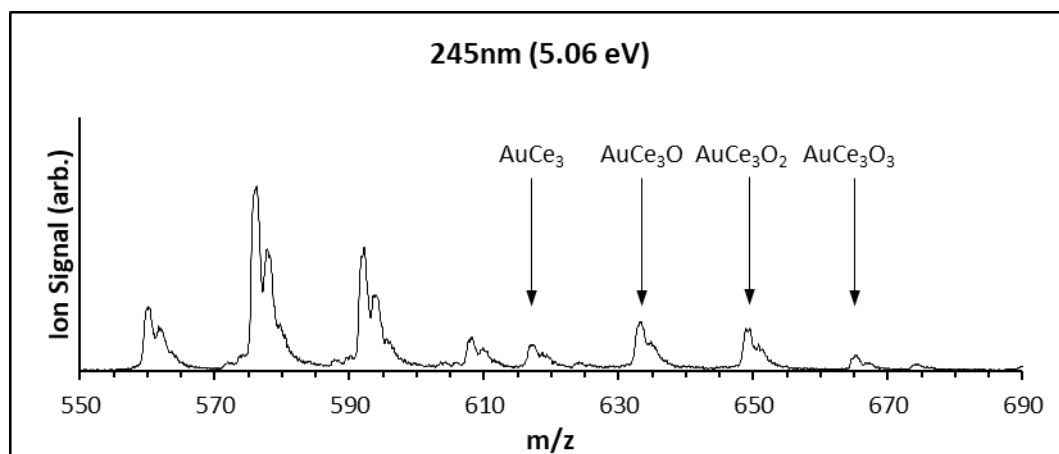


Figure 9.3(e): Mass spectrum of AuCe_3O_n clusters following photo-ionisation at 245 nm (5.06 eV). Source conditions are optimised for the production of the AuCe_3 cluster.

9.3. PIE Spectrum and DFT Results for AuCe_3

9.3.1. AuCe_3 Experimental PIE Spectrum

A PIE spectrum of the AuCe_3 cluster system recorded over the energy range 4.35 – 5.17 eV is presented in Figure 9.4. A flat region of zero intensity is recorded in the region 4.35 – 4.74 eV which is taken as the baseline. This is followed by a single onset of ion signal onset with an appearance energy of 4.74 eV. The onset is characterised with a uniform, shallow slope which extends over a broad – ca. 0.42 eV – range to 5.17 eV, corresponding to the maximum photon energy for which PIE experiments of AuCe_3O_n clusters were performed. A plateau of maximum ion signal is not recorded for the AuCe_3 species, indicating the highest FC allowed vibronic transitions has not been accessed.

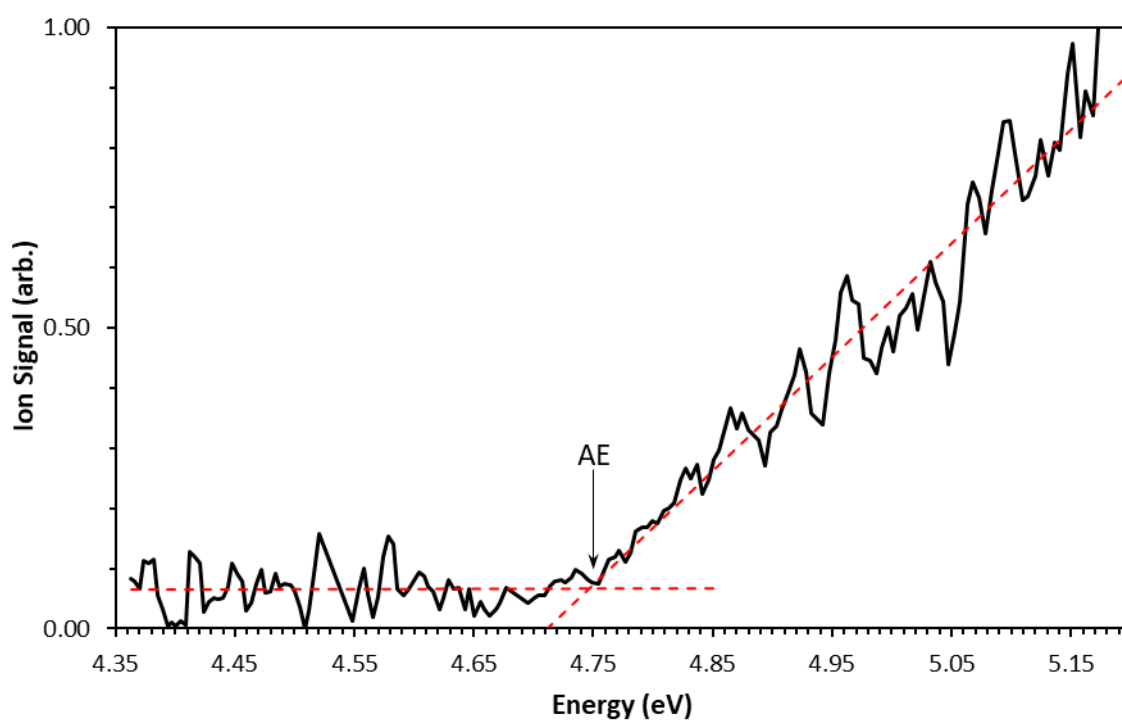


Figure 9.4: PIE spectrum for AuCe_3 . Linear trendlines for the baseline and onset are presented as red dashed lines. The appearance energy is labelled with a black arrow.

9.3.2. DFT Calculations for AuCe₃

DFT calculated neutral and cationic AuCe₃ species are presented in Figures 9.5 and 9.6. Calculated vibrational modes for all AuCe₃O_n structures are presented in Appendix B. One unique AuCe₃ structure is calculated – labelled **XVIII** – comprising a gold atom facially bound to a Ce₃ trimer. The neutral structure is calculated in $m = 8, 10, 6$ and 4 multiplicities – presented in ascending order of energy – labelled **⁸XVIII**, **¹⁰XVIII**, **⁶XVIII** and **⁴XVIII** respectively. The **⁸XVIII** LES is calculated as C_s symmetric in the $^8A''$ electronic state, while the **¹⁰XVIII**, **⁶XVIII** and **⁴XVIII** species are all calculated with C_1 symmetry. Energies of the **¹⁰XVIII**, **⁶XVIII** and **⁴XVIII** species relative to the **⁸XVIII** lowest energy structure (LES) are calculated as +0.052 eV, +0.128 eV and +0.393 eV respectively. The 0.052 eV energy difference between the **⁸XVIII** and **¹⁰XVIII** species would most likely make these isomers energetically indistinguishable. Conversely, the high energy of the **⁴XVIII** isomer would most likely preclude the formation of this species in any reasonable abundance in the cluster source. Thus, ionisation processes from the **⁴XVIII** structure are not considered to contribute to the PIE spectrum.

Calculations of AuCe₃ cationic species reveal four unique spin isomers, all of which possess the same trigonal pyramidal geometry as calculated for the neutral AuCe₃ structures. These include $m = 9, 7, 3$ and 5 species, labelled **⁹XVIII⁺**, **⁷XVIII⁺**, **⁵XVIII⁺** and **³XVIII⁺** respectively, all of which are calculated with C_1 symmetry. Calculations of the $m = 11$ species – as a potential $\Delta S = +\frac{1}{2}$ target state for the **¹⁰XVIII** neutral species – were unsuccessful due to convergence difficulties. The calculated cationic species give a total of 5 potential ionisation processes for the AuCe₃ cluster which include the $^9A \leftarrow ^8A''$ (**⁹XVIII⁺** \leftarrow **⁸XVIII**), $^7A \leftarrow ^8A''$ (**⁷XVIII⁺** \leftarrow **⁸XVIII**), $^9A \leftarrow ^{10}A$ (**⁹XVIII⁺** \leftarrow **¹⁰XVIII**), $^7A \leftarrow ^6A$ (**⁷XVIII⁺** \leftarrow **⁶XVIII**) and $^5A \leftarrow ^6A$ (**⁵XVIII⁺** \leftarrow **⁶XVIII**) transitions. IEs for these processes are calculated as 4.937 eV, 4.983 eV, 4.885 eV, 4.855 eV and 5.094 eV respectively. The ca. 0.24 eV difference between the calculated IEs is consistent – within the 0.2 eV error for calculated IEs – with the ca. 0.42 eV range over which the ion signal onset occurs in the experimental PIE spectrum. The $^9A \leftarrow ^8A''$ (**⁹XVIII⁺** \leftarrow **⁸XVIII**), $^7A \leftarrow ^8A''$ (**⁷XVIII⁺** \leftarrow **⁸XVIII**), $^9A \leftarrow ^{10}A$ (**⁹XVIII⁺** \leftarrow **¹⁰XVIII**), $^7A \leftarrow ^6A$ (**⁷XVIII⁺** \leftarrow **⁶XVIII**) and $^5A \leftarrow ^6A$ (**⁵XVIII⁺** \leftarrow **⁶XVIII**) ionisation processes are shown in Figure 9.5 as green, orange, violet, blue and magenta arrows, respectively.

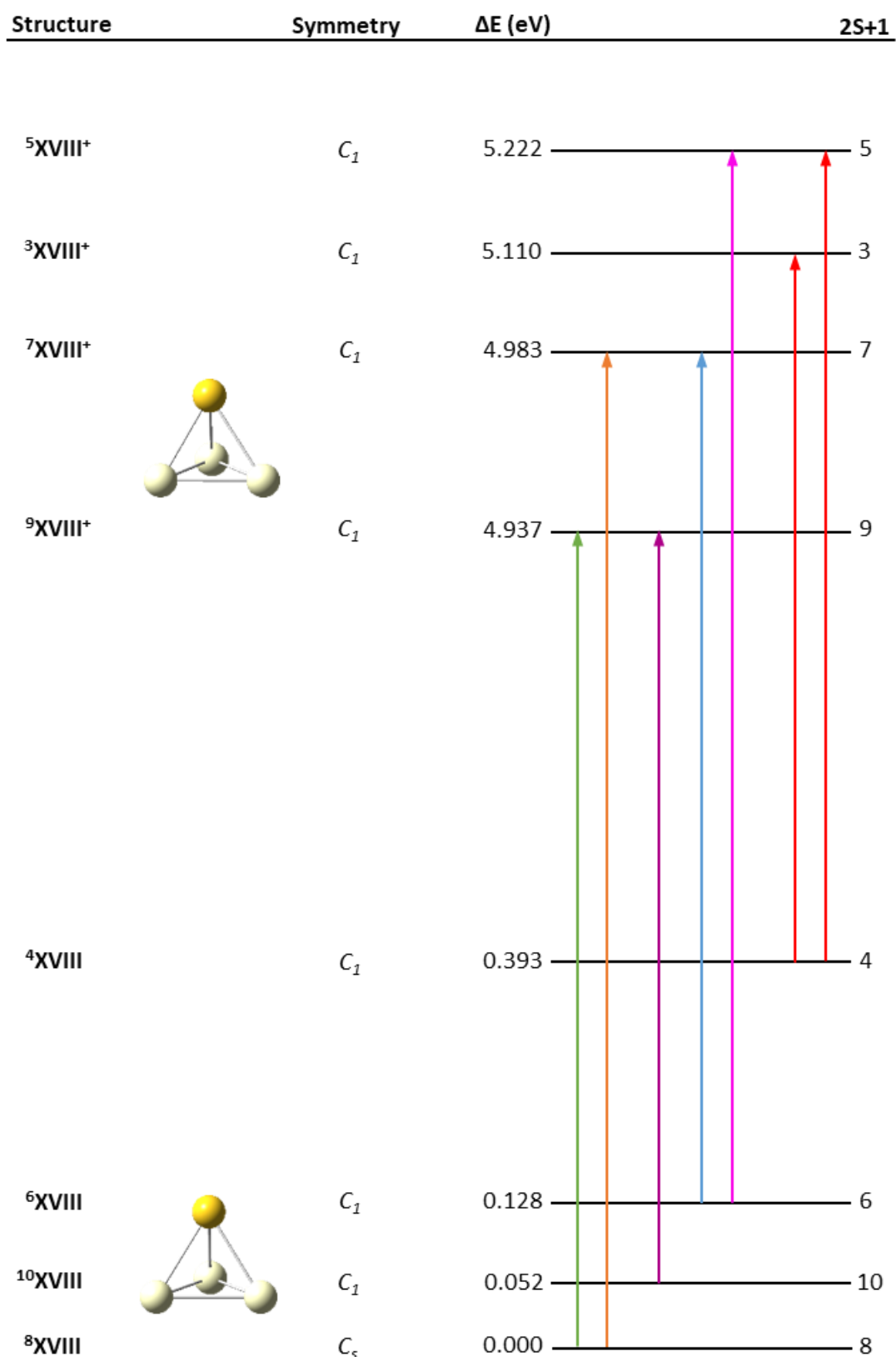


Figure 9.5: Calculated structures for AuCe_3 . Potential ionisation transitions are shown. Ionisation transitions from neutral structures with prohibitively high electronic energies are shown as solid red arrows.

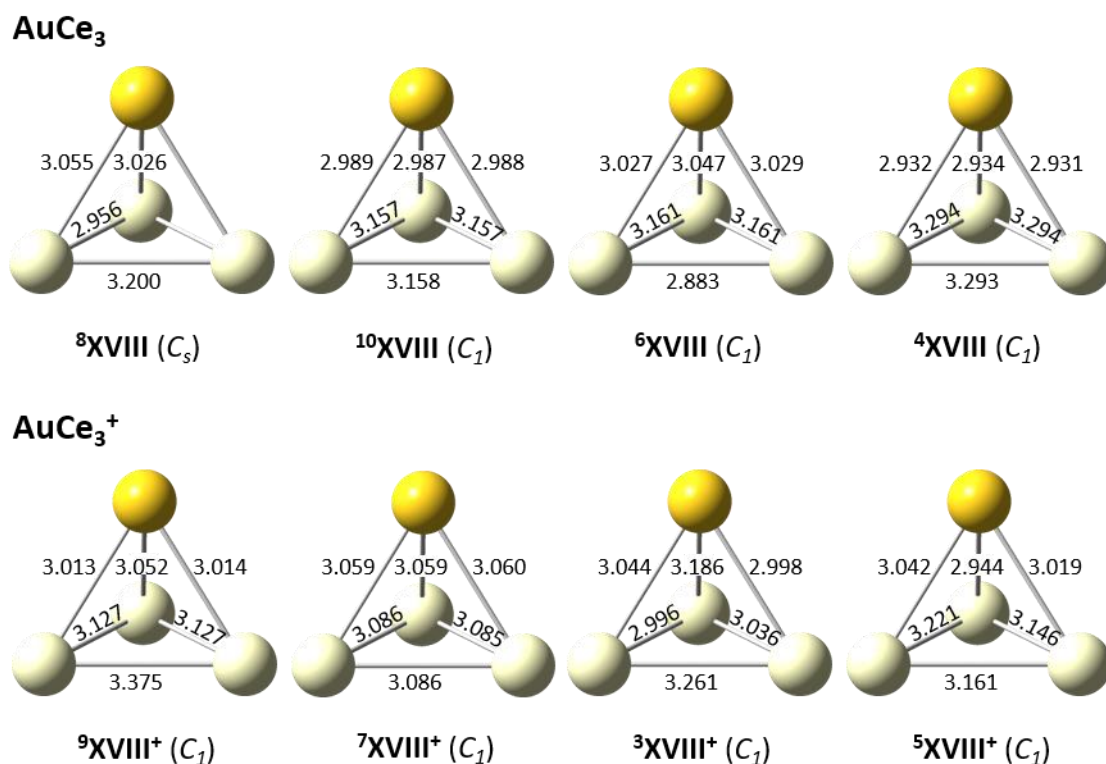


Figure 9.6: Calculated AuCe₃ neutral (top) and cationic (below) structures. Bond lengths are presented in Å. Point groups are shown in brackets.

9.3.3. ZEKE Spectral Simulations for AuCe₃

Calculated ZEKE spectra for the AuCe₃ ⁹A←⁸A" (⁹XVIII⁺←⁸XVIII), ⁷A←⁸A" (⁷XVIII⁺←⁸XVIII), ⁹A←¹⁰A (⁹XVIII⁺←¹⁰XVIII), ⁷A←⁶A (⁷XVIII⁺←⁶XVIII) and ⁵A←⁶A (⁵XVIII⁺←⁶XVIII) ionisation processes are presented in Figure 9.7. The ZEKE spectra were corrected to the experimental PIE spectrum using the method described in Chapter 3. Briefly, the lowest energy vibronic transition for the ionisation process with the lowest IE is corrected to match the experimental AE. The remaining ionisation processes are then offset from the lowest energy transition by their relative differences in calculated IEs. Energetic corrections of +0.010 eV, +0.155 eV, -0.070 eV, +0.025 eV and +0.120 eV were then applied to the ⁹A←⁸A" (⁹XVIII⁺←⁸XVIII), ⁷A←⁸A" (⁷XVIII⁺←⁸XVIII), ⁹A←¹⁰A (⁹XVIII⁺←¹⁰XVIII), ⁷A←⁶A (⁷XVIII⁺←⁶XVIII) and ⁵A←⁶A (⁵XVIII⁺←⁶XVIII) ZEKE spectra, respectively, to improve the fit of the subsequently calculated PIE spectrum (vide infra) to the experimental PIE spectrum. The corrected ZEKE spectra are shown here.

Vibronic peak intensities in each ZEKE spectrum are normalised such that the most intense peak has a value of 1.00. Comparison of the scaling factors used to normalise the ${}^9\text{A} \leftarrow {}^8\text{A}''$ (${}^9\text{XVIII}^+ \leftarrow {}^8\text{XVIII}$), ${}^7\text{A} \leftarrow {}^8\text{A}''$ (${}^7\text{XVIII}^+ \leftarrow {}^8\text{XVIII}$), ${}^9\text{A} \leftarrow {}^{10}\text{A}$ (${}^9\text{XVIII}^+ \leftarrow {}^{10}\text{XVIII}$), ${}^7\text{A} \leftarrow {}^6\text{A}$ (${}^7\text{XVIII}^+ \leftarrow {}^6\text{XVIII}$) and ${}^5\text{A} \leftarrow {}^6\text{A}$ (${}^5\text{XVIII}^+ \leftarrow {}^6\text{XVIII}$) spectra – which are 15.0, 5.9, 27.6, 14.7 and 21.0 respectively – suggests the ${}^7\text{A} \leftarrow {}^8\text{A}''$ (${}^7\text{XVIII}^+ \leftarrow {}^8\text{XVIII}$) transition – with the lowest scaling factor – is the dominant process. However, the remaining ionisation processes would contribute substantially to the PIE spectrum. The 0_0^0 transition is not calculated in any of the ZEKE spectra, inferring considerable structural change occurring between the neutral and cationic species in all ionisation processes.

ZEKE spectra for the ${}^9\text{A} \leftarrow {}^8\text{A}''$ (${}^9\text{XVIII}^+ \leftarrow {}^8\text{XVIII}$) and ${}^7\text{A} \leftarrow {}^8\text{A}''$ (${}^7\text{XVIII}^+ \leftarrow {}^8\text{XVIII}$) transitions presented in Figures 9.7(a) and 9.7(b), respectively – which both describe ionisation of the ${}^8\text{XVIII}$ LES – show similar spectral profiles. However, the ${}^9\text{A} \leftarrow {}^8\text{A}''$ (${}^9\text{XVIII}^+ \leftarrow {}^8\text{XVIII}$) spectrum is calculated with a broader range of vibronic transitions and lower vibronic peak intensities. While not all vibronic peaks in each spectrum were assigned, the prominent vibronic transitions in both spectra were found to belong to a number of vibronic progressions. The ${}^9\text{A} \leftarrow {}^8\text{A}''$ (${}^9\text{XVIII}^+ \leftarrow {}^8\text{XVIII}$) spectrum is dominated by the $3_0^2 6_0^n$, $3_0^3 6_0^n$, $3_0^4 6_0^n$ and $3_0^5 6_0^n$ progressions. The ν_3 and ν_6 modes describe symmetric Au-Ce stretching and AuCe₃ breathing modes, respectively. The ${}^7\text{A} \leftarrow {}^8\text{A}''$ (${}^7\text{XVIII}^+ \leftarrow {}^8\text{XVIII}$) spectrum largely comprises progressions of the ν_3 mode which include the $1_0^1 3$, $3_0^n 6_0^1$, $2_1^0 3_0^n$, $2_2^0 3_0^n$ and $1_0^1 3_0^n 4_0^1$ progressions. The maximum intensity FC transitions in the ${}^9\text{A} \leftarrow {}^8\text{A}''$ (${}^9\text{XVIII}^+ \leftarrow {}^8\text{XVIII}$) and ${}^7\text{A} \leftarrow {}^8\text{A}''$ (${}^7\text{XVIII}^+ \leftarrow {}^8\text{XVIII}$) are calculated as the $3_0^5 6_0^4$ and $1_0^1 3_0^4$ transitions, respectively. The more highly excited maximum intensity FC transition in this spectrum infers greater structural deformation following ionisation; this is consistent with the weaker intensity of the ${}^9\text{A} \leftarrow {}^8\text{A}''$ (${}^9\text{XVIII}^+ \leftarrow {}^8\text{XVIII}$) spectrum compared to the ${}^7\text{A} \leftarrow {}^8\text{A}''$ (${}^7\text{XVIII}^+ \leftarrow {}^8\text{XVIII}$) spectrum.

ZEKE spectra for the ${}^9\text{A} \leftarrow {}^{10}\text{A}$ (${}^9\text{XVIII}^+ \leftarrow {}^{10}\text{XVIII}$), ${}^7\text{A} \leftarrow {}^6\text{A}$ (${}^7\text{XVIII}^+ \leftarrow {}^6\text{XVIII}$) and ${}^5\text{A} \leftarrow {}^6\text{A}$ (${}^5\text{XVIII}^+ \leftarrow {}^6\text{XVIII}$) ionisation processes are presented in Figures 9.7(c), 9.7(d) and 9.7(e), respectively. The ${}^9\text{A} \leftarrow {}^{10}\text{A}$ (${}^9\text{XVIII}^+ \leftarrow {}^{10}\text{XVIII}$) and ${}^5\text{A} \leftarrow {}^6\text{A}$ (${}^5\text{XVIII}^+ \leftarrow {}^6\text{XVIII}$) ZEKE spectra are both dominated by progressions involving the ν_5 mode – which describes an in-plane bending of

the Ce₃ trimer – coupled to v_1 and v_6 modes in the former and the v_2 mode in the latter. The ${}^7\text{A} \leftarrow {}^6\text{A}$ (${}^7\text{XVIII}^+ \leftarrow {}^6\text{XVIII}$) ZEKE spectrum largely comprises the $1_0^1 6_0^n$ and $1_0^2 6_0^n$ progressions, where the v_6 mode describes the AuCe₃ breathing mode. The maximum FC transitions for the ${}^9\text{A} \leftarrow {}^{10}\text{A}$ (${}^9\text{XVIII}^+ \leftarrow {}^{10}\text{XVIII}$), ${}^7\text{A} \leftarrow {}^6\text{A}$ (${}^7\text{XVIII}^+ \leftarrow {}^6\text{XVIII}$) and ${}^5\text{A} \leftarrow {}^6\text{A}$ (${}^5\text{XVIII}^+ \leftarrow {}^6\text{XVIII}$) spectra are assigned to the $1_0^1 5_0^5 6_0^2$, $1_0^2 6_0^6$ and $2_0^2 5_0^6$ vibronic peaks, respectively. The moderately excited cationic species in all three vibronic transitions infers a small degree of structural deformation of the cation.

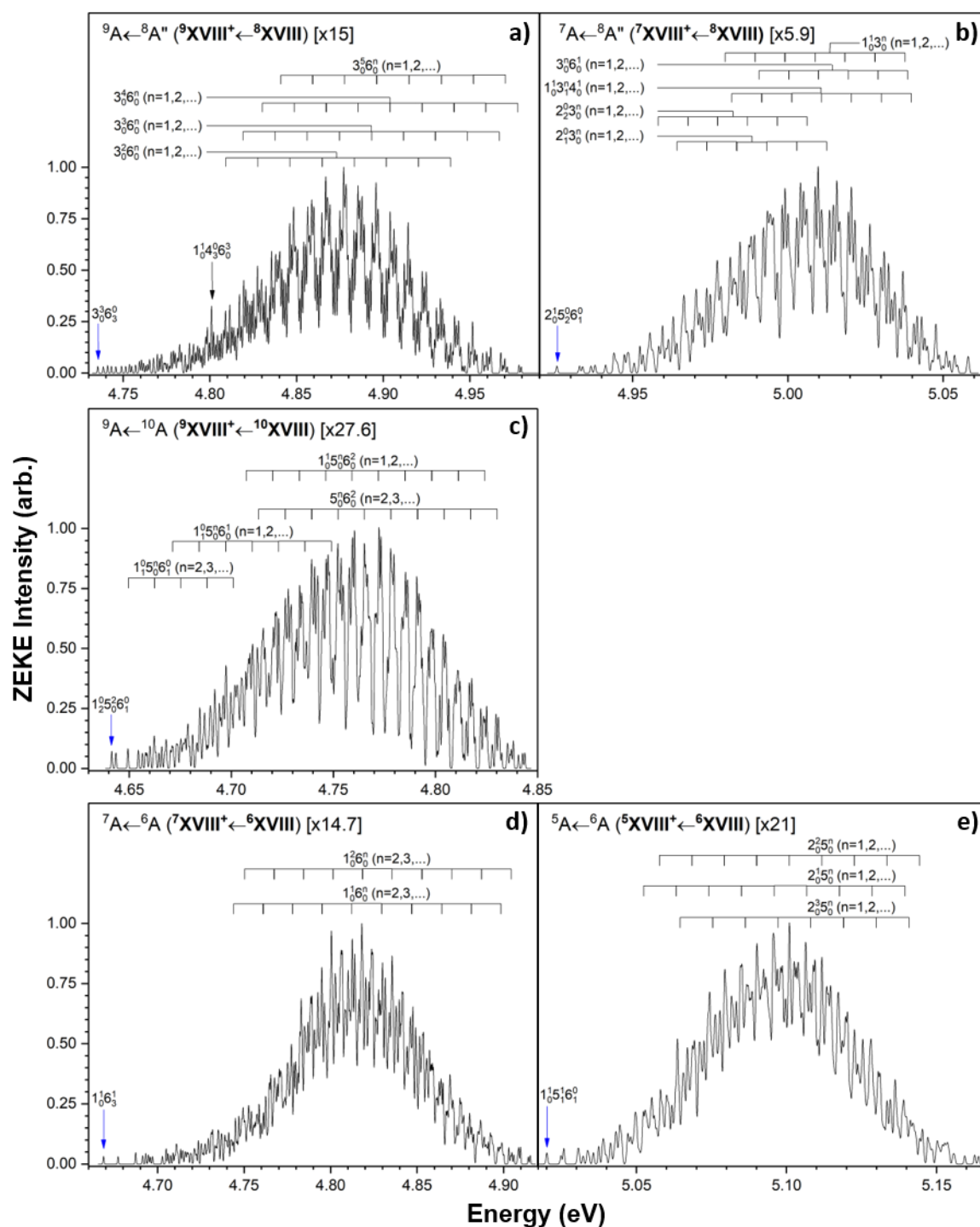


Figure 9.7: Calculated ZEKE spectra for AuCe₃ ionisation transitions: **a).** ${}^9A \leftarrow {}^8A''$ (${}^9XVIII^+ \leftarrow {}^8XVIII$), **b).** ${}^7A \leftarrow {}^8A''$ (${}^7XVIII^+ \leftarrow {}^8XVIII$), **c).** ${}^9A \leftarrow {}^{10}A$ (${}^9XVIII^+ \leftarrow {}^{10}XVIII$), **d).** ${}^7A \leftarrow {}^6A$ (${}^7XVIII^+ \leftarrow {}^6XVIII$) and **e).** ${}^5A \leftarrow {}^6A''$ (${}^5XVIII^+ \leftarrow {}^6XVIII$). Spectral intensities are normalised to the most intense peak with scaling factors shown. Prominent vibronic transitions are assigned. The vibronic transition likely to correspond to the appearance of ion signal in each spectrum is labelled with a blue arrow.

9.3.4. Comparison of Simulated and Experimental PIE Spectra for AuCe₃

A PIE spectrum for the AuCe₃ system is calculated via integration of the ${}^9\text{A} \leftarrow {}^8\text{A}''$ (${}^9\text{XVIII}^+ \leftarrow {}^8\text{XVIII}$), ${}^7\text{A} \leftarrow {}^8\text{A}''$ (${}^7\text{XVIII}^+ \leftarrow {}^8\text{XVIII}$), ${}^9\text{A} \leftarrow {}^{10}\text{A}$ (${}^9\text{XVIII}^+ \leftarrow {}^{10}\text{XVIII}$), ${}^7\text{A} \leftarrow {}^6\text{A}$ (${}^7\text{XVIII}^+ \leftarrow {}^6\text{XVIII}$) and ${}^5\text{A} \leftarrow {}^6\text{A}$ (${}^5\text{XVIII}^+ \leftarrow {}^6\text{XVIII}$) vibronic transitions. The calculated PIE spectrum is shown overlayed against the experimental PIE spectrum in Figure 9.8 with good agreement between the two spectra. However, it is assumed that no further increase in AuCe₃ ion signal – for the experimental PIE spectrum – occurs at higher energy. The IE is assigned to the ${}^9\text{A} \leftarrow {}^8\text{A}''$ (${}^9\text{XVIII}^+ \leftarrow {}^8\text{XVIII}$) process – as the lowest energy ionisation process from the lowest energy neutral structure – as 4.76 eV. It should be noted that the ${}^9\text{A} \leftarrow {}^{10}\text{A}$ (${}^9\text{XVIII}^+ \leftarrow {}^{10}\text{XVIII}$) transition would also be a viable process from which to assign the IE value, given the ${}^8\text{XVIII}$ and ${}^{10}\text{XVIII}$ species are calculated as energetically indistinguishable. Moreover, the ca. 0.04 eV difference between the calculated IEs for the two ionisation processes falls within the ± 0.05 eV error assigned to the experimental IE.

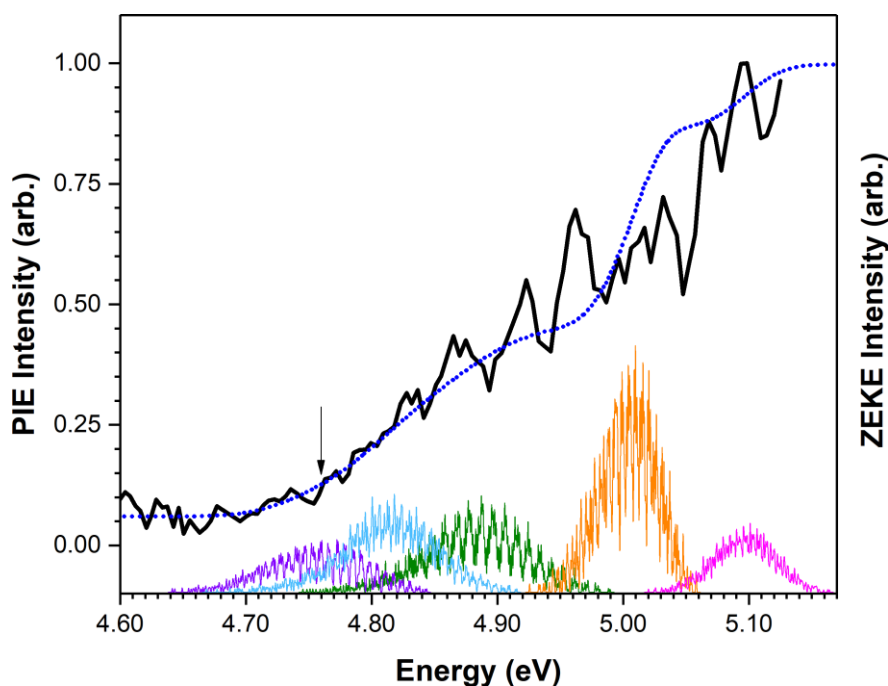


Figure 9.8: Calculated AuCe₃ PIE spectrum (blue dotted line) overlayed against the experimental PIE spectrum (solid black line). Calculated ZEKE spectra for the ${}^9\text{A} \leftarrow {}^8\text{A}''$ (${}^9\text{XVIII}^+ \leftarrow {}^8\text{XVIII}$), ${}^7\text{A} \leftarrow {}^8\text{A}''$ (${}^7\text{XVIII}^+ \leftarrow {}^8\text{XVIII}$), ${}^9\text{A} \leftarrow {}^{10}\text{A}$ (${}^9\text{XVIII}^+ \leftarrow {}^{10}\text{XVIII}$), ${}^7\text{A} \leftarrow {}^6\text{A}$ (${}^7\text{XVIII}^+ \leftarrow {}^6\text{XVIII}$) and ${}^5\text{A} \leftarrow {}^6\text{A}$ (${}^5\text{XVIII}^+ \leftarrow {}^6\text{XVIII}$) transitions are shown below the PIE spectrum in green, orange, violet, blue and magenta, respectively. The adiabatic ionisation energy is labelled with a black arrow.

9.4. PIE Spectrum and DFT Results for AuCe_3O

9.4.1. AuCe_3O Experimental PIE Spectrum

A PIE spectrum recorded for the AuCe_3O cluster system within the 4.10 – 4.90 eV energy range is presented in Figure 9.9. The PIE spectrum shows two onsets of ion signal – in the ranges 4.39 – 4.49 eV and 4.51 – 4.74 eV – which are separated by a short plateau. The lower energy onset begins at 4.39 eV and extends to the plateau at ca. 4.49 eV. This onset is characterised by a weak onset of ion signal and a shallow slope. This onset is designated as the secondary onset due to the weak ion signal; the appearance energy is thus labelled AE_2 in Figure 9.9. The higher energy onset is recorded with an appearance energy of 4.51 eV which extends to a plateau of maximum AuCe_3O ion signal at ca. 4.74 eV, indicating the highest energy FC allowed transition has been accessed. This onset encompasses the majority of ion signal increase for the AuCe_3O system and is thus designated as the primary onset, labelled AE_1 in Figure 9.9. The primary onset displays a shallow slope with a small ion signal increase in the 4.51 – 4.55 eV range. A very sharp slope is observed between 4.55 eV and 4.64 eV. The slope then becomes shallower before reaching the ion signal plateau at 4.74 eV.

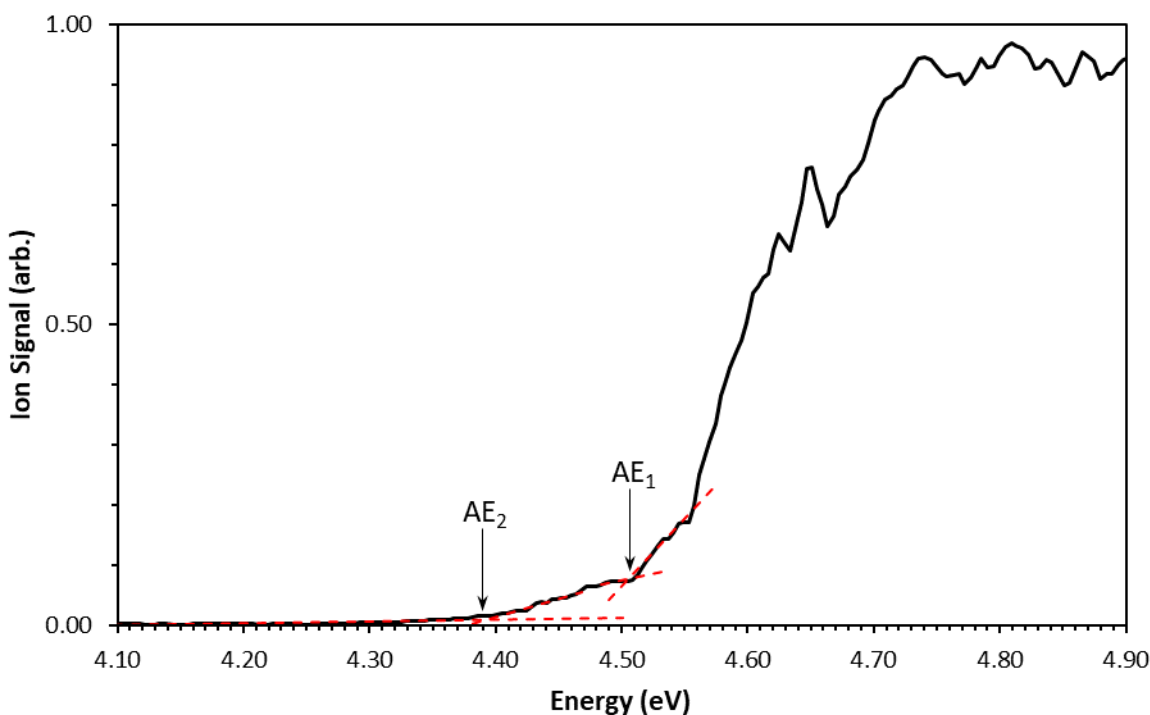


Figure 9.9: PIE spectrum for AuCe₃O. Linear trendlines for the baseline and onset are presented as red dashed lines. Appearance energies for the primary and secondary onsets – designated AE₁ and AE₂, respectively – are labelled with black arrows.

9.4.2. DFT Calculations for AuCe₃O

DFT calculated neutral and cationic AuCe₃O structures are presented in Figures 9.10 and 9.11. Calculations show two unique neutral AuCe₃O structures – labelled **XIXA** and **XIXB** – which are each calculated in two different spin states. The **XIXA** structure comprises an AuCe₃ trimer – similar to the AuCe₃ **XVIII** structure discussed previously – with an oxygen atom facially bound to the Ce₃ plane. The **XIXA** structure belongs to the C₁ point group, however approaches a C_{3v} symmetry (symmetry constrained calculations lead to convergence issues). This structure is calculated in both doublet and sextet multiplicities – labelled ²**XIXA** and ⁶**XIXA**, respectively – in the ²A and ⁶A electronic states, respectively.

The **XIXB** structure is similar to the **XIXA** structure, albeit with the oxygen atom bridging a Ce-Ce bond instead of binding to the Ce₃ face. This structure is C₁ – albeit near-C_s – symmetric and is calculated in the ⁴A and ⁶A electronic states, labelled ⁴**XIXB** and ⁶**XIXB**, respectively.

While the ²XIXA structure is calculated as the neutral LES, the small energetic separations of the ⁶XIXB, ⁴XIXB and ⁶XIXA species – which are calculated as +0.008 eV, +0.013 eV and +0.023 eV relative to the LES, respectively – effectively makes these four species energetically indistinguishable.

Calculation of the AuCe₃O cations show 7 unique species as presented in Figures 9.10 and 9.11. This gives 8 potential ionisation processes which include the ¹A←²A (¹XIXA⁺←²XIXA), ³A←²A (³XIXA⁺←²XIXA), ⁷A←⁶A (⁷XIXB⁺←⁶XIXB), ⁵A←⁶A (⁵XIXB⁺←⁶XIXB), ⁵A←⁴A (⁵XIXB⁺←⁴XIXB), ³A←⁴A (³XIXB⁺←⁴XIXB), ⁷A←⁶A (⁷XIXA⁺←⁶XIXA) and ⁵A←⁶A (⁵XIXA⁺←⁶XIXA) transitions; these transitions are shown in Figure 9.10. IEs for these processes are calculated as 4.844 eV, 4.876 eV, 4.592 eV, 4.823 eV, 4.818 eV, 4.936 eV, 4.725 eV and 4.789 eV, respectively. The ⁷A←⁶A (⁷XIXB⁺←⁶XIXB) ionisation process is assigned to the secondary ionisation onset due to the lower calculated IE of 4.592 eV. The remaining processes are assigned to the primary onset due to their comparable IE values. The 0.17 eV difference calculated between the IEs for the ⁷A←⁶A (⁷XIXB⁺←⁶XIXB) and ⁷A←⁶A (⁷XIXA⁺←⁶XIXA) processes – which describe to the lowest energy ionisation process for each onset – is consistent with the ca. 0.12 eV difference between the AE values for the primary and secondary onsets in the experimental PIE spectrum. The ¹A←²A (¹XIXA⁺←²XIXA), ⁵A←⁶A (⁵XIXB⁺←⁶XIXB), ⁷A←⁶A (⁷XIXA⁺←⁶XIXA) and ⁵A←⁶A (⁵XIXA⁺←⁶XIXA) ionisation processes – corresponding to the primary onset – are shown in Figure 9.10 as green, orange, violet and blue arrows, respectively. The ⁷A←⁶A (⁷XIXB⁺←⁶XIXB) ionisation process corresponding to the secondary onset is shown as a dark red arrow. The ³A←²A (³XIXA⁺←²XIXA), ⁵A←⁴A (⁵XIXB⁺←⁴XIXB) and ³A←⁴A (³XIXB⁺←⁴XIXB) are shown as red dotted arrows due to low vibronic peak intensities calculated for these transitions in subsequent ZEKE simulations (vide infra).

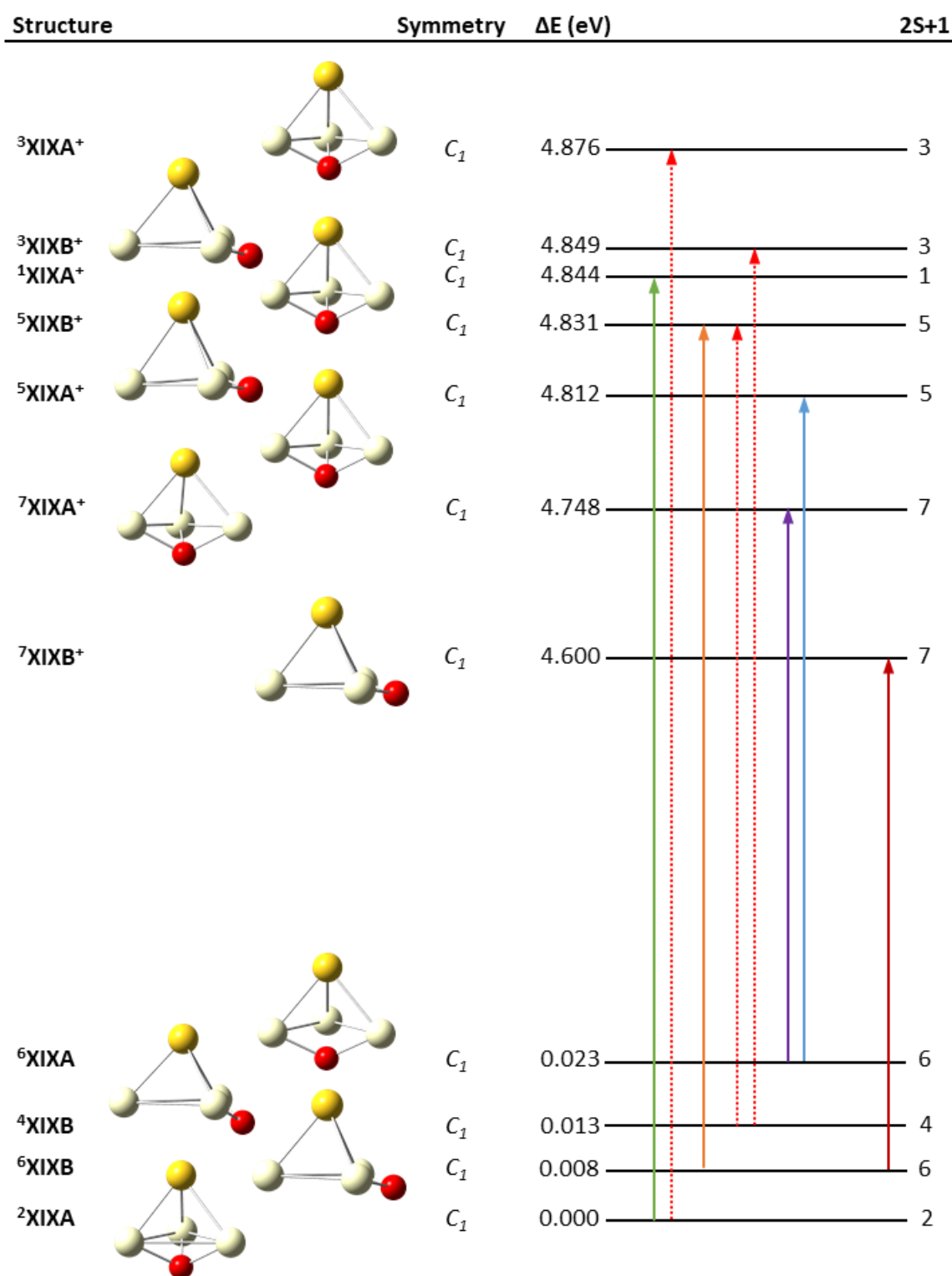


Figure 9.10: Calculated structures for AuCe_3O . Potential ionisation transitions are shown. Ionisation processes with low ZEKE intensities (*vide infra*) are shown as red dotted arrows.

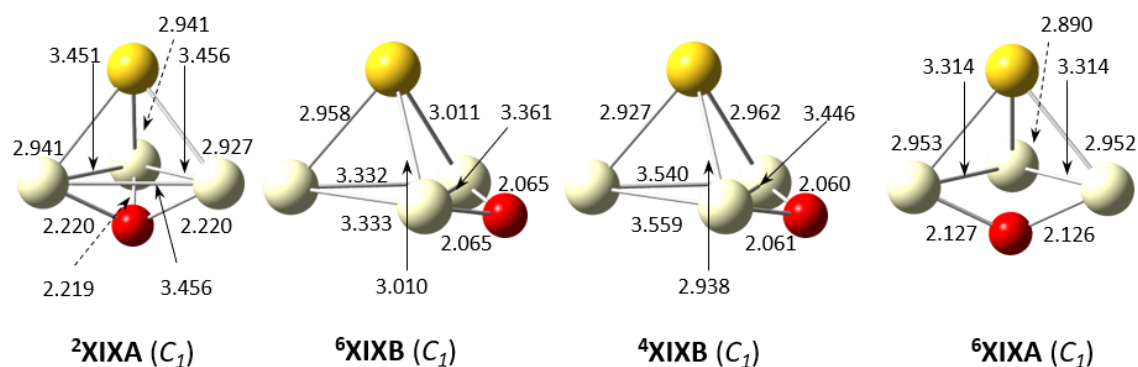
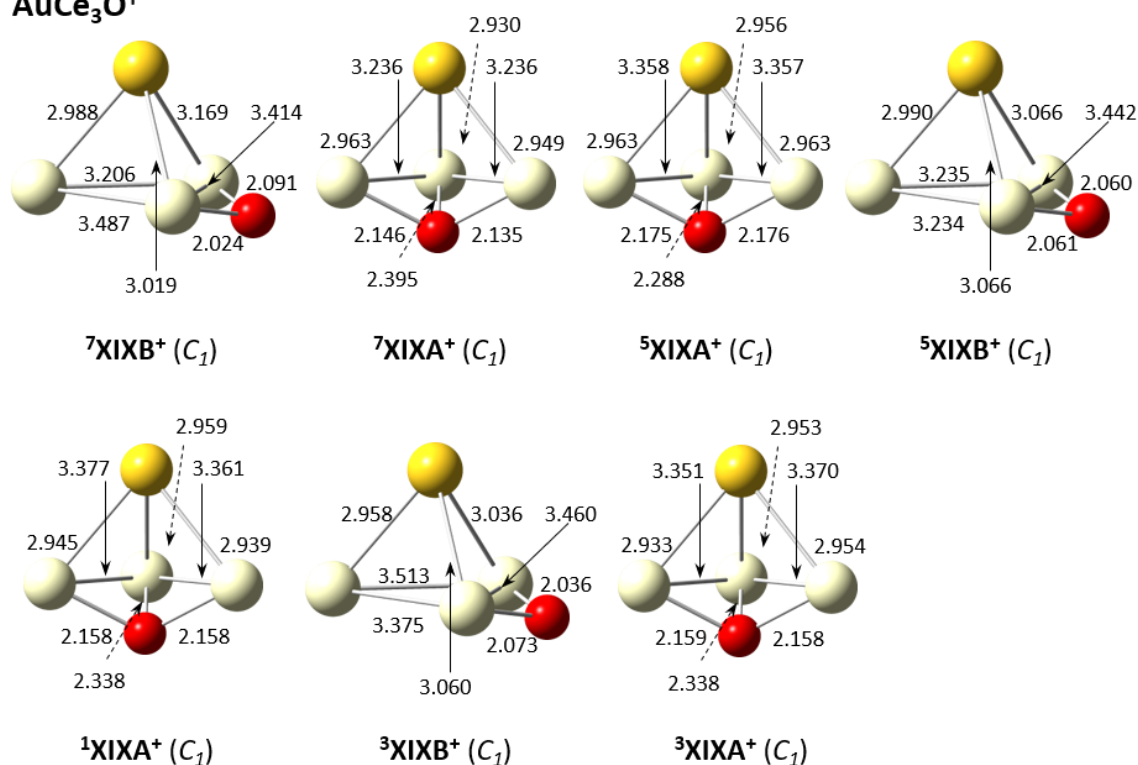
AuCe_3O  **AuCe_3O^+** 

Figure 9.11: Calculated AuCe_3O neutral (top) and cationic (below) structures. Bond lengths are presented in Å. Point groups are shown in brackets.

9.4.3. ZEKE Spectral Simulations for AuCe₃O

Calculated ZEKE spectra for the $^1A \leftarrow ^2A$ ($^1XIXA^+ \leftarrow ^2XIXA$), $^5A \leftarrow ^6A$ ($^5XIXB^+ \leftarrow ^6XIXB$), $^7A \leftarrow ^6A$ ($^7XIXA^+ \leftarrow ^6XIXA$) and $^5A \leftarrow ^6A$ ($^5XIXA^+ \leftarrow ^6XIXA$) ionisation processes corresponding to the AuCe₃O primary onset are presented in Figure 9.12. The vibronic transitions for each spectrum were corrected to the primary onset AE as detailed in Chapter 3; the corrected ZEKE spectra are shown.

ZEKE spectral simulations for the $^3A \leftarrow ^2A$ ($^3XIXA^+ \leftarrow ^2XIXA$), $^5A \leftarrow ^4A$ ($^5XIXB^+ \leftarrow ^4XIXB$) and $^3A \leftarrow ^4A$ ($^3XIXB^+ \leftarrow ^4XIXB$) transitions revealed low intensity vibronic peaks in all three spectra. These weak ionisation processes are considered to have a negligible contribution to the PIE spectrum; thus, they are not considered any further. The $^3A \leftarrow ^2A$ ($^3XIXA^+ \leftarrow ^2XIXA$), $^5A \leftarrow ^4A$ ($^5XIXB^+ \leftarrow ^4XIXB$) and $^3A \leftarrow ^4A$ ($^3XIXB^+ \leftarrow ^4XIXB$) ZEKE spectra are presented in Appendix C.

The spectral profiles of the calculated $^1A \leftarrow ^2A$ ($^1XIXA^+ \leftarrow ^2XIXA$), $^5A \leftarrow ^6A$ ($^5XIXB^+ \leftarrow ^6XIXB$) and $^5A \leftarrow ^6A$ ($^5XIXA^+ \leftarrow ^6XIXA$) ZEKE spectra – presented in Figures 9.12(a), (b) and (d), respectively – are similar in terms of both spectral width and peak intensity. Vibronic peaks within all three spectra extend over a ca. 0.15 eV energy range. Scaling factors used to normalise the most intense peaks of the $^1A \leftarrow ^2A$ ($^1XIXA^+ \leftarrow ^2XIXA$), $^5A \leftarrow ^6A$ ($^5XIXB^+ \leftarrow ^6XIXB$) and $^5A \leftarrow ^6A$ ($^5XIXA^+ \leftarrow ^6XIXA$) spectra are 14.4, 8.2 and 11.5 respectively; this infers similar contribution of all three ionisation processes to the PIE spectrum. By contrast, the $^7A \leftarrow ^6A$ ($^7XIXA^+ \leftarrow ^6XIXA$) ZEKE spectrum – presented in Figure 9.12(c) – displays a markedly smaller scaling factor – 2.64 – with the majority of vibronic peaks covering a smaller – ca. 0.09 eV – range. This would suggest the $^7A \leftarrow ^6A$ ($^7XIXA^+ \leftarrow ^6XIXA$) transition both is the dominant process in the PIE spectrum and underlies a sharper region of the primary onset than the other ionisation processes. It is therefore likely that the $^7A \leftarrow ^6A$ ($^7XIXA^+ \leftarrow ^6XIXA$) process constitutes the strong ion signal increase in the 4.55 – 4.64 eV energy region. The $^1A \leftarrow ^2A$ ($^1XIXA^+ \leftarrow ^2XIXA$), $^5A \leftarrow ^6A$ ($^5XIXB^+ \leftarrow ^6XIXB$) and $^5A \leftarrow ^6A$ ($^5XIXA^+ \leftarrow ^6XIXA$) spectra, with larger scaling factors concomitant with weaker spectral intensities, are likely to contribute to the weaker section of the primary onset in the higher energy 4.64 – 4.74 eV region near the plateau.

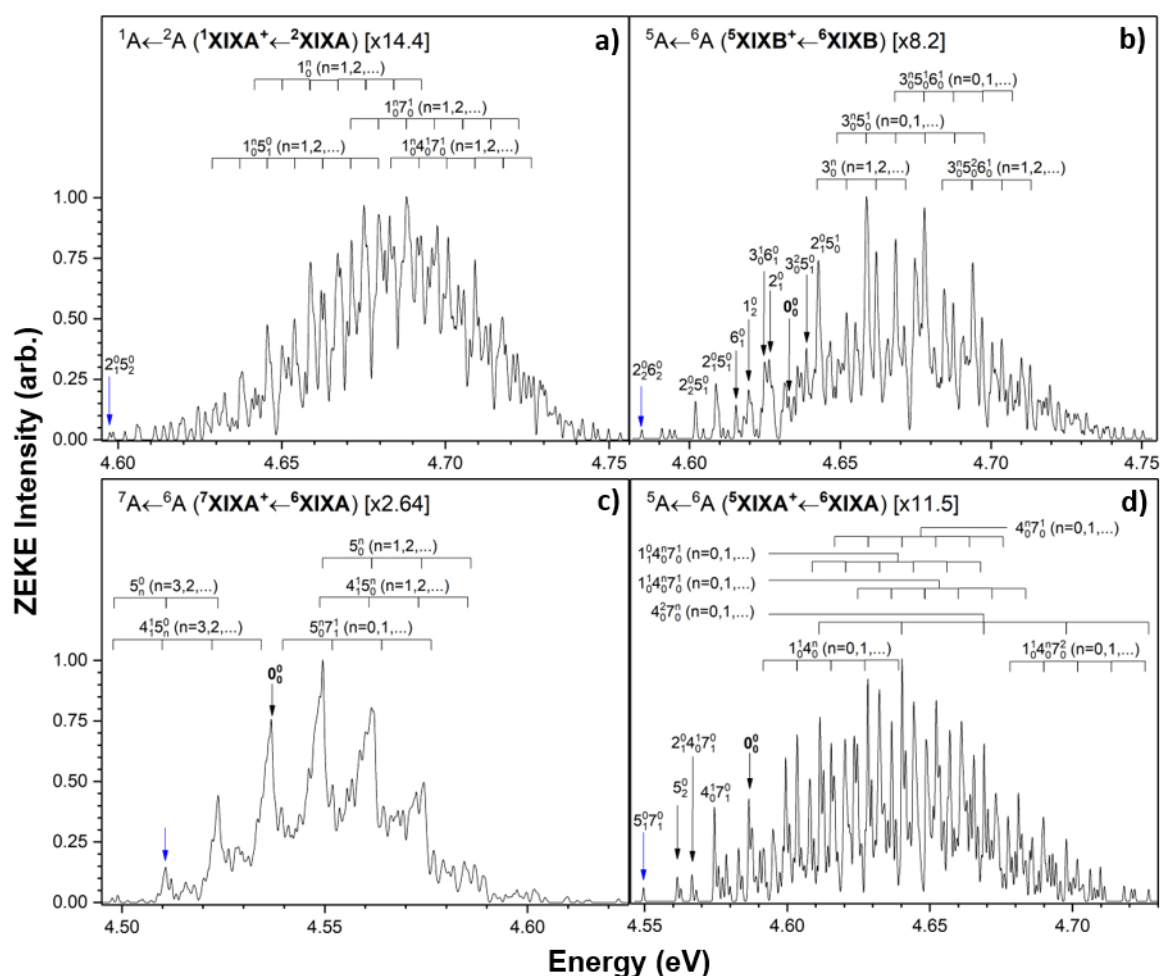


Figure 9.12: Calculated ZEKE spectra for AuCe₃O ionisation transitions corresponding to the primary onset: **a).** $^1A \leftarrow ^2A$ ($^1X1XA^+ \leftarrow ^2X1XA$), **b).** $^5A \leftarrow ^6A$ ($^5X1XB^+ \leftarrow ^6X1XB$), **c).** $^7A \leftarrow ^6A$ ($^7X1XA^+ \leftarrow ^6X1XA$) and **d).** $^5A \leftarrow ^6A$ ($^5X1XA^+ \leftarrow ^6X1XA$). Spectral intensities are normalised to the most intense peak in each spectrum with scaling factors shown. Prominent vibronic transitions are assigned. The vibronic transition likely to correspond to the appearance of ion signal in each spectrum is labelled with a blue arrow.

A calculated ZEKE spectrum for the $^7A \leftarrow ^6A$ ($^7X1XB^+ \leftarrow ^6X1XB$) ionisation process – corresponding to the AuCe₃O secondary onset – is presented in Figure 9.13. The vibronic peaks in the spectrum appear quite broad due to unresolved vibronic transitions (vibronic peaks were treated post-calculation with a series of Gaussian functions to convolute each peak to a FWHM of 5 cm⁻¹ in order to correctly describe thermal broadening effects). Due to the extensive number of vibronic transitions underlying each peak, it was not possible to assign specific vibronic transitions. The scaling factor used to normalise the $^7A \leftarrow ^6A$ ($^7X1XB^+ \leftarrow ^6X1XB$) vibronic

peak intensities – 24.3 – is considerably larger than those used for the primary onset ZEKE spectra discussed previously. This infers a lower intensity ZEKE spectrum which is consistent with the weaker secondary onset observed in the PIE spectrum compared to the primary onset.

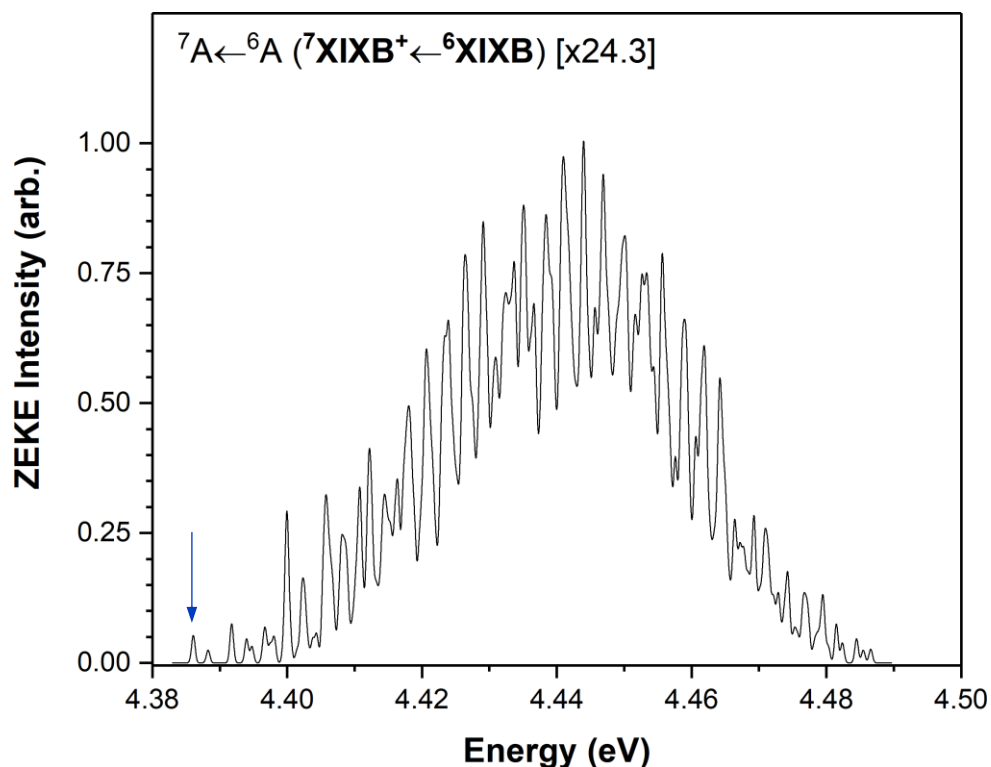


Figure 9.13: Calculated ZEKE spectrum for the AuCe_3O ${}^7\text{A} \leftarrow {}^6\text{A}$ (${}^7\text{XIXB}^+ \leftarrow {}^6\text{XIXB}$) ionisation transition corresponding to the secondary onset. The spectral intensity is normalised to the most intense peak with scaling factor shown. The vibronic transition likely to correspond to the appearance of ion signal is labelled with a blue arrow. Due to the complexity of the spectrum, vibronic peaks are not assigned.

9.4.4. Comparison of Simulated and Experimental PIE Spectra for AuCe_3O

A PIE spectrum for the AuCe_3O primary onset was calculated via integration of the ${}^1\text{A} \leftarrow {}^2\text{A}$ (${}^1\text{XIXA}^+ \leftarrow {}^2\text{XIXA}$), ${}^5\text{A} \leftarrow {}^6\text{A}$ (${}^5\text{XIXB}^+ \leftarrow {}^6\text{XIXB}$), ${}^7\text{A} \leftarrow {}^6\text{A}$ (${}^7\text{XIXA}^+ \leftarrow {}^6\text{XIXA}$) and ${}^5\text{A} \leftarrow {}^6\text{A}$ (${}^5\text{XIXA}^+ \leftarrow {}^6\text{XIXA}$) vibronic peaks. The calculated PIE spectrum is shown overlayed against the experimental PIE spectrum in Figure 9.14. A good fit is found between the simulated and experimental PIE spectra, particularly with regard to matching the slopes of the onsets in both the

4.55 – 4.64 eV and 4.64 – 4.74 eV regions. The agreement between the experimental and calculated PIE spectra means that reliable inferences about the AuCe₃O geometric and vibrational properties can be made from the DFT calculated structures. The adiabatic IE is assigned to the 0₀⁰ vibronic transition of the ¹A←²A (¹X₁A⁺←²X₁A) ionisation process, as the lowest energy ionisation process from the lowest energy structure. This gives an IE_{ad} value of 4.64 eV for the AuCe₃O cluster.

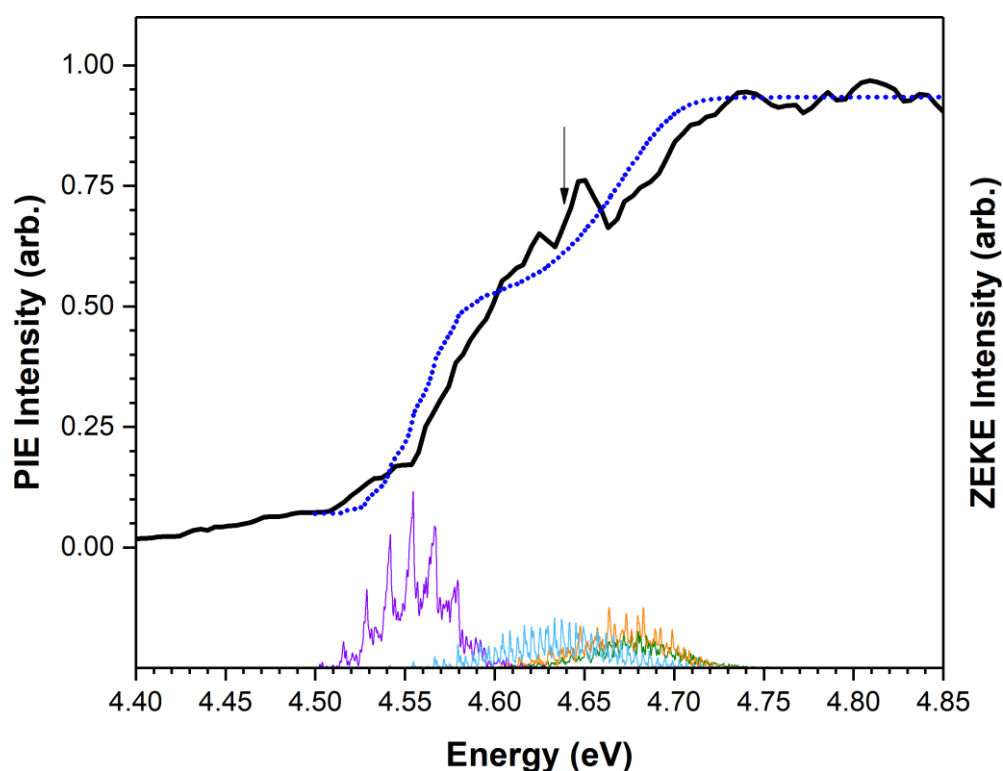


Figure 9.14: Calculated PIE spectrum for the AuCe₃O primary onset (blue dotted line) overlaid against the experimental PIE spectrum (solid black line). Calculated ZEKE spectra for the ¹A←²A (¹X₁A⁺←²X₁A), ⁵A←⁶A (⁵X₁B⁺←⁶X₁B), ⁷A←⁶A (⁷X₁A⁺←⁶X₁A) and ⁵A←⁶A (⁵X₁A⁺←⁶X₁A) ionisation transitions are shown below the PIE spectrum in green, orange, violet and blue, respectively. The adiabatic ionisation energy is labelled with a black arrow.

A simulated PIE spectrum for the AuCe₃O secondary onset – calculated via integration of the ⁷A←⁶A (⁷X₁B⁺←⁶X₁B) ZEKE spectrum – is presented in Figure 9.15. A reasonable fit is found between the simulated and experimental PIE spectra; the adiabatic IE for the secondary onset is assigned to the ⁷A←⁶A (⁷X₁B⁺←⁶X₁B) 0₀⁰ vibronic transition as 4.39 eV. However, the

secondary onset is assigned for completion only; it is not of any further interest in the context of this work.

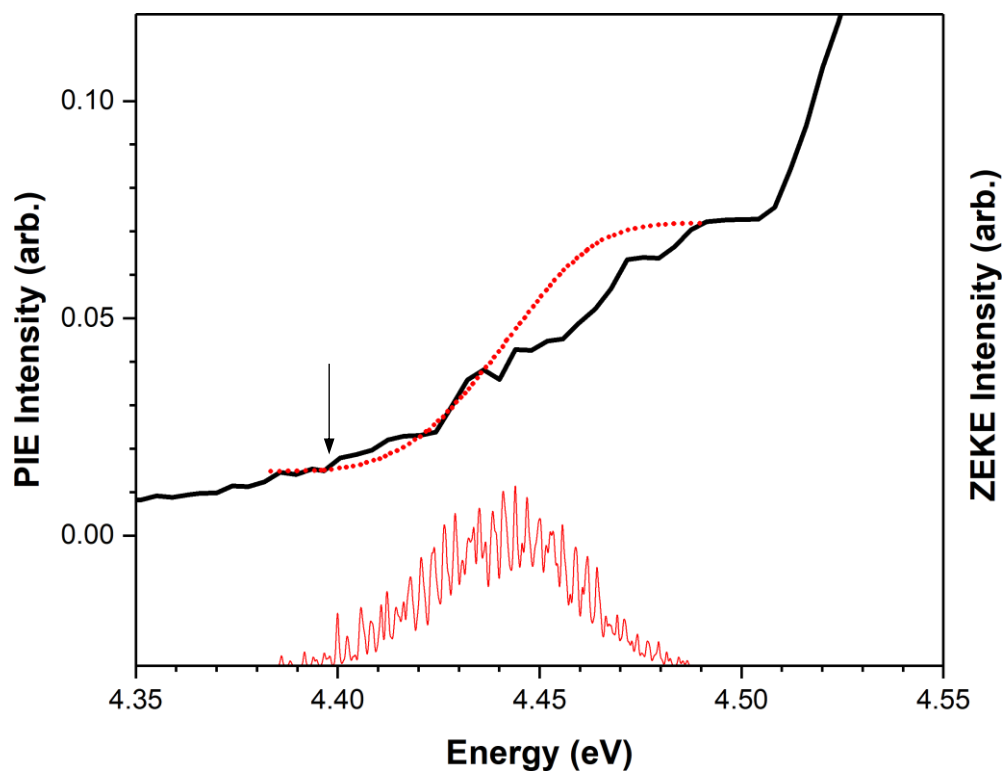


Figure 9.15: Calculated PIE spectrum for the AuCe₃O secondary onset (red dotted line) overlaid against the experimental PIE spectrum (solid black line). The calculated ZEKE spectrum for the ${}^7A \leftarrow {}^6A$ (${}^7XIXB^+ \leftarrow {}^6XIXB$) ionisation transition is shown below the PIE spectrum in red. The adiabatic ionisation energy is labelled with a black arrow.

9.5. PIE Spectrum and DFT Results for AuCe₃O₂

9.5.1. AuCe₃O₂ Experimental PIE Spectrum

The experimental AuCe₃O₂ PIE spectrum, recorded over the 3.92 – 5.00 eV energy range, is presented in Figure 9.16. From the low energy end of the spectrum, a relatively flat region of near-zero ion signal is recorded in the 3.92 – 4.31 eV region; this region is assigned as the baseline. A very small increase in ion signal is recorded over this region which is attributed to photo-ionisation processes from metastable isomers. Two onsets of ion signal are then recorded within the 3.92 – 5.00 eV energy range. The lower energy onset begins at 4.31 eV where it extends to a short plateau at ca. 4.45 eV. This onset is characterised by a moderate slope and a relatively small increase in ion signal. The lower energy onset does not describe the dominant photo-ionisation process for the AuCe₃O₂ system and is therefore designated the secondary onset – labelled AE₂ in Figure 9.16. The higher energy onset, which occurs over the 4.51 – 4.83 eV energy range, encompasses the majority of the increase in AuCe₃O₂ ion signal. This onset describes the dominant AuCe₃O₂ photo-ionisation process over the 3.92 – 5.00 eV energy range and is thus designated the primary onset – labelled AE₁ in Figure 9.16. The primary onset is characterised by a relatively sharp slope over the 4.51 – 4.69 eV range and a shallower slope from 4.69 eV to the plateau at 4.83 eV. The plateau corresponds to the maximum ion signal recorded over the region of interest, signifying the highest energy FC allowed transition has been accessed.

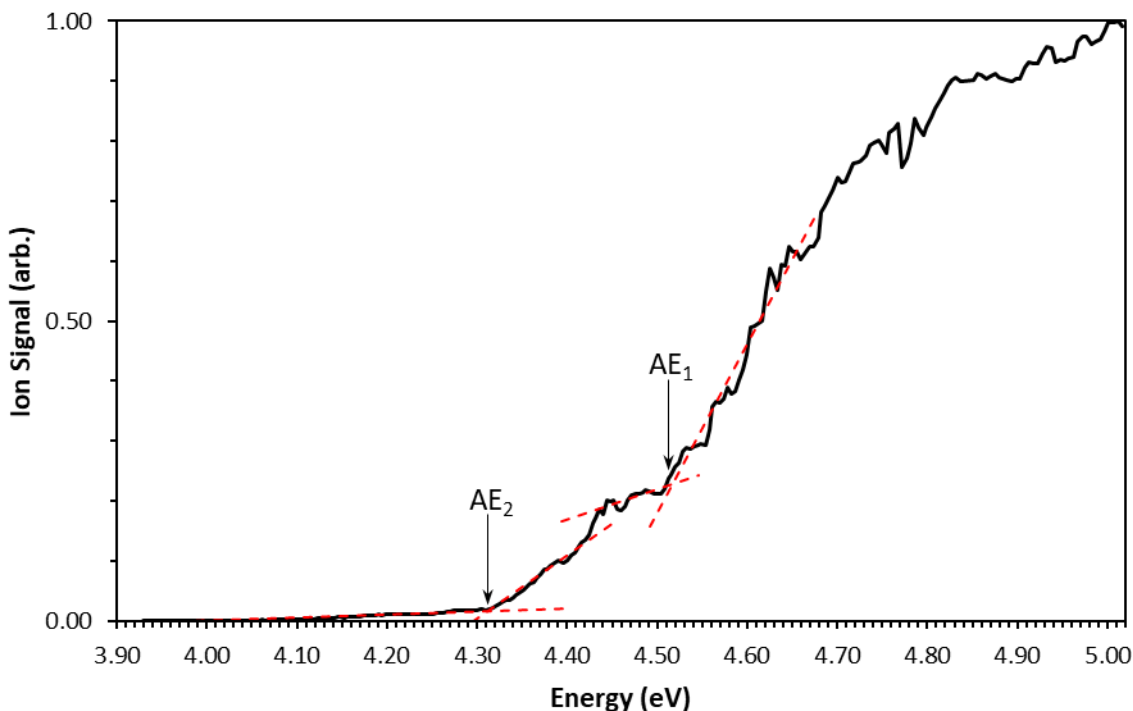


Figure 9.16: PIE spectrum for AuCe_3O_2 . Linear trendlines for the baseline and onset are presented as red dashed lines. Appearance energies for the primary and secondary onsets – designated AE_1 and AE_2 , respectively – are labelled with black arrows.

9.5.2. DFT Calculations for AuCe_3O_2

DFT Calculated AuCe_3O_2 neutral and cationic structures are presented in Figures 9.17 and 9.18. Calculations revealed only one unique neutral geometry – labelled **XX** – comprising a structure similar to the Ce_3O_3 motif discussed previously in Chapter 6, albeit with the gold atom occupying the position of the centre oxygen atom. Alternative AuCe_3O_2 structures were calculated with significantly higher energies than the **XX** structure and are not shown here. The AuCe_3O_2 LES is calculated as a sextet C_1 -symmetric species in the ${}^6\text{A}$ electronic state, labelled ${}^6\text{XX}$. Two additional low-lying spin-isomers are calculated which include a C_1 quartet in the ${}^4\text{A}$ electronic state and a C_s doublet in the ${}^2\text{A}''$ electronic state, labelled ${}^4\text{XX}$ and ${}^2\text{XX}$ respectively. Electronic and zero-point energies of the ${}^4\text{XX}$ and ${}^2\text{XX}$ species relative to the ${}^6\text{XX}$ LES are calculated as +0.035 eV and +0.068 eV, respectively. This would make both the ${}^4\text{XX}$ and ${}^2\text{XX}$ species challenging to differentiate energetically from the LES.

A total of three AuCe₃O₂ cationic species are calculated; these include quintet, triplet and septet species labelled ⁵XX⁺, ³XX⁺ and ⁷XX⁺, respectively. A singlet AuCe₃O₂⁺ cation is not presented due to convergence difficulties. The ⁵XX⁺ and ³XX⁺ species both have the same arrangements of atoms compared to their respective neutral species, albeit with a breakage of the Au-Ce bond along the centre of the structure. All other bond lengths within the ⁵XX⁺ and ³XX⁺ species are, however, within 0.02 Å of their respective bond lengths in the neutral structures; reflecting a small degree of structural deformation along these coordinates. Conversely, the ⁷XX⁺ structure not only retains the Au-Ce bond but shows a ca. 0.08 Å contraction in the Au-Ce bond length. This marked change in bond length should reflect in a poor FC overlap and consequently a weak ZEKE spectrum.

The calculated neutral and cationic AuCe₃O₂ species give a total of 5 potential ionisation processes. These include the ⁵A←⁶A (⁵XX⁺←⁶XX⁺), ⁷A'←⁶A (⁷XX⁺←⁶XX⁺), ⁵A←⁴A (⁵XX⁺←⁴XX⁺), ³A←⁴A (³XX⁺←⁴XX⁺) and ³A←²A'' (³XX⁺←²XX⁺) transitions. Ionisation energies for these processes are calculated as 4.736 eV, 4.822 eV, 4.701 eV, 4.729 eV and 4.696 eV, respectively. The ⁵A←⁶A (⁵XX⁺←⁶XX⁺), ⁵A←⁴A (⁵XX⁺←⁴XX⁺), ³A←⁴A (³XX⁺←⁴XX⁺) and ³A←²A'' (³XX⁺←²XX⁺) processes are shown in Figure 9.17 as green, orange, dark red and violet arrows, respectively. The ⁷A'←⁶A (⁷XX⁺←⁶XX⁺) process is shown as a dotted arrow due to low vibronic peak intensities calculated in subsequent ZEKE simulations (vide infra).

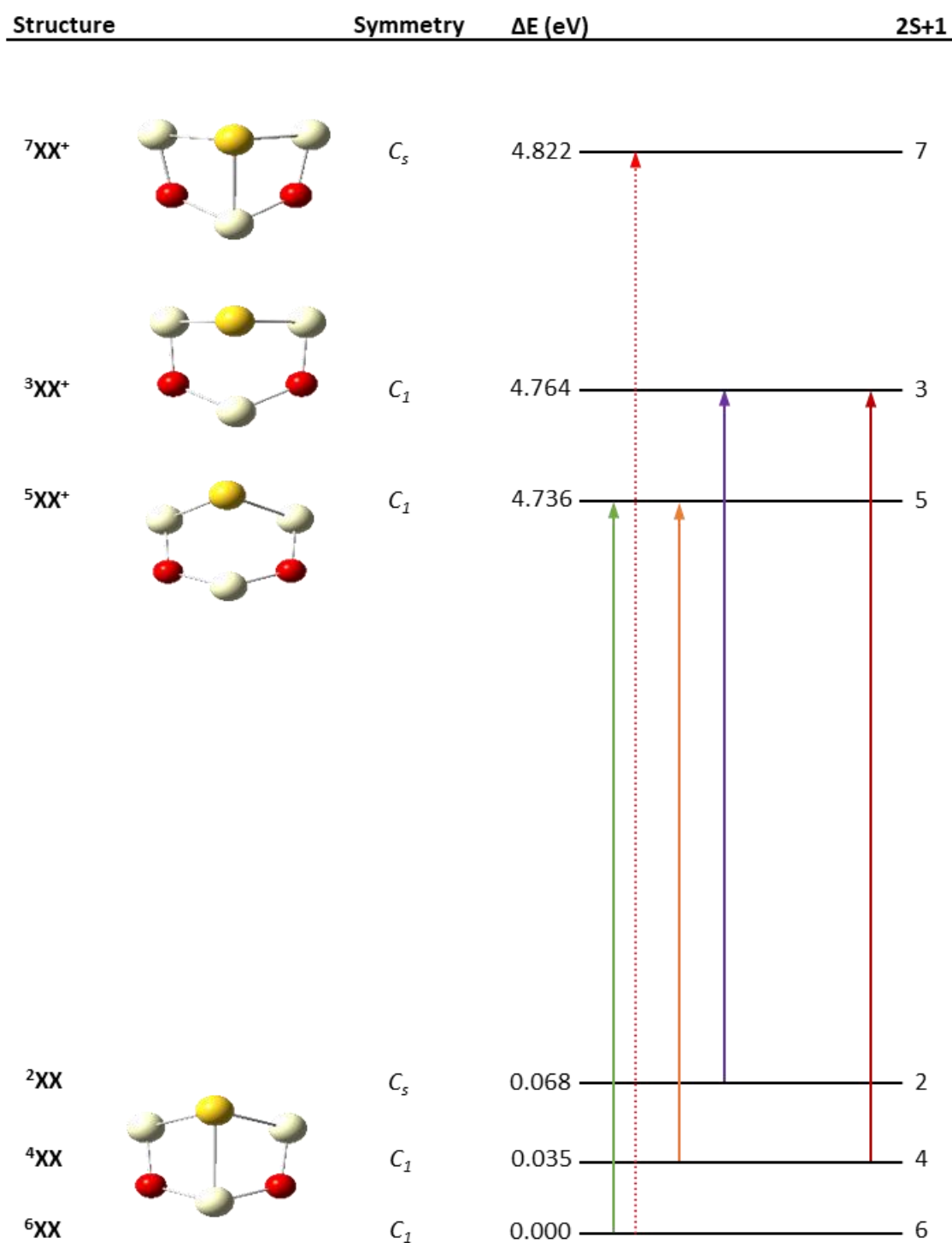


Figure 9.17: Calculated structures for AuCe₃O₂. Potential ionisation transitions are shown. Ionisation processes with low ZEKE intensities (*vide infra*) are shown as red dotted arrows.

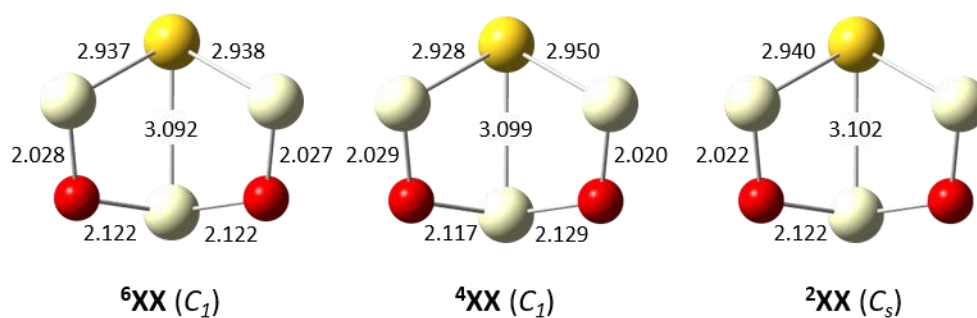
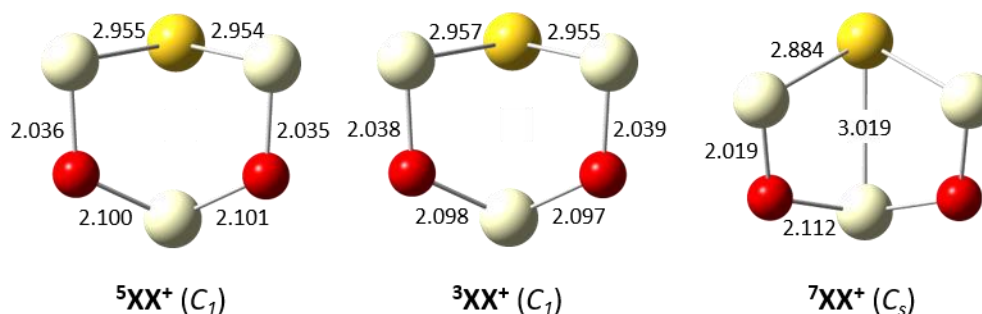
AuCe_3O_2  **$\text{AuCe}_3\text{O}_2^+$** 

Figure 9.18: Calculated AuCe_3O_2 neutral (top) and cationic (below) structures. Bond lengths are presented in Å. Point groups are shown in brackets.

9.5.3. ZEKE Spectral Simulations for AuCe_3O_2

Simulated ZEKE spectra for the AuCe_3O_2 ${}^5\text{A} \leftarrow {}^6\text{A}$ (${}^5\text{XX}^+ \leftarrow {}^6\text{XX}^+$), ${}^5\text{A} \leftarrow {}^4\text{A}$ (${}^5\text{XX}^+ \leftarrow {}^4\text{XX}^+$), ${}^3\text{A} \leftarrow {}^4\text{A}$ (${}^3\text{XX}^+ \leftarrow {}^4\text{XX}^+$) and ${}^3\text{A} \leftarrow {}^2\text{A}''$ (${}^3\text{XX}^+ \leftarrow {}^2\text{XX}^+$) transitions are presented in Figures 9.19 and 9.20. Due to the extensive number of vibrational modes for the AuCe_3O_2 system, it was not possible to afford the ZEKE simulations a full Duschinsky treatment. Thus, the Parallel Approximation was used to calculate ZEKE spectra for the AuCe_3O_2 system.

The ${}^5\text{A} \leftarrow {}^6\text{A}$ (${}^5\text{XX}^+ \leftarrow {}^6\text{XX}^+$) ZEKE spectrum shown in Figure 9.19(a) is calculated with a broad spectral profile – spanning ca. 0.2 eV – which is comprised mostly of long, closely spaced vibronic progressions. The 5_0^n , $3_0^1 8_0^1$ and $3_0^1 8_0^1$ progressions are calculated with the highest

vibronic peak intensities. The maximum FC transition is assigned to the $3_0^5 8_0^1$ vibronic peak, while the 0_0^0 transition is not calculated, inferring considerable deformation between the neutral and cationic species.

The $^5A \leftarrow ^4A$ ($^5XX^+ \leftarrow ^4XX^+$), and $^3A \leftarrow ^2A''$ ($^3XX^+ \leftarrow ^2XX^+$) ZEKE spectra, which are presented in Figures 9.19(b) and (c), respectively, show some marked similarities. Both spectra span a similar energy range – ca. 0.15 eV – which is considerably narrower than the $^5A \leftarrow ^6A$ ($^5XX^+ \leftarrow ^6XX^+$) spectrum. Moreover, the dominant vibronic progressions in both spectra all constitute v_4v_8 combination bands. The spectra differ markedly, however, with the $4_0^n 8_0^4$ progression appearing only in the $^5A \leftarrow ^4A$ ($^5XX^+ \leftarrow ^4XX^+$) spectrum; this progression gives stronger vibronic peaks toward the higher energy end of the spectrum. The calculated $^3A \leftarrow ^4A$ ($^3XX^+ \leftarrow ^4XX^+$) ZEKE spectrum presented in Figure 9.20 spans a similar energy range to both the $^5A \leftarrow ^4A$ ($^5XX^+ \leftarrow ^4XX^+$), and $^3A \leftarrow ^2A''$ ($^3XX^+ \leftarrow ^2XX^+$) ZEKE spectra discussed previously. However, the $^3A \leftarrow ^4A$ ($^3XX^+ \leftarrow ^4XX^+$) ZEKE spectrum comprises noticeably shorter progressions than both the $^5A \leftarrow ^4A$ ($^5XX^+ \leftarrow ^4XX^+$), and $^3A \leftarrow ^2A''$ ($^3XX^+ \leftarrow ^2XX^+$) spectra – which primarily include the $3_0^1 5_0^1 7_0^1$ and $3_0^1 4_0^1 5_0^1 7_0^1$ progressions – with a higher degree of vibrational mixing. In terms of the Parallel Approximation, extensive vibrational mixing is generally correlated with a weak FC overlap. Lastly, the $^7A' \leftarrow ^6A$ ($^7XX^+ \leftarrow ^6XX^+$) ZEKE spectrum was calculated with very low intensity and therefore is not considered to contribute to the PIE spectrum. The calculated $^7A' \leftarrow ^6A$ ($^7XX^+ \leftarrow ^6XX^+$) ZEKE spectrum is presented in Appendix C.

Comparable ZEKE intensities were calculated for the $^5A \leftarrow ^6A$ ($^5XX^+ \leftarrow ^6XX^+$), $^5A \leftarrow ^4A$ ($^5XX^+ \leftarrow ^4XX^+$), and $^3A \leftarrow ^2A''$ ($^3XX^+ \leftarrow ^2XX^+$) spectra shown in Figure 9.19; with scaling factors of 7.9, 13.5 and 6.95, respectively, required to normalise the intensity of the strongest peak in each spectrum. The $^3A \leftarrow ^4A$ ($^3XX^+ \leftarrow ^4XX^+$) ZEKE spectrum presented in Figure 9.20, however, was calculated with significantly lower intensity; a scaling factor of 34.4 was required to normalise the spectrum to the most intense peak. Given the similar IEs calculated for all the ionisation processes considered for the AuCe₃O₂ system, and the small energetic separation between the primary and secondary onsets in the experimental AuCe₃O₂ PIE spectrum, it would be difficult to assign ionisation processes to particular onsets from an energetic standpoint. Thus,

the ionisation processes were assigned to the experimental PIE onsets by their relative ZEKE intensities. The stronger ZEKE intensities calculated for the $^5A \leftarrow ^6A$ ($^5XX^+ \leftarrow ^6XX^+$), $^5A \leftarrow ^4A$ ($^5XX^+ \leftarrow ^4XX^+$), and $^3A \leftarrow ^2A''$ ($^3XX^+ \leftarrow ^2XX^+$) spectra are consistent with the greater ion signal increase in the primary onset. The weaker $^3A \leftarrow ^4A$ ($^3XX^+ \leftarrow ^4XX^+$) ZEKE spectrum is then assigned to the secondary onset. The relevant ZEKE spectra were energetically corrected to their respective onsets using the method described in Chapter 3; these involved corrections of -0.052 eV, $+0.213$ eV and $+0.128$ eV to the primary onset $^5A \leftarrow ^6A$ ($^5XX^+ \leftarrow ^6XX$), $^5A \leftarrow ^4A$ ($^5XX^+ \leftarrow ^4XX$) and $^3A \leftarrow ^2A''$ ($^3XX^+ \leftarrow ^2XX$) spectra, respectively, for the subsequent PIE spectrum to agree well with the experimental PIE spectrum (vide infra).

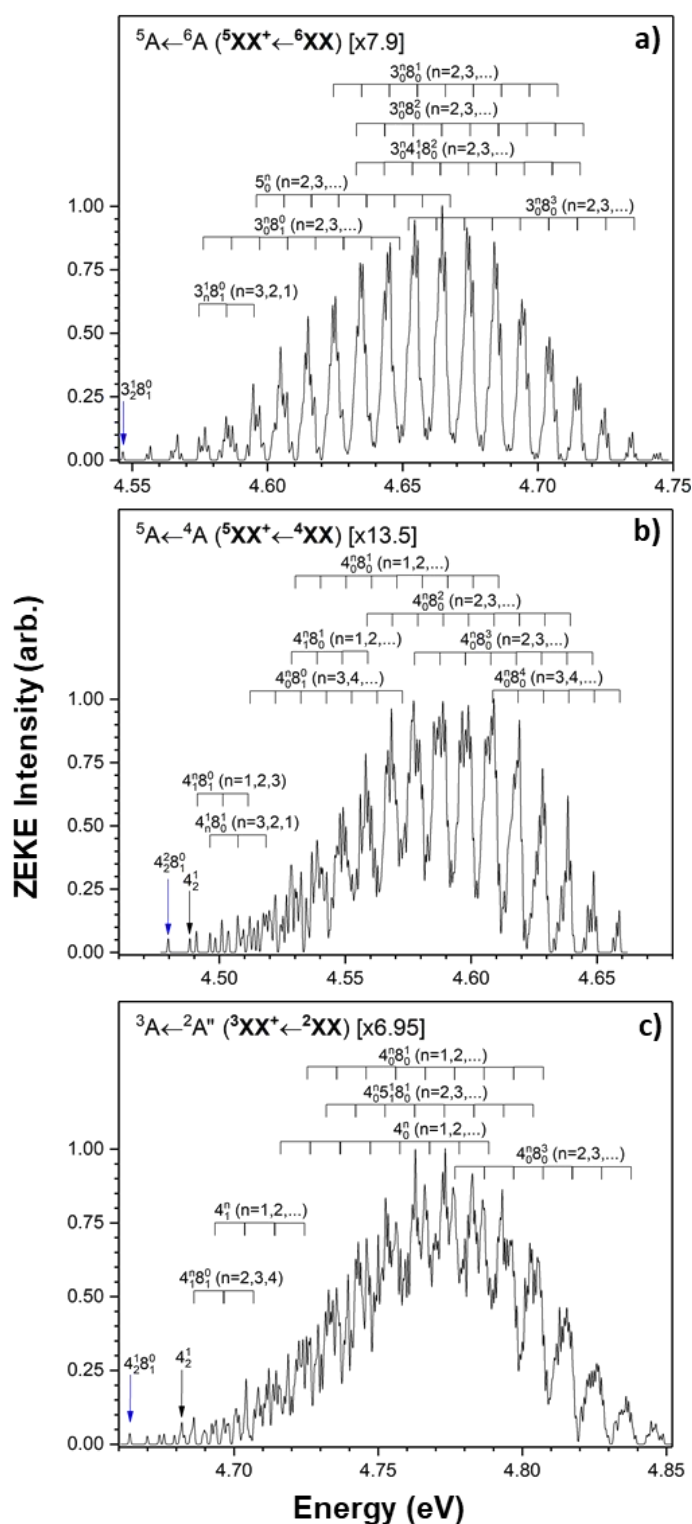


Figure 9.19: Calculated ZEKE spectra for AuCe₃O₂ ionisation transitions corresponding to the primary onset: **a).** ${}^5A \leftarrow {}^6A ({}^5XX^+ \leftarrow {}^6XX)$, **b).** ${}^5A \leftarrow {}^4A ({}^5XX^+ \leftarrow {}^4XX)$ and **c).** ${}^3A \leftarrow {}^2A'' ({}^3XX^+ \leftarrow {}^2XX)$. Spectral intensities are normalised to the most intense peak in each spectrum with scaling factors shown. Prominent vibronic transitions are assigned. The vibronic transition likely to correspond to the appearance of ion signal in each spectrum is labelled with a blue arrow.

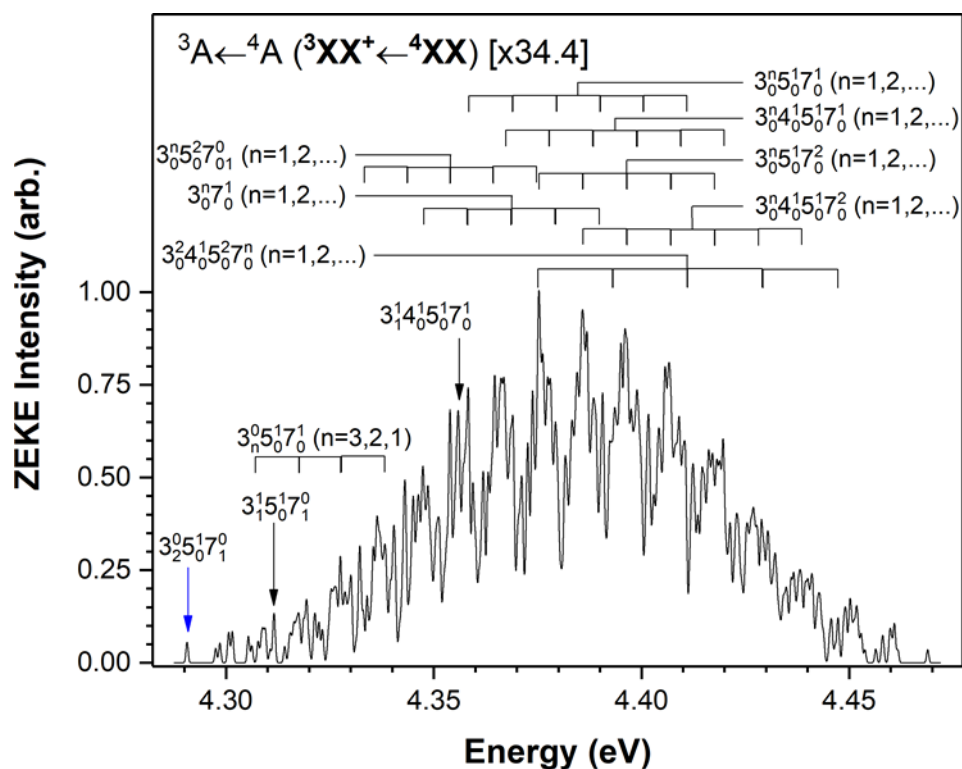


Figure 9.20: Calculated ZEKE spectrum for the AuCe₃O₂ ${}^3A \leftarrow {}^4A$ (${}^3XX^+ \leftarrow {}^4XX$) ionisation transition corresponding to the secondary onset. The spectral intensity is normalised to the most intense peak with scaling factors shown. Prominent vibronic transitions are assigned. The vibronic transition likely to correspond to the appearance of ion signal is labelled with a blue arrow.

9.5.4. Comparison of Simulated and Experimental PIE Spectra for AuCe₃O₂

A PIE spectrum for the AuCe₃O₂ primary onset was calculated by integration of the ${}^5A \leftarrow {}^6A$ (${}^5XX^+ \leftarrow {}^6XX$), ${}^5A \leftarrow {}^4A$ (${}^5XX^+ \leftarrow {}^4XX$) and ${}^3A \leftarrow {}^2A''$ (${}^3XX^+ \leftarrow {}^2XX$) ZEKE spectra. This calculated PIE spectrum is shown overlaid against the experimental PIE spectrum in Figure 9.21. An excellent fit is found between the simulated and experimental PIE spectra for the primary PIE onset. The adiabatic IE is assigned to the ${}^5A \leftarrow {}^6A$ (${}^5XX^+ \leftarrow {}^6XX$) process – as the lowest calculated ionisation process from the lowest energy calculated structure. This gives an IE value of 4.48 eV for the AuCe₃O₂ system.

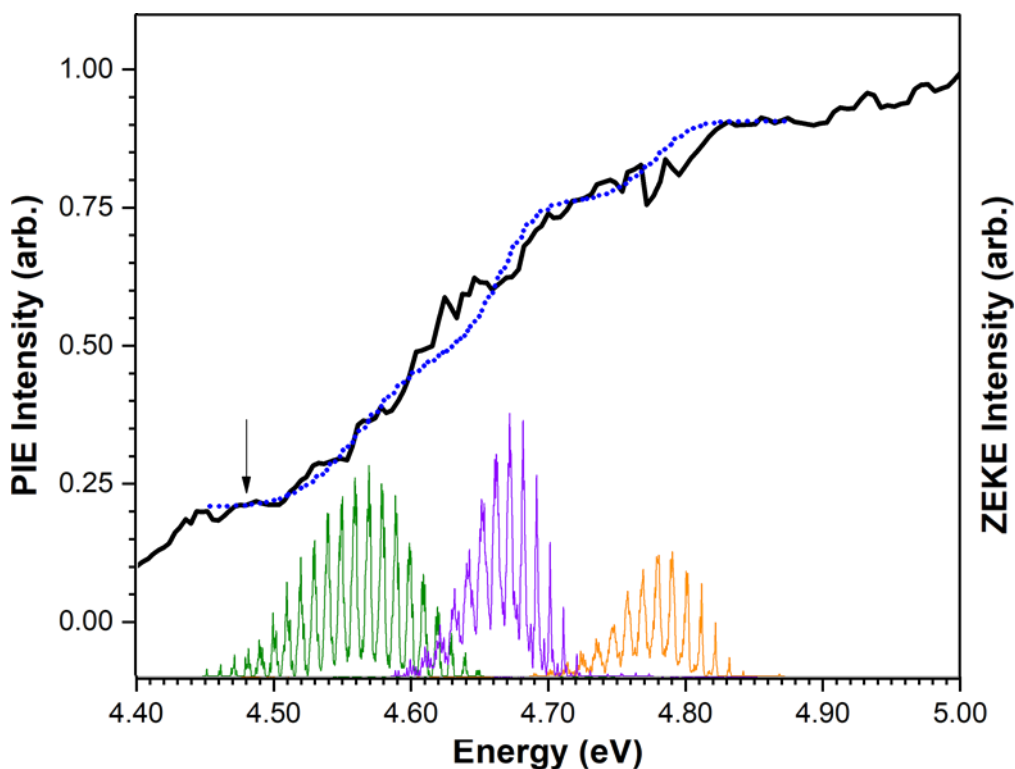


Figure 9.21: Calculated PIE spectrum for the AuCe₃O₂ primary onset (blue dotted line) overlaid against the experimental PIE spectrum (solid black line). Calculated ZEKE spectra for the $^5A \leftarrow ^6A$ ($^5XX^+ \leftarrow ^6XX^+$), $^5A \leftarrow ^4A$ ($^5XX^+ \leftarrow ^4XX^+$), and $^3A \leftarrow ^2A$ ($^3XX^+ \leftarrow ^2XX^+$) ionisation processes are shown below the PIE spectrum in green, orange and violet, respectively. The adiabatic ionisation energy is labelled with a black arrow.

A simulated PIE spectrum for the AuCe₃O₂ secondary onset – calculated by integration of the $^3A \leftarrow ^4A$ ($^3XX^+ \leftarrow ^4XX$) ZEKE spectrum – is presented in Figure 9.22. The simulated PIE spectrum presents a reasonable fit to the experimental PIE spectrum. The adiabatic IE for the secondary onset is assigned to the 0_0^0 vibronic transition; this gives an IE_{ad} value of 4.31 eV. However, the secondary onset IE_{ad} value is not of any further interest in the context of this work.

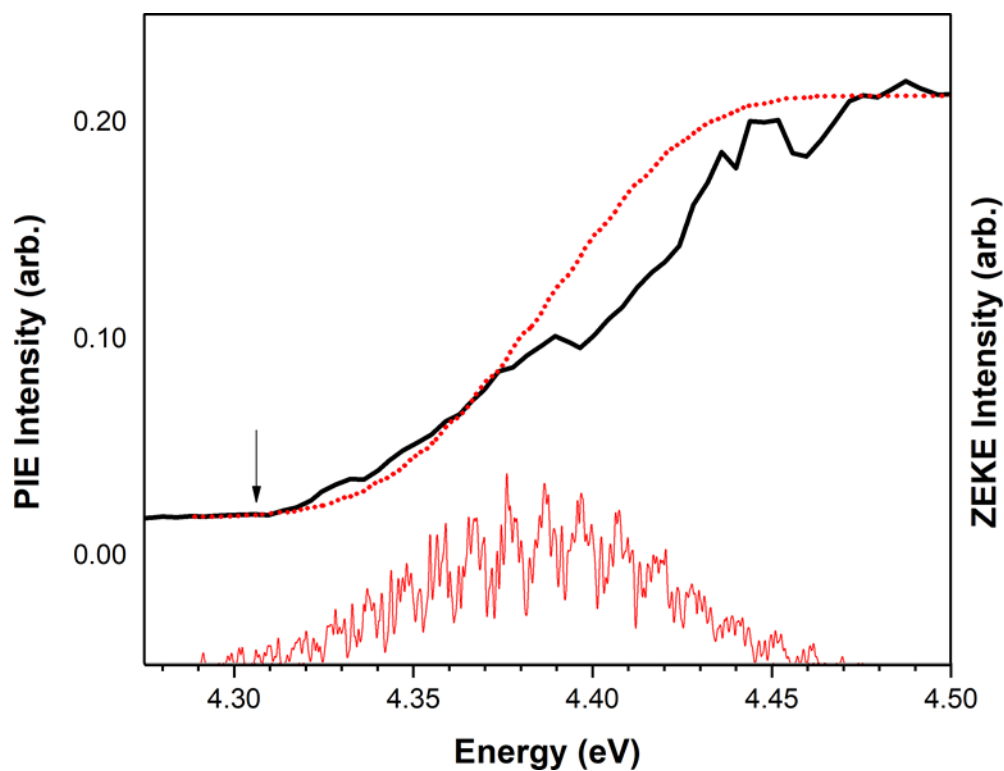


Figure 9.22: Calculated PIE spectrum for the AuCe₃O₂ secondary onset (red dotted line) overlaid against the experimental PIE spectrum (solid black line). The calculated ZEKE spectrum for the $^3A \leftarrow ^4A$ ($^3XX^+ \leftarrow ^4XX$) ionisation process is shown below the PIE spectrum in red. The adiabatic ionisation energy is labelled with a black arrow.

9.6. PIE Spectrum and DFT Results for AuCe_3O_3

9.6.1. AuCe_3O_3 Experimental PIE Spectrum

A PIE spectrum for the AuCe_3O_3 cluster system recorded within the 3.92 – 5.13 eV energy range is presented in Figure 9.23. A near-flat region of very low ion signal intensity is recorded at the low energy end of the spectrum in the 3.92 – 4.24 eV energy range. The ion signal in this region is attributed to weak metastable photo-ionisation processes which are not of interest in the context of this work. Therefore, this region is taken as the baseline of ion signal. From the AE at 4.24 eV, a gradual increase in ion signal is recorded with increased photon energy to an inflection point at 4.55 eV. From this point, a significantly sharper increase in ion signal is then recorded to a plateau of maximum ion signal at 5.00 eV. The marked difference between the two slopes in the 4.24 – 4.55 eV and 4.55 – 5.00 eV energy ranges would suggest the occurrence of overlapping photo-ionisation onsets. The higher energy onset encompasses most of the ion signal increase and is therefore labelled the primary onset – with the appearance energy shown as AE_1 in Figure 9.23. The lower energy onset displays a very small ion signal increase which is likely a product of photo-ionisation from metastable states. This region is designated the secondary onset, labelled AE_2 in Figure 9.23. It should be noted that the overlap of onsets makes the ion signal plateau of the secondary onset and the appearance energy of the primary onset difficult to resolve. This means the AE_1 value presented does not necessarily reflect the start of the primary onset, but the point where the primary onset can be differentiated from the secondary onset; vibronic transitions corresponding to the primary onset may actually begin at lower energies. Both onsets appear quite broad – the primary and secondary onsets span energy ranges of 0.45 eV and 0.31 eV, respectively – with uniform slopes. The slope of the primary onset is markedly sharper than that of the secondary onset.

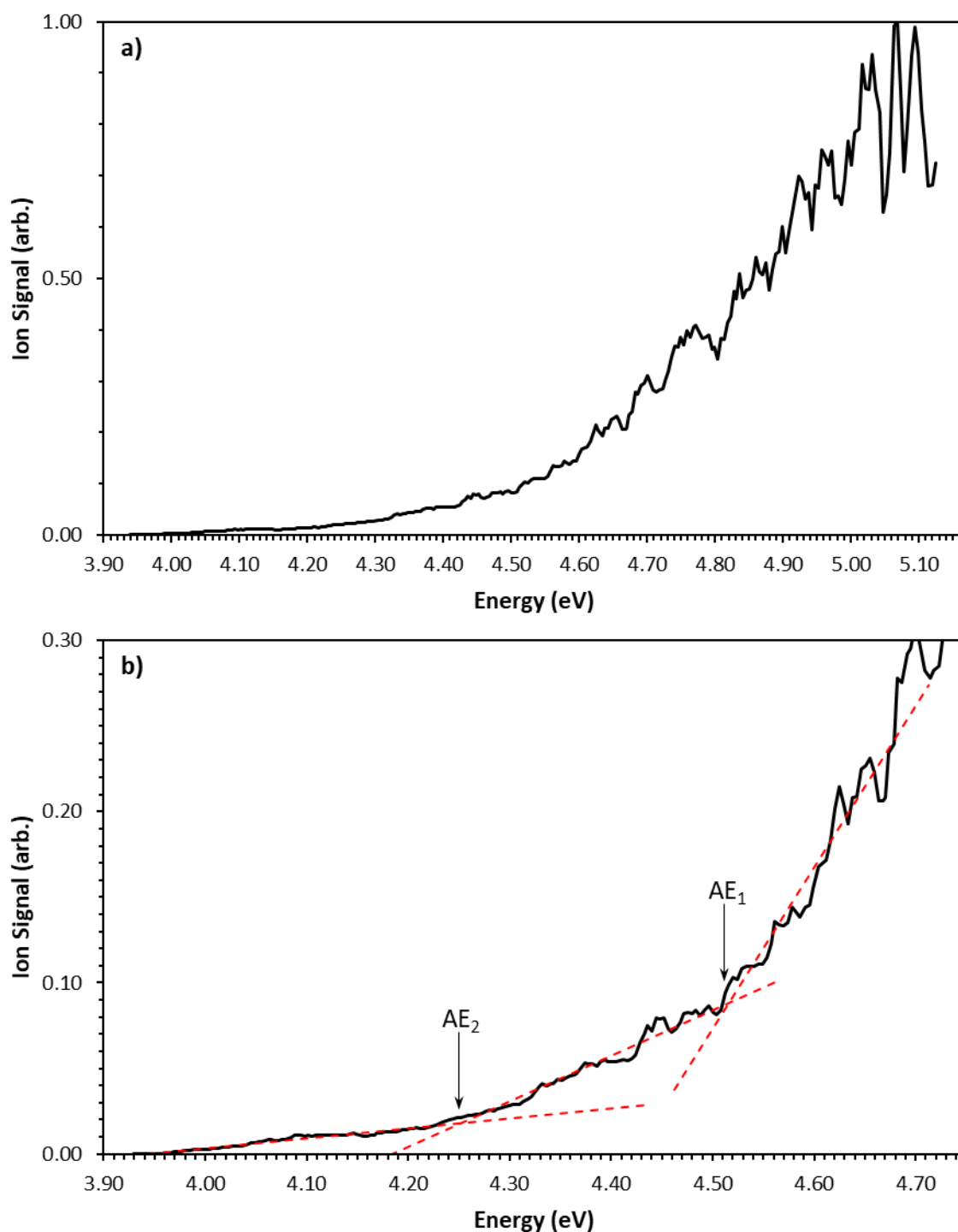


Figure 9.23: PIE spectrum for AuCe_3O_3 showing **a)** entire spectrum and **b)** primary and secondary onsets. Linear trendlines for the baseline and onset are presented as red dashed lines. Appearance energies for the primary and secondary onsets – designated AE_1 and AE_2 , respectively – are labelled with black arrows.

9.6.2. DFT Calculations for AuCe₃O₃

DFT calculated AuCe₃O₃ neutral and cationic species are presented in Figures 9.24 and 9.25. Two unique neutral geometries are calculated. The first geometry – labelled **XXIA** – comprises a Ce₃O₄-type structure with the gold atoms occupying the position of the central oxygen atom. Doublet and quartet species are calculated with this structure, labelled ²**XXIA** and ⁴**XXIA**, respectively. The ²**XXIA** species is C_{3v} symmetric in the ²A₁ electronic state, while the ⁴**XXIA** species displays a C_s symmetry in the ⁴A'' electronic state. The second AuCe₃O₃ geometry again comprises a Ce₃O₄-type motif, albeit with the gold atom adopting the position of one of the peripheral oxygen atoms. This structure is calculated in both ⁶A' and ²A electronic states – with the sextet and doublet species adopting C_s and C₁ symmetries, respectively – which are labelled ⁶**XXIB** and ⁴**XXIB**, respectively. The ²**XXIA** species is calculated as the LES, with energetic separations for the ⁶**XXIB**, ⁴**XXIA** and ²**XXIB** isomers calculated as +0.049 eV, +0.053 eV and +0.095 eV, respectively. These energies all fall well within the 0.2 eV error estimated for the DFT calculated energies in this work.

Seven AuCe₃O₃ cationic species are presented as potential target states from the ²**XXIA**, ⁶**XXIB**, ⁴**XXIA** and ²**XXIB** neutral isomers. These comprise the **XXIA** structure calculated in the ¹A', ³A and ⁵A'' cationic electronic states – labelled ¹**XXIA**⁺, ³**XXIA**⁺ and ⁵**XXIA**⁺, respectively – and the **XXIB** structure calculated in the ¹A, ³A, ⁵A'' and ⁷A' electronic states, labelled ⁵**XXIB**⁺, ³**XXIB**⁺, ¹**XXIB**⁺ and ⁷**XXIB**⁺, respectively. This gives a total of 8 potential ionisation processes, which include the ³A←²A₁ (³**XXIA**⁺←²**XXIA**), ¹A'←²A₁ (¹**XXIA**⁺←²**XXIA**), ⁵A''←⁶A' (⁵**XXIB**⁺←⁶**XXIB**), ⁷A'←⁶A' (⁷**XXIB**⁺←⁶**XXIB**), ⁵A''←⁴A'' (⁵**XXIA**⁺←⁴**XXIA**), ³A←⁴A'' (³**XXIA**⁺←⁴**XXIA**), ³A←²A (³**XXIB**⁺←²**XXIB**) and ¹A←²A (¹**XXIB**⁺←²**XXIB**) transitions. IEs for these processes are calculated as 4.373 eV, 8.021 eV, 4.438 eV, 7.706 eV, 4.304 eV, 4.320 eV, 4.405 eV and 4.461 eV, respectively. The high IEs calculated for both the ¹A'←²A₁ (¹**XXIA**⁺←²**XXIA**) and ⁷A'←⁶A' (⁷**XXIB**⁺←⁶**XXIB**) processes makes their contribution to the ionisation onsets in the experimental PIE spectrum unlikely. The comparable IEs for the remaining processes makes it highly likely that all six ionisation transitions will contribute to the same PIE onset. The ³A←²A₁ (³**XXIA**⁺←²**XXIA**), ⁵A''←⁴A'' (⁵**XXIA**⁺←⁴**XXIA**), ³A←⁴A'' (³**XXIA**⁺←⁴**XXIA**), ³A←²A (³**XXIB**⁺←²**XXIB**) and ¹A←²A (¹**XXIB**⁺←²**XXIB**) ionisation processes are shown in Figure 9.24 as green, orange, violet, blue and magenta arrows, respectively. The ⁵A''←⁶A' (⁵**XXIB**⁺←⁶**XXIB**)

transition is shown as a red dotted arrow due to low vibronic peak intensities calculated in subsequent ZEKE simulations (vide infra). The $^1A' \leftarrow ^2A_1$ ($^1XXIA^+ \leftarrow ^2XXIA$) and $^7A' \leftarrow ^6A'$ ($^7XXIB^+ \leftarrow ^6XXIB$) processes are shown as red dashed arrows due to their high calculated IEs.

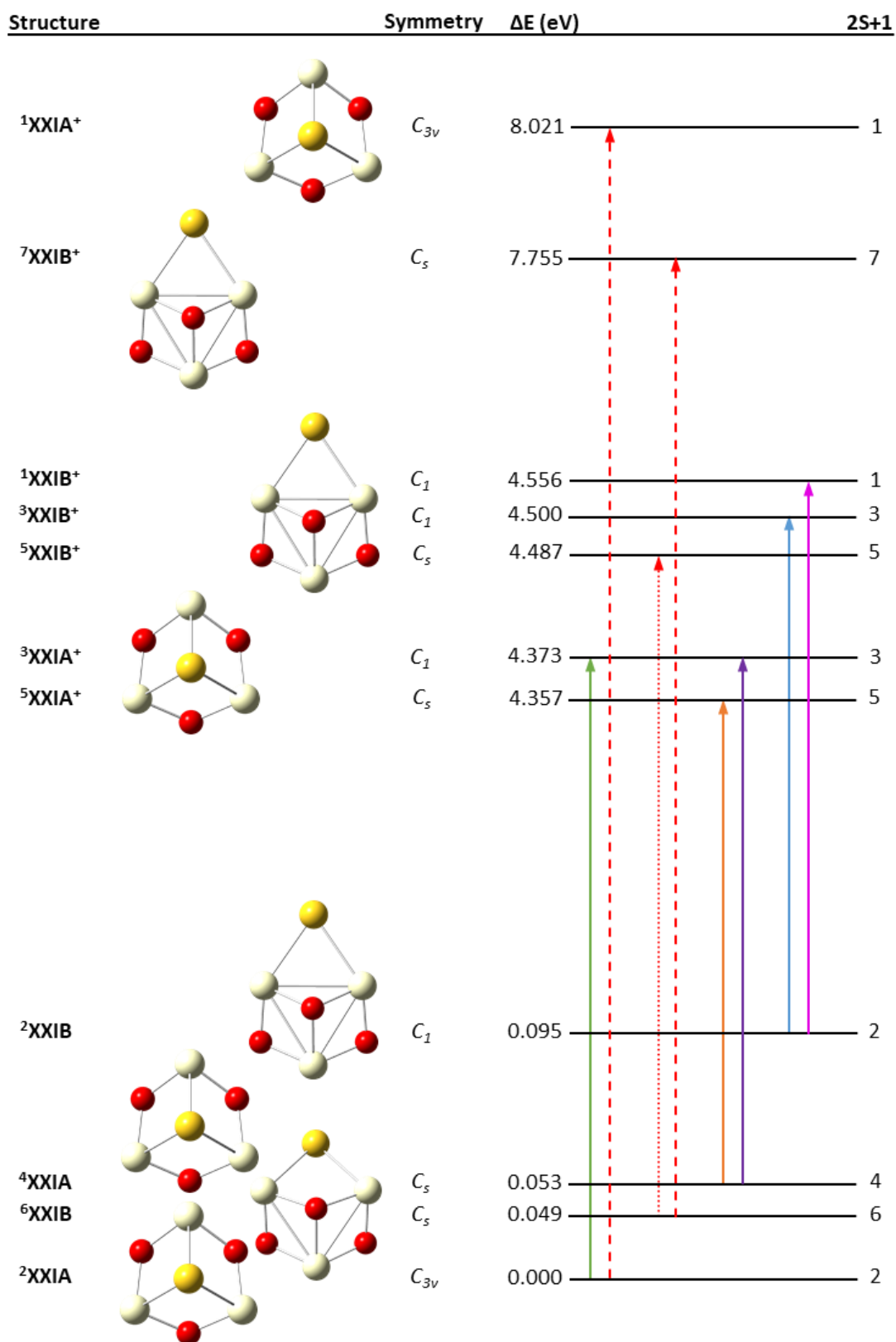


Figure 9.24: Calculated structures for AuCe_3O_3 . Potential ionisation transitions are shown. Ionisation processes with low ZEKE intensities (*vide infra*) are shown as red dotted arrows. Transitions with prohibitively high ionisation energies shown as red dashed arrows.

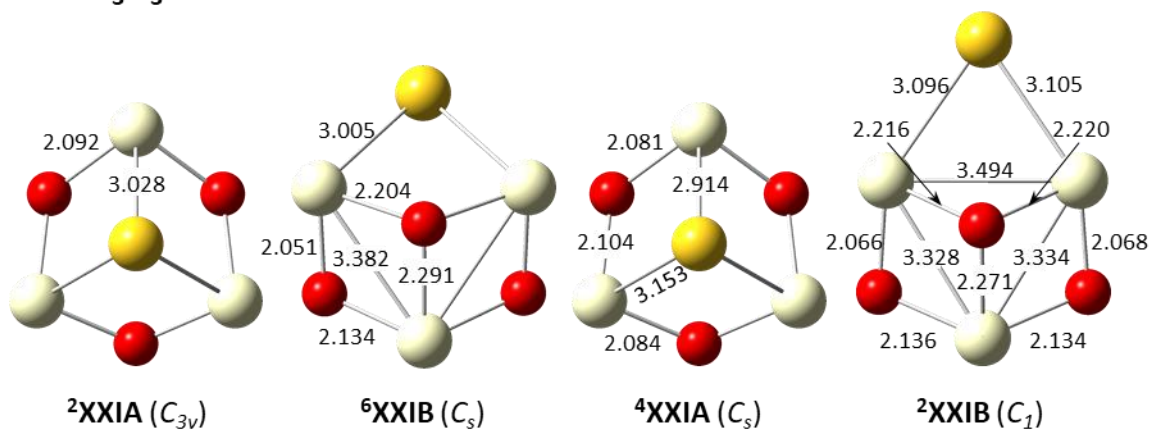
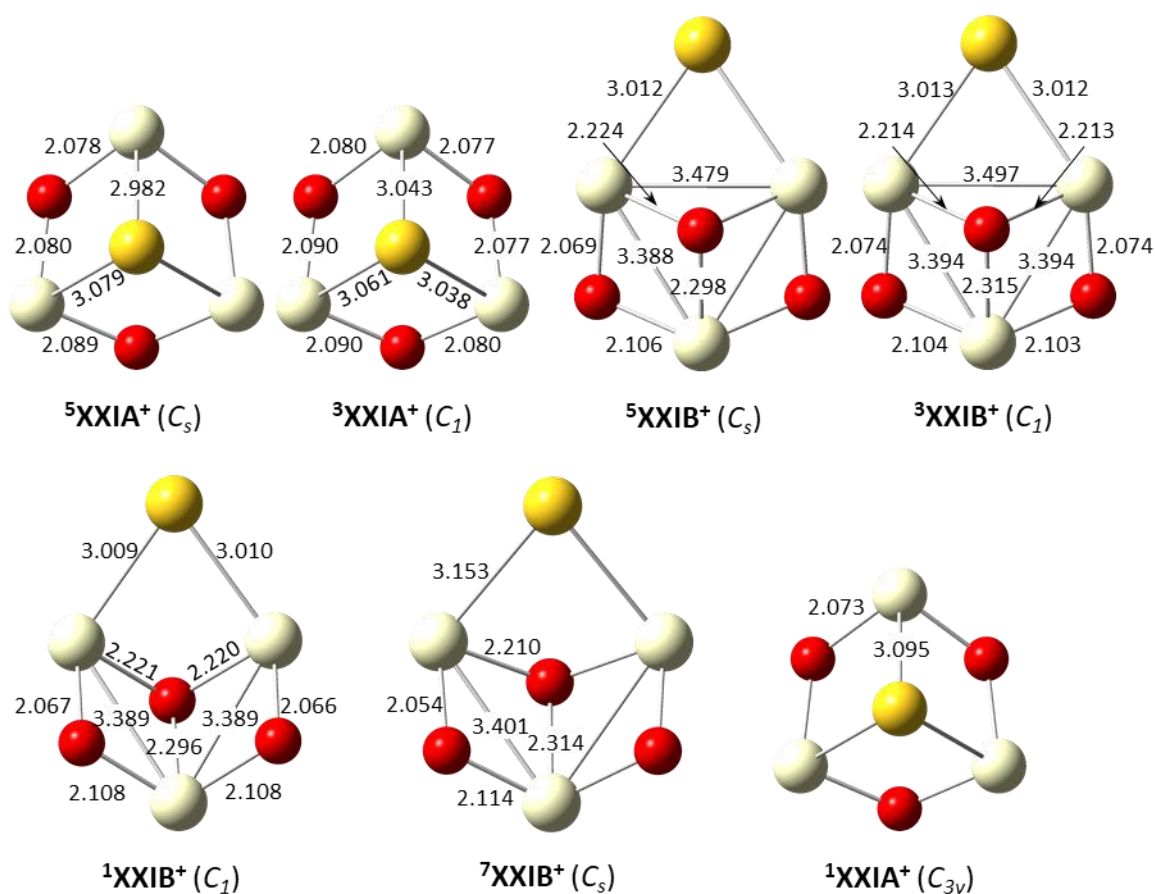
AuCe_3O_3  **$\text{AuCe}_3\text{O}_3^+$** 

Figure 9.25: Calculated AuCe_3O_3 neutral (top) and cationic (below) structures. Bond lengths are presented in Å. Point groups are shown in brackets.

DFT calculations also revealed a significant number of AuCe₃O₃ neutral species for which a cationic target state was not calculated. This was due to either convergence of the cationic structure to another geometry entirely – thus producing a very weak FC overlap between the neutral and cationic species – or convergence issues with the cationic state. These calculated neutral structures are presented in Figure 9.26.

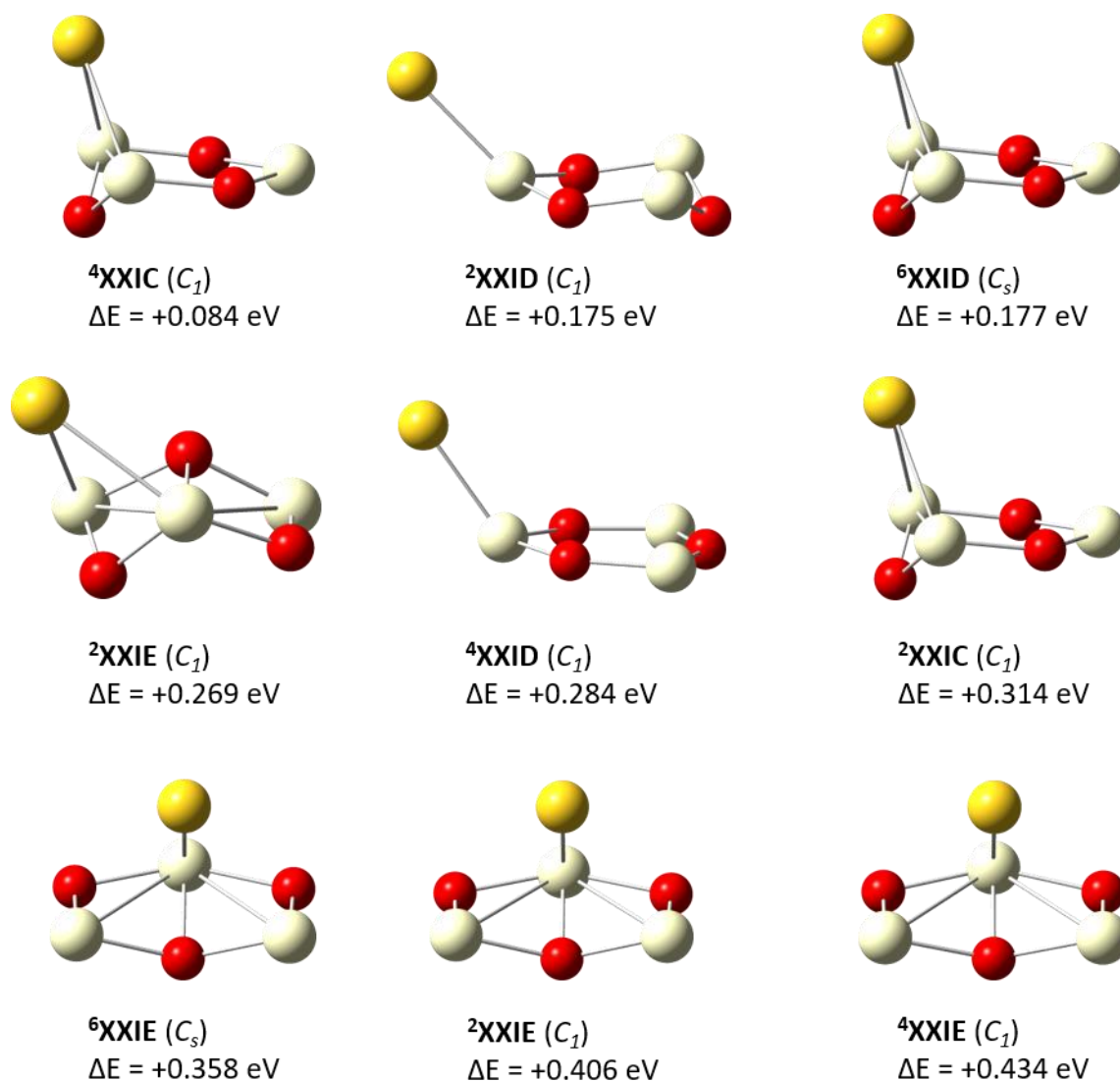


Figure 9.26: Calculated AuCe₃O₃ neutral species for which a cationic state was not calculated. Energies relative to the LES (ΔE) are shown. Point groups are shown in brackets.

9.6.3. ZEKE Spectral Simulations for AuCe₃O₃

Simulated ZEKE spectra for the AuCe₃O₃ ${}^3A \leftarrow {}^2A_1$ (${}^3XXIA^+ \leftarrow {}^2XXIA$), ${}^5A'' \leftarrow {}^4A''$ (${}^5XXIA^+ \leftarrow {}^4XXIA$), ${}^3A \leftarrow {}^4A''$ (${}^3XXIA^+ \leftarrow {}^4XXIA$), ${}^3A \leftarrow {}^2A$ (${}^3XXIB^+ \leftarrow {}^2XXIB$) and ${}^1A \leftarrow {}^2A$ (${}^1XXIB^+ \leftarrow {}^2XXIB$) ionisation processes are presented in Figure 9.27. The ${}^5A'' \leftarrow {}^6A'$ (${}^5XXIB^+ \leftarrow {}^6XXIB$) ionisation process was calculated to be extremely weak such that it would have a negligible contribution to the PIE spectrum. The ${}^5A'' \leftarrow {}^6A'$ (${}^5XXIB^+ \leftarrow {}^6XXIB$) ZEKE spectrum is therefore presented in Appendix C and not shown here. Due to the extensive number of vibrational modes inherent to the AuCe₃O₃ cluster, ZEKE simulations were performed using the Parallel Approximation to facilitate memory constraints. Energetic corrections of +0.228 eV, +0.388 eV, +0.063 eV, -0.192 eV and -0.092 eV were applied to the vibronic transition energies of the ${}^3A \leftarrow {}^2A_1$ (${}^3XXIA^+ \leftarrow {}^2XXIA$), ${}^5A'' \leftarrow {}^4A''$ (${}^5XXIA^+ \leftarrow {}^4XXIA$), ${}^3A \leftarrow {}^4A''$ (${}^3XXIA^+ \leftarrow {}^4XXIA$), ${}^3A \leftarrow {}^2A$ (${}^3XXIB^+ \leftarrow {}^2XXIB$) and ${}^1A \leftarrow {}^2A$ (${}^1XXIB^+ \leftarrow {}^2XXIB$) spectra, respectively, such that a PIE spectrum calculated via integration of the corrected ZEKE spectra showed good agreement with the experimental PIE spectrum (vide infra). The corrected ZEKE spectra are shown here.

ZEKE spectra calculated for the ${}^3A \leftarrow {}^2A_1$ (${}^3XXIA^+ \leftarrow {}^2XXIA$) and ${}^5A'' \leftarrow {}^4A''$ (${}^5XXIA^+ \leftarrow {}^4XXIA$) transitions presented in Figures 9.27(a) and 9.27(b) respectively show these two transitions to be the dominant ionisation pathways; with scaling factors of 6.8 and 7.55 respectively required to normalise the spectral intensities of the most intense peaks. Prominent vibronic peaks in the ${}^3A \leftarrow {}^2A_1$ (${}^3XXIA^+ \leftarrow {}^2XXIA$) ZEKE spectrum comprise the 5_0^n , $5_0^n 6_0^1$ and $5_0^n 9_0^1$ progressions. The 0_0^0 transition in this spectrum is calculated with good intensity, inferring a strong FC overlap between the 2XXIA and ${}^3XXIA^+$ species. The ${}^5A'' \leftarrow {}^4A''$ (${}^5XXIA^+ \leftarrow {}^4XXIA$) ZEKE spectrum primarily consists of the 3_0^n , $3_0^n 8_0^1$ and $1_1^1 3_0^n$ progressions. The vibronic peaks span a short energy range – ca. 0.15 eV, suggesting a small degree of structural change between the 4XXIA and ${}^5XXIA^+$ species.

The ${}^3A \leftarrow {}^4A''$ (${}^3XXIA^+ \leftarrow {}^4XXIA$), ${}^3A \leftarrow {}^2A$ (${}^3XXIB^+ \leftarrow {}^2XXIB$) and ${}^1A \leftarrow {}^2A$ (${}^1XXIB^+ \leftarrow {}^2XXIB$) ZEKE spectra presented in Figures 9.27(c), (d) and (e) are all calculated with considerably lower intensities than the ${}^3A \leftarrow {}^2A_1$ (${}^3XXIA^+ \leftarrow {}^2XXIA$) and ${}^5A'' \leftarrow {}^4A''$ (${}^5XXIA^+ \leftarrow {}^4XXIA$) ZEKE spectra discussed previously; particularly the (${}^3XXIB^+ \leftarrow {}^2XXIB$) and ${}^1A \leftarrow {}^2A$ (${}^1XXIB^+ \leftarrow {}^2XXIB$) spectra, with scaling

factors of 28.7 and 16.4, respectively used to normalise the vibronic peaks. The weaker intensities in these photo-ionisation processes suggests the (³XXIB⁺←²XXIB) and ¹A←²A (¹XXIB⁺←²XXIB) processes will have less contribution to the PIE spectrum than the ³A←²A₁ (³XXIA⁺←²XXIA) and ⁵A''←⁴A'' (⁵XXIA⁺←⁴XXIA) transitions discussed previously. Prominent vibronic peaks within the ³A←⁴A'' (³XXIA⁺←⁴XXIA) are assigned to the 6₀ⁿ, 2₁6₀ⁿ, 2₂6₀ⁿ and 1₁2₂6₀ⁿ progressions. However, due to the complexity of the spectrum, only a few vibronic peaks were assigned. ZEKE spectra for the (³XXIB⁺←²XXIB) and ¹A←²A (¹XXIB⁺←²XXIB) transitions – shown in Figures 9.27(d) and 9.26(e), respectively – are also quite complex; with both spectra showing considerable peak broadening from unresolved vibronic transitions. Consequentially, vibronic peaks were not assigned for either of these spectra. Both spectra present a broad profile of vibronic peaks – spanning ca. 0.2 eV ranges – with the 0₀⁰ transition not calculated in either spectrum. This suggests considerable structural deformation may be occurring during both ionisation processes.

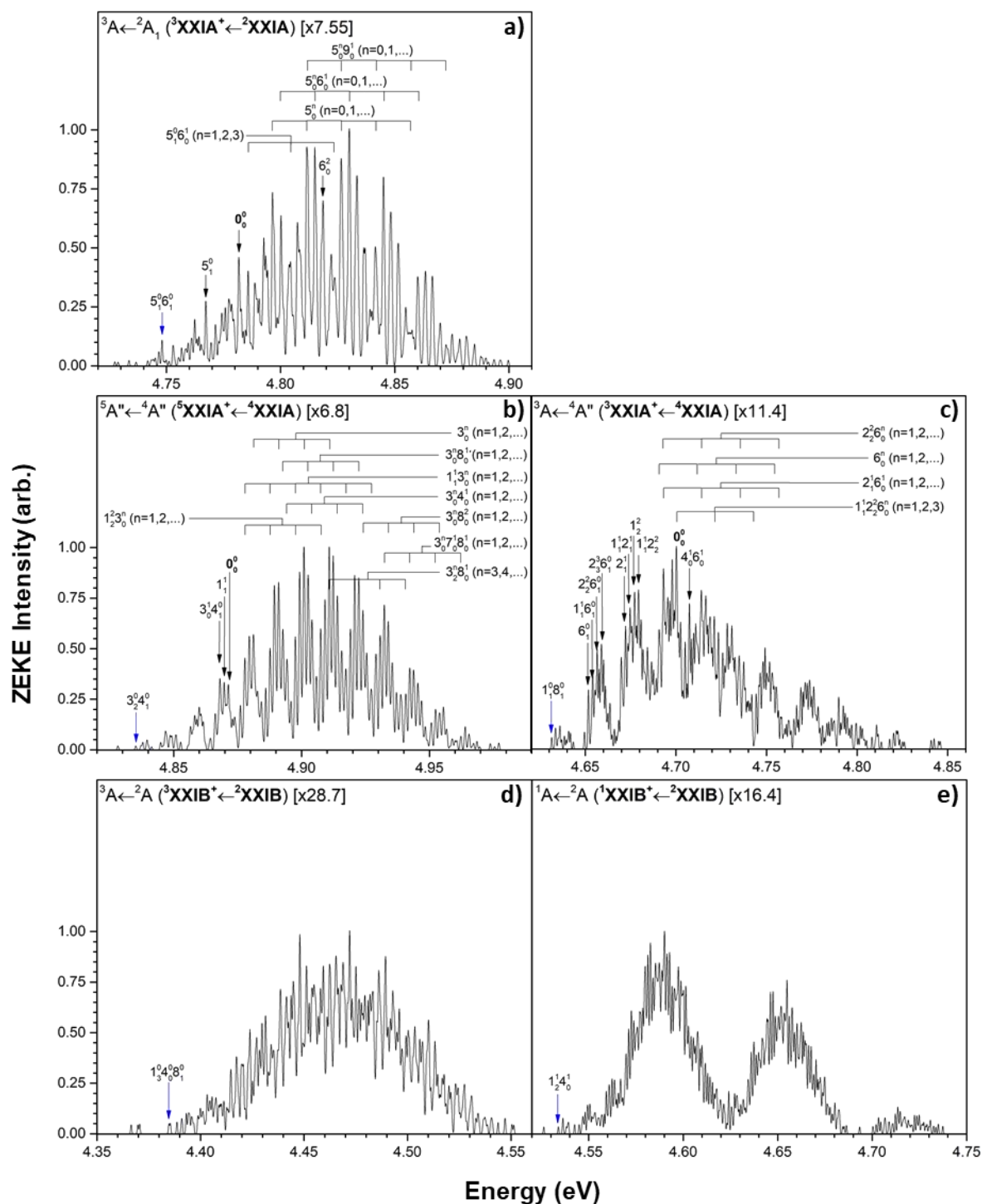


Figure 9.27: Calculated ZEKE spectra for AuCe₃O₃ ionisation transitions: **a).** ${}^3A \leftarrow {}^2A_1$ (${}^3XXIA^+ \leftarrow {}^2XXIA$), **b).** ${}^5A'' \leftarrow {}^4A''$ (${}^5XXIA^+ \leftarrow {}^4XXIA$), **c).** ${}^3A \leftarrow {}^4A''$ (${}^3XXIA^+ \leftarrow {}^4XXIA$), **d).** ${}^3A \leftarrow {}^2A$ (${}^3XXIB^+ \leftarrow {}^2XXIB$) and **e).** ${}^1A \leftarrow {}^2A$ (${}^1XXIB^+ \leftarrow {}^2XXIB$). Spectral intensities are normalised to the most intense peak in each spectrum with scaling factors shown. Prominent vibronic transitions are assigned. The vibronic transition likely to correspond to the appearance of ion signal in each spectrum is labelled with a blue arrow.

9.6.4. Comparison of Simulated and Experimental PIE Spectra for AuCe₃O₃

A simulated PIE spectrum for the AuCe₃O₃ system is calculated from a combination of the integrated ${}^3A \leftarrow {}^2A_1$ (${}^3XXIA^+ \leftarrow {}^2XXIA$), ${}^5A'' \leftarrow {}^4A''$ (${}^5XXIA^+ \leftarrow {}^4XXIA$), ${}^3A \leftarrow {}^4A''$ (${}^3XXIA^+ \leftarrow {}^4XXIA$), ${}^3A \leftarrow {}^2A$ (${}^3XXIB^+ \leftarrow {}^2XXIB$) and ${}^1A \leftarrow {}^2A$ (${}^1XXIB^+ \leftarrow {}^2XXIB$) ionisation processes. Given the small energetic separations calculated between the AuCe₃O₃ 2XXIA , 6XXIB , 4XXIA and 2XXIB neutral isomers, in addition to the comparable IEs and ZEKE intensities calculated for the ${}^3A \leftarrow {}^2A_1$ (${}^3XXIA^+ \leftarrow {}^2XXIA$), ${}^5A'' \leftarrow {}^4A''$ (${}^5XXIA^+ \leftarrow {}^4XXIA$), ${}^3A \leftarrow {}^4A''$ (${}^3XXIA^+ \leftarrow {}^4XXIA$), ${}^3A \leftarrow {}^2A$ (${}^3XXIB^+ \leftarrow {}^2XXIB$) and ${}^1A \leftarrow {}^2A$ (${}^1XXIB^+ \leftarrow {}^2XXIB$) processes – shown in Figures 9.24 and 9.27, respectively – all 5 ionisation processes are considered to underlie the primary onset. The simulated PIE spectrum for the primary PIE onset is shown overlayed against the experimental PIE spectrum in Figure 9.28. An excellent fit is found between the simulated and experimental PIE spectra. Thus, inferences about the AuCe₃O₃ geometric structure can be made from the DFT calculated structures. The adiabatic IE is assigned to the ${}^3A \leftarrow {}^2A$ (${}^3XXIB^+ \leftarrow {}^2XXIB$) process – as the lowest energy ionisation process post-correction – to give an IE value of 4.39 eV.

A PIE spectrum is not calculated for the secondary onset since all calculated ionisation processes are assigned to the primary onset. However, it is possible that the neutral AuCe₃O₃ species for which cationic states were unable to be calculated – presented in Figure 9.26 – may have ionisation processes which could be assigned to the secondary onset. Calculations of these cationic states were largely hindered by convergence issues. Future advances in either DFT optimisation algorithms¹⁻³ – to provide more reliable convergence – or computing power – to allow more refined treatments of the electronic structure for transition metal-lanthanide oxide clusters – may make these calculations viable at a later date.

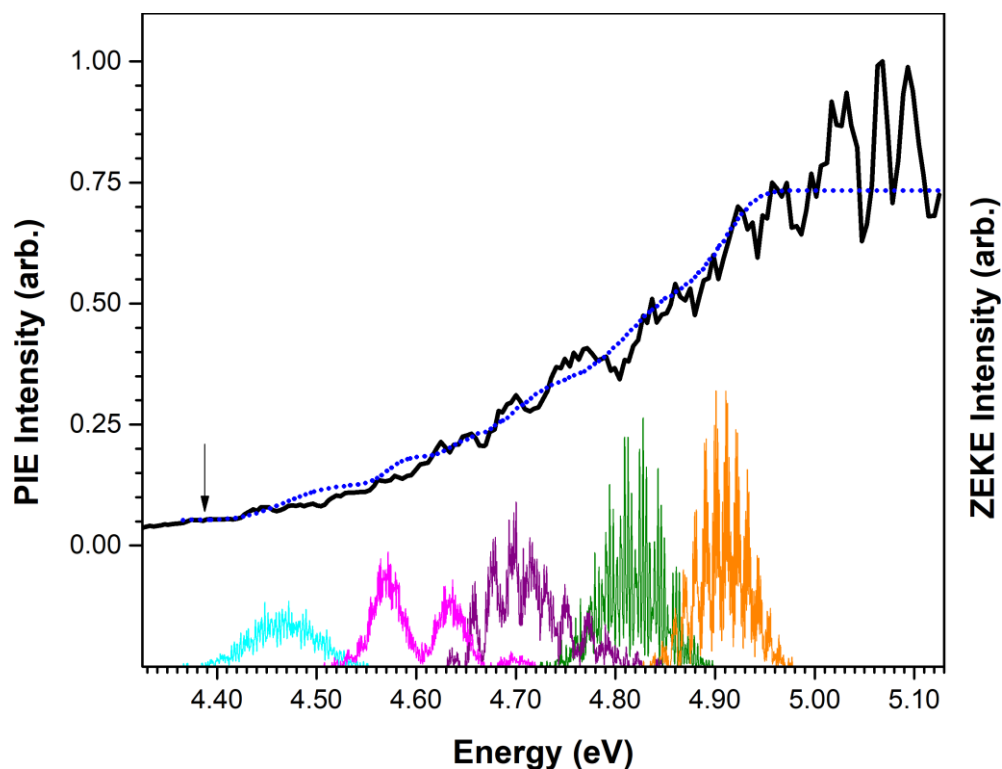


Figure 9.28: Calculated AuCe₃O₃ PIE spectrum (blue dotted line) overlaid against the experimental PIE spectrum (solid black line). Calculated ZEKE spectra for the $^3A \leftarrow ^2A_1$ ($^3XXIA^+ \leftarrow ^2XXIA$), $^5A'' \leftarrow ^4A''$ ($^5XXIA^+ \leftarrow ^4XXIA$), $^3A \leftarrow ^4A''$ ($^3XXIA^+ \leftarrow ^4XXIA$), $^3A \leftarrow ^2A$ ($^3XXIB^+ \leftarrow ^2XXIB$) and $^1A \leftarrow ^2A$ ($^1XXIB^+ \leftarrow ^2XXIB$) ionisation processes are shown below the PIE spectrum in green, orange, violet, blue and magenta, respectively. The adiabatic ionisation energy is labelled with a black arrow.

9.7. PIE Spectrum and DFT Results for AuCe₃O₄

9.7.1. AuCe₃O₄ Experimental PIE Spectrum

The AuCe₃O₄ cluster ion was not detected in any mass spectra within the 3.92 – 5.17 eV range of photo-ionisation experiments. Moreover, the AuCe₃O₄ ion peak was not detected in the mass spectrum following photo-ionisation at 213 nm (5.82 eV). Therefore, a PIE spectrum is not presented for the AuCe₃O₄ cluster. However, DFT calculated AuCe₃O₄ structures are presented in addition to ZEKE and PIE spectral simulations to provide insight into the structural and electronic properties of the AuCe₃O₄ cluster system.

9.7.2. DFT Calculations for AuCe₃O₄

DFT calculated AuCe₃O₄ neutral and cationic structures are presented in Figures 9.29 and 9.30. Only one low energy neutral geometry is calculated; other structures to be significantly higher in energy and are not shown here. This structure – labelled **XXII** – consists of a Ce₃O₄ motif with a gold atom singly attached to one of the Ce atoms. Both the gold atom and the central oxygen atom are positioned below the Ce₃ plane. The **XXVII** structure is calculated in geometrically identical doublet and quartet spin isomers – labelled ²**XXII** and ⁴**XXII**, respectively – which occupy the ²A and ⁴A electronic states, respectively. A very small energetic separation of 0.003 eV is calculated between the ²**XXII** and ⁴**XXII** species.

Calculations of AuCe₃O₄ cations reveal three unique species. These species all retain the same geometric arrangement as the neutral **XXII** structure and are calculated in triplet (³A), quintet (⁵A) and singlet (¹A') electronic states – labelled ³**XXII**⁺, ⁵**XXII**⁺ and ¹**XXII**⁺, respectively. Both the ³**XXII**⁺ and ¹**XXII**⁺ species are geometrically similar to their neutral counterparts; with the most significant difference being a ca. 0.18 Å contraction in the Au-Ce bond length of both cationic species compared to the neutral ²**XXII** and ⁴**XXII** structures. The ⁵**XXII**⁺ species, however, shows a ca. 0.39 Å elongation of the Au-Ce bond relative to the ⁴**XXII** neutral. Thus, the calculated ⁵**XXII**⁺ species may reflect a van der Waals state where the gold atom is only weakly bound to the Ce₃O₄ motif.

A total of four ionisation processes are calculated for the AuCe₃O₄ system which include the ${}^3\text{A} \leftarrow {}^2\text{A}$ (${}^3\text{XXII}^+ \leftarrow {}^2\text{XXII}$), ${}^1\text{A}' \leftarrow {}^2\text{A}$ (${}^1\text{XXII}^+ \leftarrow {}^2\text{XXII}$), ${}^3\text{A} \leftarrow {}^4\text{A}$ (${}^3\text{XXII}^+ \leftarrow {}^4\text{XXII}$) and ${}^5\text{A} \leftarrow {}^4\text{A}$ (${}^5\text{XXII}^+ \leftarrow {}^4\text{XXII}$) transitions. IEs for these processes are calculated as 6.369 eV, 8.596 eV, 6.366 eV and 7.100 eV, respectively. The calculated IEs are all significantly higher than the maximum photon energy of 5.82 eV (213 nm) available with the experimental setup and are thus consistent with the non-detection of the AuCe₃O₄ ion in any mass spectra. The near-identical IEs calculated for the ${}^3\text{A} \leftarrow {}^2\text{A}$ (${}^3\text{XXII}^+ \leftarrow {}^2\text{XXII}$) and ${}^3\text{A} \leftarrow {}^4\text{A}$ (${}^3\text{XXII}^+ \leftarrow {}^4\text{XXII}$) processes suggests both transitions will contribute to the same PIE onset. These processes are shown as green and orange arrows, respectively, in Figure 9.29. The ${}^1\text{A}' \leftarrow {}^2\text{A}$ (${}^1\text{XXII}^+ \leftarrow {}^2\text{XXII}$) and ${}^5\text{A} \leftarrow {}^4\text{A}$ (${}^5\text{XXII}^+ \leftarrow {}^4\text{XXII}$) processes, both with significantly higher IEs, will most likely contribute to higher energy onsets which are not of interest in the context of this work.

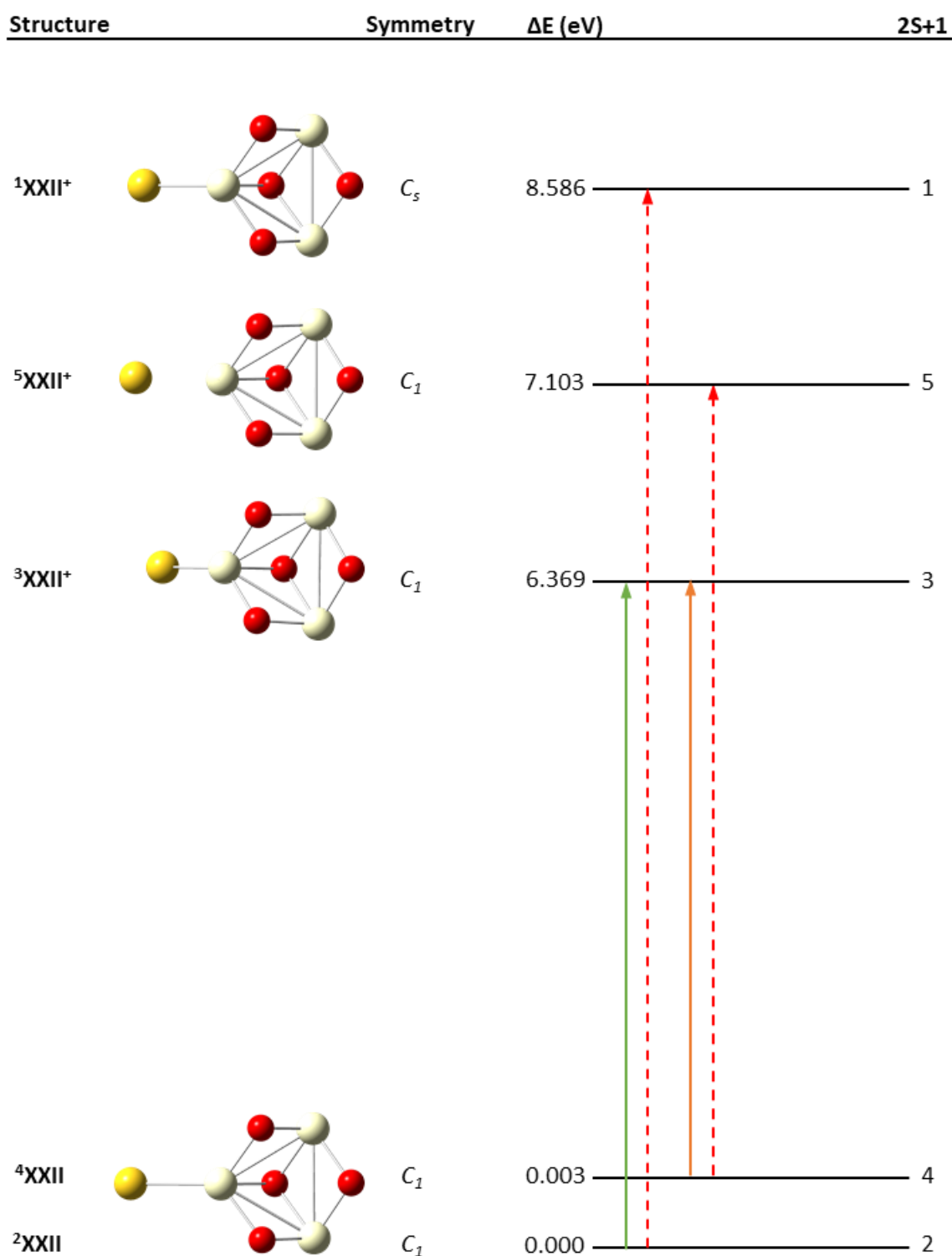


Figure 9.29: Calculated structures for AuCe_3O_4 . Potential ionisation transitions are shown. Transitions with prohibitively high ionisation energies are presented as red dashed arrows.

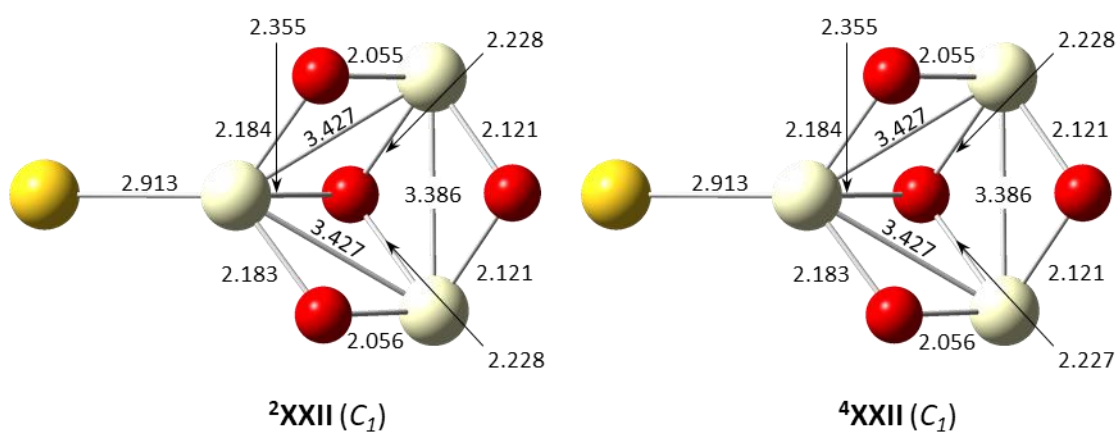
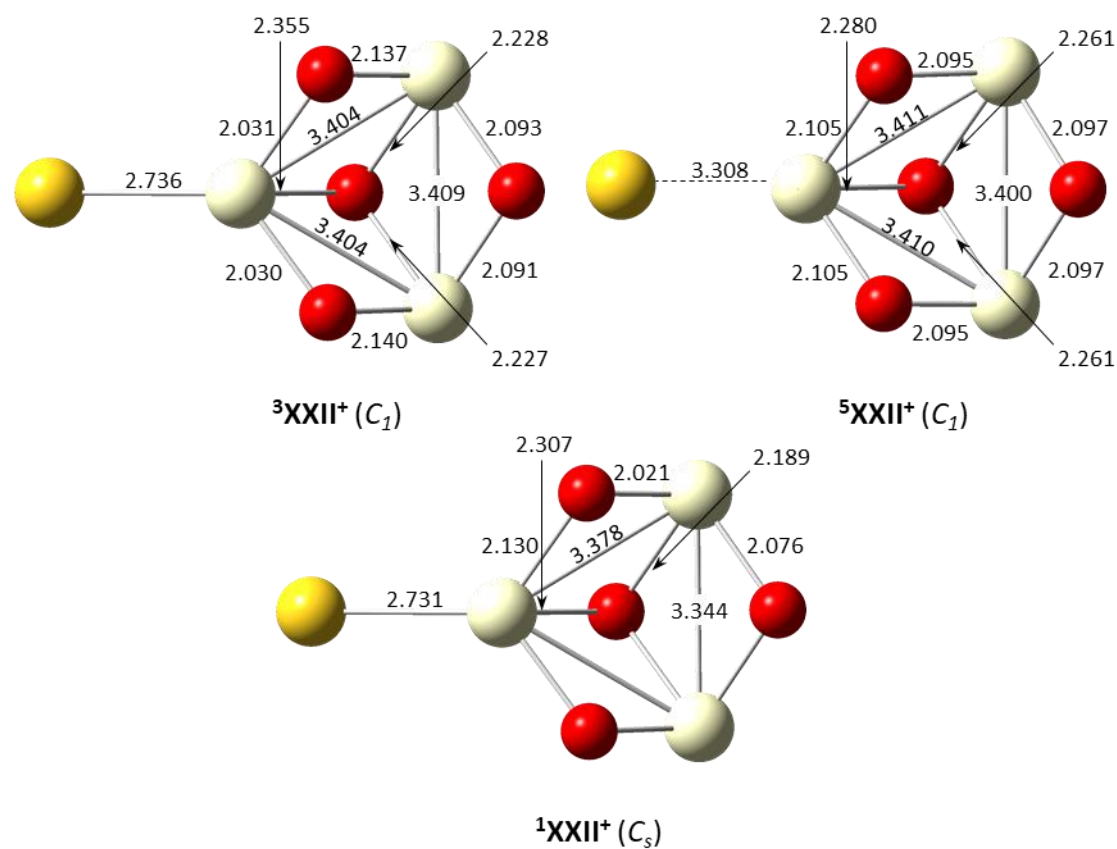
AuCe_3O_4  $\text{AuCe}_3\text{O}_4^+$ 

Figure 9.30: Calculated AuCe_3O_4 neutral (top) and cationic (below) structures. Bond lengths are presented in Å. Point groups are shown in brackets.

9.7.3. ZEKE Spectral Simulations for AuCe₃O₄

Simulated ZEKE spectra for the AuCe₃O₄ ³A←²A (³XXII⁺←²XXII) and ³A←⁴A (³XXII⁺←⁴XXII) ionisation processes are presented in Figure 9.31. ZEKE simulations were performed using the Parallel Approximation due to the extensive number of vibrational modes inherent to the AuCe₃O₄ neutral and cationic species which did not permit a full Duschinsky treatment. Due to the lack of any experimental data, the 0₀⁰ transitions for the ³A←²A (³XXII⁺←²XXII) and ³A←⁴A (³XXII⁺←⁴XXII) transitions were set to their respective calculated IE values of 6.369 eV and 6.366 eV, respectively during ZEKE simulations.

Comparable spectral profiles and vibronic peak intensities are calculated for both the ³A←²A (³XXII⁺←²XXII) and ³A←⁴A (³XXII⁺←⁴XXII) ZEKE spectra, with scaling factors of 1240 and 1090, respectively, used to normalise the most intense vibronic transition in each spectrum. Both transitions should have similar contributions to the PIE spectrum, with no dominant ionisation process. The large scaling factors applied to both spectra infers a weak FC overlap which may manifest as a weak Ce₃O₄ ion signal in any experimental mass spectra. Both spectra show several clusters of vibronic peaks separated by ca. 0.08 eV which closely aligns with the calculated ν'_{17} frequency of 651.48 cm⁻¹. Thus, the vibronic peaks in both spectra are most likely vibronic progressions of the ³XXII⁺ ν_{17} mode. The extensive number of vibronic transitions calculated for both spectra makes the assignment of vibronic peaks difficult. Therefore, only the lowest energy vibronic transitions and the maximum FC peaks are assigned. The maximum FC transitions for the ³A←²A (³XXII⁺←²XXII) ZEKE spectrum are calculated as both the $1_1^9 2_1^1 3_0^1 6_0^1 17_0^7$ and $1_0^7 3_1^0 17_0^8$ peaks, while the ³A←⁴A (³XXII⁺←⁴XXII) maximum FC transition is calculated as the highly excited $1_2^3 3_0^1 17_0^8$ vibronic transition. The 0₀⁰ transition is not calculated in either spectrum, with the lowest intensity vibronic peaks in both spectra calculated as ca. 0.35 eV higher in energy than the 0₀⁰ transition. The absence of the 0₀⁰ peak in both spectra, in addition to the highly excited maximum FC transitions, correlates with a weak FC overlap in both ionisation processes

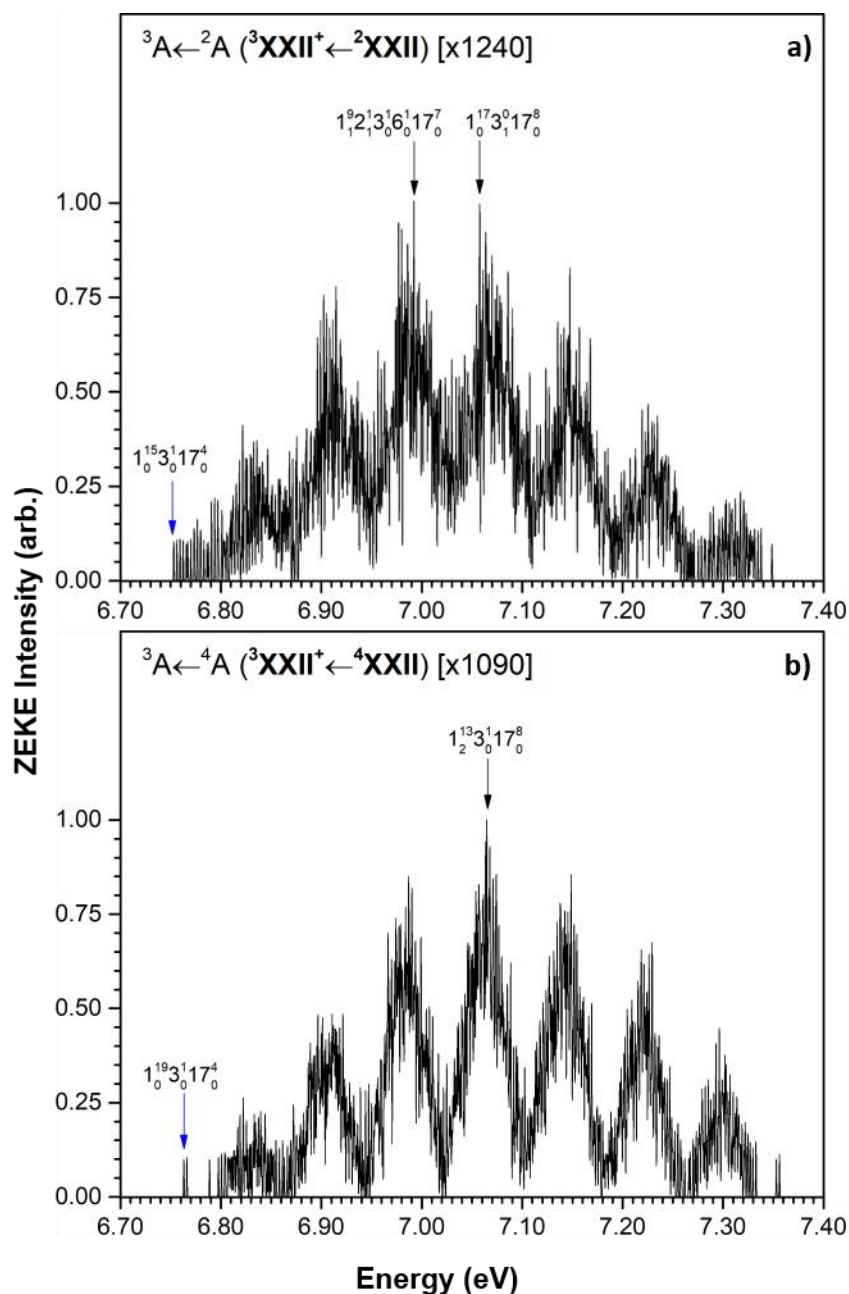


Figure 9.31: Calculated ZEKE spectra for AuCe₃O₄ ionisation transitions: **a).** ${}^3A \leftarrow {}^2A ({}^3XXII^+ \leftarrow {}^2XXII)$ and **b).** ${}^3A \leftarrow {}^4A ({}^3XXII^+ \leftarrow {}^4XXII)$. Spectral intensities are normalised to the most intense peak in each spectrum with scaling factors shown. The vibronic transition likely to correspond to the appearance of ion signal in each spectrum is labelled with a blue arrow.

9.7.4. Simulated PIE Spectrum for AuCe₃O₄

A simulated PIE spectrum for the AuCe₃O₄ cluster system is presented in Figure 9.32. The PIE spectrum was calculated via integration of the ${}^3A \leftarrow {}^2A$ (${}^3XXII^+ \leftarrow {}^2XXII$) and ${}^3A \leftarrow {}^4A$ (${}^3XXII^+ \leftarrow {}^4XXII$) vibronic peaks. A single onset of ion signal is calculated with an appearance energy of 6.75 eV. The onset is quite broad, spanning a ca. 0.35 eV range to a plateau of maximum ion signal at ca. 7.36 eV. The adiabatic IE is assigned to the ${}^3A \leftarrow {}^2A$ (${}^3XXII^+ \leftarrow {}^2XXII$) 0_0^0 transition at 6.37 eV. This assignment is arbitrary, however, given the 2XXII and 4XXII neutral species are energetically indistinguishable; the IE could equally be assigned to the ${}^3A \leftarrow {}^4A$ (${}^3XXII^+ \leftarrow {}^4XXII$) ionisation process. Due to the tendency of the DFT method used in this work to over-predict IE values – by 0.18 eV for the AuCe₃O_n series (vide infra) – the calculated IE value presented here is likely to be higher than the experimental IE_{ad} value.

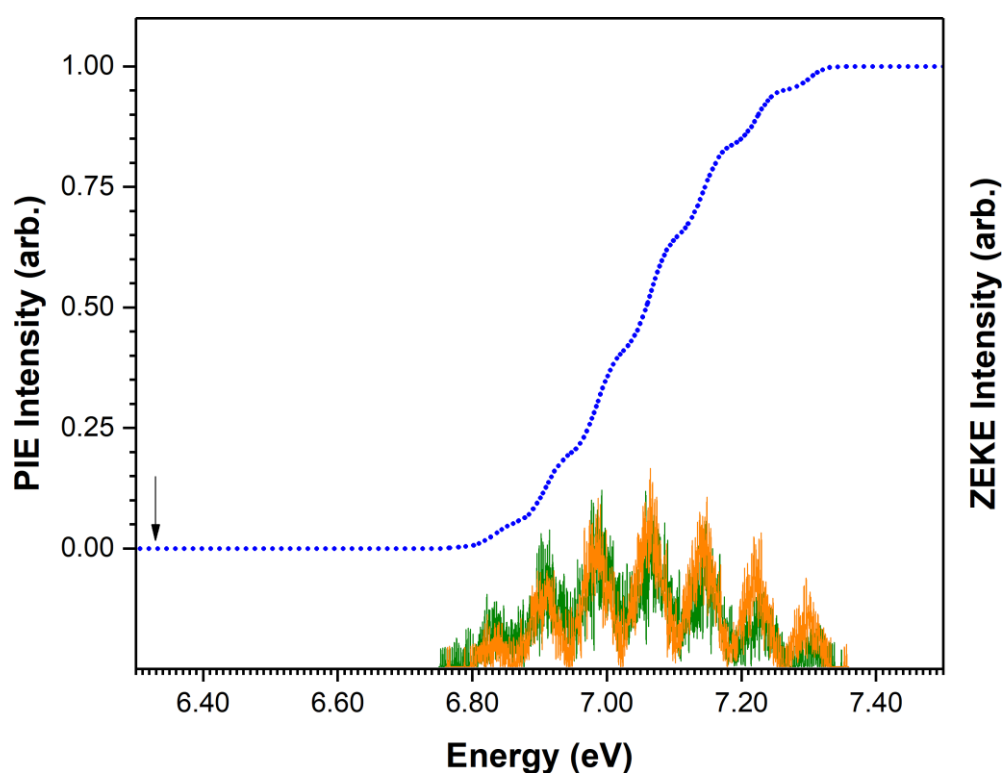


Figure 9.32: Calculated AuCe₃O₄ PIE spectrum (blue dotted line). Calculated ZEKE spectra for the ${}^3A \leftarrow {}^2A$ (${}^3XXII^+ \leftarrow {}^2XXII$) and ${}^3A \leftarrow {}^4A$ (${}^3XXII^+ \leftarrow {}^4XXII$) ionisation processes are shown below the PIE spectrum in green and orange, respectively. The adiabatic ionisation energy is labelled with a black arrow.

9.8. PIE Spectrum and DFT Results for AuCe₃O₅

9.8.1. AuCe₃O₅ Experimental PIE Spectrum

The AuCe₃O₅ ion was not detected in any mass spectra during photo-ionisation experiments. Moreover, not AuCe₃O₅ ion peak was found in the mass spectrum recorded following 213 nm (5.82 eV) photo-ionisation. Therefore, a PIE spectrum for the AuCe₃O₅ system is not presented. However, DFT calculated AuCe₃O₅ neutral and cationic structures are presented in addition to simulated ZEKE and PIE spectra. Some comments on these calculations will be made with regard to the non-detection of the AuCe₃O₅ ion in experiments.

9.8.2. DFT Calculations for AuCe₃O₅

DFT calculated AuCe₃O₅ neutral and cationic geometries are presented in Figures 9.33 and 9.34. Two unique structures are calculated which are labelled **XXIIIA** and **XXIIIB** with increasing energy. The lower energy **XXIIIA** structure shows a geometry which does not resemble any of the Ce₃O_n or AuCe₃O_n species shown previously; the gold atom is bound to both cerium and oxygen atoms. This is the first AuCe₃O_n structure discussed thus far where Au-O bonds are calculated; all previous structures have shown only Au-Ce bonds. While a detailed discussion of the interactions between gold atoms and Ce_mO_n clusters will be presented in Chapter 10, the change in Au-Ce₃O_n bonding calculated here suggests the interaction between gold and cerium oxide clusters may be strongly influenced by the oxidation state of the cerium oxide cluster. The **XXIIIA** structure is calculated in both quartet ⁴A" and doublet ²A electronic states, which are labelled ⁴**XXIIIA** and ²**XXIIIA**, respectively. The calculated energetic separation between these species of 5.2x10⁻⁴ eV is negligible; thus, the ⁴**XXIIIA** and ²**XXIIIA** species can be considered as degenerate. The **XXIIIB** structures consists of a gold atom bound to the exterior of a Ce₃O₅ **XIB** type structure. The Au atom is bound to the Ce₃O₅ structure via a Ce-Au bond, although the gold atom is also positioned near the facially bound oxygen atom atop the Ce₃ face. While the calculations do not predict a formal Au-O bond in this instance, the close proximity between the Au and O atoms – ca. 2.2 Å – strongly suggests the presence of Au-O bonding. The **XXIIIB** structure is calculated in both ⁴A and ²A electronic states – labelled ⁴**XXIIIB** and ²**XXIIIB**, respectively – with energetic separations from the LES calculated as +0.264 and +0.268 eV, respectively. The calculated

0.004 eV energetic difference between the **⁴XXIIIB** and **²XXIIIB** species makes these spin-isomers energetically indistinguishable.

Calculation of AuCe₃O₅ cations show 5 unique species which are labelled in terms of increasing energy as **³XXIIIA⁺**, **¹XXIIIA⁺**, **³XXIIIB⁺**, **⁵XXIIIA⁺** and **⁵XXIIIB⁺** (a singlet **XXIIIB⁺** cation was not calculated due to convergence difficulties). All cationic species are C₁ symmetric and – aside from the **³XXIIIB⁺** species – display similar geometric structures to their neutral counterparts. The **³XXIIIB⁺** species is quite unusual in that the gold atom is bound to the Ce₃O₅ cluster via an Au-O bond only. Given that optimised neutral geometries are used as starting structures in the cationic geometry optimisations, convergence from both **²XXIIIB** and **⁴XXIIIB** structures to the **³XXIIIB⁺** geometry suggests that not only is Au-O bonding prevalent, but the Au-Ce bond is broken during the ionisation process.

A total of 7 ionisation processes are calculated for the AuCe₃O₅ system; these include the **³A←⁴A''** (**³XXIIIA⁺←⁴XXIIIA**), **⁵A←⁴A''** (**⁵XXIIIA⁺←⁴XXIIIA**), **³A←²A** (**³XXIIIA⁺←²XXIIIA**), **¹A←²A** (**¹XXIIIA⁺←²XXIIIA**), **³A←⁴A** (**³XXIIIB⁺←⁴XXIIIB**), **⁵A←⁴A** (**⁵XXIIIB⁺←⁴XXIIIB**) and **³A←²A** (**³XXIIIB⁺←²XXIIIB**) transitions. IEs for these processes are calculated as 5.709 eV, 6.940 eV, 5.709 eV, 5.710 eV, 6.351 eV, 7.932 eV and 6.347 eV, respectively. The high IEs calculated for the **⁵A←⁴A''** (**⁵XXIIIA⁺←⁴XXIIIA**) and **⁵A←⁴A** (**⁵XXIIIB⁺←⁴XXIIIB**) transitions rules out any contribution to the PIE spectrum from these processes. The remaining ionisation processes are considered for ZEKE simulations. The **³A←⁴A''** (**³XXIIIA⁺←⁴XXIIIA**), **³A←²A** (**³XXIIIA⁺←²XXIIIA**) and **¹A←²A** (**¹XXIIIA⁺←²XXIIIA**) ionisation processes are shown in Figure 9.33 as green, orange and violet arrows, respectively. The **¹A←²A** (**¹XXIIIA⁺←²XXIIIA**) and **³A←²A** (**³XXIIIB⁺←²XXIIIB**) ionisation processes are shown as dotted red arrows due to low vibronic peak intensities calculated in subsequent ZEKE simulations (vide infra).

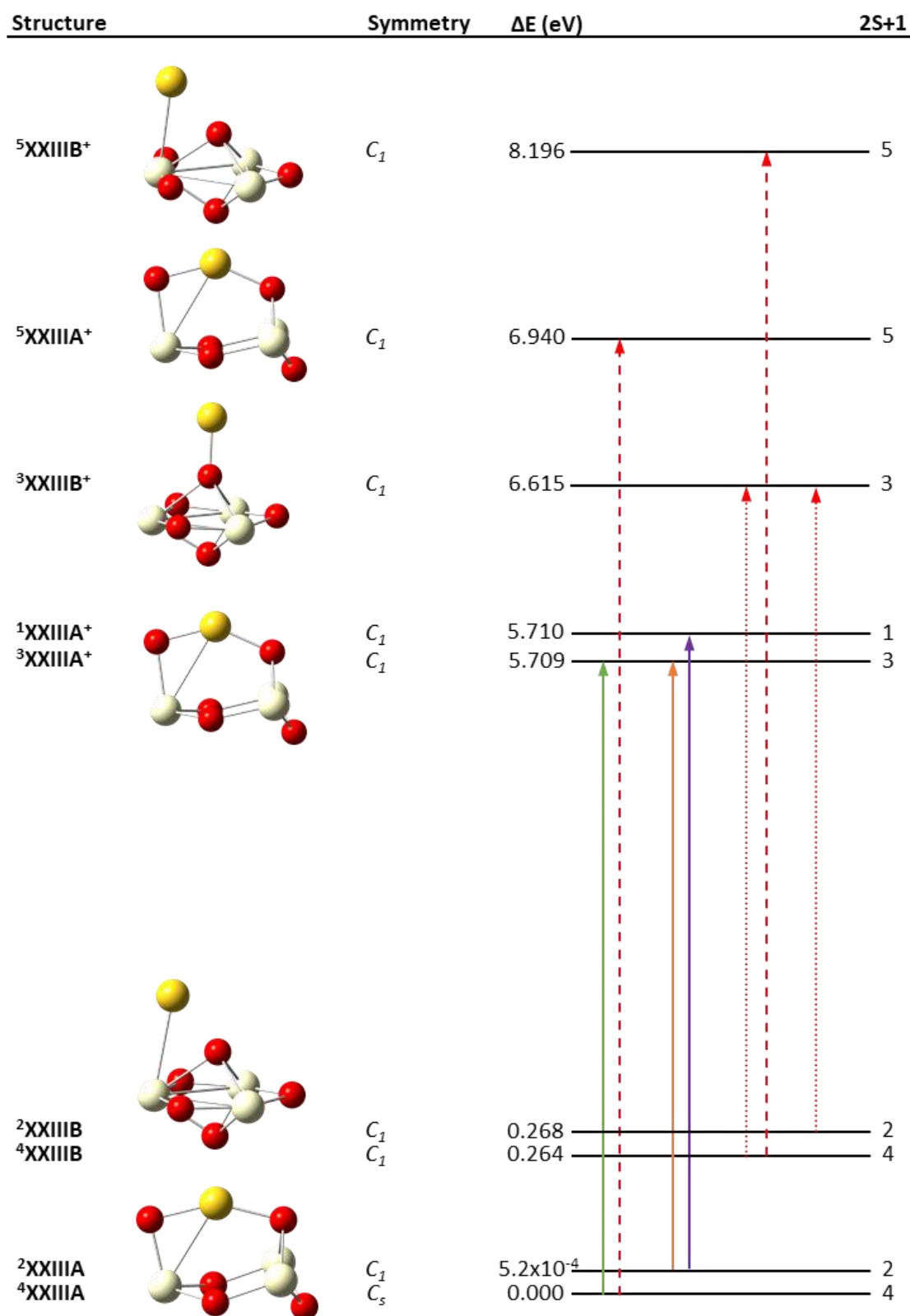


Figure 9.33: Calculated structures for AuCe₃O₅. Potential ionisation transitions are shown.. Ionisation processes with low ZEKE intensities (*vide infra*) are shown as red dotted arrows. Transitions with prohibitively high ionisation energies are shown as red dashed arrows.

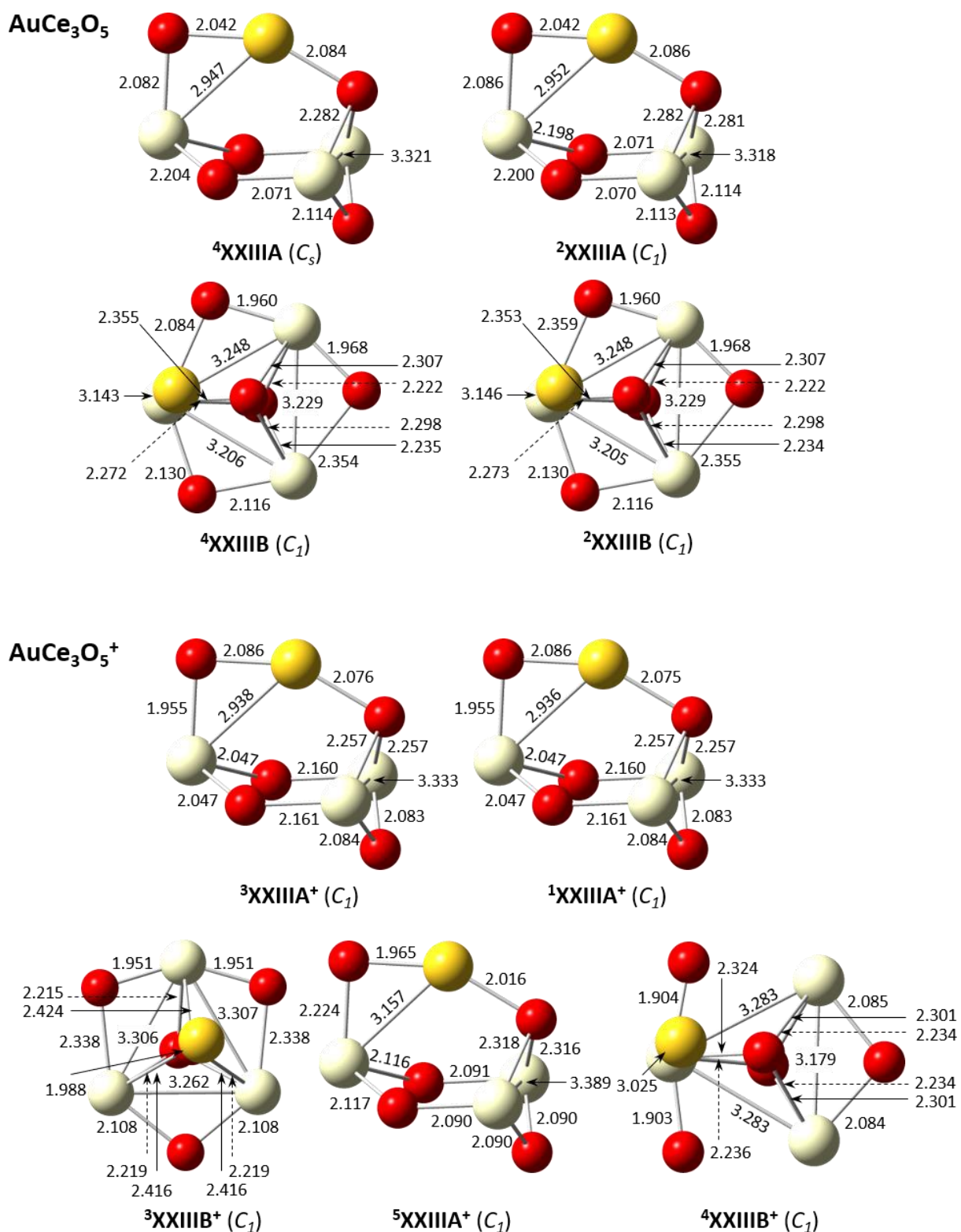


Figure 9.34: Calculated AuCe_3O_5 neutral (top) and cationic (below) structures. Bond lengths are presented in Å. Point groups are shown in brackets.

9.8.3. ZEKE Spectral Simulations for AuCe₃O₅

ZEKE spectra were calculated for the ${}^3A \leftarrow {}^4A''$ (${}^3XXIII A^+ \leftarrow {}^4XXIII A$), ${}^3A \leftarrow {}^2A$ (${}^3XXIII A^+ \leftarrow {}^2XXIII A$), ${}^1A \leftarrow {}^2A$ (${}^1XXIII A^+ \leftarrow {}^2XXIII A$), ${}^3A \leftarrow {}^4A$ (${}^3XXIII B^+ \leftarrow {}^4XXIII B$) and ${}^3A \leftarrow {}^2A$ (${}^3XXIII B^+ \leftarrow {}^2XXIII B$) ionisation transitions. Due to the extensive number of vibrational modes for the AuCe₃O₅ system, a full Duschinsky treatment was not feasible; thus, the Parallel Approximation was used.

Calculated ZEKE spectra for the ${}^3A \leftarrow {}^4A''$ (${}^3XXIII A^+ \leftarrow {}^4XXIII A$), ${}^3A \leftarrow {}^2A$ (${}^3XXIII A^+ \leftarrow {}^2XXIII A$) and ${}^1A \leftarrow {}^2A$ (${}^1XXIII A^+ \leftarrow {}^2XXIII A$) transitions are presented in Figure 9.35. ZEKE simulations for both ${}^3A \leftarrow {}^4A$ (${}^3XXIII B^+ \leftarrow {}^4XXIII B$) and ${}^3A \leftarrow {}^2A$ (${}^3XXIII B^+ \leftarrow {}^2XXIII B$) transitions were attempted; however, no vibronic peak in either spectrum was calculated above the 1×10^{-10} intensity threshold set for the ZEKE simulations. It was therefore concluded that neither the ${}^3A \leftarrow {}^4A$ (${}^3XXIII B^+ \leftarrow {}^4XXIII B$) or ${}^3A \leftarrow {}^2A$ (${}^3XXIII B^+ \leftarrow {}^2XXIII B$) transitions would contribute substantially to any PIE spectrum compared to the first onset ionisation processes. Calculated ZEKE spectra for these processes are not shown.

The spectral profiles for the ${}^3A \leftarrow {}^4A''$ (${}^3XXIII A^+ \leftarrow {}^4XXIII A$), ${}^3A \leftarrow {}^2A$ (${}^3XXIII A^+ \leftarrow {}^2XXIII A$) and ${}^1A \leftarrow {}^2A$ (${}^1XXIII A^+ \leftarrow {}^2XXIII A$) ZEKE spectra – shown in Figures 9.35(a), (b) and (c) respectively – are similar, owing to the near-identical neutral and cationic spin isomers participating in the ionisation processes. All three spectra span a broad – ca. 0.9 eV – range and are dominated by long 21_0^n , $2_0^1 21_0^n$ and $18_0^1 21_0^n$ progressions, where the ν_{21} mode describes a symmetric stretch of the Ce-O bonds for the O atom below the Ce₃ pseudo-plane, and asymmetric stretches of all other Ce-O and Au-O bonds. Comparison of the spectral intensities – via the scaling factors used to normalise vibronic peak intensities in each spectrum – shows the ${}^1A \leftarrow {}^2A$ (${}^1XXIII A^+ \leftarrow {}^2XXIII A$) ZEKE spectrum is considerably weaker than both the ${}^3A \leftarrow {}^4A''$ (${}^3XXIII A^+ \leftarrow {}^4XXIII A$) and ${}^3A \leftarrow {}^2A$ (${}^3XXIII A^+ \leftarrow {}^2XXIII A$) ZEKE spectra. Thus, the ${}^3A \leftarrow {}^4A''$ (${}^3XXIII A^+ \leftarrow {}^4XXIII A$) and ${}^3A \leftarrow {}^2A$ (${}^3XXIII A^+ \leftarrow {}^2XXIII A$) processes are expected to be dominant. The band origin transitions of the ${}^3A \leftarrow {}^4A''$ (${}^3XXIII A^+ \leftarrow {}^4XXIII A$) and ${}^3A \leftarrow {}^2A$ (${}^3XXIII A^+ \leftarrow {}^2XXIII A$) processes, which are calculated via DFT to occur at 5.709 eV, 5.709 eV and 5.710 eV, respectively, are not calculated above the intensity threshold in any of the spectra. Moreover, the lowest energy vibronic transitions in all three ZEKE spectra are calculated ca.

0.3 eV higher in energy than their respective 0_0^0 transitions. This suggests considerable structural deformation of the cationic structure following photo-ionisation.

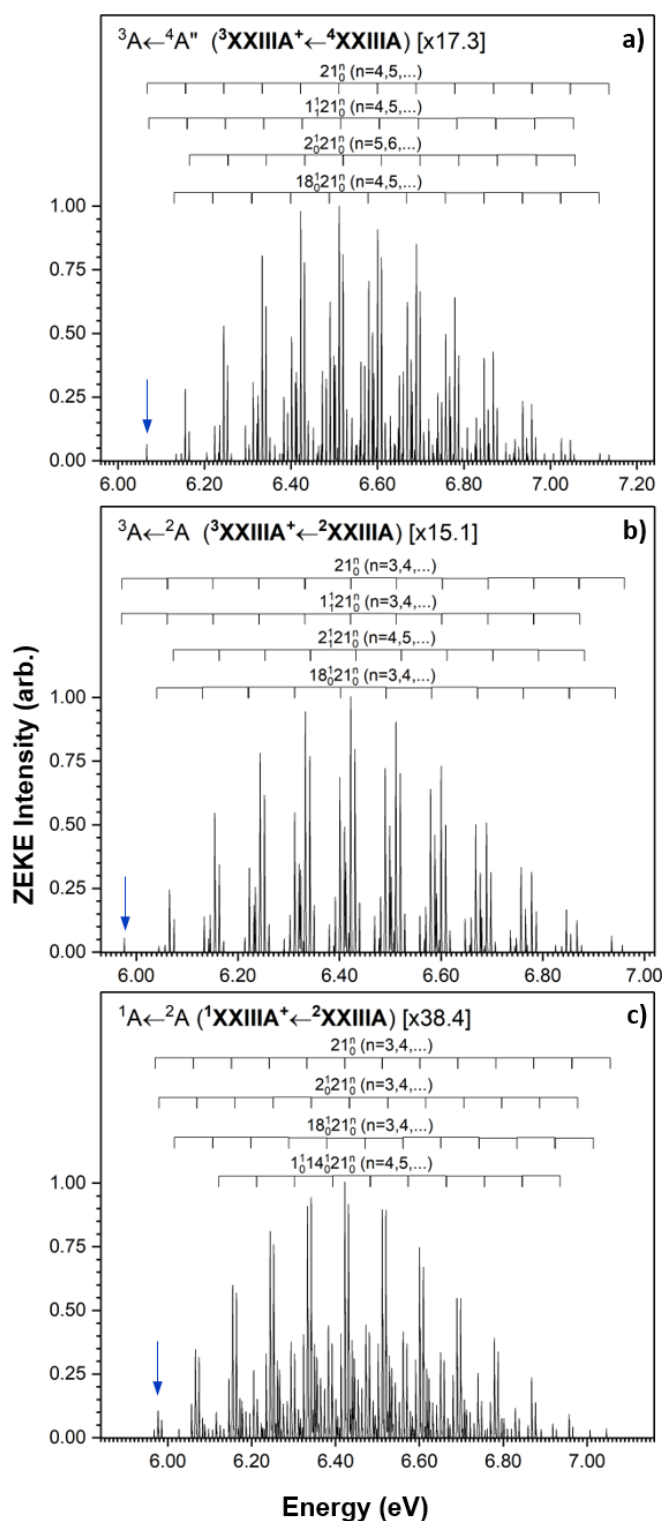


Figure 9.35: Calculated ZEKE spectra for AuCe₃O₅ ionisation transitions: **a).** ${}^3A \leftarrow {}^4A''$ (${}^3XXIII A^+ \leftarrow {}^4XXIII A$), **b).** ${}^3A \leftarrow {}^2A$ (${}^3XXIII A^+ \leftarrow {}^2XXIII A$) and **c).** ${}^1A \leftarrow {}^2A$ (${}^1XXIII A^+ \leftarrow {}^2XXIII A$). Spectral intensities are normalised to the most intense peak in each spectrum with scaling factors shown. Prominent vibronic peaks are assigned. The vibronic transition likely to correspond to the appearance of ion signal in each spectrum is labelled with a blue arrow.

9.8.4. Simulated PIE Spectrum for AuCe₃O₅

A PIE spectrum for the AuCe₃O₅ system is calculated by integration of the combined ${}^3A \leftarrow {}^4A''$ (${}^3XXIII A^+ \leftarrow {}^4XXIII A$), ${}^3A \leftarrow {}^2A$ (${}^3XXIII A^+ \leftarrow {}^2XXIII A$) and ${}^1A \leftarrow {}^2A$ (${}^1XXIII A^+ \leftarrow {}^2XXIII A$) ZEKE spectra. The simulated PIE spectrum is presented in Figure 9.36. The spectrum presents a very broad onset from ca. 6.05 eV to a plateau at ca. 6.98 eV. Vibronic transitions calculated below 6.05 eV appear to have a negligible influence on the ion signal; it is unlikely these transitions could be discerned from the ion signal baseline in the experimental PIE spectrum. Thus, the AE is assigned a value of 6.05 eV. This calculated AE value is considerably higher than the photon energies used in this work and thus consistent with the non-detection of the AuCe₃O₅ ion in any mass spectra. The calculated adiabatic IE value is assigned to the DFT-calculated IE for the ${}^3A \leftarrow {}^4A''$ (${}^3XXIII A^+ \leftarrow {}^4XXIII A$) transition as 5.71 eV. However, the calculated IE for the AuCe₃O₅ cluster system is ca. 0.34 eV lower than the calculated AE; the calculated AE value of ca. 6.05 eV is consistent with the non-detection of the AuCe₃O₅ ion in any photo-ionisation mass spectra.

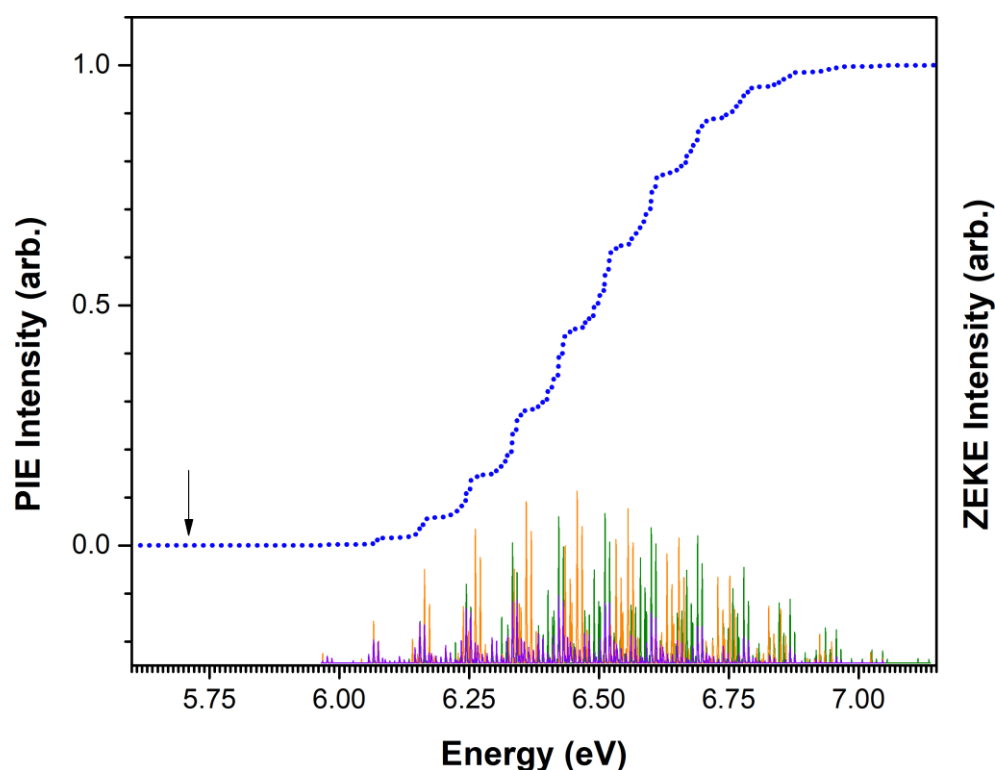


Figure 9.36: Calculated AuCe₃O₅ PIE spectrum (blue dotted line). Calculated ZEKE spectra for the ${}^3A \leftarrow {}^4A''$ (${}^{\beta}XXIII A^+ \leftarrow {}^4XXIII A$), ${}^3A \leftarrow {}^2A$ (${}^{\beta}XXIII A^+ \leftarrow {}^2XXIII A$) and ${}^1A \leftarrow {}^2A$ (${}^1XXIII A^+ \leftarrow {}^2XXIII A$) ionisation processes are shown below the PIE spectrum in green, orange and violet, respectively. The adiabatic ionisation energy is labelled with a black arrow.

9.9. PIE Spectrum and DFT Results for AuCe₃O₆

9.9.1. AuCe₃O₆ Experimental PIE Spectrum

The AuCe₃O₆⁺ cluster ion was not detected in the mass spectrum recorded following 213 nm (5.82 eV) photo-ionisation, or in any mass spectra recorded at lower photon energies. The non-detection of this species is attributed to a high IE which is supported by DFT calculations presented *vide infra*. While an experimental PIE spectrum is not presented, DFT calculated structures are presented in addition to ZEKE and PIE simulations to provide insight on the AuCe₃O₆ electronic and geometric structures.

9.9.2. DFT Calculations for AuCe₃O₆

DFT calculated AuCe₃O₆ neutral and cationic species are calculated in Figures 9.37 and 9.38. Only one unique neutral species is shown here which comprises a C_s structure in the ²A'' electronic state – labelled ²XXIV. The Ce and Au atoms are arranged in a – slightly bent – diamond geometry with four of the oxygen atoms peripherally bridging the Ce-Ce and Au-Ce bonds. The remaining two O atoms are positioned above and below the AuCe₃ pseudo-plane. One oxygen atom is facially bound to the three Ce atoms, while the other O atom bridges two Ce atoms across the centre of the cluster. Numerous alternative AuCe₃O₆ structures were calculated with energies over 1 eV higher than the ²XXIV species; these structures are unlikely to form under the experimental conditions utilised in this work and are thus not shown.

Two AuCe₃O₆⁺ cationic species are calculated; these include a C_s singlet in the ¹A' electronic state and a C₁ triplet in the ³A electronic state, labelled ¹XXIV⁺ and ³XXIV⁺ respectively. The ¹XXIV⁺ cation maintains the same geometric structure as the neutral ²XXIV species; albeit with some minor bond length changes. The ³XXIV⁺ species shows more substantial structural deformation from the neutral ²XXIV geometry, with no Au-Ce bonds calculated for the cation. IEs for the ¹A'←²A'' (¹XXIV⁺←²XXIV) and ³A←²A'' (³XXIV⁺←²XXIV) ionisation processes are calculated as 6.845 eV and 7.809 eV, respectively. The high IE values calculated for both ionisation processes are consistent with the non-detection of the AuCe₃O₆ ion peak in experimental mass spectra. The ¹A'←²A'' (¹XXIV⁺←²XXIV) process is shown in Figure 9.37 as a green arrow, while the ³A←²A'' (³XXIV⁺←²XXIV) transition is shown as a red dotted arrow due to low vibronic peak intensities calculated during ZEKE simulations (vide infra).

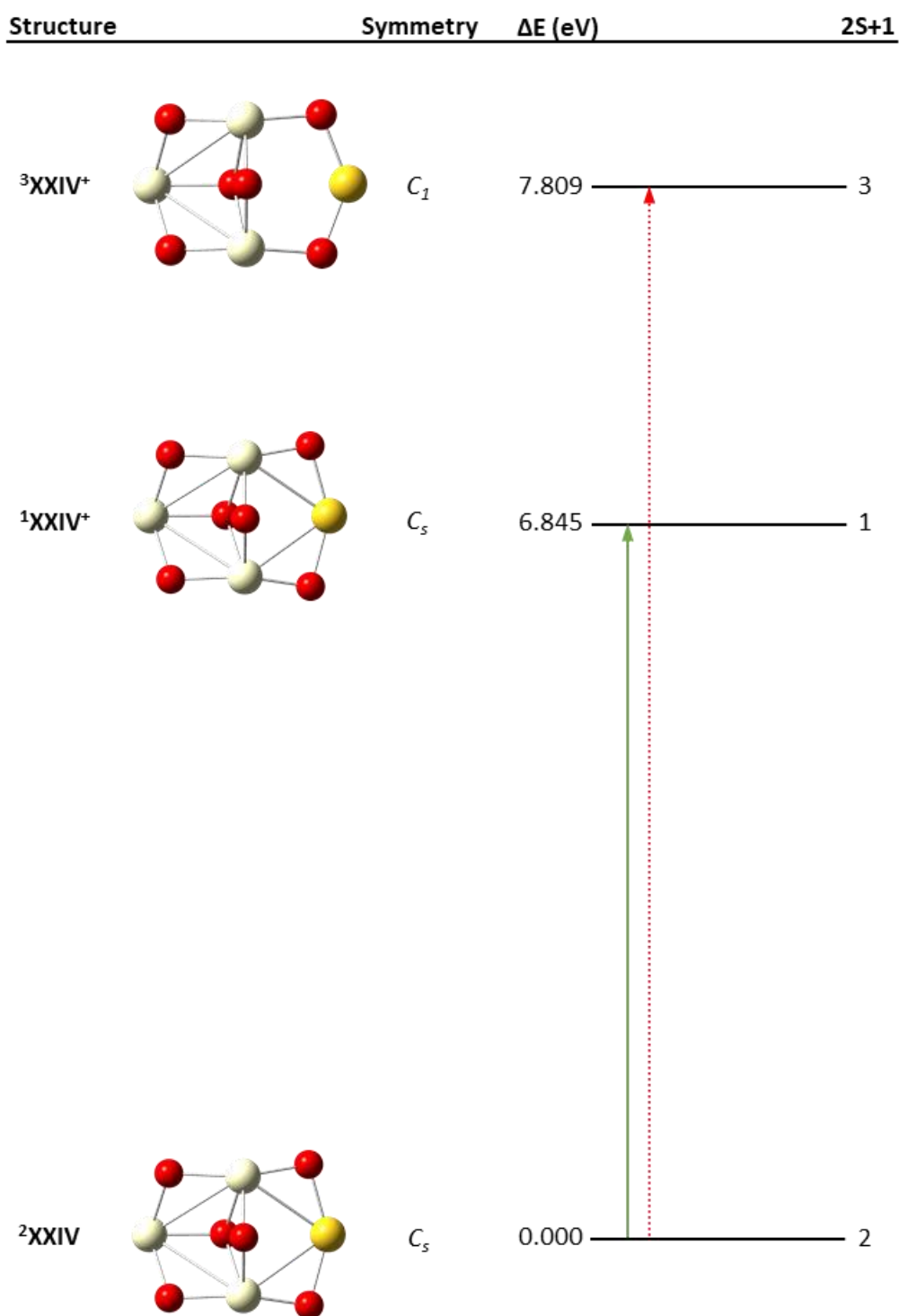


Figure 9.37: Calculated structures for AuCe_3O_6 . Potential ionisation transitions are shown. Ionisation processes with low ZEKE intensities (*vide infra*) are shown as red dotted arrows.

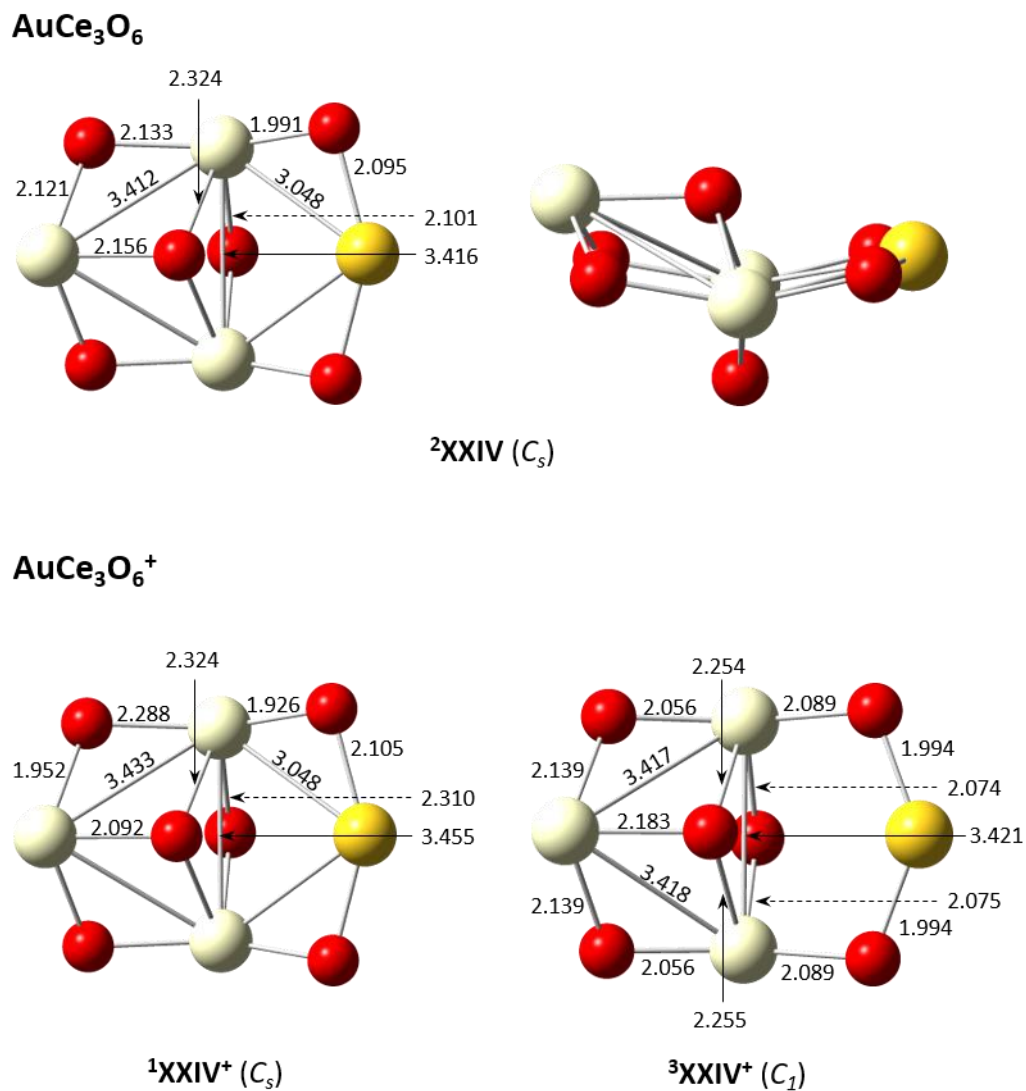


Figure 9.38: Calculated AuCe_3O_6 neutral (top) and cationic (below) structures. Top and side views of the neutral structure are shown. Bond lengths are presented in Å. Point groups are shown in brackets.

9.9.3. ZEKE Spectral Simulations for AuCe₃O₆

Calculated ZEKE spectra are shown for the $^1A' \leftarrow ^2A''$ ($^1XXIV^+ \leftarrow ^2XXIV$) and $^3A \leftarrow ^2A''$ ($^3XXIV^+ \leftarrow ^2XXIV$) ionisation processes in Figures 9.39(a) and (b), respectively. Due to extensive number of vibrational modes inherent to the AuCe₃O₆ system, a full Duschinsky treatment was not viable; calculations were instead performed using the Parallel Approximation.

Vibronic peaks of the $^1A' \leftarrow ^2A''$ ($^1XXIV^+ \leftarrow ^2XXIV$) and $^3A \leftarrow ^2A''$ ($^3XXIV^+ \leftarrow ^2XXIV$) ZEKE spectra overlap in the ca. 7.80 – 8.22 eV region. This is largely due to the broad spectrum calculated for the $^1A' \leftarrow ^2A''$ ($^1XXIV^+ \leftarrow ^2XXIV$) process, which spans a ca. 0.9 eV energy range. Thus, despite the ca. 0.95 eV difference in calculated IEs between the $^1A' \leftarrow ^2A''$ ($^1XXIV^+ \leftarrow ^2XXIV$) and $^3A \leftarrow ^2A''$ ($^3XXIV^+ \leftarrow ^2XXIV$) transitions, both transitions would be expected to underlie the same PIE onset. Comparison of the scaling factors used to normalise the most intense vibronic peaks of the $^1A' \leftarrow ^2A''$ ($^1XXIV^+ \leftarrow ^2XXIV$) and $^3A \leftarrow ^2A''$ ($^3XXIV^+ \leftarrow ^2XXIV$) ZEKE spectra – which are 351 and 11750, respectively – show the $^1A' \leftarrow ^2A''$ ($^1XXIV^+ \leftarrow ^2XXIV$) ionisation process is far more dominant than the $^3A \leftarrow ^2A''$ ($^3XXIV^+ \leftarrow ^2XXIV$) process. The contribution of the $^3A \leftarrow ^2A''$ ($^3XXIV^+ \leftarrow ^2XXIV$) ionisation process to the PIE spectrum would therefore be negligible. Thus, only the $^1A' \leftarrow ^2A''$ ($^1XXIV^+ \leftarrow ^2XXIV$) process is considered.

The $^1A' \leftarrow ^2A''$ ($^1XXIV^+ \leftarrow ^2XXIV$) ZEKE spectrum – shown in Figure 9.39(a) comprises a number of long vibronic progressions of the ν_{24} mode; the most pertinent of which include the $18_0^1 24_0^n$, $18_0^1 22_0^1 24_0^n$, $18_0^2 22_0^1 24_0^n$ and $13_0^1 18_0^1 22_0^1 24_0^n$ progressions. The ν_{24} mode describes displacement of the facially bound oxygen atom and the two peripheral oxygen atoms bridging the Ce-Ce bonds; these oxygen atoms toward the left cerium atom – in Figure 9.38 – along the coordinates of their respective Ce-O bonds. The common progression of the ν_{24} mode would suggest the neutral 2XXIV species undergoes distortion along the ν_{24} vibrational coordinate following photo-ionisation. The 0_0^0 transition at 6.845 eV is calculated ca. 0.5 eV lower in energy than the lowest energy vibronic transition. Thus, the AE would be expected to be higher in energy than the IE for the AuCe₃O₆ PIE spectrum.

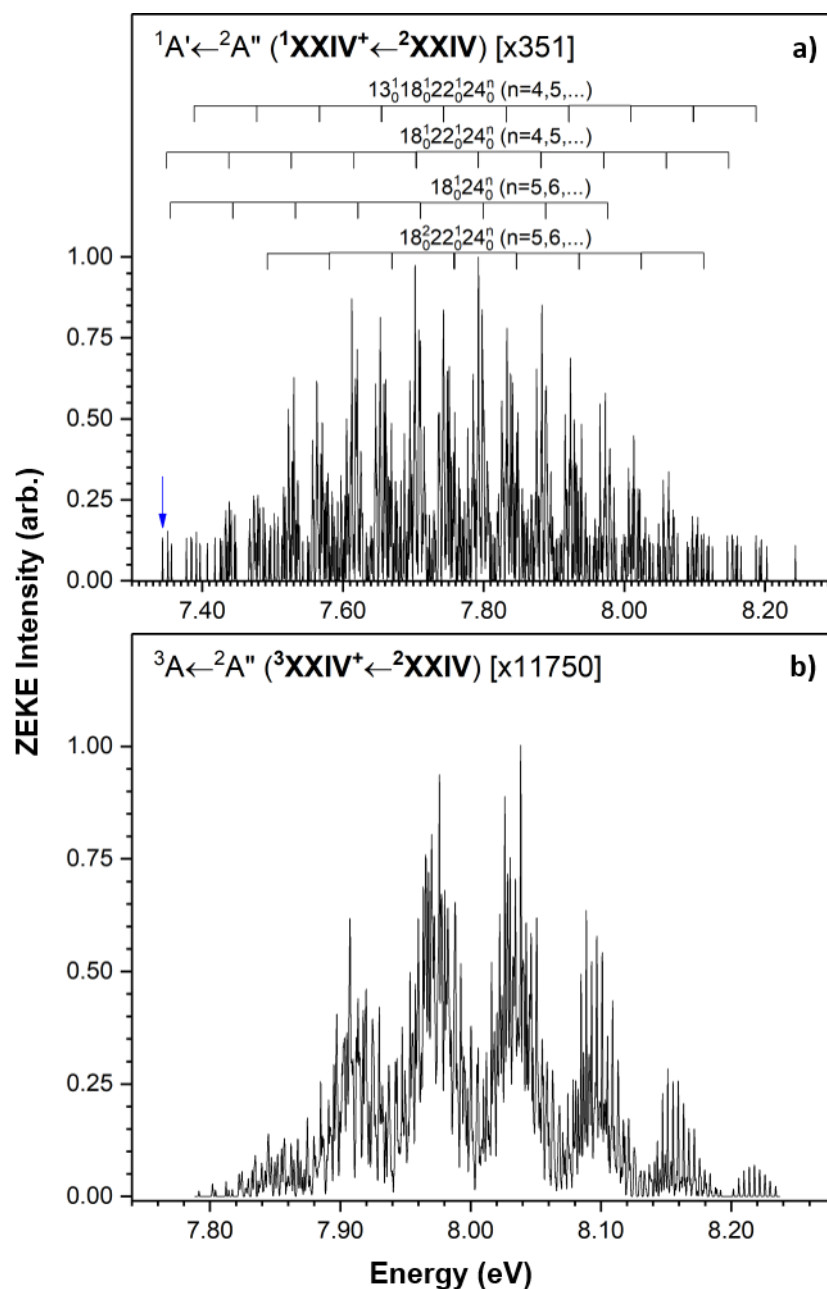


Figure 9.39: Calculated ZEKE spectra for AuCe₃O₆ ionisation transitions: **a).** ${}^1A' \leftarrow {}^2A''$ (${}^1XXIV^+ \leftarrow {}^2XXIV$) and **b).** ${}^3A \leftarrow {}^2A''$ (${}^3XXIV^+ \leftarrow {}^2XXIV$). Spectral intensities are normalised to the most intense peak in each spectrum with scaling factors shown. Prominent vibronic peaks are assigned. The vibronic transition likely to correspond to the appearance of ion signal in each spectrum is labelled with a blue arrow.

9.9.4. Simulated PIE Spectrum for AuCe_3O_6

A calculated PIE spectrum for the AuCe_3O_6 cluster system –calculated via integration of the $^1\text{A}' \leftarrow ^2\text{A}''$ ($^1\text{XXIV}^+ \leftarrow ^2\text{XXIV}$) ZEKE spectrum – is presented in Figure 9.40. The PIE spectrum presents a broad onset from the AE at 7.45 eV to a plateau of maximum ion signal at ca. 8.20 eV. The calculated AE value is considerably higher than the photon energies available in this work and is thus consistent with the non-detection of the AuCe_3O_6 ion during photo-ionisation experiments. The IE_{ad} value for the AuCe_3O_6 system is taken from the DFT-calculated IE for the $^1\text{A}' \leftarrow ^2\text{A}''$ ($^1\text{XXIV}^+ \leftarrow ^2\text{XXIV}$) ionisation transition; this gives a calculated IE value of 6.85 eV. However, the experimental IE_{ad} may be slightly lower than this value due to the tendency of the DFT method employed in this work to overpredict IEs.

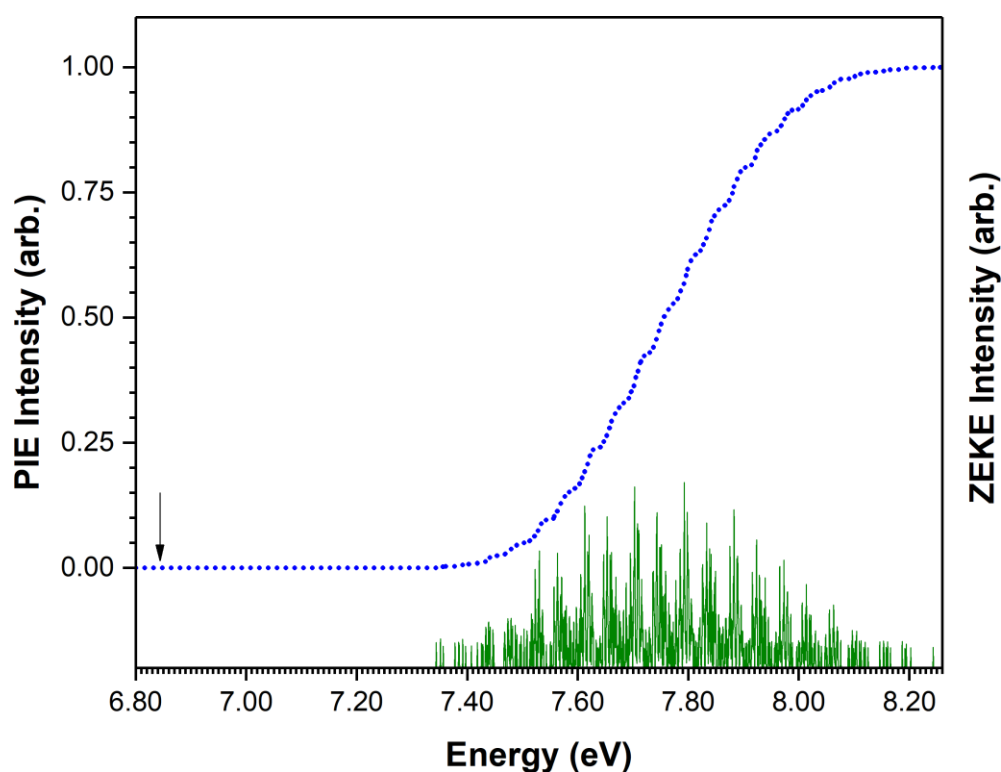


Figure 9.40: Calculated AuCe_3O_6 PIE spectrum, (blue dotted line). The calculated ZEKE spectrum for the $^1\text{A}' \leftarrow ^2\text{A}''$ ($^1\text{XXIV}^+ \leftarrow ^2\text{XXIV}$) ionisation process is shown below the PIE spectrum in green. The adiabatic ionisation energy is labelled with a black arrow.

9.10. Comparison of Experimental and Calculated AuCe₃O_n Ionisation Energies

Experimental and calculated adiabatic IEs for the AuCe₃O_n cluster series are presented in Figure 9.41. Experimental IE values are presented for the AuCe₃, AuCe₃O, AuCe₃O₂ and AuCe₃O₃ clusters. These IE values have an associated error of ±0.05 eV which is too small to be shown in Figure 9.41 and therefore not presented.

Calculated IEs are presented for the AuCe₃O_n ($n=0-6$) clusters. The calculated IE values are corrected to experimental IE values using the methods described in Chapter 3. Briefly, the calculated IE for the AuCe₃ cluster is corrected to the experimental IE (involving a correction of -0.18 eV). The same correction is then applied to the calculated IEs for the remainder of the clusters in the AuCe₃O_n series. This method of offsetting the calculated IEs is consistent with previous work by Gentleman et al.^{4,5} and Dryza et al.⁶⁻⁸ and accounts for any systematic errors in IE predictions due to the use of frozen cores. The -0.18 eV correction applied to the AuCe₃O_n clusters is consistent with the -0.20 eV, -0.18 eV and -0.22 eV correction applied to the Ce₂O_n, Ce₃O_n and AuCe₂O_n clusters, respectively. Error bars of ±0.2 eV are applied to each of the AuCe₃O_n calculated IE values to account for the inherent uncertainty associated with DFT calculations regarding both the energies of structural isomers and transition energies.

Calculated AE values are additionally presented for the AuCe₃O₄, AuCe₃O₅ and AuCe₃O₆ species since the AEs for these species were calculated to be substantially higher than their respective IEs. Calculated AE values for the AuCe₃O₄, AuCe₃O₅ and AuCe₃O₆ clusters are assigned from the lowest energy vibronic transitions in their respective calculated ZEKE spectra.

Comparison of the calculated and experimental AuCe₃O_n IEs shows both the AuCe₃O and AuCe₃O₂ IEs are calculated as slightly higher than their respective experimental IEs, while the calculated AuCe₃O₃ IE is slightly lower than the experimental value. This trend is consistent with those reported previously for the Ce₃O_n and AuCe₂O_n calculated IEs in Chapters 6 and 8, respectively: the IE of the cluster species for which any further oxidation causes a sharp

increase in IE – namely the Ce_3O_4 , AuCe_2O_2 and AuCe_3O_3 species – is calculated to be lower than the experimental value; all other calculated IEs are higher than their respective experimental values. Further benchmarking studies – using experimental IE values for more highly oxidised clusters, if available – would be required to identify the source of this anomaly. Regardless, an excellent correlation is found between the calculated and experimental IEs; with all calculated IEs within 0.2 eV of their respective experimental values. Experimental IE values are not presented for the AuCe_3O_n ($n=4-6$) clusters for comparison. However, the high IEs – and even higher AEs – calculated for these species are consistent with the non-detection of these cluster ions during photo-ionisation experiments. From the excellent agreement between both the calculated and experimental ionisation energies, and between the calculated and experimental PIE spectra shown previously, reliable inferences about the electronic and geometric structures can be made from the calculated AuCe_3O_n structures presented in this chapter.

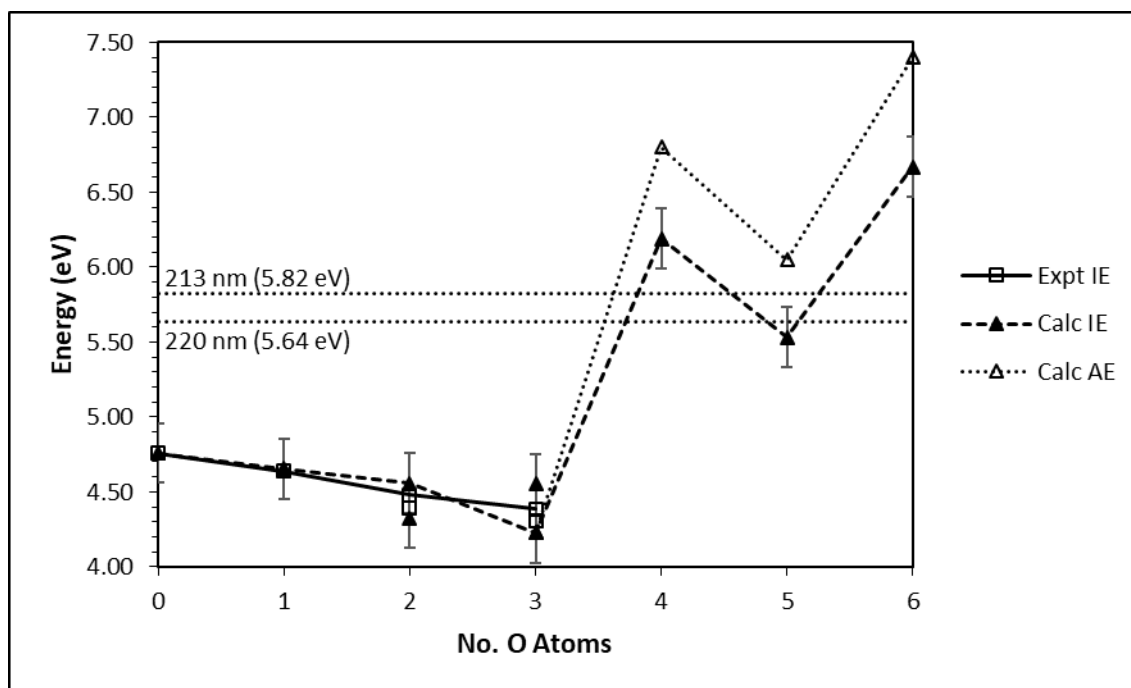


Figure 9.41: Experimental and calculated ionisation energies for the AuCe_3O_n series with sequential oxidation. Primary and secondary IEs are shown for the AuCe_3O_2 and AuCe_3O_3 species. The experimental and calculated IE trends for the primary onsets are shown as solid and dashed lines, respectively. Calculated appearance energies are presented for the AuCe_3O_4 , AuCe_3O_5 and AuCe_3O_6 species with the AE trend shown as a dotted line. Horizontal lines are drawn at 220 nm (5.64 eV) and 213 nm (5.82 eV) to represent the upper energy bound of the tuneable laser source and the highest energy for which photo-ionisation mass spectra can be recorded, respectively.

9.11. Comparison of Experimental Appearance Energies for Ce_3O_n and AuCe_3O_n Clusters

A comparison of the experimental appearance energies for the undoped Ce_3O_n clusters and gold-doped AuCe_3O_n clusters provides a rudimentary analysis on the effects of gold doping of cerium oxide clusters using experimental data. Experimental appearance energies for both the Ce_3O_n and AuCe_3O_n clusters are presented in Figure 9.42 (with a detailed analysis on the effects of gold doping on cerium oxide cluster properties – using DFT calculations – presented in Chapter 10). Appearance energies for both the first onset of ion signal and the primary onset ion signal – which corresponds to the onset with the greatest increase in ion signal – are presented as dashed and solid lines, respectively, in Figure 9.42. The Ce_3O_5 AE value is approximated as 5.73 eV – which represents the midpoint of the bracketed 5.64 – 5.82 eV AE value presented earlier – with the Ce_3O_4 – Ce_3O_5 AE trends presented as dotted lines. The

AuCe_3O_4 and AuCe_3O_5 AEs are not presented due to these species not being detected in any mass spectra.

Comparison of the first onset AE values for the Ce_3O_n and AuCe_3O_n clusters (shown as blue and gold dashed lines in Figure 9.42, respectively) shows a general trend where the AuCe_3O_n AEs are higher than their respective Ce_3O_n AE values by 0.25 – 0.40 eV. Similarly, the AuCe_3O_n primary onset AE values are generally 0.30 – 0.45 eV higher in energy than their respective Ce_3O_n primary onset AE values (shown as solid gold and blue lines in Figure 9.42, respectively). The exception to this is the AuCe_3O cluster, which has an AE value 0.02 eV higher than the respective Ce_3O AE. Thus, Au adsorption appears to have minimal effect on the Ce_3O – lowest energy neutral – cluster species. This is further verified by calculations presented in Chapter 10.

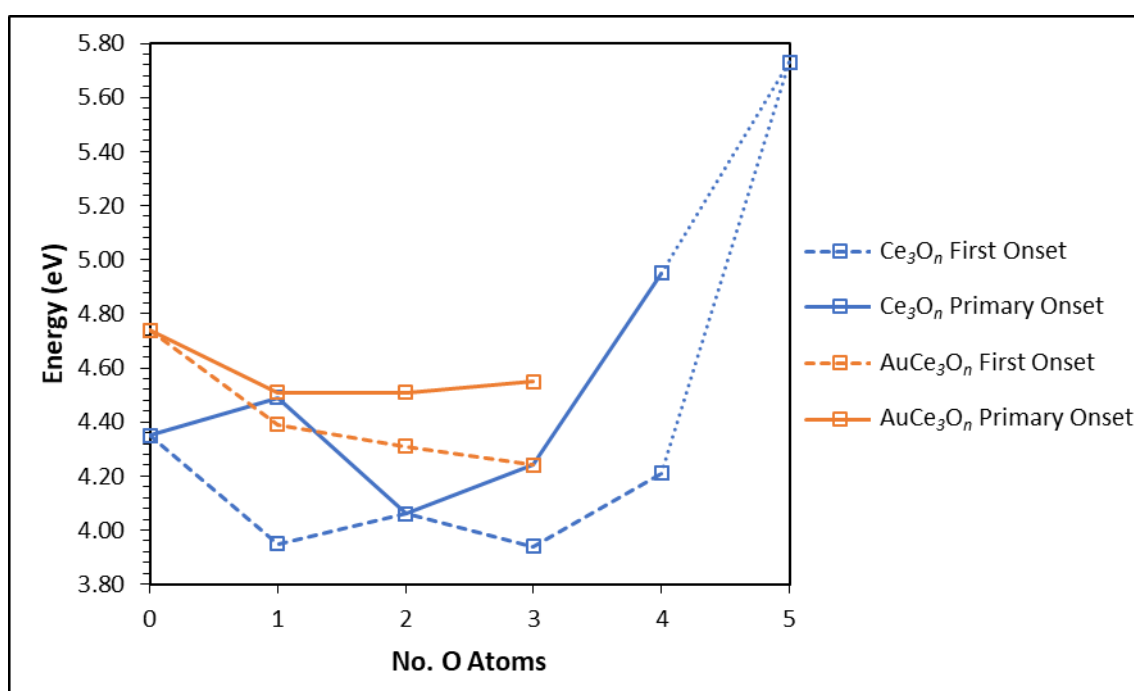


Figure 9.42: Experimental appearance energies for the Ce_3O_n (blue) and AuCe_3O_n (gold) cluster series with sequential oxidation. Appearance energy trends are shown for both the first onset of ion signal (dashed lines) and the primary onset (solid lines). The Ce_3O_5 AE is approximated; therefore, the Ce_3O_4 - Ce_3O_5 AE trends are presented as dotted lines.

9.12. References

- (1) Young, D. C. *Computational Chemistry: A Practical Guide for Applying Techniques to Real-World Problems*; John Wiley & Sons: New York, 2001.
- (2) Addicoat, M. A. *Computational Investigations into the Structure and Reactivity of Small Transition Metal Clusters*, PhD Thesis, The University of Adelaide, 2009.
- (3) Dolg, M. *Computational Methods in Lanthanide and Actinide Chemistry*; John Wiley & Sons, Ltd.: West Sussex, 2015.
- (4) Gentleman, A. S. *The Effect of Sequential Oxidation and Composition on the Structural and Electronic Properties of Gas Phase Transition-Lanthanide Bimetallic Clusters*, PhD Thesis, The University of Adelaide, 2014.
- (5) Gentleman, A. S.; Addicoat, M. A.; Dryza, V.; Gascooke, J. R.; Buntine, M. A.; Metha, G. F. *J. Chem. Phys.* **2009**, *130* (16), 64311.
- (6) Dryza, V.; Addicoat, M. A.; Gascooke, J. R.; Buntine, M. A.; Metha, G. F. *J. Phys. Chem. A* **2005**, *109* (49), 11180.
- (7) Dryza, V.; Addicoat, M. A.; Gascooke, J. R.; Buntine, M. A.; Metha, G. F. *J. Phys. Chem. A* **2008**, *112* (25), 5582.
- (8) Dryza, V.; Gascooke, J. R.; Buntine, M. A.; Metha, G. F. *Phys. Chem. Chem. Phys.* **2009**, *11* (7), 1060.

Chapter Ten

Effects of Gold Adsorption on the Catalytic Properties of AuCe_mO_n (m=2,3; n=0-2m) Clusters

This chapter investigates the interactions between the Ce_mO_n cluster and the Au adatom. The structures of Ce_mO_n and their respective gold doped AuCe_mO_n clusters are compared to provide insight to the deposition sites of gold atoms on the Ce_mO_n cluster surface. The potential charge transfer mechanisms occurring within each of the AuCe_mO_n (m=2,3; n=0–2m) clusters are then investigated via an analysis of calculated Hirshfeld charges. Finally, the effects of Au adsorption on the Ce_mO_n cluster surface are explored with respect to a catalytic CO oxidation cycle. This includes an analysis of the effects of Au adsorption on the HOMO and LUMO energies and the oxygen affinities of the AuCe_mO_n clusters.

10.1. Au Deposition Site: Ce Vacancy or O vacancy?

One of the pertinent questions regarding the interaction between gold and cerium oxide concerns the preferred deposition site of the gold atom on the cerium oxide surface^{1–4}. Specifically, does the gold atom deposit on an oxygen vacancy site, a cerium vacancy site, or on the defect-free surface? This point of contention is investigated here by comparison of the calculated AuCe₂O_n and AuCe₃O_n clusters – previously shown in Chapters 8 and 9, respectively – to Ce₂O_n and Ce₃O_n calculated cluster geometries – previously shown in Chapters 6 and 7, respectively. A comparison between the relevant AuCe_mO_n cluster and the most geometrically aligned Ce_mO_n cluster species may provide insight into the preferred deposition sites of Au atoms on various cerium oxide surfaces; favourable substitution of either cerium or oxygen atoms with a gold atom should result in minimal structural deformation.

Calculated AuCe₂O_n ($n=0–4$) cluster geometries are presented in Figure 10.1. The calculated Ce_mO_{n+1} or Ce_{m+1}O_n structure most geometrically aligned with each AuCe₂O_n cluster is presented below the respective AuCe₂O_n species. The AuCe₂, AuCe₂O, AuCe₂O₂ and AuCe₂O₃ structures show similar geometries to their respective Ce₂O_{n+1} clusters which include the Ce₂O, Ce₂O₂, Ce₂O₃ and Ce₂O₄ species, respectively. The gold atom is clearly substituting an oxygen atom in each of these AuCe₂O_n ($n=0–3$) structures, inferring preferable Au deposition at an oxygen vacancy site. However, the specific oxygen vacancy site appears to vary with oxidation of the Ce_mO_n cluster. For example, the gold atom substitutes a bridging oxygen in both the AuCe₂ and AuCe₂O species. By contrast, the gold atom substitutes a singly attached oxygen atom in the AuCe₂O₂ and AuCe₂O₃ clusters, when bridging sites are available. This highlights the versatility of the Au atom in bonding to the cerium oxide surface. While Au attachment atop F-centres on bulk ceria surfaces has typically been reported with the Au atom bridging two Ce atoms^{2,5} (as shown in Figure 10.3(a)), the calculations presented here suggest Au attachment to oxygen deficient sites via a single Au-Ce bond is also viable. Thus, Au adsorption to reduced ceria sites may vary depending on the extent to which the site is reduced.

In contrast to the AuCe_2O_n ($n=0-3$) clusters, where the bonding arrangements are consistent with Au deposition at an O vacancy, the AuCe_2O_4 structure appears to be more geometrically aligned with the Ce_3O_4 cluster than any Ce_2O_n cluster species. This would suggest Au substitution with a cerium atom. The bonding arrangement of the AuCe_2O_4 cluster shows the Au atom bonded to both O and Ce atoms; whereas the AuCe_2O_n ($n=0-3$) clusters show no Au-O bonding arrangement. This is consistent with the Au atom replacing a Ce atom, which in all calculated structures binds to both O atoms and other Ce atoms. Moreover, the bridging arrangement of the Au atom between two O atoms is consistent with previous calculations by Nolan et al.^{6,7} of Au deposition to Ce vacancy sites on bulk surfaces (as shown in Figure 10.3(b)). The stoichiometric ratio of Ce and O atoms within the AuCe_2O_4 cluster is, however, more consistent with Au deposition at a CeO_2 vacancy site than a Ce^{4+} vacancy (which would be modelled by an AuCe_3O_8 cluster). Moreover, CeO_2 vacancy sites have been shown via DFT calculations to form in preference to Ce^{4+} vacancies since they are electronically neutral¹.

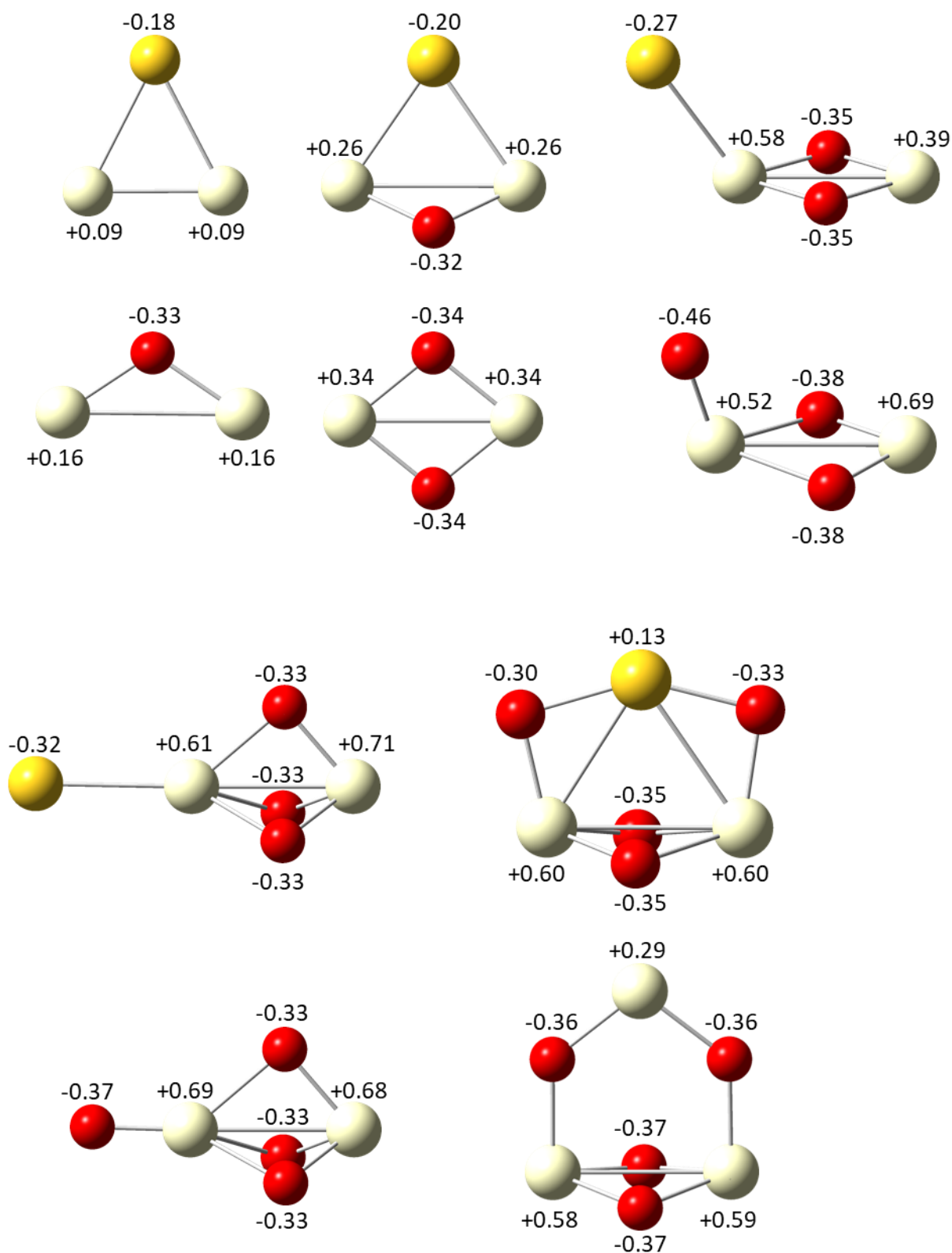


Figure 10.1: Calculated $AuCe_2O_n$ ($n=0-4$) neutral structures with Hirshfeld atomic charges. Corresponding Ce_mO_{n+1} or $Ce_{m+1}O_n$ structures are shown below each $AuCe_2O_n$ structure to highlight potential Au deposition sites.

Calculated AuCe_3O_n ($n=0-6$) clusters are presented in Figure 10.2. The calculated $\text{Ce}_m\text{O}_{n+1}$ cluster geometries which best correlate with each of the AuCe_3O_n ($n=0-4$) clusters are also shown in Figure 10.2. Similar geometries are found between the AuCe_3 , AuCe_3O , AuCe_3O_2 and AuCe_3O_3 clusters and their respective Ce_3O , Ce_3O_2 , Ce_3O_3 and Ce_3O_4 species; in all cases an oxygen atom can be substituted for a gold atom with minimal change in structure. Thus, the preferred Au deposition site on the Ce_3O , Ce_3O_2 , Ce_3O_3 and Ce_3O_4 cluster surfaces appears to be an oxygen vacancy. Moreover, the Au atom in each of the AuCe_3O_n ($n=0-4$) species is bound to cerium atoms only; no Au-O bonding is observed. This is consistent with Au deposition at an oxygen vacancy site (shown in Figure 10.3(a)) since no direct O-O bonding is observed in any calculated Ce_mO_n or AuCe_mO_n cluster.

The nature of Au-Ce bonding within each of the AuCe_3O_n ($n=1-4$) species follows a similar trend to the AuCe_2O_n clusters which appears to be dependent on the degree of oxidation of the cluster. The AuCe_3 , AuCe_3O and AuCe_3O_2 species each describe a gold atom bound to a Ce_3 face with the oxygen atoms in the AuCe_3O and AuCe_3O_2 clusters forming bridging arrangements between two cerium atoms. The AuCe_3O_3 cluster is calculated with two low-lying structures in which the gold atom is bound either along a Ce-Ce bridge or to the Ce_3 face (the bridging arrangement is shown here; the facially bound arrangement is presented in Chapter 9). Thus, both facial and bridging arrangements for the Au-Ce interaction are favourable. Finally, the AuCe_3O_4 species has the gold atom singly bound to one cerium atom; the oxygen atoms then occupy bridging and facial positions across the Ce-Ce bonds and the Ce_3 face, respectively. Comparison to the AuCe_2O_n clusters discussed previously shows some general trends with regard to the Au-Ce bonding arrangement for oxygen deficient AuCe_mO_n cluster species; the Au atom will adsorb in either a facial or bridging Au-Ce arrangement to the highly oxygen deficient species, and form single Au-Ce bonds in moderately oxygen deficient clusters.

The AuCe_3O_5 and AuCe_3O_6 cluster geometries are both calculated to be vastly different from any of the Ce_3O_n structures shown in this work. Thus, no correlating Ce_3O_n species are shown. Both the AuCe_3O_5 and AuCe_3O_6 clusters are calculated with the gold atom inserted between

two oxygen atoms – similar to the $AuCe_2O_4$ structure – consistent with occupation of a Ce vacancy site, as shown in Figure 9.3(b). Moreover, the gold atoms in both the $AuCe_3O_5$ and $AuCe_3O_6$ species display Au-O bonding – in addition to Au-Ce bonding – which is not found in any of the $AuCe_3O_n$ ($n=0-4$) species discussed previously. The Au-ceria interactions displayed by both the $AuCe_3O_5$ and $AuCe_3O_6$ clusters appear to be consistent with an Au atom deposited at a CeO_2 vacancy, where the Au atom bridges two sub-surface O atoms¹. This unexpected finding – since the Ce_3O_5 and Ce_3O_6 clusters are stoichiometrically consistent with an oxygen vacancy site and the defect-free surface, respectively – again draws from previous work by Jenkins et al.¹, who showed that CeO_2 vacancies form quite readily on the bulk ceria surface. Thus, the $AuCe_3O_5$ and $AuCe_3O_6$ clusters can also be considered as stoichiometrically consistent models for Au deposition to a Ce_4O_8 cluster with CeO_3 and CeO_2 vacancies, respectively. Jenkins et al. have reported in their calculations of gold-doped ceria surfaces that the Au atom prefers to adsorb to a CeO_2 vacancy site than either an oxygen vacancy site or the defect-free surface; this is consistent with the calculations shown here. However, the surprising result from these calculations, that Au adsorbs readily to both CeO_2 and O vacancy sites, may explain the previous conflicting works regarding the preferred Au deposition site on the ceria surface¹⁻¹⁰.

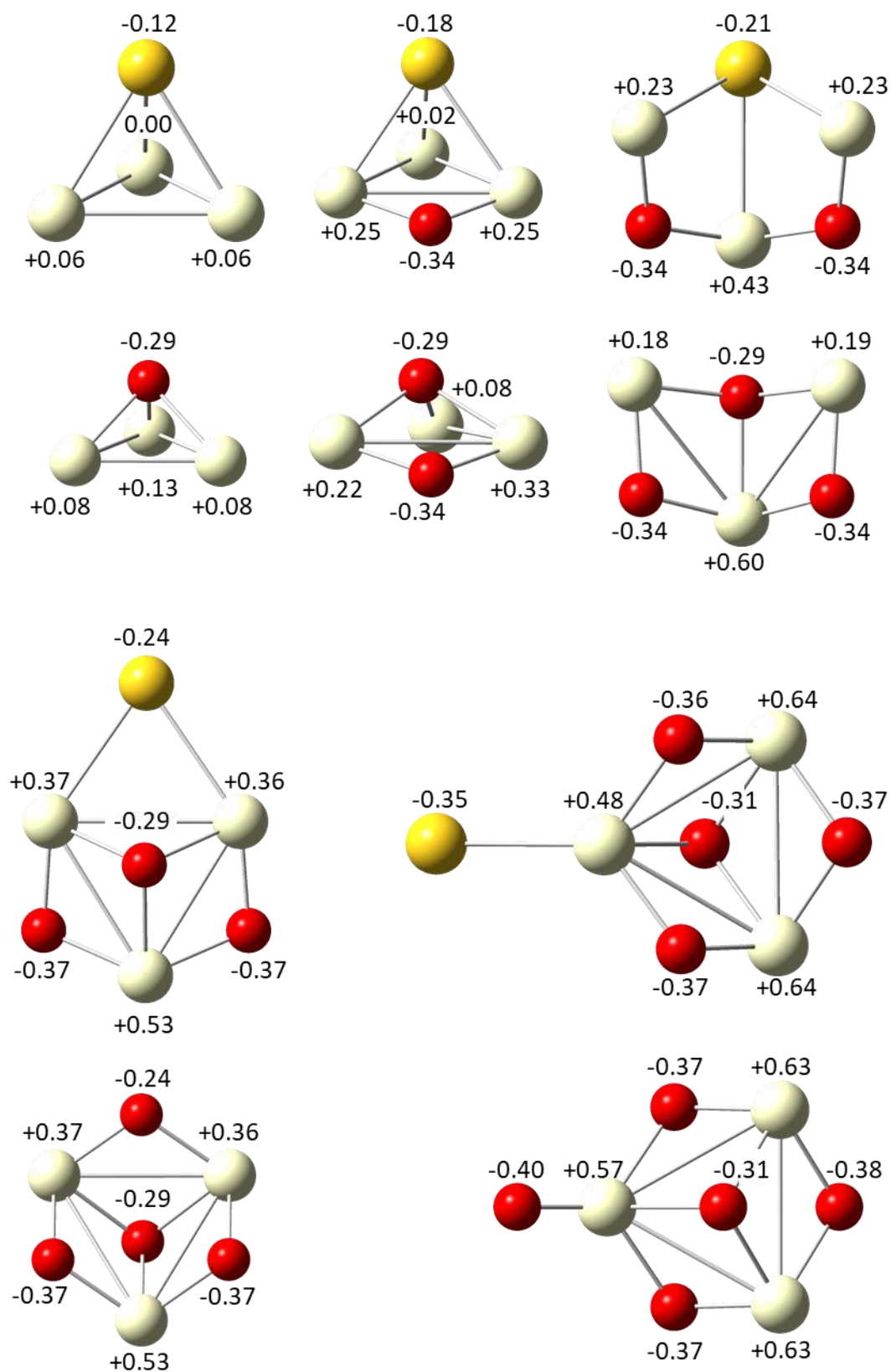


Figure 10.2(a): Calculated AuCe_3O_n ($n=0-4$) neutral structures with Hirshfeld atomic charges. Corresponding $\text{Ce}_m\text{O}_{n+1}$ structures are shown below each AuCe_3O_n structure to highlight potential Au deposition sites.

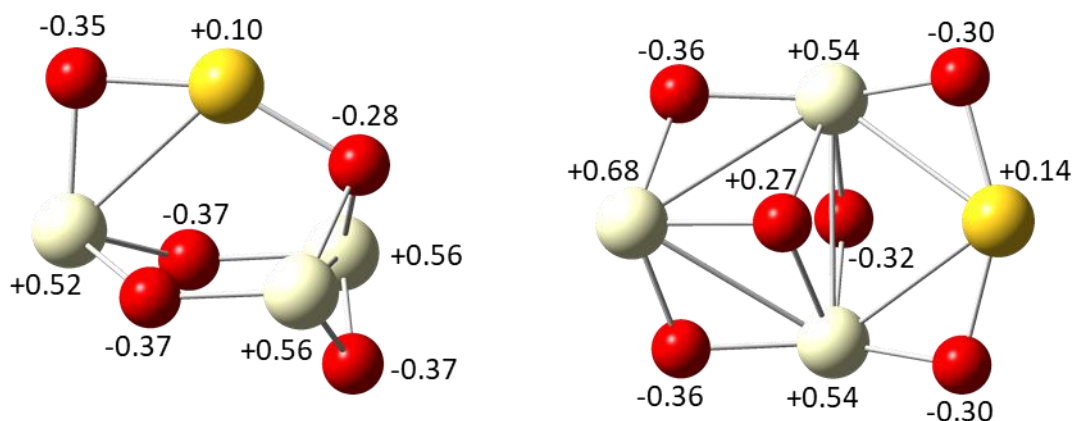


Figure 10.2(b): Calculated $AuCe_3O_n$ ($n=5,6$) neutral structures with Hirshfeld atomic charges. Corresponding Ce_mO_n structures for these species were not calculated.

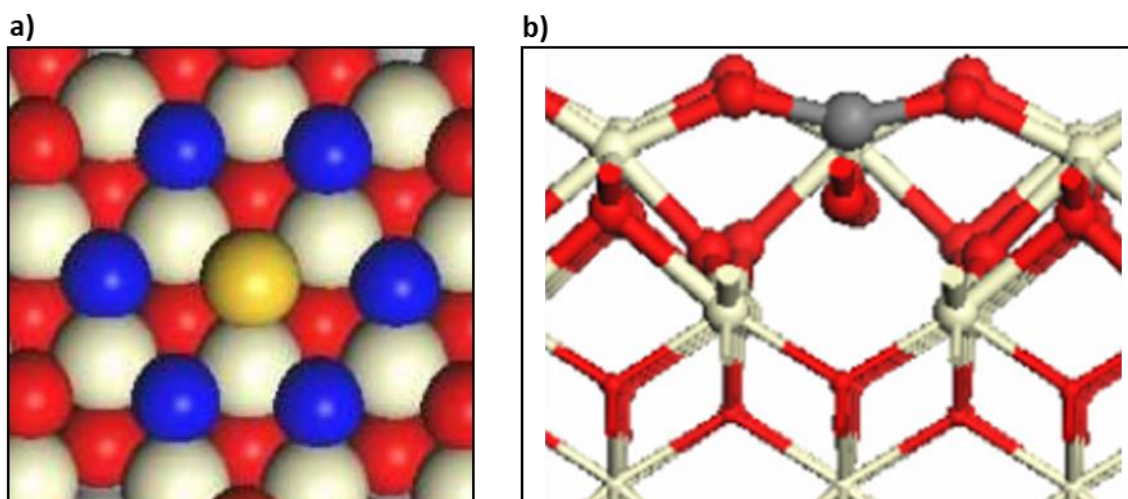


Figure 10.3: DFT-optimised bulk ceria showing Au deposited at defect sites. **a)** Au deposited at an oxygen vacancy site on the [111] surface. Neighbouring oxygen atoms on the surface layer are highlighted in blue. Reprinted figure with permission from Liu, Z. P.; Jenkins, S. J.; King, D. A. *Phys. Rev. Lett.* **2005**, 94 (19), 196102. Copyright 2005 by the American Physical Society. **b)** Au deposited at a Ce vacancy site on the [100] surface. The Au atom is highlighted in grey. Reprinted figure from Nolan, M.; Verdugo, V. S.; Metiu, H. *Surf. Sci.* **2008**, 602 (16), 2734 with permission from Elsevier.

10.2. Hirshfeld Charge Analysis

10.2.1. Au Atomic Charge

A second point of contention regarding the interaction between gold and cerium oxide surfaces concerns both the charge of the adsorbed gold atom – specifically, whether the Au adatom holds a δ^- or δ^+ charge – and the nature of charge transfer interaction between the Au adatom and the Ce atoms neighbouring the adsorption site. Both Au→Ce and Ce→Au charge transfer mechanisms have been proposed previously (as discussed in Chapter 1)^{2-4,11}.

Calculated atomic Hirshfeld charges for the AuCe₂O_n and AuCe₃O_n cluster species are presented in Figures 10.1 and 10.2. Negative Au atomic charges are calculated for the AuCe₂, AuCe₂O, AuCe₂O₂ and AuCe₂O₃ clusters while a positive atomic charge is calculated for the Au atom in the AuCe₂O₄ cluster. Similarly, for the AuCe₃O_n cluster series, the Au atom in the AuCe₃, AuCe₃O, AuCe₃O₂, AuCe₃O₃ and AuCe₃O₄ clusters is calculated with a negative charge while the AuCe₃O₅ and AuCe₃O₆ clusters are calculated with a positively charged Au atom. These results suggest that the Au adatom may hold either a positive or negative charge. Furthermore, the sign of the Au charge appears to be dependent on the deposition site. The AuCe₂O_n ($n=0-3$) and AuCe₃O_n ($n=0-4$) clusters, which are structurally consistent with Au deposition to an oxygen vacancy site, all show the Au atom as negatively charged. The magnitude of the δ^- charge on the Au atom appears to be quite strong, particularly for the AuCe₂O₂ and AuCe₃O₄ species where the Au atom shows a comparable charge to the oxygen atoms. Conversely, the AuCe₂O₄, AuCe₃O₅ and AuCe₃O₆ clusters, which are analogous to a gold atom occupying a Ce-type vacancy site (i.e. CeO₂ and CeO₃ vacancies), have a positively charged gold atom. The amphoteric nature of gold calculated here may explain discrepancies in previous works regarding the charge state of gold atoms and clusters adsorbed to the ceria surface^{1,2,11,3-10}. Moreover, the ability of gold to transition between δ^- and δ^+ charged species depending on the oxidation state of the ceria adsorption site may be key to the enhanced catalytic properties observed in gold-ceria systems; particularly with regard to CO oxidation. Calculations by Wu et al.¹² have shown CO adsorbs more strongly to cationic Au clusters than either neutral or anionic species. Conversely, a combination of experimental work and calculations by Socaciu et al.^{13,14}, Mills et al.¹⁵, Okumura et al.¹⁶, Yoon et al.¹⁷ and

Franceschetti et al.¹⁸ have found preferential O₂ adsorption to anionic Au clusters and nanoparticles (which has also been shown by Socaciu et al. to facilitate CO co-adsorption). Franceschetti et al. report dissociative O₂ adsorption, with the two oxygen atoms forming an O-Au-O bridge similar to the Au-O bonding arrangements calculated here for the AuCe₂O₄, AuCe₃O₅ and AuCe₃O₆ clusters. The ability of Au-Ce_mO_n to adsorb CO when in an oxidised state, and adsorb O₂ when in a reduced state, may be pertinent towards catalytic CO oxidation.

10.2.2. Au-Ce_mO_n Charge Transfer Interactions

The charge transfer mechanisms within the AuCe_mO_n ($m=2,3$; $n=0-2m$) clusters are investigated by consideration of the average charge per atom type. These changes in atomic charge with gold doping may provide insight into the underlying charge transfer interactions. A comparison of the average Ce and O charges in the Ce₂O_n and Ce₃O_n clusters, and their corresponding gold-doped AuCe₂O_n and AuCe₃O_n clusters, allows the effect of Au doping on both the Ce and O atomic charges to be quantified. Thus, the underlying charge transfer mechanisms occurring following Au adsorption to each Ce_mO_n cluster can be explored.

The averaged charges per atom type for the Ce₂O_n and AuCe₂O_n clusters are presented in Figure 10.4. The average charge on the Ce₂O_n oxygen atoms – shown as a dashed green line – remains relatively constant with increased oxidation while the average charge of the Ce₂O_n Ce atoms – displayed by a dashed blue line – shows a linear increase with oxidation, as expected. The AuCe₂O_n average O atomic charge – represented by a solid green line – remains constant with oxidation and is nearly identical to the Ce₂O_n average O charge. Thus, the Au atom does not undergo any charge transfer with the oxygen atoms within the AuCe₂O_n species. The average Ce charge for the AuCe₂O, AuCe₂O₂ and AuCe₂O₃ clusters – shown as a solid blue line – is ca. 0.1e more positive than for the undoped Ce₂O_m, Ce₂O₂ and Ce₂O₃ species (represented by a dashed blue line). The Au atom holds a negative charge in these AuCe₂O_n species. Thus, a Ce→Au charge transfer mechanism can be assigned to these clusters. By contrast, the average Ce charge for the AuCe₂O₄ cluster is ca. 0.1e less positive than the average Ce charge within the undoped Ce₂O₄ species; while the Au charge is now positive. This infers a charge

transfer of $\text{Au} \rightarrow \text{Ce}$ for the AuCe_2O_4 cluster. Similar trends are observed for the Ce_3O_n and AuCe_3O_n clusters as shown in Figure 10.5. The average oxygen charge remains constant and is unaffected by gold doping. The average Ce charges for the AuCe_3O , AuCe_3O_2 , AuCe_3O_3 and AuCe_3O_4 clusters – which are consistent with Au deposition at an oxygen vacancy site – are ca. 0.1e more positive than those of the respective undoped Ce_3O , Ce_3O_2 , Ce_3O_3 and Ce_3O_4 species, with the Au atom holding a negative charge. A $\text{Ce} \rightarrow \text{Au}$ charge transfer mechanism can be proposed for these clusters. Conversely, the AuCe_3O_5 and AuCe_3O_6 species – which are both consistent with Au deposition at a cerium-type vacancy site – both show a reduced Ce charge compared to their respective undoped Ce_3O_5 and Ce_3O_6 clusters; the Au atom is then positively charged. This is consistent with an $\text{Au} \rightarrow \text{Ce}$ charge transfer. Thus, the charge transfer interaction between cerium oxide surface defects and the adsorbed gold atom appears to be dependent on the nature of the defect site; Au adsorption to O vacancy sites favours a $\text{Ce} \rightarrow \text{Au}$ charge transfer, while Au deposition to a cerium-type vacancy site yields an $\text{Au} \rightarrow \text{Ce}$ charge transfer process.

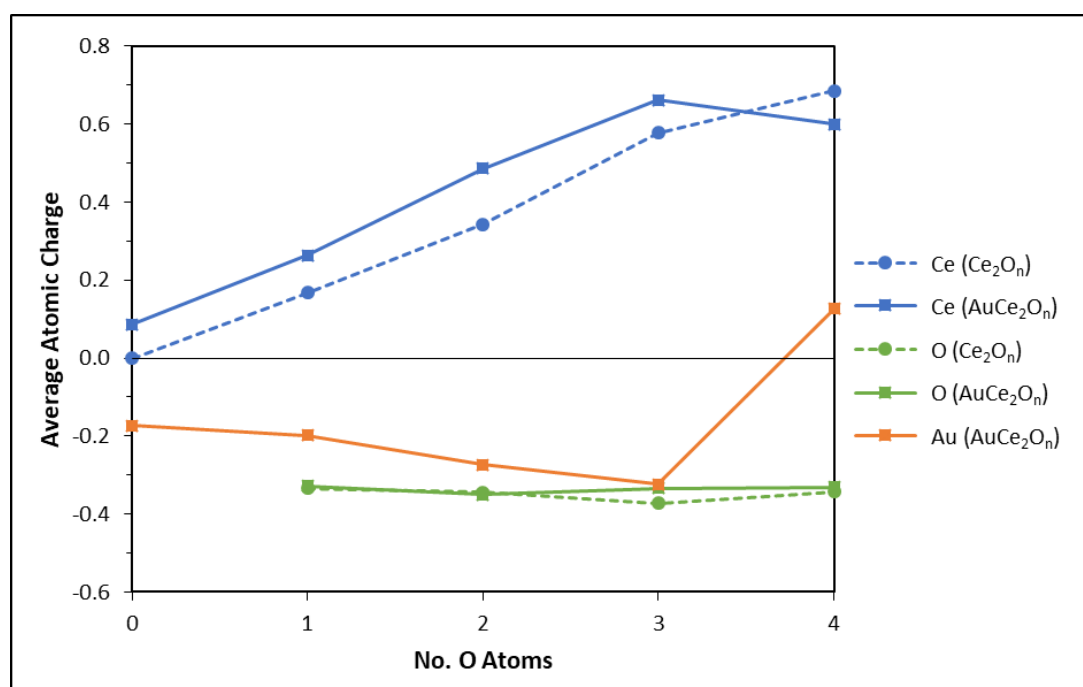


Figure 10.4: Calculated Hirshfeld charges for the Ce_2O_n and AuCe_2O_n neutral clusters, averaged per atom type.

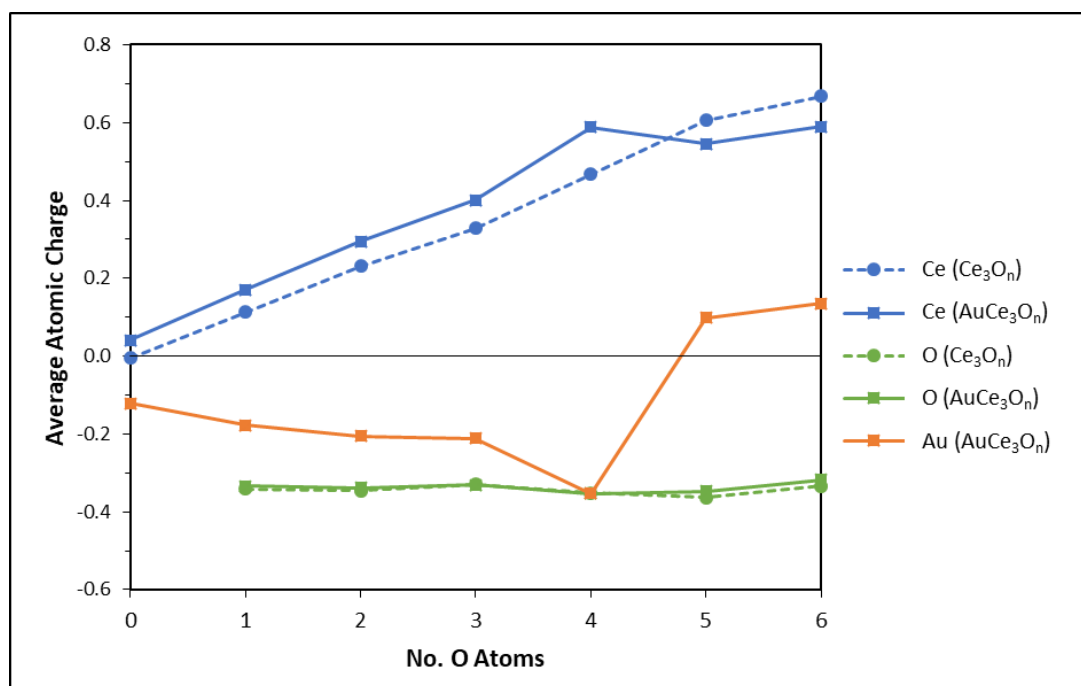


Figure 10.5: Calculated Hirshfeld charges for the Ce_3O_n and $AuCe_3O_n$ neutral clusters, averaged per atom type.

10.3. Effects of Au on $AuCe_mO_n$ Catalytic Properties

10.3.1. HOMO and LUMO Energies

The abilities of Ce_mO_n and $AuCe_mO_n$ systems to facilitate oxidative catalysis reactions are highly dependent on their capacity to donate or accept electrons. Specifically, the fully oxidised Ce_2O_4 and Ce_3O_6 species both function as electron acceptors to become reduced. The reduced Ce_2O_3 and Ce_3O_5 species, respectively, may then function either as electron donors – to be oxidised back to their respective Ce_2O_4 and Ce_3O_6 species – or electron acceptors to become further reduced. To effectively function as a catalyst, both oxidation and reduction processes must be viable such that a catalytic cycle can occur. It is assumed here that a similar process would apply for the $AuCe_mO_n$ clusters. Reduction of the Ce_2O_4 and Ce_3O_6 species – both of which are calculated in closed shell singlet states – is dependent on the Lowest Energy Unoccupied Orbital (LUMO) while all reduced Ce_mO_n species are calculated in open shell electronic states making both oxidation and reduction processes dependent on the singly occupied Highest Energy Occupied Orbital (HOMO). Oxidation and reduction of all $AuCe_mO_n$ species which possess an odd number of electrons are dependent on the HOMO only.

The HOMO energies of all cluster systems can be determined directly from their IEs using Koopmans Theorem¹⁹ as follows:

$$E_{HOMO} \cong -IE_{corrected} \quad (10.1)$$

Where $IE_{corrected}$ refers to the experimentally-corrected calculated IE values from Chapters 5, 6, 8 and 9. The $IE_{corrected}$ values are used in preference to the calculated HOMO energies since they have been shown in this work to agree with experimental IE values. However, a comparison of calculated HOMO energies and $-IE_{corrected}$ values for the Ce₂O_n, AuCe₂O_n, Ce₃O_n and AuCe₃O_n cluster systems – presented in Figures 10.6, 10.7, 10.8 and 10.9, respectively – reveals similar trends in both the $-IE_{corrected}$ and calculated HOMO energies with sequential oxidation across each cluster series.

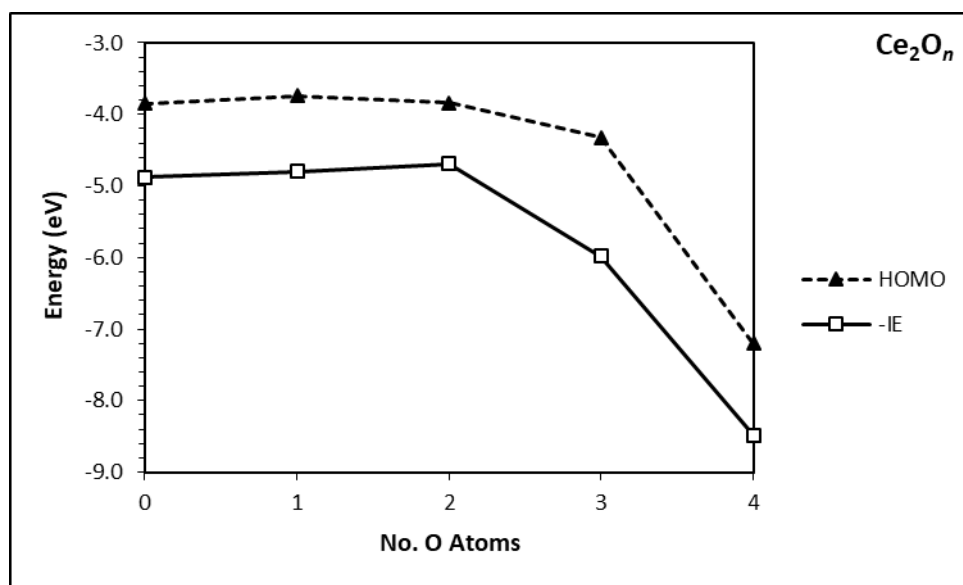


Figure 10.6: Comparison of calculated HOMO energies and negative IEs for the Ce₂O_n (n=0–4) cluster series. Calculated IEs are corrected to the experimental IE of the bare metal cluster.

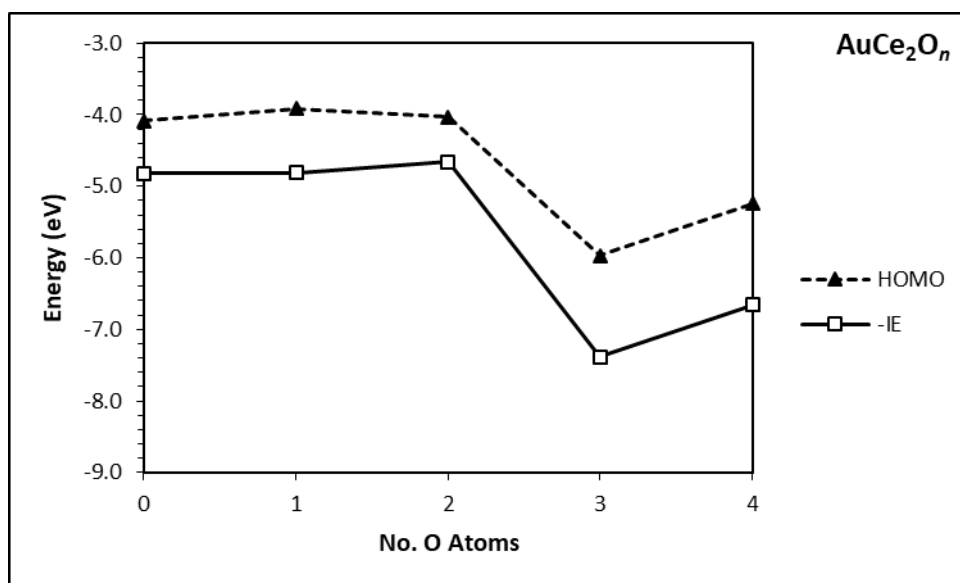


Figure 10.7: Comparison of calculated HOMO energies and negative IEs for the AuCe_2O_n ($n=0-4$) cluster series. Calculated IEs are corrected to the experimental IE of the bare metal cluster.

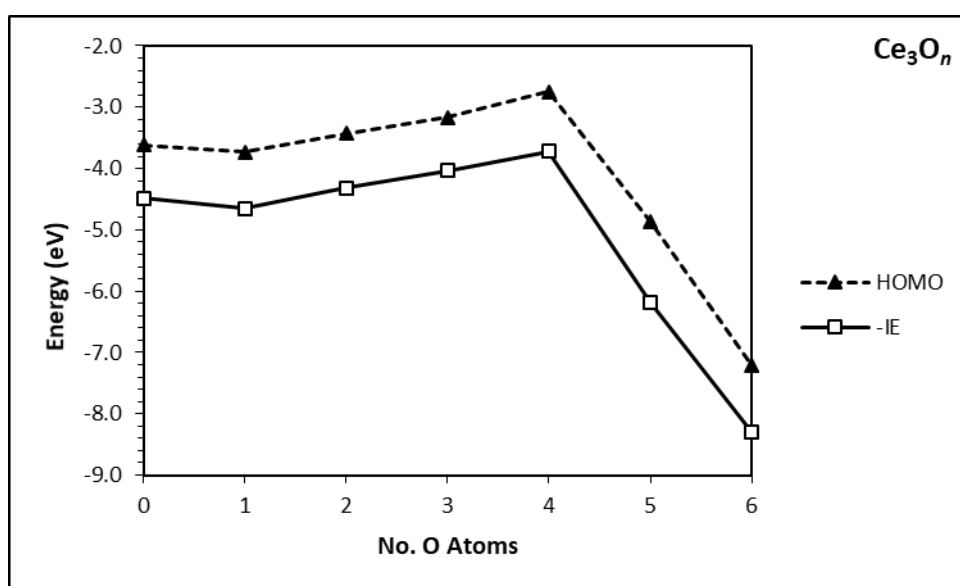


Figure 10.8: Comparison of calculated HOMO energies and negative IEs for the Ce_3O_n ($n=0-6$) cluster series. Calculated IEs are corrected to the experimental IE of the bare metal cluster.

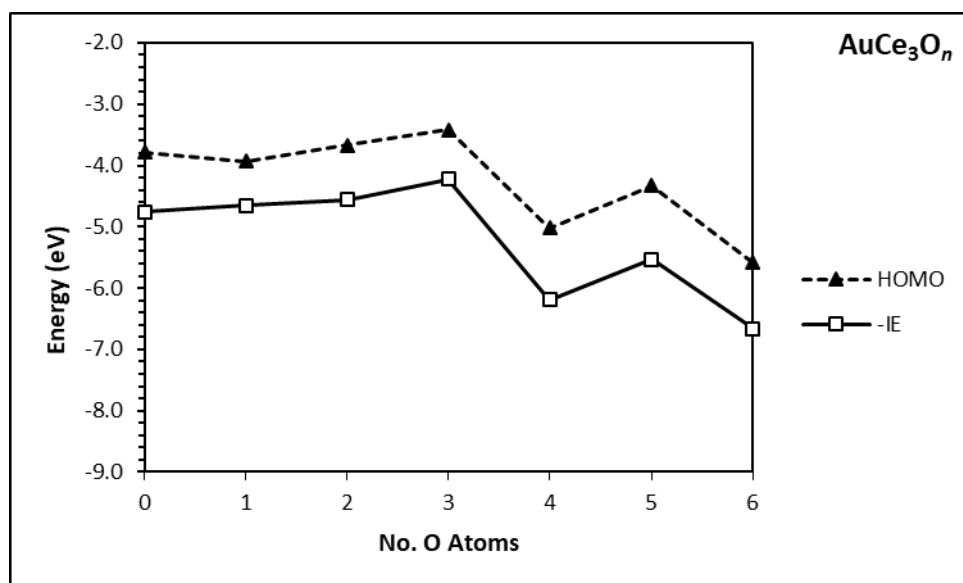


Figure 10.9: Comparison of calculated HOMO energies and negative IEs for the AuCe₃O_n ($n=0-6$) cluster series. Calculated IEs are corrected to the experimental IE of the bare metal cluster.

The LUMO energies for each system can be calculated as follows:

$$E_{LUMO} = E_{HOMO} + \Delta E_{HOMO-LUMO} \quad (10.2)$$

Where $\Delta E_{HOMO-LUMO}$ is the DFT calculated energy of the HOMO-LUMO gap. Using the approximation in Equation 10.1, the LUMO energy can be expressed as follows:

$$E_{LUMO} = -IE_{corrected} + \Delta E_{HOMO-LUMO} \quad (10.3)$$

Calculated HOMO and LUMO energies for the Ce₂O_n and AuCe₂O_n clusters are presented in Figure 10.10. Both cluster systems tend to show an increase in their respective HOMO-LUMO gaps with sequential oxidation. The Ce₂O₄ and AuCe₂O₄ HOMO-LUMO gaps are calculated as 4.09 eV and 2.49 eV, respectively, both of which are considerably lower than the bulk ceria bandgap which has been reported to be around 6 eV²⁰⁻²³. The increased HOMO-LUMO energies of the higher oxide species are largely due to the stabilisation of their respective

HOMOs which is consistent with the IE trends shown previously. While the LUMO energies of both the Ce₂O_n and AuCe₂O_n species also decrease with oxidation, the effect is less pronounced.

Similar HOMO energies are calculated for the Ce₂, Ce₂O and Ce₂O₂ species and their respective gold-doped AuCe₂, AuCe₂O and AuCe₂O₂ species. The stabilities of the Ce₂, Ce₂O and Ce₂O₂ clusters are thus largely unaffected by Au adsorption. HOMO energies of the Ce₂O₃ and AuCe₂O₃ species are calculated as -5.98 eV and -7.38 eV, respectively, inferring significant stabilisation of the AuCe₂O₃ HOMO from the Au adatom. Moreover, the AuCe₂O₃ HOMO shows a σ -type bonding orbital – as shown in Figure 10.10 – largely centred on the Au atom. Thus, the low energy HOMO may act to stabilise the strong negative charge held by the Au atom in the AuCe₂O₃ cluster; this may assist the Au atom to function as a nucleophile toward adsorbed reactants. The Ce₂O₄ and AuCe₂O₄ HOMO energies are calculated as -8.48 eV and -6.66 eV, respectively, inferring destabilisation of the HOMO following Au adsorption. However, the singly occupied AuCe₂O₄ HOMO energy is considerably lower than the Ce₂O₄ LUMO energy of -4.39 eV. Despite the destabilised HOMO, the AuCe₂O₄ cluster is still a better electron acceptor than the Ce₂O₄ cluster. Moreover, the calculated AuCe₂O₄ LUMO energy of -4.17 eV is only slightly higher than that of the Ce₂O₄ LUMO. Therefore, the AuCe₂O₄ cluster can accept both a single electron and an electron pair more readily than the Ce₂O₄ species. Comparison of the HOMO energies for the Ce₂O₃ and Ce₂O₄ clusters finds an energetic difference of 2.50 eV which may present a significant energetic barrier for the reduction process. Conversely, the significantly lower energetic separation of 0.72 eV between the AuCe₂O₃ and AuCe₂O₄ HOMOs suggests neither species is significantly more electronically stable than the other; this may present a lower barrier to the cyclic oxidation/reduction process which is required to facilitate catalysis.

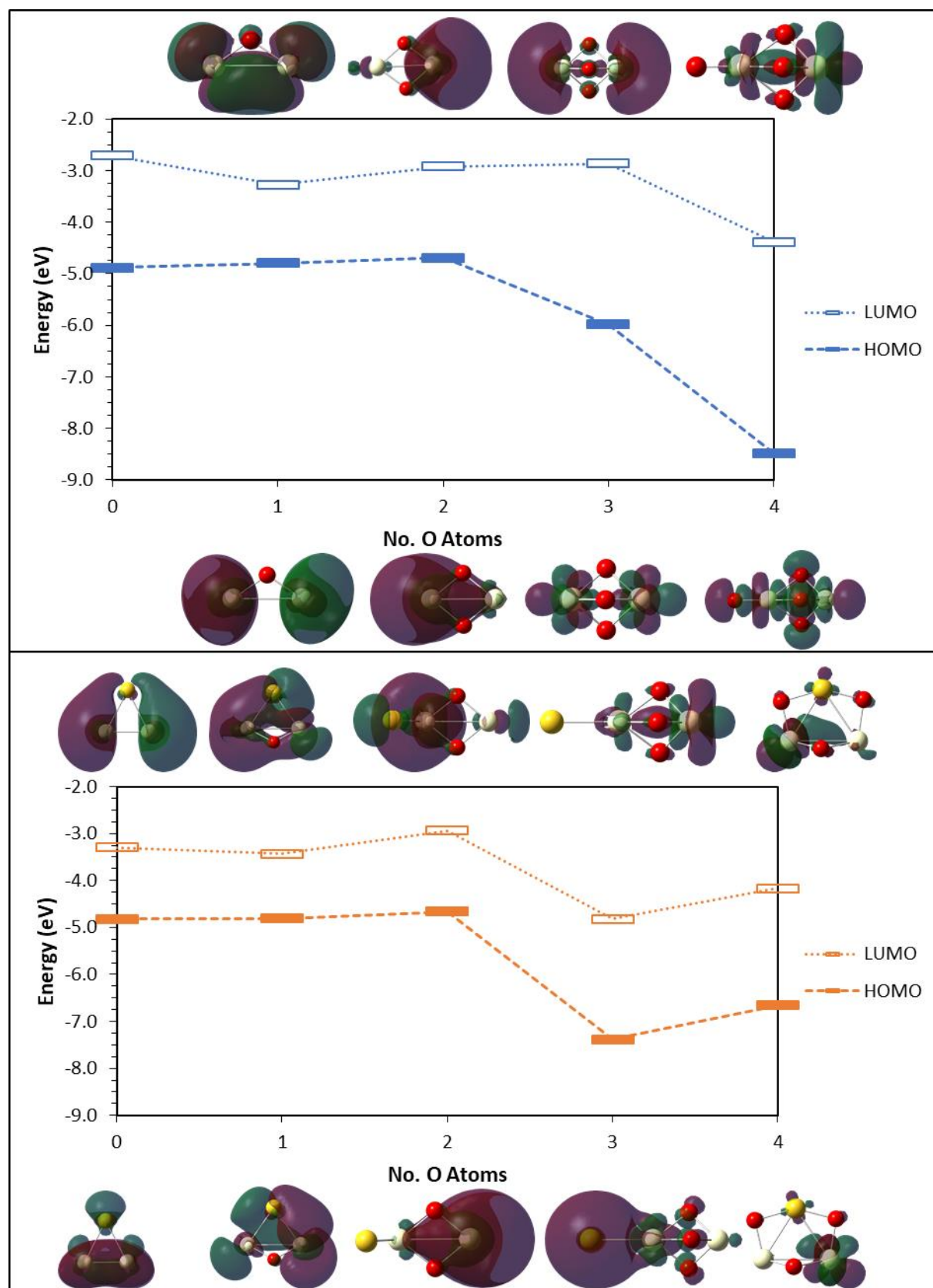


Figure 10.10: Calculated HOMO and LUMO energies for the Ce_2O_n and AuCe_2O_n cluster series (top and bottom, respectively). HOMO and LUMO orbitals are presented below and above each graph, respectively.

Calculated HOMO and LUMO energies for the Ce_3O_n and AuCe_3O_n clusters are presented in Figure 10.11. The HOMO-LUMO gap energies again increase with sequential oxidation; however, the Ce_3O_6 and AuCe_3O_6 HOMO-LUMO gap energies of 4.55 eV and 3.72 eV respectively are considerably lower than the bulk ceria bandgap (ca. 6 eV). The HOMO energies of both the Ce_3O_n and AuCe_3O_n species tend to decrease with increased oxidation, consistent with IE trends shown previously. The LUMO energies remain constant to a good approximation with increased oxidation; the exceptions are the Ce_3O_6 and AuCe_3O_6 species, which both show a slight stabilisation of their LUMOs. Similar HOMO energies are calculated for the Ce_3 , Ce_3O , Ce_3O_2 and Ce_3O_3 species compared to their respective Au-adsorbed AuCe_3 , AuCe_3O , AuCe_3O_2 and AuCe_3O_3 clusters. Thus, gold adsorption has minimal effect on the electronic structures for these species. The Ce_3O_4 and AuCe_3O_4 HOMO energies are calculated as -3.71 eV and -6.19 eV, respectively, inferring significant stabilisation of the AuCe_3O_4 HOMO from Au adsorption. The AuCe_3O_4 HOMO comprises a σ^* anti-bonding orbital centred on the gold atom and the neighbouring cerium atom (as shown in Figure 10.11). The low AuCe_3O_4 HOMO energy may stabilise the electrons on the negatively charged Au atom, thereby allowing the Au atom to act as a nucleophile to adsorbed reactants.

The Ce_3O_5 and AuCe_3O_5 HOMO energies are calculated as -6.19 eV and -5.53 eV, respectively, indicating a small destabilisation of the AuCe_3O_5 HOMO following Au adsorption. This suggests the AuCe_3O_5 cluster acts as a slightly poorer electron acceptor, and a better electron donor, than the Ce_3O_5 cluster. The AuCe_3O_5 HOMO orbital – which comprises non-bonding f-type orbitals on two Ce centres, as shown in Figure 10.11 – implies any electron transfer will involve the Ce atoms and not the Au atom. Thus, the Au atom may indirectly enhance the ability of the Ce atoms in the AuCe_3O_5 cluster to undergo oxidation by destabilising the HOMO. However, comparison between the AuCe_3O_4 and AuCe_3O_5 HOMO energies shows the AuCe_3O_5 HOMO to be slightly higher in energy – by $+0.66$ eV – suggesting that further reduction of the AuCe_3O_5 cluster to AuCe_3O_4 is also favourable. This presents a contrast to the Ce_3O_4 and Ce_3O_5 clusters, where the Ce_3O_4 HOMO energy is $+2.48$ eV higher in energy than the Ce_3O_5 HOMO, making reduction of the Ce_3O_5 cluster energetically unfavourable.

The Ce₃O₆ and AuCe₃O₆ HOMO energies are calculated as -8.30 eV and -6.67 eV, respectively, inferring destabilisation of the Ce₃O₆ HOMO from Au adsorption. The calculated HOMO energies presented here tend to denote a trend where the ceria cluster HOMO is stabilised by Au upon adsorption to an oxygen vacancy site and destabilised by Au following adsorption to a cerium-type vacancy site. However, the singly occupied AuCe₃O₆ HOMO energy is calculated to be significantly lower than the Ce₃O₆ LUMO energy of -4.55 eV, suggesting the AuCe₃O₆ cluster may still act as a better electron acceptor.

The calculated HOMO energies for the AuCe₃O₆, AuCe₃O₅ and AuCe₃O₄ clusters are quite comparable – spanning a 1.13 eV energy range – suggesting neither species is significantly more stable than any other. This may facilitate a low-energy redox cycle between the AuCe₃O₄, AuCe₃O₅ and AuCe₃O₆ clusters. Conversely, the Ce₃O₄ and Ce₃O₅ HOMO energies are calculated to be $+2.10$ eV and $+4.58$ eV higher than the Ce₃O₆ HOMO energy, respectively, suggesting significantly more energy may be required to facilitate reduction of the Ce₃O₆ and Ce₃O₅ clusters.

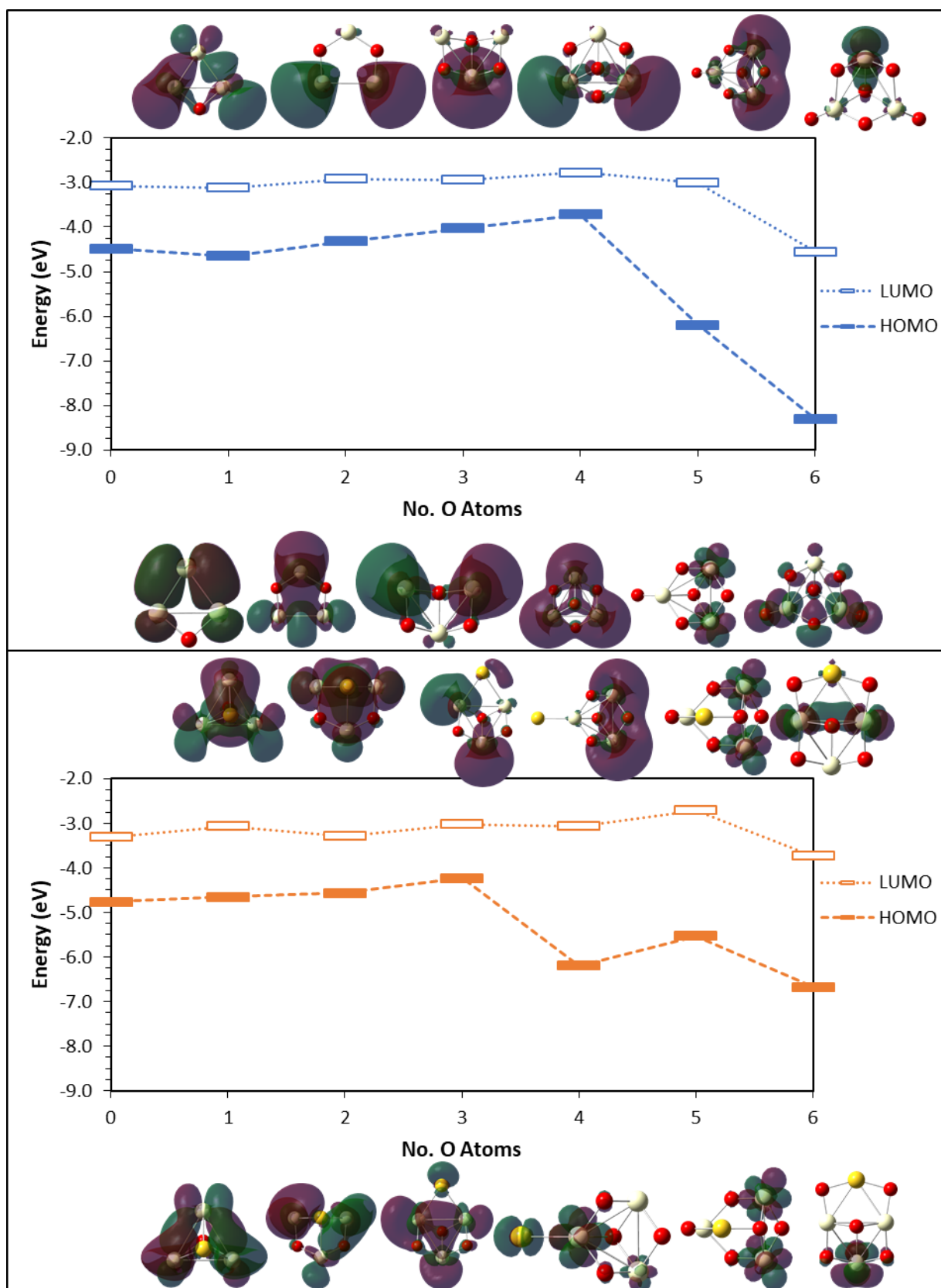


Figure 10.11: Calculated HOMO and LUMO energies for the Ce_3O_n and $AuCe_3O_n$ cluster series (top and bottom, respectively). HOMO and LUMO orbitals are presented below and above each graph, respectively.

10.3.2. Bonding Energies of Au, O and CeO₂ Fragments

The intramolecular bonding energies of Au, CeO₂ and O within the Ce_mO_n and AuCe_mO_n ($m=2,3$; $n=0-2m$) clusters are calculated and presented in Figures 10.12 and 10.13. These particular bonding energies within the cluster framework are pertinent to the ability of ceria – and gold-doped ceria – to function as an oxidative catalyst. Prospective Au adsorption sites on the ceria surface involve either an O vacancy site or a CeO₂ vacancy site, as shown previously. Formation of these active sites would require the loss of an O atom or a CeO₂ unit, respectively, from the cluster surface; weak O and CeO₂ bonding energies would therefore be beneficial in this context. A comparison of the Au bonding energies to oxygen vacancy and CeO₂ vacancy sites allows the preferential Au adsorption site to be determined. Finally, the oxygen release/healing capacity of the cerium oxide and gold-cerium oxide surfaces – which has been purported to be one of the key mechanisms by which ceria performs oxidative catalysis^{6,24-27} – can be explored and compared. The vacancy formation and healing processes considered here only involve atomic oxygen and not molecular O₂; none of the cluster structures calculated in this work contain an O₂ unit and are therefore unlikely to lose O₂ through any simple fragmentation process. Moreover, the healing of vacancy sites with molecular oxygen is considerably more complex than processes involving atomic oxygen and is beyond the context of this work.

Bonding energies were calculated as the energetic difference between the relevant cluster and the optimised fragmented cluster following loss of either an O, Au or CeO₂ fragment (reported as E_O , E_{Au} and E_{CeO_2} , respectively). The energy of the fragmented system was calculated with the O/Au/CeO₂ fragment placed at a distance of 20 Å from the fragmented cluster (to minimise the effects of Basis Set Superposition Error). The E_O and E_{Au} values were calculated for the Ce₂O_n/AuCe₂O_n and Ce₃O_n/AuCe₃O_n ($m=2,3$; $n=0-2m$) clusters. The CeO₂ bonding energies were only calculated for the Ce₃O_n/AuCe₃O_n ($n=0-6$) clusters; the Ce₂O_n/AuCe₂O_n clusters were considered to be too small for fragmentation of a CeO₂ unit to be of particular interest.

Oxygen and gold bonding energies for the $\text{Ce}_2\text{O}_n/\text{AuCe}_2\text{O}_n$ clusters are presented in Figure 10.12. Very high E_O values of 8.61 eV and 9.00 eV are calculated for both the Ce_2O and Ce_2O_2 species, respectively. The Ce_2O_3 species is calculated with a slightly lower, albeit still very high E_O value of 7.00 eV while a significantly lower E_O of 5.22 eV is calculated for Ce_2O_4 . The E_O values calculated for the AuCe_2O and AuCe_2O_2 clusters – calculated as 8.60 eV and 8.81 eV, respectively – are almost identical to those of Ce_2O and Ce_2O_2 , respectively. Thus, Au adsorption has minimal effect on the oxygen affinities of these species. The calculated AuCe_2O_3 and AuCe_2O_4 E_O values of 5.84 eV and 4.58 eV, respectively, are lower than the corresponding Ce_2O_3 and Ce_2O_4 E_O values by 1.46 eV and 0.65 eV, respectively. Au adsorption may therefore enhance the oxygen release capability of both the AuCe_2O_3 and AuCe_2O_4 species (which stoichiometrically correspond to an Au atom deposited at O and CeO_2 vacancy sites, respectively). However, the near-identical oxygen affinities calculated for the Ce_2O_2 and AuCe_2O_2 species suggests that Au adsorption has a minimal effect on the vacancy healing process.

The calculated E_{Au} values for the AuCe_2O_n clusters (calculated as 3.22 eV, 4.48 eV, 3.02 eV, 1.88 eV and 1.18 eV for $n=0-4$) are quite low, and considerably lower than their respective E_O values. This would suggest the Au atoms are quite weakly bound to the Ce_2O_n clusters. The E_{Au} values show a trend where the Au bonding energy tends to decrease with oxidation (the exception being the AuCe_2O cluster, which has a E_{Au} value ca. 1.26 eV higher than that of the AuCe_2 species). Thus, the Au atom appears to be more strongly bound to the oxygen deficient clusters – where bonding is consistent with adsorption to an O vacancy site – than the stoichiometric AuCe_2O_4 cluster which represents Au deposition at a CeO_2 vacancy. These results are consistent with Jenkins et al.¹ who calculated Au adsorption to an O vacancy site on the bulk ceria surface as more energetically favourable than adsorption to either a Ce or CeO_2 vacancy site.

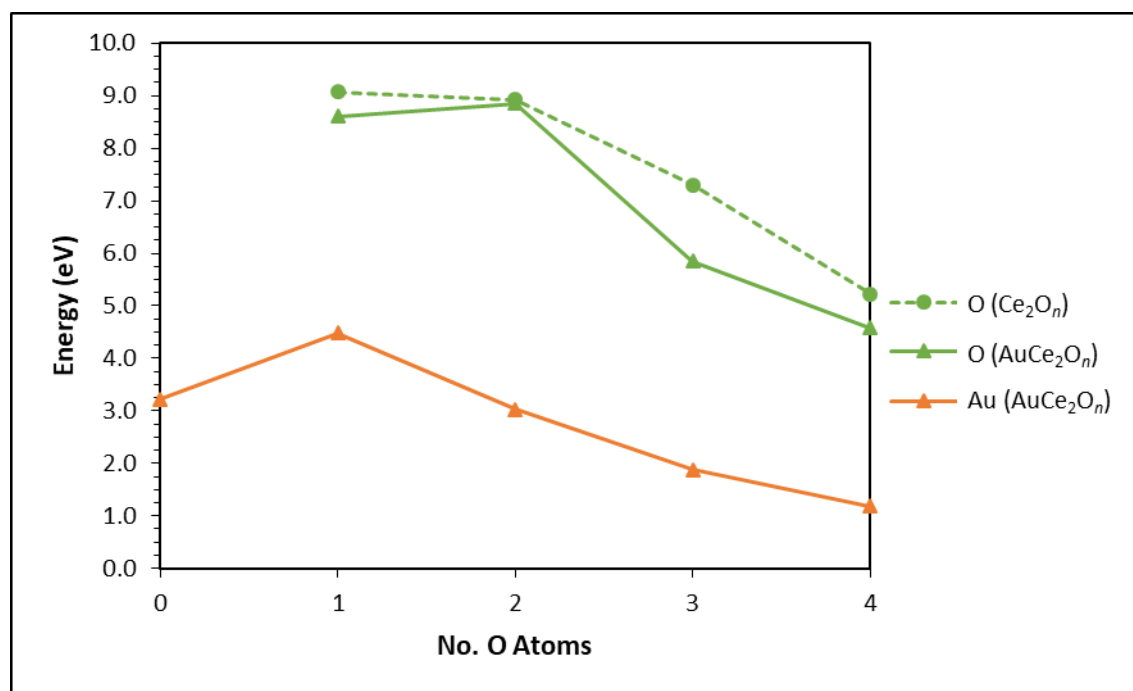


Figure 10.12: Calculated Au (gold) and O (green) bonding energies for neutral Ce_2O_n (dashed line) and AuCe_2O_n (solid line) clusters.

Calculated oxygen bonding energies for the Ce_3O_n and AuCe_3O_n clusters are presented in Figure 10.13. Very high E_O values of 9.34 eV, 9.73 eV, 9.60 eV and 9.24 eV are calculated for the Ce_3O , Ce_3O_2 , Ce_3O_3 and Ce_3O_4 clusters, respectively. Comparable, albeit slightly lower E_O values of 9.27 eV, 9.48 eV, 8.94 eV and 8.46 eV are calculated for the AuCe_3O , AuCe_3O_2 , AuCe_3O_3 and AuCe_3O_4 species, respectively. A small decrease in oxygen bonding energy from Au adsorption can thus be inferred. E_O values for the Ce_3O_5 and AuCe_3O_5 clusters are calculated as 6.25 eV and 4.49 eV, respectively, suggesting Au adsorption may enhance the ability of the AuCe_3O_5 cluster to release oxygen to adsorbed reactants. Conversely, a comparison between the Ce_3O_6 and AuCe_3O_6 calculated E_O values of 4.57 eV and 5.12 eV, respectively, infers the Au atom may hinder the oxygen release capacity of the AuCe_3O_6 cluster. However, the relatively small E_O difference of 0.55 eV between the doped and undoped clusters may not be significant; both the Ce_3O_6 and AuCe_3O_6 species may be able to release oxygen quite readily. Unusually, the E_O of the AuCe_3O_5 cluster is less than that of the AuCe_3O_6 cluster and implies that the release of an oxygen atom by the AuCe_3O_6 species could potentially be followed by the spontaneous release of a second oxygen atom. This would suggest a potential catalytic cycle occurring between the AuCe_3O_4 , AuCe_3O_5 and AuCe_3O_6

species. The AuCe_3O_6 and AuCe_3O_5 species both undergo reduction via their low oxygen bonding energies, while the high E_O of the AuCe_3O_4 cluster facilitates healing of the oxygen vacancy sites.

CeO_2 bonding energies for the Ce_3O_n clusters (calculated as 6.17 eV, 5.59 eV, 5.15 eV, 3.92 eV and 3.30 eV for $n=2-6$) show a near-linear decrease in bonding energy with sequential oxidation. Similar E_{CeO_2} values are calculated for the respective AuCe_3O_n clusters (with E_{CeO_2} values of 5.73 eV, 5.64 eV, 5.17 eV, 3.07 eV and 3.61 eV calculated for $n=2-6$, respectively), suggesting that gold doping generally does not have a significant effect on CeO_2 vacancy formation (an exception is the AuCe_3O_5 cluster, where gold doping appears to cause a slight reduction in both the CeO_2 and O vacancy formation energies). However, the considerably lower E_{CeO_2} values calculated for both the Ce_3O_n and AuCe_3O_n clusters compared to their respective E_O values suggests that CeO_2 vacancies may form more readily than O vacancies. This contrasts Jenkins et al.¹, who calculated CeO_2 vacancy formation to be ca. 3 eV more unfavourable than O vacancy formation in their DFT studies on bulk ceria surfaces, however is consistent with photo-dissociation studies of small oxygen-deficient ceria clusters by Akin et al.²⁸ who observed the loss of CeO_2 fragments in preference to atomic or molecular oxygen. Jenkins et al. also noted that O and CeO_2 vacancy formation becomes competitive in oxygen rich environments. This certainly appears to be the case here; the E_O and E_{CeO_2} values for both the Ce_3O_n and AuCe_3O_n clusters tend to converge with increased oxidation.

The calculated Au bonding energies are considerably lower than both the O and CeO_2 bonding energies for all AuCe_3O_n species. Thus, as with the AuCe_2O_n clusters, the Au atoms are quite weakly bound compared to both the O atoms and CeO_2 fragments. The E_{Au} values for the AuCe_3O_n ($n=0-4$) clusters are all quite similar (calculated as 3.77 eV, 3.48 eV, 3.83 eV, 3.52 eV and 3.50 eV, respectively), as are the AuCe_3O_5 and AuCe_3O_6 E_{Au} values (calculated as 1.00 eV and 1.50 eV, respectively). However, the considerably lower E_{Au} values calculated for the AuCe_3O_5 and AuCe_3O_6 clusters – which stoichiometrically represent Au deposition at CeO_3 and CeO_2 vacancies, respectively – than the oxygen deficient AuCe_3O_n ($n=0-4$) clusters suggests Au deposition occurs preferentially to O vacancy sites than to $\text{CeO}_2/\text{CeO}_3$ vacancies.

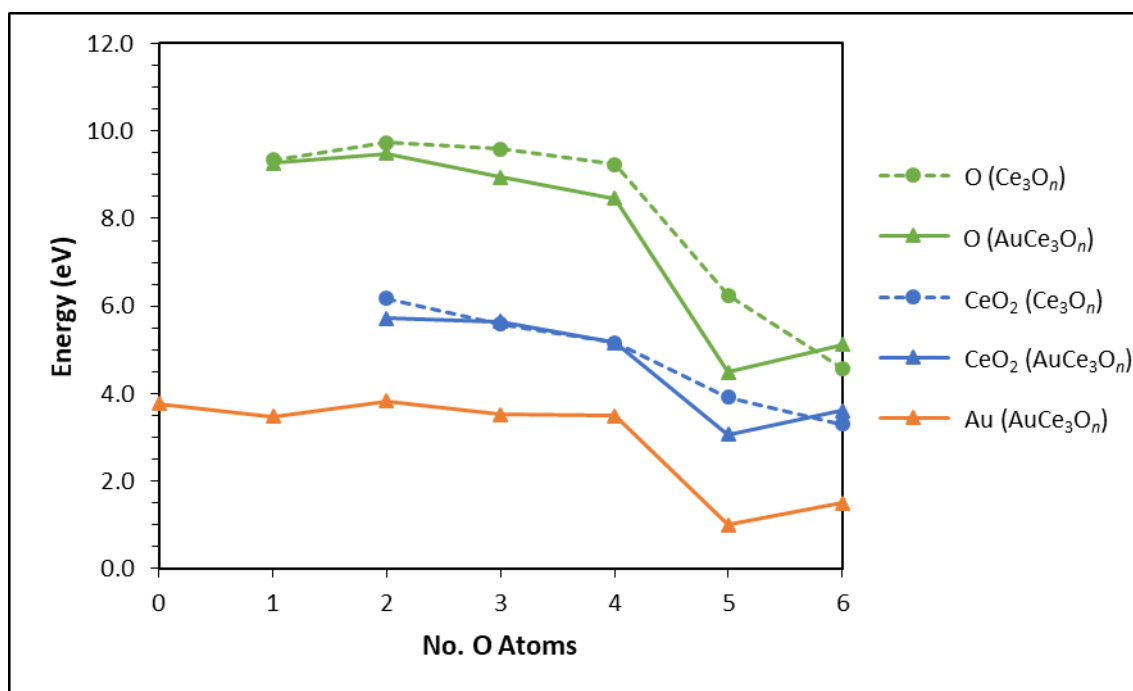


Figure 10.13: Calculated Au (gold), O (green) and CeO₂ (blue) bonding energies for neutral Ce₃O₄ (dashed line) and AuCe₃O₄ (solid line) clusters.

10.4. Ce_mO_n and AuCe_mO_n Photon Absorption Pathways

The relatively low bonding energies and high IEs calculated for the higher oxide Ce_mO_n and AuCe_mO_n clusters, in addition to the low E_{Au} values calculated for all AuCe_mO_n species, suggests that the photon absorption processes for some cluster species may contain competing photo-dissociation pathways in addition to photo-ionisation. Therefore, the photon absorption pathways for the Ce_mO_n and AuCe_mO_n ($m=2,3$; $n=0-2m$) clusters were considered from the energetic differences between their respective photo-dissociation and photo-ionisation processes, as follows:

$$E_x - IE_{corrected} \begin{cases} > 0: \text{Photo-ionisation is thermodynamically preferred} \\ < 0: \text{Photo-dissociation is thermodynamically preferred} \end{cases} \quad (10.4)$$

Where E_x and $IE_{corrected}$ represent the bonding energies ($x = O, Au, CeO_2$) and ionisation energies for each cluster species, respectively. Only the relative energies of the initial and fragmented clusters are considered here; activation barriers which may be present during the

dissociation process are not calculated at this time. These activation barriers may be considered in future work.

The calculated photon absorption pathways for the Ce_mO_n and AuCe_mO_n ($m=2,3; n=0-2m$) clusters are presented in Figures 10.14 and 10.15. For all AuCe_mO_n species, the E_{Au} value is less than the respective IE. Photo-dissociation involving the loss of Au therefore appears to be a preferred pathway – from a purely energetic standpoint – to photo-ionisation. However, the AuCe_mO_n clusters detected in experimental mass spectra during this work – namely AuCe₂, AuCe₂O, AuCe₂O₂, AuCe₃, AuCe₃O, AuCe₃O₂ and AuCe₃O₃ – all have E_{Au} values within ca. 1.2 eV of their calculated IEs. Thus, while dissociation may be preferred, the comparable energies of both the dissociation and ionisation processes may still allow some photo-ionisation to occur. This low-energy photo-dissociation process may explain the difficulties encountered with obtaining good AuCe_mO_n ion signal during photo-ionisation experiments. It is also worthwhile mentioning at this point that the Ce_mO_n PIE spectra presented in this work were all drawn from mass spectra recorded without any Au ablation. Therefore, none of the Ce_mO_n PIE spectra are contaminated by ion signal evolving from Au fragmentation of AuCe_mO_n clusters.

Comparison of the IE and E_O values for the Ce₂O_n/AuCe₂O_n and Ce₃O_n/AuCe₃O_n clusters shows the Ce₂O_n ($n=0-3$), AuCe₂O_n ($n=0-2$), Ce₃O_n ($n=0-4$) and AuCe₃O_n ($n=0-4$) clusters favour photo-ionisation as the lower energy pathway in preference to photo-dissociation involving O loss. All of these species were detected in experimental mass spectra with the exception of the AuCe₃O₄ cluster (the non-detection of AuCe₃O₄ was attributed to an ionisation energy greater than the photon energies available in the experimental setup). The Ce₃O₅ cluster is calculated with energetically identical photo-ionisation and E_O values but is not detected due to a very high AE (which is significantly higher than the IE). Calculations show the Ce₂O₄, Ce₃O₆, AuCe₂O₃, AuCe₂O₄, AuCe₃O₅ and AuCe₃O₆ species to have O fragmentation pathways with lower energies than their respective photo-ionisation processes. This is consistent with the non-detection of these species in any photo-ionisation mass spectra during this work.

Comparison of the IE and E_{CeO_2} values for the $\text{Ce}_3\text{O}_n/\text{AuCe}_3\text{O}_n$ clusters shows preferable photo-ionisation pathways for the Ce_3O_2 , Ce_3O_3 , Ce_3O_4 , AuCe_3O_2 and AuCe_3O_3 clusters – which were all detected during this work – and low-energy fragmentation pathways involving loss of CeO_2 for the Ce_3O_5 , Ce_3O_6 , AuCe_3O_4 , AuCe_3O_5 and AuCe_3O_6 species which were not detected. Moreover, all clusters are calculated with lower E_{CeO_2} values than their respective E_{O} values which suggests fragmentation involving the loss of a CeO_2 unit may occur in preference to loss of atomic oxygen. The low energy fragmentation pathways – through loss of either O or CeO_2 – calculated for the Ce_2O_4 , Ce_3O_5 , Ce_3O_6 , AuCe_2O_3 , AuCe_2O_4 , AuCe_3O_5 and AuCe_3O_6 species could make photo-ionisation experiments unfeasible since these clusters may simply dissociate when exposed to high energy photons. Future work involving these particular cluster species may therefore be limited to studies of nascent cations or anions, which are already being investigated by several other groups^{28–37}.

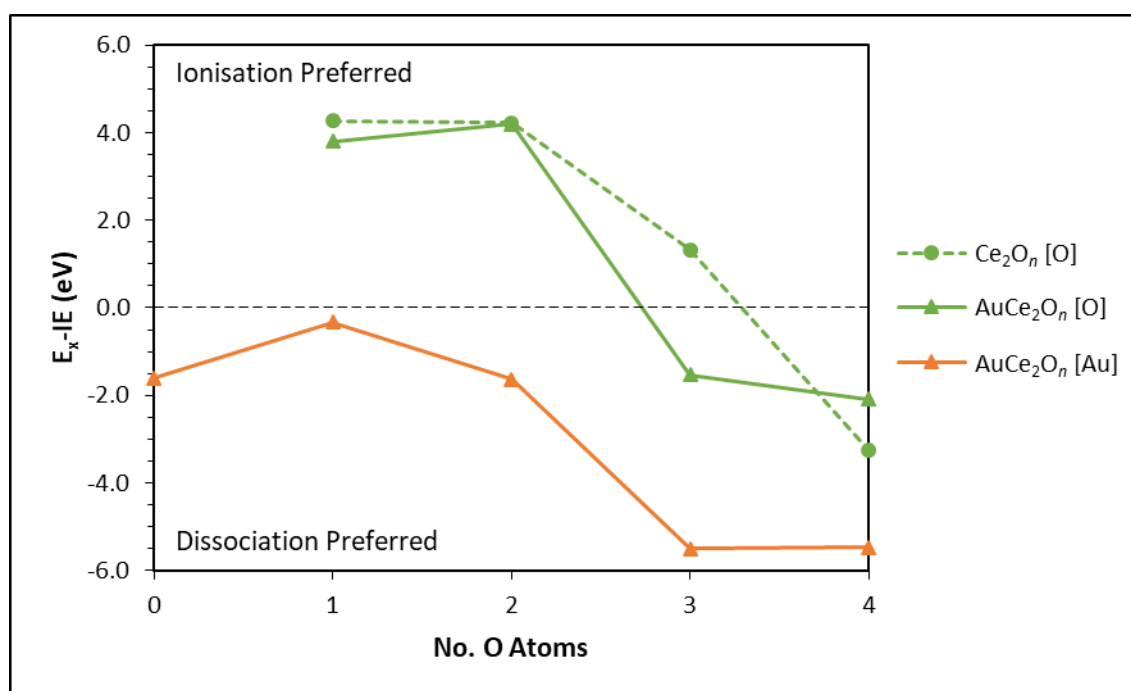


Figure 10.14: Calculated photon absorption pathways for Ce_2O_n and AuCe_2O_n clusters. Potential dissociation pathways are calculated to involve loss of either O (green) or Au (gold). Photo-dissociation fragments are shown in square brackets. The photo-ionisation pathway is preferred when $E_x - \text{IE} > 0$. The photo-dissociation pathway is preferred when $E_x - \text{IE} < 0$.

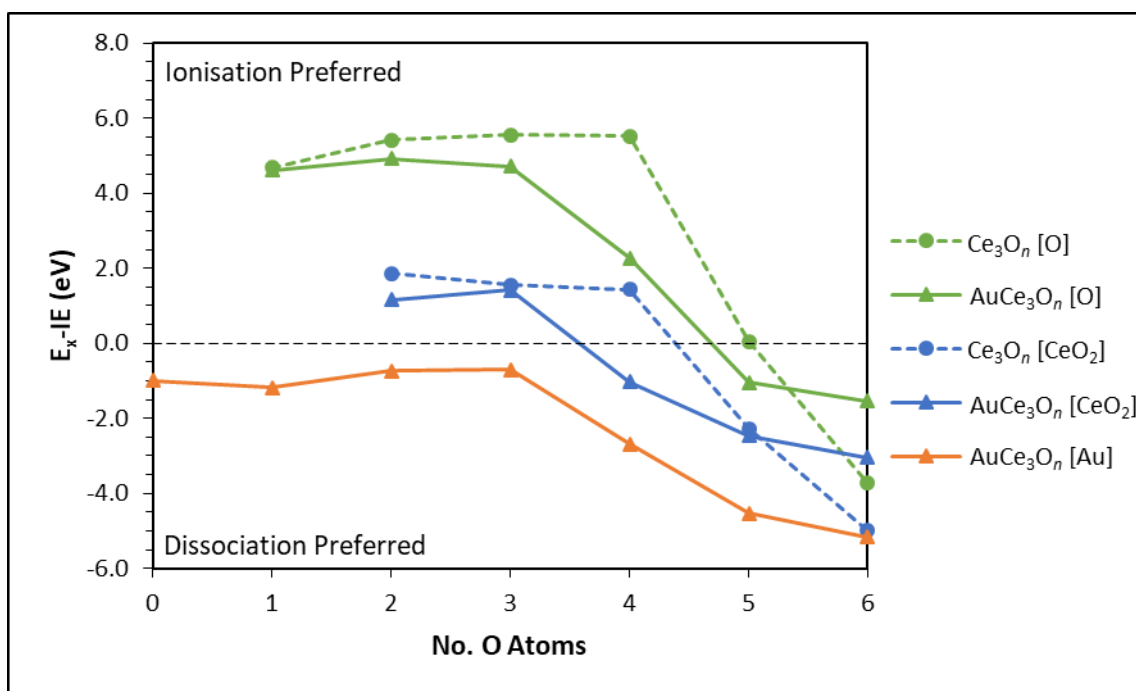


Figure 10.15: Calculated photon absorption pathways for Ce_3O_n and AuCe_3O_n clusters. Potential dissociation pathways are calculated to involve loss of either O (green), Au (gold) or CeO_2 (blue). Photo-dissociation fragments are shown in square brackets. The photo-ionisation pathway is preferred when $E_x\text{-IE} > 0$. The photo-dissociation pathway is preferred when $E_x\text{-IE} < 0$.

10.5. References

- (1) Zhang, C.; Michaelides, A.; King, D. A.; Jenkins, S. J. *J. Phys. Chem. C* **2009**, *113* (16), 6411.
- (2) Liu, Z. P.; Jenkins, S. J.; King, D. A. *Phys. Rev. Lett.* **2005**, *94* (19), 196102.
- (3) Zhang, C.; Michaelides, A.; King, D. A.; Jenkins, S. J. *J. Chem. Phys.* **2008**, *129* (19), 1.
- (4) Zhang, C.; Michaelides, A.; King, D. A.; Jenkins, S. J. *J. Am. Chem. Soc.* **2010**, *132* (7), 2175.
- (5) Camellone, M. F.; Fabris, S. *J. Am. Chem. Soc.* **2009**, *131* (30), 10473.
- (6) Nolan, M. *J. Chem. Phys.* **2009**, *130* (14), 144702.
- (7) Nolan, M.; Verdugo, V. S.; Metiu, H. *Surf. Sci.* **2008**, *602* (16), 2734.
- (8) Tibiletti, D.; Amieiro-Fonseca, A.; Burch, R.; Chen, Y.; Fisher, J. M.; Goguet, A.; Hardacre, C.; Hu, P.; Thompsett, D. *J. Phys. Chem. B* **2005**, *109* (47), 22553.
- (9) Fu, Q.; Deng, W.; Saltsburg, H.; Flytzani-Stephanopoulos, M. *Appl. Catal. B Environ.* **2005**, *56* (1–2), 57.
- (10) Yi, N.; Si, R.; Saltsburg, H.; Flytzani-Stephanopoulos, M. *Energy Environ. Sci.* **2010**, *3*, 831.
- (11) Wang, X.; Rodriguez, J. A.; Hanson, J. C.; Pérez, M.; Evans, J. *J. Chem. Phys.* **2005**, *123* (22), 221101.
- (12) Wu, X.; Senapati, L.; Nayak, S. K.; Selloni, A.; Hajaligol, M. *J. Chem. Phys.* **2002**, *117* (8), 4010.
- (13) Socaciu, L. D.; Hagen, J.; Bernhardt, T. M.; Wo, L.; Heiz, U.; Ha, H.; Landman, U. *J. Am. Chem. Soc.* **2003**, *125* (34), 10437.
- (14) Hagen, J.; Socaciu, L. D.; Elijazyfer, M.; Heiz, U.; Bernhardt, T. M.; Woste, L. *Phys. Chem. Chem. Phys.* **2002**, *4* (10), 1707.
- (15) Mills, G.; Gordon, M. S.; Metiu, H. *J. Chem. Phys.* **2003**, *118* (9), 4198.
- (16) Okumura, M.; Kitagawa, Y.; Haruta, M.; Yamaguchi, K. *Chem. Phys. Lett.* **2001**, *346* (1–2), 163.

- (17) Yoon, B.; Häkkinen, H.; Landman, U. *J. Phys. Chem. A* **2003**, *107* (20), 4066.
- (18) Franceschetti, A.; Pennycook, S. J.; Pantelides, S. T. *Chem. Phys. Lett.* **2003**, *374* (5–6), 471.
- (19) Koopmans, T. *Physica* **1934**, *1*, 104.
- (20) Marabelli, F.; Wachter, P. *Phys. Rev. B* **1987**, *36* (2), 1238.
- (21) Mullins, D. .; Overbury, S. .; Huntley, D. . *Surf. Sci.* **1998**, *409* (2), 307.
- (22) Wuilloud, E.; Delley, B.; Schneider, W.-D.; Baer, Y. *Phys. Rev. Lett.* **1984**, *53* (2), 202.
- (23) Pfau, A.; Schierbaum, K. D. *Surf. Sci.* **1994**, *321* (1–2), 71.
- (24) Nolan, M.; Parker, S. C.; Watson, G. W. *Phys. Chem. Chem. Phys.* **2006**, *8*, 216.
- (25) Nolan, M. *J. Mater. Chem* **2011**, *21*, 9160.
- (26) Nolan, M.; Watson, G. W. *J. Phys. Chem. B* **2006**, *110*, 16600.
- (27) Nolan, M.; Parker, S. C.; Watson, G. W. *J. Phys. Chem. B* **2006**, *110* (5), 2256.
- (28) Akin, S. T.; Ard, S. G.; Dye, B. E.; Schaefer, H. F.; Duncan, M. A. *J. Phys. Chem. A* **2016**, *120* (15), 2313.
- (29) Himeno, H.; Miyajima, K.; Yasuike, T.; Mafuné, F. *J. Phys. Chem. A* **2011**, *115* (42), 11479.
- (30) Mafuné, F.; Masuzaki, D.; Nagata, T. *Top. Catal.* **2018**, *61* (1–2), 42.
- (31) Miyajima, K.; Mafuné, F. *Chem. Phys. Lett.* **2016**, *660*, 261.
- (32) Nagata, T.; Miyajima, K.; Mafuné, F. *J. Phys. Chem. A* **2016**, *120* (39), 7624.
- (33) Nagata, T.; Miyajima, K.; Mafuné, F. *J. Phys. Chem. A* **2015**, *119* (41), 10255.
- (34) Nagata, T.; Miyajima, K.; Hardy, R. A.; Metha, G. F.; Mafuné, F. *J. Phys. Chem. A* **2015**, *119* (22), 5545.
- (35) Nagata, T.; Miyajima, K.; Mafuné, F. *J. Phys. Chem. A* **2015**, *119* (10), 1813.
- (36) Zhou, Z.-X.; Wang, L.; Li, Z.-Y.; He, S.-G.; Ma, T.-M. *J. Phys. Chem. A* **2016**, *120* (22), 3843.
- (37) Wu, X.; Ding, X.; Bai, S.; Xu, B.; He, S.; Shi, Q. *J. Phys. Chem. C* **2011**, *115*, 13329.

Conclusions and Future Directions

The properties of small cerium oxide and gold-cerium oxide clusters have been investigated with specific regard to the catalytic potential of gold-ceria systems. Cerium oxide (Ce_2 , Ce_2O , Ce_2O_2 , Ce_3 , Ce_3O , Ce_3O_2 , Ce_3O_3 , Ce_3O_4 , Ce_4O , Ce_4O_2 , Ce_4O_3 , Ce_4O_4 , Ce_4O_5) and gold-cerium oxide (AuCe_2 , AuCe_2O , AuCe_2O_2 , AuCe_3 , AuCe_3O , AuCe_3O_2 , AuCe_3O_3) clusters were successfully prepared in the gas phase via dual laser ablation of separate gold and cerium rods. The ionisation energies (IEs) of these clusters were accurately determined using Photo-Ionisation Efficiency (PIE) experiments, which were compared to calculated PIE spectra drawn from Zero Electron Kinetic Energy (ZEKE) simulations of DFT-calculated neutral and cationic species. Excellent agreement was found between the spectral profiles of the experimental and calculated PIE spectra and between the experimental and calculated adiabatic IE trends with sequential oxidation of each metal cluster base. This allowed the geometric and electronic properties of the clusters of interest to be inferred from the calculated structures. A comparison between appearance energies for the Ce_2O_n and AuCe_2O_n clusters with sequential oxidation did not reveal any discernible trends. The AuCe_2 and AuCe_2O primary onset AEs were lower than their respective undoped Ce_2 and Ce_2O AEs by 0.09 eV and 0.31 eV, respectively, while the AuCe_2O_2 primary onset AE was 0.25 eV higher than the Ce_2O_2 AE value. Comparison between the Ce_3O_n and AuCe_3O_n experimental AEs revealed a more distinct trend where Au adsorption caused an increase in the AE of all AuCe_3O_n species compared to their relative undoped Ce_3O_n cluster. First onset AEs for the AuCe_3O_n clusters were 0.25 – 0.45 eV higher than their respective Ce_3O_n species, while AE values for the AuCe_3O_n primary onsets were higher than those of their respective Ce_3O_n clusters by 0.02 – 0.45 eV.

A geometric comparison between gold-doped AuCe_mO_n and undoped Ce_mO_n clusters was used to investigate potential deposition sites of adsorbed gold atoms on a cerium oxide surface. The adsorbed Au atom appeared to occupy oxygen vacancy sites in highly reduced cerium oxide clusters, and cerium vacancy sites – specifically, CeO_2 vacancy sites – in moderately reduced and stoichiometric clusters. Hirshfeld charge analysis showed the adsorbed Au atom possesses a strong negative charge when deposited in an oxygen vacancy site and a moderate positive charge when deposited in a cerium vacancy site. Further comparison of atomic

Hirshfeld charges in the Ce_mO_n and $AuCe_mO_n$ species inferred two different charge transfer mechanisms between the cerium oxide cluster and the adsorbed Au atom; an Au→Ce mechanism was calculated for the Au atom in an oxygen vacancy site (e.g. $AuCe_2$, $AuCe_2O$, $AuCe_2O_2$, $AuCe_2O_3$, $AuCe_3$, $AuCe_3O$, $AuCe_3O_2$, $AuCe_3O_3$, $AuCe_3O_4$), while a Ce→Au mechanism was calculated when the Au atom occupied a cerium vacancy site (e.g. $AuCe_2O_4$, $AuCe_3O_5$, $AuCe_3O_6$).

Comparison of the HOMO and LUMO energies for the calculated Ce_mO_n and $AuCe_mO_n$ neutral clusters showed Au adsorption lead to a stabilisation of the ceria cluster HOMO when adsorbed to an oxygen vacancy site. Conversely, Au adsorption to a cerium vacancy site – which included the $AuCe_2O_4$, $AuCe_3O_5$ and $AuCe_3O_6$ clusters – showed a destabilisation of the HOMO compared to the undoped species. Au adsorption did not have a significant effect on the LUMO energies of the ceria clusters. Comparison of the HOMO energies for the Ce_mO_n and $AuCe_mO_n$ clusters suggested Au doping may influence the potential of $AuCe_mO_n$ clusters to catalyse CO oxidation by several means. These include an increase in the electron accepting ability of the fully oxidised species; an increase in the nucleophilic character of reduced $AuCe_mO_n$ species towards adsorbed reactants by stabilising a strong negative charge on the Au atom; and a small difference between the HOMO energies of the fully oxidized and partially reduced $AuCe_mO_n$ species which may potentially facilitate a low-energy redox cycle. An investigation into the calculated oxygen bonding energies of the Ce_mO_n and $AuCe_mO_n$ clusters showed Au doping may increase the amount of oxygen available for abstraction by adsorbed reactants without having any significant effect on subsequent healing processes of the reduced cluster.

A comparison between the calculated bonding energies (O, CeO_2 and Au) and ionisation energies for the Ce_mO_n and $AuCe_mO_n$ clusters highlighted potential photo-dissociation pathways – involving loss of either O or CeO_2 – for the Ce_2O_4 , Ce_3O_5 , Ce_3O_6 , $AuCe_2O_3$, $AuCe_2O_4$, $AuCe_3O_5$ and $AuCe_3O_6$ species which may either occur instead of, or concurrently with, photo-ionisation. These energetically preferable photo-dissociation pathways are consistent with the non-detection – or detection in weak abundance – of these above-mentioned species in

all photo-ionisation mass spectra recorded throughout this work. Consequentially, studies of these clusters may be limited to experiments involving nascent cations (or anions). The unusually low bonding energies calculated for the Au atoms within all AuCe_mO_n clusters were consistent with the limited AuCe_mO_n ion signal detected during photo-ionisation experiments.

Future work may be extended to studies of larger Ce_mO_n and AuCe_mO_n clusters as faster computational facilities and more refined computational methods become available. Many of the calculations attempted in this work were problematic due to wavefunction convergence issues. This included both failure of the software to diagonalize the wavefunction, causing the calculation to terminate, and stalled calculations where the time required to complete one optimisation step exceeded the maximum time allocated for the calculation itself. The latter issue may be alleviated as faster computational facilities become available. The former issue may be resolved through the use of improved DFT algorithms, including Density Functional Tight Binding (DFTB) — which would assist in optimising structures to reasonable geometries — and could potentially facilitate calculations of larger cluster systems.

Many of the ZEKE simulations performed in this work were problematic due to in-built memory limitations associated with the ezSpectrum software (although the memory requirements for the ZEKE calculations themselves were well within the capabilities of a modern PC or laptop). Consequently, a full Duschinsky treat was not feasible for many of the cluster systems considered in this work; calculations were instead restricted to a Parallel Approximation of the vibrational mode overlap between the neutral and cationic states. Considerable advances in FC simulation software have been made in recent years; with vibronic spectral simulation algorithms now becoming embedded in modern commercial computational packages such as Gaussian16. Preliminary calculations of ZEKE spectra using Gaussian16 have shown considerable improvement over ezSpectrum with regard to both computational speed and available memory. Improvements in both the DFT and ZEKE calculation methods may facilitate a larger study of cluster species over a broad size regime. This can assist in identifying trends for the interactions between the cerium oxide cluster and

adsorbed gold species. Changes in those trends can be then explored as the cerium oxide cluster approaches the bulk size regime.

It would be interesting to examine the photo-ionisation/photo-dissociation pathways of the cluster species not detected – or detected in trace quantities – in this work. This would require a tunable laser source capable of producing higher photon energies than those available in the current experimental setup, which could be achieved using third harmonic generation of the existing tunable laser output coupled with mixing after doubling.

The interactions of Ce_mO_n and $AuCe_mO_n$ clusters with gas phase reactants, specifically CO and O_2 , can be investigated with some small modifications to the experimental setup. This experiment would involve monitoring the change in ion signal of the $Ce_mO_n/AuCe_mO_n$ clusters when CO and/or O_2 gases are introduced to a reaction channel downstream of the condensing tube in the cluster source. Some of this work can be – and is currently being – performed using nascent cations which would reduce the requirement for a tunable photo-ionisation source. Moreover, nascent cation studies would allow clusters not detectable via photo-ionisation to be studied in the experiment. These experimental results can be coupled with intrinsic reaction coordinate (IRC) calculations to identify possible reaction pathways for Ce_mO_n and $AuCe_mO_n$ clusters with CO and O_2 . A full catalytic CO oxidation cycle could potentially be derived for both the undoped Ce_mO_n and gold-doped $AuCe_mO_n$ cluster species.

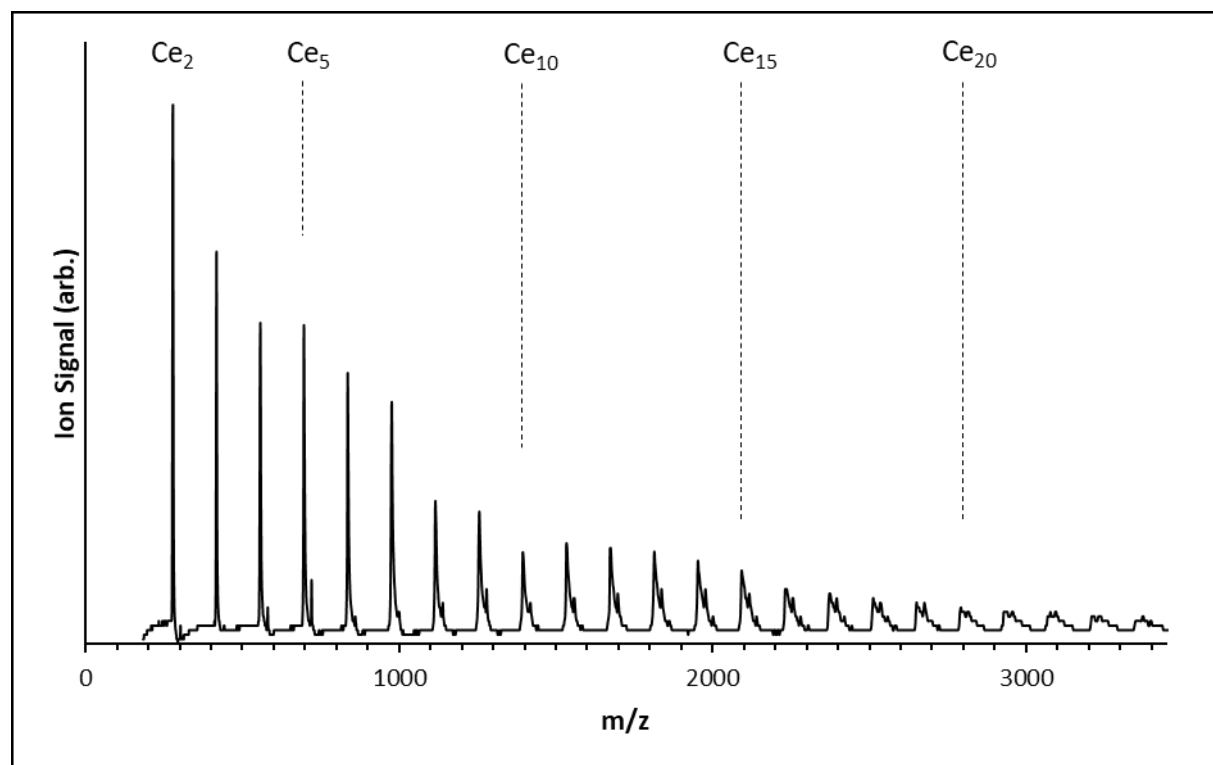
Appendix A: Mass Spectra of Ce_mO_n Clusters

Figure A1: Mass spectrum for Ce_m clusters recorded following photo-ionisation at 220 nm (5.64 eV). Prominent mass peaks are labelled.

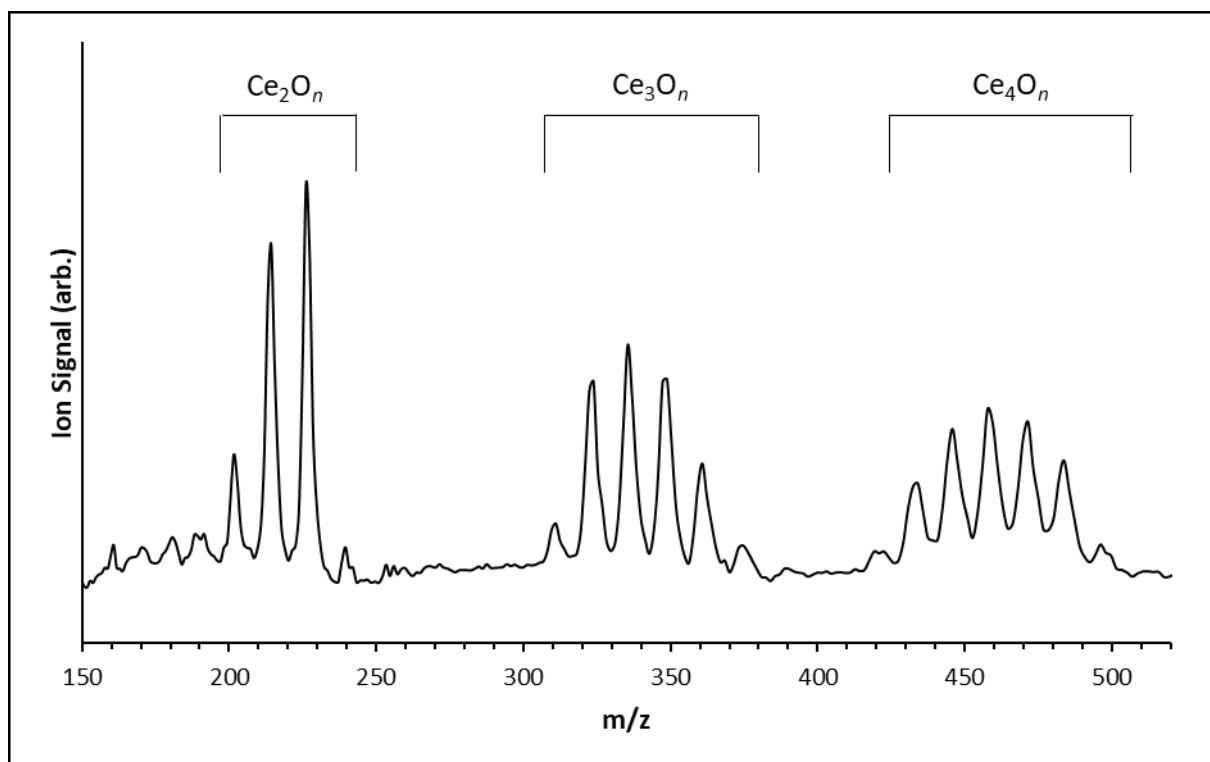


Figure A2: Mass spectrum of Ce_mO_n ($m=2,3,4$) clusters following photo-ionisation at 220 nm (5.64 eV). Mass ranges for each base metal cluster and corresponding oxide species are shown.

Appendix B: Calculated Vibrational Frequencies of Ce_mO_n and $AuCe_mO_n$ ($m=2,3$; $n=0-2m$) Clusters

Appendix B1: Calculated Vibrational Frequencies for Ce_2O_n ($n=1-4$) Clusters

Calculated Vibrational Frequencies for Ce_2O Clusters

Mode	Description ^a	Symmetry	¹ I A ω (cm ⁻¹)	⁵ I B ω (cm ⁻¹)	³ I B ω (cm ⁻¹)
ν_1	δ_s	a'	23.2	102.3	130.0
ν_2	ν_a Ce-O	a'	262.6	398.6	393.7
ν_3	ν_s Ce-O-Ce	a'	521.1	505.2	537.1
Mode	Description ^a	Symmetry	⁴ I B ⁺ ω (cm ⁻¹)	² I B ⁺ ω (cm ⁻¹)	⁶ I B ⁺ ω (cm ⁻¹)
ν_1	δ_s	a'	138.7	131.6	122.2
ν_2	ν_a Ce-O	a'	448.6	440.2	313.8
ν_3	ν_s Ce-O-Ce	a'	547.7	549.1	572.9

Appendix B1-1: Calculated vibrational modes for the Ce_2O neutral and cationic structures.

^a ν_a : asymmetric stretch; ν_s : symmetric stretch; δ_s : symmetric bend

Calculated Vibrational Frequencies for Ce_2O_2 Clusters

Mode	Description ^b	³ III		⁵ III		⁴ III ⁺	
		Symmetry	ω (cm ⁻¹)	Symmetry	ω (cm ⁻¹)	Symmetry	ω (cm ⁻¹)
v ₁	π Ce-O-Ce	b _{3u}	143.9	b _{3u}	176.1	b _{3u}	100.1
v ₂	δ_s Ce-O-Ce	a _g	231.6	a _g	237.8	a _g	243.1
v ₃	v _a Ce-O	b _{3g}	348.0	b _{3g}	326.0	b _{3g}	338.4
v ₄	v _s Ce-O/ v _a Ce-O	b _{2u}	522.9	b _{2u}	513.5	b _{1u}	436.5
v ₅	v _s Ce-O	a _g	603.8	a _g	602.0	b _{2u}	530.1
v ₆	v _a Ce-O/ v _s Ce-O	b _{1u}	609.0	b _{1u}	628.0	a _g	623.1

Appendix B1-2: Calculated vibrational modes for the Ce_2O_2 neutral and cationic structures.

^b δ_s : symmetric bend; v_s: symmetric stretch; v_a: asymmetric stretch; π : out-of-plane bend

Calculated Vibrational Frequencies for Ce_2O_3 Clusters

Mode	³ IVA		¹ IVA		² IVA ⁺	
	Symmetry	ω (cm ⁻¹)	Symmetry	ω (cm ⁻¹)	Symmetry	ω (cm ⁻¹)
v ₁	a''	208.6	a	199.9	a	152.1
v ₂	a''	215.3	a	206.8	a	156.0
v ₃	a'	281.7	a	278.1	a	294.4
v ₄	a'	333.0	a	326.8	a	352.8
v ₅	a'	335.8	a	330.9	a	353.6
v ₆	a'	544.9	a	545.8	a	581.4
v ₇	a'	546.9	a	547.4	a	596.0
v ₈	a''	605.3	a	583.2	a	598.3
v ₉	a'	623.5	a	619.5	a	722.2

Appendix B1-3: Calculated vibrational modes for the Ce_2O_3 neutral and cationic structures.

Calculated Vibrational Frequencies for Ce_2O_4 Clusters

Mode	¹ VA		² VA ⁺		¹ VB		² VB ⁺	
	Symmetry	ω (cm ⁻¹)	Symmetry	ω (cm ⁻¹)	Symmetry	ω (cm ⁻¹)	Symmetry	ω (cm ⁻¹)
v ₁	b _u	59.1	a	59.5	a''	2.25	a'	101.9
v ₂	a _u	83.4	a	68.3	a'	28.5	a''	123.3
v ₃	a _g	90.5	a	88.1	a''	118.5	a'	144.2
v ₄	b _g	123.3	a	108.7	a'	125.5	a''	168.7
v ₅	b _u	233.4	a	168.5	a'	253.6	a'	279.9
v ₆	a _g	240.1	a	226.7	a'	332.8	a''	318.0
v ₇	b _g	252.5	a	327.0	a''	334.0	a'	339.8
v ₈	a _u	497.9	a	474.5	a'	482.2	a'	388.2
v ₉	a _g	582.8	a	565.7	a''	586.2	a'	644.3
v ₁₀	b _u	623.4	a	650.4	a'	588.8	a''	686.0
v ₁₁	b _u	831.5	a	673.7	a'	737.0	a'	699.0
v ₁₂	a _g	840.7	a	904.2	a'	821.6	a'	806.2

Appendix B1-4: Calculated vibrational modes for Ce_2O_4 neutral and cationic structures.

Appendix B2: Calculated Vibrational Frequencies for Ce_3O_n ($n=0-6$) ClustersCalculated Vibrational Frequencies for Ce_3 Clusters

Mode	Description ^c	Symmetry	³ VIB ω (cm ⁻¹)	⁵ VIB ω (cm ⁻¹)	⁶ VIA ⁺ ω (cm ⁻¹)	² VIA ⁺ ω (cm ⁻¹)	⁴ VIA ⁺ ω (cm ⁻¹)
v ₁	v _a	a'	71	88	91	108	108
v ₂	δ	a'	180	187	133	180	177
v ₃	v _s	a'	201	202	182	204	209

Appendix B2-1: Calculated vibrational modes for the Ce_3 neutral and cationic structures.

^c v_a: asymmetric stretch; v_s: symmetric stretch; δ : in-plane bend

Calculated Vibrational Frequencies for Ce_3O Clusters

Mode	⁵ VIIA			⁶ VIIA ⁺		
	Description ^d	Symmetry	ω (cm ⁻¹)	Description ^d	Symmetry	ω (cm ⁻¹)
v ₁	v _a Ce ₃	a'	16	v _a Ce ₃	a'	71
v ₂	v _s Ce ₃	a'	138	π O	a''	108
v ₃	π O	a''	167	v _s Ce ₃	a'	125
v ₄	δ OCe ₂	a'	190	δ OCe ₂	a'	145
v ₅	v _a OCe ₂	a'	400	v _a OCe ₂	a'	468
v ₆	v _s OCe ₂	a'	564	v _s OCe ₂	a'	524

Appendix B2-2: Calculated vibrational modes for the Ce_3O neutral and cationic structures.

^d v_a: asymmetric stretch; v_s: symmetric stretch; δ : in-plane bend; π : out-of-plane bend

Calculated Vibrational Frequencies for Ce_3O_2 Clusters

Mode	$^5V_{IIIA}$		$^6V_{IIIA}^+$		$^4V_{IIIA}^+$		$^3V_{IIIB}$	
	Symmetry	ω (cm $^{-1}$)	Symmetry	ω (cm $^{-1}$)	Symmetry	ω (cm $^{-1}$)	Symmetry	ω (cm $^{-1}$)
ν_1	b_1	41.69	a''	63.91	a	64.65	a	63.91
ν_2	a_1	56.66	a''	83.85	a	80.82	a	83.85
ν_3	a_2	93.70	a''	113.73	a	97.37	a	133.73
ν_4	a_1	115.63	a''	171.91	a	107.96	a	171.91
ν_5	b_2	116.68	a''	256.40	a	120.79	a	256.40
ν_6	b_2	419.05	a''	371.66	a	427.88	a	371.66
ν_7	a_1	441.42	a'	418.10	a	443.70	a	418.10
ν_8	b_2	479.96	a''	464.82	a	502.38	a	464.82
ν_9	a_1	543.30	a'	538.92	a	543.73	a	538.92
Mode	$^5V_{IIIB}$		$^6V_{IIIB}^+$		$^4V_{IIIB}^+$		$^2V_{IIIB}^+$	
	Symmetry	ω (cm $^{-1}$)	Symmetry	ω (cm $^{-1}$)	Symmetry	ω (cm $^{-1}$)	Symmetry	ω (cm $^{-1}$)
ν_1	a	61.56	a	39.57	a	88.11	a	89.69
ν_2	a	84.39	a	121.71	a	114.15	a	114.60
ν_3	a	134.28	a	150.00	a	128.00	a	129.42
ν_4	a	172.35	a	182.82	a	183.92	a	184.06
ν_5	a	255.68	a	248.64	a	263.27	a	258.71
ν_6	a	369.06	a	384.29	a	387.86	a	385.50
ν_7	a	421.10	a	430.39	a	433.48	a	427.14
ν_8	a	462.42	a	454.12	a	479.42	a	479.78
ν_9	a	534.71	a	544.92	a	545.56	a	547.24

Appendix B2-3: Calculated vibrational modes for the Ce_3O_2 neutral and cationic structures.

Calculated Vibrational Frequencies for Ce_3O_3 Clusters

Mode	5I_X		3I_X	
	Symmetry	ω (cm^{-1})	Symmetry	ω (cm^{-1})
V ₁	a'	67.74	a	68.97
V ₂	a''	101.72	a	96.88
V ₃	a'	139.53	a	137.91
V ₄	a''	161.57	a	160.68
V ₅	a'	205.17	a	204.81
V ₆	a'	278.26	a	279.20
V ₇	a''	362.67	a	361.67
V ₈	a'	370.29	a	371.55
V ₉	a''	451.35	a	451.52
V ₁₀	a'	532.04	a	533.16
V ₁₁	a''	548.92	a	551.66
V ₁₂	a'	571.20	a	571.29

Appendix B2-4a: Calculated vibrational modes for the Ce_3O_3 neutral structures.

Mode	$2 X^+$		$4 X^+$		$6 X^+$	
	Symmetry	ω (cm^{-1})	Symmetry	ω (cm^{-1})	Symmetry	ω (cm^{-1})
v_1	a	104.08	a'	104.99	a	64.54
v_2	a	137.69	a''	139.46	a	81.59
v_3	a	168.68	a''	168.78	a	128.24
v_4	a	168.80	a'	169.31	a	167.07
v_5	a	207.85	a'	208.20	a	206.38
v_6	a	303.02	a'	304.16	a	259.98
v_7	a	375.14	a''	374.20	a	355.31
v_8	a	411.22	a'	410.49	a	381.30
v_9	a	454.40	a''	453.92	a	471.99
v_{10}	a	549.25	a'	548.66	a	535.38
v_{11}	a	566.93	a''	566.72	a	565.32
v_{12}	a	629.57	a'	629.92	a	583.32

Appendix B2-4b: Calculated vibrational modes for the Ce_3O_3 cationic structures.

Calculated Vibrational Frequencies for Ce_3O_4 Clusters

Mode	5X_A ω (cm^{-1})	3X_A ω (cm^{-1})	1X_A ω (cm^{-1})	5X_B ω (cm^{-1})	3X_B ω (cm^{-1})
V ₁	131.61	131.29	132.69	63.99	63.17
V ₂	131.94	132.86	133.10	102.29	102.92
V ₃	155.17	151.21	151.32	110.95	110.30
V ₄	155.68	151.30	157.33	144.25	144.74
V ₅	183.01	184.90	187.05	200.09	200.15
V ₆	235.43	236.08	236.38	234.49	234.82
V ₇	308.58	302.43	318.91	267.30	266.87
V ₈	310.20	328.70	327.72	317.62	318.78
V ₉	328.65	335.05	337.56	357.88	359.34
V ₁₀	368.64	363.61	381.66	392.89	394.31
V ₁₁	371.60	412.46	413.53	401.60	401.66
V ₁₂	411.44	433.34	415.94	502.06	502.30
V ₁₃	517.99	517.08	516.03	570.29	570.16
V ₁₄	519.74	526.99	535.22	668.66	668.76
V ₁₅	530.66	539.14	535.29	687.14	685.62

Appendix B2-5a: Calculated vibrational modes for Ce_3O_4 neutral structures. All calculated structures are C_1 symmetric; therefore, vibrational symmetries are not shown.

Mode	${}^2X_A^+$ ω (cm $^{-1}$)	${}^4X_A^+$ ω (cm $^{-1}$)	${}^4X_B^+$ ω (cm $^{-1}$)	${}^2X_B^+$ ω (cm $^{-1}$)	${}^6X_B^+$ ω (cm $^{-1}$)	${}^6X_A^+$ ω (cm $^{-1}$)
v ₁	145.22	147.33	19.64	20.45	73.33	69.44
v ₂	147.02	147.90	105.94	105.79	94.27	107.61
v ₃	159.23	159.59	111.28	111.10	110.45	135.57
v ₄	159.60	159.74	161.02	161.39	110.59	162.93
v ₅	205.89	206.65	217.41	217.00	139.86	163.48
v ₆	257.91	258.57	244.28	243.97	189.46	197.25
v ₇	329.20	331.79	267.27	267.92	214.29	292.12
v ₈	342.64	343.59	324.23	323.78	240.26	308.72
v ₉	343.66	344.42	329.94	330.35	361.12	356.98
v ₁₀	432.94	432.57	387.92	388.44	377.66	357.55
v ₁₁	519.80	519.90	459.82	460.25	384.30	406.63
v ₁₂	521.48	521.75	514.64	514.75	394.19	446.39
v ₁₃	552.31	552.22	590.07	590.93	504.89	529.89
v ₁₄	652.15	653.08	690.15	689.79	653.69	535.58
v ₁₅	653.12	654.43	739.66	738.48	686.85	626.99

Appendix B2-5a: Calculated vibrational modes for Ce_3O_4 cationic structures. All calculated structures are C_1 symmetric; therefore, vibrational symmetries are not shown.

Calculated Vibrational Frequencies for Ce_3O_5 Clusters

Mode	3XIA ω (cm $^{-1}$)	1XIB ω (cm $^{-1}$)	3XIB ω (cm $^{-1}$)	1XIA ω (cm $^{-1}$)
V ₁	69.17	128.14	128.35	53.60
V ₂	76.04	128.91	128.94	70.88
V ₃	135.29	164.30	164.40	97.23
V ₄	142.52	171.02	171.11	127.69
V ₅	156.80	210.70	211.06	155.63
V ₆	171.20	219.36	219.36	173.04
V ₇	202.99	268.64	268.61	190.12
V ₈	249.90	320.77	320.81	245.01
V ₉	297.22	322.80	323.00	281.19
V ₁₀	309.59	368.45	368.68	302.70
V ₁₁	352.77	382.61	382.48	407.26
V ₁₂	436.72	441.78	441.92	462.07
V ₁₃	491.33	454.04	454.18	479.92
V ₁₄	492.01	511.95	512.01	522.81
V ₁₅	519.94	553.81	553.73	551.29
V ₁₆	634.48	563.80	563.81	676.28
V ₁₇	651.58	633.91	633.59	695.22
V ₁₈	805.71	660.27	660.11	820.93

Appendix B2-6a: Calculated vibrational modes for Ce_3O_5 neutral structures. All calculated structures are C_1 symmetric; therefore, vibrational symmetries are not shown.

Mode	${}^2XIB^+$ ω (cm $^{-1}$)	${}^2XIA^+$ ω (cm $^{-1}$)	${}^4XIA^+$ ω (cm $^{-1}$)	${}^4XIB^+$ ω (cm $^{-1}$)
v ₁	112.94	59.91	74.77	91.66
v ₂	123.61	80.45	83.05	107.85
v ₃	150.71	128.13	144.98	128.60
v ₄	188.18	137.93	147.64	130.97
v ₅	210.89	144.75	155.52	169.24
v ₆	245.22	160.66	168.76	226.39
v ₇	272.69	197.53	204.19	246.72
v ₈	305.10	247.52	247.52	267.13
v ₉	350.57	263.25	298.89	302.27
v ₁₀	391.90	314.19	340.20	306.93
v ₁₁	395.46	352.63	349.71	376.38
v ₁₂	457.96	466.93	437.19	449.63
v ₁₃	499.09	480.51	482.78	449.71
v ₁₄	539.48	496.14	500.33	538.68
v ₁₅	564.30	579.69	547.29	549.08
v ₁₆	584.97	674.23	562.08	572.93
v ₁₇	666.47	741.15	644.56	590.04
v ₁₈	684.88	865.95	657.47	635.04

Appendix B2-6b: Calculated vibrational modes for Ce_3O_5 cationic structures. All calculated structures are C_1 symmetric; therefore, vibrational symmetries are not shown.

Calculated Vibrational Frequencies for Ce_3O_6 Clusters

Mode	1XII		$^2XII^+$	
	Symmetry	ω (cm $^{-1}$)	Symmetry	ω (cm $^{-1}$)
V ₁	a''	64.80	a	51.88
V ₂	a'	65.71	a	76.03
V ₃	a'	69.28	a	91.00
V ₄	a''	74.46	a	98.69
V ₅	a''	128.42	a	142.81
V ₆	a'	133.08	a	131.34
V ₇	a''	149.46	a	167.05
V ₈	a'	167.73	a	175.80
V ₉	a'	195.14	a	192.95
V ₁₀	a'	233.73	a	233.85
V ₁₁	a''	252.91	a	266.88
V ₁₂	a'	307.00	a	290.22
V ₁₃	a''	333.14	a	356.50
V ₁₄	a'	421.40	a	451.66
V ₁₅	a'	485.20	a	471.75
V ₁₆	a'	501.25	a	481.29
V ₁₇	a''	537.96	a	584.45
V ₁₈	a''	651.73	a	737.43
V ₁₉	a'	741.78	a	610.70
V ₂₀	a''	817.63	a	658.85
V ₂₁	a'	832.11	a	850.49

Appendix B2-7: Calculated vibrational modes for Ce_3O_6 neutral and cationic structures.

Appendix B3: Calculated Vibrational Frequencies for $AuCe_2O_n$ ($n=0-4$) ClustersCalculated Vibrational Frequencies for $AuCe_2$ Clusters

Mode	Description ^e	Symmetry	⁶ XIIIA ω (cm ⁻¹)	⁷ XIIIA ⁺ ω (cm ⁻¹)	⁵ XIIIA ⁺ ω (cm ⁻¹)
ν_1	ν_a Au-Ce	a'	56.4	69.0	83.2
ν_2	ν_s	a'	102.5	118.2	116.5
ν_3	δ_s Au-Ce	a'	161.4	166.1	164.9
Mode	Description ^e	Symmetry	⁸ XIIIB ω (cm ⁻¹)	⁷ XIIIB ⁺ ω (cm ⁻¹)	⁶ XIIIB ω (cm ⁻¹)
ν_1	ν_a Au-Ce	b ₂	66.8	84.7	68.1
ν_2	δ_s	b ₂	95.5	122.4	115.3
ν_3	ν_s Au-Ce	b ₂	133.2	167.7	176.5

Appendix B3–1: Calculated vibrational modes for $AuCe_2$ neutral and cationic structures.

^e : ν_a : asymmetric stretch; ν_s : symmetric stretch; δ_s : in-plane bend

Calculated Vibrational Frequencies for $AuCe_2O$ Clusters

Mode	Description ^f	Symmetry	⁴ XIV (cm ⁻¹)	² XIV ω (cm ⁻¹)	³ XIVB ⁺ ω (cm ⁻¹)	¹ XIVB ⁺ ω (cm ⁻¹)
v ₁	ν_a Au-Ce	a	68.5	68.8	73.3	73.9
v ₂	π O δ Au-Ce	a	92.3	91.6	108.9	105.1
v ₃	π O ν_s Au-Ce	a	113.2	112.3	132.5	132.6
v ₄	π O ν_s Ce-Ce	a	155.2	157.1	160.7	162.2
v ₅	ν_a O-Ce	a	430.0	435.6	396.7	408.0
v ₆	ν_s O-Ce	a	510.2	512.2	553.2	555.9

Appendix B3-2: Calculated vibrational modes for $AuCe_2O$ neutral and cationic structures.

^f : ν_a : asymmetric stretch; ν_s : symmetric stretch; δ_s : in-plane bend; π : out-of-plane bend

Calculated Vibrational Frequencies for $AuCe_2O_2$ Clusters

Mode	Description [§]	⁴ XVA		² XVA		² XVB	
		Symmetry	ω (cm ⁻¹)	Symmetry	ω (cm ⁻¹)	Symmetry	ω (cm ⁻¹)
ν_1	δ Ce-Ce-Au	a'	23.18	a	22.84	a	22.1
ν_2	τ Ce ₂ O ₂	a''	70.72	a	70.36	a	72.1
ν_3	ν Au-Ce	a'	119.87	a	120.07	a	118.7
ν_4	π O-Ce ₂	a'	184.89	a	186.87	a	180.7
ν_5	ν Ce-Ce δ O-Ce	a'	234.50	a	234.75	a	231.0
ν_6	ν_a Ce-O	a''	318.10	a	317.45	a	327.8
ν_7	ν_s O-Ce (alternating)	a''	519.86	a	519.71	a	516.5
ν_8	ν_s O-Ce (Ce ₁) δ O-Ce (Ce ₂)	a'	591.81	a	594.89	a	593.1
ν_9	δ O-Ce (Ce ₁) ν_s O-Ce (Ce ₂)	a'	610.02	a	613.20	a	560.6

Appendix B3-3a: Calculated vibrational modes for $AuCe_2O_2$ neutral structures.

[§] : ν_a : asymmetric stretch; ν_s : symmetric stretch; δ_s : in-plane bend; π : out-of-plane bend; τ : twist; λ : wag.

Ce₁ and Ce₂ denote Ce atoms closest and furthest from the Au atom, respectively. Alternating modes (i.e. where atoms on either side of a σ plane or pseudo-plane move in opposite directions) are specified.

Mode	Description [§]	Symmetry	¹ XVA ⁺ ω (cm ⁻¹)	³ XVA ⁺ ω (cm ⁻¹)
V ₁	ν_a Au-Ce	a	62.8	63.5
V ₂	ν_s Au-Ce	a	112.0	111.9
V ₃	τ Ce ₂ O ₂	a	146.7	148.9
V ₄	λ O-Ce δ AuCe	a	230.4	228.7
V ₅	ν_a O-Ce (alternating)	a	287.8	274.8
V ₆	λ O-Ce	a	299.3	299.7
V ₇	ν_s O-Ce (alternating)	a	549.6	545.9
V ₈	ν_a O-Ce	a	620.1	611.1
V ₉	ν_s O-Ce	a	624.9	620.0

Appendix B3-3b: Calculated vibrational modes for $AuCe_2O_2$ cationic structures.

[§] ν_a : asymmetric stretch; ν_s : symmetric stretch; δ_s : in-plane bend; π : out-of-plane bend; τ : twist; λ : wag.

Ce₁ and Ce₂ denote Ce atoms closest and furthest from the Au atom, respectively. Alternating modes (i.e. where atoms on either side of a σ plane or pseudo-plane move in opposite directions) are specified.

Calculated Vibrational Frequencies for $AuCe_2O_3$ Clusters

Mode	2XVIA		2XVIB		$^1XVI^+$	
	Symmetry	ω (cm $^{-1}$)	Symmetry	ω (cm $^{-1}$)	Symmetry	ω (cm $^{-1}$)
ν_1	a	11.6	a'	12.2	a'	28.1
ν_2	a	15.5	a''	17.2	a''	32.2
ν_3	a	99.2	a'	100.8	a'	111.1
ν_4	a	156.1	a'	137.9	a'	135.5
ν_5	a	157.8	a''	144.7	a''	136.1
ν_6	a	270.3	a'	295.5	a'	311.0
ν_7	a	337.0	a'	338.6	a'	345.5
ν_8	a	338.7	a''	340.0	a''	353.7
ν_9	a	504.2	a'	562.4	a'	444.9
ν_{10}	a	589.1	a''	566.3	a''	641.3
ν_{11}	a	590.1	a'	577.1	a'	655.4
ν_{12}	a	732.0	a'	647.1	a'	767.3

Appendix B3-4: Calculated vibrational modes for $AuCe_2O_3$ neutral and cationic structures.

Calculated Vibrational Frequencies for $AuCe_2O_4$ Clusters

Mode	2XVII		$^1XVII^+$		$^3XVII^+$	
	Symmetry	ω (cm^{-1})	Symmetry	ω (cm^{-1})	Symmetry	ω (cm^{-1})
V ₁	a'	94.9	b_2	94.0	a'	76.7
V ₂	a'	111.5	b_1	94.5	a'	83.7
V ₃	a''	118.3	a_2	121.9	a''	114.8
V ₄	a''	146.7	b_1	140.6	a''	120.8
V ₅	a''	200.6	b_1	197.5	a''	181.8
V ₆	a'	211.0	a_2	206.9	a'	225.8
V ₇	a''	256.8	a_1	230.0	a''	266.0
V ₈	a'	273.8	a_1	290.7	a'	269.4
V ₉	a'	390.3	b_2	382.9	a'	321.7
V ₁₀	a'	475.9	a_1	448.3	a'	496.2
V ₁₁	a'	507.8	b_1	522.1	a'	503.6
V ₁₂	a''	523.7	b_2	550.7	a''	539.2
V ₁₃	a'	568.4	a_1	620.1	a'	583.9
V ₁₄	a'	616.5	a_1	692.0	a'	614.5
V ₁₅	a'	688.0	b_2	705.8	a'	711.7

Appendix B3-5: Calculated vibrational modes for $AuCe_2O_4$ neutral and cationic structures.

Appendix B4: Calculated Vibrational Frequencies for $AuCe_3O_n$ ($n=0-6$) ClustersCalculated Vibrational Frequencies for $AuCe_3$ Clusters

Mode	⁸ XVIII		Symmetry	¹⁰ XVIII	⁶ XVIII	⁴ XVIII
	Symmetry	ω (cm ⁻¹)		ω (cm ⁻¹)	ω (cm ⁻¹)	ω (cm ⁻¹)
v ₁	a''	50.00	a	63.92	36.90	67.74
v ₂	a''	59.27	a	63.93	60.25	68.00
v ₃	a''	76.85	a	78.45	67.69	93.45
v ₄	a''	83.41	a	97.43	82.64	94.68
v ₅	a''	88.77	a	97.53	109.27	94.88
v ₆	a''	147.91	a	152.40	150.21	145.73

Mode	Symmetry	⁹ XVIII ⁺	⁷ XVIII ⁺	³ XVIII ⁺	⁵ XVIII ⁺
		ω (cm ⁻¹)	ω (cm ⁻¹)	ω (cm ⁻¹)	ω (cm ⁻¹)
v ₁	a	58.41	48.68	29.42	13.01
v ₂	a	60.35	50.98	56.42	45.44
v ₃	a	84.16	86.36	59.40	72.88
v ₄	a	84.67	87.06	89.05	77.30
v ₅	a	104.62	90.65	101.41	87.02
v ₆	a	149.57	141.56	146.54	145.92

Appendix B4-1: Calculated vibrational modes for $AuCe_3$ neutral and cationic structures.

Calculated Vibrational Frequencies for $AuCe_3O$ Clusters

Mode	2XIXA ω (cm^{-1})	6XIXB ω (cm^{-1})	4XIXB ω (cm^{-1})	6XIXA ω (cm^{-1})
v_1	72.78	50.72	42.54	61.66
v_2	75.90	54.37	66.42	63.86
v_3	99.35	77.36	74.01	94.10
v_4	101.16	79.17	89.68	103.95
v_5	104.98	121.57	105.71	105.34
v_6	157.19	142.46	120.23	157.47
v_7	230.30	163.31	152.34	200.34
v_8	253.92	434.75	462.93	412.63
v_9	405.25	505.71	493.62	413.69

Mode	$^7XIXB^+$ ω (cm^{-1})	$^7XIXA^+$ ω (cm^{-1})	$^5XIXA^+$ ω (cm^{-1})	$^5XIXB^+$ ω (cm^{-1})	$^1XIXA^+$ ω (cm^{-1})	$^3XIXB^+$ ω (cm^{-1})	$^3XIXA^+$ ω (cm^{-1})
v_1	55.41	47.82	67.26	41.98	65.54	55.76	64.28
v_2	70.91	60.16	72.71	68.47	76.59	66.22	78.43
v_3	76.64	84.31	93.86	79.33	91.85	74.09	85.98
v_4	80.56	97.90	96.45	81.86	102.86	77.52	96.41
v_5	129.73	102.26	104.09	121.39	162.54	121.76	118.23
v_6	155.63	159.33	161.74	147.39	178.28	128.88	164.72
v_7	176.67	220.55	232.37	163.82	238.86	154.53	234.20
v_8	458.79	385.49	310.76	461.19	373.63	470.60	364.92
v_9	510.93	428.77	415.53	522.82	418.81	512.19	415.68

Appendix B4-2: Calculated vibrational modes for $AuCe_3O$ neutral and cationic structures. All calculated structures are C_1 symmetric; therefore, vibrational symmetries are not shown.

Calculated Vibrational Frequencies for $AuCe_3O_2$ Clusters

Mode	6XX		4XX		2XX	
	Symmetry	ω (cm^{-1})	Symmetry	ω (cm^{-1})	Symmetry	ω (cm^{-1})
ν_1	a	67.86	a	65.81	a''	60.26
ν_2	a	80.85	a	79.86	a''	79.04
ν_3	a	81.06	a	81.82	a''	80.53
ν_4	a	93.37	a	90.11	a''	96.21
ν_5	a	121.83	a	121.70	a''	120.24
ν_6	a	131.09	a	128.55	a''	129.27
ν_7	a	135.80	a	137.62	a''	131.52
ν_8	a	152.88	a	151.17	a'	145.56
ν_9	a	409.52	a	410.33	a''	411.22
ν_{10}	a	451.90	a	447.58	a'	443.41
ν_{11}	a	510.58	a	512.75	a''	511.27
ν_{12}	a	555.88	a	565.26	a'	569.70

Appendix B4-3a: Calculated vibrational modes for $AuCe_3O_2$ neutral structures.

Mode	$^5XX^+$		$^3XX^+$		$^7XX^+$	
	Symmetry	ω (cm^{-1})	Symmetry	ω (cm^{-1})	Symmetry	ω (cm^{-1})
V ₁	a	50.35	a	50.61	a''	50.14
V ₂	a	79.36	a	75.52	a''	47.73
V ₃	a	82.22	a	83.54	a''	86.23
V ₄	a	87.63	a	87.37	a''	112.80
V ₅	a	100.01	a	102.77	a''	117.37
V ₆	a	130.79	a	132.78	a''	136.68
V ₇	a	142.88	a	142.00	a''	157.95
V ₈	a	154.68	a	159.74	a'	176.27
V ₉	a	422.54	a	423.23	a''	404.98
V ₁₀	a	448.01	a	445.33	a'	452.90
V ₁₁	a	488.79	a	483.30	a''	497.26
V ₁₂	a	566.98	a	571.57	a'	574.74

Appendix B4-3b: Calculated vibrational modes for $AuCe_3O_2$ cationic structures.

Calculated Vibrational Frequencies for $AuCe_3O_3$ Clusters

Mode	2XXIA		6XXIB		4XXIA		2XXIB	
	Symmetry	ω (cm $^{-1}$)	Symmetry	ω (cm $^{-1}$)	Symmetry	ω (cm $^{-1}$)	Symmetry	ω (cm $^{-1}$)
v ₁	e	50.44	a'	27.94	a''	24.94	a	24.34
v ₂	e	53.33	a'	71.25	a''	57.05	a	49.38
v ₃	a ₁	104.69	a''	83.04	a''	91.10	a	74.35
v ₄	e	110.54	a'	105.59	a''	107.02	a	88.11
v ₅	e	115.76	a''	112.82	a''	109.19	a	100.85
v ₆	e	154.52	a'	129.95	a''	146.55	a	118.40
v ₇	e	165.86	a''	161.57	a''	163.55	a	132.37
v ₈	e	168.87	a'	195.56	a''	244.52	a	144.71
v ₉	a ₁	245.34	a'	299.81	a''	383.46	a	207.15
v ₁₀	a ₂	385.10	a'	356.35	a''	420.74	a	363.20
v ₁₁	e	423.83	a''	374.67	a''	423.29	a	428.93
v ₁₂	e	442.89	a'	445.12	a''	433.65	a	440.32
v ₁₃	a ₁	450.63	a''	456.03	a''	578.77	a	485.38
v ₁₄	e	564.62	a'	528.73	a''	600.28	a	547.68
v ₁₅	e	572.48	a''	557.03	a''		a	585.55

Appendix B4-4a: Calculated vibrational modes for $AuCe_3O_3$ neutral structures.

Mode	$^5XXIA^+$		$^3XXIA^+$		$^5XXIB^+$		$^3XXIB^+$	
	Symmetry	ω (cm^{-1})	Symmetry	ω (cm^{-1})	Symmetry	ω (cm^{-1})	Symmetry	ω (cm^{-1})
V1	a''	12.15	a	52.90	a'	27.57	a	25.74
V2	a''	58.29	a	76.98	a''	71.29	a	70.48
V3	a''	79.35	a	105.98	a'	71.51	a	70.79
V4	a'	106.03	a	115.52	a'	117.18	a	113.22
V5	a'	114.89	a	128.60	a''	145.75	a	145.21
V6	a''	133.95	a	167.94	a''	166.63	a	164.23
V7	a'	158.67	a	174.42	a'	169.45	a	167.69
V8	a'	173.52	a	246.73	a'	199.23	a	193.22
V9	a'	243.06	a	321.17	a'	312.19	a	310.66
V10	a''	370.28	a	385.86	a''	350.56	a	349.87
V11	a'	421.43	a	431.64	a'	415.29	a	411.95
V12	a''	439.23	a	455.16	a''	435.86	a	438.33
V13	a'	453.98	a	457.59	a'	540.40	a	535.82
V14	a''	579.95	a	612.01	a''	540.75	a	538.79
V15	a'	619.26	a	949.28	a'	619.63	a	623.45
Mode	$^1XXIB^+$		$^7XXIB^+$		$^1XXIA^+$			
	Symmetry	ω (cm^{-1})	Symmetry	ω (cm^{-1})	Symmetry	ω (cm^{-1})		
V1	a	25.47	a'	20.96	e	36.91		
V2	a	70.93	a''	45.05	e	51.18		
V3	a	72.34	a'	51.39	e	65.26		
V4	a	114.29	a'	75.05	e	88.67		
V5	a	144.32	a''	126.78	e	107.90		
V6	a	165.04	a'	130.45	a ₁	119.08		
V7	a	166.66	a''	167.64	e	130.72		

V ₈	a	197.81	a'	192.54	e	142.08
V ₉	a	312.57	a'	291.96	a ₁	196.60
V ₁₀	a	353.29	a'	354.24	a ₂	375.49
V ₁₁	a	410.08	a''	369.30	e	447.12
V ₁₂	a	435.10	a''	439.92	e	453.80
V ₁₃	a	538.61	a''	533.09	e	456.87
V ₁₄	a	543.39	a''	549.69	e	467.07
V ₁₅	a	615.06	a'	590.50	e	468.77

Appendix B4-4b: Calculated vibrational modes for $AuCe_3O_3$ cationic structures.

Calculated Vibrational Frequencies for $AuCe_3O_4$ Clusters

Mode	2XXII ω (cm $^{-1}$)	4XXII ω (cm $^{-1}$)	$^3XXII^+$ ω (cm $^{-1}$)	$^5XXII^+$ ω (cm $^{-1}$)	$^1XXII^+$ ω (cm $^{-1}$)
V ₁	21.14	21.13	8.88	9.83	21.38
V ₂	24.97	25.22	25.31	11.66	24.72
V ₃	88.50	88.05	112.26	45.22	110.75
V ₄	142.26	142.55	149.58	146.46	149.18
V ₅	144.37	144.80	154.22	147.62	150.60
V ₆	163.25	163.48	166.39	159.45	171.84
V ₇	167.12	167.75	167.42	160.65	175.81
V ₈	203.81	204.26	207.37	205.99	205.25
V ₉	255.01	255.27	265.65	255.88	241.18
V ₁₀	316.76	317.38	299.33	336.18	316.26
V ₁₁	320.97	318.55	350.77	342.25	321.81
V ₁₂	358.60	358.38	356.20	343.73	353.62
V ₁₃	436.17	435.86	438.57	428.03	398.09
V ₁₄	495.48	495.49	518.25	513.71	424.44
V ₁₅	507.36	506.08	540.56	519.46	458.09
V ₁₆	520.09	519.70	558.85	548.40	549.73
V ₁₇	633.33	633.15	651.48	642.12	553.96
V ₁₈	648.97	649.09	656.14	652.96	571.03

Appendix B4-5: Calculated vibrational modes for $AuCe_3O_4$ neutral and cationic structures. All calculated structures are C_1 symmetric; therefore, vibrational symmetries are not shown.

Calculated Vibrational Frequencies for $AuCe_3O_5$ Clusters

Mode	$^4XIII A$		Symmetry	$^2XIII A$	$^4XIII B$	$^2XIII B$
	Symmetry	ω (cm^{-1})		ω (cm^{-1})	ω (cm^{-1})	ω (cm^{-1})
v ₁	a''	61.61	a	61.10	29.30	28.21
v ₂	a'	74.64	a	73.76	59.49	59.07
v ₃	a''	92.08	a	91.17	81.99	81.77
v ₄	a'	110.63	a	110.31	140.82	140.46
v ₅	a'	135.74	a	133.88	147.15	146.69
v ₆	a''	144.95	a	144.78	160.40	160.47
v ₇	a'	173.65	a	171.40	164.58	164.57
v ₈	a''	200.73	a	200.74	209.65	208.92
v ₉	a'	206.83	a	206.52	222.11	221.92
v ₁₀	a'	255.50	a	253.29	255.57	255.42
v ₁₁	a''	287.58	a	285.19	323.92	323.84
v ₁₂	a''	329.76	a	330.77	326.46	326.63
v ₁₃	a'	372.07	a	371.42	363.92	364.16
v ₁₄	a'	391.22	a	390.86	379.22	378.86
v ₁₅	a''	403.13	a	401.53	442.91	442.68
v ₁₆	a'	453.06	a	450.64	451.61	451.43
v ₁₇	a'	509.72	a	507.10	499.57	499.20
v ₁₈	a'	533.49	a	532.62	540.55	540.25
v ₁₉	a'	548.09	a	546.21	568.63	568.25
v ₂₀	a''	628.28	a	627.96	635.56	634.99
v ₂₁	a'	668.51	a	669.01	664.17	663.92

Appendix B4-6a: Calculated vibrational modes for $AuCe_3O_5$ neutral structures.

Mode	Symmetry	$^3XXIII A^+$ ω (cm $^{-1}$)	$^1XXIII A^+$ ω (cm $^{-1}$)	$^3XXIII B^+$ ω (cm $^{-1}$)	$^5XXIII A^+$ ω (cm $^{-1}$)	$^5XXIII B^+$ ω (cm $^{-1}$)
V ₁	a	60.54	60.65	25.02	57.72	30.97
V ₂	a	71.21	71.28	26.68	78.66	62.37
V ₃	a	95.50	95.58	106.86	93.75	81.67
V ₄	a	108.11	108.45	132.27	96.88	97.60
V ₅	a	138.93	139.04	133.88	116.34	125.21
V ₆	a	146.17	146.19	159.22	138.52	127.59
V ₇	a	180.55	180.63	159.47	178.59	154.22
V ₈	a	198.92	199.01	216.18	189.70	170.34
V ₉	a	214.59	214.55	223.61	197.59	230.59
V ₁₀	a	252.49	252.57	243.38	253.87	244.31
V ₁₁	a	290.47	290.32	321.93	280.11	256.50
V ₁₂	a	318.51	318.36	337.15	318.52	292.29
V ₁₃	a	385.51	385.54	374.76	361.12	323.82
V ₁₄	a	401.91	401.99	376.03	380.94	386.37
V ₁₅	a	403.89	404.14	451.14	381.36	419.22
V ₁₆	a	439.30	439.91	469.58	392.15	443.91
V ₁₇	a	509.82	510.17	542.35	519.83	515.52
V ₁₈	a	549.29	549.32	561.68	563.61	524.11
V ₁₉	a	602.96	602.80	645.28	569.34	565.46
V ₂₀	a	648.71	648.89	647.43	660.36	584.85
V ₂₁	a	719.00	718.74	681.95	696.28	611.60

Appendix B4-6b: Calculated vibrational modes for $AuCe_3O_5$ cationic structures.

Calculated Vibrational Frequencies for $AuCe_3O_6$ Clusters

Mode	2XXIV		$^1XXIV^+$		$^3XXIV^+$	
	Symmetry	ω (cm $^{-1}$)	Symmetry	ω (cm $^{-1}$)	Symmetry	ω (cm $^{-1}$)
v ₁	a'	44.15	a'	41.34	a	38.40
v ₂	a''	90.24	a''	85.24	a	68.93
v ₃	a'	99.33	a'	90.35	a	82.11
v ₄	a''	109.17	a'	99.68	a	106.65
v ₅	a'	143.22	a''	136.86	a	144.16
v ₆	a''	154.74	a''	142.675	a	144.79
v ₇	a''	159.08	a''	145.13	a	152.13
v ₈	a'	171.47	a'	156.97	a	152.96
v ₉	a'	182.33	a'	174.02	a	176.38
v ₁₀	a'	217.97	a'	210.61	a	184.57
v ₁₁	a''	241.29	a''	218.18	a	222.34
v ₁₂	a'	270.82	a'	264.87	a	266.14
v ₁₃	a'	342.86	a'	327.10	a	271.03
v ₁₄	a''	349.25	a''	345.24	a	345.89
v ₁₅	a''	395.10	a''	395.76	a	361.78
v ₁₆	a'	427.24	a'	435.75	a	428.18
v ₁₇	a'	462.59	a'	452.57	a	481.27
v ₁₈	a'	494.00	a'	483.99	a	508.25
v ₁₉	a''	499.67	a''	527.28	a	526.90
v ₂₀	a''	525.02	a'	531.99	a	528.28
v ₂₁	a'	530.61	a''	586.03	a	553.70
v ₂₂	a'	609.78	a'	665.21	a	586.27
v ₂₃	a'	639.84	a''	692.68	a	649.92
v ₂₄	a''	648.28	a'	726.20	a	665.37

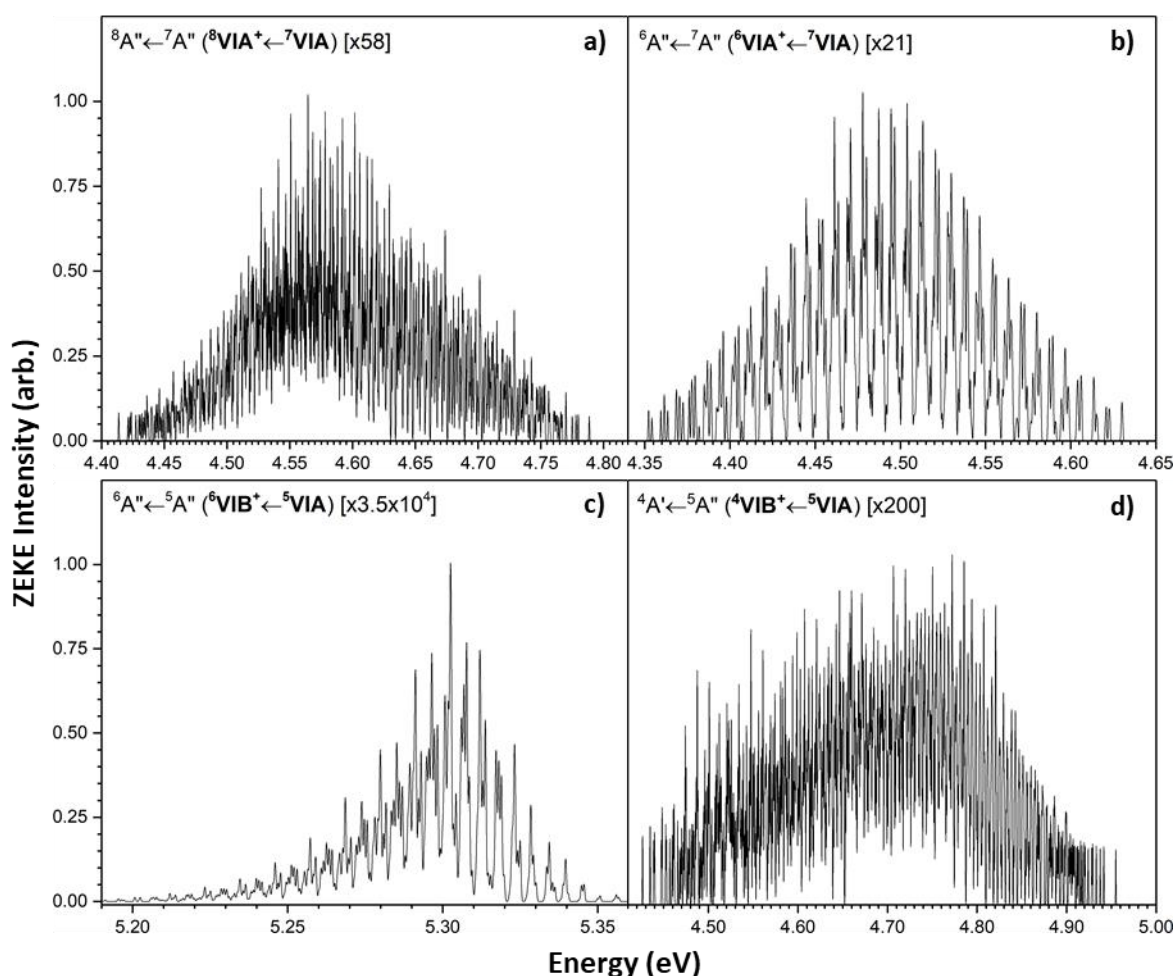
Appendix B4-7: Calculated vibrational modes for $AuCe_3O_6$ neutral and cationic structures.

Appendix C: Calculated Low-Intensity Ce_mO_n and $AuCe_mO_n$ ($m=2,3; n=0-2m$) ZEKE Spectra

(Note: low-intensity ZEKE spectra for the Ce_2O_n ($n=0-4$) ionisation processes are all presented in Chapter 5).

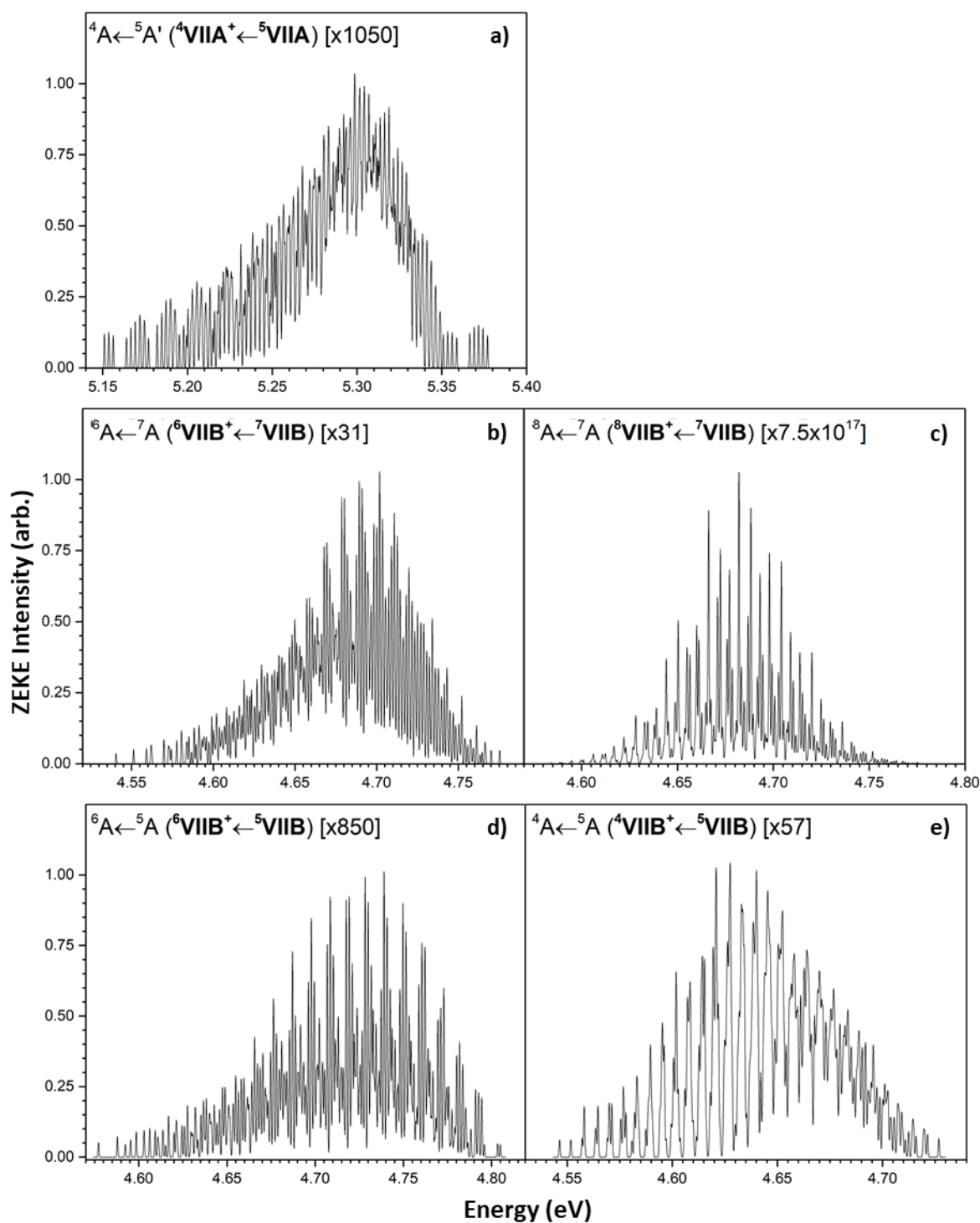
Appendix C1: Calculated Low-Intensity Ce_3O_n ($n=0-6$) ZEKE Spectra

Ce_3

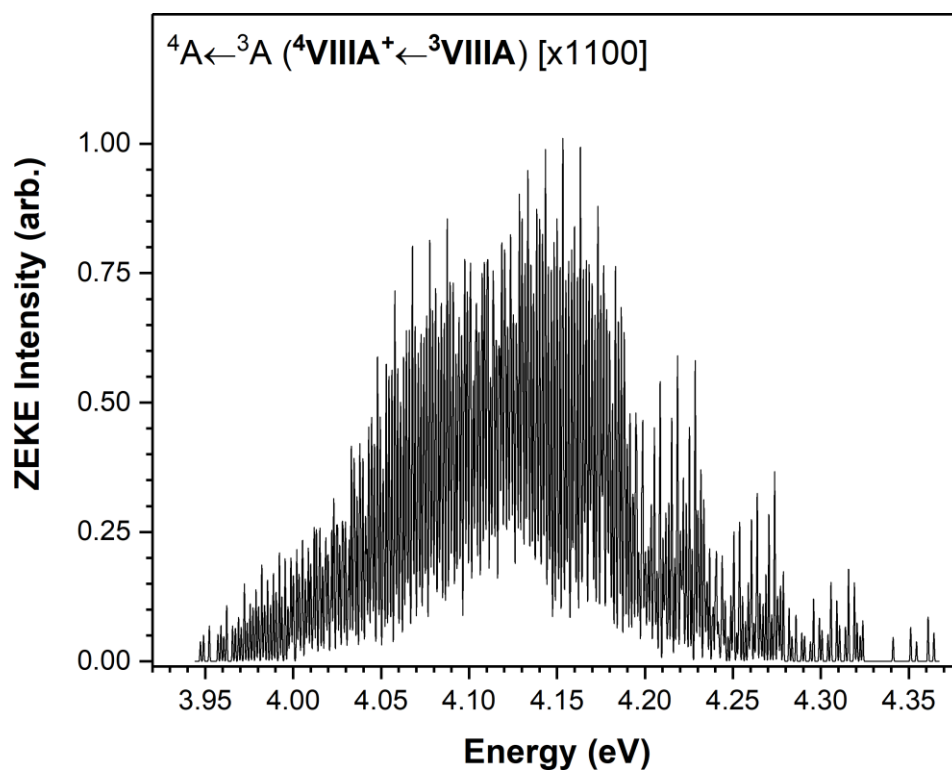


Appendix C1-1: Calculated ZEKE spectra for the Ce_3 low-intensity ionisation transitions: **a).** ${}^8A'' \leftarrow {}^7A''$ (${}^8VIA^+ \leftarrow {}^7VIA$), **b).** ${}^6A'' \leftarrow {}^7A''$ (${}^6VIA^+ \leftarrow {}^7VIA$), **c).** ${}^6A'' \leftarrow {}^7A''$ (${}^6VIB^+ \leftarrow {}^7VIA$) and **d).** ${}^4A'' \leftarrow {}^5A''$ (${}^8VIB^+ \leftarrow {}^7VIA$). Spectral intensities are normalised to the most intense peak in each spectrum with scaling factors shown.

Ce_3O

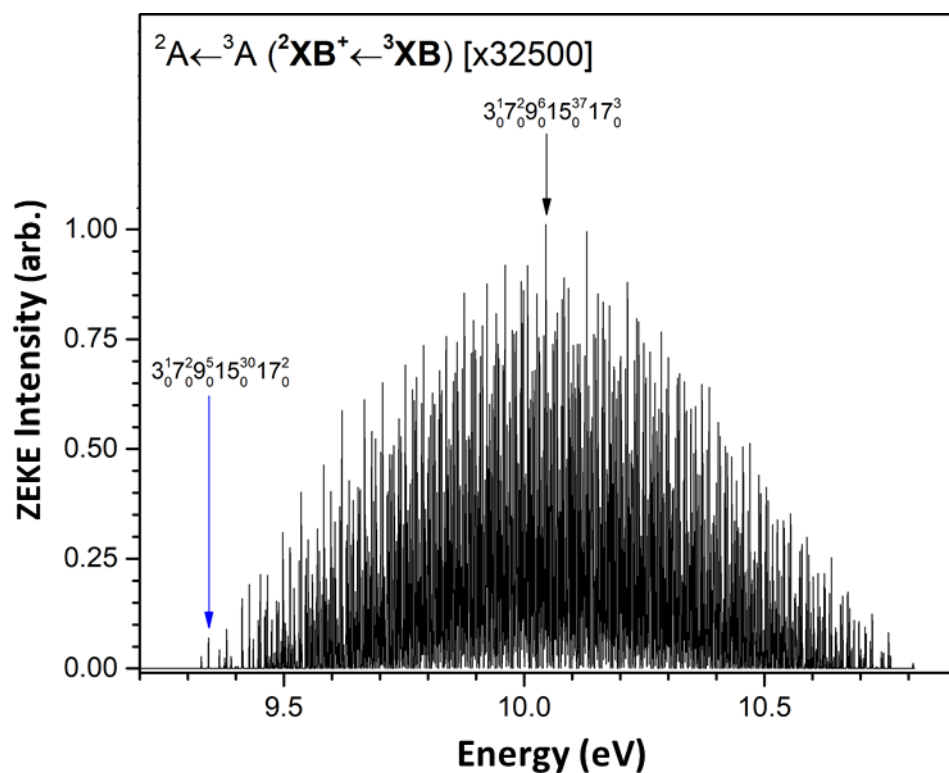


Appendix C1-2: Calculated ZEKE spectra for the Ce_3O low-intensity ionisation transitions: **a).** $^4A \leftarrow ^5A'$ ($^4VIIA^+ \leftarrow ^5VIIA$), **b).** $^6A \leftarrow ^7A$ ($^6VIIB^+ \leftarrow ^7VIIB$), **c).** $^8A \leftarrow ^7A$ ($^8VIIB^+ \leftarrow ^7VIIB$), **d).** $^6A \leftarrow ^5A$ ($^6VIIB^+ \leftarrow ^5VIIB$) and **e).** $^4A \leftarrow ^5A$ ($^4VIIB^+ \leftarrow ^5VIIB$). Spectral intensities are normalised to the most intense peak in each spectrum with scaling factors shown.

Ce₃O₂

Appendix C1-3: Calculated ZEKE spectrum for the Ce₃O₂ low-intensity $^4A \leftarrow ^3A$ ($^4V^{IIIA^+} \leftarrow ^3V^{IIIA}$) ionisation transition. The spectral intensity is normalised to the most intense peak with scaling factor shown.

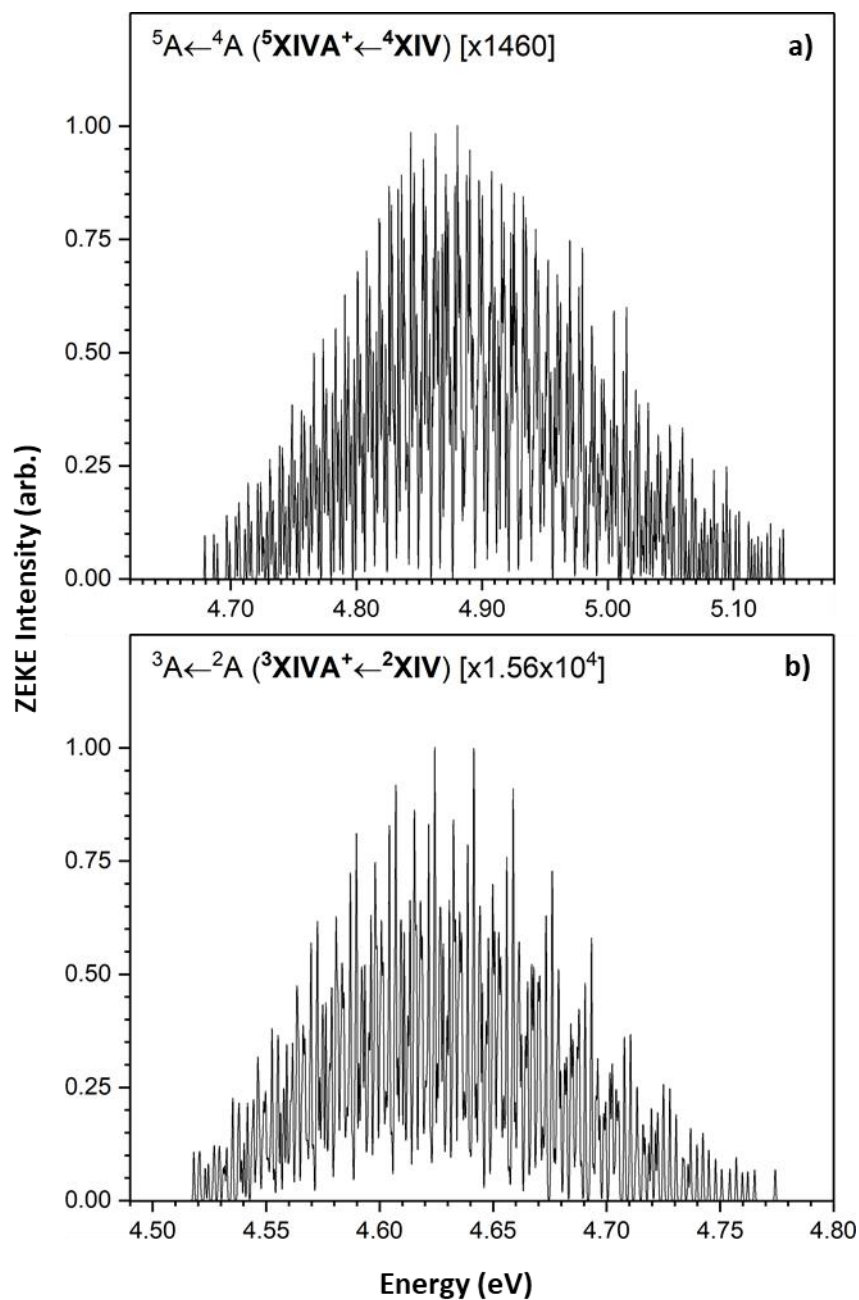
Ce_3O_5



Appendix C1-4: Calculated ZEKE spectrum for the Ce_3O_5 low-intensity ${}^2A \leftarrow {}^1A$ (${}^2XIB^+ \leftarrow {}^1XIB$) ionisation transition. The spectral intensity is normalised to the most intense peak with scaling factor shown.

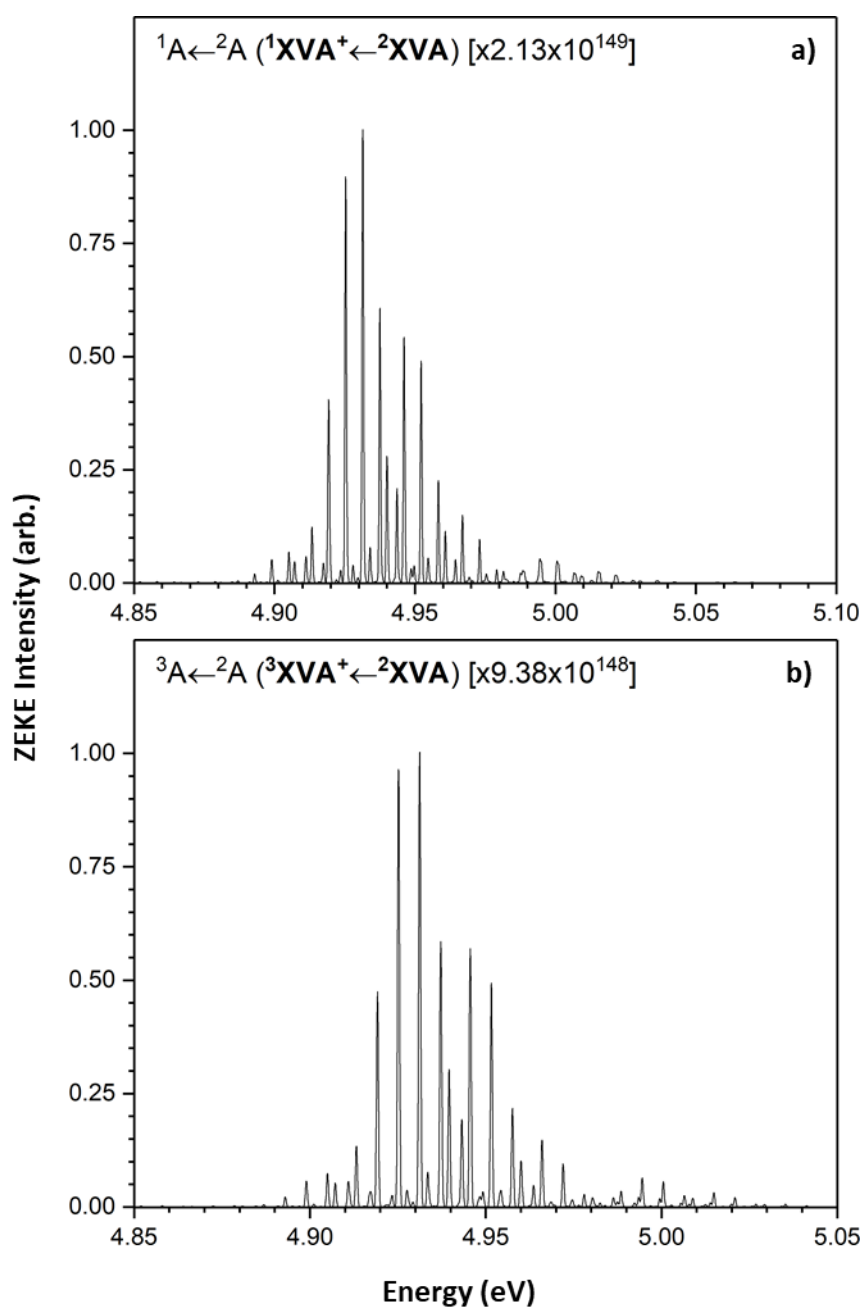
Appendix C2: Calculated Low-Intensity $AuCe_2O_n$ ($n=0-4$) ZEKE Spectra

$AuCe_2O$



Appendix C2-1: Calculated ZEKE spectra for the $AuCe_2O$ low-intensity ionisation transitions: **a).** ${}^5A \leftarrow {}^4A$ (${}^5XIVA^+ \leftarrow {}^4XIV$) and **b).** ${}^3A \leftarrow {}^2A$ (${}^3XIVA^+ \leftarrow {}^2XIV$). Spectral intensities are normalised to the most intense peak in each spectrum with scaling factors shown.

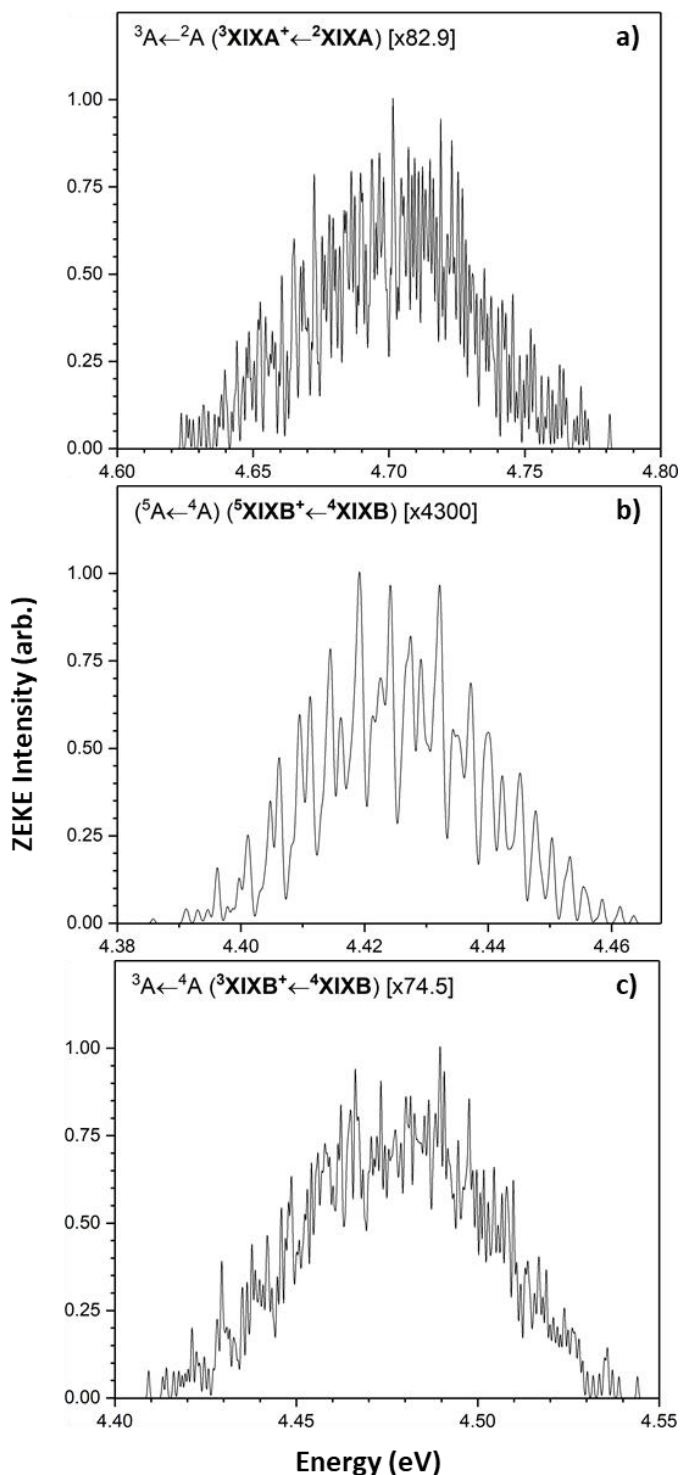
$AuCe_2O_2$



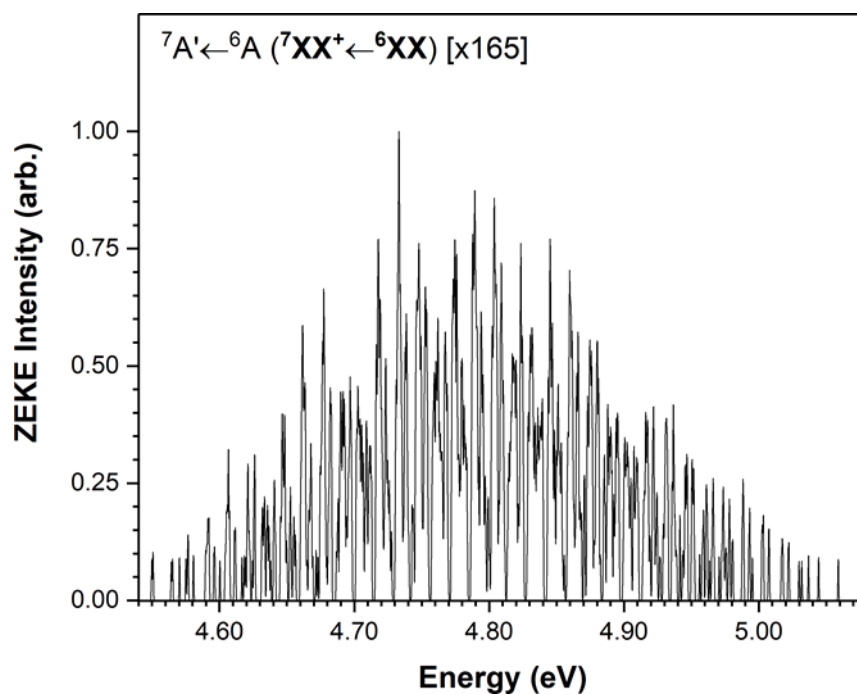
Appendix C2-2: Calculated ZEKE spectra for the $AuCe_2O_2$ low-intensity ionisation transitions: **a).** $^1A \leftarrow ^2A (^1XVA^+ \leftarrow ^2XVA)$ and **b).** $^3A \leftarrow ^2A (^3XVA^+ \leftarrow ^2XVA)$. Spectral intensities are normalised to the most intense peak in each spectrum with scaling factors shown.

Appendix C3: Calculated Low-Intensity $AuCe_3O_n$ ($n=0-6$) ZEKE Spectra

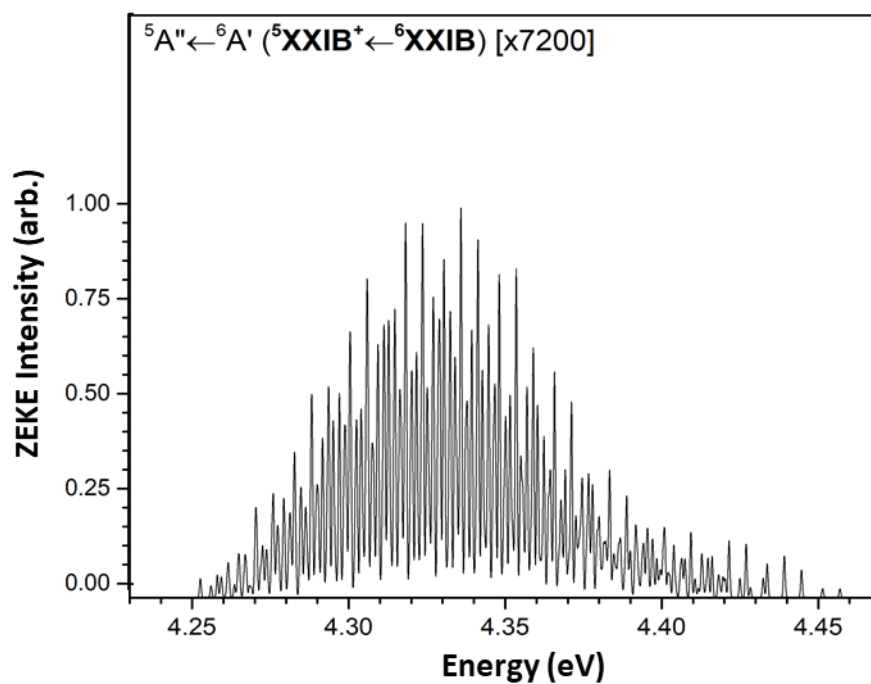
$AuCe_3O$



Appendix C3-1: Calculated ZEKE spectra for the $AuCe_3O$ low-intensity ionisation transitions: **a).** ${}^3A \leftarrow {}^2A$ (${}^3XIXA^+ \leftarrow {}^2XIXA$), **b).** ${}^5A \leftarrow {}^4A$ (${}^5XIXB^+ \leftarrow {}^4XIXB$) and **c).** ${}^3A \leftarrow {}^4A$ (${}^3XIXB^+ \leftarrow {}^4XIXB$). Spectral intensities are normalised to the most intense peak in each spectrum with scaling factors shown.

AuCe₃O₂

Appendix C3-2: Calculated ZEKE spectrum for the AuCe₃O₂ low-intensity ${}^7A' \leftarrow {}^6A$ (${}^7XX^+ \leftarrow {}^6XX$) ionisation transition. The spectral intensity is normalised to the most intense peak with scaling factor shown.

AuCe₃O₃

Appendix C3-3: Calculated ZEKE spectrum for the AuCe₃O₃ low-intensity ${}^5A'' \leftarrow {}^6A'$ (${}^5XXIB^+ \leftarrow {}^6XXIB$) ionisation transition. The spectral intensity is normalised to the most intense peak with scaling factor shown.

Appendix D: ZEKE Simulation Parameters and Test Calculations

Appendix D1: Parameters for ZEKE Simulations

System	Treatment	Transition	Omitted Modes
Ce ₂	Duschinsky	All	Nil
Ce ₂ O	Duschinsky	All	Nil
Ce ₂ O ₂	Duschinsky	All	Nil
Ce ₂ O ₃	Duschinsky	$^2A \leftarrow ^3A'' (^2IVA^+ \leftarrow ^3IVA)$	Nil
		$^2A \leftarrow ^1A (^2IVA^+ \leftarrow ^1IVA)$	0 1 3 6
Ce ₂ O ₄	Duschinsky	$^2A \leftarrow ^1A_g (^2VA^+ \leftarrow ^1VA)$	Nil
		$^2A \leftarrow ^1A' (VB^+ \leftarrow VB)$	Nil
Ce ₃	Duschinsky	All	Nil
Ce ₃ O	Duschinsky	All	Nil
Ce ₃ O ₂	Duschinsky	All	Nil
Ce ₃ O ₃	Parallel	$^4A'' \leftarrow ^5A' (^4IX^+ \leftarrow ^5IX)$	Nil
		$^2A \leftarrow ^3A (^2IX^+ \leftarrow ^3IX)$	Nil
		$^4A \leftarrow ^3A (^4IX^+ \leftarrow ^3IX)$	Nil
		$^6A \leftarrow ^5A' (^6IX^+ \leftarrow ^5IX)$	Nil
Ce ₃ O ₄	Duschinsky	$^4A \leftarrow ^5A (^4XA^+ \leftarrow ^5XA)$	Nil
		$^2A \leftarrow ^3A (^4XA^+ \leftarrow ^3XA)$	3 4 5
		$^4A \leftarrow ^3A (^4XA^+ \leftarrow ^3XA)$	Nil
		$^2A \leftarrow ^1A (^2XA^+ \leftarrow ^1XA)$	Nil
		$^4A \leftarrow ^5A (^4XB^+ \leftarrow ^5XB)$	2 3 5 7
		$^4A \leftarrow ^3A (^4XB^+ \leftarrow ^3XB)$	2 3 5 7
		$^2A \leftarrow ^3A (^4XB^+ \leftarrow ^3XB)$	2 3 5 7
Ce ₃ O ₅	Parallel	$^2A \leftarrow ^3A (^2XIA^+ \leftarrow ^3XIA)$	3 4 5 7 8 9 10 12 15 17
		$^2A \leftarrow ^1A (^2XIB^+ \leftarrow ^1XIB)$	Nil

		${}^2A \leftarrow {}^3A$ (${}^2XIB^+ \leftarrow {}^3XIB$)	0 1 3 4 5 7 9 10 11 12 13 15 17
		${}^2A \leftarrow {}^1A$ (${}^2XIA^+ \leftarrow {}^1XIA$)	Nil
Ce ₃ O ₆	Parallel	${}^2A \leftarrow {}^1A'$ (${}^2XIIA^+ \leftarrow {}^1XIIA$)	0 1 8 9 10 11 12 13 14 15 16

Appendix D-1a: Parameters used for ZEKE simulations of Ce_mO_n (m=2,3; n=0–2m) ionisation processes. Parameters shown include the method of vibrational wavefunction overlap (Duschinsky or Parallel Approximation) and any modes omitted from calculations. Mode numbers are presented as per ezSpectrum settings; i.e. mode $v_1 = "0"$, $v_2 = "1"$, etc.

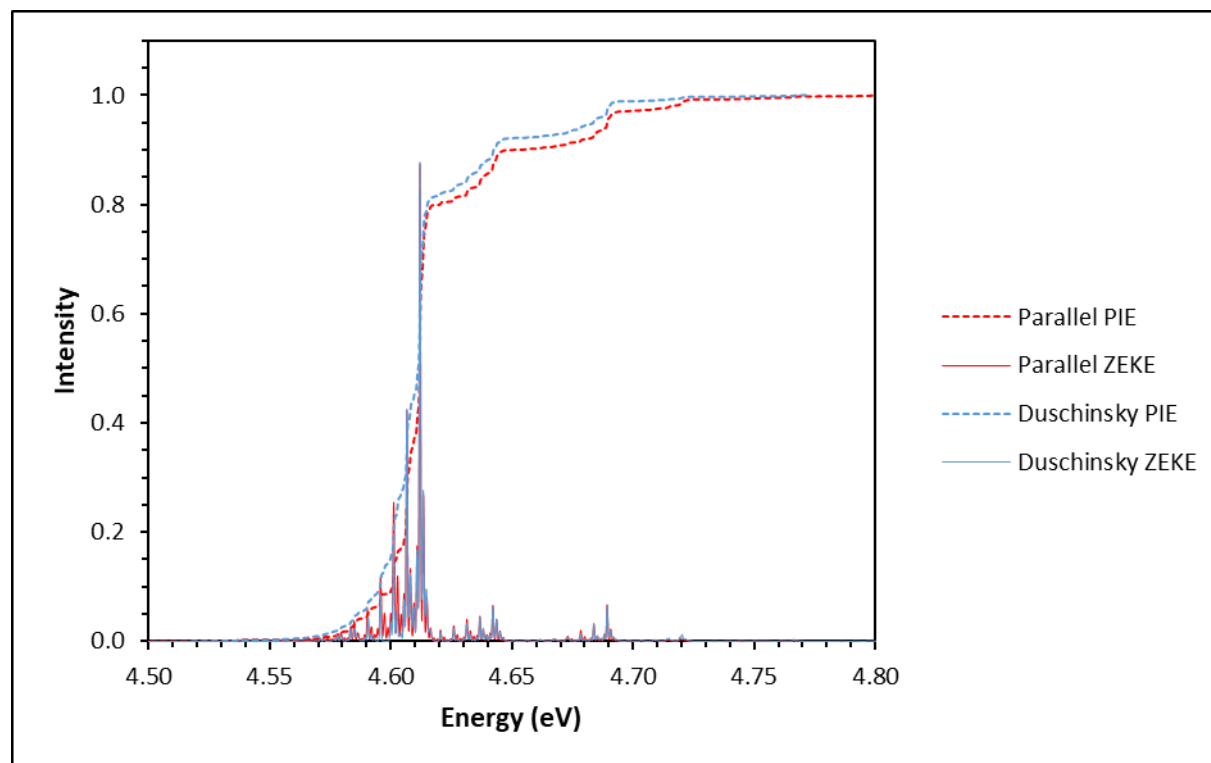
System	Treatment	Transition	Omitted Modes
AuCe ₂	Duschinsky	All	Nil
AuCe ₂ O	Duschinsky	All	Nil
AuCe ₂ O ₂	Duschinsky	³ A' ← ⁴ A' (³ XVA ⁺ ← ⁴ XVA)	8
		¹ A ← ² A (¹ XVA ⁺ ← ² XVA)	1 2 3 4
		³ A' ← ² A (³ XVA ⁺ ← ² XVA)	1 2 4
		¹ A ← ² A (¹ XVA ⁺ ← ² XVB)	1 2 4
		³ A' ← ² A (³ XVA ⁺ ← ² XVB)	1 2 4
AuCe ₂ O ₃	Duschinsky	¹ A ← ² A (¹ XVI ⁺ ← ² XVIA)	Nil
		¹ A ← ¹ A' (¹ XVI ⁺ ← ² XVIB)	Nil
AuCe ₂ O ₄	Duschinsky	¹ A ₁ ← ² A' (¹ XVII ⁺ ← ² XVII)	Nil
AuCe ₃	Duschinsky	All	Nil
AuCe ₃ O	Duschinsky	All	Nil
AuCe ₃ O ₂	Parallel	⁵ A ← ⁶ A (⁵ XX ⁺ ← ⁶ XX ⁺)	Nil
		⁷ A' ← ⁶ A (⁷ XX ⁺ ← ⁶ XX ⁺)	Nil
		⁵ A ← ⁴ A (⁵ XX ⁺ ← ⁴ XX ⁺)	Nil
		³ A ← ⁴ A (³ XX ⁺ ← ⁴ XX ⁺)	Nil
		³ A ← ² A'' (³ XX ⁺ ← ² XX ⁺)	Nil
AuCe ₃ O ₃	Parallel	³ A ← ² A ₁ (³ XXIA ⁺ ← ² XXIA)	0
		⁵ A'' ← ⁶ A' (⁵ XXIB ⁺ ← ⁶ XXIB)	1 4 6 10
		⁵ A'' ← ⁴ A'' (⁵ XXIA ⁺ ← ⁴ XXIA)	Nil
		³ A ← ⁴ A'' (³ XXIA ⁺ ← ⁴ XXIA)	Nil
		³ A ← ² A (³ XXIB ⁺ ← ² XXIB)	5 6 8 9 10 11 12 13 14
		¹ A ← ² A (¹ XXIB ⁺ ← ² XXIB)	5 8 9 10 11 13 14
AuCe ₃ O ₄	Parallel	³ A ← ² A (³ XXII ⁺ ← ² XXII)	4 6 7 8 9 10 11 12 13 14 17
		³ A ← ⁴ A (³ XXII ⁺ ← ⁴ XXII)	10 11 12 13 14 15 17
AuCe ₃ O ₅	Parallel	³ A ← ⁴ A'' (³ XXIII ⁺ ← ⁴ XXIII)	4 6 7 8 9 10 11 13 14 15 16 18 19

		$^3A \leftarrow ^2A$ ($^3XXIII A^+ \leftarrow ^2XXIII A$)	4 6 7 8 11 12 13 14 15 16 18 19
		$^1A \leftarrow ^2A$ ($^1XXIII A^+ \leftarrow ^2XXIII A$)	0 8 9 10 11 12 14 15 16 17 18 19
		$^3A \leftarrow ^4A$ ($^3XXIII B^+ \leftarrow ^4XXIII B$)	Nil
		$^3A \leftarrow ^2A$ ($^3XXIII B^+ \leftarrow ^2XXIII B$)	Nil
AuCe ₃ O ₆	Parallel	$^1A' \leftarrow ^2A''$ ($^1XXIV^+ \leftarrow ^2XXIV$)	5 6 7 8 9 10 11 13 14 15 16
		$^3A \leftarrow ^2A''$ ($^3XXIV^+ \leftarrow ^2XXIV$)	Nil

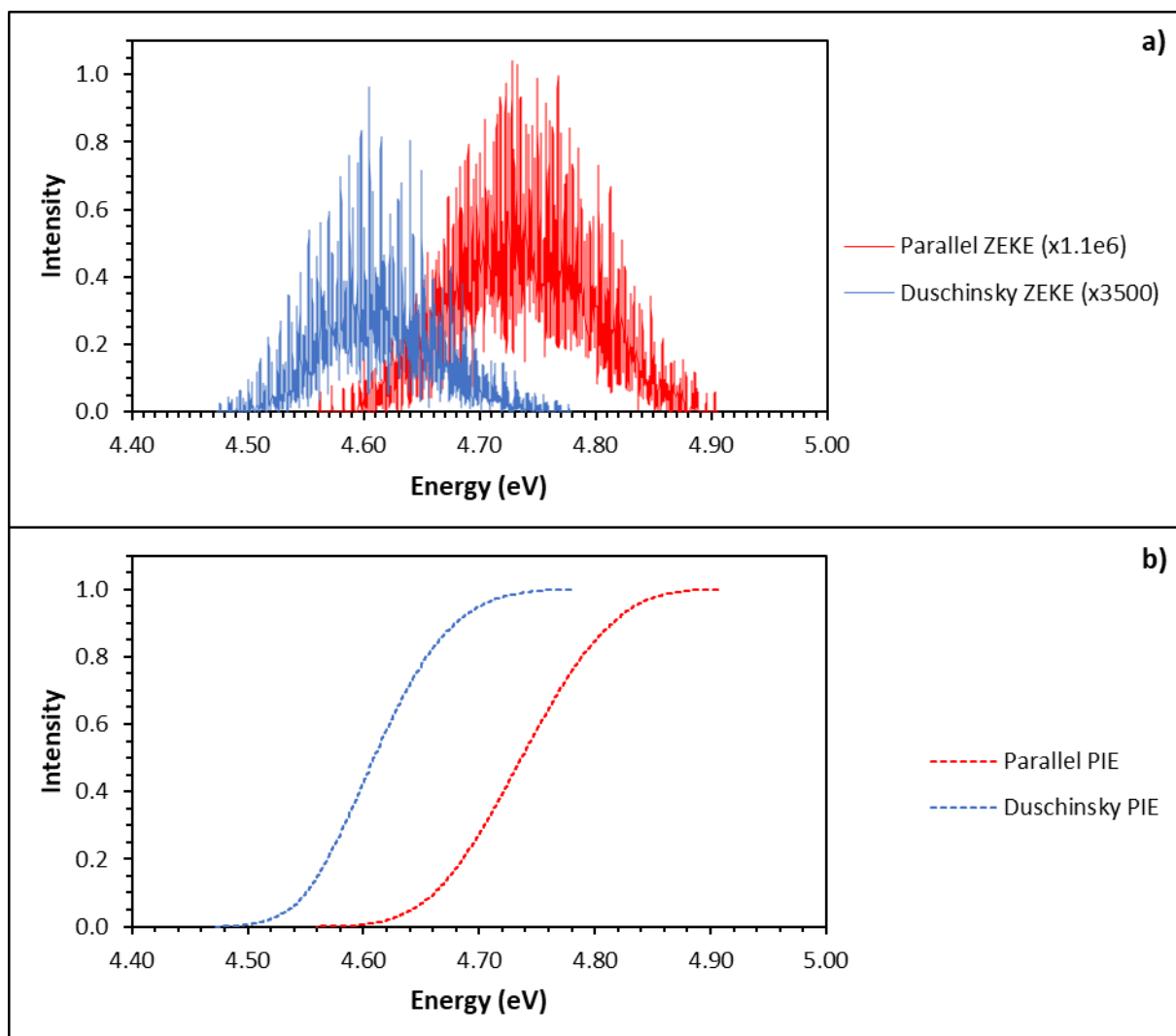
Appendix D-1b: Parameters used for ZEKE simulations of AuCe_mO_n ($m=2,3$; $n=0-2m$) ionisation processes. Parameters shown include the method of vibrational wavefunction overlap (Duschinsky or Parallel Approximation) and any modes omitted from calculations. Mode numbers are presented as per ezSpectrum settings; i.e. mode $v_1 = "0"$, $v_2 = "1"$, etc.

Appendix D2: ZEKE and PIE Test Calculations

Appendix D2-1: Comparison of Calculated ZEKE Spectra using Parallel Approximation and Duschinsky Treatment

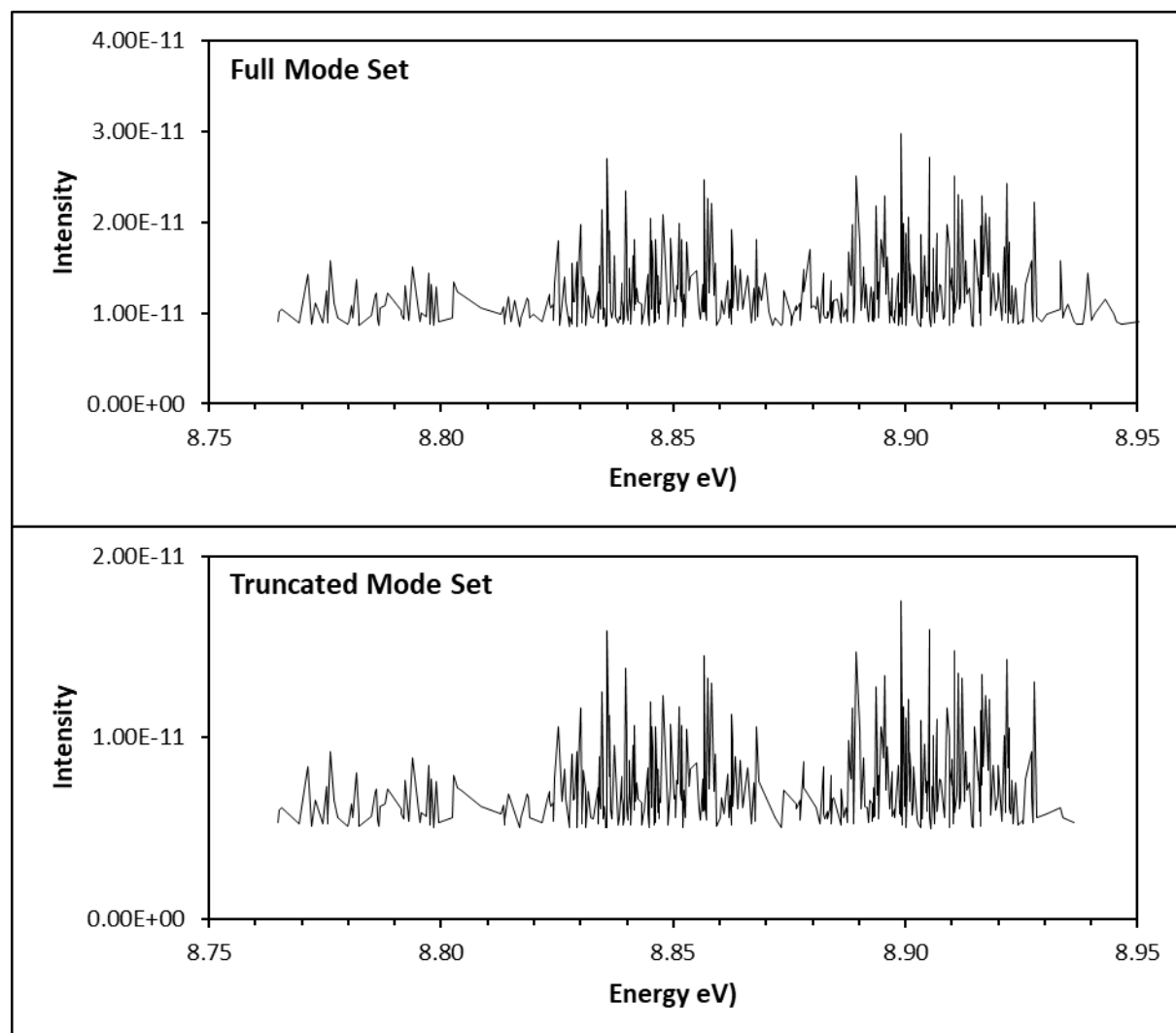


Appendix D2-1a: Simulated ZEKE and PIE spectra for the Ce_2O_2 $^4B_{1u} \leftarrow ^3B_{1u}$ ($^4III^* \leftarrow ^3III$) ionisation process. This ionisation process shows minimal structural change with ionisation. ZEKE and PIE spectra are calculated using the Parallel Approximation (red) and full Duschinsky treatment (blue) of vibrational wavefunctions.



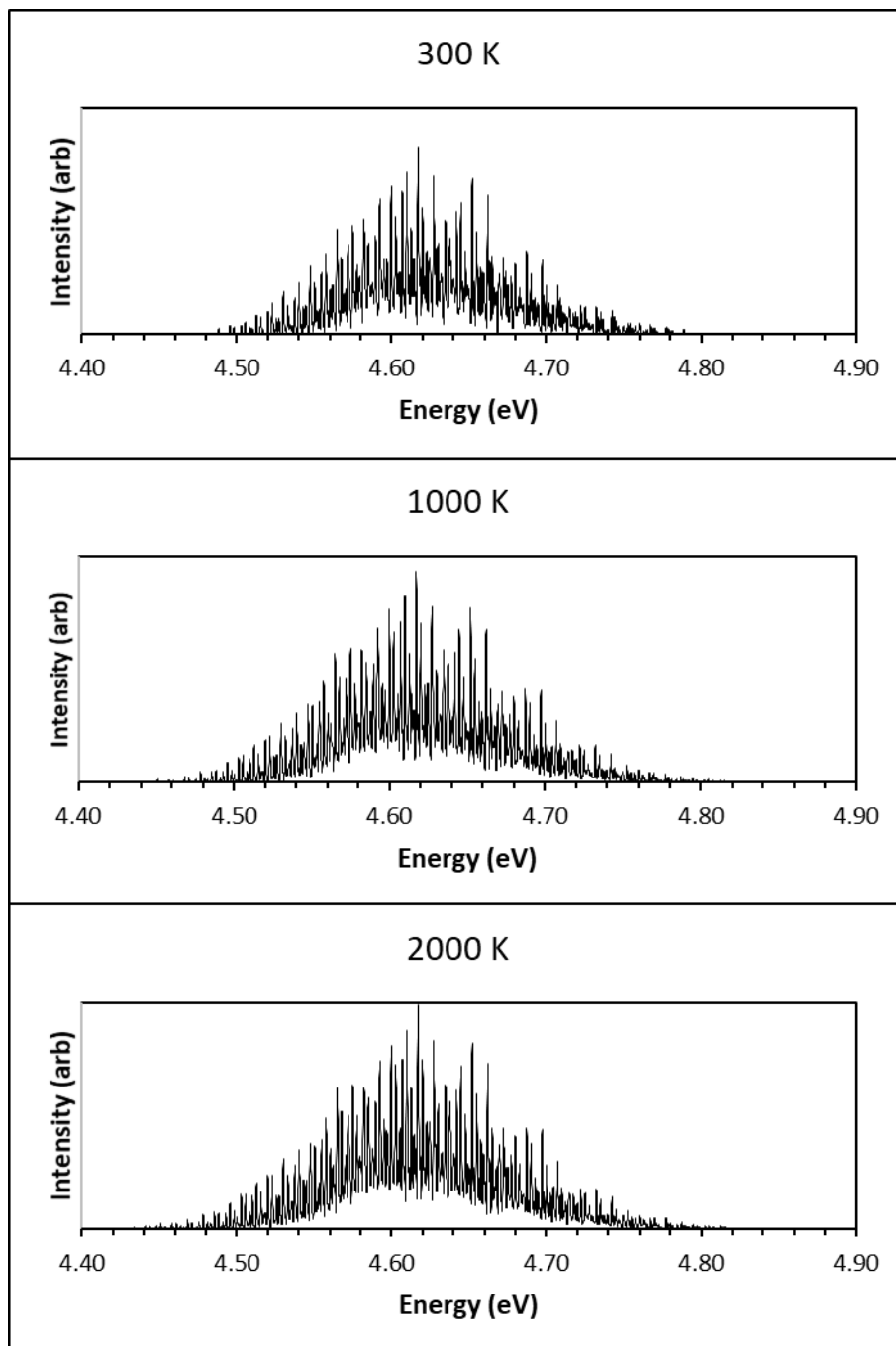
Appendix D2-1b: Simulated ZEKE and PIE spectra for the AuCe_2O_3 ${}^3\text{A} \leftarrow {}^4\text{A}$ (${}^3\text{XIVB}^+ \leftarrow {}^4\text{XIV}$) ionisation process. This ionisation process shows moderate structural change with ionisation. ZEKE and PIE spectra are calculated using the Parallel Approximation (red) and full Duschinsky treatment (blue) of vibrational wavefunctions.

Appendix D2-2: Comparison of ZEKE Spectra Calculated Using Full Vibrational Mode Set and Truncated Vibrational Mode Set

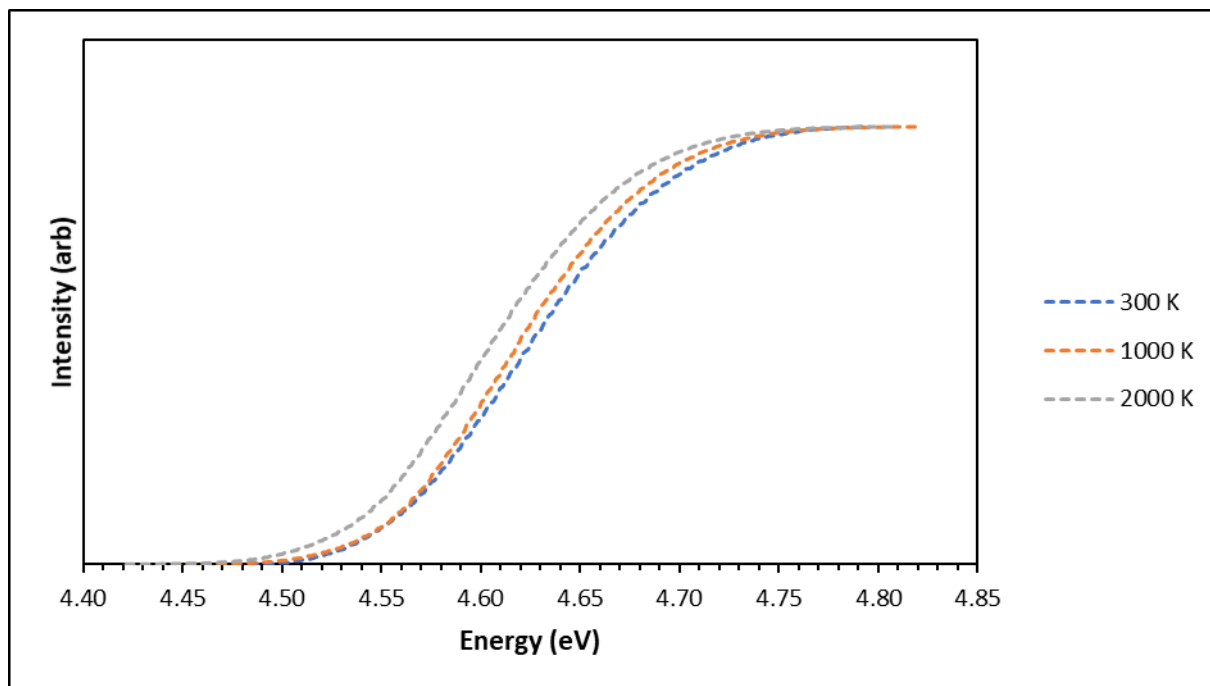


Appendix D2-2: Calculated ZEKE spectra for the Ce_3O_6 ${}^2A \leftarrow {}^1A'$ (${}^2XIIA^+ \leftarrow {}^1XIIA$) ionisation process. Calculations are performed with a full mode set (i.e. all vibrational modes are considered) and a truncated mode set (modes ν_1 , ν_2 , ν_9 , ν_{10} , ν_{11} , ν_{12} , ν_{13} , ν_{14} , ν_{15} , ν_{16} and ν_{17} are omitted). The Parallel Approximation is used in both calculations.

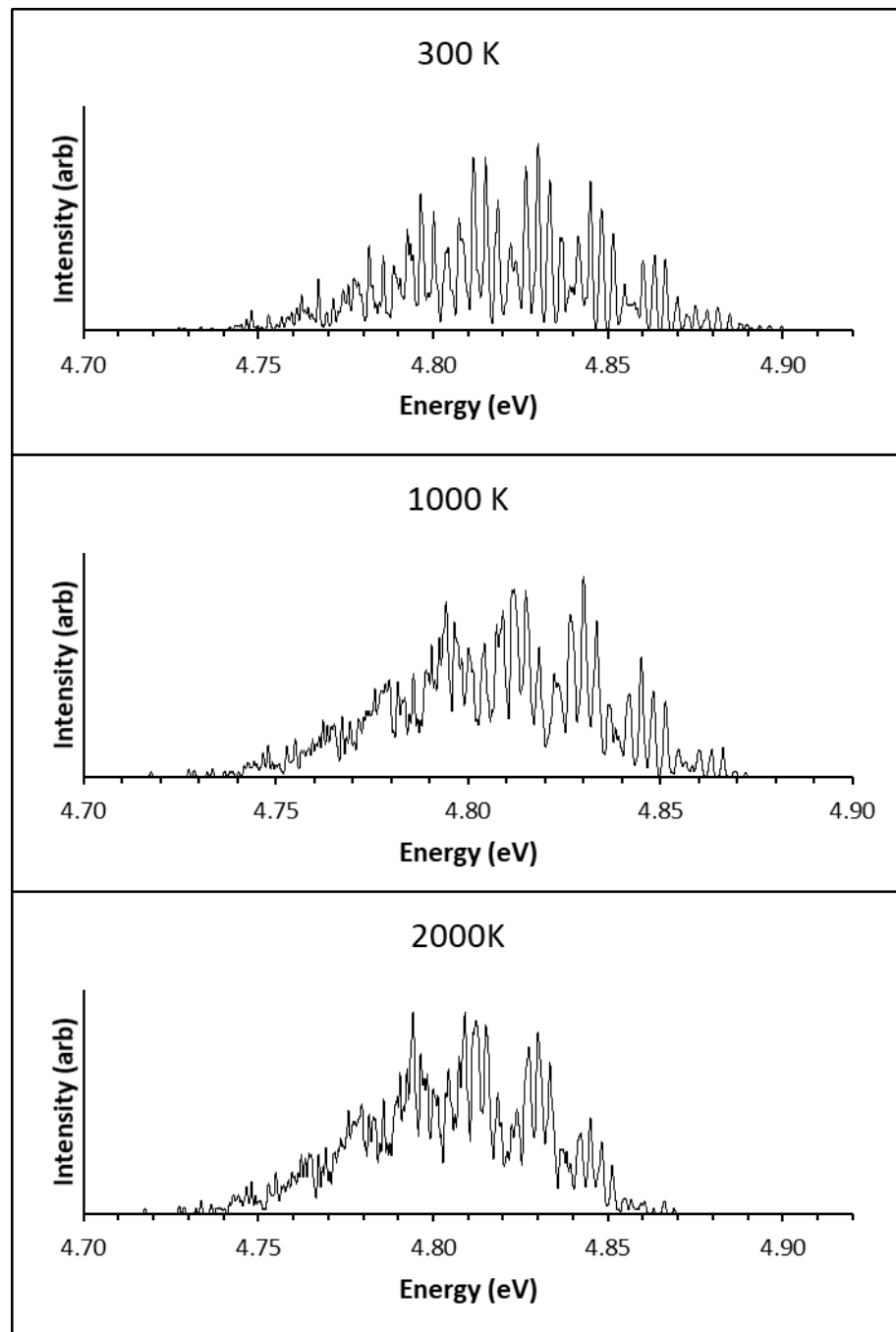
Appendix D2-3: Temperature Dependence on ZEKE and PIE Spectral Simulations

AuCe₂O ZEKE and PIE Spectra (Duschinsky Treatment)

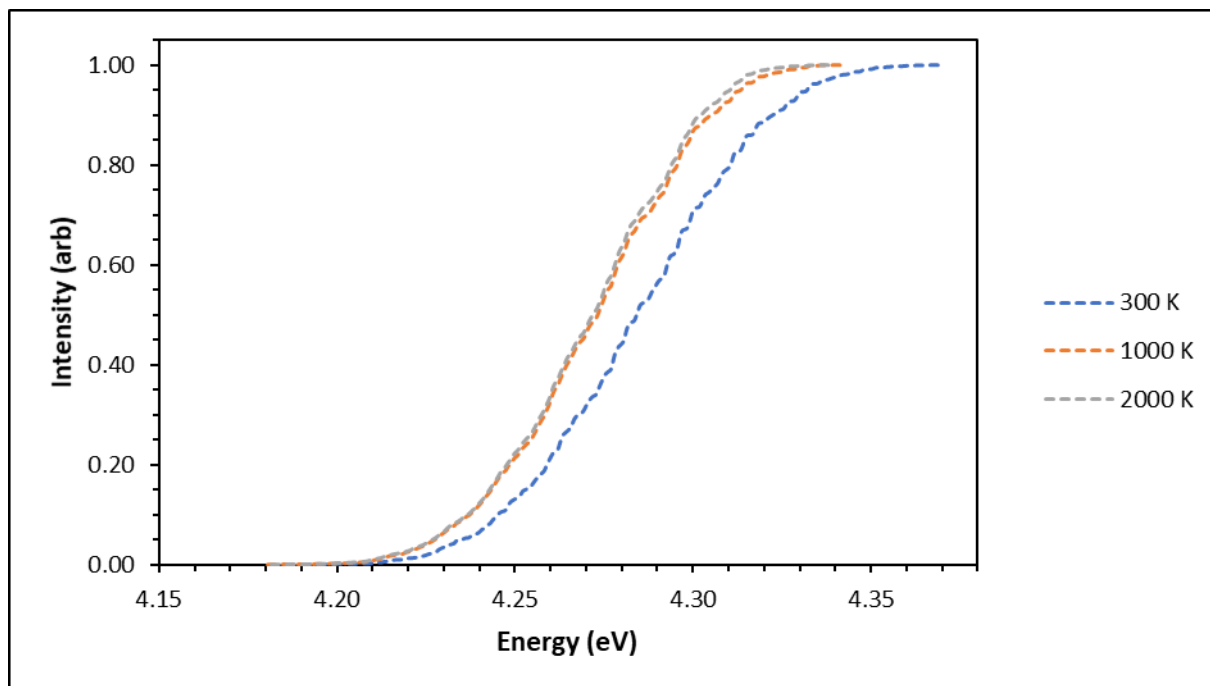
Appendix D2-3a: Calculated ZEKE spectra for the AuCe₂O ${}^3A \leftarrow {}^4A$ (${}^3XIVB^+ \leftarrow {}^4XIV$) transition at 300 K, 1000 K and 2000 K. A full Duschinsky treatment of vibrational modes is used in simulations.



Appendix D2-3b: Calculated PIE spectra for the $\text{AuCe}_2\text{O } ^3\text{A} \leftarrow ^4\text{A} (^3\text{XIVB}^+ \leftarrow ^4\text{XIV})$ transition at 300 K, 1000 K and 2000 K. A full Duschinsky treatment of vibrational modes is used in simulations.

AuCe₃O₃ PIE and ZEKE Spectra (Parallel Approximation)

Appendix D2-3c: Calculated ZEKE spectra for the AuCe_3O_3 $^3A \leftarrow ^2A_1$ ($^3XXIA^+ \leftarrow ^2XXIA$) transition at 300 K, 1000 K and 2000 K. The Parallel Approximation is used in simulations.



Appendix D2-3d: Calculated PIE spectra for the AuCe_3O_3 ${}^3A \leftarrow {}^2A_1$ (${}^3XXIA^+ \leftarrow {}^2XXIA$) transition at 300 K, 1000 K and 2000 K. The Parallel Approximation is used in simulations.